

FEBRUARY 2018

AJNR

VOLUME 39 • PP 207-404

AJNR

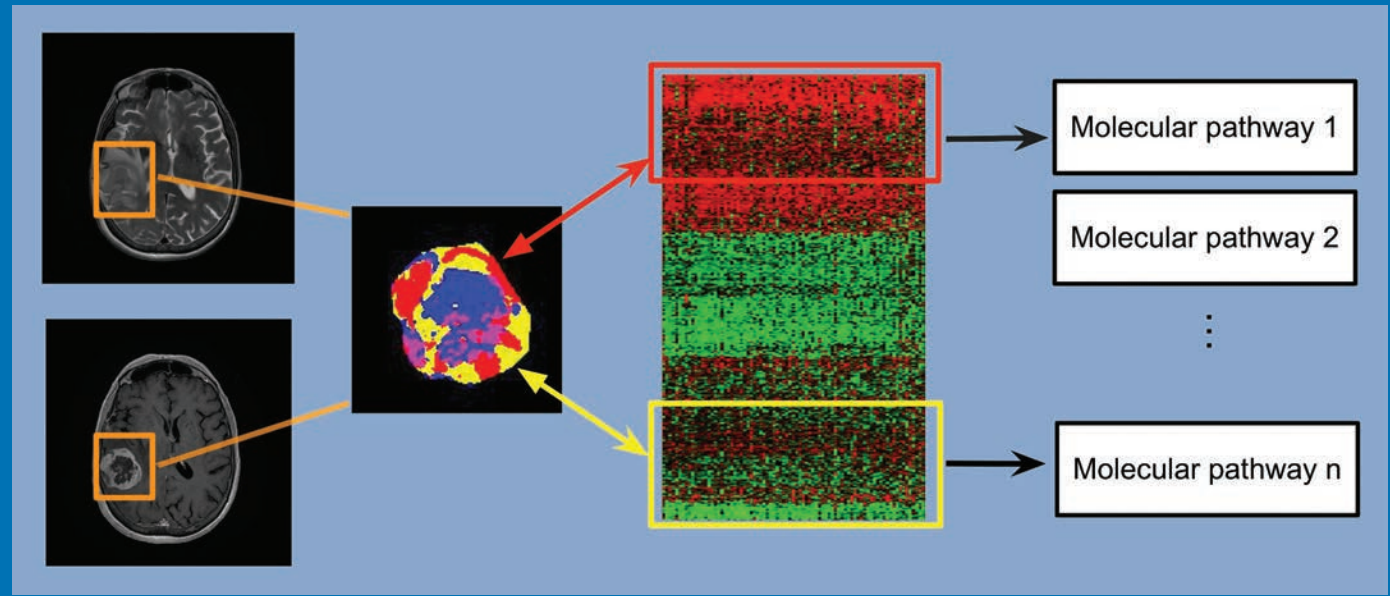
AMERICAN JOURNAL OF NEURORADIOLOGY

FEBRUARY 2018
VOLUME 39
NUMBER 2
WWW.AJNR.ORG

THE JOURNAL OF DIAGNOSTIC AND
INTERVENTIONAL NEURORADIOLOGY

Brain tumor radiomics
QSM and myelin water fraction in multiple sclerosis
Noninvasive assessment of intracranial pressure

Official Journal ASNR • ASFNR • ASHNR • ASPNR • ASSR



A Complete Coil Portfolio

MicroVention's comprehensive portfolio features clinically proven Hydrogel coils, which can be used exclusively or in combination with our trusted Platinum coils to treat a wide range of aneurysms and neurovascular lesions.



Aneurysm
Therapy
Solutions

Breakthrough Hydrogel Technology

- Less Retreatment Compared to Platinum¹
- Less Recurrence Compared to Platinum¹
- More Progressive Occlusion^{1,2}

REFERENCES:

1. ISC 2017 Meeting – Houston, TX – MV Symposium – Results of the GREAT Study – Presented by Christian Taschner, MD, Department of Neuroradiology, Medical Centre – University of Freiburg, Germany
2. LINNC 2017 Meeting – Paris, France – MV Symposium – Results of the GREAT Study – Presented by Alain Bonafe, MD, Professor of Neuroradiology, Head of the Neuroradiology department, Hôpital Gui de Chauliac, CHRU Montpellier, France



INDICATIONS FOR USE:

The HydroCoil® Embolic System (HES) and MicroPlex® Coil System (MCS) are intended for the endovascular embolization of intracranial aneurysms and other neurovascular abnormalities such as arteriovenous malformations and arteriovenous fistulae. The HES and MCS are also intended for vascular occlusion of blood vessels within the neurovascular system to permanently obstruct blood flow to an aneurysm or other vascular malformation and for arterial and venous embolizations in the peripheral vasculature.

The device should only be used by physicians who have undergone pre-clinical training in all aspects of HES/MCS procedures as prescribed by MicroVention.



**For more information or a product demonstration,
contact your local MicroVention representative:**



**MicroVention Worldwide
Innovation Center**
35 Enterprise
Aliso Viejo, CA 92656 USA
MicroVention UK Limited
MicroVention Europe, S.A.R.L.
MicroVention Deutschland GmbH
microvention.com

PH +1.714.247.8000

PH +44 (0) 191 258 6777

PH +33 (1) 39 21 77 46

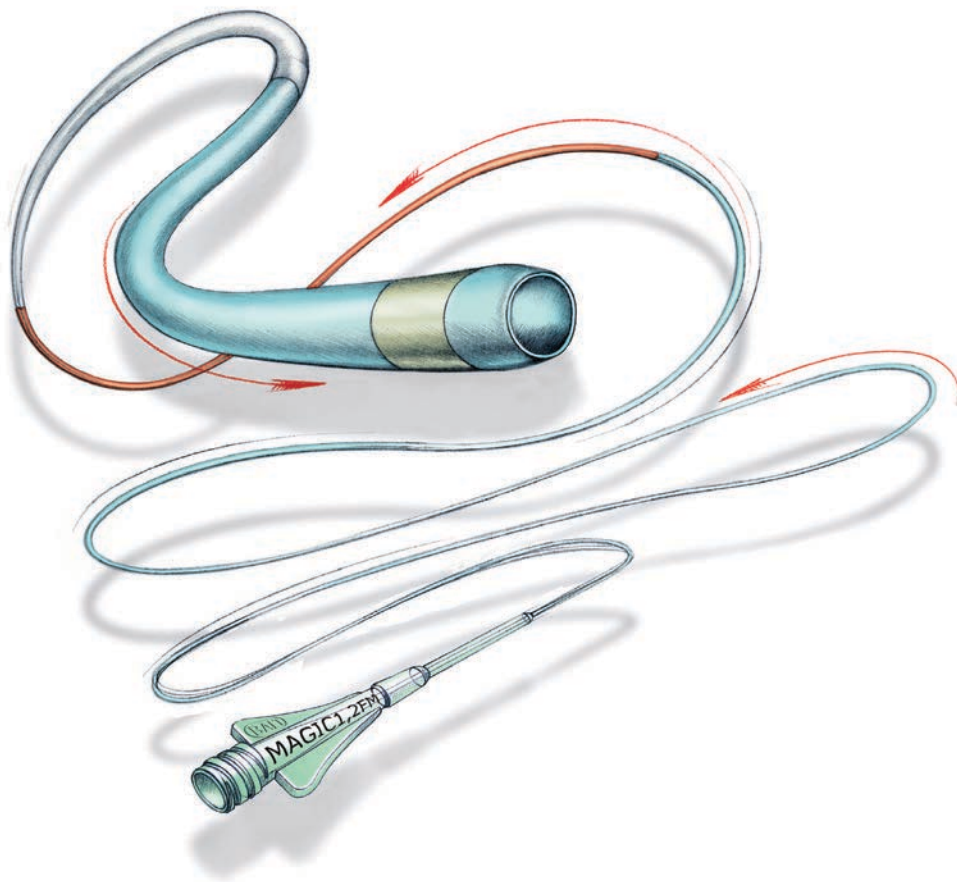
PH +49 211 210 798-0

Magic[®]



FLOW-DEPENDENT MICROCATHETER SERIES

Now available through Balt USA



ordermagics@balt-usa.com

MAGIC catheters are designed for general intravascular use. They may be used for the controlled, selective regional infusion of therapeutic agents or embolic materials into vessels.¹

Federal (USA) law restricts this device to sale, distribution by or on the order of a physician. Indications, contraindications, warnings and instructions for use can be found in the product labeling supplied with each device.

1. Magic Catheters IFU - Ind 19



BALT USA
18 Technology Drive #169, Irvine, CA 92618
P 949.788.1443 F 949.788.1444

© 2017 BALT USA MKTG-068 Rev. B

ASNR 56th Annual Meeting & The Foundation of the ASNR Symposium 2018

June 2 - 7, 2018 | Vancouver, B.C., CANADA



ASNR 2018 KEYNOTE PRESENTATION *by Andy DeLaO*

The Radiology Renaissance: Shaping the Future of Healthcare

This keynote will highlight the changing world of radiology inside of healthcare. Radiologists at one point were referred to as the "doctor's doctor." Radiologists were the trusted advisors to help physicians from primary care to specialists such as surgeons and oncologists make clinical decisions based on imaging. As technology evolves, the role of the radiologist undergoes transformation. Today we are seeing the emergence of another technology evolution in healthcare. It presents an opportunity for radiologists to transition once again, but the choices they face today will determine the future role of radiology.



The Vancouver Convention Centre East © 2013 Vancouver Convention Centre

Welcome and Greetings

Please join us in Vancouver, CANADA for the **56th Annual Meeting of the American Society of Neuroradiology** on June 2-7, 2018 at the Vancouver Convention Centre East. Surrounded by the coastal mountains and located on the waterfront, you can enjoy these spectacular views in the heart of downtown Vancouver. With its undeniable charm and friendly atmosphere, Vancouver is known around the world as both a popular tourist attraction and one of the best places to live. ASNR enthusiastically presents **Neuroradiology: Adding Value and Improving Healthcare** at the Symposium of the Foundation of the ASNR, as well as the common thread throughout the Annual Meeting. Implementing a value-based strategy in imaging has grasped the attention of nearly every healthcare provider; in particular with Radiologists understanding that the future will demand their imaging practices deliver better value. Value in healthcare is typically defined as those imaging strategies that yield improved outcomes, lower costs, or both. As payment transitions from a fee-for-service to a value-based system, thus creating a fundamentally different marketplace dynamic, measuring good outcomes are at the center of this changeover. At this time of uncertainty what little remains clear is that without a well-defined knowledge of their outcomes, no medical specialty will be able to succeed in the future value-based system. The Symposium will feature how Neuroradiology, in its many subspecialty areas, adds value to clinical care pathways by directing healthcare practice towards better outcomes. The annual meeting programming will continue on this theme emphasizing imaging that improves health outcomes, while considering costs, thus adding value. Our discussions will incorporate many innovative approaches to how neuroimaging currently does and will continue to improve overall healthcare performance.

As the Program Chair for ASNR 2018, it is my pleasure and honor to welcome you to Vancouver, CANADA for our annual meeting! Vancouver is known for being a very walkable city with a compact downtown core hosting many places to enjoy. So pack your comfortable walking shoes and let's tour together with our colleagues and friends!

Pina Sanelli

Pina C. Sanelli, MD, MPH, FACR
ASNR 2018 Program Chair/President-Elect



ASNR 2018 ■ VANCOUVER

ASFNR ASHNR ASPNR ASSR SNIS

THE FOUNDATION OF THE ASNR



Pina C. Sanelli, MD, MPH, FACR

ASNR 2018 Program Chair/President-Elect

Programming developed in cooperation with the...

American Society of Functional Neuroradiology (ASFNR)

Max Wintermark, MD

American Society of Head and Neck Radiology (ASHNR)

Deborah R. Shatzkes, MD

American Society of Pediatric Neuroradiology (ASPNR)

Ashok Panigrahy, MD

American Society of Spine Radiology (ASSR)

John D. Barr, MD, FACR, FSIR, FAHA

Society of NeuroInterventional Surgery (SNIS)

Mahesh V. Jayaraman, MD

ASNR Health Policy (HPC) Committee

William D. Donovan, MD, MPH, FACR | Gregory N. Nicola, MD, FACR

ASNR Computer Sciences & Informatics (CSI) Committee

John L. Go, MD, FACR

ASNR Research Scientist Programming Committee

Dikoma C. Shungu, PhD | Timothy P.L. Roberts, PhD

The International Hydrocephalus Imaging Working Group (IHIWG) / CSF Flow Group

Ari M Blitz, MD | Harold L. Rekaté, MD | Bryn A. Martin, PhD

Check out Meeting Registration/Housing!

Please visit 2018.asnr.org for more information

ASNR 56th Annual Meeting

c/o American Society of Neuroradiology

800 Enterprise Drive, Suite 205

Oak Brook, Illinois 60523-4216

Phone: 630-574-0220 + Fax: 630 574-0661

2018.asnr.org



CALL FOR AJNR EDITORIAL FELLOWSHIP CANDIDATES

ASNR and AJNR are pleased once again to join efforts with other imaging-related journals that have training programs on editorial aspects of publishing for trainees or junior staff (3–5 years after training), including Radiology (Olmsted fellowship), AJR (Figley and Rogers fellowships), JACR (Bruce J. Hillman fellowship), and Radiologia.

2018 Candidate Information and Requirements

GOALS

- Increase interest in “editorial” and publication-related activities in younger individuals.
- Increase understanding and participation in the AJNR review process.
- Incorporate into AJNR’s Editorial Board younger individuals who have previous experience in the review and publication process.
- Fill a specific need in neuroradiology not offered by other similar fellowships.
- Increase the relationship between “new” generation of neuroradiologists and more established individuals.
- Increase visibility of AJNR among younger neuroradiologists.

ACTIVITIES OF THE FELLOWSHIP

- Serve as Editorial Fellow for one year. This individual will be listed on the masthead as such.
- Review at least one manuscript per month for 12 months. Evaluate all review articles submitted to AJNR.
- Learn how electronic manuscript review systems work.
- Be involved in the final decision of selected manuscripts together with the Editor-in-Chief.
- Participate in all monthly Senior Editor telephone conference calls.
- Participate in all meetings of the Editors and Publications Committee during the annual meetings of ASNR and RSNA as per candidate’s availability. The Foundation of the ASNR will provide \$2000 funding for this activity.
- Evaluate progress and adjust program to specific needs in annual meeting or telephone conference with the Editor-in-Chief.
- Embark on an editorial scientific or bibliometric project that will lead to the submission of an article to AJNR or another appropriate journal as determined by the Editor-in-Chief. This project will be presented by the Editorial Fellow at the ASNR annual meeting.
- Serve as liaison between AJNR and ASNR’s Young Professionals Network and the 3 YPs appointed to AJNR as special consultants. Participate in meetings and telephone calls with this group. Design one electronic survey/year, polling the group regarding readership attitudes and wishes.
- Recruit trainees as reviewers as determined by the Editor-in-Chief.
- Organize and host a Fellows’ Journal Club podcast.
- Serve as Guest Editor for an issue of AJNR’s News Digest with a timely topic.

QUALIFICATIONS

- Be a fellow in neuroradiology from North America, including Canada (this may be extended to include other countries).
- Be a junior faculty neuroradiology member (< 3 years) in either an academic or private environment.
- Be an “in-training” or member of ASNR in any other category.

APPLICATION

- Include a short letter of intent with statement of goals and desired research project. CV must be included.
- Include a letter of recommendation from the Division Chief or fellowship program director. A statement of protected time to perform the functions outlined is desirable.
- Applications will be evaluated by AJNR’s Senior Editors and the Chair of the Publications Committee prior to the ASNR meeting. The name of the selected individual will be announced at the meeting.
- Applications should be received by March 1, 2018 and sent to Ms. Karen Halm, AJNR Managing Editor, electronically at khalm@asnr.org.

We're Inside Every Great Neuroradiologist!

ASNR MEMBERS RECEIVE

American Journal of Neuroradiology (AJNR)

The leading neuroradiology research journal, published monthly

Neurographics

Bimonthly educational journal with CME for members

ASNR Annual Meeting

Discounts for members on the field's premier conference

eCME

Online collection of lectures and articles with SA-CME and Category 1 credit

Advocacy

Coding/reimbursement, quality standards and practice guidelines; demonstrating neuroradiology's value!

Networking

Access to 5,000 peers

... And More!

TR 4730.0
TE 108.0
TA 03.27
BW 70.0
M/ND
A1
HL1.2;HS1.2
*tseR2d1_9 / 180
SP F17.7
SL 5.0
FoV 194*230
190*256s
Tra>Cor(8.7)
w 1469
c 705
MF 1.14
D
R
5cm
5cm

Join the leaders in neuroradiology today!

Learn more at www.asnr.org/join

ASNR

American Society of Neuroradiology

800 Enterprise Dr., Suite 205, Oak Brook, IL 60523 • (630)574-0220 • membership@asnr.org • www.asnr.org

Neuroform Atlas™ Stent System

See package insert for complete indications, contraindications, warnings and instructions for use.

Humanitarian Device Authorized by Federal law for use with neurovascular embolic coils in patients who are ≥ 18 years of age for the treatment of wide neck, intracranial, saccular aneurysms arising from a parent vessel with a diameter of ≥ 2 mm and ≤ 4.5 mm that are not amenable to treatment with surgical clipping. Wide neck aneurysms are defined as having a neck > 4 mm or a dome-to-neck ratio < 2. The effectiveness of this device for this use has not been demonstrated.

INDICATIONS FOR USE

The Neuroform Atlas™ Stent System is indicated for use with neurovascular embolic coils in patients who are ≥ 18 years of age for the treatment of wide neck, intracranial, saccular aneurysms arising from a parent vessel with a diameter of ≥ 2 mm and ≤ 4.5 mm that are not amenable to treatment with surgical clipping. Wide neck aneurysms are defined as having a neck > 4 mm or a dome-to-neck ratio of < 2.

CONTRAINDICATIONS

Patients in whom antiplatelet and/or anticoagulation therapy is contraindicated.

POTENTIAL ADVERSE EVENTS

The potential adverse events listed below, as well as others, may be associated with the use of the Neuroform Atlas™ Stent System or with the procedure:

Allergic reaction to nital metal and medications, Aneurysm perforation or rupture, Coil herniation through stent into parent vessel, Death, Embolus, Headache, Hemorrhage, In-stent stenosis, Infection, Ischemia, Neurological deficit/intracranial sequelae, Pseudoaneurysm, Stent fracture, Stent migration/embolization, Stent misplacement, Stent thrombosis, Stroke, Transient ischemic attack, Vasospasm, Vessel occlusion or closure, Vessel perforation/rupture, Vessel dissection, Vessel trauma or damage, Vessel thrombosis, Visual impairment, and other procedural complications including but not limited to anesthetic and contrast media risks, hypotension, hypertension, access site complications.

WARNINGS

- Contents supplied STERILE using an ethylene oxide (EO) process. Do not use if sterile barrier is damaged. If damage is found, call your Stryker Neurovascular representative.
- For single use only. Do not reuse, reprocess or resterilize. Reuse, reprocessing or resterilization may compromise the structural integrity of the device and/or lead to device failure which, in turn, may result in patient injury, illness or death. Reuse, reprocessing or resterilization may also create a risk of contamination of the device and/or cause patient infection or cross-infection, including, but not limited to, the transmission of infectious disease(s) from one patient to another. Contamination of the device may lead to injury, illness or death of the patient.
- After use, dispose of product and packaging in accordance with hospital, administrative and/or local government policy.
- This device should only be used by physicians who have received appropriate training in interventional neuroradiology or interventional radiology and preclinical training on the use of this device as established by Stryker Neurovascular.
- Select a stent size (length) to maintain a minimum of 4 mm on each side of the aneurysm neck along the parent vessel. An incorrectly sized stent may result in damage to the vessel or stent migration. Therefore, the stent is not designed to treat an aneurysm with a neck greater than 22 mm in length.
- If excessive resistance is encountered during the use of the Neuroform Atlas™ Stent System or any of its components at any time during the procedure, discontinue use of the stent system. Continuing to use the stent system against resistance may result in damage to the vessel or a system component.
- Persons allergic to nickel titanium (Nitinol) may suffer an allergic response to this stent implant.
- Purge the system carefully to avoid the accidental introduction of air into the stent system.
- Confirm there are no air bubbles trapped anywhere in the stent system.

CAUTIONS / PRECAUTIONS

- Federal Law (USA) restricts this device to sale by or on the order of a physician.
- Use the Neuroform Atlas Stent System prior to the "Use By" date printed on the package.
- Carefully inspect the sterile package and Neuroform Atlas Stent System prior to use to verify that neither has been damaged during shipment. Do not use kinked or damaged components; contact your Stryker Neurovascular representative.
- The stent delivery microcatheter and the Neuroform Atlas Stent delivery wire should not be used to recapture the stent.
- Exercise caution when crossing the deployed stent with adjunctive devices.
- After deployment, the stent may foreshorten from up to 6.3%.
- The max OD of the coiling microcatheter should not exceed the max OD of the stent delivery microcatheter.

- Standard interventional devices with distal tips > 1.8 F may not be able to pass through the interstices of the stent.
- Safety of the Neuroform Atlas Stent System in patients below the age of 18 has not been established.
- In cases where multiple aneurysms are to be treated, start at the most distal aneurysm first.

MAGNETIC RESONANCE IMAGING (MRI)

Specific Information Magnetic Resonance Conditional

Non-clinical testing and analysis have demonstrated that the Neuroform Atlas Stent is MR Conditional alone, or when overlapped with a second stent, and adjacent to a Stryker Neurovascular coil mass. A patient with the Neuroform Atlas Stent can be safely scanned immediately after placement of this implant, under the following conditions:

- Static magnetic field of 1.5 and 3.0 Tesla
- Maximum spatial gradient field up to 2500 Gauss/cm (25 Tesla/m)
- Maximum MRI system reported whole body averaged specific absorption rate of 2 W/kg (Normal Operating Mode) and head averaged specific absorption rate of 3.2 W/kg.

Under the scan conditions defined above, the Neuroform Atlas Stent is expected to produce a maximum temperature rise of 4°C after 15 minutes of continuous scanning. The Neuroform Atlas Stent should not migrate in this MRI environment.

In non-clinical testing, the image artifact caused by the device extends approximately 2 mm from the Neuroform Atlas Stent when imaged with a spin echo pulse sequence and 3 Tesla MRI System. The artifact may obscure the device lumen. It may be necessary to optimize MRI imaging parameters for the presence of this implant.

Excelsior® XT-17™ Microcatheter

See package insert for complete indications, contraindications, warnings and instructions for use.

INTENDED USE / INDICATIONS FOR USE

Stryker Neurovascular's Excelsior XT-17 Microcatheters are intended to assist in the delivery of diagnostic agents, such as contrast media, and therapeutic agents, such as occlusion coils, into the peripheral, coronary and neuro vasculature.

CONTRAINDICATIONS

None known.

POTENTIAL ADVERSE EVENTS

Potential adverse events associated with the use of microcatheters or with the endovascular procedures include, but are not limited to: access site complications, allergic reaction, aneurysm perforation, aneurysm rupture, death, embolism (air, foreign body, plaque, thrombus), hematoma, hemorrhage, infection, ischemia, neurological deficits, pseudoaneurysm, stroke, transient ischemic attack, vasospasm, vessel dissection, vessel occlusion, vessel perforation, vessel rupture, vessel thrombosis

WARNINGS

- The accessories are not intended for use inside the human body.
- Limited testing has been performed with solutions such as contrast media, saline and suspended embolic particles. The use of these microcatheters for delivery of solutions other than the types that have been tested for compatibility is not recommended. Do not use with glue or glue mixtures.
- Carefully inspect all devices prior to use. Verify shape, size and condition are suitable for the specific procedure.
- Exchange microcatheters frequently during lengthy procedures that require extensive guidewire manipulation or multiple guidewire exchanges.
- Never advance or withdraw an intravascular device against resistance until the cause of the resistance is determined by fluoroscopy. Movement of the microcatheter or guidewire against resistance could dislodge a clot, perforate a vessel wall, or damage microcatheter and guidewire. In severe cases, tip separation of the microcatheter or guidewire may occur.
- Contents supplied STERILE using an ethylene oxide (EO) process. Do not use if sterile barrier is damaged. If damage is found, call your Stryker Neurovascular representative.
- For single use only. Do not reuse, reprocess or resterilize. Reuse, reprocessing or resterilization may compromise the structural integrity of the device and/or lead to device failure which, in turn, may result in patient injury, illness or death. Reuse, reprocessing or resterilization may also create a risk of contamination of the device and/or cause patient infection or cross-infection, including, but not limited to, the transmission of infectious disease(s) from one patient to another. Contamination of the device may lead to injury, illness or death of the patient.
- After use, dispose of product and packaging in accordance with hospital, administrative and/or local government policy.
- These devices are intended for use only by physicians trained in performing endovascular procedures.
- Inspect product before use for any bends, kinks or damage. Do not use a microcatheter that has been damaged. Damaged microcatheters may rupture causing vessel trauma or tip detachment during steering maneuvers.
- The shaping mandrel is not intended for use inside the human body.

- Discontinue use of microcatheter for infusion if increased resistance is noted. Resistance indicates possible blockage. Remove and replace blocked microcatheter immediately. DO NOT attempt to clear blockage by over-pressure. Doing so may cause the microcatheter to rupture, resulting in vascular damage or patient injury.
- Do not exceed 2,070 kPa (300 psi) infusion pressure. Excessive pressure could dislodge a clot, causing thromboemboli, or could result in a ruptured microcatheter or severed tip, causing vessel injury.

CAUTIONS / PRECAUTIONS

- To reduce the probability of coating damage in tortuous vasculature, use a guide catheter with a minimum internal diameter as specified in Table 1 above, and is recommended for use with Stryker Neurovascular hydrophilically coated microcatheters.
- To control the proper introduction, movement, positioning and removal of the microcatheter within the vascular system, users should employ standard clinical angiographic and fluoroscopic practices and techniques throughout the interventional procedure.
- Exercise care in handling of the microcatheter during a procedure to reduce the possibility of accidental breakage, bending or kinking.
- Use the product prior to the "Use By" date printed on the label.
- Limited testing indicates that Excelsior XT-17 Microcatheter is compatible with Dimethyl Sulfoxide (DMSO). The compatibility of Excelsior XT-17 Microcatheter with individual agents suspended in DMSO has not been established.
- Federal Law (USA) restricts this device to sale by or on the order of a physician.
- Wet dispenser coil or packaging tray and hydrophilically coated outer shaft of microcatheters prior to removal from packaging tray. Once the microcatheter has been wetted, do not allow to dry.
- The packaging mandrel is not intended for reuse. The packaging mandrel is not intended for use inside the human body.
- Check that all fittings are secure so that air is not introduced into guide catheter or microcatheter during continuous flush.
- In order to achieve optimal performance of Stryker Neurovascular Microcatheters and to maintain the lubricity of the Hydrolene® Coating surface, it is critical that a continuous flow of appropriate flush solution be maintained between the Stryker Neurovascular Microcatheter and guide catheter, and the microcatheter and any intraluminal device. In addition, flushing aids in preventing contrast crystal formation and/or clotting on both the intraluminal device and inside the guide catheter and/or the microcatheter lumen.
- Do not position microcatheter closer than 2.54 cm (1 in) from the steam source. Damage to the microcatheter may result.
- Excessive tightening of a hemostatic valve onto the microcatheter shaft may result in damage to the microcatheter. Removing the peel away introducer with a guidewire inserted in the crystal formation and/or clotting on both the intraluminal device and inside the guide catheter and/or the microcatheter lumen.
- Do not position microcatheter closer than 2.54 cm (1 in) from the steam source. Damage to the microcatheter may result.
- Excessive tightening of a hemostatic valve onto the microcatheter shaft may result in damage to the microcatheter. Removing the peel away introducer with a guidewire inserted in the crystal formation and/or clotting on both the intraluminal device and inside the guide catheter and/or the microcatheter lumen.
- Do not position microcatheter closer than 2.54 cm (1 in) from the steam source. Damage to the microcatheter may result.
- Check that all fittings are secure so that air is not introduced into guide catheter or microcatheter during continuous flush.

Excelsior® SL-10™ Microcatheter

See package insert for complete indications, contraindications, warnings and instructions for use.

INTENDED USE / INDICATIONS FOR USE

Stryker Neurovascular Excelsior SL-10 Microcatheter is intended to assist in the delivery of diagnostic agents, such as contrast media, and therapeutic agents, such as occlusion coils, into the peripheral, coronary, and neurovasculature.

CONTRAINDICATIONS

None known.

POTENTIAL ADVERSE EVENTS

Potential adverse events associated with the use of microcatheters or with the endovascular procedures include, but are not limited to: access site complications, allergic reaction, aneurysm perforation, aneurysm rupture, death, embolism (air, foreign body, plaque, thrombus), hematoma, hemorrhage, infection, ischemia, neurological deficits, pseudoaneurysm, stroke, transient ischemic attack, vasospasm, vessel dissection, vessel perforation, vessel rupture, vessel thrombosis.

WARNINGS

- Contents supplied STERILE using an ethylene oxide (EO) process. Do not use if sterile barrier is damaged. If damage is found, call your Stryker Neurovascular representative.
- For single patient use only. Do not reuse, reprocess or resterilize. Reuse, reprocessing or resterilization may compromise the structural integrity of the device and/or lead to device failure which, in turn, may result in patient injury, illness or death. Reuse, reprocessing or resterilization may also create a risk of contamination of the device and/or cause patient infection or cross-infection, including, but not limited to, the transmission of infectious disease(s) from one patient to another. Contamination of the device may lead to injury, illness or death of the patient.
- After use, dispose of product and packaging in accordance with hospital, administrative and/or local government policy.
- These devices are intended for use only by physicians trained in performing endovascular procedures.
- Inspect product before use for any bends, kinks or damage. Do not use a microcatheter that has been damaged. Damaged microcatheters may rupture causing vessel trauma or tip detachment during steering maneuvers.
- The shaping mandrel is not intended for use inside the human body.

- beyond the alignment marker when the fluoro-saver marker reaches the microcatheter hub.
- If the fluoro-saver marker is not visible, do not advance the coil without fluoroscopy.
- Do not rotate delivery wire during or after delivery of the coil. Rotating the Target Detachable Coil delivery wire may result in a stretched coil or premature detachment of the coil from the delivery wire, which could result in coil migration.
- Verify there is no coil loop protrusion into the parent vessel after coil placement and prior to coil detachment. Coil loop protrusion after coil placement may result in thromboembolic events if the coil is detached.
- Verify there is no movement of the coil after coil placement and prior to coil detachment. Movement of the coil after coil placement may indicate that the coil could migrate once it is detached.
- Failure to properly close the RHV compression fitting over the delivery wire before attaching the InZone® Detachment System could result in coil movement, aneurysm rupture or vessel perforation.
- Verify repeatedly that the distal shaft of the catheter is not under stress before detaching the Target Detachable Coil. Axial compression or tension forces could be stored in the 2-tip microcatheter causing the tip to move during coil delivery. Microcatheter tip movement could cause the aneurysm or vessel to rupture.
- Advancing the delivery wire beyond the microcatheter tip once the coil has been detached involves risk of aneurysm or vessel perforation.
- The long term effect of this product on extravascular tissues has not been established so care should be taken to retain this device in the intravascular space.

CAUTIONS / PRECAUTIONS

- Federal Law (USA) restricts this device to sale by or on the order of a physician.
- Besides the number of InZone Detachment System units needed to complete the case, there must be an extra InZone Detachment System unit as backup.
- Removing the delivery wire without grasping the introducer sheath and delivery wire together may result in the detachable coil sliding out of the introducer sheath.
- Failure to remove the introducer sheath after inserting the delivery wire into the RHV of the microcatheter will interrupt normal infusion of flush solution and allow back flow of blood into the microcatheter.
- Some low level overhead light near or adjacent to the patient is required to

- to injury, illness or death of the patient.
- After use, dispose of product and packaging in accordance with hospital, administrative and/or local government policy.
- **These devices are intended for use only by physicians trained in performing endovascular procedures.**
- Limited testing has been performed with solutions such as contrast media, saline and suspended embolic particles. The use of these catheters for delivery of solutions other than the types that have been tested for compatibility is not recommended. Do not use with glue or glue mixtures.
- The accessories are not intended for use inside the human body.
- Carefully inspect all devices prior to use. Verify shape, size and condition are suitable for the specific procedure.
- Exchange microcatheters frequently during lengthy procedures that require extensive guidewire manipulation or multiple guidewire exchanges.
- Never advance or withdraw an intravascular device against resistance until the cause of the resistance is determined by fluoroscopy. Movement of the microcatheter or guidewire against resistance could dislodge a clot, perforate a vessel wall, or damage microcatheter and guidewire. In severe cases, tip separation of the microcatheter or guidewire may occur.
- Inspect product before use for any bends, kinks or damage. Do not use a microcatheter that has been damaged. Damaged microcatheters may rupture causing vessel trauma or tip detachment during steering maneuvers.
- Shaping mandrel is not intended for use inside the human body.
- Discontinue use of microcatheter for infusion if increased resistance is noted. Resistance indicates possible blockage. Remove and replace blocked microcatheter immediately. DO NOT attempt to clear blockage by over-pressure. Doing so may cause the microcatheter to rupture, resulting in vascular damage or patient injury.
- Do not exceed 2,070 kPa (300 psi) infusion pressure. Excessive pressure could dislodge a clot, causing thromboemboli, or could result in a ruptured microcatheter or severed tip, causing vessel injury.

CAUTIONS / PRECAUTIONS

- Federal Law (USA) restricts this device to sale by or on the order of a physician.
- To facilitate microcatheter handling, the proximal portion of the microcatheter does not have the hydrophilic surface. Greater resistance may be encountered when this section of the microcatheter is advanced into the RHV.
- Exercise care in handling of the microcatheter during a procedure to reduce the possibility of accidental breakage, bending or kinking.
- To reduce the probability of coating damage in tortuous vasculature, use a guide catheter with a minimum internal diameter as specified in Table 1 above, and is recommended for use with Stryker Neurovascular hydrophilically coated microcatheters.
- To control the proper introduction, movement, positioning and removal of the microcatheter within the vascular system, users should employ standard clinical angiographic and fluoroscopic practices and techniques throughout the interventional procedure.
- Flush dispenser coil of hydrophilically coated microcatheters prior to removal from dispenser coil. Once the microcatheter has been wetted, do not allow to dry. Do not reinsert the microcatheter into dispenser coil.
- Do not position microcatheter closer than 2.54 cm (1 in) from the steam source. Damage to the microcatheter may result.
- Check that all fittings are secure so that air is not introduced into guide catheter or microcatheter during continuous flush.
- In order to achieve optimal performance of Stryker Neurovascular Microcatheters and to maintain the lubricity of the Hydrolene® Coating surface, it is critical that a continuous flow of appropriate flush solution be maintained between the Stryker Neurovascular Microcatheter and guide catheter, and the microcatheter and any intraluminal device. In addition, flushing aids in preventing contrast crystal formation and/or clotting on both the intraluminal device and inside the guide catheter and/or the microcatheter lumen.
- Excessive tightening of a hemostatic valve onto the microcatheter shaft may result in damage to the microcatheter.



Stryker Neurovascular
47900 Bayside Parkway
Fremont, CA 94538

strykerneurovascular.com

Date of Release: NOV/2017

EX_EN_US

Copyright © 2017 Stryker

AP001839 v1.0 | Page 2 of 2

Target® Detachable Coil

See package insert for complete indications, contraindications, warnings and instructions for use.

INTENDED USE / INDICATIONS FOR USE

Target Detachable Coils are intended to endovascularly obstruct or occlude blood flow in vascular abnormalities of the neurovascular and peripheral vessels.

Target Detachable Coils are indicated for endovascular embolization of:

- Intracranial aneurysms
- Other neurovascular abnormalities such as arteriovenous malformations and arteriovenous fistulae
- Arterial and venous embolizations in the peripheral vasculature

CONTRAINDICATIONS

None known.

POTENTIAL ADVERSE EVENTS

Potential complications include, but are not limited to: allergic reaction, aneurysm perforation and rupture, arrhythmia, death, edema, embolus, headache, hemorrhage, infection, ischemia, neurological/intracranial sequelae, post-embolization syndrome (fever, increased white blood cell count, discomfort), TIA/stroke, vasospasm, vessel occlusion or closure, vessel perforation, dissection, trauma, vessel rupture, vessel thrombosis. Other procedural complications including but not limited to: anesthetic and contrast media risks, hypotension, hypertension, access site complications.

WARNINGS

- Contents supplied STERILE using an ethylene oxide (EO) process. Do not use if sterile barrier is damaged. If damage is found, call your Stryker Neurovascular representative.
- For single use only. Do not reuse, reprocess or resterilize. Reuse, reprocessing or resterilization may compromise the structural integrity of the device and/or lead to device failure which, in turn, may result in patient injury, illness or death. Reuse, reprocessing or resterilization may also create a risk of contamination of the device and/or cause patient infection or cross-infection, including, but not limited to, the transmission of infectious disease(s) from one patient to another. Contamination of the device may lead to injury, illness or death of the patient.
- After use, dispose of product and packaging in accordance with hospital, administrative and/or local government policy.

This device should only be used by physicians who have received appropriate training in interventional neuroradiology or interventional radiology and preclinical training on the use of this device as established by Stryker Neurovascular.

- Patients with hypersensitivity to 316LVM stainless steel may suffer an allergic reaction to this implant.
- MRI temperature testing was not conducted in arteriovenous malformations or fistulae and performance characteristics of the Target Detachable Coil System (Target Detachable Coils, InZone Detachment Systems, delivery systems and accessories) have not been demonstrated with other manufacturer's devices (whether coils, coil delivery devices, coil detachment systems, catheters, guidewires, and/or other accessories). Due to the potential incompatibility of non Stryker Neurovascular devices with the Target Detachable Coil System, the use of other manufacturer's devices with the Target Detachable Coil System is not recommended.
- To reduce risk of coil migration, the diameter of the first and second coil should never be less than the width of the ostium.
- In order to achieve optimal performance of the Target Detachable Coil System and to reduce the risk of thromboembolic complications, it is critical that a continuous infusion of appropriate flush solution be maintained between a) the femoral sheath and guiding catheter, b) the 2-tip microcatheter and guiding catheter, and c) the 2-tip microcatheter and Stryker Neurovascular guidewire and delivery wire. Continuous flush also reduces the potential for thrombus formation on, and crystallization of infusate around, the detachment zone of the Target Detachable Coil.
- Do not use the product after the "Use By" date specified on the package.
- Reuse of the packaging hoop or use with any coil other than the original coil may result in contamination of, or damage to, the coil.

Damaged delivery wires may cause detachment failures, vessel injury or unpredictable distal tip response during coil deployment. If a delivery wire is damaged at any point during the procedure, do not attempt to straighten or otherwise repair it. Do not proceed with deployment or detachment. Remove the entire coil and replace with undamaged product.

- Utilization of damaged coils may affect coil delivery to, and stability inside, the vessel or aneurysm, possibly resulting in coil migration and/or stretching.
- The fluoro-saver marker is designed for use with a Rotating Hemostatic Valve (RHV). If used without an RHV, the distal end of the coil may be

Copyright © 2017 Stryker

NV00018669 v2.0 | Page 2 of 2



Stryker Neurovascular
47900 Bayside Parkway
Fremont, CA 94538

strykerneurovascular.com

Date of Release: NOV/2017

EX_EN_US



LVIS®

Intraluminal Support Device

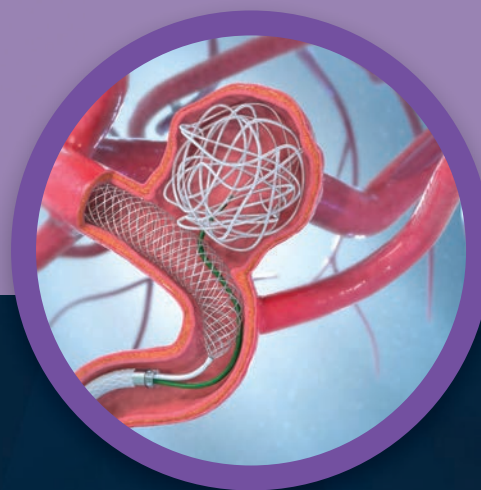
Low-profile Visualized Intرالuminal Support

Stent Deployment. Refined.

Braided Coil Assist Stents with
High Neck Coverage, Excellent Visibility
and Improved Conformability*



Aneurysm
Therapy
Solutions



For more information or a product demonstration,
contact your local MicroVention representative:

MicroVention Worldwide
Innovation Center
35 Enterprise

Aliso Viejo, CA 92656 USA

MicroVention UK Limited

MicroVention Europe, S.A.R.L.

MicroVention Deutschland GmbH

microvention.com

PH +1.714.247.8000

PH +44 (0) 191 258 6777

PH +33 (1) 39 21 77 46

PH +49 211 210 798-0

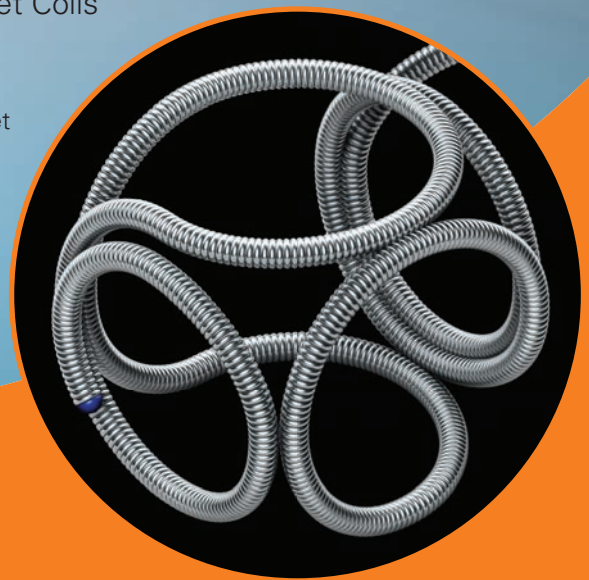
**Humanitarian Device: Authorized by Federal Law for use with bare platinum embolic coils for the treatment of unruptured, wide neck (neck \geq 4 mm or dome to neck ratio $<$ 2), intracranial, saccular aneurysms arising from a parent vessel with a diameter \geq 2.5 mm and \leq 4.5 mm. The effectiveness of this device for this use has not been demonstrated.*



Smooth and stable.

Target Detachable Coils deliver consistently smooth deployment and exceptional microcatheter stability. Designed to work seamlessly together for framing, filling and finishing. Target Coils deliver the high performance you demand.

For more information, please visit www.strykerneurovascular.com/Target or contact your local Stryker sales representative.



Target[®]
DETACHABLE COILS



Bending expectations of conformability and stability.

Enhanced conformability – The hybrid cell structure is designed to enhance stent opening and conformability in bifurcations and tight curves.

Ease of use – All sizes of the Neuroform Atlas Stent are deliverable through Excelsior® SL-10® and Excelsior XT-17™ Microcatheters.

Higher deployment accuracy – The Neuroform Atlas Stent is designed to have very low foreshortening, which enables very high deployment accuracy.



Neuroform Atlas™

STENT SYSTEM

AJNR

AMERICAN JOURNAL OF NEURORADIOLOGY

FEBRUARY 2018
VOLUME 39
NUMBER 2
WWW.AJNR.ORG

Publication Preview at www.ajnr.org features articles released in advance of print. Visit www.ajnrblog.org to comment on AJNR content and chat with colleagues and AJNR's News Digest at <http://ajnrndigest.org> to read the stories behind the latest research in neuroimaging.

207 **PERSPECTIVES** *T.A. Tomsick*

REVIEW ARTICLE

- 🔑 208 **Radiomics in Brain Tumor: Image Assessment, Quantitative Feature Descriptors, and Machine-Learning Approaches** *M. Zhou, et al.* **ADULT BRAIN**

PRACTICE PERSPECTIVES

- 217 **John Nash and the Organization of Stroke Care** *M. Goyal, et al.*

GENERAL CONTENTS

- 🔑 219 **MR Perfusion to Determine the Status of Collaterals in Patients with Acute Ischemic Stroke: A Look Beyond Time Maps** *K. Nael, et al.* **ADULT BRAIN**
- 🔑 226 **On the Reproducibility of Inversion Recovery Intravoxel Incoherent Motion Imaging in Cerebrovascular Disease** *S.M. Wong, et al.* **ADULT BRAIN**
- 232 **The CT Swirl Sign Is Associated with Hematoma Expansion in Intracerebral Hemorrhage** *D. Ng, et al.* **ADULT BRAIN**
- 238 **Dural Arteriovenous Fistulas: A Characteristic Pattern of Edema and Enhancement of the Medulla on MRI** *A.Z. Copelan, et al.* **ADULT BRAIN**
- ★🔑 245 **White Matter Changes Related to Subconcussive Impact Frequency during a Single Season of High School Football** *S.J. Kuzminski, et al.* **ADULT BRAIN**
- 🔑📄 252 **MR Imaging Characteristics Associate with Tumor-Associated Macrophages in Glioblastoma and Provide an Improved Signature for Survival Prognostication** *J. Zhou, et al.* **ADULT BRAIN**
- 260 **Diagnostic Accuracy of Centrally Restricted Diffusion in the Differentiation of Treatment-Related Necrosis from Tumor Recurrence in High-Grade Gliomas** *N. Zakhari, et al.* **ADULT BRAIN**
- 🔑📄 265 **Addition of Amide Proton Transfer Imaging to FDG-PET/CT Improves Diagnostic Accuracy in Glioma Grading: A Preliminary Study Using the Continuous Net Reclassification Analysis** *A. Sakata, et al.* **ADULT BRAIN**
- 273 **Diffusion-Weighted Imaging of Brain Metastasis from Lung Cancer: Correlation of MRI Parameters with the Histologic Type and Gene Mutation Status** *W.S. Jung, et al.* **ADULT BRAIN**

-  280 Diagnostic Accuracy of Amino Acid and FDG-PET in Differentiating Brain Metastasis Recurrence from Radionecrosis after Radiotherapy: A Systematic Review and Meta-Analysis *H. Li, et al.* **ADULT BRAIN**
-   289 Feasibility of Brain Atrophy Measurement in Clinical Routine without Prior Standardization of the MRI Protocol: Results from MS-MRIUS, a Longitudinal Observational, Multicenter Real-World Outcome Study in Patients with Relapsing-Remitting MS *R. Zivadinov, et al.* **ADULT BRAIN**
- 296 Improved Precision of Automatic Brain Volume Measurements in Patients with Clinically Isolated Syndrome and Multiple Sclerosis Using Edema Correction *J.B.M. Warntjes, et al.* **ADULT BRAIN**
-   303 Combining Quantitative Susceptibility Mapping with Automatic Zero Reference (QSM0) and Myelin Water Fraction Imaging to Quantify Iron-Related Myelin Damage in Chronic Active MS Lesions *Y. Yao, et al.* **ADULT BRAIN**
-  311 Noninvasive Assessment of Intracranial Pressure Status in Idiopathic Intracranial Hypertension Using Displacement Encoding with Stimulated Echoes (DENSE) MRI: A Prospective Patient Study with Contemporaneous CSF Pressure Correlation *A.M. Saindane, et al.* **ADULT BRAIN**
-   317 Leukoaraiosis Attenuates Diagnostic Accuracy of Large-Vessel Occlusion Scales *Y. Mayasi, et al.* **ADULT BRAIN**
INTERVENTIONAL
-   323 The Role of Hemodynamics in Intracranial Bifurcation Arteries after Aneurysm Treatment with Flow-Diverter Stents *A.P. Narata, et al.* **INTERVENTIONAL**
-   331 Feasibility of Permanent Stenting with Solitaire FR as a Rescue Treatment for the Reperfusion of Acute Intracranial Artery Occlusion *H.G. Woo, et al.* **INTERVENTIONAL**
-   337 Better Than Nothing: A Rational Approach for Minimizing the Impact of Outflow Strategy on Cerebrovascular Simulations *C. Chnafa, et al.* **INTERVENTIONAL**
-  344 Intranasal Esthesioneuroblastoma: CT Patterns Aid in Preventing Routine Nasal Polypectomy *M.E. Peckham, et al.* **HEAD & NECK**
-  350 Lymphographic-Like Technique for the Treatment of Microcystic Lymphatic Malformation Components of <3 mm *V. Da Ros, et al.* **HEAD & NECK**
- 355 Semiautomated Middle Ear Volume Measurement as a Predictor of Postsurgical Outcomes for Congenital Aural Atresia *S.J. Kabadi, et al.* **HEAD & NECK**
-  362 Optimal Fat Suppression in Head and Neck MRI: Comparison of Multipoint Dixon with 2 Different Fat-Suppression Techniques, Spectral Presaturation and Inversion Recovery, and STIR *S. Gaddikeri, et al.* **HEAD & NECK**
- 369 Optic Nerve Measurement on MRI in the Pediatric Population: Normative Values and Correlations *C.E. Al-Haddad, et al.* **PEDIATRICS**
-   375 Measuring Cerebral and Cerebellar Glutathione in Children Using ¹H MEGA-PRESS MRS *F. Raschke, et al.* **PEDIATRICS**
-  380 Temporal Lobe Malformations in Achondroplasia: Expanding the Brain Imaging Phenotype Associated with *FGFR3*-Related Skeletal Dysplasias *S.A. Manikkam, et al.* **PEDIATRICS**
-  385 Systematic Radiation Dose Reduction in Cervical Spine CT of Human Cadaveric Specimens: How Low Can We Go? *M. Tozakidou, et al.* **SPINE**
PATIENT SAFETY
-   392 Clinical and Radiologic Characteristics of Deep Lumbosacral Dural Arteriovenous Fistulas *F. Jablawi, et al.* **SPINE**
- 399 Cervical Cord Atrophy and Long-Term Disease Progression in Patients with Primary-Progressive Multiple Sclerosis *F.X. Aymerich, et al.* **SPINE**

ONLINE FEATURES

WHITE PAPER

- E9 Carotid Artery Wall Imaging: Perspective and Guidelines from the ASNR Vessel Wall Imaging Study Group and Expert Consensus Recommendations of the American Society of Neuroradiology *L. Saba, et al.* **EXTRACRANIAL VASCULAR**

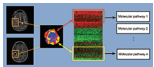
LETTERS

- E32 **Multiparametric Imaging Improves Confidence in the Diagnosis of Multinodular and Vacuolating Neuronal Tumor of the Cerebrum** *A. Lecler, et al.*
- E34 **Reply** *R.H. Nunes, et al.*
- E35 **The Anesthesiologist, Rather Than the Anesthesia, May Influence the Outcomes following Stroke Thrombectomy** *W. Fandino*
- E36 **Economic Considerations in MR Imaging of Patients with Cardiac Devices** *M.U. Antonucci, et al.*
- E37 **Reply** *A.W. Korutz, et al.*

BOOK REVIEWS

R.M. Quencer, Section Editor

Please visit www.ajnrblog.org to read and comment on Book Reviews.



Schematic showing the linking of subregional imaging to molecular profiles in glioblastoma. Tumor subregions (B) are defined by clustering on contrast-enhanced T1WI and T2WI (A). These subregions correspond to red (high T1WI and high T2WI), yellow (high T1WI and low T2WI), blue (low T1WI and high T2WI), and pink (low T1WI and low T2WI) areas. The defined tumor subregions enable quantitative spatial characterization, allowing noninvasive assessment of specific molecular activities (C) with molecular pathways (D).



Indicates Editor's Choices selection



Indicates Fellows' Journal Club selection



Indicates open access to non-subscribers at www.ajnr.org



Indicates article with supplemental on-line table



Indicates article with supplemental on-line photo



Indicates article with supplemental on-line video



Evidence-Based Medicine Level 1



Evidence-Based Medicine Level 2

Official Journal:

American Society of Neuroradiology
American Society of Functional Neuroradiology
American Society of Head and Neck Radiology
American Society of Pediatric Neuroradiology
American Society of Spine Radiology

EDITOR-IN-CHIEF

Jeffrey S. Ross, MD

Professor of Radiology, Department of Radiology,
Mayo Clinic College of Medicine, Phoenix, AZ

SENIOR EDITORS

Harry J. Cloft, MD, PhD

Professor of Radiology and Neurosurgery,
Department of Radiology, Mayo Clinic College of
Medicine, Rochester, MN

Thierry A.G.M. Huisman, MD

Professor of Radiology, Pediatrics, Neurology, and
Neurosurgery, Chairman, Department of Imaging
and Imaging Science, Johns Hopkins Bayview,
Director, Pediatric Radiology and Pediatric
Neuroradiology, Johns Hopkins Hospital,
Baltimore, MD

Yvonne W. Lui, MD

Associate Professor of Radiology,
Chief of Neuroradiology,
New York University School of Medicine,
New York, NY

C.D. Phillips, MD, FACR

Professor of Radiology, Weill Cornell Medical
College, Director of Head and Neck Imaging,
New York-Presbyterian Hospital, New York, NY

Pamela W. Schaefer, MD

Clinical Director of MRI and Associate Director of
Neuroradiology, Massachusetts General Hospital,
Boston, Massachusetts, Associate Professor,
Radiology, Harvard Medical School, Cambridge, MA

Charles M. Strother, MD

Professor of Radiology, Emeritus, University of
Wisconsin, Madison, WI

STATISTICAL SENIOR EDITOR

Bryan A. Comstock, MS

Senior Biostatistician,
Department of Biostatistics,
University of Washington, Seattle, WA

EDITORIAL BOARD

Ashley H. Aiken, *Atlanta, GA*
Lea M. Alhilali, *Phoenix, AZ*
John D. Barr, *Dallas, TX*
Ari Blitz, *Baltimore, MD*
Barton F. Branstetter IV, *Pittsburgh, PA*
Jonathan L. Brisman, *Lake Success, NY*
Julie Bykowski, *San Diego, CA*
Keith Cauley, *Danville, PA*
Asim F. Choudhri, *Memphis, TN*
Alessandro Cianfoni, *Lugano, Switzerland*
J. Matthew Debnam, *Houston, TX*
Seena Dehkharghani, *New York, NY*
Colin Derdeyn, *Iowa City, IA*
Rahul S. Desikan, *San Francisco, CA*
Yonghong Ding, *Rochester, MN*
Clifford J. Eskey, *Hanover, NH*
Saeed Fakhraan, *Phoenix, AZ*
Massimo Filippi, *Milan, Italy*
Allan J. Fox, *Toronto, Ontario, Canada*
Wende N. Gibbs, *Los Angeles, CA*
Christine M. Glastonbury, *San Francisco, CA*
John L. Go, *Los Angeles, CA*
Allison Grayev, *Madison, WI*
Brent Griffith, *Detroit, MI*
Wan-Yuo Guo, *Taipei, Taiwan*
Ajay Gupta, *New York, NY*
Rakesh K. Gupta, *Lucknow, India*
Lotfi Hachein-Bey, *Sacramento, CA*
Christopher P. Hess, *San Francisco, CA*
Andrei Holodny, *New York, NY*
Benjamin Huang, *Chapel Hill, NC*
George J. Hunter, *Boston, MA*
Mahesh V. Jayaraman, *Providence, RI*
Valerie Jewells, *Chapel Hill, NC*
Christof Karmonik, *Houston, TX*
Timothy J. Kaufmann, *Rochester, MN*
Hillary R. Kelly, *Boston, MA*
Toshitomi Kinoshita, *Akita, Japan*
Kenneth F. Layton, *Dallas, TX*
Michael M. Lell, *Nürnberg, Germany*
Michael Lev, *Boston, MA*
Karl-Olof Lovblad, *Geneva, Switzerland*
Franklin A. Marden, *Chicago, IL*
M. Gisele Matheus, *Charleston, SC*
Joseph C. McGowan, *Merion Station, PA*
Stephan Meckel, *Freiburg, Germany*
Christopher J. Moran, *St. Louis, MO*
Takahisa Mori, *Kamakura City, Japan*
Suresh Mukherji, *Ann Arbor, MI*
Amanda Murphy, *Toronto, Ontario, Canada*
Alexander J. Nemeth, *Chicago, IL*
Sasan Partovi, *Cleveland, OH*
Laurent Pierot, *Reims, France*
Jay J. Pillai, *Baltimore, MD*

Whitney B. Pope, *Los Angeles, CA*
M. Judith Donovan Post, *Miami, FL*
Tina Young Poussaint, *Boston, MA*
Joana Ramalho, *Lisbon, Portugal*
Otto Rapalino, *Boston, MA*
Álex Rovira-Cañellas, *Barcelona, Spain*
Paul M. Ruggieri, *Cleveland, OH*
Zoran Rumboldt, *Rovinj-Rovigno, Croatia*
Amit M. Saindane, *Atlanta, GA*
Erin Simon Schwartz, *Philadelphia, PA*
Lubdha M. Shah, *Salt Lake City, UT*
Aseem Sharma, *St. Louis, MO*
J. Keith Smith, *Chapel Hill, NC*
Maria Vittoria Spampinato, *Charleston, SC*
Gordon K. Sze, *New Haven, CT*
Krishnamoorthy Thamburaj, *Hershey, PA*
Cheng Hong Toh, *Taipei, Taiwan*
Thomas A. Tomsick, *Cincinnati, OH*
Aquila S. Turk, *Charleston, SC*
Willem Jan van Rooij, *Tilburg, Netherlands*
Arastoo Vossough, *Philadelphia, PA*
Elysa Widjaja, *Toronto, Ontario, Canada*
Max Wintermark, *Stanford, CA*
Ronald L. Wolf, *Philadelphia, PA*
Kei Yamada, *Kyoto, Japan*
Carlos Zamora, *Chapel Hill, NC*

EDITORIAL FELLOW

Vahe Zohrabian, *New Haven, CT*

SPECIAL CONSULTANTS TO THE EDITOR

AJNR Blog Editor

Neil Lall, *Denver, CO*

Case of the Month Editor

Nicholas Stence, *Aurora, CO*

Case of the Week Editors

Juan Pablo Cruz, *Santiago, Chile*
Sapna Rawal, *Toronto, Ontario, Canada*

Classic Case Editor

Sandy Cheng-Yu Chen, *Taipei, Taiwan*

Facebook Editor

Peter Yi Shen, *Sacramento, CA*

Health Care and Socioeconomics Editor

Pina C. Sanelli, *New York, NY*

Physics Editor

Greg Zaharchuk, *Stanford, CA*

Podcast Editor

Wende N. Gibbs, *Los Angeles, CA*

Twitter Editor

Jennifer McCarty, *Atlanta, Georgia*

YOUNG PROFESSIONALS ADVISORY COMMITTEE

Asim K. Bag, *Birmingham, AL*
Anna E. Nidecker, *Sacramento, CA*
Peter Yi Shen, *Sacramento, CA*

Founding Editor
Juan M. Taveras

Editors Emeriti
Mauricio Castillo, Robert I. Grossman,
Michael S. Huckman, Robert M. Quencer

Managing Editor
Karen Halm

Assistant Managing Editor
Laura Wilhelm

Digital Publications and Social Media Coordinator
Kylie Mason

Executive Director, ASNR
Mary Beth Hepp



Title: Stereoscopic Mardi Gras Masks. These are two 9" × 12" palette-knife oil paintings, mounted on a 16" × 20" base module with a gold background and masks in Mardi Gras yellow, green, and purple. The 2 masks form a stereoscopic pair, such that when the module-artist or observer, at a distance of 9" to 12" from this page, fixes his or her gaze between the 2 masks and allows the eyes to converge, or views through a simple stereoscopic viewer, the masks will converge as well, with the purple color aligning with the green, as the yellow "disappears." Stereoscopy has been a radiograph-viewing technique for the better part of a century, especially for viewing of the facial bones.

Thomas A. Tomsick, MD, Department of Radiology, University of Cincinnati Academic Health Center, University Hospital, Cincinnati, Ohio

Radiomics in Brain Tumor: Image Assessment, Quantitative Feature Descriptors, and Machine-Learning Approaches

M. Zhou, J. Scott, B. Chaudhury, L. Hall, D. Goldgof, K.W. Yeom, M. Iv, Y. Ou, J. Kalpathy-Cramer, S. Napel, R. Gillies, O. Gevaert, and R. Gatenby



ABSTRACT

SUMMARY: Radiomics describes a broad set of computational methods that extract quantitative features from radiographic images. The resulting features can be used to inform imaging diagnosis, prognosis, and therapy response in oncology. However, major challenges remain for methodologic developments to optimize feature extraction and provide rapid information flow in clinical settings. Equally important, to be clinically useful, predictive radiomic properties must be clearly linked to meaningful biologic characteristics and qualitative imaging properties familiar to radiologists. Here we use a cross-disciplinary approach to highlight studies in radiomics. We review brain tumor radiologic studies (eg, imaging interpretation) through computational models (eg, computer vision and machine learning) that provide novel clinical insights. We outline current quantitative image feature extraction and prediction strategies with different levels of available clinical classes for supporting clinical decision-making. We further discuss machine-learning challenges and data opportunities to advance radiomic studies.

ABBREVIATIONS: LBP = local binary patterns; HOG = histogram of oriented gradients; QIN = Quantitative Imaging Network; SIFT = scale-invariant feature transform

Clinical imaging captures enormous amounts of information, but most radiologic data are reported in qualitative and subjective terms. Radiomics^{1,2} in neuro-oncology seeks to improve the understanding of the biology and treatment in brain tumors by extracting quantitative features from clinical imaging arrays. These data can then be “mined” with machine-learning methods and validated as quantitative imaging biomarkers³ to characterize intratumoral dynamics throughout the course of treatment. The recent growth of cancer imaging analytic methods⁴⁻⁶ has produced novel insights into early indicators of treatment response, risk factors, and subsequent tailoring of optimal treatment strategies.^{2,5,7,8} Image-based computational models are, thus, becoming

an important enabling technology that permits identification, analysis, and validation of extracted quantitative features. In this review, we discuss available methodologies in radiomics that can be used as predictive markers for diagnosis, prognosis, and therapeutic planning in the context of adult brain tumors. We will also address the interpretive challenges that emerge from the computationally based data generated by radiomic methods. While statistical correlations between computational features and clinical outcomes exist, this approach will likely not gain wide clinical acceptance until there is a better link between the quantitative metric and traditional imaging features and the underlying biology.

Radiomics incorporates several important disciplines, including radiology (eg, imaging interpretation), computer vision (eg, quantitative feature extraction), and machine learning (eg, classifier evaluation). A central goal is the identification of quantitative imaging indicators that predict important clinical outcomes, including prognosis and response or resistance to a specific cancer treatment. Here, we discuss recent studies in the development of radiomics with the following goals: 1) understanding the functionality of clinical imaging as a necessary prerequisite for developing radiomic models; 2) extracting quantitative image features extraction in computer vision that can be used to exploit tumor imaging traits; 3) identifying radiomic signatures shown to be surrogate markers of underlying molecular properties of tumors, enabling a noninvasive means to characterize biologic activities of

From the Stanford Center for Biomedical Informatic Research (M.Z., O.G.) and Department of Radiology (K.W.Y., M.I.), Stanford University, Stanford, California; Department of Radiology (J.S., B.C., S.N., R. Gillies, R. Gatenby), Moffitt Cancer Research Center, Tampa, Florida; Department of Computer Science and Engineering (L.H., D.G.), University of South Florida, Tampa, Florida; and Department of Radiology (Y.O., J.K.-C.), Massachusetts General Hospital, Boston, Massachusetts.

This work is supported by the National Institute of Biomedical Imaging and Bioengineering of the National Institutes of Health under award No. R01EB020527.

The content is solely the responsibility of the authors and does not necessarily represent the official views of the National Institutes of Health.

Please address correspondence to Olivier Gevaert, PhD, Stanford Center for Biomedical Informatics Research, 1265 Welch Rd, Stanford, CA, 94305; e-mail: Olivier.gevaert@stanford.edu; and Robert Gatenby, MD, Moffitt Cancer Center, 12902 USF Magnolia Drive, Tampa, FL 33612; e-mail: Robert.gatenby@moffitt.org

Indicates open access to non-subscribers at www.ajnr.org

<http://dx.doi.org/10.3174/ajnr.A5391>

cancer⁹; and 4) performing predictive analysis with machine-learning techniques to classify clinical outcomes and assessing the physiologic status of cancer.¹⁰ Through this convergence of radiology, computer vision, and machine-learning techniques, radiomics provides a mechanism for multidisciplinary research on brain tumors.

Clinical MR Imaging Assessment of Brain Tumors

MR imaging permits noninvasive characterization of mesoscopic features (ie, the “radiologic phenotype”) of brain tumors and is an indispensable tool for early tumor detection, monitoring, and diagnosis.¹¹ Radiomic analysis is built on the central hypothesis that tumor imaging reflects the underlying morphology and dynamics of smaller-scale biologic phenomena, including gene expression patterns, tumor cell proliferation, and blood vessel formation.¹²

MR imaging plays an essential role in the management of patients with glioblastoma for 3 important reasons. First, MR imaging has an excellent capacity for the detection of soft-tissue contrast by providing superior anatomic information (eg, spatial location). Second, different MR imaging sequences can be sensitive to key components of tumor physiology, such as blood flow and cellular density, and can distinguish regions of the tumor that contain different environments (eg, variations in blood flow) that are likely to affect local cellular phenotypes and genotypes. Third, MR imaging can noninvasively and nondestructively interrogate the tumor repeatedly to assess response to treatment and can, therefore, be integrated into therapeutic strategies. Understanding these image-based features is critical because they represent a key data resource in radiomic analysis.¹

Contrast enhancement in MR imaging using gadolinium-based contrast agents is an important and useful feature in evaluating brain tumors.¹³ The tumor zone that enhances following gadolinium injection typically defines the tumor region that is well-perfused with high tumor cell density but also one in which there is a breakdown of the blood-brain barrier. Compared with noncontrast imaging, contrast-enhanced images are often used to provide a delineation of gross tumor margins and allow earlier detection of additional small metastatic lesions. In general, tumor sizes based on these images are used for monitoring tumor response to therapy.¹³ Thus, radiomic models for brain tumor analysis¹⁴⁻¹⁶ often focus on contrast-enhanced sequences.

Spatial heterogeneity of brain tumors is well-recognized in MR imaging. Different MR imaging sequences exploit various biomedical properties of brain tumors more effectively than other imaging modalities (eg, CT can only show differences in electron density). Postgadolinium T1-weighted images can show enhancing regions (characterized as T1-shortening or T1 high signal) within the tumor due to gadolinium leakage from the intravascular space into the tumor because of a disrupted blood-brain barrier. Consequently, necrosis and solid tumors can be visually distinguished. In addition, T2-weighted sequences are sensitive to water tissue content and can be used to estimate cellular density and the presence of edema. Next, fluid-attenuated inversion-recovery sequences are frequently used in conjunction with T2-weighted images to provide a better distinction between edema and solid tumor.¹⁷ In addition, diffusion-weighted imaging al-

lows characterization of tissue cellularity based on the free diffusion of water molecules along structural tissue pathways in different tissue types.¹⁸ Advanced MR imaging methods, including perfusion, proton density-weighted, fast spin-echo, and short tau inversion-recovery imaging, have also been applied to depict specific tissue contrast.¹⁹ Therefore, mining radiomic data from these advanced imaging arrays will likely offer additional information with respect to tissue discrimination, treatment measurement, and clinical usefulness.

Quantitative Image Feature Extraction

While the quality, resolution, and flexibility of MR imaging technology has greatly increased in past decades, the interpretation of images remains largely descriptive, subjective, and nonquantitative. Thus, the central goal of radiomics is the development of image analytic techniques that can reproducibly extract objective, quantitative data from MR imaging scans. Linking these quantitative features and underlying tissue dynamics that govern tumor growth and response to therapy has the potential to rapidly expand the scope of cancer imaging research.¹ Here, we focus on many related computer vision techniques that are particularly useful in quantitative cancer imaging science.

Computational Image Descriptors

Radiomics relies on computational techniques in computer vision to extract many quantitative features from radiologic images.²⁰ The extracted quantitative features are typically within a defined ROI that could include the whole tumor or specific regions within it. Computational image descriptors quantify visual characteristics at different scales from ROIs, which can be readily translated into radiologic image analysis pertaining to tumor volumetric shapes and visual appearance dynamics. For example, the scale-invariant feature transform (SIFT)^{21,22} is computed through key point detection using a difference of Gaussian function and local image gradient measurement with radius and scale selections (as illustrated in Fig 1). This permits a quantitative measurement of the tumor shape so that subtle variations during treatment (ie, increasingly round or increasingly elliptic) can be observed and quantified. Several recent studies have demonstrated the accuracy and reproducibility of computational image extraction approaches to capture characteristics of tumor shape and texture information from brain tumor MR imaging.²³⁻²⁵ Thus, these approaches have the potential for large-scale, rapid throughput and reproducible evaluation and may be applied to routine clinical imaging studies that are widely available.

Here, we describe 2 primary image feature extraction strategies with local- or global-level computations in the context of computer vision. First, local-level feature extraction provides an image descriptor used to compare a pixel being tested with its immediate pixel neighborhood.²⁶ This allows identification of a small, but biologically important, tumor niche area (a small number of pixels) within an otherwise homogeneous, larger tumor region. This can be achieved, for example, with local binary patterns (LBP).²⁷ These are local image descriptors sensitive to small monotonic gray-level differences²⁸ that may not be apparent to a human observer. In contrast, global-level feature extraction em-

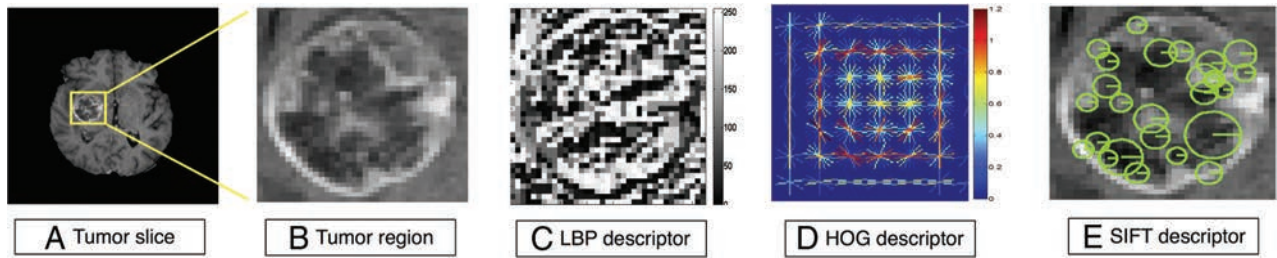


FIG 1. Visualization of computational image feature descriptors. A T1-weighted brain tumor section (A and B) is displayed, and feature visualizations (C–E) are given of LBP (C), HOG (D), and SIFT (E) descriptors. LBP quantifies local pixel structures through a binary coding scheme. HOG computes block-wise histogram gradients with multiple orientations. SIFT detects distributed key points with radius on tumor images. These multiparametric features create a rich image-driven data base to characterize tumors in MR imaging at different scales.

Examples of quantitative features with their potential clinical relevance

Quantitative Feature Descriptors	Potential Clinical Relevance
Histogram of contrast-enhanced tumor MRI ⁴⁵	Distinguish molecular subtypes
Contrast information between co-occurring subregions ⁵	Survival predictor
Pretreatment ADC histograms ⁸²	Indicator to bevacizumab treatment
HOG ³⁴	Measure tumor microenvironment
LBP ²⁷	Measure tumor microenvironment
SIFT ²²	Measure tumor spatial characteristics

Biologically Inspired Feature Descriptor

Biologically inspired feature descriptors build on specific biologic hypotheses that transfer the recognized radiology knowledge into quantitative representation, as opposed to pure computational approaches for feature extraction. Understanding disease characteristics is necessary to propose biologically inspired features because they can be disease-specific. For example, a recent study³⁷ suggested that MR imaging–derived pharmacokinetic features (eg, extracellular space per unit volume of tissue) were potential biomarkers for separating outcomes of treatment with concurrent radiation therapy and chemotherapy.

phasizes the quantification of the overall composition of an entire ROI. For example, a computational descriptor²⁹ was designed to develop a low-dimensional representation of the image, emphasizing spatial structure variations (eg, roughness, openness, and expansion). In addition, high-order statistical features, known as texture features,³⁰ have been widely applied to brain cancer and other cancer imaging analyses.^{14,31} Examples of texture features include gray-level co-occurrence matrices³² and gray-level size zone matrices,³³ which examine the spatial relationships of pixels through a series of statistical measures. Histogram of oriented gradients (HOG)³⁴ features have also proved to be efficient feature descriptors for quantifying image-gradient statistics with multiple directions not obvious to radiologists. A recent study³⁵ suggested that co-occurring gradients in MR imaging were useful for distinguishing brain tumor subtypes.

Despite these advances of computational image descriptors, they may be suboptimal because feature extraction inherently distills a complex dataset of more than a million voxels per MR imaging sequence into a handful of numeric descriptors. To identify a strong radiomic feature, one needs 2 important factors. First, the proposed descriptor must be able to capture distinctive patterns correlated with the clinical outcomes of patients. Moreover, the descriptor must be stable under various image-acquisition parameters. Although MR imaging signals exhibit tumor geometric shapes, appearances, and voxelwise variations with underlying biologic characteristics at molecular, tissue, and organ levels,¹² the potential dynamics and temporal variations in blood flow increase the difficulty in acquiring useful radiomic features. Thus, test-retest and interobserver stability³⁶ are strongly suggested for measuring robust computational image features in radiomic studies. Figure 1 highlights several hand-crafted computational descriptors that capture different visual characteristics of brain tumor MR imaging. Despite the promise of computational image descriptors, the underlying biologic meanings of these features have not been fully exploited, with links to promising therapies and outcome prediction of patients.

Biologically inspired MR imaging features can be used to define organ-level tumor data variation and distribution, offering an opportunity to observe spatial variations and temporal evolution of tumors.¹² For example, a spatial distance measurement³⁸ was defined to quantitatively explore brain tumor heterogeneity. The proposed spatial distances suggested that the variations among biologically defined tumor subregions can reflect distinct prognostic information. Also, early temporal changes and spatial heterogeneity during radiation therapy in heterogeneous regions of high and low perfusion in gliomas might predict different physiologic responses to radiation therapy.³⁹ Other work¹⁶ has proposed a novel concept of imaging habitats that quantifies distinctive tumor subregions by their local contrast enhancement, edema, and cellularity in MR imaging. Moreover, a recent study measured the relationships between MR signal and cell density using radiographically localized biopsies,⁴⁰ revealing that T2-FLAIR and ADC sequences were inversely correlated with cell density. The Table highlights several feature descriptors with their clinical potentials.

Biologically inspired features correlate with corresponding MR imaging sequences because different MR imaging sequences come with various clinical imaging protocols. As a result, selection of MR imaging sequences can directly affect image feature definition and corresponding biologic interpretation. For example, 1 study⁴¹ used apparent diffusion coefficient histograms for the early prediction of drug treatment responses of glioblastomas. In this study, diffusion- and T1-weighted data were used separately for ADC computation and tumor segmentation. The ADC was used to describe the diffusion processes that reflect different

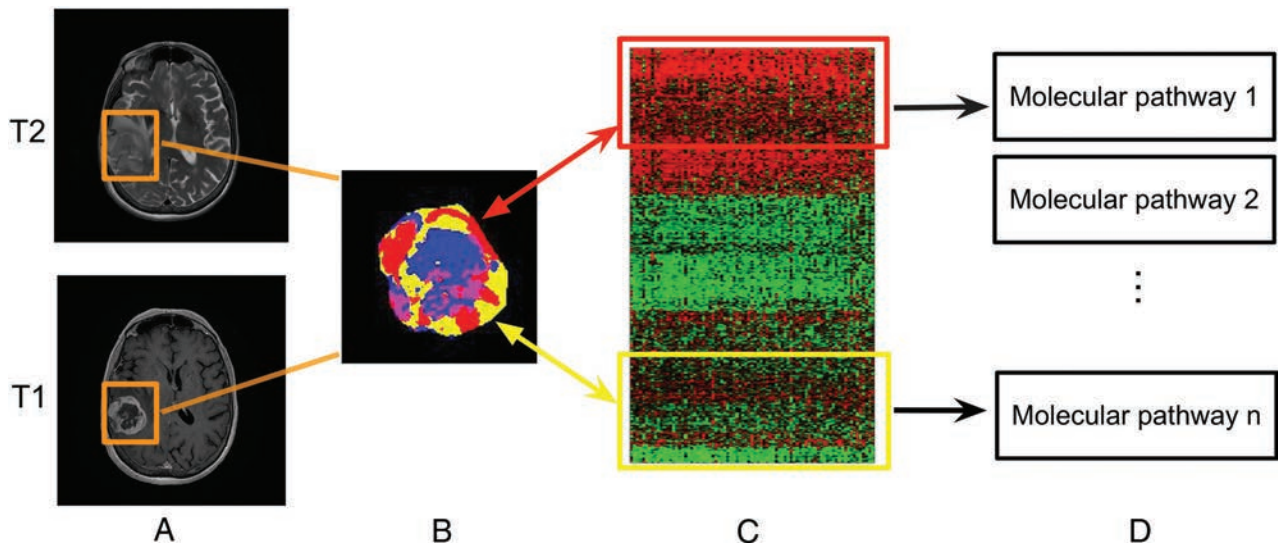


FIG 2. Linking subregional imaging to molecular profiles in glioblastoma. In this example, tumor subregions (B) are defined by jointly clustering on contrast-enhanced T1WI and T2WI (A). These subregions correspond to red (high T1WI and high T2WI), yellow (high T1WI and low T2WI), blue (low T1WI and high T2WI), and pink (low T1WI and low T2WI) areas. The defined tumor subregions enable quantitative spatial characterization, offering a means to noninvasively assess specific molecular activities (C) with enriched molecular pathways (D).

biomedical mechanisms.⁴² These biologically inspired features are quantitative rather than qualitative semantic features annotated by radiologists to describe the tumor environment.⁴³ The VASARI semantic feature set (<https://wiki.cancerimagingarchive.net/display/Public/VASARI+Research+Project>), for example, is used to describe the morphology of brain tumors (eg, tumor location, shape, and geometric properties) on contrast-enhanced MR imaging.⁷

Imaging and Genomics in Glioblastoma

Imaging genomics, also known as radiogenomics, is a growing field that studies the association between imaging biomarkers and genomic characteristics of a disease.^{7,44,45} Inherent in this definition is the goal of enabling noninvasive imaging assessment as a surrogate for molecular signatures that were previously only available through molecular testing. A handful of studies^{7,44,45} identified associations between quantitative image features and gene expression profiles of glioblastoma (eg, *TP53*, *EGFR*, *NF1*, and *IDH1*) and its molecular subtypes (eg, classical, mesenchymal, proneural, and neural). Additional studies indicated that quantitative MR imaging features derived from entire tumor volumes can be used to identify glioblastoma subtypes with distinct molecular pathway activities.^{15,46} The value of such whole-tumor comparisons is limited by the spatial variations in both the imaging features and molecular tumor properties of tumor cells in, for example, glioblastoma multiforme. However, this extensive intratumoral heterogeneity also provides a compelling research opportunity if spatial characteristics in MR imaging, largely governed by mesoscopic tumor properties (eg, blood flow and cell density), could be used to define the spatial distribution of glioblastoma molecular subtypes within the same tumor.⁴⁷ To better define imaging-to-genomic relationships, the development of subregional imaging analysis enabling spatial characterization is biologically valuable (Fig 2) because it provides a means to characterize molecular variations in the spatially distinct tumor fragments.

Machine Learning in Radiomics

Machine learning offers an approach for discovering predictive radiomic features. Here, the investigator does not begin with an a priori biologic hypothesis. Thus, the parameter space is searched for an imaging feature statistically associated with clinical outcome. Before one evaluates machine-learning models, a specification for the medical diagnostic task is needed so that models can be appropriately trained. For example, supervised, unsupervised, and semisupervised learning models are fundamental learning strategies used in accordance with the different levels of available clinical outcome labels. In supervised learning, the goal is to learn from a certain portion of trained samples with known class labels and to predict classes or numeric values for unknown patterns from large and noisy datasets.⁴⁷ Conversely, unsupervised learning finds the natural structure from data without having any prior labels. As a hybrid setting, semisupervised learning needs only a small portion of labeled training data. The unlabeled data samples, instead of being discarded, are also used in the learning process. More recently, the rise of deep learning as a new frontier in machine learning has advanced large-scale medical image analysis.⁴⁸ We describe these learning strategies and highlight specific clinical applications in the context of brain tumors.

Supervised Learning

Supervised learning is a primary learning scheme that has been applied in recent radiomic studies.^{16,23} Supervised learning is conceptually divided into 2 phases. First, training samples with available class labels are used to build a classifier by finding a set of parameters to define a decision boundary among classes. Second, the learned classifier is used to predict class labels of unknown testing samples. Notably, the selection of classifiers depends on the desired properties of the classifier, including convergence and modeling assumptions.⁴⁹ An example of this approach is a study⁵⁰ that showed the selection of machine-learning classifiers for supervised radiomic applications in detecting radiomic biomarkers. More examples include tumor-subtype classification and survival

time prediction, and these are discussed in clinical applications below.

Unsupervised Learning

Without knowing any prior labels of data, unsupervised learning algorithms group the data according to their similarity. For example, a knowledge-based unsupervised fuzzy clustering approach⁵¹ was proposed to automate brain tumor segmentation. It showed that tumor and healthy intracranial regions could be grouped using this clustering algorithm through a rule-based expert system. The growth of clinical imaging results in the onerous task of manually annotating tumors on imaging volumes. Therefore, there has been growing interest in exploring scalable algorithms for annotating large volumes of tumor imaging data¹⁵ and evaluating human interrater variability.⁵²

Semisupervised Learning

Semisupervised learning is designed specifically for tasks for which it is difficult to obtain class labels for certain patients (eg, the estimation of tumor progression). In other words, the advance of semisupervised learning overcomes a limitation of conventional supervised learning that is incapable of using data with missing labels in training. Semisupervised models have a great potential to effectively enable predictive analysis with uncompleted clinical labels in training. For example, 1 study⁵³ predicted states of brain tumor prognosis using a semisupervised learning model. With <26% of the available staging labels, a discriminative analysis was performed using the staging labels of patients with glioblastoma.

Deep Learning

Recently, deep learning^{54,55} has emerged as a powerful technique that defines a network architecture, concatenating multiple neural-like processing layers with multiple levels of abstraction. Deep learning methods have achieved record-breaking performances for numerous computer vision applications when the number of available training samples is sufficiently large.⁵⁶ Convolutional neural networks,⁵⁷ for example, are deep learning models that incorporate concatenated convolutional layers and pooling layers, followed by fully connected layers to learn the high-level representation of input data. A growing set of studies has shown superior results in the field of medical image analysis by applying convolutional neural networks models.^{48,58-60} A recent study⁶¹ specifically introduced a convolutional neural networks–based approach for brain tumor segmentation. With the designed network architecture containing multiple small 3×3 kernels and deep layers, the model achieved strong segmentation performance (DICE score = 0.88) on the Brain Tumor Segmentation Challenge 2013 data base (<http://braintumorsegmentation.org/>).

Specific Clinical Applications of Radiomics

Survival Time Prediction. Predicting prognostic performance of glioblastomas using clinical imaging alone is challenging due to the radiographic heterogeneity of tumors. Stratification of clinical groups will directly impact image-guided diagnosis and targeted treatment.¹⁶ In contrast to qualitative assessment (enhancing tumor, edema, and multifocal lesions)⁶² made by radiologists, a

recent study⁵ introduced quantitative spatial imaging biomarkers to predict survival time for patients with glioblastomas. Such work requires a labeled training set with survival information. It suggested that contrast information gained from co-occurring subregions on FLAIR and T2-weighted images was useful to separate long-term (>400 days) and short-term (<400 days) survival groups.

Classification of Glioblastoma Subtypes. An example of the classification of brain tumor histologic groups²⁵ demonstrated the usefulness of radiomic features to rapidly classify gliomas, metastases, and high- (grade III and grade IV) and low-grade (grade II) neoplasms. The quantitative image analysis collected brain tumor identification, raw intensity values, and MR imaging–based texture features to demonstrate the capability of multiparametric MR imaging features to separate histologic classes of brain tumors. In addition, a recent study⁴⁵ showed the possibility of classifying molecular subtypes of glioblastomas using radiomic features alone. In this approach, histograms of MR imaging intensity in enhanced tumors were identified to provide added value for predicting molecular subtypes of glioblastoma.⁴⁵

Tumor–Tissue Discriminative Analysis. Differentiating radiation necrosis from tumor recurrence is difficult in patients with glioblastoma undergoing chemoradiation because traditional qualitative interpretation of conventional contrast-enhanced MR imaging is unlikely to differentiate chemoradiation-induced necrosis and pseudoprogression.⁶³ By contrast, quantitative MR imaging features⁶⁴ were shown to differentiate radiation necrosis from recurrent tumor. Results revealed that a set of quantitative intensity features obtained from multiple MR imaging arrays (eg, T1, T2, relative CBF, and ADC) was useful for detecting radiation necrosis tissue in resected patients with glioblastoma multiforme undergoing chemoradiation.

Research Opportunities and Challenges

Substantial progress has been made from recent radiomic studies to deepen our understanding of imaging characteristics in cancer.^{1,2} The identified quantitative features can be used to alert radiologists to suspicious abnormalities because radiomic models can even capture subtle variations in tumor environment not easily perceived by human experts. We highlighted the convergence of quantitative image feature extraction and machine-learning techniques for supporting diagnosis, prognosis, and treatment predictions. Next, we discuss challenges and opportunities that are not only related to brain tumor MR imaging but also applicable to other types of cancer studies in radiomics.

Development of Treatment-Specific Radiomics

There is a growing need to develop radiomic signatures that can be used to directly inform specific treatment options. With diffusion-weighted MR imaging, emerging evidence revealed that ADC maps were useful to differentiate treatment outcomes in glioblastoma with radiation therapy concurrent with temozolomide.⁶⁵ Also, early changes of ADC maps were identified for predicting glioblastoma recurrence.⁶⁶ In addition, a decrease in the volume of FLAIR signal and contrast enhancement⁶⁷ was shown to predict the response to bevacizumab treatment for patients

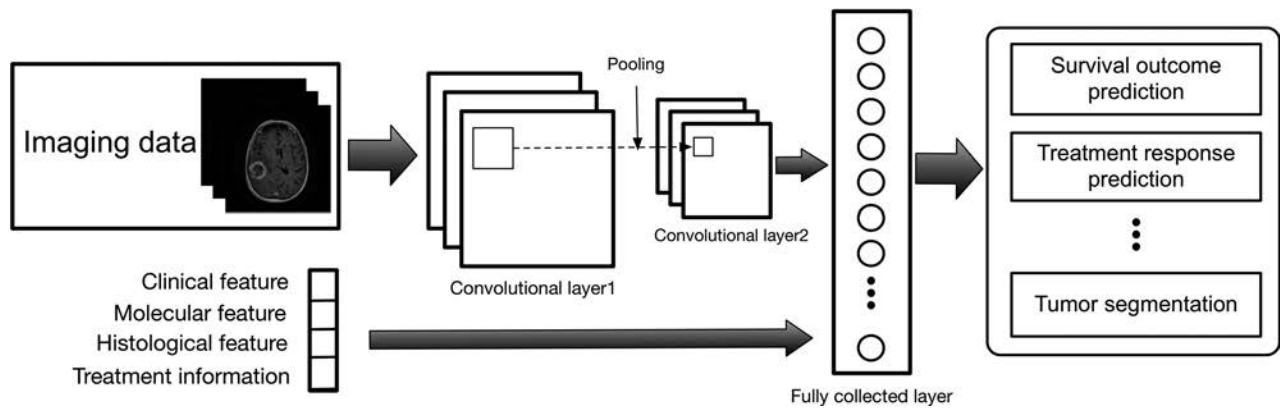


FIG 3. Illustration of the convolutional neural networks model using imaging and other biomedical data for brain tumor analysis. The convolutional neural networks model consists of multiple convolutional layers, pooling layers, and fully connected layers to learn an abstraction of the input data, such as imaging and clinical features for a variety of outcome evaluations.

with glioblastomas. To better understand the biologic implications of these imaging findings, the collection of temporal imaging at multiple diagnostic periods will offer an opportunity to consistently characterize biologic tumor evolution before and after treatment.⁶⁸ Currently, distinguishing tumor response between pseudoprogression and pseudoresponse continues to be challenging in tumor MR imaging⁶⁹; thus, development of radiomic features to contribute to treatment outcome analysis will be appealing. Although the type of radiomic features that will eventually be validated as true predictors responsive to different treatments is still to be determined, the vast quantity of radiomic findings, in conjunction with the growth of molecular data, will increase the possibility of a redefinition of tumor subtypes and novel biomarker discovery to inform treatment decisions in the coming years.

Machine Learning

Extracting large-scale radiomic features from a variety of imaging arrays creates a rich data base containing clinically relevant information. Both computational and biologically inspired feature descriptors are important and useful for machine learning. Thus, development of scalable machine-learning techniques is vital to search for and identify useful image features associated with outcome variables and clinical records. We discuss 2 representative techniques to address this need. First, a suggested approach is to investigate sparse-learning models, also known as lasso regularization,⁷⁰ for finding a useful set of reduced features from a high-dimensional feature vector. Emerging evidence suggests that sparse learning is useful for identifying multiparametric prognostic imaging biomarkers in non-small cell lung cancer.⁷¹

Second, recent breakthroughs in deep learning with applications in radiology, such as lung nodule malignancy classification^{58,59} and lymph node detection,⁷² have been encouraging in finding disease-specific imaging biomarkers. However, the availability of labeled medical data poses a challenge for developing efficient deep-learning models. For example, cancer images with pathologically proved labels are costly to collect at scale; thus, data integration with different types of clinical labels may present an alternative means to overcome such obstacles for deep-learning models, which need large datasets as input.⁷³ Although how we gain clinical insight from these deep-learning outcomes and how

we optimize network architectures for the better use of multiscale medical data (eg, serial MR imaging, genomics, and clinical data) are uncertain,⁷⁴ the extraction of compact patterns via hierarchical networks presents enormous opportunities for large-scale radiomic applications (Fig 3).

The Role of Radiomics in Big Data

Radiomic studies follow the theme of emerging big data in health care that concerns mining vast quantities of biomedical data.^{75,76} A typical concern of radiomics in big data relates to the management of growing image data, gene expression profiles, and the associated clinical records. Multiple data sources (eg, medical institutions) and various data types (eg, multitechnique imaging data) make data sharing and collective administration an especially complex problem. Enabling data standardization across different image protocols and parameters becomes a prerequisite for collective study. The pilot project of the Cancer Genome Atlas⁷⁷ is an initiative to provide a large portion of clinical data and generic information. As a parallel effort, The Cancer Imaging Archive⁴ is growing rapidly for sharing radiologic images. Also, the Quantitative Imaging Network⁷⁸ is designed to promote efficient data integration that helps validate imaging biomarkers that are impactful in treating cancer. More recently, MR fingerprinting⁷⁹ was introduced to advance the role of quantitative MR imaging using pseudorandomized acquisition parameters. However, large-scale, high-quality benchmark datasets, including complete clinical labels, standard radiomic features, and molecular profiles, are not widely available for data sharing, experimental evaluation, and reproducibility of radiomics toward precision medicine.^{80,81}

CONCLUSIONS

The rapid discovery rate of novel imaging biomarkers in radiomics allows integrating information from interdisciplinary approaches in radiology, computer vision, and machine learning. With the growth of clinical imaging data, novel image-based computational models are playing an increasingly important role for precise diagnosis and treatment guidance in neuro-oncology. Only when these models align well with tumor biology will radiomic findings maximize their likelihood for clinical utility. Research challenges remain for exploring cancer heterogeneity, scalable computational models, and the clinical significance of

radiomic findings. We believe that the newly emerging diagnostic hypotheses and scalable machine-learning algorithms have the potential for enhancing the current performance of predictive cancer diagnosis and accelerating quantitative cancer imaging findings to reach their true clinical potential.

Disclosures: Mu Zhou—*RELATED: Grant:* National Institutes of Health, *Comments:* National Institute of Biomedical Imaging and Bioengineering of the National Institutes of Health under award No. R01EB020527. Jayashree Kalpathy-Cramer—*RELATED: Grant:* National Institutes of Health, *Comments:* National Institutes of Health/National Cancer Institute U24CA180927, National Institutes of Health/National Cancer Institute U24CA180918, National Institutes of Health/National Cancer Institute U01CA154601*; *Consulting Fee or Honorarium:* Infotech Software, *Comments:* amount of <\$2000. Sandy Napel—*UNRELATED: Board Membership:* EchoPixel, Fovia, Radlogics, *Comments:* scientific advisory boards; *Consultancy:* Algotec. Robert Gillies—*RELATED: Grant:* National Institutes of Health*; *UNRELATED: Stock/Stock Options:* HealthMyne, *Comments:* a radiomics PACS system not used in the current article. Olivier Gevaert—*RELATED: Grant:* National Institutes of Health*, *Comments:* National Institutes of Health No. R01EB020527; *UNRELATED: Grants/Grants Pending:* National Institutes of Health*. *Money paid to the institution.

REFERENCES

- Gillies RJ, Kinahan PE, Hricak H. **Radiomics: images are more than pictures, they are data.** *Radiology* 2016;278:563–77 CrossRef Medline
- Kumar V, Gu YH, Basu S, et al. **Radiomics: the process and the challenges.** *Magn Reson Imaging* 2012;30:1234–48 CrossRef Medline
- Ludwig JA, Weinstein JN. **Biomarkers in cancer staging, prognosis and treatment selection.** *Nat Rev Cancer* 2005;5:845–56 CrossRef Medline
- Prior FW, Clark K, Commean P, et al. **TCIA: an information resource to enable open science.** In: *Proceedings of the 35th Annual International Conference of the IEEE Engineering in Medicine and Biological Society*, Osaka, Japan. July 3–7, 2013:1282–85
- Zhou M, Chaudhury B, Hall LO, et al. **Identifying spatial imaging biomarkers of glioblastoma multiforme for survival group prediction.** *J Magn Reson Imaging* 2016;46:115–23
- Aerts HJ, Velazquez ER, Leijenaar RTH, et al. **Decoding tumour phenotype by noninvasive imaging using a quantitative radiomics approach.** *Nat Commun* 2014;5:4006 CrossRef Medline
- Gutman DA, Cooper LA, Hwang SN, et al. **MR imaging predictors of molecular profile and survival: multi-institutional study of the TCGA glioblastoma data set.** *Radiology* 2013;267:560–69 CrossRef Medline
- Kotrotsou A, Zinn PO, Colen RR. **Radiomics in brain tumors: an emerging technique for characterization of tumor environment.** *Magn Reson Imaging Clin North Am* 2016;24:719–29 CrossRef Medline
- Jaffe CC. **Imaging and genomics: is there a synergy?** *Radiology* 2012; 264:329–31 CrossRef Medline
- Michaelis LC, Ratain MJ. **Measuring response in a post-RECIST world: from black and white to shades of grey.** *Nat Rev Cancer* 2006; 6:409–14 CrossRef Medline
- Kheifets LI. **Electric and magnetic field exposure and brain cancer: a review.** *Bioelectromagnetics* 2001;(suppl 5):S120–31 Medline
- Gatenby RA, Grove O, Gillies RJ. **Quantitative imaging in cancer evolution and ecology.** *Radiology* 2013;269:8–15 CrossRef Medline
- Drevelgas A, Papanikolaou N. **Imaging modalities in brain tumors.** In: Drevelgas A. *Imaging of Brain Tumors with Histological Correlations*. Berlin: Springer; 2011:13–33
- Kickingreder P, Götz M, Muschelli J, et al. **Large-scale radiomic profiling of recurrent glioblastoma identifies an imaging predictor for stratifying anti-angiogenic treatment response.** *Clin Cancer Res* 2016;22:5765–71 CrossRef Medline
- Itakura H, Achrol AS, Mitchell LA, et al. **Magnetic resonance image features identify glioblastoma phenotypic subtypes with distinct molecular pathway activities.** *Sci Transl Med* 2015;7:303ra138 CrossRef Medline
- Zhou M, Hall L, Goldof D, et al. **Radiologically defined ecological dynamics and clinical outcomes in glioblastoma multiforme: preliminary results.** *Transl Oncol* 2014;7:5–13 CrossRef Medline
- Tsuchiya K, Inaoka S, Mizutani Y, et al. **Fast fluid-attenuated inversion-recovery MR of intracranial infections.** *AJNR Am J Neuroradiol* 1997;18:909–13 Medline
- Padhani AR, Liu G, Koh DM, et al. **Diffusion-weighted magnetic resonance imaging as a cancer biomarker: consensus and recommendations.** *Neoplasia* 2009;11:102–25 CrossRef Medline
- Bitar R, Leung G, Perng R, et al. **MR pulse sequences: what every radiologist wants to know but is afraid to ask.** *Radiographics* 2006; 26:513–37 CrossRef Medline
- Lambin P, Rios-Velazquez E, Leijenaar R, et al. **Radiomics: extracting more information from medical images using advanced feature analysis.** *Eur J Cancer* 2012;48:441–46 CrossRef Medline
- Ambrosini RD, Wang P, O'Dell WG. **Computer-aided detection of metastatic brain tumors using automated three-dimensional template matching.** *J Magn Reson Imaging* 2010;31:85–93 CrossRef Medline
- Lowe DG. **Object recognition from local scale-invariant features.** In: *Proceedings of the Seventh IEEE International Conference on Computer Vision*, Corfu, Greece. September 20–25, 1999:1150–57
- Zikic D, Glocker B, Konukoglu E, et al. **Decision forests for tissue-specific segmentation of high-grade gliomas in multi-channel MR.** In: Ayache N, Delingette H, Golland P, et al, eds; *Medical Image Computing and Computer-Assisted Intervention—MICCAI 2012*. Berlin: Springer; 2012:369–76
- Reddy KK, Solmaz B, Yan P, et al. **Confidence guided enhancing brain tumor segmentation in multi-parametric MRI.** In: *Proceedings of the 9th IEEE International Symposium on Biomedical Imaging*, Barcelona, Spain. May 2–5, 2012:366–69
- Zacharaki EI, Wang S, Chawla S, et al. **Classification of brain tumor type and grade using MRI texture and shape in a machine learning scheme.** *Magn Reson Med* 2009;62:1609–18 CrossRef Medline
- Tuytelaars T, Mikolajczyk K. **Local invariant feature detectors: a survey.** *Foundations and Trends in Computer Graphics and Vision* 2008;3:177–280
- Ojala T, Pietikäinen M, Mäenpää T. **Multiresolution gray-scale and rotation invariant texture classification with local binary patterns.** *IEEE Transactions on Pattern Analysis and Machine Intelligence* 2002; 24:971–87 CrossRef
- Heikkilä M, Pietikäinen M, Schmid C. **Description of interest regions with local binary patterns.** *Pattern Recognition* 2009;42:425–36 CrossRef
- Oliva A, Torralba A. **Modeling the shape of the scene: a holistic representation of the spatial envelope.** *International Journal of Computer Vision* 2001;42:145–75 CrossRef
- Kassner A, Thornhill RE. **Texture analysis: a review of neurologic MR imaging applications.** *AJNR Am J Neuroradiol* 2010;31:809–16 CrossRef Medline
- Aerts HJ, Velazquez ER, Leijenaar RT, et al. **Decoding tumour phenotype by noninvasive imaging using a quantitative radiomics approach.** *Nat Commun* 2014;5:4006 CrossRef Medline
- Haralick RM, Shanmugam K, Dinstein I. **Textural features for image classification.** *IEEE Transactions on Systems Man Cybernetics* 1973;Smc3:610–21
- Galloway MM. **Texture analysis using gray level run lengths.** *Computer Graphics and Image Processing* 1975;4:172–79 CrossRef
- Dalal N, Triggs B. **Histograms of oriented gradients for human detection.** In: *Proceedings of the 2005 IEEE Computer Society Conference on Computer Vision and Pattern Recognition*, San Diego, California. June 20–26, 2005:886–93
- Prasanna P, Tiwari P, Madabhushi A. **Co-occurrence of Local Anisotropic Gradient Orientations (CoLIAGe): distinguishing tumor confounders and molecular subtypes on MRI.** In: Ayache N, Delingette H, Golland P, et al, eds. *Medical Image Computing and Computer-Assisted Intervention—MICCAI 2012*. Berlin: Springer; 2012:369–76
- Leijenaar RT, Carvalho S, Velazquez ER, et al. **Stability of FDG-PET**

- radiomics features: an integrated analysis of test-retest and inter-observer variability.** *Acta Oncol* 2013;52:1391–97 CrossRef Medline
37. Yun TJ, Park CK, Kim TM, et al. **Glioblastoma treated with concurrent radiation therapy and temozolomide chemotherapy: differentiation of true progression from pseudoprogression with quantitative dynamic contrast-enhanced MR imaging.** *Radiology* 2015;274:830–40 CrossRef Medline
 38. Zhou M, Hall LO, Goldgof DB, et al. **Survival time prediction of patients with glioblastoma multiforme tumors using spatial distance measurement.** *SPIE Proceedings* 2013;8670:86702O CrossRef
 39. Cao Y, Tsien CI, Nagesh V, et al. **Survival prediction in high-grade gliomas by MRI perfusion before and during early stage of RT.** *Int J Radiat Oncol Biol Phys* 2006;64:876–85 CrossRef Medline
 40. Chang PD, Malone HR, Bowden SG, et al. **A multiparametric model for mapping cellularity in glioblastoma using radiographically localized biopsies.** *AJNR Am J Neuroradiol* 2017;38:890–98 CrossRef Medline
 41. Huo J, Kim HJ, Pope WB, et al. **Histogram-based classification with Gaussian mixture modeling for GBM tumor treatment response using ADC map.** *SPIE Proceedings* 2009;7260:72601Y CrossRef
 42. Le Bihan D, Breton E, Lallemand D, et al. **MR imaging of intravoxel incoherent motions: application to diffusion and perfusion in neurologic disorders.** *Radiology* 1986;161:401–07 CrossRef Medline
 43. Mazurowski MA, Desjardins A, Malof JM. **Imaging descriptors improve the predictive power of survival models for glioblastoma patients.** *Neuro Oncol* 2013;15:1389–94 CrossRef Medline
 44. Zinn PO, Mahajan B, Majadan B, et al. **Radiogenomic mapping of edema/cellular invasion MRI-phenotypes in glioblastoma multiforme.** *PLoS One* 2011;6:e25451 CrossRef Medline
 45. Macyszyn L, Akbari H, Pisapia JM, et al. **Imaging patterns predict patient survival and molecular subtype in glioblastoma via machine learning techniques.** *Neuro Oncol* 2016;18:417–25 CrossRef Medline
 46. Gevaert O, Mitchell LA, Achrol AS, et al. **Glioblastoma multiforme: exploratory radiogenomic analysis by using quantitative image features.** *Radiology* 2014;273:168–74 CrossRef Medline
 47. Cruz JA, Wishart DS. **Applications of machine learning in cancer prediction and prognosis.** *Cancer Inform* 2007;2:59–77 Medline
 48. Shen D, Wu G, Suk HI. **Deep learning in medical image analysis.** *Annu Rev Biomed Eng* 2017;19:221–48 CrossRef Medline
 49. Mitchell T. **The discipline of machine learning.** Carnegie Mellon University, School of Computer Science, Machine Learning Department; 2006. <http://docplayer.net/19055685-The-discipline-of-machine-learning.html>. Accessed September 26, 2017
 50. Parmar C, Grossmann P, Bussink J, et al. **Machine learning methods for quantitative radiomic biomarkers.** *Sci Rep* 2015;5:13087 CrossRef Medline
 51. Clark MC, Hall LO, Goldgof DB, et al. **Automatic tumor segmentation using knowledge-based techniques.** *IEEE Trans Med Imaging* 1998;17:187–201 CrossRef Medline
 52. Menze BH, Jakab A, Bauer S, et al. **The multimodal Brain Tumor Image Segmentation Benchmark (BRATS).** *IEEE Trans Med Imaging* 2015;34:1993–2024 CrossRef Medline
 53. Cruz-Barbosa R, Vellido A. **Semi-supervised analysis of human brain tumours from partially labeled MRS information, using manifold learning models.** *Int J Neural Syst* 2011;21:17–29 CrossRef Medline
 54. LeCun Y, Bengio Y, Hinton G. **Deep learning.** *Nature* 2015;521:436–44 CrossRef Medline
 55. Szegedy C, Liu W, Jia YQ, et al. **Going deeper with convolutions.** In: *Proceedings of the 2009 IEEE Conference on Computer Vision and Pattern Recognition*, Miami, Florida. June 20–25, 2015:1–9
 56. Deng J, Dong W, Socher R, et al. **ImageNet: a large-scale hierarchical image database.** In: *Proceedings of the 2009 IEEE Conference on Computer Vision and Pattern Recognition*, Miami, Florida. June 20–25, 2015:248–55
 57. Karpathy A, Toderici G, Shetty S, et al. **Large-scale video classification with convolutional neural networks.** In: *Proceedings of the 2014 IEEE Conference on Computer Vision and Pattern Recognition*, Columbus, Ohio. June 23–28, 2014:1725–32
 58. Shen W, Zhou M, Yang F, et al. **Multi-scale convolutional neural networks for lung nodule classification.** *Inf Process Med Imaging* 2015;24:588–99 Medline
 59. Shen W, Zhou M, Yang F, et al. **Multi-crop convolutional neural networks for lung nodule malignancy suspiciousness classification.** *Pattern Recognition* 2017;61:663–73 CrossRef
 60. Setio AA, Ciompi F, Litjens G, et al. **Pulmonary nodule detection in CT images: false positive reduction using multi-view convolutional networks.** *IEEE Trans Med Imaging* 2016;35:1160–69 CrossRef Medline
 61. Pereira S, Pinto A, Alves V, et al. **Brain tumor segmentation using convolutional neural networks in MRI images.** *IEEE Trans Med Imaging* 2016;35:1240–51 CrossRef Medline
 62. Pope WB, Sayre J, Perlina A, et al. **MR imaging correlates of survival in patients with high-grade gliomas.** *AJNR Am J Neuroradiol* 2005;26:2466–74 Medline
 63. Siu A, Wind JJ, Iorgulescu JB, et al. **Radiation necrosis following treatment of high grade glioma: a review of the literature and current understanding.** *Acta Neurochir (Wien)* 2012;154:191–201; discussion 201 CrossRef Medline
 64. Hu X, Wong KK, Young GS, et al. **Support vector machine multiparametric MRI identification of pseudoprogression from tumor recurrence in patients with resected glioblastoma.** *J Magn Reson Imaging* 2011;33:296–305 CrossRef Medline
 65. Chu HH, Choi SH, Ryoo I, et al. **Differentiation of true progression from pseudoprogression in glioblastoma treated with radiation therapy and concomitant temozolomide: comparison study of standard and high-b-value diffusion-weighted imaging.** *Radiology* 2013;269:831–40 CrossRef Medline
 66. Chang PD, Chow DS, Yang PH, et al. **Predicting glioblastoma recurrence by early changes in the apparent diffusion coefficient value and signal intensity on FLAIR images.** *AJR Am J Roentgenol.* 2017;208:57–65 CrossRef Medline
 67. Ellingson BM, Cloughesy TF, Lai A, et al. **Quantitative volumetric analysis of conventional MRI response in recurrent glioblastoma treated with bevacizumab.** *Neuro Oncol* 2011;13:401–09 CrossRef Medline
 68. Zhou M, Hall LO, Goldgof DB, et al. **Decoding brain cancer dynamics: a quantitative histogram-based approach using temporal MRI.** *SPIE Proceedings* 2015;9414
 69. Hygino da Cruz LC Jr, Rodriguez I, Domingues RC, et al. **Pseudoprogression and pseudoresponse: imaging challenges in the assessment of posttreatment glioma.** *AJNR Am J Neuroradiol* 2011;32:1978–85 CrossRef Medline
 70. Tibshirani R. **Regression shrinkage and selection via the lasso.** *Journal of the Royal Statistical Society. Series B (Methodological)* 1996;58:267–88
 71. Gevaert O, Xu J, Hoang CD, et al. **Non-small cell lung cancer: identifying prognostic imaging biomarkers by leveraging public gene expression microarray data—methods and preliminary results.** *Radiology* 2012;264:387–96 CrossRef Medline
 72. Shin HC, Roth HR, Gao MC, et al. **Deep convolutional neural networks for computer-aided detection: CNN architectures, dataset characteristics and transfer learning.** *IEEE Trans Med Imaging* 2016;35:1285–98 CrossRef Medline
 73. Shen W, Zhou M, Yang F, et al. **Learning from experts: developing transferable deep features for patient-level lung cancer prediction.** In: *Proceedings of the 19th Medical Image Computing and Computer-Assisted Intervention Conference*, Athens, Greece. October 17–21, 2016:124–31
 74. Mamoshina P, Vieira A, Putin E, et al. **Applications of deep learning in biomedicine.** *Mol Pharm* 2016;13:1445–54 CrossRef Medline
 75. Manyika J, Chui M, Brown B, et al. **Big data: the next frontier for innovation, competition, and productivity.** McKinsey Global Institute. 2011. <http://www.mckinsey.com/business-functions/digital-mckinsey/our-insights/big-data-the-next-frontier-for-innovation>. Accessed September 26, 2017

76. Bates DW, Saria S, Ohno-Machado L, et al. **Big data in health care: using analytics to identify and manage high-risk and high-cost patients.** *Health Aff (Millwood)* 2014;33:1123–31 CrossRef Medline
77. Cancer Genome Atlas Research Network. **Comprehensive genomic characterization defines human glioblastoma genes and core pathways.** *Nature* 2008;455:1061–68 CrossRef Medline
78. Kalpathy-Cramer J, Freymann JB, Kirby JS, et al. **Quantitative imaging network: data sharing and competitive algorithm validation leveraging The Cancer Imaging Archive.** *Transl Oncol* 2014;7:147–52 CrossRef Medline
79. Badve C, Yu A, Dastmalchian S, et al. **MR fingerprinting of adult brain tumors: initial experience.** *AJNR Am J Neuroradiol* 2017;38:492–99 CrossRef Medline
80. Aerts HJ. **The potential of radiomic-based phenotyping in precision medicine: a review.** *JAMA Oncol* 2016;2:1636–42 CrossRef Medline
81. O'Connor JP, Aboagye EO, Adams JE, et al. **Imaging biomarker roadmap for cancer studies.** *Nat Rev Clin Oncol* 2017;14:169–86 CrossRef Medline
82. Ellingson B, Sahebjam S, Kim HJ, et al. **Pretreatment ADC histogram analysis is a predictive imaging biomarker for bevacizumab treatment but not chemotherapy in recurrent glioblastoma.** *AJNR Am J Neuroradiol* 2014;35:673–79 CrossRef Medline

John Nash and the Organization of Stroke Care

 M. Goyal,  A.T. Wilson,  D. Mayank,  N. Kamal,  D.H. Robinson,  D. Turkel-Parrella, and  J.A. Hirsch

ABSTRACT

SUMMARY: The concept of Nash equilibrium, developed by John Forbes Nash Jr, states that an equilibrium in noncooperative games is reached when each player takes the best action for himself or herself, taking into account the actions of the other players. We apply this concept to the provision of endovascular thrombectomy in the treatment of acute ischemic stroke and suggest that collaboration among hospitals in a health care jurisdiction could result in practices such as shared call pools for neurointervention teams, leading to better patient care through streamlined systems.

John Forbes Nash Jr was a renowned mathematician whose groundbreaking work in the domain of game theory earned him the Nobel Prize in Economics in 1994. His theories have been key to our understanding of decision-making processes in economics and every other aspect of life involving complex strategic interactions.¹

Nash became a household name due to a critically acclaimed depiction of his life in the film *A Beautiful Mind*. There is a scene where Nash is struck by an epiphany because of a discussion about an imaginary interaction with some young women. He realizes that Adam Smith's theory of systems fails to take into account that people choose the action that confers the greatest benefit (within the constraints of law and decency). If you have not seen the film or do not remember the scene, check it out at <https://www.youtube.com/watch?v=LJS7lgvk6ZM>. The important message is that in game theory as in life, systems work best when every person does what is best for himself or herself, taking into consideration the decisions of the other players. A system in this state is in Nash equilibrium.²⁻⁴

In acute ischemic stroke due to large-vessel occlusion, we know that the natural history of the disease is generally poor and devastating, endovascular thrombectomy is highly effective, and "time is brain."⁵ Our biggest challenge moving forward is to improve the organization of systems of care, getting each patient to

the correct hospital the first time around.⁶ Additionally, individual cities, jurisdictions, and groups of physicians need to organize themselves so that they can provide endovascular thrombectomy 24/7/365. Neurointerventionists are often hired mainly on the basis of adequate availability of daytime work and where a hospital is located, the population denominator, and the presence of other neurointervention centers in the vicinity. Thus, hospitals may be limited in increasing their call pool, making the frequency of calls for each neurointerventionist quite onerous.

In game theory, a game comprises 3 parts: the players, the set of actions available to each player, and a utility function for each player.⁴ Here, the players are the health care providers, the actions are the choices they make regarding patient admission and treatment, and the primary utility measure of these actions is the patient's well-being. To achieve optimization (both for patient outcome and use of resources, decent call schedules, and work-life balance) based on Nash's work would require all the players (in this case, all the health care providers in a particular jurisdiction) to evaluate not only their own choices and strategy but also the choices and strategies of the other players.

Nash's work suggests that patients with stroke could be better served in their community if hospitals or neurointervention groups engaged in collaborative practices, rather than each institution working exclusively to its best interest in isolation. In this sense, each player would show his or her "hand" and, subsequently, take the best action for himself or herself based on every other player's hand. This would constitute a mutually beneficial cooperative Nash equilibrium in which the system is in a stable state, with each player maximally benefitting.^{4,7} In this sense, outcomes of patients with stroke (the shortest possible onset-to-reperfusion time in appropriately chosen patients⁸) will be improved in the community as a whole.

Received October 3, 2017; accepted October 9.

From the Department of Radiology and Clinical Neurosciences (M.G., A.T.W., N.K.), University of Calgary, Calgary, Alberta, Canada; Faculty of Applied Science and Engineering (D.M.), University of Toronto, Toronto, Ontario, Canada; Department of Radiology (D.H.R.), Virginia Mason Medical Center, Seattle, Washington; Department of Neurology (D.T.-P.), Division of Neurointerventional Radiology, NYU School of Medicine, New York, New York; and Department of Neurointerventional Radiology (J.A.H.), Massachusetts General Hospital, Harvard Medical School, Boston, Massachusetts.

Please address correspondence to Mayank Goyal, MD, FRCPC, Department of Radiology, Seaman Family MR Research Centre, Foothills Medical Centre, 1403 29th St NW, Calgary AB T2N2T9, Canada; e-mail: mgoyal@ucalgary.ca

<http://dx.doi.org/10.3174/ajnr.A5481>

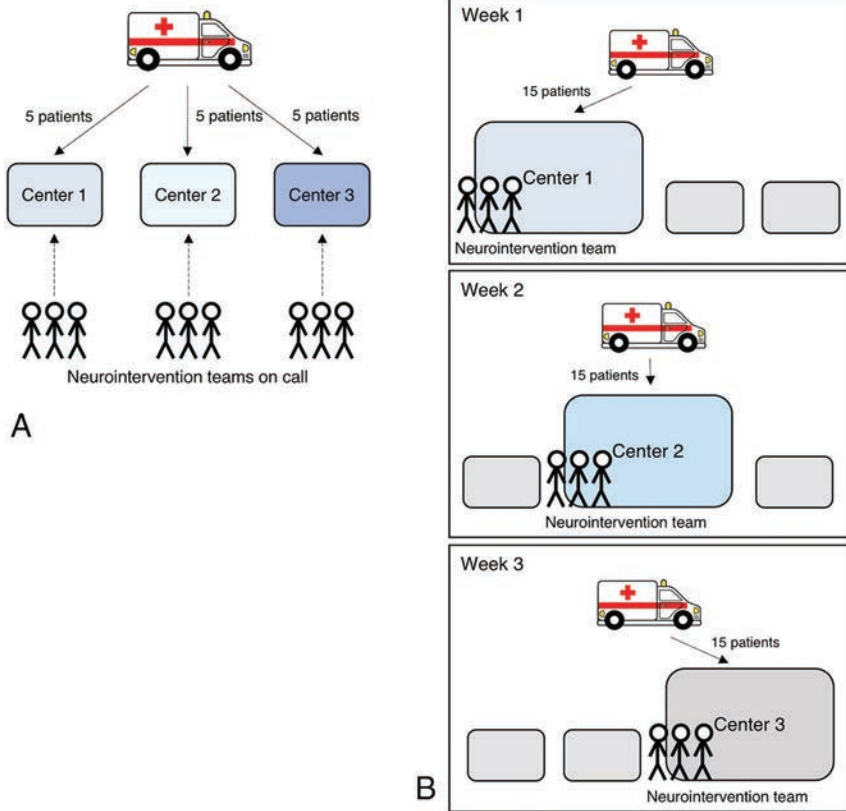


FIGURE. Schematic demonstrating different approaches to the neurointervention service for acute stroke in a community. *A*, In an isolationist setting, each stroke center has its own call schedule and receives patients. The patient volume is divided among the centers. Nearly all components of the neurointervention team are called from home. *B*, In a more cooperative setting, a call schedule is shared among the 3 centers and parts of the neurointervention team are in-house (eg, angiography nurse and technologist, stroke fellow/nurse practitioner) when that center is the active center. The active center receives a higher patient volume, making use of the neurointervention team more effective. The presence of an in-house team allows better workflow and increased efficiency. It is likely that stroke patients who are not eligible for endovascular thrombectomy (intracranial hematoma, no large-vessel occlusion) will also receive better care. Note that the total volume of patients treated by each hospital remains unchanged.

When one starts thinking this way, the obvious conclusion is to have a shared city- or jurisdiction-wide call schedule (Figure). This could be communicated well in advance to the paramedic staff so that they could determine where to bring the patient on the basis of a predetermined call schedule. In jurisdictions where many patients are brought directly to the hospital by family and friends, an alternative approach could be for the neurointerventionist on call to have privileges in all the relevant hospitals and to therefore travel to the patient. There are simple solutions to overcome the variances of catheterization laboratory setup and individual choices of tools: Physicians could carry a Brisk Recanalization Ischemic Stroke Kit (BRISK) in their cars and walk in with all the tools they need.⁹ Of course, establishing such a system will require cooperation and trust; however, this is easier to achieve

when one is backed by a Nobel-winning mathematician's math and game theory. Is it time to start this discussion?

Disclosures: Mayank Goyal—UNRELATED: Consultancy: Medtronic, Stryker, MicroVention, Comments: teaching engagements and product advice regarding acute stroke; Grants/Grants Pending: Medtronic, Stryker, Comments: Medtronic funding for HERMES collaboration provided to the University of Calgary, Stryker funding for UNMASK EVT provided to the University of Calgary*; Patents (Planned, Pending or Issued): GE Healthcare, Comments: Systems of Stroke Diagnosis. David Turkeltaub—UNRELATED: Consultancy: Alpha Insights; Travel/Accommodations/Meeting Expenses Unrelated to Activities Listed: Stryker. Joshua A. Hirsch—UNRELATED: Consultancy: Medtronic, Globus, Codman Neurovascular, Whale Imaging; Other Relationships: I am the recipient of a grant from the Neiman Policy Institute, where I serve as a senior affiliate research fellow. *Money paid to the institution.

REFERENCES

1. John Nash Jr.—Biographical. https://www.nobelprize.org/nobel_prizes/economic-sciences/laureates/1994/nash-bio.html. Accessed September 18, 2017
2. Nash JF. **Equilibrium points in N-person games.** *Proc Natl Acad Sci U S A* 1950;36:48–49 CrossRef Medline
3. Nash JF. **Non-cooperative games.** *The Annals of Mathematics* 1951;54:286–95 CrossRef
4. Dufwenberg M. **Game theory.** *Wiley Interdiscip Rev Cogn Sci* 2011;2:167–73 CrossRef Medline
5. Goyal M, Menon BK, van Zwam WH, et al; HERMES collaborators. **Endovascular thrombectomy after large-vessel ischaemic stroke: a meta-analysis of individual patient data from five randomised trials.** *Lancet* 2016;387:1723–31 CrossRef Medline
6. Goyal M, Jadhav AP, Wilson AT, et al. **Shifting bottlenecks in acute stroke treatment.** *J Neurointerv Surg* 2016;8:1099–100 CrossRef Medline
7. Saposni G, Johnston SC. **Applying principles from the game theory to acute stroke care: learning from the prisoner's dilemma, stag-hunt, and other strategies.** *Int J Stroke* 2016;11:274–86 CrossRef Medline
8. Menon BK, Sajobi TT, Zhang Y, et al. **Analysis of workflow and time to treatment on thrombectomy outcome in the Endovascular Treatment for Small Core and Proximal Occlusion Ischemic Stroke (ESCAPE) randomized, controlled trial.** *Circulation* 2016;133:2279–86 CrossRef Medline
9. Goyal M, Menon BK, Hill MD, et al. **Consistently achieving computed tomography to endovascular recanalization <90 minutes: solutions and innovations.** *Stroke* 2014;45:e252–56 CrossRef Medline

MR Perfusion to Determine the Status of Collaterals in Patients with Acute Ischemic Stroke: A Look Beyond Time Maps

 K. Nael,  A. Doshi,  R. De Leacy,  J. Puig,  M. Castellanos,  J. Bederson,  T.P. Naidich,  J. Mocco, and  M. Wintermark



ABSTRACT

BACKGROUND AND PURPOSE: Patients with acute stroke with robust collateral flow have better clinical outcomes and may benefit from endovascular treatment throughout an extended time window. Using a multiparametric approach, we aimed to identify MR perfusion parameters that can represent the extent of collaterals, approximating DSA.

MATERIALS AND METHODS: Patients with anterior circulation proximal arterial occlusion who had baseline MR perfusion and DSA were evaluated. The volume of arterial tissue delay (ATD) at thresholds of 2–6 seconds ($ATD^{2-6 \text{ seconds}}$) and >6 seconds ($ATD^{>6 \text{ seconds}}$) in addition to corresponding values of normalized CBV and CBF was calculated using VOI analysis. The association of MR perfusion parameters and the status of collaterals on DSA were assessed by multivariate analyses. Receiver operating characteristic analysis was performed.

RESULTS: Of 108 patients reviewed, 39 met our inclusion criteria. On DSA, 22/39 (56%) patients had good collaterals. Patients with good collaterals had significantly smaller baseline and final infarct volumes, smaller volumes of severe hypoperfusion ($ATD^{>6 \text{ seconds}}$), larger volumes of moderate hypoperfusion ($ATD^{2-6 \text{ seconds}}$), and higher relative CBF and relative CBV values than patients with insufficient collaterals. Combining the 2 parameters into a Perfusion Collateral Index (volume of $ATD^{2-6 \text{ seconds}} \times$ relative $CBV^{2-6 \text{ seconds}}$) yielded the highest accuracy for predicting collateral status: At a threshold of 61.7, this index identified 15/17 (88%) patients with insufficient collaterals and 22/22 (100%) patients with good collaterals, for an overall accuracy of 94.1%.

CONCLUSIONS: The Perfusion Collateral Index can predict the baseline collateral status with 94% diagnostic accuracy compared with DSA.

ABBREVIATIONS: ASITN = American Society of Interventional and Therapeutic Neuroradiology; ATD = arterial tissue delay; PCI = Perfusion Collateral Index; rCBF = relative cerebral blood flow; rCBV = relative cerebral blood volume; ROC = receiver operating characteristic; Tmax = time-to-maximum

In patients with acute ischemic stroke, the status of collateral blood supply can be an independent predictor of reperfusion success and can impact the clinical outcome.^{1,2} In addition, promising data suggest that good collateral status can prolong the

time that tissue-at-risk remains salvageable,³⁻⁵ which, in turn, may allow extension of the therapeutic window. Therefore, noninvasive evaluation of the collateral blood supply may be helpful in identifying patients who may benefit from endovascular thrombectomy.

Noninvasive imaging of collateral status can be assessed by direct visualization of the collateral vessels with CTA^{6,7} or MRA^{8,9} or by the assessment of the efficiency of collateral perfusion with CT perfusion^{10,11} or MR perfusion.¹²⁻¹⁴ These techniques are complementary: CTA and MRA provide anatomic information about collateral vessels, while perfusion techniques provide functional and circulatory information on leptomeningeal and secondary collateral pathways.¹⁵ Although various perfusion parameters have been used to measure collateral status, specific perfusion criteria to assess collateral status have yet to be defined. Most research has focused on time-based perfusion maps, assuming that patients with good collaterals have less severe delays¹² and larger perfusion delay volumes.^{13,16} Some investigators have also looked into using CBV and CBF from raw perfusion data to assess collateral status.^{12,17}

Received June 11, 2017; accepted after revision September 14.

From the Departments of Radiology (K.N., A.D., T.P.N.) and Neurosurgery (R.D.L., J.B., J.M.), Icahn School of Medicine at Mount Sinai, New York, New York; Department of Radiology (J.P.), Girona Biomedical Research Institute, Diagnostic Imaging Institute, Hospital Universitari Dr Josep Trueta, Girona, Spain; Department of Neurology (M.C.), A Coruña University Hospital, A Coruña Biomedical Research Institute, A Coruña, Spain; and Department of Radiology (M.W.), Neuroradiology Section, Stanford University, Palo Alto, California.

This article has not been submitted or published elsewhere in whole or in part, except as an abstract (oral presentation, No. A61) at: 2016 International Stroke Conference, February 16–19, 2016; Los Angeles, California; and as an oral presentation at: Radiological Society of North America 102nd Scientific Assembly and Annual Meeting, November 27–December 2, 2016; Chicago, Illinois.

Please address correspondence to Kambiz Nael, MD, Department of Radiology, Icahn School of Medicine at Mount Sinai, One Gustave L. Levy Place, Box 1234, New York, NY 10029-6574; e-mail: Kambiznael@gmail.com; @kambiznael

 Indicates open access to non-subscribers at www.ajnr.org

<http://dx.doi.org/10.3174/ajnr.A5454>

In this study, we hypothesized that MR perfusion time maps, which show only delayed perfusion, are insufficient to predict the status of collaterals if used alone. By applying a multiparametric approach, we aimed to identify perfusion parameters that can represent the extent of collaterals, approximating DSA.

MATERIALS AND METHODS

Patients

Patients with anterior circulation acute ischemic stroke who presented within 9 hours of symptom onset and who were considered for revascularization treatment were retrospectively reviewed under an approved institutional review board protocol. Inclusion criteria were the following: 1) large unilateral proximal arterial occlusion (internal carotid or proximal middle cerebral artery), 2) baseline MR imaging including DSC perfusion and DSA, and 3) follow-up imaging to determine the final infarction volume. Patients were excluded if DSC perfusion was nondiagnostic or DSA studies did not allow adequate evaluation of collaterals.

We recorded clinical data, including patient age, sex, baseline NIHSS scores, time from stroke onset, time from onset to groin puncture, and treatment type, including intravenous tissue plasminogen activator (IV tPA) and/or mechanical thrombectomy when available.

Image Analysis

DWI was acquired using a single-shot spin-echo EPI sequence with following parameters: TR/TE, 4900/98 ms; flip angle, 90°; FOV, 22 × 22 cm; matrix, 128 mm; sections, 30 × 5 mm. Diffusion gradients were applied along 6 noncollinear directions with b-values of 0 and 1000 s/mm², resulting in a 51-second acquisition time. DSC perfusion was performed with a single-shot gradient-echo EPI sequence with the following parameters: TR/TE, 1450/22 ms; flip angle, 90°; FOV, 22 × 22 cm; matrix, 128 mm; sections, 30 × 4 mm. Sixty dynamic frames were obtained during a 90-second acquisition time. A generalized autocalibrating partially parallel acquisition technique with an acceleration factor of 2 was used for both DWI and DSC.

DSC perfusion was processed with US Food and Drug Administration–approved software (Olea Sphere; Olea Medical, La Ciotat, France) by applying a Bayesian probabilistic method.¹⁸ Bayesian is a delay-insensitive probabilistic method in which the Bayes rule is applied to combine experimental perfusion data and a priori information about the parameters, to compute a posteriori probability distribution functions for every parameter of interest. From these distributions, parameter estimates and errors on those estimates can be derived (eg, the mean and SD of the posteriori distributions). Arterial tissue delay (ATD), defined as time-to-maximum of the Bayesian-estimated tissue residue function, CBF, and CBV, was generated. The software used a 6-*df* transformation and a mutual information cost function to coregister DWI and all perfusion maps for each patient. DSC maps were normalized to an ROI placed in normal-appearing white matter in the centrum semiovale, contralateral to the infarct side, to calculate the ratios for CBV and CBF values.

Because ATD is essentially a Bayesian-estimated time-to-maximum (Tmax), previously used time-delay thresholds of 2

and 6 seconds^{12,13,19} were used to differentiate brain tissue perfusion properties. ATD > 2 seconds defined any visually perceptible delayed perfusion, and ATD maps with thresholds of 2 and 6 seconds were generated. We applied the following designations: 1) Tissue with ATD > 6 seconds was defined as having severe delayed perfusion; 2) tissue with 2 seconds < ATD ≤ 6 seconds was defined as having moderately delayed perfusion.

Subsequently, a VOI from the above-described ATD maps was calculated using a voxel-based signal intensity threshold method subsuming the entire region of hypoperfusion within the defined threshold. The volume of each VOI and its corresponding relative cerebral blood flow (rCBF) and relative cerebral blood volume (rCBV) were calculated for each patient. Assuming that most blood volume in the moderate hypoperfused tissue is likely via collaterals, we calculated a new perfusion index as the Perfusion Collateral Index (PCI), defined as the volume of moderately hypoperfused tissue (ATD^{2–6 seconds}) multiplied by its corresponding mean rCBV (PCI = Volume of ATD^{2–6 seconds} × rCBV^{2–6 seconds}).

We defined the baseline infarct volume as the volume of tissue with an apparent diffusion coefficient < 600 × 10⁻⁶ mm²/s on the baseline MR diffusion images.²⁰ Final infarct volume was calculated from the follow-up imaging (obtained within 7 days from the initial imaging) using the volume of FLAIR-hyperintense tissue or CT-hypodense tissue.

DSA Analysis

Angiographic collateral grading was performed with the American Society of Interventional and Therapeutic Neuroradiology (ASITN)/Society of Interventional Radiology Collateral Flow Grading System on baseline angiography (ASITN grades 0–4)²¹: grade 0: no collaterals visible; grade 1: slow collaterals to the periphery of the ischemic site with persistence of some of the defect; grade 2: rapid collaterals to the periphery of the ischemic site with persistence of some of the defect; grade 3: collaterals with slow-but-complete angiographic blood flow of the ischemic bed by the late venous phase; and grade 4: complete and rapid collateral blood flow to the vascular bed in the entire ischemic territory by retrograde perfusion.

Patients were dichotomized to those with good collaterals (ASITN grades 3 and 4) and insufficient collaterals (ASITN grades 0, 1, and 2). Primary revascularization following mechanical thrombectomy was assessed with the TICI scale.²² Data were dichotomized with TICI ≥ 2b as an indication of successful revascularization.

Statistical Analysis

Baseline characteristics and neuroimaging variables were compared between subjects with insufficient-versus-good collaterals using the Fisher exact and Wilcoxon rank sum tests as appropriate. For multivariate analysis, a Classification Tree (binary recursive partition) model was used to simultaneously evaluate all (*n* = 12) included imaging (baseline infarction volume, final infarction volume, ATD^{>6 seconds}, ATD^{2–6 seconds}, rCBF, rCBV, and PCI) and clinical (age, sex, baseline NIHSS score, IV tPA administration, time-to-groin puncture from last known well) parameters of insufficient-versus-good collaterals.

Table 1: Baseline and clinical data in patients with insufficient-versus-good collateral flow

Variable	Overall (n = 39)	Good Collaterals (n = 22)	Insufficient Collaterals (n = 17)	P Value
Age (mean) (SD) (yr)	63.3 (13.3)	62.8 (15.3)	63.9 (10.2)	.85
Sex (M/F)	(22:17)	(11:11)	(11:6)	.52
Baseline NIHSS score (median) (IQR)	17, 14–19	16, 13–18	18, 15–20	.19
IV tPA (No.) (%)	18 (46%)	10 (45%)	8 (47%)	.45
Hr to groin puncture from last known well (median) (IQR)	6.10, 5.54–7.14	5.98, 5.67–7.54	6.08, 5.27–7.10	.93
Hr from MRI to groin puncture (median) (IQR) ^a	1.40, 0.80–2.20	1.10, 0.70–1.75	1.5, 0.90–2.14	.58

Note:—IQR indicates interquartile range.

^a Subset analysis (only available for 20 patients, 13 patients with good collaterals and 7 patients with insufficient collaterals).

Table 2: Imaging data in patients with insufficient-versus-good collateral flow

Variable	Good Collaterals (n = 22)	Insufficient Collaterals (n = 17)	P Value
Baseline infarct volume (mean) (SD)	29.7 (18.7)	48.3 (30.0)	.021 ^a
Final infarct volume (mean) (SD)	51.1 (32.4)	81.0 (44.7)	.030 ^a
ATD ^{>6 s} (vol) (mean) (SD)	24.7 (17.4)	42.4 (18.2)	.004 ^a
ATD ^{2–6 s} (vol) (mean) (SD)	64.6 (25.0)	28.2 (17.1)	<.001 ^a
rCBF ^{2–6 s} (mean) (SD)	1.16 (0.18)	0.98 (0.25)	.026 ^a
rCBV ^{2–6 s} (mean) (SD)	1.92 (0.32)	1.17 (0.38)	<.001 ^a
PCI (mean) (SD)	120.70 (47.6)	36.0 (25.8)	<.001 ^a
Primary revascularization (DSA-TICI) (No.) (%) ^b	12 (54.5)	5 (29.4)	.190

Note:—vol indicates volume.

^a Significant.

^b Primary revascularization based on the outcome of thrombectomy, dichotomized to 0 and 1 using TICI \geq 2b.

Accuracy statistics were computed with a nonparametric receiver operating characteristic (ROC) analysis. Thresholds for separating insufficient from good collaterals were chosen to maximize the unweighted overall accuracy, defined as the weighted average of the percentage of insufficient and good collateral vessels. Sensitivity, specificity, overall accuracy defined as (sensitivity + specificity) / 2, and the area under the ROC curve were reported. The significance level was set at $P = .05$ in our statistical analysis.

RESULTS

Among 108 charts reviewed, 39 patients met our inclusion criteria. In 61 patients, baseline DSA was inadequate to provide a score of collateral vessels (lack of an adequate number of phases and injections). Eight patients were excluded due to inadequate and nondiagnostic MR perfusion data. Of those patients included in the analysis, 22 were men, 17 were women (mean age, 63.3 years; range, 37–85 years). The median and interquartile range of the NIHSS scores were 17 and 14–19. Five patients had distal internal carotid occlusion, and 34 patients had proximal MCA occlusion. Twenty-two (56%) patients were classified as having good collaterals defined by ASITN \geq 3 on baseline conventional angiography.

Clinical Data

Demographic data and basic clinical information for patients with insufficient-versus-good collaterals are provided in Table 1. Among the 39 patients included, 18 (46%) received IV tPA before undergoing conventional angiography. Administration of IV tPA was not significantly different ($P = .45$) between patients with good (10/22, 45%) versus insufficient collaterals

(8/17, 47%) (Table 1). The time gap between MR imaging and DSA was not significantly different between patients with good collaterals (mean, 100 ± 45 minutes) versus insufficient collaterals (mean, 128 ± 39 minutes). Endovascular treatment was performed with a Merci retriever (Concentric Medical, Mountain View, California) catheter ($n = 12$) or the Penumbra (Penumbra, Alameda, California) suction thrombectomy catheter ($n = 16$) and stent retrieval device ($n = 11$).

Imaging Data

Univariate analysis showed significantly smaller baseline infarction volume, final infarction volume, and volume of severe (ATD^{>6 seconds}) delayed perfusion in patients with good collaterals (Table 2). On the other hand, rCBF, rCBV, PCI, and the volume of moderate (ATD^{2–6 seconds}) delayed perfusion were significantly higher in patients with good collaterals (Table 2). The rate of primary postprocedural revascularization did not differ significantly between the 2 groups (Table 2). Figs 1 and 2 show examples of our image analysis in 2 patients with right proximal MCA occlusion; one had good and the other had insufficient collaterals, respectively.

The Classification Tree (binary recursive partition) model in the simultaneous evaluation of all 12 included predictive parameters of insufficient-versus-good collaterals showed that the 2 best single parameters with the highest predictive ability were rCBV^{2–6 seconds} and volume of moderate (ATD^{2–6 seconds}) hypoperfusion, with an overall diagnostic accuracy of 85% and 82.1%, respectively. Both rCBV^{2–6 seconds} (at a threshold of >1.6) and volume of ATD^{2–6 seconds} (at a threshold of >38.28 mL) could identify 18/22 (81.8%) patients with good collaterals when used alone. A combination of the 2 parameters used in our newly defined Perfusion Collateral Index (Volume of ATD^{2–6 seconds} \times rCBV^{2–6 seconds}) resulted in improved predictive accuracy over each measure alone to correctly identify all 22 patients (100%) with good collaterals. Model accuracy statistics, including sensitivity, specificity, overall accuracy, and area under the ROC curve in addition to the optimal threshold for the variables that reached statistical significance, are reported in Table 3. In further analysis of our Classification Tree model, a combination of PCI and baseline infarction volume showed further improvement in predictive accuracy, providing the best tree model with a nominal (not validated) 100% accuracy and ROC area = 1.0 (Fig 3).

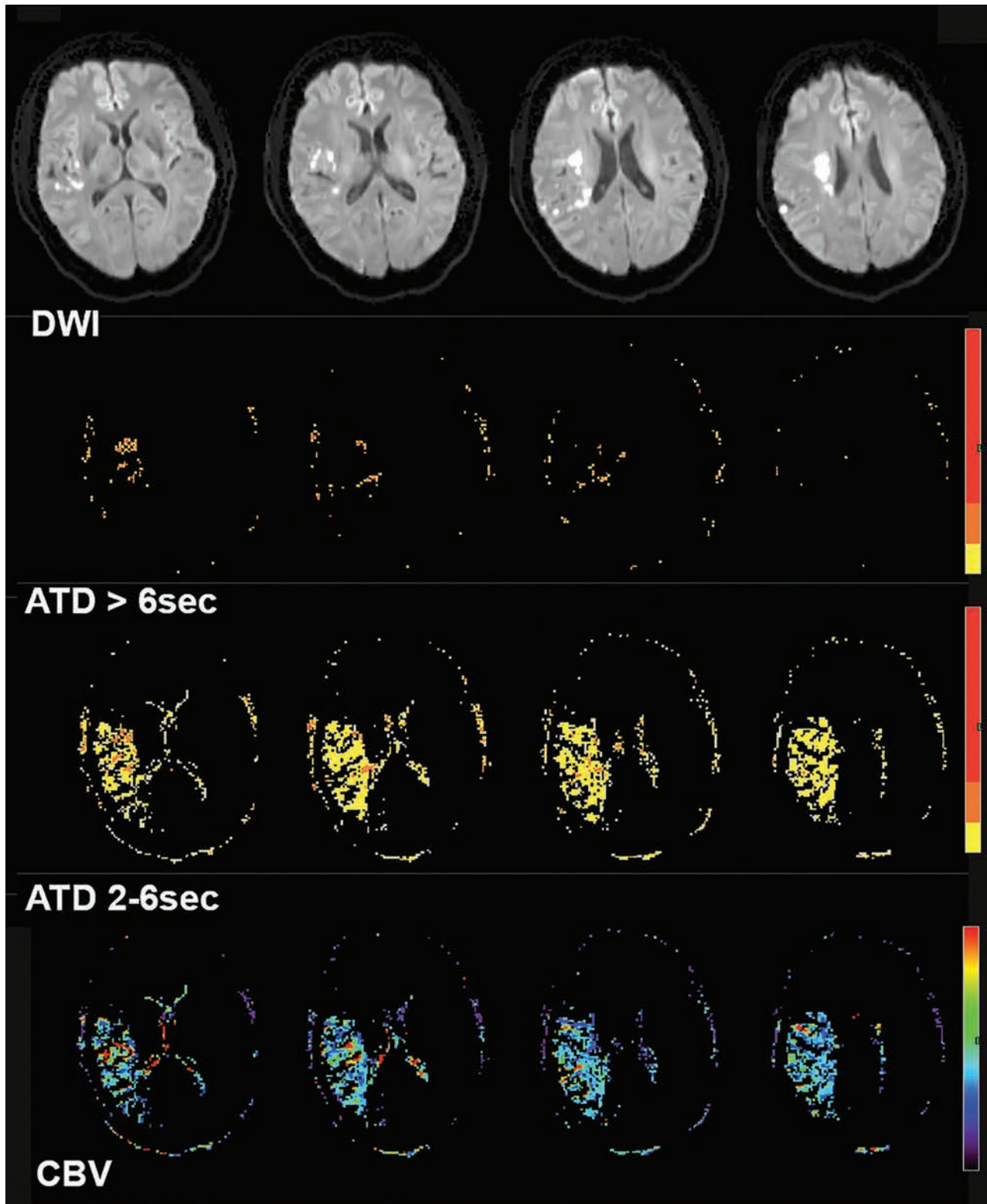


FIG 1. A 61-year-old woman with left hemiparesis who had right MCA (M1) occlusion (not shown) but sufficient collaterals on baseline conventional angiography. DWI shows right MCA territorial infarction. Processed perfusion maps show 3.5 mL of severe ($ATD^{>6 \text{ seconds}}$) hypoperfusion, 42 mL of moderate ($ATD^{2-6 \text{ seconds}}$) hypoperfusion, and a mean $rCBV^{2-6 \text{ seconds}}$ of 1.7 within the hypoperfused area. The Perfusion Collateral Index is $42 \times 1.7 = 71.4$.

DISCUSSION

In this study, we showed that multiparametric MR perfusion enables accurate assessment of collateral status in patients with anterior circulation proximal arterial occlusion who may be candi-

dates for endovascular revascularization. By incorporating $rCBV$ in addition to commonly used perfusion time maps, we defined the Perfusion Collateral Index as a new perfusion parameter superior to other baseline imaging variables to predict the status of

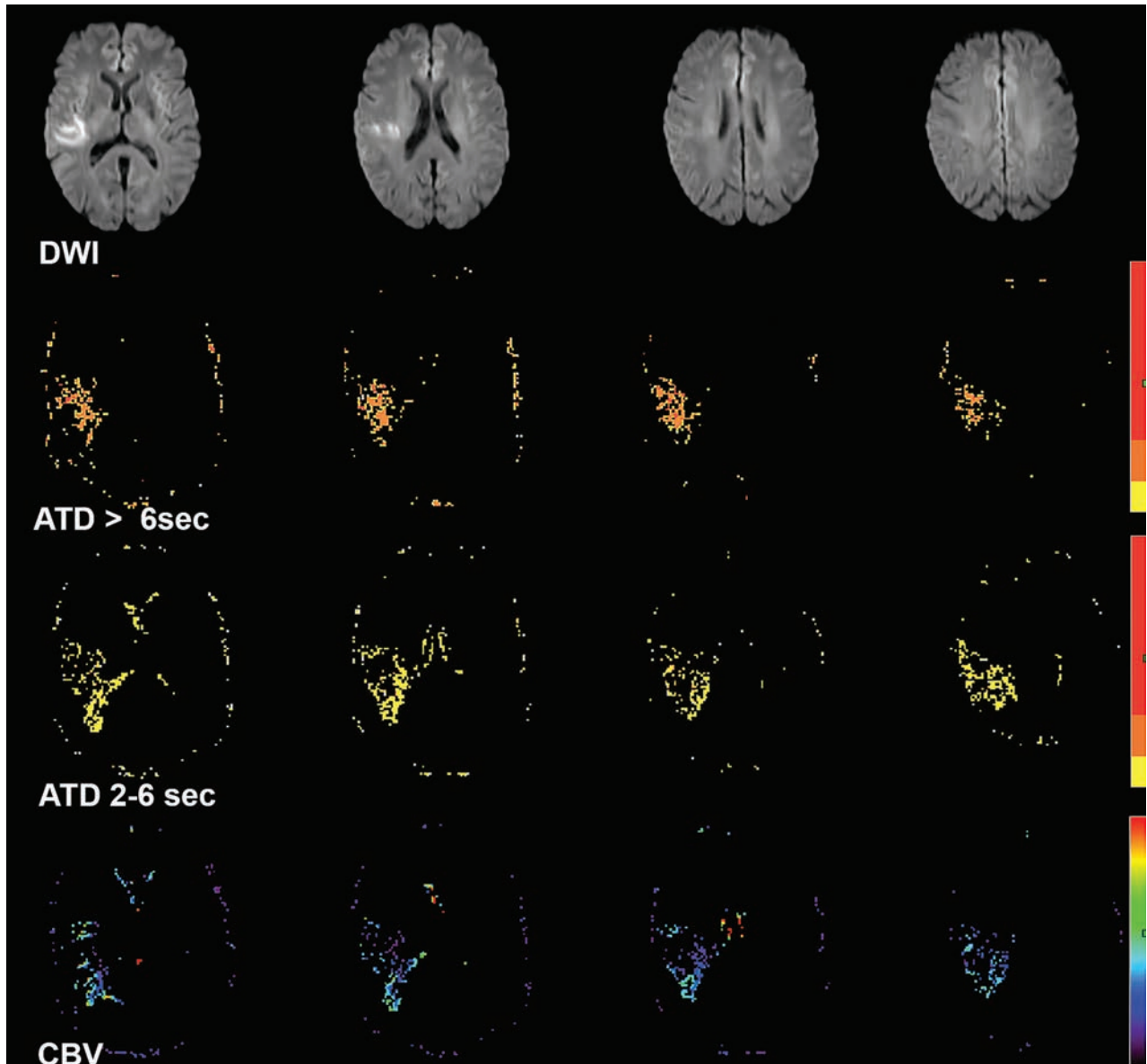


FIG 2. A 70-year-old woman with left paresis who had right MCA (M1) occlusion (not shown) and insufficient collaterals on baseline conventional angiography. DWI showed right MCA territorial infarction. Processed perfusion maps show 17 mL of severe ($ATD^{>6 \text{ seconds}}$) hypoperfusion, 20 mL of moderate ($ATD^{2-6 \text{ seconds}}$) hypoperfusion, and a mean $rCBV^{2-6 \text{ seconds}}$ of 0.9 within the hypoperfused area. The perfusion collateral index is $20 \times 0.9 = 18$.

Table 3: Optimal threshold, sensitivity, specificity, overall accuracy, and ROC area imaging variables that were significant with univariate analysis

Variable	Threshold	Specificity	Sensitivity	Overall Accuracy	ROC Area
Base infarct volume (mL)	24.1	76.5%	63.6%	70.1%	0.717
Final infarct volume (mL)	45	82.4%	59.1%	70.7%	0.706
Volume of $ATD^{>6 \text{ s}}$ (mL)	27.77	88.2%	63.6%	75.9%	0.777
Volume of $ATD^{2-6 \text{ s}}$ (mL)	38.28	82.4%	81.8%	82.1%	0.906
rCBF	1	58.8%	90.9%	74.9%	0.709
$rCBV^{2-6 \text{ s}}$	1.6	88.2%	81.8%	85.0%	0.900
PCI ^a	61.70	88.2%	100.0%	94.1%	0.973

^a PCI = Volume of $ATD^{2-6 \text{ seconds}} \times rCBV^{2-6 \text{ seconds}}$.

collaterals with a diagnostic accuracy of 94% in comparison with baseline DSA.

There are several studies on the use of MR perfusion for assessing the collateral status in patients with acute ischemic

stroke with predominant focus on the use of perfusion time maps. In 2008, Bang et al⁵ showed that patients with good collaterals had a larger volume of mild ($2 \text{ seconds} \leq T_{\text{max}} < 4 \text{ seconds}$) delayed perfusion, but they found no relationship between collateral status and perfusion-diffusion mismatch using $T_{\text{max}} \geq 4 \text{ seconds}$. Later, in 2013, Campbell et al¹² showed that better baseline collateral flow measured by

digitally subtracted perfusion MR imaging was associated with a larger diffusion-perfusion mismatch using $T_{\text{max}} > 6 \text{ seconds}$. In 2014, good collateral status was shown to be associated with a smaller volume of severe hypoperfusion using

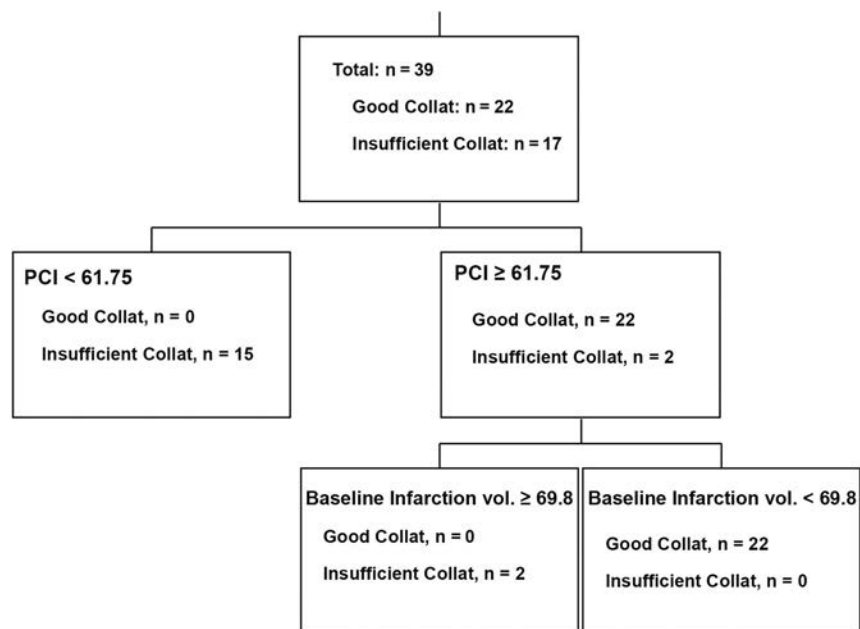


FIG 3. The Classification Tree model using a combination of the PCI (Volume of $ATD^{2-6 \text{ seconds}} \times rCBV^{2-6 \text{ seconds}}$) and baseline infarction volume provides a nominal (not validated) 100% accuracy and ROC area = 1.0.

$T_{max} \geq 6 \text{ seconds}$ ¹³ and $ATD \geq 6 \text{ seconds}$.¹⁹ Later, Olivot et al²³ showed that a smaller hypoperfusion intensity ratio (defined as the proportion of $T_{max} > 6$ -second lesion volume with a $T_{max} > 10$ -second delay) was associated with good collateral status. Most interesting, in 2015, by applying a probabilistic method, Lee et al¹⁴ showed that good collaterals were associated with more severe delayed perfusion with a T_{max} of 16–22 seconds.

In our study, in addition to commonly used perfusion time maps, we incorporated additional information obtained via rCBV to improve our prediction of collateral status. The hallmarks of collateral perfusion are delay and dispersion.²⁴ Perfusion deficits noted on MR perfusion time maps (such as T_{max}) encompass both delayed perfusion due to underlying arterial occlusion and delayed flow via collateral circulation. The addition of CBV to routinely used time maps may provide information regarding the amount of blood flow to the ischemic region of the brain (dispersion component); although the arterial source of sustained perfusion may not be evident, in the presence of large arterial occlusion, most of it will be from the collateral circulation.

We showed that in the presence of proximal arterial occlusion, rCBV provides essential information about the status of collaterals and is insightful concerning the distribution and dispersion of collateral flow, a component that may be overlooked using perfusion time maps alone. We showed that mean rCBV values calculated from the region with moderate hypoperfusion have an overall diagnostic performance (85%) similar to that of the volume of $ATD^{2-6 \text{ seconds}}$ (82.1%) for predicting good baseline collaterals. However, when used in combination with our newly defined PCI (Volume of $ATD^{2-6 \text{ seconds}} \times rCBV^{2-6 \text{ seconds}}$), it further improved the overall diagnostic performance to 94.1%. This translated into identifying 4 additional (20%) patients

with good collaterals who were falsely categorized by rCBV or a volume of $ATD^{2-6 \text{ seconds}}$ alone.

Our results also showed that a larger volume of moderate ($ATD^{2-6 \text{ seconds}}$) hypoperfusion is a better indicator of good baseline collateral status, with higher specificity (81.8%) compared with a smaller volume of severe ($ATD^{>6 \text{ seconds}}$) hypoperfusion (specificity of 63.6%). This finding is interesting and somewhat different from prior reports in which a better association between good collateral status and a smaller volume of severe hypoperfusion has been shown using $T_{max} > 6 \text{ seconds}$.^{12,13,23} This may be explained by intrinsic technical differences between Bayesian-estimated ATD and singular value decomposition-estimated T_{max} .

To increase the broad acceptance of perfusion imaging in the stroke neurology community, further improve-

ment of methodology in image postprocessing is required, especially when dealing with a noisy imaging environment such as DSC perfusion. In this study, we used ATD rather than T_{max} to take advantage of inherent noise-resistance behavior of the Bayesian postprocessing. Although Bayesian-derived ATD is equivalent to deconvolution-derived T_{max} in terms of definition (maximum time-to-peak of the residue function), they do not share the same properties. The Bayesian method is a robust probabilistic method that minimizes effects of oscillation, tracer delay, and low SNR during residue function estimation compared with other deconvolution methods.^{18,25} The inherent delay insensitivity of the Bayesian technique is essential for accurate evaluation of the perfusion time delay to minimize the effect of existing underlying arterial occlusion.²⁶ In addition, simulation studies in agreement with the recommendations from the Acute Stroke Research Imaging Roadmap II²⁷ have shown highly reproducible and accurate data for ATD estimation.¹⁸ A follow-up study between ATD and T_{max} -estimated PCI may be helpful for exploring potential differences between these techniques.

Our study has several limitations. First, we acknowledge potential selection bias associated with retrospective studies. Second, our small sample size may affect some part of our results. For example, we showed that patients with good baseline collaterals tend to have a higher recanalization rate, but this trend was not statistically significant ($P = .19$), which may have been a function of the small sample size. In our Classification Tree model, combining PCI and baseline infarct volume yielded a nominal accuracy of 100% (Fig 3). However, this result must be interpreted in the context of our small sample, and like any predictive model, our results need to be validated in a large prospective cohort. Finally, we excluded 61 patients due to inadequate DSA data for collateral scoring. This is an inevitable challenge in acute ischemic

stroke because performing a complete diagnostic angiography for collateral assessment poses a delay in treatment. This further highlights the need for development of an advanced noninvasive collateral grading system such as ours from which accurate collateral status may be imputed. To establish the accuracy of our perfusion parameters, we had to compare our results with the current standard of reference (DSA). It is, however, plausible that perfusion imaging may outperform rough collateral grading obtained from 2D DSA as shown by prior reports.¹²

CONCLUSIONS

Using a multiparametric MR imaging approach, we identified the Perfusion Collateral Index, defined as $\text{Volume of ATD}^{2-6 \text{ seconds}} \times \text{rCBV}^{2-6 \text{ seconds}}$, as a new perfusion parameter that provides accurate noninvasive estimation of baseline collateral status with a diagnostic accuracy of 94% compared with DSA. If its potential is realized, the PCI can be used to accurately identify patients with good collaterals, potentially extending the treatment window and increasing the number of patients who may benefit from endovascular treatment in the current era of endovascular therapy.

Disclosures: Kambiz Nael—UNRELATED: Board Membership: Olea Medical, Comments: Medical Advisory Board; Consultancy: Olea Medical. Thomas Naidich—UNRELATED: Consulting Fee or Honorarium: Elsevier. J Mocco—UNRELATED: Consultancy: Rebound Medical, EndoStream, Synchron, Cerebrotech Medical; Other: Apama, The Stroke Project, EndoStream, Synchron, Cerebrotech Medical, Neurvana, NeuroTechnology Investors, Comments: investment. Max Wintermark—UNRELATED: Board Membership: GE-NFL Advisory Board.

REFERENCES

- Bang OY, Saver JL, Kim SJ, et al. **Collateral flow predicts response to endovascular therapy for acute ischemic stroke.** *Stroke* 2011;42:693–99 CrossRef Medline
- Liebeskind DS, Tomsick TA, Foster LD, et al; IMS III Investigators. **Collaterals at angiography and outcomes in the Interventional Management of Stroke (IMS) III trial.** *Stroke* 2014;45:759–64 CrossRef Medline
- Jung S, Gilgen M, Slotboom J, et al. **Factors that determine penumbral tissue loss in acute ischaemic stroke.** *Brain* 2013;136:3554–60 CrossRef Medline
- Galimanis A, Jung S, Mono ML, et al. **Endovascular therapy of 623 patients with anterior circulation stroke.** *Stroke* 2012;43:1052–57 CrossRef Medline
- Bang OY, Saver JL, Buck BH, et al; UCLA Collateral Investigators. **Impact of collateral flow on tissue fate in acute ischaemic stroke.** *J Neurol Neurosurg Psychiatry* 2008;79:625–29 Medline
- Menon BK, O'Brien B, Bivard A, et al. **Assessment of leptomeningeal collaterals using dynamic CT angiography in patients with acute ischemic stroke.** *J Cereb Blood Flow Metabol* 2013;33:365–71 CrossRef
- Lima FO, Furie KL, Silva GS, et al. **The pattern of leptomeningeal collaterals on CT angiography is a strong predictor of long-term functional outcome in stroke patients with large vessel intracranial occlusion.** *Stroke* 2010;41:2316–22 CrossRef Medline
- Hernández-Pérez M, Puig J, Blasco G, et al. **Dynamic magnetic resonance angiography provides collateral circulation and hemodynamic information in acute ischemic stroke.** *Stroke* 2016;47:531–34 CrossRef Medline
- Ernst M, Forkert ND, Brehmer L, et al. **Prediction of infarction and reperfusion in stroke by flow- and volume-weighted collateral signal in MR angiography.** *AJNR Am J Neuroradiol* 2015;36:275–82 CrossRef Medline
- Shuaib A, Butcher K, Mohammad AA, et al. **Collateral blood vessels in acute ischaemic stroke: a potential therapeutic target.** *Lancet Neurol* 2011;10:909–21 CrossRef Medline
- Wintermark M, Rowley HA, Lev MH. **Acute stroke triage to intravenous thrombolysis and other therapies with advanced CT or MR imaging: pro CT.** *Radiology* 2009;251:619–26 CrossRef Medline
- Campbell BC, Christensen S, Tress BM, et al; EPITHET Investigators. **Failure of collateral blood flow is associated with infarct growth in ischemic stroke.** *J Cereb Blood Flow Metabol* 2013;33:1168–72 CrossRef Medline
- Marks MP, Lansberg MG, Mlynash M, et al; Diffusion and Perfusion Imaging Evaluation for Understanding Stroke Evolution 2 Investigators. **Effect of collateral blood flow on patients undergoing endovascular therapy for acute ischemic stroke.** *Stroke* 2014;45:1035–39 CrossRef Medline
- Lee MJ, Son JP, Kim SJ, et al. **Predicting collateral status with magnetic resonance perfusion parameters: probabilistic approach with a Tmax-derived prediction model.** *Stroke* 2015;46:2800–07 CrossRef Medline
- Keedy AW, Fischette WS, Soares BP, et al. **Contrast delay on perfusion CT as a predictor of new, incident infarct: a retrospective cohort study.** *Stroke* 2012;43:1295–301 CrossRef Medline
- Vagal A, Menon BK, Foster LD, et al. **Association between CT angiogram collaterals and CT perfusion in the Interventional Management of Stroke III Trial.** *Stroke* 2016;47:535–38 CrossRef Medline
- Kim SJ, Son JP, Ryoo S, et al. **A novel magnetic resonance imaging approach to collateral flow imaging in ischemic stroke.** *Ann Neurol* 2014;76:356–69 CrossRef Medline
- Boutelier T, Kudo K, Pautot F, et al. **Bayesian hemodynamic parameter estimation by bolus tracking perfusion weighted imaging.** *IEEE Trans Med Imaging* 2012;31:1381–95 CrossRef Medline
- Nicoli F, Scalzo F, Saver JL, et al; UCLA Stroke Investigators. **The combination of baseline magnetic resonance perfusion-weighted imaging-derived tissue volume with severely prolonged arterial-tissue delay and diffusion-weighted imaging lesion volume is predictive of MCA-M1 recanalization in patients treated with endovascular thrombectomy.** *Neuroradiology* 2014;56:117–27 CrossRef Medline
- Dardzinski BJ, Sotak CH, Fisher M, et al. **Apparent diffusion coefficient mapping of experimental focal cerebral ischemia using diffusion-weighted echo-planar imaging.** *Magn Reson Med* 1993;30:318–25 CrossRef Medline
- Higashida RT, Furlan AJ, Roberts H, et al; Technology Assessment Committee of the American Society of Interventional and Therapeutic Neuroradiology, Technology Assessment Committee of the Society of Interventional Radiology. **Trial design and reporting standards for intra-arterial cerebral thrombolysis for acute ischemic stroke.** *Stroke* 2003;34:e109–37 CrossRef Medline
- Tomsick T, Broderick J, Carrozella J, et al; Interventional Management of Stroke II Investigators. **Revascularization results in the Interventional Management of Stroke II trial.** *AJNR Am J Neuroradiol* 2008;29:582–87 CrossRef Medline
- Olivot JM, Mlynash M, Inoue M, et al; DEFUSE 2 Investigators. **Hypoperfusion intensity ratio predicts infarct progression and functional outcome in the DEFUSE 2 cohort.** *Stroke* 2014;45:1018–23 CrossRef Medline
- Liebeskind DS. **Collateral circulation.** *Stroke* 2003;34:2279–84 CrossRef Medline
- Mouridsen K, Friston K, Hjort N, et al. **Bayesian estimation of cerebral perfusion using a physiological model of microvasculature.** *Neuroimage* 2006;33:570–79 CrossRef Medline
- Sasaki M, Kudo K, Boutelier T, et al. **Assessment of the accuracy of a Bayesian estimation algorithm for perfusion CT by using a digital phantom.** *Neuroradiology* 2013;55:1197–203 CrossRef Medline
- Wintermark M, Albers GW, Broderick JP, et al. **Acute Stroke Imaging Research Roadmap II.** *Stroke* 2013;44:2628–39 CrossRef Medline

On the Reproducibility of Inversion Recovery Intravoxel Incoherent Motion Imaging in Cerebrovascular Disease

S.M. Wong, W.H. Backes, C.E. Zhang, J. Staals, R.J. van Oostenbrugge, C.R.L.P.N. Jeukens, and J.F.A. Jansen



ABSTRACT

BACKGROUND AND PURPOSE: Intravoxel incoherent motion imaging can measure both microvascular and parenchymal abnormalities simultaneously. The contamination of CSF signal can be suppressed using inversion recovery preparation. The clinical feasibility of inversion recovery–intravoxel incoherent motion imaging was investigated in patients with cerebrovascular disease by studying its reproducibility.

MATERIALS AND METHODS: Sixteen patients with cerebrovascular disease (66 ± 8 years of age) underwent inversion recovery–intravoxel incoherent motion imaging twice. The reproducibility of the perfusion volume fraction and parenchymal diffusivity was calculated with the coefficient of variation, intraclass correlation coefficient, and the repeatability coefficient. ROIs included the normal-appearing white matter, cortex, deep gray matter, white matter hyperintensities, and vascular lesions.

RESULTS: Values for the perfusion volume fraction ranged from 2.42 to 3.97×10^{-2} and for parenchymal diffusivity from 7.20 to 9.11×10^{-4} mm^2/s , with higher values found in the white matter hyperintensities and vascular lesions. Coefficients of variation were $<3.70\%$ in normal-appearing tissue and $<9.15\%$ for lesions. Intraclass correlation coefficients were good to excellent, showing values ranging from 0.82 to 0.99 in all ROIs, except the deep gray matter and cortex, with intraclass correlation coefficients of 0.66 and 0.54, respectively. The repeatability coefficients ranged from 0.15 to 0.96×10^{-2} and 0.10 to 0.37×10^{-4} mm^2/s for perfusion volume fraction and parenchymal diffusivity, respectively.

CONCLUSIONS: Good reproducibility of inversion recovery–intravoxel incoherent motion imaging was observed with low coefficients of variation and high intraclass correlation coefficients in normal-appearing tissue and lesion areas in cerebrovascular disease. Good reproducibility of inversion recovery–intravoxel incoherent motion imaging in cerebrovascular disease is feasible in monitoring disease progression or treatment responses in the clinic.

ABBREVIATIONS: CV = coefficient of variation; D = parenchymal diffusivity; f = perfusion volume fraction; ICC = intraclass correlation coefficient; IR = inversion recovery; IVIM = intravoxel incoherent motion; NAWM = normal-appearing white matter; RC = repeatability coefficient

Perfusion imaging using an exogenous contrast agent is commonly used in the clinic in patients with cerebrovascular diseases.^{1,2} This technique is sensitive to the microcirculatory con-

dition and provides insight into the cerebral hemodynamics in, for example, patients with ischemic stroke. Because this technique is contraindicated in patients with impaired renal function, there is interest in techniques that avoid contrast agents. For example, by labeling endogenous blood as a tracer, arterial spin-labeling has been used to measure perfusion. However, this technique is associated with low signal-to-noise ratios and is dependent on the arterial transit time. Changes in flow conditions due to disease (eg, stroke) can complicate selecting the correct arterial transit time.³ Another technique without the use of a contrast agent that has received attention is intravoxel incoherent motion (IVIM) imaging. IVIM is a DWI technique that measures the diffusion properties of water molecules in static tissue and in blood flowing into the capillary networks. Therefore, it can measure perfusion and diffusion properties in the brain simultaneously.⁴ The resulting perfusion volume fraction (f) and parenchymal diffusivity (D)

Received June 4, 2017; accepted after revision October 3.

From the Departments of Radiology and Nuclear Medicine (S.M.W., W.H.B., C.R.L.P.N.J., J.F.A.J.), Neurology (C.E.Z., J.S., R.J.v.O.), School for Mental Health and Neuroscience (S.M.W., W.H.B., C.E.Z., R.J.v.O., J.F.A.J.), and Cardiovascular Research Institute Maastricht (C.E.Z., J.S., R.J.v.O.), Maastricht University Medical Centre, Maastricht, the Netherlands.

This project was funded by the Netherlands Organization for Scientific Research, (grant: 017.009.048), Hersenstichting (grant: 2013(I)-195), and Stichting de Weijerhorst Foundation.

Please address correspondence to J.F.A. Jansen, PhD, Department of Radiology and Nuclear Medicine, Maastricht University Medical Centre, PO Box 5800, 6202 AZ, Maastricht, the Netherlands; e-mail: jacobus.jansen@mumc.nl; @jfajansenphd

Indicates open access to non-subscribers at www.ajnr.org

<http://dx.doi.org/10.3174/ajnr.A5474>

provide information on the microvasculature and parenchymal microstructure, respectively, and have shown promising results in assisting in the assessment of stroke.^{5,6} Moreover, with this technique, the affected microvasculature and parenchyma in patients with cerebral small-vessel disease have been demonstrated previously.⁷

Unfortunately, the IVIM signal and the resulting measures can be affected by partial volume effects of CSF. The contamination of CSF has been previously demonstrated to be relevant for DWI, and an improved accuracy of diffusion measures was shown when suppressing the CSF signal.^{8,9} Recently, this suppression has been applied to IVIM.¹⁰ This so-called inversion recovery–based IVIM technique (ie, IR-IVIM) can be particularly helpful for patients with cerebrovascular disease because these patients often have brain atrophy,¹¹ which can increase the CSF contamination.

The reproducibility of IR-IVIM has not yet been fully studied. Several groups have investigated the reproducibility of conventional IVIM and have shown good results (eg, low coefficients of variation [CVs]) for both the perfusion volume fraction and parenchymal diffusivity.¹²⁻¹⁵ Thus far, only 1 reproducibility study has been performed on IR-IVIM. This study examined only *f* and healthy participants.¹⁰

We aimed to assess the clinical feasibility of IR-IVIM using the reproducibility of the perfusion volume fraction and parenchymal diffusivity.

MATERIALS AND METHODS

Study Population

For this study, we enrolled patients with varying manifestations of cerebrovascular disease ($n = 17$): 1) cerebral small vessel disease ($n = 11$), 2) cortical stroke ($n = 5$), and 3) intracerebral hemorrhage ($n = 1$). Patients were recruited in either the transient ischemic attack outpatient service or the stroke unit of the department of neurology of the hospital. A more detailed description of the study population has been published previously.¹⁶

All patients were scanned twice on separate days. The patient with intracerebral hemorrhage did not complete both sessions and was excluded from analysis. This exclusion resulted in 16 patients (14 men and 2 women; mean age, 66 ± 8 years; 1.9 ± 2.2 mean days between the 2 sessions) suitable for image analysis.

Standard Protocol Approvals, Registrations, and Patient Consents

The medical ethics committee of our institution approved this study. Written informed consent was obtained from patients before participation.

Imaging Protocol

Participants underwent brain imaging on an MR imaging system (3T, Achieva TX; Philips Healthcare, Best, the Netherlands) using a 32-element head coil suitable for parallel imaging. For IVIM imaging, a Stejskal-Tanner DWI single-shot spin-echo EPI pulse sequence was used (TR/TE, 6800/84 ms; FOV, $221 \times 269 \times 139$ mm³; 2.4-mm cubic voxel size). To suppress the CSF signal, an inversion pulse (TI, 2230 ms) was given before the DWI sequence.¹⁰ The total scan time of IVIM imaging using the inversion pulse was 14 minutes. Fifteen DWIs were acquired in 3 orthogo-

nal directions using multiple diffusion-sensitive b-values (0, 5, 7, 10, 15, 20, 30, 40, 50, 60, 100, 200, 400, 700, and 1000 s/mm²). IVIM images were aligned with the corpus callosum (ie, the line connecting the center of the genu and splenium of the corpus callosum). The number of signal averages for the highest 2 b-values was 2 and 3, instead of 1, respectively, to increase the signal-to-noise ratio at high b-values.

For anatomic reference, a T1-weighted sequence (TR/TI/TE, 8.3/800/3.8 ms; FOV, $256 \times 256 \times 160$ mm³; cubic voxel, 1.0 mm³) and T2-weighted FLAIR sequence (TR/TI/TE, 4800/1650/299 ms; FOV, $250 \times 256 \times 180$ mm³; cubic voxel, 1.0 mm³) were performed.

Image Analysis

Brain Segmentation. T1-weighted images were segmented into white matter, cortex, and deep gray matter using FreeSurfer software (<http://surfer.nmr.mgh.harvard.edu>)¹⁷ and FSL (Version 5.0; <http://www.fmrib.ox.ac.uk/fsl>).¹⁸ Subsequently, the normal-appearing white matter (NAWM) was separated from the white matter hyperintensities on FLAIR using a semiautomated segmentation algorithm¹⁹ followed by visual checks. Visible vascular lesions were identified ($n = 4$) by a neuroradiologist (>20 years of experience). Because a range of cerebrovascular diseases was included (ie, cerebral small-vessel disease and cortical infarction), we explored various ROIs: NAWM, cortex, deep gray matter, white matter hyperintensities, and vascular lesions (Fig 1A, -B). For patients ($n = 5$) with an acute infarct, only the contralateral hemisphere was considered for analysis.

IVIM Analysis. IVIM images were corrected for distortions and head displacements by registering to a corresponding T1-weighted image, using ExploreDTI Version 4.8.3 (<http://exploredti.com/>).²⁰ Subsequently, trace images were obtained by calculating the geometric mean of the DWIs measured in 3 orthogonal directions. Henceforth, spatial smoothing was performed on the trace images with a 3-mm (full width at half maximum) Gaussian kernel. The signal-to-noise ratio²¹ of cerebral tissue of the trace images was 60; and of the images obtained in 1 direction, it was 45 with a b-value of 1000 s/mm², which was higher than the recommended value (ie, 30) for reliable IVIM estimation.²²

Model Fitting. We used a 2-compartment model representing a vascular and nonvascular component, which also accounts for CSF contamination and differences in the relaxation time of blood and tissue.⁷ The IVIM signal was fitted biexponentially using a 2-step approach, which has been described previously^{7,23,24}: 1) The parenchymal diffusivity was obtained by fitting a monoexponential decay to the signal attenuation curve, obtained with b-values of >200 s/mm²; and 2) a biexponential decay was fitted to the signal attenuation curve, using all b-values and a fixed *D*, to obtain the perfusion volume fraction. This fitting was performed in a voxelwise manner; and for each ROI, the average IVIM measure was calculated. This calculation was performed with in-house software in Matlab R2012a (MathWorks, Natick, Massachusetts).

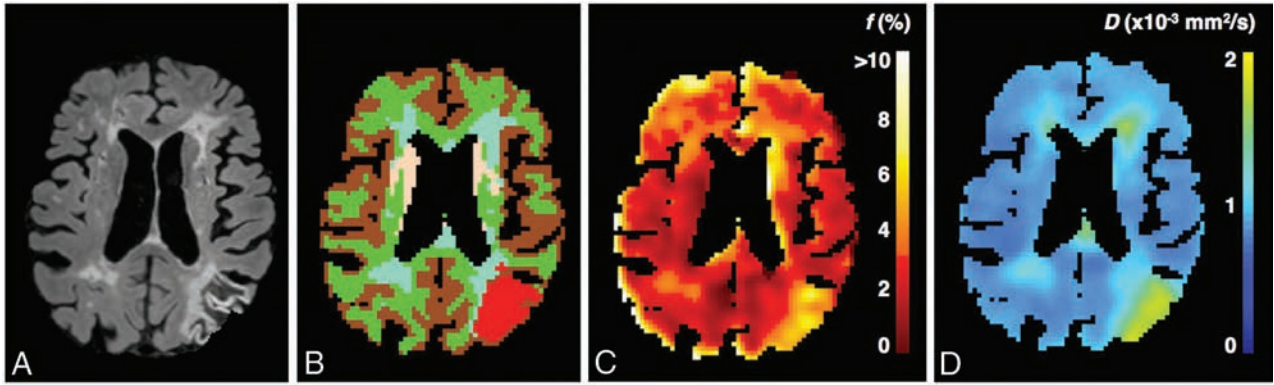


FIG 1. A, FLAIR image of a patient with a cortical infarct. Cerebral tissue was segmented (B) into normal-appearing white matter (green), cortex (brown), deep gray matter (pink), white matter hyperintensities (light blue), and vascular lesion (red). C and D, The calculated perfusion volume fraction map and parenchymal diffusivity map are shown, respectively.

Reproducibility Assessment and Statistical Analysis

All IVIM measures obtained with the trace images were calculated for 2 sessions and compared between sessions to evaluate the reproducibility using the coefficient of variation (CV), the repeatability coefficient (RC), and the intraclass correlation coefficient (ICC).²⁵ The CV expresses the relative variation within the subject from 1 session to the second session, whereas the ICC provides information on the effect of this variation with respect to the biologic variation of the study population. Furthermore, the RC indicates the minimal difference needed between the 2 measurements obtained from the same method to be considered an actual change rather than a test-retest error.²⁶

CV was calculated to express the relative within-subject variation and is defined as

$$CV = \frac{\sigma_{ws}}{\mu_{ws}} \times 100\%,$$

where σ_{ws} is the population SD during 2 sessions within the same subject and μ_{ws} the mean value during 2 sessions within the same subject.

The repeatability coefficient was calculated as

$$RC = 1.96 \times \sqrt{2} \times \sigma_{ws}.$$

Both the CV and RC were calculated per participant and averaged over all subjects to represent the overall CV and RC. Low CV and RCs represented good test-retest reproducibility.

Third, the intraclass correlation coefficient was used, defined as

$$ICC = \frac{\sigma_{bs}^2}{\sigma_{bs}^2 + \sigma_{ws}^2},$$

where σ_{bs}^2 denotes the biologic variance, which was obtained by calculating the variance over the average values of both sessions in all patients. The ICC expresses the effect of the biologic variance on the total variance rather than the test-retest error (σ_{ws}^2). ICC values toward 1 represent good reproducibility. The ICC was categorized as follows: poor, $ICC < 0.40$; moderate, $0.40 \leq ICC < 0.60$; good, $0.60 \leq ICC < 0.75$; and excellent, $0.75 \leq ICC \leq 1.00$.²⁷

Reproducibility values of the perfusion fraction and parenchymal diffusivity

Region	Session 1 ^a (mean) (SD)	Session 2 ^a (mean) (SD)	CV (%)	RC ^b	ICC
<i>f</i>					
NAWM	2.42 (0.23)	2.42 (0.22)	2.27	0.15	0.86
Cortex	2.79 (0.37)	2.76 (0.38)	2.89	0.21	0.89
DGM	2.90 (0.27)	2.81 (0.31)	3.70	0.29	0.66
WMH	3.22 (0.33)	3.23 (0.31)	2.47	0.22	0.84
VL	3.46 (0.79)	3.97 (1.33)	9.15	0.96	0.82
<i>D</i>					
NAWM	7.20 (0.19)	7.27 (0.22)	0.49	0.10	0.88
Cortex	7.35 (0.12)	7.44 (0.17)	0.68	0.14	0.54
DGM	7.36 (0.28)	7.42 (0.27)	0.46	0.09	0.95
WMH	9.02 (0.64)	9.11 (0.69)	0.70	0.18	0.97
VL	8.83 (1.88)	9.09 (2.10)	1.30	0.37	0.99

Note:—DGM indicates deep gray matter; WMH, white matter hyperintensities; VL, vascular lesion.

^a Mean and SD were calculated for all participants.

^b Units: $\times 10^{-2}$ (*f*); $\times 10^{-4}$ mm²/s (*D*).

Effect of Smoothing

To analyze the effect of smoothing on the reproducibility, we smoothed DWIs with a Gaussian kernel with increasing full width at half maximum ranging from 0 to 6 mm. Subsequently, CV values were calculated and used for comparing the reproducibility for increased smoothing. This calculation was performed for both *f* and *D* and for the ROIs in the white and gray matter.

RESULTS

The Table shows the results of the reproducibility of the IVIM parameter perfusion volume fraction and parenchymal diffusivity. Figure 1C, -D shows examples of *f* and *D* maps. The measured *f* (2.42 – 2.90×10^{-2}) and *D* (7.20 – 7.44×10^{-4} mm²/s) seen in patients with cerebrovascular disease are in the range of expected values in NAWM and gray matter. White matter hyperintensities and vascular lesions had values for *f* and *D* ranging from 3.22 – 3.97×10^{-2} and 8.83 – 9.11×10^{-4} mm²/s, respectively. CVs of $\leq 3.7\%$ for *f* and *D* were observed for the white and gray matter. Vascular lesions showed relatively higher CVs for *f* and *D* of 9.15 and 1.30%, respectively. Excellent ICCs (0.82–0.97) were observed for both IVIM parameters, except for *f* in the deep gray matter and *D* in the cortex showing moderate-to-good ICCs. Fur-

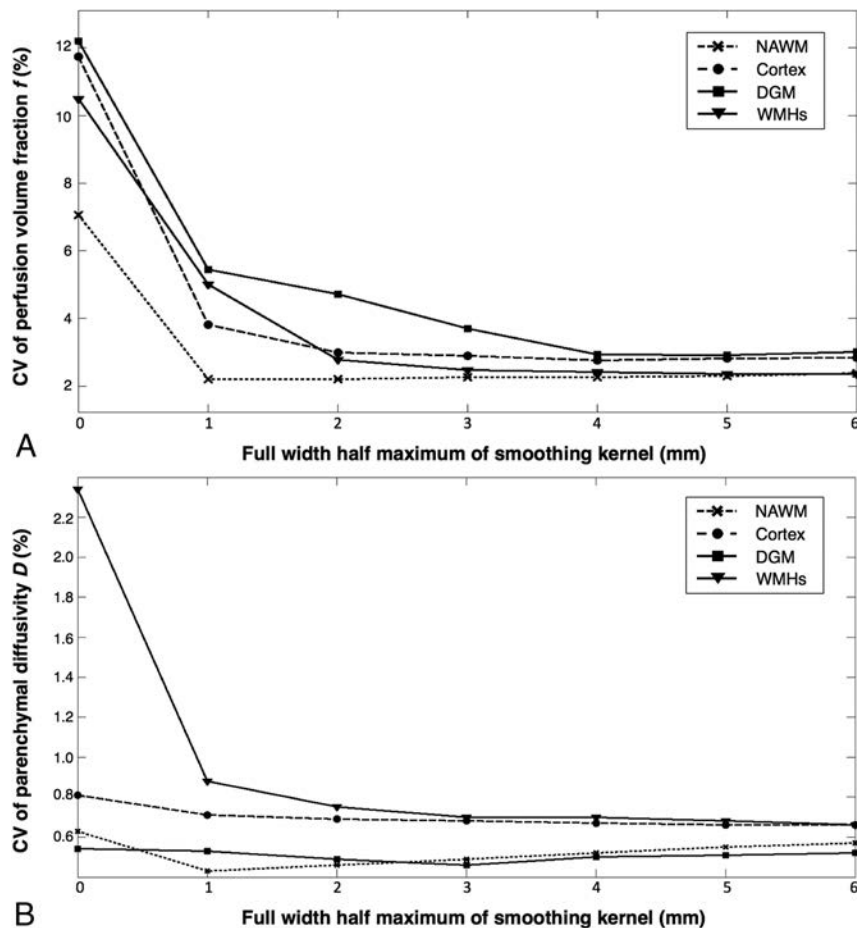


FIG 2. Coefficients of variation as a function of the full width at half maximum of the smoothing kernels ranging from 0 to 6 mm for the perfusion volume fraction (A) and parenchymal diffusivity (B). Higher CVs are present when no smoothing was performed. CVs decreased up to 3 times when smoothing was applied.

thermore, RCs ranged from $0.15\text{--}0.96 \times 10^{-2}$ for f and from $0.09\text{--}0.37 \times 10^{-4}$ mm^2/s for D .

When comparing our CVs obtained with smoothing (ie, full width at half maximum = 3 mm) with CVs without smoothing (ie, full width at half maximum = 0 mm), we observed lower CVs for f (CV, 2.27%–3.70%) when smoothing was applied than when no smoothing was applied (CV, 7.05%–12.20%) in the white and gray matter. For D , lower CVs were also found when smoothing was applied (CV, 0.49%–0.70%) than without smoothing (CV, 0.54%–2.34%) in the white and gray matter. In Fig 2, the CVs for an increasing size of the smoothing kernel are shown. For f , CVs without smoothing ranged from 7.05%–12.20%, and with smoothing, from 2.20%–5.45% in the white and gray matter. For D , CVs without smoothing ranged from 0.54%–2.34%, and with smoothing, from 0.43%–0.88% in the white and gray matter.

DISCUSSION

In this study, we assessed the reproducibility of IR-IVIM. Low CVs and moderate-to-excellent ICCs were observed for both normal-appearing tissue and lesion areas. Furthermore, low values for RCs were observed for all regions.

Several groups have evaluated the reproducibility of conventional IVIM in the brain.^{12–15} In patients with gliomas, CVs of

6.5% and 0.6% in the NAWM outside the tumor mass for f and D were reported, respectively.¹² Furthermore, Peterson et al¹⁵ investigated healthy participants and reported moderate-to-excellent ICCs for f in the deep gray matter. In a multicenter study¹⁴ also in healthy participants, CVs of f were 5.8% and 11.1%, and CVs of D were 1.7% and 2.1% in the white matter and gray matter, respectively. In comparison with these results, we reported somewhat lower CVs of f and D for the white and gray matter, not exceeding 3.70% and 0.70%, respectively, and comparable ICCs. An explanation for the lower CV values might be the effect of smoothing. We have shown that our CVs with smoothing (ie, full width at half maximum = 3 mm) were generally 3 times lower than when no smoothing was applied. When one assesses CVs with no smoothing (f , CV \leq 12.20%; and D , CV \leq 2.34%), it can be observed that CVs are in the same range as in the other studies (ie, f , 5.8%–11.1%; and D , 0.6%–2.1%^{12,15,14}). This finding indicates that the reproducibility of IR-IVIM is like that of conventional IVIM. Nevertheless, differences exist between our study and other studies that can influence the accurate comparison between IR-IVIM and IVIM, including the study population (ie, healthy controls^{14,15} versus pa-

tients with disease and cerebrovascular disease versus brain gliomas¹²); the exact method used (eg, IVIM versus IR-IVIM and selection of ROIs to analyze the reproducibility); and image-acquisition settings, which can contribute to a better signal-to-noise ratio (eg, the number of averages and the number of diffusion-sensitizing directions).

A study that used a similar IR-IVIM technique also explored the reproducibility of f in 5 healthy adults at 1.5T in the gray matter.¹⁰ They reported high-repeatability indices (dissimilar to the repeatability coefficient but comparable with CV) ranging from 27.3% to 65.2%, with a smoothing window full width at half maximum of 0–6 mm. The seemingly higher reproducibility we show from our CVs (ie, full width at half maximum, 0–6 mm: CVs, 2.77%–12.20%) may be explained by several factors: First, our study was performed at a higher field strength (ie, 3T versus 1.5T). At a higher field strength, a better signal-to-noise ratio and/or a higher spatial resolution can be acquired, which may contribute to better reproducibility. Second, the methods used to calculate the reproducibility values were different. Whereas we have calculated reproducibility values from the mean IVIM measure taken over an ROI (ie, “mean method”), they calculated the reproducibility values in a voxelwise manner. An earlier study has shown that CVs calculated in a voxelwise manner are approxi-

mately twice as high as CVs obtained with the mean method.²⁵ On the basis of this observation, our CV values of f for the voxelwise method can be roughly estimated to be approximately $\leq 7.40\%$ for the white and gray matter, which is lower than that reported by Hales and Clark (27.3%–65.2%)¹⁰ and is indicative of good reproducibility.

In our study, we applied spatial smoothing, which is beneficial because it improves the signal-to-noise ratio and corrects for small movement or spatial registration errors. We observed that smoothing might lead to improved CVs (f , 2.20%–5.45%; D , 0.43%–0.88%), which were generally up to 3 times lower compared with CVs without smoothing (f , 7.05%–12.20%; D , 0.54%–2.34%). This finding is in accordance with a previous study that reported better reproducibility with an increasing full width at half maximum of the smoothing kernel.¹⁰

Lower ICCs in the cortex and DGM can be observed, which indicate lower reproducibility in those areas. We argue that partial volume effects in general can still contribute to the lower reproducibility values. Even though CSF is suppressed and contamination of CSF is reduced, other tissue (eg, white matter) can still contribute to partial volume effects leading to lower reproducibility values.

The clinical contribution of IVIM in neuroimaging is an active research topic. IR-IVIM shows good reproducibility in both normal-appearing tissue and lesion area, which is required when monitoring disease progression or treatment responses. The clinical applicability of our reproducibility results can be demonstrated by the following: A difference in f and D in the stroke region (f , $2.6\% \pm 1.9\%$; D , $3.9 \pm 0.79 \times 10^{-4} \text{ mm}^2/\text{s}$) compared with the contralateral side (f , $5.6\% \pm 2.5\%$; D , versus $7.5\% \pm 0.86 \times 10^{-4} \text{ mm}^2/\text{s}$) has been reported.⁶ Our RC values in the vascular lesions of 1.0 and 0.4 for f and D , respectively, show that this difference can be easily detected with IR-IVIM. Furthermore, another benefit of IR-IVIM, as opposed to contrast-enhanced techniques, is that it can be performed multiple times to assess both diffusion and perfusion properties without the concern of contrast deposition in the brain. In addition, the advantage of DWI in ischemic stroke has already been widely reported,² and the IR-IVIM–derived D was corrected for microvascular contributions; this process resulted in a more accurate D (ie, less biased).

The strength of this study is that it was performed in a patient group in which both normal-appearing tissue and lesion areas (ie, white matter hyperintensities and vascular lesions) were investigated. On the contrary, in this study, only 2 sessions were performed, whereas multiple scan sessions could have improved the reproducibility evaluation. Furthermore, IVIM imaging without suppression of the CSF would have provided a more accurate comparison of reproducibility between IVIM with and without CSF suppression. However, IVIM without CSF suppression was not acquired because there was limited scan time. In addition, only a few patients ($n = 4$) had an acute infarct that we could use to investigate the vascular lesion area. However, we were able to provide some preliminary results. Last, in this study, we assumed a random microvascular network and hence an isotropic f . However, in a recent study, f was shown to be anisotropic in the gray

matter.²⁸ Further investigation is needed to study the effect on the reproducibility of fitting the anisotropic f .

CONCLUSIONS

IR-IVIM shows good reproducibility in its clinical feasibility in patients with cerebrovascular disease. Good reproducibility is a primary requirement in monitoring disease progression or treatment responses in the clinical setting.

ACKNOWLEDGMENTS

The authors greatly appreciate the effort and help of Professor P. Hofman in evaluating MR images on vascular lesions.

Disclosures: Sau May Wong—RELATED: Other: Stichting de Weijerhorst, Comments: Salary. Walter H. Backes—RELATED: Grant: Stichting de Weijerhorst*. *Money paid to the institution.

REFERENCES

1. Wintermark M, Sesay M, Barbier E, et al. **Comparative overview of brain perfusion imaging techniques.** *J Neuroradiol* 2005;32:294–314 CrossRef Medline
2. Latchaw RE, Alberts MJ, Lev MH, et al; American Heart Association Council on Cardiovascular Radiology and Intervention, Stroke Council, and the Interdisciplinary Council on Peripheral Vascular Disease. **Recommendations for imaging of acute ischemic stroke: a scientific statement from the American Heart Association.** *Stroke* 2009;40:3646–78 CrossRef Medline
3. Alsop DC, Detre JA, Golay X, et al. **Recommended implementation of arterial spin-labeled perfusion MRI for clinical applications: a consensus of the ISMRM perfusion study group and the European consortium for ASL in dementia.** *Magn Reson Med* 2015;73:102–116 CrossRef Medline
4. Le Bihan D, Breton E, Lallemand D, et al. **Separation of diffusion and perfusion in intravoxel incoherent motion MR imaging.** *Radiology* 1988;168:497–505 Medline
5. Yao Y, Zhang S, Tang X, et al. **Intravoxel incoherent motion diffusion-weighted imaging in stroke patients: initial clinical experience.** *Clin Radiol* 2016;71:938.e11–16 CrossRef
6. Federau C, Sumer S, Becce F, et al. **Intravoxel incoherent motion perfusion imaging in acute stroke: initial clinical experience.** *Neuroradiology* 2014;56:629–35 CrossRef Medline
7. Wong SM, Eleana Zhang C, van Bussel FC, et al. **Simultaneous investigation of microvasculature and parenchyma in cerebral small vessel disease using intravoxel incoherent motion imaging.** *Neuroimage Clin* 2017;14:216–21 CrossRef Medline
8. Latour LL, Warach S. **Cerebral spinal fluid contamination of the measurement of the apparent diffusion coefficient of water in acute stroke.** *Magn Reson Med* 2002;48:478–86 CrossRef Medline
9. Bhagat YA, Beaulieu C. **Diffusion anisotropy in subcortical white matter and cortical gray matter: changes with aging and the role of CSF-suppression.** *J Magn Reson Imaging* 2004;20:216–27 CrossRef Medline
10. Hales PW, Clark C. **Combined arterial spin labeling and diffusion-weighted imaging for noninvasive estimation of capillary volume fraction and permeability-surface product in the human brain.** *J Cereb Blood Flow Metab* 2013;33:67–75. CrossRef Medline
11. Nitkunan A, Lanfranconi S, Charlton RA, et al. **Brain atrophy and cerebral small vessel disease a prospective follow-up study.** *Stroke* 2011;42:133–38 CrossRef Medline
12. Bisdas S, Koh TS, Roder C, et al. **Intravoxel incoherent motion diffusion-weighted MR imaging of gliomas: feasibility of the method and initial results.** *Neuroradiology* 2013;55:1189–96 CrossRef Medline
13. Rydhög A, van Osch MJP, Lindgren E, et al. **Intravoxel incoherent motion (IVIM) imaging at different magnetic field strengths: what is feasible?** *Magn Reson Imaging* 2014;32:1247–58 CrossRef Medline

14. Grech-Sollars M, Hales PW, Miyazaki K, et al. **Multi-centre reproducibility of diffusion MRI parameters for clinical sequences in the brain.** *NMR Biomed* 2015;28:468–85 CrossRef Medline
15. Peterson ET, Zahr NM, Kwon D, et al. **Intra voxel incoherent motion (IVIM) in brain regions: a repeatability and aging study.** In: *Proceedings of the International Society for Magnetic Resonance in Medicine 24th Scientific Meeting & Exhibition*, Singapore. May 7–13, 2016: 3410
16. Wong SM, Jansen JFA, Zhang CE, et al. **Measuring subtle leakage of the blood-brain barrier in cerebrovascular disease with DCE-MRI: test-retest reproducibility and its influencing factors.** *J Magn Reson Imaging* 2017;46:159–66 CrossRef Medline
17. Fischl B, Salat DH, Busa E, et al. **Whole brain segmentation: automated labeling of neuroanatomical structures in the human brain.** *Neuron* 2002;33:341–55 CrossRef Medline
18. Jenkinson M, Bannister P, Brady M, et al. **Improved optimization for the robust and accurate linear registration and motion correction of brain images.** *Neuroimage* 2002;17:825–41 CrossRef Medline
19. de Boer R, Vrooman H, van der Lijn F, et al. **White matter lesion extension to automatic brain tissue segmentation on MRI.** *Neuroimage* 2009;45:1151–61 CrossRef Medline
20. Leemans A, Jeurissen B, Sijbers J, et al. **ExploreDTI: a graphical toolbox for processing, analyzing, and visualizing diffusion MR data.** In: *Proceedings of the International Society for Magnetic Resonance in Medicine 17th Scientific Meeting & Exhibition*, Honolulu, Hawaii. April 18–24, 2009: 3537
21. The Association of Electrical Equipment and Medical Imaging Manufacturers. Determination of signal-to-noise ratio (SNR) in diagnostic magnetic resonance imaging. EMA MS 1–2008 (R2014.) April, 30, 2015. <https://www.nema.org/Standards/Pages/Determination-of-Signal-to-Noise-Ratio-in-Diagnostic-Magnetic-Resonance-Imaging.aspx>. Accessed September 1, 2017
22. Wu WC, Chen YF, Tseng HM, et al. **Caveat of measuring perfusion indexes using intravoxel incoherent motion magnetic resonance imaging in the human brain.** *Eur Radiol* 2015;25:2485–92 CrossRef Medline
23. van Bussel FC, Backes WH, Hofman PA, et al. **On the interplay of microvasculature, parenchyma, and memory in type 2 diabetes.** *Diabetes Care* 2015 38:876–82 CrossRef Medline
24. Federau C, O'Brien K, Meuli R, et al. **Measuring brain perfusion with intravoxel incoherent motion (IVIM): initial clinical experience.** *J Magn Reson Imaging* 2014;39:624–32 CrossRef Medline
25. Jansen JFA, Kooi ME, Kessel AG, et al. **Reproducibility of quantitative cerebral T2 relaxometry, diffusion tensor imaging, and 1H magnetic resonance spectroscopy at 3.0 Tesla.** *Invest Radiol* 2007;42:327–37 CrossRef Medline
26. Bland JM, Altman DG. **Measurement error.** *BMJ* 1996;312:1654 CrossRef Medline
27. Cicchetti DV. **Guidelines, criteria, and rules of thumb for evaluating normed and standardized assessment instruments in psychology.** *Psychol Assess* 1994;6:284–90 CrossRef
28. Finkenstaedt T, Klarhoefer M, Eberhardt C, et al. **The IVIM signal in the healthy cerebral gray matter: a play of spherical and non-spherical components.** *Neuroimage* 2017;152:340–47 CrossRef Medline

The CT Swirl Sign Is Associated with Hematoma Expansion in Intracerebral Hemorrhage

 D. Ng,  L. Churilov,  P. Mitchell,  R. Dowling, and  B. Yan

ABSTRACT

BACKGROUND AND PURPOSE: Hematoma expansion is an independent determinant of poor clinical outcome in intracerebral hemorrhage. Although the “spot sign” predicts hematoma expansion, the identification requires CT angiography, which limits its general accessibility in some hospital settings. Noncontrast CT, without the need for CT angiography, may identify sites of active extravasation, termed the “swirl sign.” We aimed to determine the association of the swirl sign with hematoma expansion.

MATERIALS AND METHODS: Patients with spontaneous intracerebral hemorrhage between 2007 and 2014 who underwent an initial and subsequent noncontrast CT at a single center were retrospectively identified. The swirl sign, on noncontrast CT, was defined as iso- or hypodensity within a hyperdense region that extended across 2 contiguous 5-mm axial CT sections.

RESULTS: A total of 212 patients met the inclusion criteria. The swirl sign was identified in 91 patients with excellent interobserver agreement ($\kappa = 0.87$). The swirl sign was associated with larger initial hematoma ($P < .001$) and earlier initial CT ($P < .001$) and hematoma expansion ($P = .028$). Multivariable regression modeling demonstrated that if one assumed similar initial hematoma volume, onset-to-first scan, and time between CT scans, the median absolute hematoma growth was 5.77 mL (95% CI, 2.37–9.18 mL; $P = .001$) and relative growth was 35.6% (95% CI, 18.5%–52.6%; $P < .001$) higher in patients with the swirl sign compared with those without.

CONCLUSIONS: The NCCT swirl sign was reliably identified and is associated with hematoma expansion. We propose that the swirl sign be included in risk stratification of intracerebral hemorrhage and considered for inclusion in clinical trials.

ABBREVIATIONS: ICH = intracerebral hemorrhage; IQR = interquartile range

The annual incidence of intracerebral hemorrhage (ICH) worldwide is estimated at 4 million with a large proportion occurring in low- to middle-income countries.¹ ICH confers a poorer prognosis compared with ischemic stroke with morbidity and mortality approaching 50% at 30 days.²

Established prognostic factors include initial hematoma volume, age, low Glasgow Coma Scale score, and shorter time from onset to presentation.^{3,4} These factors may not reflect the dynamic nature of hematoma evolution and expansion, which are important in the clinical outcome.⁵ Hematoma growth due to active extravasation and rebleeding has been reported in 38% of patients after initial CT.⁶ Hematoma expansion has been shown

to be an independent determinant of poorer clinical outcome.⁵ Consequently, identification of patients at increased risk of hematoma expansion and the development of strategies to limit hematoma growth have been a focus of clinical trials.^{1,5,7–10}

Current Phase II trials, the Spot Sign and Tranexamic Acid On Preventing ICH Growth—AUStralasia Trial (STOP-AUST), “Spot Sign” Selection of Intracerebral Hemorrhage to Guide Hemostatic Therapy (SPOTLIGHT), Intensive Blood Pressure Reduction in Acute Cerebral Hemorrhage Trial 2 (INTERACT 2), and Antihypertensive Treatment of Acute Cerebral Hemorrhage (ATACH II), investigated the reduction of hematoma growth using tranexamic acid, recombinant factor VIIa, and blood pressure control.^{1,9–11} STOP-AUST and SPOTLIGHT used the CTA “spot sign” as a basis for patient selection. The spot sign is a biomarker for active hemorrhage and independently predicts relative and absolute hematoma expansion.^{12–17} Currently, CT angiography is widely performed in cases in which an ischemic stroke is suspected, while it is less commonly performed in the hemorrhagic subtype. Limitations for contrast administration include nephrotoxicity, contraindications in moderate-to-severe renal impair-

Received July 31, 2017; accepted September 19.

From the Department of Radiology (D.N., P.M., R.D., B.Y.), and Melbourne Brain Centre (B.Y.), University of Melbourne, Royal Melbourne Hospital, Parkville, Victoria, Australia; and Statistics and Decision Analysis (L.C.), Florey Institute of Neuroscience and Mental Health, Heidelberg, Victoria, Australia.

Please address correspondence to Bernard Yan, MD, Melbourne Brain Centre, Royal Melbourne Hospital, 300 Grattan St, Parkville Victoria 3050 Australia; e-mail: bernard.yan@mh.org.au

<http://dx.doi.org/10.3174/ajnr.A5465>

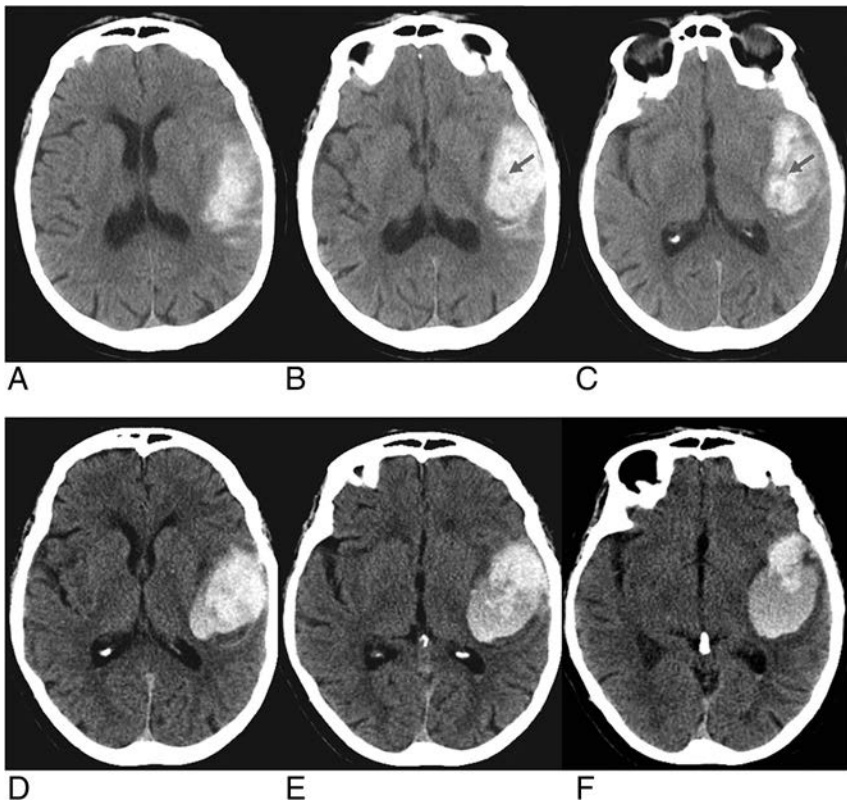


FIGURE. Noncontrast brain CT of a 73-year-old woman who presented with right-sided weakness. Initial brain CT (A–C) demonstrates a left parietal hematoma measuring 33 mL, demonstrating hypodense hematoma with hypodense foci, the swirl sign. Follow-up CT (D–F) performed 8 hours later demonstrates increased hematoma volume, 46 mL.

ment, prior contrast reaction, and access and availability of staff or infrastructure in rural areas, which preclude the use of this prognostic tool.^{18,19} Thus, there remains a role for noncontrast CT in identifying patients at risk for hematoma growth.

The “swirl sign” has been previously described as a hypo- or isodensity within a region of a hyperdensity that correlates with active hemorrhage on surgical evacuation.²⁰ It is reproducible and an independent predictor of 1-month mortality and functional outcomes.²¹ The utility of the swirl sign in predicting hematoma growth has not been thoroughly investigated.^{21,22} We aimed to further define the swirl sign and evaluate its value in predicting hematoma expansion. With the CT swirl sign, it may be possible to identify patients with intracerebral hemorrhage most likely to have hematoma expansion in the absence of CT angiography and for whom hemostatic therapy will be of benefit.

MATERIALS AND METHODS

Study Population

This was a retrospective analysis of all patients who presented to the Royal Melbourne Hospital, a quaternary stroke referral center, with a spontaneous intracerebral hemorrhage diagnosed between September 2007 and August 2014. All potential cases were identified with our prospective stroke data base. The diagnosis was made on CT by a neuroradiologist. The exclusion criteria were an absence of an initial CT at our institution or a repeat CT scan, imaging performed 96 hours after symptom onset (including interhospital transfers) or subsequent CT performed 96 hours

after initial CT, surgical decompression between CT1 and CT2 (for which the hematoma volume on subsequent CT could not be assessed), concurrent vascular abnormalities (intracranial aneurysms, arteriovenous malformations, cavernomas, hemangiomas), trauma, or tumor. The study adhered to the principles of the Declaration of Helsinki and was approved by the Melbourne Health Human Research Ethics Committee.

Demographic and Clinical Data

Demographic and clinical data were obtained via a prospectively organized stroke data base compiled after review of patient medical records. Parameters included age, sex, history (previous stroke/transient ischemic attack, diabetes mellitus, hypertension), medications, time of onset, and initial examination findings (Glasgow Coma Scale, initial systolic blood pressure). The modified Rankin Scale score on admission was also calculated. Interventions, including warfarin reversal, were also noted.

Biochemical results including hemoglobin level, platelet level, and coagulation profile (international normalized ratio, activated partial thromboplastin time, fibrinogen levels) were obtained

using the electronic pathology data base of Melbourne Health, clinical information service.

Radiologic Findings

Initial noncontrast CT scans were reviewed independently by the primary investigator (D.N., 6 months of neuroimaging experience) and an interventional neuroradiologist (R.D., 18 years of neuroimaging experience) for the presence or absence of the swirl sign. They were blinded to clinical data and the presence of hematoma enlargement. The swirl sign was defined as an area of low density (30–50 HU, hypo- or isodense to brain parenchyma) surrounded by a hyperdense region (Figure). The hypodensity had to extend across 2 contiguous 5-mm axial CT sections. The sign represents active hemorrhage within an area of acute hematoma.

Hematoma volume, location (supra- or infratentorial in relation to the tentorium cerebelli), presence of midline shift, and intraventricular extension were obtained from previously published data in our stroke data base.²³ Hematoma growth was calculated as absolute (hematoma volume measured on CT2–CT1) and relative values (hematoma volume measured on CT2–CT1) / Volume on CT1).

Statistical Analysis

Statistical analysis was conducted by using STATA 13 IC (StataCorp, College Station, Texas). *P* values < .05 were indicative of statistical significance.

Patient characteristics of those included and excluded from

Table 1: Comparison of included and excluded patients

Patient Characteristics	Patients with Spontaneous ICH (n = 212)	Patients Excluded (n = 460)	P Value
Age (median) (IQR) (yr)	68 (61–77.5)	75 (64.5–83)	<.001
Male sex (No.) (%)	86 (40.6)	210 (45.7)	.21
Time to initial CT (median) (IQR) (hr)	4.5 (2.29–17.5)	4.4 (2.0–11.6) [n = 299]	.06
Time to second CT (median) (IQR) (hr)	11.92 (5.38–29.27)	19.9 (4.6–56.64) [n = 287]	.005
PMHx (No.) (%)			
Hypertension	166 (78.3)	329 (71.8)	.09
Hypercholesterolemia	68 (32.1)	114 (30.6)	.71
Statin use	68 (32.1)	145 (31.5)	.92
Diabetes	54 (25.6)	108 (23.8)	.32
Ischemic heart disease	39 (18.4)	79 (17.6)	.83
Atrial fibrillation	47 (22.2)	93 (20.7)	.68
Previous stroke			
Transient ischemic attack	13 (6.2)	29 (6.5)	1.00
Ischemic stroke (n = 207)	21 (9.9)	43 (11.5)	.68
Hemorrhagic stroke	12 (5.8)	35 (9.4)	.15
Anticoagulant (No.) (%)			
Warfarin	42 (19.8)	87 (18.9)	.83
Antiplatelet	70 (33.0)	164 (35.6)	.54
GCS on presentation (median) (IQR)	14 (11–15) [n = 207]	14 (10–15) [n = 355]	.52
Radiologic (No.) (%)			
Location supratentorial	173 (81.6)	309 (67.2)	.42
IV extension (n = 326)	88 (41.5)	60 (52.6)	.06
Midline shift (n = 499)	78 (36.8)	142 (49.5)	.006

Note.—GCS indicates Glasgow Coma Scale; PMHx, past medical history; IV, intraventricular.

Table 2: Comparison of patients positive and negative for the swirl sign

Patient Characteristics	Swirl Sign -ve (n = 121)	Swirl Sign +ve (n = 91)	P Value
Age (median) (IQR) (yr)	69 (51–76)	68 (51–72)	.4
Male sex (No.) (%)	50 (41.3)	36 (39.6)	.89
Time to initial CT (median) (IQR) (hr)	16.1 (1.1–95.3)	8.0 (0.37–94)	<.001
Time to second CT (median) (IQR) (hr)	21.0 (10.3–28.5)	16.5 (5.9–29.5)	.12
Initial hematoma volume (median) (IQR) (mL)	8.56 (3.83–14.95)	23.2 (11.65–43.3)	<.001
PMHx (No.) (%)			
Hypertension	99 (81.8)	67 (73.6)	.18
Hypercholesterolemia	45 (37.3)	23 (25.3)	.08
Statin use	40 (33.1)	28 (30.8)	.77
Diabetes	33 (27.5)	21 (23.1)	.52
Ischemic heart disease	21 (17.4)	18 (19.8)	.72
Atrial fibrillation	21 (17.4)	26 (28.6)	.06
Previous stroke			
Transient ischemic attack	9 (7.5)	4 (4.4)	.40
Ischemic stroke (n = 207)	10 (8.5)	11 (12.2)	.49
Hemorrhagic stroke	8 (6.8)	4 (4.4)	.56
Anticoagulant (No.) (%)			
Warfarin	19 (15.7)	23 (25.3)	.12
Antiplatelet	42 (34.7)	28 (30.8)	.56
GCS on presentation (median) (IQR) (n = 207)	14 (12–15)	13 (11–14)	.018
INR (median) (IQR)	1.1 (1.0–1.2)	1.1 (1.0–1.4)	.13
Radiologic (No.) (%)			
Location supratentorial	95 (78.5)	78 (85.7)	.21
IV extension (n = 145)	50 (63.3)	38 (57.6)	1.00
Midline shift	27 (22.3)	51 (56.0)	<.001

Note.—INR indicates international normalized ratio; -ve, negative; +ve, positive; PMHx, past medical history; GCS, Glasgow Coma Scale; IV, intraventricular.

the study, those positive or negative for the swirl sign, and those with the swirl sign with and without hematoma growth were summarized as median and interquartile range (IQR) for continuous variables and counts and proportions for categorical variables and were compared using the Wilcoxon-Mann-Whitney and Fisher exact tests, respectively.

Interobserver agreement for the presence of the swirl sign was estimated using the Cohen κ score, with a κ of 0.81–1.00 corresponding to almost perfect agreement; 0.61–0.80, substantial; 0.41–0.60,

moderate; 0.21–0.40, fair; 0.00–0.20, slight; and <0.00, poor agreement.²⁴

To investigate the association between the presence or absence of the swirl sign and hematoma growth, we created 2 kinds of models in which hematoma growth was expressed as either an absolute or a relative change. Multiple median regression was performed with hematoma growth as an output; the swirl sign as a factor; and hematoma volume on the initial CT, time difference between the first and second CT, and onset of symptoms to the first CT, as covariates. The resulting models were further validated by running linear least-squares regression models with the same input but with the output transformed by using fifth-root transformation to ensure satisfaction of model assumptions.

RESULTS

Patient Characteristics

A total of 672 patients were treated for spontaneous ICH and had an assessable initial CT scan between October 2007 and August 2014. Four hundred sixty were excluded from the analysis, including 405 who did not have a repeat CT, 30 in whom the interval between onset and initial CT exceeded 4 days, 8 in whom the interval between CT1 and CT2 exceeded 4 days, 15 who underwent surgical decompression between CT1 and CT2 (13 demonstrated the swirl sign on initial CT), and 2 who could not be assessed due to poor image quality.

A total of 212 patients met the inclusion criteria, including 86 (40.6%) men with a median age of 68 years (IQR, 61–77.5 years).

Previous stroke was documented in 33 (15.9%) patients with a hemorrhagic etiology in 12 (5.8%) and ischemic in 21 (9.9%). Clinical risk factors for ICH included hypertension (n = 166, 78.3%), antiplatelet use 70 (33%), and anticoagulant use 42 (19.8%). On presentation, patients had a median international normalized ratio of 1.1 (IQR, 1.0–1.2) and a Glasgow Coma Scale score of 14 (IQR, 12–15).

The median time from symptom onset to initial CT was 4.5 hours (IQR, 2.29–17.5 hours). The hemorrhage was supratentorial in 173 (81.6%) patients, associated with intraventricular extension in 88/145 (60.7%), and midline shift in 78 (36.8%).

Comparison between Included and Excluded Patients

The excluded patients were older ($P < .001$) and were more likely to have midline shift ($P = .006$) (Table 1). No statistically signif-

Table 3: Comparison of patients positive for the swirl sign with and without hematoma growth

Patient Characteristics	Increased Hematoma Volume (n = 65)	Stable/Reduced Hematoma Volume (n = 26)	P Value
Age (median) (IQR) (yr)	71 (63–76)	66 (55–72)	.06
Male sex (No.) (%)	25 (38.5)	11 (42.3)	.81
Time to initial CT (median) (IQR) (hr)	3 (1.7–6.6)	4 (2.6–12.7)	.01
Time to second CT (median) (IQR) (hr)	12 (4.2–23.8)	26.8 (14.7–36.0)	<.001
Initial hematoma volume (median) (IQR) (mL)	24 (12.2–49.6)	21.6 (10.3–38.5)	.37
PMHx (No.) (%)			
Hypertension	46 (70.7)	21 (80.8)	.43
Hypercholesterolemia	17 (26.2)	6 (23.8)	1.00
Statin use	22 (33.9)	6 (23.8)	.45
Diabetes	16 (24.6)	5 (19.2)	.78
Ischemic heart disease	15 (23.1)	3 (11.5)	.26
Atrial fibrillation	23 (35.4)	3 (11.5)	.018
Previous stroke			
Transient ischemic attack	3 (4.6)	1 (3.9)	1.00
Ischemic stroke (n = 207)	8 (12.3)	3 (11.5)	1.00
Hemorrhagic stroke	3 (4.6)	1 (3.9)	1.00
Anticoagulant (No.) (%)			
Warfarin	22 (33.9)	1 (3.9)	.003
Antiplatelet	22 (33.9)	6 (23.8)	.45
GCS on presentation (median) (IQR)	14 (9.8–14)	13 (11–14)	.13
INR (median) (IQR)	1.2 (1.0–1.8)	1.1 (1.0–1.1)	.01
Radiologic (No.) (%)			
Location supratentorial	55 (84.6)	23 (88.5)	.75
IV extension	17 (26.2)	11 (42.3)	.35
Midline shift	33 (50.8)	18 (69.2)	.16

Note:—GCS indicates Glasgow Coma Scale; PMHx, past medical history; IV, intraventricular; INR, international normalized ratio.

Table 4: Multiple median regression model (follow-up volume)

Follow-Up Volume	Median Absolute Growth (mL)	P Value	95% CI
Swirl sign	5.77	.001	2.37 to 9.18
Initial hematoma volume (mL)	1.01	.000	0.95 to 1.06
Time between CT1 and CT2 (hr)	−0.07	.028	−0.12 to −0.007
Time between onset and CT1 (hr)	−0.0003	.251	−0.0008 to 0.0002

Table 5: Multiple median regression model (relative hematoma volume change)

Relative Hematoma Volume Change	Median Relative Growth (%)	P Value	95% CI
Swirl sign	35.6	<.001	18.5 to 52.6
Initial hematoma volume (mL)	−0.23	.158	−0.56 to 0.09
Time between CT1 and CT2 (hr)	−0.42	.008	−0.73 to −0.11
Time between onset and CT1 (hr)	0.0	.424	−0.01 to 0.00

icant differences in sex, time to initial CT, traditional cardiovascular risk factors, previous stroke, and use of anticoagulants between included and excluded patients were observed (Table 1).

Interobserver Agreement

A random sample of 60 CT scans demonstrated excellent interobserver agreement in identifying the swirl sign ($\kappa = 0.87$; 95% CI, 0.75–0.99). There was disagreement about the presence of the swirl sign in 4 of 60 patients. Three of these patients had a small hematoma volume (<10 mL).

The Swirl Sign and Clinical Variables

The swirl sign was present in 91 (42.9%; 95% CI, 36.2%–49.9%) patients. Hematoma expansion occurred in 65 (71%; 95% CI,

61%–80.4%) patients with positive swirl signs compared with 33 (27%; 95% CI, 19.6%–36.1%) of those without the swirl sign (Table 2). On univariate analysis, no significant difference in the age, sex, presence of hypertension, diabetes, previous stroke of any cause, ischemic heart disease, or antiplatelet use was observed between those with and those without the swirl sign (Table 2). No statistically significant association between the presence of the swirl sign and the initial Glasgow Coma Scale score, initial mRS, or international normalized ratio was observed (Table 2). No statistically significant association between the presence of the swirl sign and time of symptom onset to initial CT ($P = .08$), atrial fibrillation ($P = .06$), or anticoagulant use ($P = .12$) was observed (Table 2).

Association between the Swirl Sign and Hematoma Growth

Patients positive for the swirl sign had larger initial hematoma volumes ($P < .001$) and a shorter time between symptom onset and initial CT ($P < .001$) and were more likely to have midline shift ($P < .001$) compared with those without (Table 2). No statistically significant differences in the hemorrhage location or time taken for repeat imaging were observed.

Patients with the swirl sign and hematoma growth were more likely to have atrial fibrillation ($P = .018$), be on warfarin ($P = .003$) with a higher international normalized ratio ($P = .01$), and have a shorter interval between onset and CT1 ($P = .01$) and between CT1 and CT2 ($P < .001$) (Table 3).

Multivariable regression modeling demonstrated that if we assumed similar initial hematoma volume, onset-to-first

scan time, and time between CT scans, the median absolute hematoma growth was 5.77 mL (95% CI, 2.37–9.18 mL; $P = .001$) higher and the median relative hematoma growth was 35.6% (95% CI, 18.5%–52.6%; $P < .001$) higher in patients with the swirl sign compared with those without (Tables 4 and 5).

Qualitatively similar associations were observed on a robustness analysis using least-squares linear regression models with the same input and the output transformed by using fifth-root transformation.

DISCUSSION

Our retrospective study demonstrates that if we assume similar initial hematoma volume and time between CT scans, the median

absolute hematoma growth (5.77 mL; 95% CI, 2.37–9.18 mL; $P = .001$) and relative hematoma growth (35.6%; 95% CI, 18.5%–52.6%; $P < .001$) in patients with the swirl sign were higher than in those without. The swirl sign was common and present in 43% (91/212) of our study population.

Hematoma evolution in ICH is a dynamic process that begins as a primary hemorrhagic insult. Multiple studies have shown that a significant proportion of patients (38%) undergo hematoma expansion on repeat CT imaging.⁶ The currently recognized clinical prognostic factors (including initial hematoma volume, neurologic deficit at presentation, age, and infratentorial location) do not directly reflect the dynamic nature of hematoma evolution. Hematoma growth is thought to be due to active hemorrhage and rebleeding and has been shown to be an independent determinant of mortality and morbidity.⁵ Early identification and hematoma limitation have become a treatment goal.⁵

The swirl sign on noncontrast CT is iso- or hypodense within a hyperdense region and is thought to represent an area of active hemorrhage within an acute hematoma.²⁰ The swirl sign was first described in traumatic extra-axial hematomas.²⁵ Greenberg et al²⁶ and Al-Nakshabandi²⁰ documented that following surgical exploration, the swirl sign correlated with areas of active hemorrhage in subdural hematomas.

Selariu et al²¹ demonstrated that the swirl sign was reproducible and correlated with increased mortality and poorer functional outcomes. The swirl sign was present in 30% (61/203) of the study population. The patients positive for the swirl sign were more likely to demonstrate midline shift and intraventricular hematoma extension and have larger initial hematoma volumes (mean, 52 versus 15 mL). Our study supports these findings.

Gökçe et al²² studied the CT findings of 45 patients with ICH on antihypertensive and anticoagulant agents. The median initial hematoma volume was 46 mL, with the swirl sign identified in 32 (71%) patients. All patients with the swirl sign demonstrated hematoma enlargement on repeat imaging.²² Kim et al²⁷ found that the swirl sign, among other prognostic factors, was associated with increased mortality but did not independently predict mortality and hematoma growth.

To our knowledge, no previous study has specifically examined the association between the swirl sign and hematoma growth. The CTA spot sign has been extensively investigated and prospectively validated as an independent determinant of hematoma expansion, morbidity, and mortality.^{3,12,13,28} Currently, the spot sign is the imaging benchmark for hematoma growth in large national trials investigating hemostatic agents.¹ However, CT angiography is contraindicated in patients with prior contrast reactions and renal impairment and has reduced availability. Identification of baseline CT predictors of ICH expansion is important to aid selection in hemostatic trials when CTA is not possible. This study supports the swirl sign as a reproducible marker of hematoma growth that can be used as an adjunct to the spot sign.

The strengths of our study include the study population size and length of the recruitment period. The swirl sign was further defined to improve reproducibility and attempt to reduce the impact of imaging artifacts.

Limitations of the study include a selection bias, which may have been introduced by our exclusion criteria. The excluded pa-

tients were older ($P < .001$) and more likely to demonstrate midline shift ($P = .006$) on initial CT. These features probably reflect the effects of a larger hematoma, and it is postulated that a higher proportion of these patients would be swirl-positive. Thus, this understates the incidence and strength of the association of the swirl sign and hematoma growth. In addition, a number of patients were transferred from another hospital, resulting in a longer time to imaging, which may underestimate the degree of active hemorrhage. Furthermore, the impetus for repeat CT imaging was dependent on the degree of clinical concern of the treating neurology team. Consequently, the interval between initial and subsequent CT varied; this difference may underestimate the degree of hematoma expansion in delayed imaging due to clot retraction.

CONCLUSIONS

The noncontrast CT swirl sign was reliably identified with excellent interrater agreement. The presence of the swirl sign was associated with hematoma expansion. We propose that the swirl sign should be included in the risk stratification of intracerebral hemorrhage and should be considered for inclusion in clinical trials.

REFERENCES

1. Meretoja A, Churilov L, Campbell BC, et al. **The spot sign and tranexamic acid on preventing ICH growth: AUstralasia Trial (STOP-AUST)—protocol of a phase II randomized, placebo-controlled, double-blind, multicenter trial.** *Int J Stroke* 2014;9:519–24 CrossRef Medline
2. Flaherty ML, Haverbusch M, Sekar P, et al. **Long-term mortality after intracerebral hemorrhage.** *Neurology* 2006;66:1182–86 CrossRef Medline
3. Hemphill JC 3rd, Bonovich DC, Besmertis L, et al. **The ICH score: a simple, reliable grading scale for intracerebral hemorrhage.** *Stroke* 2001;32:891–97 CrossRef Medline
4. Curtze S, Strbian D, Meretoja A, et al. **Higher baseline international normalized ratio value correlates with higher mortality in intracerebral hemorrhage during warfarin use.** *Eur J Neurol* 2014;21: 616–22 CrossRef Medline
5. Davis SM, Broderick J, Hennerici M, et al; Recombinant Activated Factor VII Intracerebral Hemorrhage Trial Investigators. **Hematoma growth is a determinant of mortality and poor outcome after intracerebral hemorrhage.** *Neurology* 2006;66:1175–81 Medline
6. Brott T, Broderick J, Kothari R, et al. **Early hemorrhage growth in patients with intracerebral hemorrhage.** *Stroke* 1997;28:1–5 CrossRef Medline
7. Edavettal M, Rogers A, Rogers F, et al. **Prothrombin complex concentrate accelerates international normalized ratio reversal and diminishes the extension of intracranial hemorrhage in geriatric trauma patients.** *Am Surg* 2014;80:372–76 Medline
8. Romero JM, Heit JJ, Delgado Almandoz JE, et al. **Spot sign score predicts rapid bleeding in spontaneous intracerebral hemorrhage.** *Emerg Radiol* 2012;19:195–202 CrossRef Medline
9. Hill MD, Muir KW. **INTERACT-2: should blood pressure be aggressively lowered acutely after intracerebral hemorrhage?** *Stroke* 2013; 44:2951–52 CrossRef Medline
10. Gladstone D. “Spot Sign” Selection of Intracerebral Hemorrhage to Guide Hemostatic Therapy (SPOTLIGHT). 2011. <https://clinicaltrials.gov/ct2/show/NCT01359202>. Accessed May 1, 2017
11. Qureshi AI, Palesch YY. **Antihypertensive Treatment of Acute Cerebral Hemorrhage (ATACH) II: design, methods, and rationale.** *Neurocrit Care* 2011;15:559–76 CrossRef Medline
12. Huynh TJ, Demchuk AM, Dowlatshahi D, et al; PREDICT/Sunny-

- brook ICH CTA Study Group. **Spot sign number is the most important spot sign characteristic for predicting hematoma expansion using first-pass computed tomography angiography: analysis from the PREDICT study.** *Stroke* 2013;44:972–77 CrossRef Medline
13. Demchuk AM, Dowlatshahi D, Rodriguez-Luna D, et al; PREDICT/Sunnybrook ICH CTA study group. **Prediction of haematoma growth and outcome in patients with intracerebral haemorrhage using the CT-angiography spot sign (PREDICT): a prospective observational study.** *Lancet Neurol* 2012;11:307–14 CrossRef Medline
 14. Delgado Almandoz JE, Yoo AJ, Stone MJ, et al. **Systematic characterization of the computed tomography angiography spot sign in primary intracerebral hemorrhage identifies patients at highest risk for hematoma expansion: the spot sign score.** *Stroke* 2009;40:2994–3000 CrossRef Medline
 15. Rost NS, Smith EE, Chang Y, et al. **Prediction of functional outcome in patients with primary intracerebral hemorrhage: the FUNC score.** *Stroke* 2008;39:2304–09 CrossRef Medline
 16. Broderick JP, Dinger MN, Hill MD, et al; Recombinant Activated Factor VII Intracerebral Hemorrhage Trial Investigators. **Determinants of intracerebral hemorrhage growth: an exploratory analysis.** *Stroke* 2007;38:1072–75 CrossRef Medline
 17. Godoy DA, Piñero G, Di Napoli M. **Predicting mortality in spontaneous intracerebral hemorrhage: can modification to original score improve the prediction?** *Stroke* 2006;37:1038–44 CrossRef Medline
 18. Leys D, Cordonnier C, Debette S, et al; Executive committee of the European Stroke Initiative (EUSI). **Facilities available in French hospitals treating acute stroke patients: comparison with 24 other European countries.** *J Neurology* 2009;256:867–73 CrossRef Medline
 19. Goldstein LB. **Statewide hospital-based stroke services in North Carolina: changes over 10 years.** *Stroke* 2010;41:778–83 CrossRef Medline
 20. Al-Nakshabandi NA. **The swirl sign.** *Radiology* 2001;218:433 CrossRef Medline
 21. Selariu E, Zia E, Brizzi M, et al. **Swirl sign in intracerebral haemorrhage: definition, prevalence, reliability and prognostic value.** *BMC Neurol* 2012;12:109 CrossRef Medline
 22. Gökçe E, Beyhan M, Acu B. **Evaluation of oral anticoagulant-associated intracranial parenchymal hematomas using CT findings.** *Clin Neuroradiol* 2015;25:151–59 CrossRef Medline
 23. Ma M, Meretoja A, Churilov L, et al. **Warfarin-associated intracerebral hemorrhage: volume, anticoagulation intensity and location.** *J Neurol Sci* 2013;332:75–79 CrossRef Medline
 24. Landis JR, Koch GG. **The measurement of observer agreement for categorical data.** *Biometrics* 1977;33:159–74 CrossRef Medline
 25. Zimmerman RA, Bilaniuk LT. **Computed tomographic staging of traumatic epidural bleeding.** *Radiology* 1982;144:809–12 CrossRef Medline
 26. Greenberg J, Cohen WA, Cooper PR. **The “hyperacute” extra-axial intracranial hematoma: computed tomographic findings and clinical significance.** *Neurosurgery* 1985;17:48–56 CrossRef Medline
 27. Kim J, Smith A, Hemphill JC 3rd, et al. **Contrast extravasation on CT predicts mortality in primary intracerebral hemorrhage.** *AJNR Am J Neuroradiol* 2008;29:520–25 CrossRef Medline
 28. Hallevi H, Abraham AT, Barreto AD, et al. **The spot sign in intracerebral hemorrhage: the importance of looking for contrast extravasation.** *Cerebrovasc Dis* 2010;29:217–20 CrossRef Medline

Dural Arteriovenous Fistulas: A Characteristic Pattern of Edema and Enhancement of the Medulla on MRI

A.Z. Copelan, A. Krishnan, H. Marin, and R. Silbergleit

ABSTRACT

SUMMARY: Medullary edema with enhancement is rarely reported at initial MR imaging in intracranial dural arteriovenous fistulas. We report a series of 5 patients with dural arteriovenous fistulas, all of whom demonstrated a characteristic pattern of central medullary edema and medullary enhancement at initial MR imaging. Cognard type V dural arteriovenous fistula, defined by drainage into the perimedullary veins and the veins surrounding the brain stem, is a rare yet well-described pathologic entity. Even more rarely reported, however, is its clinical presentation with predominantly bulbar symptoms and MR imaging findings of central medullary edema with enhancement. This constellation of findings frequently leads to a convoluted clinical picture, prompting work-up for alternative disease processes and delaying diagnosis. Because an expedited diagnosis is critical in preventing poor outcomes, it is paramount to make the referring physician and neuroradiologist more cognizant of this rare-yet-characteristic imaging manifestation of dural arteriovenous fistula.

ABBREVIATION: DAVF = dural arteriovenous fistula

Intracranial dural arteriovenous fistulas (DAVFs) result from a meshwork of anomalous communications between dural arteries and dural venous sinuses or cortical veins, without an intervening capillary network or nidus, and account for approximately 10%–15% of intracranial vascular malformations.¹ The rare Cognard type V DAVF is defined by its drainage into veins around the brain stem and further caudally into the perimedullary veins.² Consequently, this subtype often presents with symptoms related to swelling of the cervical cord, including a slowly progressive myelopathy initially involving the upper limbs. The imaging findings include an enlarged cervical cord and engorged perimedullary veins.

What is less commonly understood and described here is the clinical presentation with bulbar symptoms related to brain stem involvement.³ The imaging findings within the brain stem are even more rarely reported, though intuitively, a brain MR may be

the initial imaging test ordered by clinicians in these patients. MR imaging may reveal central medullary edema with occasional intense medullary enhancement.⁴ Engorged perimedullary veins may not be evident. These findings may lead the clinician further astray and prompt a work-up for a neoplasm and infectious or inflammatory processes. Ultimately, improper management and, in some reported instances, biopsy for a suspected neoplasm may occur.⁵

We report a series of 5 patients who presented at 2 nearby academic institutions from 2012 to 2016 with DAVFs demonstrating medullary edema and enhancement at initial imaging. Most interesting, the unique pattern of edema was nearly identical in all 5 cases and, retrospectively, has been anecdotally mentioned previously.^{5–7} All 5 patients underwent CT and MR imaging examinations, and 2 patients underwent MR spectroscopy/perfusion because there was concern for a neoplasm. All patients eventually underwent conventional angiography.

This multicenter retrospective study was approved by the institutional review board of each institution with data compiled into a single Health Insurance Portability and Accountability Act-compliant data base.

Cases

Case 1. A 59-year-old man presented with new-onset dizziness and severe nausea and vomiting. He reported positional vertigo that had commenced 5 weeks before presentation. MR imaging

Received July 30, 2017; accepted after revision September 16.

From the Department of Diagnostic Radiology and Medical Imaging (A.Z.C., A.K., R.S.), Beaumont Health - Royal Oak, Oakland University William Beaumont School of Medicine, Royal Oak, Michigan; and Department of Radiology (H.M.), Henry Ford Hospital, Detroit, Michigan.

Several of these cases were previously presented at: Annual Meeting of the American Society of Neuroradiology and the Foundation of the ASNR Symposium, May 21–26, 2016; Washington, DC.

Please address correspondence to Alexander Z. Copelan, MD, Hospital of the University of Pennsylvania, Radiology Department, Neuroradiology Division, 3400 Spruce St, Philadelphia, PA 19104; e-mail: alexander.copelan@uphs.upenn.edu

<http://dx.doi.org/10.3174/ajnr.A5460>

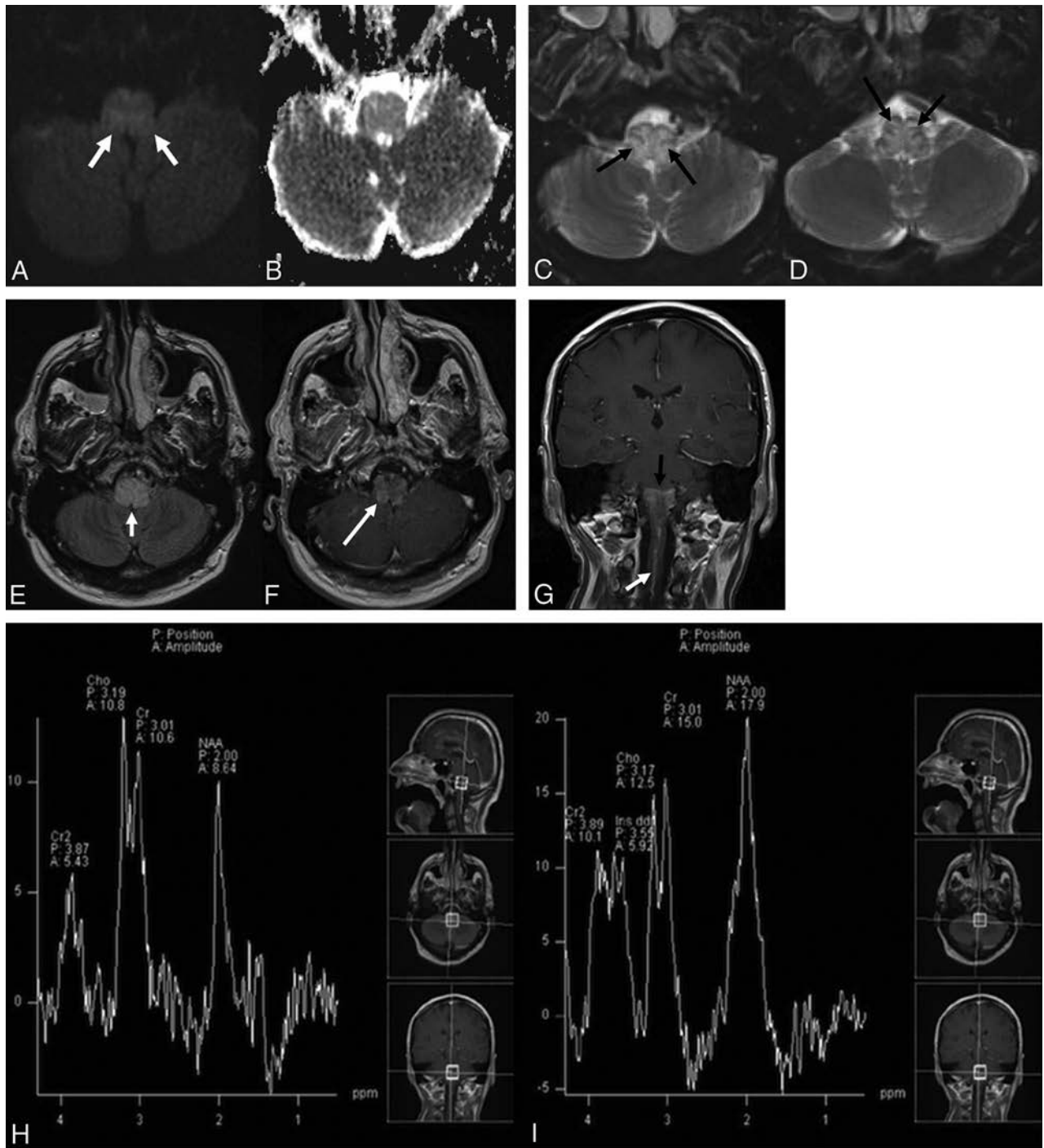


FIG 1. A 59-year-old man who presented with new-onset dizziness and severe nausea and vomiting. Initial MR imaging demonstrates mild hyperintense signal on axial DWI ($b = 1000$) (white arrows, *A*) without definite restricted diffusion on the corresponding ADC map (*B*). There is relatively diffuse hyperintense signal abnormality within the medulla on axial T2WI with fat suppression (*C* and *D*) with sparing of the periphery and several internal linear regions (black arrows). This pattern of sparing was not initially recognized. *E*, Axial FLAIR imaging demonstrates relatively diffuse hyperintense signal abnormality within the medulla (short white arrow). Axial postcontrast T1WI (*F*) demonstrates mild patchy enhancement (long white arrow). *G*, Coronal postcontrast T1WI reveals a dilated perimedullary vein (white arrow) extending inferiorly from the patchy enhancement within the medulla (black arrow) and coursing caudally along the upper cervical cord. MR spectroscopy with TEs of 135 (*H*) and 35 (*I*) ms demonstrates no significant elevation in choline with decreased NAA. MR perfusion imaging (*J*) reveals slightly decreased relative CBV within the medulla. Suspicion was raised for an underlying DAVF. Left external carotid injection on digital subtraction angiography arterial phase lateral (*K*) and delayed venous phase anteroposterior (*L*) views demonstrates a DAVF in the wall of the left superior petrosal sinus (long white arrow) fed by meningeal branches of the occipital (short white arrow), ascending pharyngeal (long black arrow), and middle meningeal (short black arrows) arteries, with retrograde venous drainage via the petrosal vein to the pial perimedullary veins running to the cervical cord as the anterior and posterior spinal veins (black dashed arrows).

revealed a relatively diffuse T2 hyperintense signal within the medulla, with peripheral and internal linear areas of sparing, as well as associated mild medullary enhancement (Fig 1*A–F*). CTA was

also performed, and no vascular malformation was identified. MR imaging with spectroscopy/perfusion was performed several days later to exclude neoplasms (Fig 1*G–J*). This repeat MR imaging

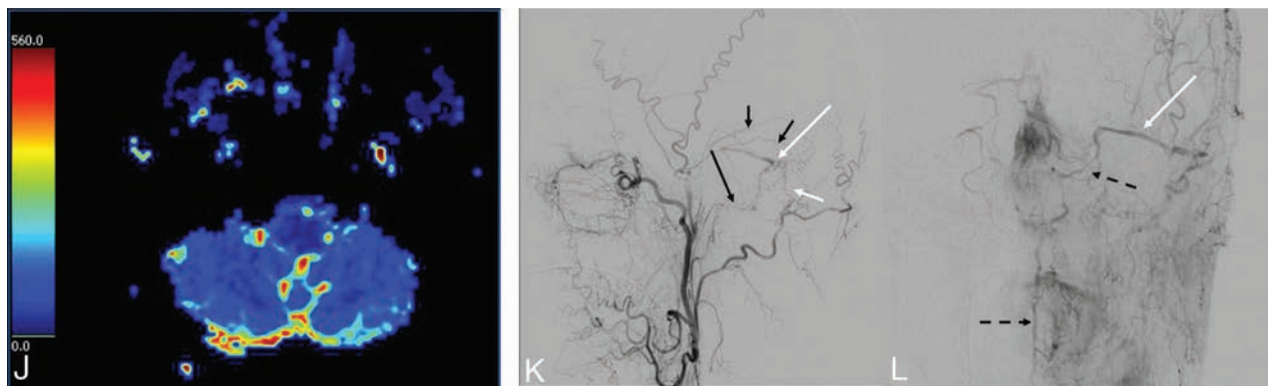


FIG 1. Continued.

demonstrated prominent vessels along the surface of the medulla and upper cervical cord (Fig 1G). Spectroscopy did not reveal findings concerning for an aggressive neoplasm, and MR perfusion demonstrated decreased relative cerebral blood volume (Fig 1J) and flow within the medulla. Concern was raised for a potential DAVF, and catheter angiography was recommended. Angiography revealed a DAVF in the wall of the left superior petrosal sinus (Fig 1K, -L). The patient underwent a combination of endovascular embolization and surgical resection of the DAVF, and repeat angiography showed no recurrence. His symptoms markedly improved with no recurrence at 3-year follow-up.

Case 2. A 72-year-old man presented with 3 months of imbalance, slurred speech, and dysphagia. He had a vestibular schwannoma resected 15 years prior. MR imaging demonstrated relatively diffuse T2 hyperintense signal within the medulla, with peripheral and internal linear regions of sparing, with intense enhancement in the medulla and adjacent cerebellar flocculus (Fig 2A–D). Additionally, an unusual enhancing vascular structure, near but separate from the right vertebral artery, was identified (Fig 2D). Concern was initially raised for a DAVF. The patient underwent 4-vessel cerebral angiography outside our department, but no vascular malformation was identified. Subsequent clinical work-up, including multiple lumbar punctures for cytology, failed to demonstrate evidence of malignancy. MR spectroscopy/perfusion revealed a lactate/lipid peak and prolongation of the mean transit time and mildly decreased cerebral blood volume within the medulla (Fig 2E, -F). The case was reviewed by the tumor board, and one of the authors strongly suggested a DAVF, despite the prior negative findings on angiography (which did not include selective injections of the external carotid arteries). Repeat cerebral angiography in our department with selective external carotid and, potentially, spinal artery injections, was recommended. Arteriovenous shunting in the region of the anterior condylar vein was identified on repeat angiography (Fig 2G). Dilated draining veins along the brain stem and upper cord were present (Fig 2H). Embolization was performed with Onyx injection (Covidien, Irvine, California) in the neuromeningeal division of the ascending pharyngeal artery feeding the fistula. No evidence of residual DAVF was seen, and the patient had improvement in symptoms, particularly his dysphagia. Five-month follow-up angiography did not show recurrence, and follow-up MR imaging revealed resolution of edema and enhancement.

Case 3. A 35-year-old woman with a medical history significant for pilocytic astrocytoma as a child presented with 4 weeks of progressive unsteady gait and lower extremity weakness as well as dysphonia and nasal speech. MR imaging demonstrated patchy T2 hyperintensity within the medulla, with peripheral and several internal linear regions of sparing, and subtle intramedullary enhancement (Fig 3A, -B). Serpiginous vessels on postcontrast sequences and flow voids were seen along the surface of the medulla and brain stem. CTA revealed prominent perimedullary and ventral and dorsal spinal veins (Fig 3C). Cerebral angiography demonstrated a DAVF in the wall of the superior petrosal sinus (Fig 3D, -E). Endovascular embolization was performed with injection of Onyx into the mastoid branch of the occipital artery. The patient experienced marked clinical improvement with mild residual left lower extremity weakness. A 3-month follow-up angiogram showed no recurrence.

Case 4. A 64-year-old woman presented to an outside hospital with progressive bilateral arm and leg weakness for the prior 6 months that gradually evolved to tetraparesis. MR imaging of the cervical spine revealed diffuse T2 hyperintensity within the medulla and cervical spinal cord, with peripheral and internal linear regions of sparing, with relatively diffuse enhancement. This was initially diagnosed as transverse myelitis and managed with steroids, intravenous immunoglobulin, and plasma exchange. The patient's symptoms progressed for the next 5 months, and she was seen at our institution. MR imaging revealed mild expansion of the medulla and cervical spinal cord with a similar pattern of T2 hyperintensity and enhancement. Subtle prominent vessels were now evident along the ventral pial surface of the medulla. CTA revealed venous congestion at the cervicomedullary junction, and cerebral angiography demonstrated a DAVF along the superior petrosal sinus supplied by the tentorial branch of the inferolateral trunk with perimedullary venous drainage. The DAVF was initially treated with an Onyx injection into the occipital arterial supply; however, residual shunting was seen without successful penetration of Onyx on the venous side. Surgical resection was performed the following day, and 1-week angiographic follow-up demonstrated no residual fistula. Clinical recovery, however, was limited, with persistent tetraparesis 12 months after treatment.

Case 5. A 50-year-old man presented with new-onset upper and lower extremity weakness. He was initially diagnosed with trans-

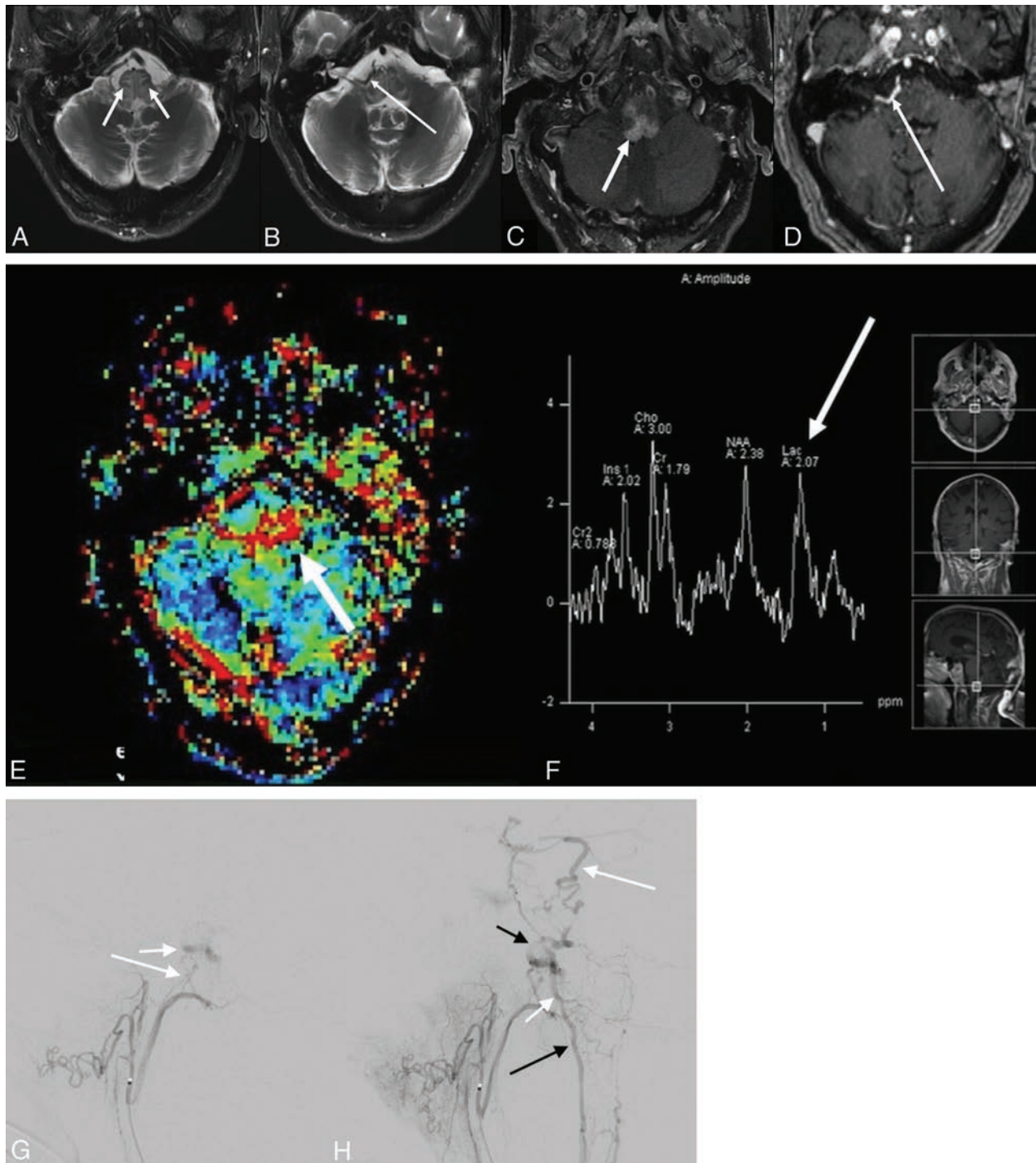


FIG 2. A 72-year-old man with 2- to 3-month history of imbalance and dysphagia. A and B, Axial T2WI with fat suppression from initial MR imaging demonstrates diffuse hyperintense signal in the medulla with segments of linear sparing (*short white arrows*), creating a geographic pattern, as well as an unusual vascular structure (*long white arrow*). C and D, Axial postcontrast T1-weighted fat-suppression imaging demonstrates intense enhancement within the medulla (*short white arrow*) and again depicts the unusual vascular structure (*long white arrow*), which appears separate from the vertebral arteries. Dynamic susceptibility contrast MR perfusion imaging reveals prolongation in mean transit time (*short white arrow, E*), and MR spectroscopy with a TE of 35 ms (*F*) reveals a lactate/lipid peak (*long white arrow*) without significant elevation in choline. G, Lateral view from a selective right ascending pharyngeal injection on DSA demonstrates arteriovenous shunting with early opacification of the anterior condylar vein (*short white arrow*) supplied by feeders from the neuromeningeal division of the ascending pharyngeal artery (*long white arrow*). H, More delayed lateral image demonstrates dilated veins along the surface of the brain stem and upper cord (*short white arrow*), draining both superiorly along the anterolateral surface of the pons toward the petrosal vein (*long white arrow*) and inferiorly toward the anterior spinal vein (*long black arrow*). The tortuous vein (*short black arrow*) likely corresponds to the anomalous venous structure seen on the original MR imaging.

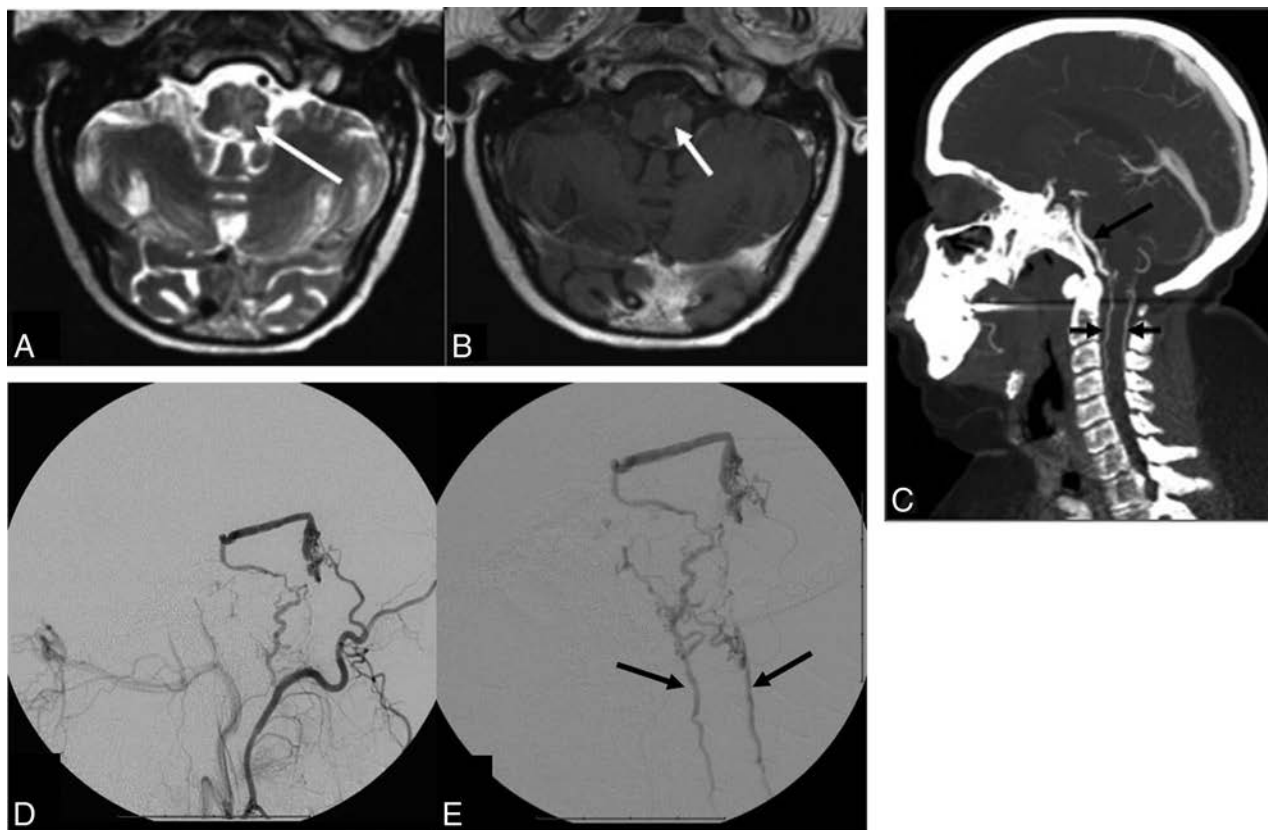


FIG 3. A 35-year-old woman with a history of pilocytic astrocytoma as a child now presenting with 4 weeks of progressive difficulty in walking. *A*, Axial T2WI reveals patchy hyperintensity within the medulla (*long white arrow*) with peripheral sparing. *B*, Axial postcontrast T1WI demonstrates subtle intramedullary enhancement (*short white arrow*). *C*, Sagittal CTA reformatted image depicts prominent perimedullary (*long black arrow*) as well as ventral and dorsal spinal veins (*short black arrows*). Selective DSA of the occipital (*D*) and mastoid branch via microcatheter (*E*) demonstrates the fistulous connection in the wall of the superior petrosal sinus with retrograde pial reflux via the petrosal vein to the perimedullary and spinal veins (*black arrows*).

verse myelitis and came to our institution for a second opinion. MR imaging of the cervical spine revealed expansion of the lower medulla and cervical cord with T2 hyperintensity, sparing the periphery, and faint enhancement with prominent vessels along the ventral cervical cord. Cerebral angiography revealed a spinal DAVF in the left C1 foramen with perimedullary venous drainage to the anterior spinal vein. Due to the short arterial pedicle, endovascular management was deferred. Surgical management was initially unsuccessful with persistence of the DAVF. His symptoms progressed for the next 6 weeks to marked lower extremity weakness, bowel and bladder dysfunction, and dysphagia, with an inability to maintain secretions, requiring percutaneous endoscopic gastrostomy tube placement and tracheostomy. A second operation was then performed and was successful; however, clinical examination findings remained unchanged.

DISCUSSION

While an intracranial DAVF with perimedullary spinal venous drainage is rare, even more uncommon is its presentation with medullary or pontomedullary edema, with only 31 cases previously reported in the English language medical literature. Because timely diagnosis is paramount in minimizing the potential for catastrophic outcomes, it is critical to make the referring physician and neuroradiologist more cognizant of this rare-yet-characteristic imaging manifestation of a DAVF.

This series illustrates the challenges in diagnosing this atypical presentation of DAVF. Because symptomatology is related to the distribution of venous drainage rather than the site of the fistula, the clinical presentation may mimic demyelinating and inflammatory disorders, brain stem and spinal cord infarction, or neoplasms. Symptom onset may be sudden or gradual, with our patients' presentations ranging from sudden onset of nausea and vomiting to gradually progressive tetraparesis.⁸⁻¹² As exemplified in our patients, the challenges in recognizing this rare disease entity often lead to a significant delay in diagnosis, on the order of several months from the time of initial investigation and months to years from the time of initial symptoms.

Imaging findings of DAVF often overlap more common disease entities, convoluting the diagnostic dilemma. Prominent perimedullary flow voids on T2WI, a feature suggestive of an underlying vascular malformation, are present in only 37% of cases.⁴ With contrast-enhanced imaging, the detection rate of atypical perimedullary vessels increases to 76% but is often subtle.⁵ Use of MRA increases the detection rate to 85%.⁵ Four of our 5 patients (80%) retrospectively demonstrated atypical perimedullary vessels or flow voids on initial MR imaging, subtle in some instances. Prominent veins are likely a later sign.⁵ In Cognard type V lesions, the perimedullary venous drainage is predominantly through the anterior spinal veins, making them less prominent on MR imaging.⁴

Central medullary or pontomedullary edema has been reported in 73% of patients with Cognard type V DAVFs.⁵ All our patients demonstrated a nearly identical pattern of geographic central medullary edema with sparing of the periphery as well as internal linear segments in a tigroid pattern. In this series, not all cases of Cognard type V DAVFs were reviewed; rather, only those cases demonstrating central medullary edema were included, so the proportion of total cases of type V DAVFs from our institutions with the aforementioned specific imaging features is unknown. This peripheral sparing appearance has been mentioned in case reports.¹³ This pattern contrasts with the infiltrative process seen in brain stem tumors. Maintenance of the normal signal of the peripheral subpial tissue may be secondary to direct drainage of the extracellular vasogenic edema into the CSF through the permeable pia mater.^{14,15} Perivascular spaces may also play a role in draining the peripheral tissue.¹⁶

Of the 20 cases in the literature reporting on the presence of medullary contrast enhancement for Cognard type V DAVFs, 11 cases (55%) demonstrated enhancement. Medullary enhancement was demonstrated in all our cases, 4 of which were initially scanned on a 1.5T scanner and 1 on a 3T scanner, with 3 different vendors used. Medullary enhancement was demonstrated in all our cases. The combination of medullary edema and enhancement may lead to the consideration of neoplastic or inflammatory etiologies, as was the case in 3 of our 5 cases, and has reportedly led to inappropriate brain stem biopsies.⁵ Two of our patients underwent MR perfusion/spectroscopy because a neoplasm was considered. MR perfusion and spectroscopy in DAVF are also uncommonly reported. A prolonged mean transit time with decreased cerebral blood volume may be present secondary to venous congestion with ischemia, seen in both of our patients.^{17,18} Additionally, spectroscopy may reveal increased lactate, which was demonstrated in 1 of our patients.

Four of our 5 patients had true intracranial DAVFs. Case 5 revealed the site of the fistula at the craniocervical junction along the C1 foramen. In 3 of our 4 cases of true intracranial DAVFs, conventional angiography revealed the site of the fistula to be along the superior petrosal sinus, and in 1 case, the anterior condylar vein. The goal of treatment is closure of the draining vein proximally as it exits the fistula. Successful endovascular embolization with Onyx was performed in 2 of our patients; combined embolization and an operation, in 2 patients; and 2 operations, in 1 patient. As in case 2, the medullary edema might resolve following treatment.⁵

Bulbar symptoms were present in 3 of our 5 (60%) cases: case 2 (slurred speech and dysphagia), case 3 (dysphonia and nasal speech), and case 5 (inability to maintain secretions). A systematic review of the literature on Cognard type V DAVFs identified bulbar symptoms in 31% of patients and found no significant difference in prognosis between those with versus those without bulbar symptoms.¹⁹ In our series, 2 of 3 patients with clinical improvement and 1 of 2 patients without clinical improvement had bulbar symptoms, further exemplifying a lack of relationship between the presence of bulbar symptoms and prognosis.

Three of our 5 patients (60%) had near-complete resolution of symptoms and angiographically complete occlusion of the DAVF. Unfortunately, the 2 patients with the most significant delay in

diagnosis and treatment did not show significant clinical improvement following treatment, further exemplifying the importance of early diagnosis and management.

CONCLUSIONS

This relatively unusual-but-characteristic pattern of medullary edema with areas of sparing and patchy enhancement should prompt scrutiny for atypical perimedullary vessels. If no such vessels are identified, MRA/CTA or conventional angiography should be recommended. Of utmost importance, selective injection of the external carotid arteries is mandated at the time of conventional angiography to avoid false-negative results as was the case in 1 of our patients.

Disclosures: Richard Silbergleit—UNRELATED: Consultancy: Relievant Medsystems.

REFERENCES

1. Kwon BJ, Han MH, Kang HS, et al. **MR imaging findings of intracranial dural arteriovenous fistulas: relations with venous drainage patterns.** *AJNR Am J Neuroradiol* 2005;26:2500–07 Medline
2. Cognard C, Gobin YP, Pierot L, et al. **Cerebral dural arteriovenous fistulas: clinical and angiographic correlation with a revised classification of venous drainage.** *Radiology* 1995;194:671–80 CrossRef Medline
3. van Rooij WJ, Sluzewski M, Beute GN. **Intracranial dural fistulas with exclusive perimedullary drainage: the need for complete cerebral angiography for diagnosis and treatment planning.** *AJNR Am J Neuroradiol* 2007;28:348–51 Medline
4. Haryu S, Endo T, Sato K, et al. **Cognard type V intracranial dural arteriovenous shunt: case reports and literature review with special consideration of the pattern of spinal venous drainage.** *Neurosurgery* 2014;74:E135–42; discussion E142 CrossRef Medline
5. Roelz R, Van Velthoven V, Reinacher P, et al. **Unilateral contrast-enhancing pontomedullary lesion due to an intracranial dural arteriovenous fistula with perimedullary spinal venous drainage: the exception that proves the rule.** *J Neurosurg* 2015;123:1534–39 CrossRef Medline
6. Ricolfi F, Manelfe C, Meder JF, et al. **Intracranial dural arteriovenous fistulae with perimedullary venous drainage: anatomical, clinical and therapeutic considerations.** *Neuroradiology* 1999;41:803–12 CrossRef Medline
7. Brunereau L, Gobin YP, Meder JF, et al. **Intracranial dural arteriovenous fistulas with spinal venous drainage: relation between clinical presentation and angiographic findings.** *AJNR Am J Neuroradiol* 1996;17:1549–54 Medline
8. Gaensler EH, Jackson DE Jr, Halbach VV. **Arteriovenous fistulas of the cervicomedullary junction as a cause of myelopathy: radiographic findings in two cases.** *AJNR Am J Neuroradiol* 1990;11:518–21 Medline
9. Hähnel S, Jansen O, Geletneky K. **MR appearance of an intracranial dural arteriovenous fistula leading to cervical myelopathy.** *Neurology* 1998;51:1131–35 CrossRef Medline
10. Li J, Ezura M, Takahashi A, et al. **Intracranial dural arteriovenous fistula with venous reflux to the brainstem and spinal cord mimicking brainstem infarction: case report.** *Neurol Med Chir (Tokyo)* 2004;44:24–28 CrossRef Medline
11. Cahan LD, Higashida RT, Halbach VV, et al. **Variants of radiculomeningeal vascular malformations of the spine.** *J Neurosurg* 1987;66:333–37 CrossRef Medline
12. Hassler W, Thron A. **Flow velocity and pressure measurements in spinal dural arteriovenous fistulas.** *Neurosurg Rev* 1994;17:29–36 CrossRef Medline
13. Hurst RW, Grossman RI. **Peripheral spinal cord hypointensity on T2-weighted MR images: a reliable imaging sign of venous hypertensive myelopathy.** *AJNR Am J Neuroradiol* 2000;21:781–86 Medline

14. Nicholas DS, Weller RO. **The fine anatomy of the human spinal meninges: a light and scanning electron microscopy study.** *J Neurosurg* 1988;69:276–82 CrossRef Medline
15. Hutchings M, Weller RO. **Anatomical relationships of the pia mater to cerebral blood vessels in man.** *J Neurosurg* 1986;65:316–25 CrossRef Medline
16. Fleury J, Gherardi R, Poirier J. **Pathology of perivascular spaces in the central nervous system** [in French]. *Ann Pathol* 1984;4:249–57 Medline
17. Doege CA, Tavakolian R, Kerskens CM, et al. **Perfusion and diffusion magnetic resonance imaging in human cerebral venous thrombosis.** *J Neurol* 2001;248:564–71 CrossRef Medline
18. Kim DJ, Krings T. **Whole-brain perfusion CT patterns of brain arteriovenous malformations: a pilot study in 18 patients.** *AJNR Am J Neuroradiol* 2011;32:2061–66 CrossRef Medline
19. El Asri AC, El Mostarchid B, Akhaddar A, et al. **Factors influencing the prognosis in intracranial dural arteriovenous fistulas with perimedullary drainage.** *World Neurosurg* 2013;79:182–91 CrossRef Medline

White Matter Changes Related to Subconcussive Impact Frequency during a Single Season of High School Football

 S.J. Kuzminski,  M.D. Clark,  M.A. Fraser,  C.C. Haswell,  R.A. Morey,  C. Liu,  K.R. Choudhury,  K.M. Guskiwicz, and  J.R. Petrella



ABSTRACT

BACKGROUND AND PURPOSE: The effect of exposing the developing brain of a high school football player to subconcussive impacts during a single season is unknown. The purpose of this pilot study was to use diffusion tensor imaging to assess white matter changes during a single high school football season, and to correlate these changes with impacts measured by helmet accelerometer data and neurocognitive test scores collected during the same period.

MATERIALS AND METHODS: Seventeen male athletes (mean age, 16 ± 0.73 years) underwent MR imaging before and after the season. Changes in fractional anisotropy across the white matter skeleton were assessed with Tract-Based Spatial Statistics and ROI analysis.

RESULTS: The mean number of impacts over a 10-g threshold sustained was 414 ± 291 . Voxelwise analysis failed to show significant changes in fractional anisotropy across the season or a correlation with impact frequency, after correcting for multiple comparisons. ROI analysis showed significant ($P < .05$, corrected) decreases in fractional anisotropy in the fornix-stria terminalis and cingulum hippocampus, which were related to impact frequency. The effects were strongest in the fornix-stria terminalis, where decreases in fractional anisotropy correlated with worsening visual memory.

CONCLUSIONS: Our findings suggest that subclinical neurotrauma related to participation in American football may result in white matter injury and that alterations in white matter tracts within the limbic system may be detectable after only 1 season of play at the high school level.

ABBREVIATIONS: CTE = chronic traumatic encephalopathy; FA = fractional anisotropy; FXST = fornix-stria terminalis; TBSS = Tract-Based Spatial Statistics

The association between head injury and neurodegeneration in contact sport athletes has been well established. Multiple postmortem case reports of former American football players with this neurodegenerative process, termed “chronic traumatic

encephalopathy” (CTE), are present in the literature.^{1,2} Although most available data are from middle-aged or elderly individuals, there is a troubling report of early CTE pathologic changes in a deceased high school football player.³ CTE is believed to be related to repetitive brain injuries accrued across time, and the long-term consequences of exposing the developing brain of a high school football athlete to several hundred head impacts during a season have yet to be determined. With >1 million high school athletes playing football, there is a commensurately large need to elucidate the neurologic consequences of repetitive, subconcussive impacts.⁴

There is a growing body of evidence that diffusion tensor imaging can detect injuries to the white matter tracts related to contact sports exposure. One study, for example, found alterations in DTI measures of mean diffusivity and fractional anisotropy (FA) in high school football athletes that differed from those in controls.⁵ Most interesting, these alterations in DTI metrics were even more extensive in the single concussed subject in that study. These findings are corroborated by studies in which a greater risk-weighted head impact exposure index was associated with

Received June 11, 2017; accepted after revision October 3.

From the Department of Radiology (S.J.K., C.L., K.R.C., J.R.P.), Brain Imaging and Analysis Center (C.C.H., R.A.M., C.L., J.R.P.), and Department of Translational Neuroscience (R.A.M.), Duke University, Durham, North Carolina; Department of Exercise and Sport Science (M.D.C., M.A.F., K.M.G.), University of North Carolina, Chapel Hill, North Carolina; and Department of Radiological Sciences (S.J.K.), University of Oklahoma Health Sciences Center, Oklahoma City, Oklahoma.

This work was supported by Department Seed Funding, Department of Radiology, Duke University, Durham, North Carolina, and the National Institutes of Health under the Ruth L. Kirschstein National Research Service Award F30NS090816 from the National Institute of Neurological Disorders and Stroke.

Paper previously presented, in part, as a scientific poster at: Annual Meeting of the Radiological Society of North America, November 30–December 5, 2014; Chicago, Illinois.

Please address correspondence to Samuel J. Kuzminski, MD, Department of Radiological Sciences, University of Oklahoma Health Sciences Center, College of Medicine, P.O. Box 2690, Garrison Tower, Suite 4G4250, Oklahoma City, OK 73126; e-mail: sam@kuzminskis.com; @Skuzmi8

 Indicates open access to non-subscribers at www.ajnr.org

<http://dx.doi.org/10.3174/ajnr.A5489>

Table 1: Demographic information and subconcussive head impact burden for study participants^a

Primary Position	Age (yr)	Football Experience (yr)	No. of Prior Concussions	No. of Impacts >10 g	Cumulative Sum of Peak Linear Accelerations (g)	Cumulative Sum of Peak Rotational Accelerations (g)
OL	15	5	0	894	24,564.4	1,810,771.7
DL	15	4	0	875	31,184.3	2,153,609.4
RB	15	10	0	860	28,593.6	1,822,181.9
OL	16	11	0	746	19,564.8	1,239,304.9
LB ^a	16 ^a	10 ^a	3 ^a	642 ^a	18,424.9 ^a	1,281,591.5 ^a
LB	17	6	0	549	15,968.8	1,119,530.6
TE	16	11	3	533	15,452.3	1,030,314.1
WR	16	6	0	387	13,497.6	903,651
DB	16	7	3	323	8164.3	595,068.9
DB	17	12	1	283	8190.2	592,990.3
DB	17	4	0	209	5733.8	354,013.8
WR	16	7	0	207	5017.5	365,631.7
QB	17	7	0	171	4962.7	278,609.3
QB	16	11	0	155	5634.1	368,306.5
WR	16	6	0	99	2589	147,352.9
WR	15	9	3	78	1845.5	130,116.5
QB	17	7	3	20	363.6	25,190.1

Note:—OL indicates offensive lineman; DL, defensive lineman; RB, running back; LB, linebacker; TE, tight end; WR, wide receiver; DB, defensive back; QB, quarterback.

^a Concussed subject.

a greater number of voxels with altered FA.^{6,7} Expanding to other sports, the burden of heading events in adult soccer athletes has been associated with alterations in white matter diffusion metrics and diminished performance on computerized cognitive assessment.^{8,9}

Given the evidence linking subconcussive impacts to neurophysiological and neuroanatomic alterations, the purpose of this pilot study was to use diffusion tensor imaging to assess white matter changes during a single season of high school football. Furthermore, we sought to correlate imaging data with helmet accelerometer and neurocognitive data collected during the same period. We hypothesized that alterations in white matter diffusion tensor metrics from preseason to postseason would correlate with cumulative subconcussive impacts, as measured by helmet accelerometers, and that these DTI changes would also correlate with alterations in neurocognitive measures.

MATERIALS AND METHODS

Subjects

This was a prospective, longitudinal pilot study to investigate the effects of cumulative head impacts during 1 high school football season. An initial MR imaging study was performed for each subject before the start of fall contact practice (average, 4.6 ± 5.0 days before the first contact practice). Within 4 weeks of the end of the season (average, 14.5 ± 8.5 days after the final game), the subjects returned for the postseason MR imaging using the same protocol. If a subject was injured and missed a portion of the season, they were scanned after the completion of the team's season. Any subjects who experienced a diagnosed concussion were asked to undergo an additional MR imaging within 48 hours of the injury in addition to the pre- and postseason scans.

Institutional review board approval was obtained at both participating institutions, Duke University and University of North Carolina, Chapel Hill, before enrollment. Subjects were recruited from a local high school football team by an informational meeting held with players and parents following a noncontact pre-season practice. Because all the subjects were minors, informed

consent was obtained from the subject's legal guardian with assent from the subject before enrollment in the research study.

Any participant with a contraindication to MR imaging was excluded. Individuals with metallic dental or surgical implants that would excessively degrade the echo-planar images were also excluded. Any subject with a structural abnormality on MR imaging, including but not limited to tumors, hematomas, or intraparenchymal hemorrhages, was also excluded.

Neurocognitive Data

Before the start of the season and after the last game of the season, the subjects were administered a computer-based neurocognitive assessment using CNS Vital Signs (<http://cnsvs.com/>). The validity and reliability of CNS Vital Signs have been previously described.^{10,11} Main outcome measures included standard scores for the following domains: verbal memory, visual memory, psychomotor speed, cognitive flexibility, complex attention, processing speed, reasoning, reaction time, and executive functioning. Standard scores are based on a normative dataset that matches participants by age. Subjects also underwent assessment with Neuropsychological Assessment Metrics, which contained scores of physical and verbal aggression, anger, and hostility; aggressiveness, the Buss-Perry Aggression Questionnaire; anxiety, the State-Trait Anxiety Inventory; and impulsivity, the Barratt Impulsiveness Scale.¹²⁻¹⁴

Accelerometer Data

Head impact biomechanics were measured using the Head Impact Telemetry System (Simbex; Lebanon, New Hampshire) mounted in the helmets, which recorded the incidence, direction, and severity of head impacts received by the players. The subjects wore the accelerometer-fitted helmets in all contact practices and games. Head impacts exceeding 10 g of linear acceleration were collected via radiofrequency communication to a sideline unit. Head Impact Telemetry System data were preprocessed by time-gating practice and game sessions and removing non-impact artifacts.

MR Imaging

All pre- and postseason MR imaging was performed at the Brain Imaging and Analysis Center at Duke University Hospital on a 3T scanner (MR750; GE Healthcare, Milwaukee, Wisconsin) with an 8-channel head coil. Diffusion tensor imaging was acquired using the following parameters: b-value = 1000 s/mm², 31 directions, TR/TE = 10,000/96 ms, FOV = 256 × 256 mm², matrix size = 128 × 128, section thickness = 2 mm, 71 axial sections with no interslice gap, resolution = 2 × 2 × 2 mm³. 3D sagittal T1-weighted spoiled gradient-recalled echo was performed for anatomic reference (TE = 1.9 ms, TI = 400 ms, flip angle = 11°, voxel size = 0.93 × 0.93 × 1.2 mm³).

Image Preprocessing

Preprocessing was performed with the FMRIB Diffusion Toolbox (<http://fsl.fmrib.ox.ac.uk/fsl/fslwiki/FDT>) to remove eddy current distortions and to correct for simple head motion. Eddy current distortion was corrected using the FSL software tool, eddy (<https://fsl.fmrib.ox.ac.uk/fsl/fslwiki/eddy>). It simultaneously models the effects of diffusion eddy currents and subject movements on the image. After preprocessing, all images were visually inspected for quality assurance.

Fractional anisotropy was chosen as the single DTI metric to be analyzed in this study for 2 primary reasons: First, FA is the most commonly studied metric in traumatic brain injury, allowing the results to be considered in the context of other available data. Second, given the small sample size and large number of regions studied, FA was chosen as the focus of the study to limit errors due to multiple comparisons. FA is a scalar value describing the degree to which diffusion is asymmetric, or anisotropic, and reflects the presence of underlying ordered microstructure within the tissue, such intact axons and/or myelin sheaths.¹⁵

Fractional anisotropy was calculated for each voxel, and the data were projected onto a group white matter skeleton using Tract-Based Spatial Statistics (TBSS; <http://fsl.fmrib.ox.ac.uk/fsl/fslwiki/TBSS>)¹⁶ in the following manner: The subjects in the sample were coregistered using a method that ensured white matter alignment using an intermediate *df* and nonlinear registration to a 1 × 1 × 1 mm template (FMRIB58_FA; https://fsl.fmrib.ox.ac.uk/fsl/fslwiki/FMRIB58_FA). Mean FA images were generated by averaging these normalized resampled images, and a mean FA skeleton was created in TBSS. After thresholding the skeleton to exclude low FA values (<0.2), we projected each subject's aligned FA image onto the mean FA skeleton.

TBSS Analysis

White matter skeleton difference images of postseason minus pre-season were created to assess changes in FA across the season using a 1-sample *t* test. The difference images were also used to model the mean-centered, continuous covariate of the number of impacts across the season. Design matrices were created using the FSL General Linear Model tool (<http://fsl.fmrib.ox.ac.uk/fsl/fslwiki/GLM>), and the FSL Randomize tool (<http://fsl.fmrib.ox.ac.uk/fsl/fslwiki/Randomise/UserGuide>)¹⁷ was used to perform nonparametric, permutation-based statistical inference with threshold-free cluster enhancement and correction for multiple comparisons.¹⁸ These methods have been described in detail elsewhere.¹⁶ *T*-statistics were used to determine main or interaction effects with an a priori α of .05

Table 2: Parameter estimates from a mixed linear model^a

Parameter	Mean Change in FA ($\times 10^3$)	P Value
(Intercept)	-1.372	.339
ACR	5.360	.058
ALIC	1.906	.499
BCC	-2.767	.326
CC	-1.386	.623
CGC	-1.487	.598
CGH	2.145	.447
CR	2.908	.302
CST	-2.916	.301
EC	0.985	.727
FX ^b	6.677	.018
FXST ^b	-6.268	.027
GCC	-1.024	.716
IC	-1.028	.715
IFO	2.183	.439
PCR	1.698	.547
PLIC	-1.709	.544
PTR	-0.666	.813
RLIC	-3.181	.259
SCC	0.224	.937
SCR	0.772	.784
SFO	-0.132	.963
SLF	-0.744	.792
SS	-0.229	.935
Impacts	-0.00178	.722
Impacts × ACR	-0.00194	.841
Impacts × ALIC	0.00005	.996
Impacts × BCC	0.00811	.402
Impacts × CC	-0.00330	.733
Impacts × CGC	0.01671	.085
Impacts × CGH ^b	-0.02059	.034
Impacts × CR	0.00312	.747
Impacts × CST	0.00699	.471
Impacts × EC	-0.00440	.650
Impacts × FX	0.00951	.326
Impacts × FXST ^b	-0.02641	.007
Impacts × GCC	-0.01075	.267
Impacts × IC	0.00009	.992
Impacts × IFO	-0.01002	.301
Impacts × PCR	0.00327	.735
Impacts × PLIC	0.00033	.973
Impacts × PTR	0.01127	.245
Impacts × RLIC	-0.00015	.988
Impacts × SCC	-0.01306	.178
Impacts × SCR	0.00874	.367
Impacts × SFO	0.01579	.104
Impacts × SLF	0.00970	.317
Impacts × SS	-0.00291	.764

Note:—CGH indicates cingulum hippocampus; CGC, cingulate gyrus; ACR, anterior corona radiata; ALIC, anterior limb of internal capsule; BCC, body of corpus callosum; CC, corpus callosum; CR, corona radiata; CST, corticospinal tracts; EC, external capsule; FX, fornix; IC, internal capsule; GCC, genu of corpus callosum; IFO, inferior fronto-occipital fasciculus; PCR, posterior corona radiata; PLIC, posterior limb of internal capsule; PTR, posterior thalamic radiation; RLIC, retrolenticular part of internal capsule; SCC, splenium of corpus callosum; SCR, superior corona radiata; SFO, superior fronto-occipital fasciculus; SLF, superior longitudinal fasciculus; SS, sagittal stratum.

^a Parameters for region main effects are centered at the mean number of impacts.

^b Indicates statistical significance ($P < .05$).

and 5000 conditional Monte Carlo permutations (giving a confidence limit of $.05 \pm .0062$ for the *P* value).

TBSS ROI Analysis

Mean FA values were derived from the WM skeleton for 24 ROIs using the ENIGMA DTI Protocol (<http://enigma.ini.usc.edu/protocols/dti-protocols/#eDTI>) and applying the ICBM-JHU-

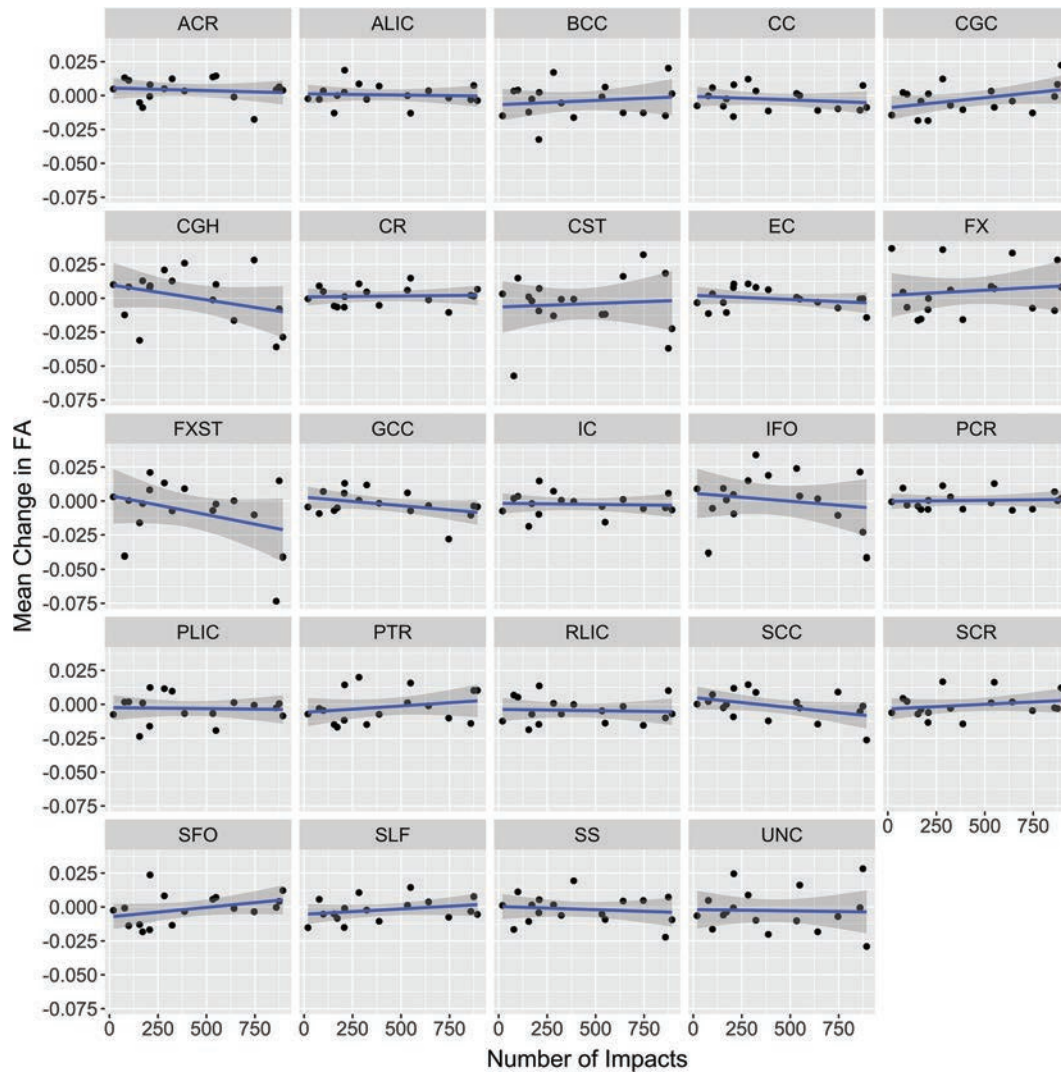


FIG 1. Mean change in FA for each ROI against the frequency of impacts across the season. Ninety-five percent confidence bands are presented as shadows around the linear regression line. CGH indicates cingulum hippocampus; CGC, cingulate gyrus; ACR, anterior corona radiata; ALIC, anterior limb of internal capsule; BCC, body of corpus callosum; CC, corpus callosum; CR, corona radiata; CST, corticospinal tract; EC, external capsule; FX, fornix; IC, internal capsule; GCC, genu of corpus callosum; IFO, inferior fronto-occipital fasciculus; PCR, posterior corona radiata; PLIC, posterior limb of internal capsule; PTR, posterior thalamic radiation; RLIC, retrolenticular part of internal capsule; SCC, splenium of corpus callosum; SCR, superior corona radiata; SFO, superior fronto-occipital fasciculus; SLF, superior longitudinal fasciculus; SS, sagittal stratum; UNC, uncinate fasciculus.

DTI-81 whitematter atlas (<http://neuro.debian.net/pkgs/fsl-jhdti-whitematter-atlas.html>).¹⁹ Pre- to postseason differences in these mean FA values by region were modeled using a mixed linear model with region, number of impacts, and their interaction as fixed effects and subject as a random effect, as depicted in the following equation:

$$\text{Change in FA}_i = \beta_0 + \beta_1 X_{\text{Region}} + \beta_2 X_{\text{Impacts}} + \beta_3 X_{\text{Region}} \times X_{\text{Impacts}} + u_{\text{Subject}} + e_i,$$

where β_0 represents the intercept (mean FA change across all regions at the mean number of impacts); β_1 through β_3 , the coefficients for region, impact number, and their interaction, respectively; u , a subject-specific random effect; and e_i , the residual error term for an arbitrary measurement i . We chose this model to take into account the variability in individual subject responses, recognizing that repeat measurements across regions in the same

subject are likely to be more similar to each other than to measurements from different subjects.²⁰ Parameter estimates for main effects and interactions in each region were determined, with corresponding F -tests. Correlation of FA changes with neuropsychological measures was performed for regions showing a significant interaction. Statistical analyses were performed with R statistical software (<http://www.r-project.org/>),²¹ the statistical package nlme (<https://cran.r-project.org/web/packages/nlme/index.html>),²² SAS 9.3 (SAS Institute, Cary, North Carolina), and JMP 11.2.0 (SAS Institute).

RESULTS

Subjects

Our cohort consisted of 17 male athletes with a mean age of 16 ± 0.73 years and mean football experience of 7.8 ± 2.53 years. Six athletes reported at least 1 previous concussion using

a standard definition of concussion²³; of these 6, five subjects reported 3 previous concussions and 1 subject had 1 prior concussion. The mean number of impacts sustained across the season was 414 ± 291 , with mean cumulative linear and rotational sums of $12,338 \pm 9274$ g and $836,367 \pm 635,830$ rad/s², respectively. Eleven subjects played an offensive primary position, and the rest played defense primarily. Three subjects were linemen, and the remainder were skill positions (any other position except punter or kicker). Subject demographics and subconcussive impact burdens are presented in Table 1, sorted in descending order by the number of impacts. One subject (data listed by footnote a) was concussed on day 93 of the study. He underwent MR imaging the following day, in addition to his postseason scan 39 days after the injury; data from the concussed subject's pre- and postseason scans are included in all group analyses.

TBSS Analysis

No clusters demonstrated a change in FA across the season that was significantly different from zero, after correcting for multiple comparisons. Similarly, no clusters demonstrated a linear relationship between a change in FA across the season and the number of impacts during the season.

TBSS ROI Analysis

Parameter estimates of fixed effects for region, number of impacts, and their interaction terms are provided in Table 2. For the overall mean of the regions, there was no significant main effect across the season or interaction with impacts. The change in FA for each region is plotted as a function of the number of impacts in Fig 1. Of the specific regions examined, 2 were observed to have an interaction with the number of impacts: the cingulum hippocampus and the fornix-stria terminalis (FXST). The parameter estimates for these 2 interactions were both negative, indicating a negative change in FA with a higher number of impacts. Of these 2 regions, the FXST demonstrated a greater magnitude of interaction and a significant main effect, indicating an overall loss of FA at the mean number of impacts across all players. FA reduction in the FXST correlated with a decline in the visual memory score during the season, but not with other available CNS Vital Signs or Neuropsychological Assessment data. Pre- and postseason visual memory scores were available in 14 of the 17 players (Fig 2). Regarding the subject who was concussed during the season, FA in the FXST demonstrated a 4.7% reduction within 24 hours of the concussion. The FA value returned to its baseline level at his post-season follow-up scan (Fig 3).

DISCUSSION

In this pilot study, we used diffusion tensor imaging to examine the effects of subconcussive head trauma in high school football athletes during 1 season. We examined multiple white matter tracts across the brain for changes in FA as a function of the number of linear impacts exceeding a minimal threshold and observed decreases in fractional anisotropy with an increasing number of impacts in 2 tracts, the FXST and the cingulum hippocampus, both of which are components of the limbic system. Overall, the observed effects were greatest in the FXST, where there was also a significant main effect, meaning a fixed

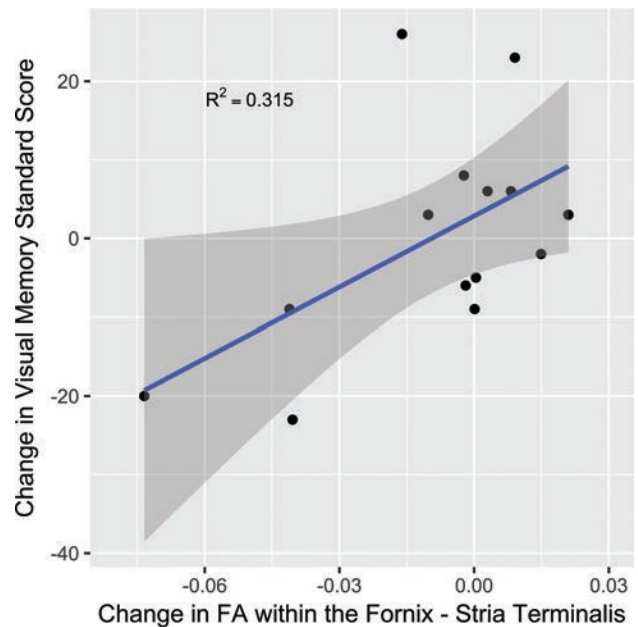


FIG 2. Scatterplot of changes in FXST FA versus change in the visual memory domain standard score from CNS Vital Signs. The 95% confidence band is presented as a shadow around the linear regression line.

pre- to postseason decline in FA in the FXST, compared with other regions.

These results suggest that alterations in white matter tracts within the limbic system may be detectable after only 1 season of play at the high school level. Comparison of limbic system white matter changes with the CNS Vital Signs data revealed a correlation between change in FA in the FXST and visual memory; a reduction in FA corresponded to a worsening of visual memory scores. This same association of FA alterations in the fornix-hippocampal pathway and declining verbal memory scores has previously been found in concussed individuals, suggesting that neural networks involving memory are susceptible to injury and that these alterations in our subjects might be related to repetitive neurotrauma.²⁴

The ROI-labeled fornix-stria terminalis (FXST) correlates anatomically with the crus of the fornix and stria terminalis, which cannot be individually resolved on the white matter skeleton. The fornix is largely implicated in memory formation,^{25,26} whereas the stria terminalis parallels the fornix and is believed to be important in emotional processing, mood, and anxiety.^{27,28} Aside from alterations in visual memory, there were no clinical findings in our study to suggest changes in emotional processing, though it is possible that the lack of detectable changes may be due to the subtle, subclinical nature of white matter injury during a limited period of a single football season.

There are limitations to our study. First, the sample size was small and did not include a group of nonexposed, age-matched controls; therefore, it is not possible to control for alterations in white matter fractional anisotropy related to brain maturation during the season. Second, data suggest that the reproducibility of the ENIGMA-DTI protocol (<http://enigma.usc.edu/protocols/dti-protocols/>) overall is excellent, though the fornix is a region where there is a greater degree of variability among imaging stud-

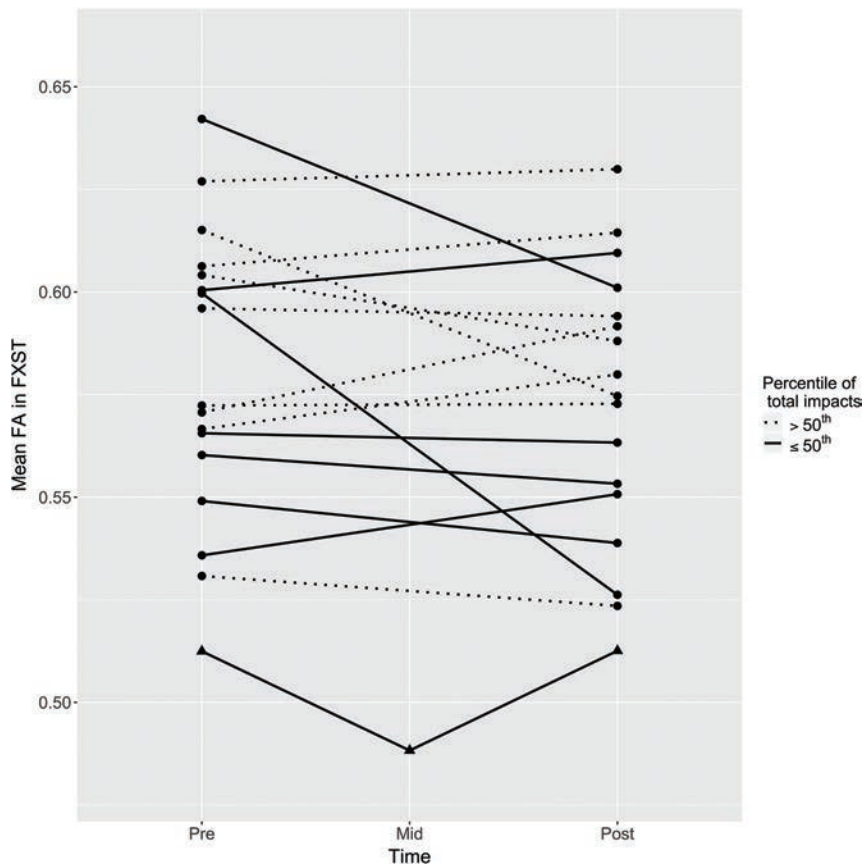


FIG 3. Scatterplot of changes in FXST FA for all subjects across the season. Individual player data are connected by solid or dotted lines based on the median split of the total number of impacts during the season, as depicted in the legend. The concussed subject is plotted with triangles.

ies.²⁹ It is therefore possible that the observed changes in the FXST are due to type I error in our small sample and are not generalizable; however, despite these factors, the finding remained robust to correction for multiple comparisons in the context of our mixed linear model. Nevertheless, we consider this pilot study exploratory and hypothesis-generating, necessitating confirmation in a larger sample. Third, given the small sample size, heterogeneity of trauma, and subtle alterations in white matter FA, type II error is a possibility as well. Perhaps for this reason, voxelwise analysis, with appropriate corrections for multiple comparisons, failed to detect relationships found with the ROI analysis. We believe that using an ROI approach in conjunction with the Tract-Based Spatial Statistics analysis increased sensitivity to subtle changes in white matter without relying on perfect registration, as would be the case in a voxelwise comparison. Moreover, the mixed model allowed a more flexible statistical approach, incorporating a random variable for subject, recognizing that response to head impacts might differ across individuals as a function of a variety of genetic, physiologic, and/or environmental factors.

It is unclear whether most of the measured changes during a single football season might be reversible with rest. Our data in a single subject who sustained a concussion during the season showed an approximately 5% decrease in FXST FA within 24 hours after the concussion, but these values normalized at the postseason scan after several weeks of rest. Although anecdotal,

this evidence confirms the need in future studies for imaging follow-up after sustained periods of rest from contact exposure.

CONCLUSIONS

This pilot study revealed subtle decreases in fractional anisotropy within the white matter tracts of the limbic system that worsened with an increasing number of accelerometer-measured impacts during the season. The white matter changes observed on imaging in the FXST correlated with declines in visual memory, but not other neurocognitive measures. These findings suggest the possibility of white matter injury due to repetitive subclinical impacts while participating in a single season of high school football; however, they will require validation with appropriately powered, hypothesis-driven studies including age-matched controls. Longitudinal studies spanning multiple sequential football seasons with a cohort of subjects will also be useful to evaluate the effects of cumulative trauma, normalization of white matter alterations after rest, and the presence of white matter changes too subtle to manifest in the short period of 1 football season.

Disclosures: Michael D. Clark—RELATED: Grant: National Institute of Neurological Disorders and Stroke, Comments: grant No. F30NS090816.* Money paid to the institution.

REFERENCES

- Omalu BI, Hamilton RL, Kamboh MI, et al. **Chronic traumatic encephalopathy (CTE) in a National Football League player: case report and emerging medicolegal practice questions.** *J Forensic Nurs* 2010;6:40–46 CrossRef Medline
- McKee AC, Cantu RC, Nowinski CJ, et al. **Chronic traumatic encephalopathy in athletes: progressive tauopathy after repetitive head injury.** *J Neuropathol Exp Neurol* 2009;68:709–35 CrossRef Medline
- Stern RA, Daneshvar DH, Baugh CM, et al. **Clinical presentation of chronic traumatic encephalopathy.** *Neurology* 2013;81:1122–29 CrossRef Medline
- Badgeley MA, McIlvain NM, Yard EE, et al. **Epidemiology of 10,000 high school football injuries: patterns of injury by position played.** *Phys Act Health* 2013;10:160–69 CrossRef Medline
- Bazarian JJ, Zhu T, Blyth B, et al. **Subject-specific changes in brain white matter on diffusion tensor imaging after sports-related concussion.** *Magn Reson Imaging* 2012;30:171–80 CrossRef Medline
- Davenport EM, Whitlow CT, Urban JE, et al. **Abnormal white matter integrity related to head impact exposure in a season of high school varsity football.** *J Neurotrauma* 2014;31:1617–24 CrossRef Medline
- Bahrani N, Sharma D, Rosenthal S, et al. **Subconcussive head impact exposure and white matter tract changes over a single season of youth football.** *Radiology* 2016;281:919–26 CrossRef Medline

8. Lipton ML, Kim N, Zimmerman ME, et al. **Soccer heading is associated with white matter microstructural and cognitive abnormalities.** *Radiology* 2013;268:850–57 CrossRef Medline
9. Koerte IK, Ertl-Wagner B, Reiser M, et al. **White matter integrity in the brains of professional soccer players without a symptomatic concussion.** *JAMA* 2012;308:1859–61 CrossRef Medline
10. Gualtieri CT, Johnson LG. **Reliability and validity of a computerized neurocognitive test battery: CNS Vital Signs.** *Arch Clin Neuropsychol* 2006;21:623–43 CrossRef Medline
11. Littleton AC, Register-Mihalik JK, Guskiewicz KM. **Test-retest reliability of a computerized concussion test: CNS Vital Signs.** *Sports Health* 2015;7:443–47 CrossRef Medline
12. Stanford MS, Mathias CW, Dougherty DM, et al. **Fifty years of the Barratt Impulsiveness Scale: an update and review.** *Personality and Individual Differences* 2009;47:385–95 CrossRef
13. Buss AH, Perry M. **The aggression questionnaire.** *J Pers Soc Psychol* 1992;63:452–59 CrossRef
14. Spielberger CD, Gorsuch RL. *Manual for the State-Trait Anxiety Inventory: STAI (Form Y).* Palo Alto: Consulting Psychologists Press; 1983
15. Edlow BL, Copen WA, Izzy S, et al. **Diffusion tensor imaging in acute-to-subacute traumatic brain injury: a longitudinal analysis.** *BMC Neurol* 2016;16:2 CrossRef Medline
16. Smith SM, Jenkinson M, Johansen-Berg H, et al. **Tract-Based Spatial Statistics: voxelwise analysis of multi-subject diffusion data.** *Neuroimage* 2006;31:1487–505 CrossRef Medline
17. Winkler AM, Ridgway GR, Webster MA, et al. **Permutation inference for the general linear model.** *Neuroimage* 2014;92:381–97 CrossRef Medline
18. Smith SM, Nichols TE. **Threshold-free cluster enhancement: addressing problems of smoothing, threshold dependence and localisation in cluster inference.** *Neuroimage* 2009;44:83–98 CrossRef Medline
19. Oishi K, Zilles K, Amunts K, et al. **Human brain white matter atlas: identification and assignment of common anatomical structures in superficial white matter.** *Neuroimage* 2008;43:447–57 CrossRef Medline
20. Detry MA, Ma Y. **Analyzing repeated measurements using mixed models.** *JAMA* 2016;315:407–08 CrossRef Medline
21. Dean CB, Nielsen JD. **Generalized linear mixed models: a review and some extensions.** *Lifetime Data Anal* 2007;13:497–512 CrossRef Medline
22. Pinheiro JC, Bates DM, DebRoy S, et al; R Core Team. *nlme: Linear and Nonlinear Mixed Effects Models.* R package version 3.1–131; 2017
23. McCrory P, Meeuwisse WH, Aubry M, et al. **Consensus statement on concussion in sport: the 4th International Conference on Concussion in Sport held in Zurich, November 2012.** *Br J Sports Med* 2013;47:250–58 CrossRef Medline
24. Alhilali LM, Delic J, Fakhran S. **Differences in callosal and forniceal diffusion between patients with and without postconcussive migraine.** *AJNR Am J Neuroradiol* 2017;38:691–95 CrossRef Medline
25. Sutherland RJ, Rodriguez AJ. **The role of the fornix/fimbria and some related subcortical structures in place learning and memory.** *Behav Brain Res* 1989;32:265–77 CrossRef Medline
26. Markowska AL, Olton DS, Murray EA, et al. **A comparative analysis of the role of fornix and cingulate cortex in memory: rats.** *Exp Brain Res* 1989;74:187–201 Medline
27. Davis M, Walker DL, Miles L, et al. **Phasic vs sustained fear in rats and humans: role of the extended amygdala in fear vs anxiety.** *Neuropsychopharmacology* 2010;35:105–35 CrossRef Medline
28. Lebow MA, Chen A. **Overshadowed by the amygdala: the bed nucleus of the stria terminalis emerges as key to psychiatric disorders.** *Mol Psychiatry* 2016;21:450–63 CrossRef Medline
29. Acheson A, Wijtenburg SA, Rowland LM, et al. **Reproducibility of tract-based white matter microstructural measures using the ENIGMA-DTI protocol.** *Brain Behav* 2017;7:e00615 CrossRef Medline

MR Imaging Characteristics Associate with Tumor-Associated Macrophages in Glioblastoma and Provide an Improved Signature for Survival Prognostication

J. Zhou, M.V. Reddy, B.K.J. Wilson, D.A. Blair, A. Taha, C.M. Frampton, R.A. Eiholzer, P.Y.C. Gan, F. Ziad, Z. Thotathil, S. Kirs, N.A. Hung, J.A. Royds, and T.L. Slatter



ABSTRACT

BACKGROUND AND PURPOSE: In glioblastoma, tumor-associated macrophages have tumor-promoting properties. This study determined whether routine MR imaging features could predict molecular subtypes of glioblastoma that differ in the content of tumor-associated macrophages.

MATERIALS AND METHODS: Seven internally derived MR imaging features were assessed in 180 patients, and 25 features from the Visually AcceSABle Rembrandt Images feature set were assessed in 164 patients. Glioblastomas were divided into subtypes based on the telomere maintenance mechanism: alternative lengthening of telomeres positive (ALT+) and negative (ALT-) and the content of tumor-associated macrophages (with [M+] or without [M-] a high content of macrophages). The 3 most frequent subtypes (ALT+/M-, ALT-/M+, and ALT-/M-) were correlated with MR imaging features and clinical parameters. The fourth group (ALT+/M+) did not have enough cases for correlation with MR imaging features.

RESULTS: Tumors with a regular margin and those lacking a fungating margin, an expansive T1/FLAIR ratio, and reduced ependymal extension were more frequent in the subgroup of ALT+/M- ($P < .05$). Radiologic necrosis, lack of cystic component (by both criteria), and extensive peritumoral edema were more frequent in ALT-/M+ tumors ($P < .05$). Multivariate testing with a Cox regression analysis found the cystic imaging feature was additive to tumor subtype, and *O6-methylguanine methyltransferase* (*MGMT*) status to predict improved patient survival ($P < .05$).

CONCLUSIONS: Glioblastomas with tumor-associated macrophages are associated with routine MR imaging features consistent with these tumors being more aggressive. Inclusion of cystic change with molecular subtypes and *MGMT* status provided a better estimate of survival.

ABBREVIATIONS: ALT = alternative lengthening of telomeres; ALT- = alternative lengthening of telomeres negative; ALT+ = alternative lengthening of telomeres positive; *IDH* = *isocitrate dehydrogenase*; M+ = a tumor with a high content of tumor-associated macrophages; M- = a tumor with a low content of tumor-associated macrophages; *MGMT* = *O6-methylguanine methyltransferase*; PTE = peritumoral edema; VASARI = Visually AcceSABle Rembrandt Images

Glioblastomas are the most common and aggressive primary malignant brain tumor, with an incidence of 5.26 per 100,000 population.¹ With temozolomide and radiation therapy, the median survival is 14.6 months.¹ Patients' response to treatment and prognosis are notoriously variable. Many studies have attributed heterogeneous outcomes to molecular differences

among glioblastomas, such as different means to maintain telomere integrity (telomerase activity or an alternative method known as the alternative lengthening of telomeres [ALT]).² In 2003, the presence of the ALT telomere maintenance mechanism was associated with longer patient survival compared with ALT negative (ALT-) tumors, including those that were telomerase positive (ALT+) and those where the telomere maintenance mechanism was unknown.³

It has been recently found that most tumors without a defined telomere maintenance mechanism contain a high con-

Received March 20, 2017; accepted after revision September 7.

From the Departments of Radiology (J.Z., M.V.R., B.K.J.W.) and Neurosurgery (A.T.), Southern District Health Board, Dunedin, New Zealand; Department of Pathology (J.Z., R.A.E., N.A.H., J.A.R., T.L.S.) and Surgical Sciences (A.T., S.K.), Dunedin School of Medicine, University of Otago, Dunedin, New Zealand; Departments of Radiology (D.A.B.), Neurosurgery (P.Y.C.G.), Pathology (F.Z.), and Medical Oncology (Z.T.), Waikato District Health Board, Hamilton, New Zealand; and Department of Medicine (C.M.F.), University of Otago, Christchurch, New Zealand.

This work was supported by the Health Research Council of New Zealand.

Paper previously presented at: American Roentgen Ray Society Annual Meeting, April 17–26, 2016; Los Angeles, California.

Please address correspondence to Dr. Jean Zhou, Department of Radiology, Dunedin Hospital, Southern District Health Board, 201 Great King St, Private Bag 1921, Dunedin, New Zealand; e-mail: jean.zhou@southerndhb.govt.nz

Indicates open access to non-subscribers at www.ajnr.org

Indicates article with supplemental on-line tables.

<http://dx.doi.org/10.3174/ajnr.A5441>

tent of tumor-associated macrophages (M+) that affects assays assigning telomere maintenance.⁴ The revised subgroups were ALT positive tumors with and without (M-) a high content of macrophages (ALT+/M+ and ALT+/M-) and ALT negative tumors with and without a high content of macrophages (ALT-/M+ and ALT-/M-). With temozolomide treatment, patients with ALT-/M- tumors have improved survival compared with patients with ALT-/M+ tumors,⁴ suggesting that identifying the increased macrophage content will distinguish those with a poor outcome.

MR imaging is a diagnostic tool that evaluates tumor as well as peritumoral characteristics. Improving prognostic determination based on MR imaging features alone has associated radiologic necrosis and peritumoral edema (PTE) with poorer survival.⁵⁻⁸ Tumors with a cystic component have been associated with improved patient survival.^{9,10} However, inconsistencies occur between studies, and MR imaging features are not always found as independent factors associated with survival.¹¹⁻¹⁴

Imaging features have been attributed to differences in tumor biology, suggesting an analysis of MR imaging features combined with molecular characteristics may improve prognostic prediction. *Isocitrate dehydrogenase 1 (IDH1)* mutations, *O6-methylguanine methyltransferase (MGMT)* promoter methylation, and epidermal growth factor receptor overexpressing tumors have been correlated with MR imaging features.^{13,15-19} That tumor biology influences imaging features is further evident in studies that investigate subgroups of glioblastomas based on multiple gene expression differences.²⁰

This study aimed to determine whether MR imaging features were associated with the telomere maintenance mechanism and tumor-associated macrophage content-based subtypes. The inclusion of MR imaging parameters with the molecular subtyping and *MGMT* promoter methylation status²¹ was also investigated to determine whether it could better predict outcome for patients with glioblastoma.

MATERIALS AND METHODS

Study Participants

One hundred eighty patients from Dunedin, Christchurch, and Waikato hospitals in New Zealand with a diagnosis of glioblastoma between the years 2004 and 2014 were included in the study. The cohort was aged between 16–82 years (mean, 61 years; 95% CI, 59–63); 39% were female and 61% male; and 93% were white, 3% Maori, and 4% identified with other ethnic groups. All patients were eligible for standard of care therapy (surgery, radiation therapy, and temozolomide), and no patients received other therapies. The participants were all diagnosed with glioblastoma after the Stupp protocol was used in New Zealand.¹

Participant Selection/Inclusion Criteria

The inclusion criteria were a diagnosis of glioblastoma (as assessed by 2 pathologists independently), no previous lower-grade brain tumor or other brain surgery, and no previous radiation or chemotherapy. No patients received corticosteroids at the time of the preoperative MR imaging scan. Survival time was defined as the time interval (months) between the time of diagnosis (defined as the time of the initial preoperative MR imaging scan) and death.

MR Imaging Features and Interpretation

Preoperative MR imaging scans were evaluated including T1, T2, FLAIR, and postcontrast T1-weighted sequences after intravenous infusion of 10 mL of gadolinium. Images were taken by clinical 1.5T (Siemens, Erlangen, Germany or GE Healthcare, Milwaukee, Wisconsin) scanners. All study scans had routine tumor protocol sequences (T1, T2, FLAIR, DWI, ADC, and postcontrast gadolinium T1), and some had additional susceptibility-weighted sequences. At least 3 reviewers (3 neuroradiologists [M.V.R., B.K.J.W., and D.A.B.] and 1 radiology registrar [J.Z.]) read each MR imaging scan independently in the Public Hospital PACS. All readers were blinded to patient demographics, treatment regimen, and tumor molecular subtypes. The term “overall agreement” was defined as when 3 or more examiners agreed and the term “overall disagreement” was defined as when 2 or more examiners disagreed. In cases with disagreement between reviewers, the cases were reanalyzed in a collaborative fashion by at least 3 examiners, and a consensus score was reached and used in the final analysis.

Based on the current available MR imaging literature and the cumulative experiences from the 2 tertiary centers, 7 imaging features were analyzed, as detailed in Table 1. These features included tumor margin: regular or irregular (Fig 1A, regular margin being a tumor with a smooth enhancing margin on postgadolinium T1 and irregular margin being a tumor that lacks a smooth enhancing margin on postgadolinium T1), fungating or nonfungating (Fig 1B, a fungating margin being a tumor with a thick heterogeneous “brush”-like enhancing rim and nonfungating margin being a tumor that lacks a thick heterogeneous “brush”-like enhancing rim), cystic component (Fig 1C), radiologic necrosis (Fig 1D), limited or extensive PTE (Fig 1E), multifocality (Fig 1F), and hemorrhage (Fig 1G).

The protocol for measuring PTE grade was based on that developed by Wu⁵ and Hartmann.²² The degree of the white matter edema was estimated on the basis of the maximal distance from the tumor margin to the furthest point of the white matter edema. The tumor’s maximal dimension was estimated based on the maximal diameter of the tumor on any axis. When the degree of white matter edema was less or similar (no more than 4 mm greater) to the tumor’s maximal dimension, the edema was considered low grade, and when the degree of white matter edema was greater (more than 4 mm) than the tumor’s maximal dimension, the edema was considered a high-grade.

Furthermore, the Visually Accessible Rembrandt Images (VASARI) feature set was analyzed on 164 cases (<https://wiki.cancerimagingarchive.net/display/Public/VASARI+Research+Project>^{18,23,24}); 16 cases were missing some sequences required for the VASARI analysis.

Telomere Maintenance Mechanism Subtyping

Tumors were classified into 4 subgroups: ALT positive tumors with or without a high content of tumor associated macrophages (ALT+/M+ and ALT+/M-, respectively) and ALT negative tumors with or without a high content of tumor associated macrophages (ALT-/M+ and ALT-/M-, respectively) based on established methods by using paraffin-embedded tumor sections.^{4,25} Tumors from 80 cases were typed for

Table 1: Specific classification of MRI features

Imaging Feature with:	Classification Criteria
Regular enhancing margin	
Yes	Smooth enhancing margin on post-Gd T1
No	Lack of smooth enhancing margin on post-Gd T1
Fungating margin	
Yes	Thick heterogeneous brushlike enhancing rim on post-Gd T1
No	Lack of thick heterogeneous brushlike enhancing rim on post-Gd T1
Cystic	
Yes	A well-circumscribed region with low T1 and high T2 signal; loses signal on the FLAIR sequence
No	Lack of well-circumscribed region with low T1 and high T2 signal; does not lose signal on the FLAIR sequence
Proportion of necrosis	
Yes	An area within the tumor that had high signal on T2 and low signal on T1; had heterogeneous enhancement on post-Gd T1; the proportion of the tumor estimated to represent more than 5% necrosis
No	Less than 5% or none
Proportion of edema ^a	
Limited (<50% of the entire abnormality)	Less than half of the entire abnormality is estimated to represent vasogenic edema
Extensive (> 50% of the entire abnormality)	More than half of the entire abnormality is estimated to represent vasogenic edema
Multifocal and multicentric lesion	
Yes	Two or more enhancing intra-axial tumors on post-Gd T1
No	One intra-axial tumor on post-Gd T1
Hemorrhage	
Yes	Tumor has an area of internal high or isolated T1 and low T2; area of internal high T1 and high T2; area of internal low T1 and low T2. Takes into account that the signal characteristics differ depending on the age of the hemorrhage. SWI sequences were also used.
No	No hemorrhage

Note:—Gd indicates gadolinium.

^a The protocol for measuring PTE grade was based on that by Wu et al⁵ and Hartmann et al.²²

telomere maintenance mechanisms as part of an earlier study, and 100 tumors were new to this study.⁴ The tumor-associated macrophage content was identified by immunohistochemistry staining for CD163 positive macrophages. The CD163 antibody used was EPR19518 (Abcam, Cambridge, United Kingdom), and the macrophage content was estimated as described previously.⁴

Mutant IDH1 and IDH2 Determination

The presence of the R132H IDH1 mutation was estimated by using immunohistochemistry.²⁶ To confirm the presence and frequency of IDH1 mutations and to estimate the number of IDH2 mutations, exon 4 of IDH1 and IDH2 were amplified from tumor-extracted DNA and sequenced.²⁷ Tumor DNA was extracted from paraffin embedded tumor sections or frozen tumor.

MGMT Promoter Methylation Determination

The method to determine whether tumors had a methylated or unmethylated MGMT promoter was based on published methods.^{21,28} In this study, genomic DNA was extracted from paraffin-embedded tumors by using the QIAmp DNA FFPE tissue Kit

(QIAGEN, Tokyo, Japan), and bisulfite DNA conversion was performed by using the EpiTect Bisulfite kit (QIAGEN).

Statistical Methods

The clinico-demographic and MR imaging features were compared between the 3 telomere maintenance–based subtypes by using Pearson χ^2 tests and 1-way ANOVA as appropriate. The κ statistical test was performed to assess the concordance between interobserver agreement. Logistic regression was used to test if imaging could predict the ALT+/M– and ALT–/M+ subtypes and used imaging features as covariants. Survival was compared between the subtypes by using the log-rank test and the independent association of the MR imaging features in addition to the subtype effects. To test multiple variants on survival, Cox proportional hazards regression models were used. A 2-tailed *P* value <.05 was taken to indicate statistical significance.

RESULTS

Whether the 7 internally derived MR imaging features could be consistently identified was investigated by comparing MR imaging scores from the 3 different readers and calculating the percentage of scans on which all 3 blinded reviewers agreed on the presence or absence of each MR imaging feature. κ statistical analyses were performed. The interobserver data including

κ value demonstrated reproducible results (Table 2). The interobserver agreement rate was highest for the glioblastoma cystic component feature (86.2%, $\kappa = 0.71$), followed by multifocal lesion (85.6%, $\kappa = 0.71$). The margin-based parameters had the lowest interobserver agreement percentages (regular margin, 62.9%, $\kappa = 0.23$; fungating margin, 64.6%, $\kappa = 0.28$).

MR Imaging Features Predictive of ALT+ and M+ Status

In the 7 internally derived MR imaging feature groups, the clinico-demographic features and the frequency of IDH1 and IDH2 mutations and MGMT promoter methylation among the telomere maintenance subtypes are given in Table 3. Three telomere maintenance–based subtypes had sufficient numbers to investigate MR imaging features (ALT+/M–, *n* = 26; ALT–/M–, *n* = 92; and ALT–/M+, *n* = 56). Because of the lack of glioblastomas in the ALT+/M+ group (*n* = 6), these cases were not included in the subsequent analyses. The frequency of each MR imaging feature among the telomere-based subtypes is given in Table 4. Five MR imaging features—regular margin, fungating margin, tumor cystic component, radiologic necrosis, and limited

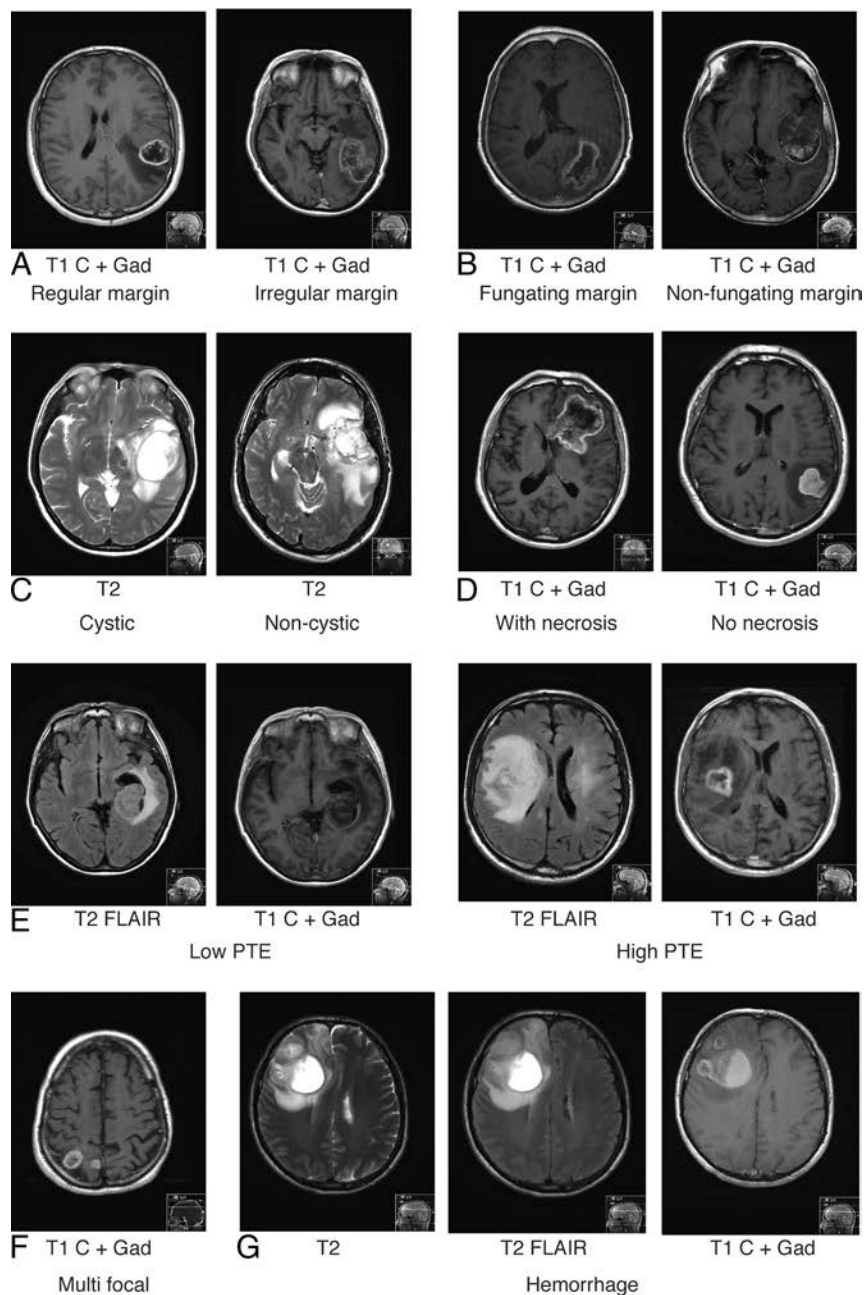


FIG 1. Examples of MR imaging features in glioblastoma. A, Tumor classified with a regular (*left*) or irregular margin (*right*). B, Tumor classified with a fungating (*left*) or nonfungating margin (*right*). C, Tumors classified with a cystic component (*left*) or noncystic component (*right*). D, Tumor classified with (*left*) and without (*right*) radiologic necrosis. E, Tumor classified with low (*limited, left*) and high (*extensive, right*) PTE. F, Tumor classified as being multifocal. G, tumor classified with hemorrhage. Gd indicated gadolinium; C, contrast.

Table 2: Interobserver reliability assessment for MRI features in glioblastoma

MRI Feature	% Where All 3 Reviewers Agree	κ Value
Regular margin	62.9%	0.23
Fungating margin	64.6%	0.28
Cystic	86.2%	0.71
Necrosis	72.6%	0.50
Limited PTE	70.7%	0.43
Hemorrhage	78.3%	0.56
Multifocal lesion	85.6%	0.71

or extensive PTE—showed altered frequency among the 3 tumor subgroups.

The ALT−/M+ subgroup had the lowest incidence of tumors with a cystic component (10.7%) compared with the ALT+/M− (38.5%) and the ALT−/M− (23.9%) groups ($P = .014$). This subtype had the highest incidence of tumors with extensive PTE (44.6% versus 23.1% for ALT+/M− and 22.8% for ALT−/M−, $P = .014$) and the highest incidence of tumors with radiologic necrosis (85.7% versus 72.8% for ALT−/M− and 58% for ALT+/M−; $P = .021$).

The ALT+/M− subgroup had the highest incidence of tumors with a regular margin (58% versus 30% in both the ALT−/M− and ALT−/M+ groups; $P = .026$) and the lowest incidence of tumors with a fungating margin (19% versus 53% and 61% in the ALT−/M− and ALT−/M+ groups, respectively; $P = .002$).

With the exception of PTE, the other MR imaging features were strongly associated with each other. Cystic tumors were more likely to have regular margins with no necrosis, and noncystic tumors were more likely to have irregular margins with necrosis (cystic association with regular margin, $P < .0001$; cystic with no necrosis, $P < .0001$).

To test whether imaging could predict ALT+/M− or an ALT−/M+ status, a logistic regression analysis was performed. For predicting ALT+/M− tumors, 3 features—cystic component (standard error, 1.18; $P = .0077$; OR, 0.04; 95% CI, 0.004–0.43), radiologic necrosis (standard error, 1.16; $P = .0001$; OR, 84; 95% CI, 8.6–821), and fungating margin (standard error, 0.61; $P = .015$; OR, 0.23; 95% CI, 0.07–0.75) showed statistical differences and were included in the final model. For predicting ALT−/M+ tumors, 2 features—extensive PTE (standard error, 0.48; $P = .007$; OR, 0.27; 95% CI, 0.11–0.7) and fungating margin (standard error, 0.36; $P = .014$; OR, 2.5; 95% CI, 1.2–4.8) showed statistical differences and were included in the final model.

Using the VARSARI feature set, 6 VASARI features—side of lesion center (F2), proportion of necrosis (F7), cysts (F8), T1/FLAIR ratio (F10), proportion of edema (F14), and ependymal extension (F19)—were found to be correlated with the 3 tumor subgroups. The full set of VASARI features and the associations with telomere maintenance glioblastoma subtypes is detailed in On-line Table 1.

Table 3: Clinico-demographic features among telomere maintenance glioblastoma subtypes

Demographics	Telomere Maintenance Subtype			Pearson χ^2 (or F-Ratio) and P Values ^a
	ALT+/M- (n = 26)	ALT-/M- (n = 92)	ALT-/M+ (n = 56)	
% Male (no.)	57.7 (15)	63 (58)	57.1 (32)	0.6, .742
Mean age (range), yrs	45.9 (16–66)	64.1 (40–81)	63.2 (39–82)	34.8, <.001
Median survival, mo	21.0	10.6	7.1	40.1, <.001
% Treated with at least 4 cycles of temozolomide (no.)	42.3 (11)	38 (35)	32 (18)	0.63, .629
% Treated with radiotherapy (no.)	84.6 (22)	78.3 (72)	92.9 (52)	5.5, .064
Type of surgery				
Biopsy, % (no.)	15.4 (4)	24 (22)	16 (9)	37.9, <.0001
Near total, % (no.)	76.9 (20)	61 (56)	27.3 (15)	
Partial	8 (2)	15.2 (14)	56.4 (31)	
MGMT promoter methylation status, % (no.)	61.5 (16)	45 (36)	48 (25)	NS
IDH1 and IDH2 mutation status, % (no.)	73 (19)	9 (8)	5 (3)	67, <.0001

Note:—NS indicates not significant.

^a Statistical comparisons were made between 3 groups: ALT+/M-, ALT-/M-, and ALT-/M+.

Table 4: MRI features among telomere maintenance glioblastoma subtypes

MRI Feature	Telomere Maintenance Subtype			Pearson χ^2 and P Values ^a	ALT+/M+
	ALT+/M-	ALT-/M-	ALT-/M+		
No. of patients	26	92	56		6
Regular margin, % (no.)	58 (15)	30 (28)	30 (17)	7.3, .026	33 (2)
Fungating margin, % (no.)	19 (5)	53 (49)	61 (34)	12.8, .002	67 (4)
Cystic component, % (no.)	39 (10)	24 (22)	11 (6)	8.5, .014	50 (3)
Radiologic necrosis, % (no.)	58 (15)	73 (67)	86 (48)	7.7, .021	83 (5)
Extensive PTE, % (no.)	23 (6)	23 (21)	45 (25)	8.6, .014	17 (1)
Multifocal lesion, % (no.)	15 (4)	12 (11)	23 (13)	NS	33 (2)
Hemorrhage, % (no.)	8 (2)	20 (18)	7 (4)	NS	3 (2)

Note:—NS indicates not significant.

^a Statistical comparisons were made between 3 groups: ALT+/M-, ALT-/M-, and ALT-/M+.

Table 5: MRI features among mutant IDH1 and IDH2 tumors

MRI Feature	Tumor Type		Pearson χ^2 and P Values
	IDH1 and IDH2 Mutant (n = 30)	IDH1 and IDH2 Wild-Type (n = 150)	
Regular margin	50%	31%	NS
Fungating margin	33%	55%	4.8 .028
Cystic component	37%	17%	5.7 .017
Radiologic necrosis	63%	77%	NS
Extensive PTE	23%	32%	NS
Multifocal lesion	10%	16%	NS
Hemorrhage	10%	15%	NS

Note:—NS indicates not significant.

The ALT-/M+ subgroup had the lowest incidence of tumors with a cyst (4%) compared with the ALT+/M- (30%) and the ALT-/M- (12%) groups ($P = .007$), the highest incidence of tumors with a higher proportion of necrosis (71%) versus 49% for ALT-/M- and 42% for ALT+/M- ($P = .026$), and the highest incidence of tumors with the highest grade of edema (grade 5; 53%) compared with 32% in the ALT-/M- and 14% in the ALT+/M- group ($P = .002$).

The ALT+/M- subgroup had the highest incidence of tumors with an expansive T1/FLAIR ratio (79%) compared with 41% in the ALT-/M- and 37% in the ALT-/M+ group ($P = .0003$), the lowest incidence of tumors located in the right side of the brain (17%) compared with 41% in the ALT-/M- and 54% in the ALT-/M+ group ($P = .007$), and the lowest incidence of tumors with ependymal extension (30%) compared

with 60% in the ALT-/M- and 49% in the ALT-/M+ group ($P = .036$).

To test whether the VASARI imaging features could predict ALT+/M- or an ALT-/M+ status, a logistic regression analysis was performed. For predicting ALT+/M- tumors, 3 features were significant—F2 side of lesion center % left (standard error, 0.52; $P = .049$; OR, 2.8; 95% CI, 1.01–7.8), F8 cysts (standard error, 0.57; $P = .04$; OR, 3.2, 95% CI, 1.05–9.8), and F10 T1/FLAIR ratio % expansive (standard error, 0.52; $P = .016$; OR, 3.5; 95% CI, 1.26–9.7). To predict ALT-/M+ status, only 1 feature was significant: F8 cysts (standard error, 0.77; $P = .03$; OR, 0.19; 95% CI, 0.04–0.87).

MR Imaging Features Correlated with IDH1 and IDH2 Mutations

In the 7 internally derived MR imaging feature groups, the mutant IDH1 or mutant IDH2 was present in 30 tumors; this included most ALT+/M- ($n = 19/26$, 73%; Table 3) tumors and was less frequent in ALT-/M- ($n = 8/92$, 9%) and ALT-/M+ tumors ($n = 3/56$, 5%).

Tumors with mutant IDH1 and IDH2 had a higher incidence of the cystic component feature (37%) compared with tumors with wild-type IDH1 and IDH2 (17%, $P = .017$) and fewer incidences of tumors with a fungating margin (33%) compared with wild-type tumors (55%, $P = .028$; Table 5). Using the VASARI features, patients with mutant IDH1 and IDH2 glioblastomas had a higher incidence of tumors with an expansive T1/FLAIR ratio (80%) compared with the wild-type tumors (40%, $P < .0001$) and a lower incidence of grade 5 edema (17%) compared with wild-type tumors (38%, $P = .024$; On-line Table 2).

MR Imaging Features Predict Survival Beyond Molecular Status

Consistent with earlier studies, the ALT+/M- subgroup patients had the best survival (Fig 2), and the ALT-/M- subgroup patients had an improved overall survival compared with the

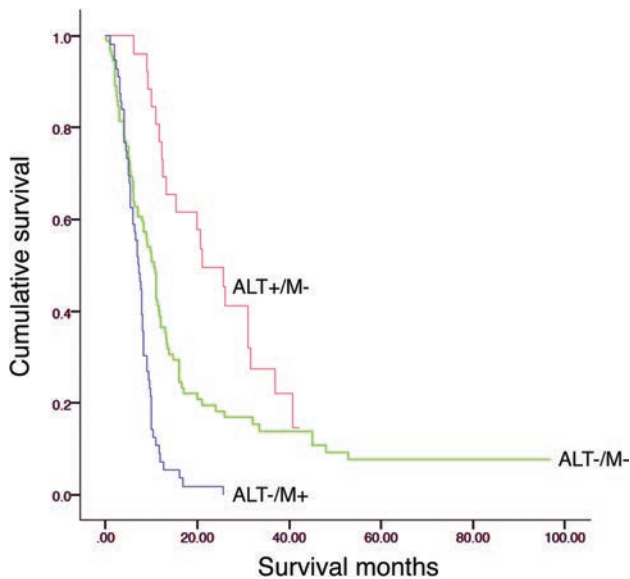


FIG 2. The 3 telomere maintenance mechanism subtypes are associated with differences in patient survival. Eighty cases were those used in a previous study,⁴ and 100 cases were new to this study.

Table 6: Cox regression analysis to test if radiologic features added to telomere maintenance subtype and MGMT promoter methylation status in predicting patient survival

Category Variable	Wald Value	df	Significance P
Molecular subtype	26	2	<.0001
MGMT	6.89	1	.009
Cystic	4	1	.045

ALT-/M+ group (Fig 2, $P < .009$ ALT+/M- versus ALT-/M-, $P < .0001$ ALT+/M- versus ALT-/M+, and ALT-/M- versus ALT-/M+ $P < .001$).^{3,4,29} There were no significant differences ($P > .05$) among telomere maintenance-based subgroups in relation to the amount of patients treated with radiation therapy, concurrent temozolomide, or adjuvant temozolomide. In an earlier study and in this study (Table 4), the ALT-/M+ subgroup was associated with an increased frequency of partial resections compared with near-total resections.⁴

A Cox regression analysis by using forward and backward stepwise models was used to determine whether 4 imaging features (margin regularity, cystic, necrosis, and PTE grade) added to telomere maintenance-based subtype and MGMT promoter methylation status to better determine patient prognosis. Cystic feature was significant ($P = .045$) in predicting patients' survival independent of tumor subtype and MGMT promoter methylation status (Table 6).

DISCUSSION

An assessment of MR imaging features is an advantage to using histologic-based subtypes alone because the characteristics of whole tumor in situ can be assessed before surgery. In this study, we found radiologic features (including the VASARI MR imaging) associated with telomere maintenance and tumor-associated macrophage content-based subtypes, consistent with MR imaging features being informative in identifying differences in tumor biology. A cystic component was additive in predicting an improved patient outcome, suggesting that inclusion of this MR

imaging feature along with an assessment of telomere maintenance subtypes and MGMT promoter methylation status will improve patient outcome prediction. Both feature sets had imaging parameters that predicted the ALT+/M- and the ALT-/M+ subgroups.

Because temozolomide use ALT-/M+ tumors are associated with the poorest survival independent of patient age, extent of surgery, and treatment received.⁴ ALT-/M+ tumors were associated with a higher proportion of necrosis, extensive edema, and lack of a cystic component. Whether the increased macrophage content directly contributes to the associated MR imaging features is unknown. Tumor-associated macrophages have many tumor-promoting activities including proinvasive and proangiogenesis properties.³⁰ Increased edema may result from increased vascular permeability. Increased vascular endothelial growth factor and angiogenesis correlated with edema,^{31,32} and a molecular marker found on endothelial cells (deltalike ligand 4) that functions in angiogenesis was associated with PTE and poorer patient survival.³³ Consistent with a link between PTE and angiogenesis, patients treated with the vascular endothelial growth factor inhibitor bevacizumab had reduced PTE.³⁴

Increased edema has been associated with poorer prognosis.⁶⁻⁸ In the study by Carillo et al,¹³ edema was additive for survival for MGMT methylated but not unmethylated tumors. In the current study, edema was not additive to survival by tumor subtype; this is likely attributable to edema being closely associated with the ALT-/M+ subtype. In a future study, we aim to incorporate quantitative MR imaging techniques, more specifically DTI in vivo to demonstrate the PTE grade.³⁵ The imaging features associated with the ALT-/M+ group are consistent with this subgroup comprising aggressive tumors. The increased content of macrophages in the ALT-/M+ subtype, combined with these tumors having a poorer prognosis that has not changed with temozolomide, suggests this subtype would be an ideal target for immunotherapies, particularly those that could activate macrophages to remove the malignant cells or those that inhibit the tumor-promoting activities of tumor-associated macrophages.^{4,36}

Alternative lengthening of telomere-positive tumors is associated with the best overall patient survival independent of patient age, extent of surgery, treatment received, and IDH1 mutant status.^{3,4,29} In this study, ALT+ tumors were more likely to have a regular margin, lack of a fungating margin, cystic component, expansive T1/FLAIR ratio, and lack of ependymal extension, consistent with ALT+ tumors being less aggressive. The MR imaging data from other studies support ALT+ tumors being less aggressive.^{29,37,38} Sharper margins and less contrast enhancement by MR imaging have been associated with features of ALT+ tumors, including mutant IDH1, mutant tumor protein p53 (TP53), or proneural tumors.^{13,16,18,20,39,40} Considering that most ALT+ tumors in this study had mutant IDH1 or IDH2, MR imaging features of ALT may be due to mutant IDH. The expansive T1/FLAIR VASARI feature had greater significance when tumors were compared based on IDH mutant status rather than telomere maintenance subtype.

The presence of the cystic component was associated with improved survival. A cystic component has been associated with improved survival in some,^{9,10} but not all studies.^{6,12,13} If molec-

ular differences are driving phenotypes that are detected by MR imaging, inconsistencies between studies may be improved if the molecular subgroups are included in analyses of MR imaging features. Tumors that were ALT+/M- and ALT-/M- had a higher cystic component compared with non-ALT+/M+ tumors. In a study by Carrillo et al,¹³ a cystic component was one of 4 features that could predict mutant *IDH1* glioma with 94% accuracy. A cystic component associated with mutant *IDH1* could explain the higher incidence of the cystic component in ALT+ tumors. Similarities exist between clinical parameters for those with cystic glioblastoma and those with secondary glioblastoma, suggesting the cystic component may indicate those with previously undiagnosed low-grade glioma. This may be the case for those with ALT+ tumors because ALT+/M- is more frequent in secondary glioblastoma. A cystic component was present in a considerable portion of ALT-/M- tumors; fewer of these had mutant *IDH1* ($n = 3/22$, 13%), and most are thought to arise de novo.

The cystic component in ALT-/M- tumors may arise because of a different mechanism to that in ALT+ tumors. Why ALT-/M- tumors with a cystic component are associated with improved survival is unclear. The cystic component may represent a distinct tumor biology that responds well to treatment, or it may directly aid in the acquisition or detainment of temozolomide. The cystic component was reproducibly identified among different radiologists. A larger study to investigate whether ALT-/M- tumors with a cystic component are those that respond well to temozolomide is warranted.

Limitations of this study include its retrospective nature. The study excluded patients previously treated with radiation therapy to prevent factors that would affect MR imaging interpretation. This would exclude more patients with secondary glioblastoma that are more likely to be ALT+. Thus, the MR imaging features of the ALT+ group will be representative of a subset of ALT+ tumors.

CONCLUSIONS

The radiologic feature of cystic component was a predictive factor for survival and could be combined with telomere maintenance mechanism and macrophage content-based subtypes and *MGMT* promoter methylation status to provide a better estimation of survival. A lack of cystic component, a lack of left-sided tumor epicenter, higher necrosis and edema, along with a higher ependymal extension are more often present in tumors with a high tumor-associated macrophage content, suggesting that the presence of macrophages leads to a more invasive tumor behavior and a greater difficulty in obtaining near total resection, which could be predicted by MR imaging.

ACKNOWLEDGMENTS

We would like to acknowledge Dr James Fulton for his MR imaging expertise, Mrs Amanda Fisher, Ms Sara Bowie, and Ms Janine Neill for their technical assistance, Ms Helen Morrin and the Cancer Society Tissue Bank, and Mr David Wong for his contribution to data collection.

Disclosures: Jean Zhou—RELATED: Grant: Health Research Council of New Zealand, Comments: titled "Molecular subtypes of glioblastoma predicts tumour behavior"; UNRELATED: Employment: Southern District Health Board, Comments: Radiology

registrar in Dunedin Hospital, Otago, New Zealand; Grants/Grants Pending: Health Research Council, Comments: grant will be used to work on glioblastoma subtyping and imaging clinical trial with ultrasmall superparamagnetic iron oxide particles*. Michael V. Reddy—UNRELATED: Board Membership: Pacific Radiology Group, Comments: a private diagnostic radiology practice; Employment: Pacific Radiology Group and Southern District health Board, Comments: public and private radiology groups for whom I provide radiology services. Ramona A. Eiholzer—RELATED: Grant: Health Research Council of New Zealand*. Tania Slatter—RELATED: Grant: Health Research Council New Zealand*. *Money paid to the institution.

REFERENCES

1. Stupp R, Mason WP, van den Bent MJ, et al. **Radiotherapy plus concomitant and adjuvant temozolomide for glioblastoma.** *N Engl J Med* 2005;352:987–96 CrossRef Medline
2. Pickett HA, Reddel RR. **Molecular mechanisms of activity and derepression of alternative lengthening of telomeres.** *Nat Struct Mol Biol* 2015;22:875–80 CrossRef Medline
3. Hakin-Smith V, Jellinek DA, Levy D, et al. **Alternative lengthening of telomeres and survival in patients with glioblastoma multiforme.** *Lancet* 2003;361:836–38 CrossRef Medline
4. Hung NA, Eiholzer RA, Kirs S, et al. **Telomere profiles and tumor-associated macrophages with different immune signatures affect prognosis in glioblastoma.** *Mod Pathol* 2016;29:212–26 CrossRef Medline
5. Wu CX, Lin GS, Lin ZX, et al. **Peritumoral edema on magnetic resonance imaging predicts a poor clinical outcome in malignant glioma.** *Oncol Lett* 2015;10:2769–76 CrossRef Medline
6. Pope WB, Sayre J, Perlina A, et al. **MR imaging correlates of survival in patients with high-grade gliomas.** *AJNR Am J Neuroradiol* 2005; 26:2466–74 Medline
7. Li WB, Tang K, Chen Q, et al. **MRI manifestations correlate with survival of glioblastoma multiforme patients.** *Cancer Biol Med* 2012;9: 120–23 CrossRef Medline
8. Schoenegger K, Oberndorfer S, Wuschitz B, et al. **Peritumoral edema on MRI at initial diagnosis: an independent prognostic factor for glioblastoma?** *Eur J Neurol* 2009;16:874–78 CrossRef Medline
9. Maldaun MV, Suki D, Lang FF, et al. **Cystic glioblastoma multiforme: survival outcomes in 22 cases.** *J Neurosurg* 2004;100: 61–67 CrossRef Medline
10. Utsuki S, Oka H, Suzuki S, et al. **Pathological and clinical features of cystic and noncystic glioblastomas.** *Brain Tumor Pathol* 2006;23: 29–34 CrossRef Medline
11. Hammoud MA, Sawaya R, Shi W, et al. **Prognostic significance of preoperative MRI scans in glioblastoma multiforme.** *J Neurooncol* 1996;27:65–73 CrossRef Medline
12. Kaur G, Bloch O, Jian BJ, et al. **A critical evaluation of cystic features in primary glioblastoma as a prognostic factor for survival.** *J Neurosurg* 2011;115:754–59 CrossRef Medline
13. Carrillo JA, Lai A, Nghiemphu PL, et al. **Relationship between tumor enhancement, edema, *IDH1* mutational status, *MGMT* promoter methylation, and survival in glioblastoma.** *AJNR Am J Neuroradiol* 2012;33:1349–55 CrossRef Medline
14. Pierallini A, Bonamini M, Osti MF, et al. **Supratentorial glioblastoma: neuroradiological findings and survival after surgery and radiotherapy.** *Neuroradiology* 1996;38 Suppl 1:S26–30 CrossRef Medline
15. Drabycz S, Roldán G, de Robles P, et al. **An analysis of image texture, tumor location, and *MGMT* promoter methylation in glioblastoma using magnetic resonance imaging.** *Neuroimage* 2010;49:1398–405 CrossRef Medline
16. Qi S, Yu L, Li H, et al. **Isocitrate dehydrogenase mutation is associated with tumor location and magnetic resonance imaging characteristics in astrocytic neoplasms.** *Oncol Lett* 2014;7:1895–902 CrossRef Medline
17. Liu XY, Gerges N, Korshunov A, et al. **Frequent *ATRX* mutations and loss of expression in adult diffuse astrocytic tumors carrying *IDH1/IDH2* and *TP53* mutations.** *Acta Neuropathol* 2012;124: 615–25 CrossRef Medline
18. Gutman DA, Dunn WD Jr, Grossmann P, et al. **Somatic mutations**

- associated with MRI-derived volumetric features in glioblastoma. *Neuroradiology* 2015;57:1227–37 CrossRef Medline
19. Aghi M, Gaviani P, Henson JW, et al. **Magnetic resonance imaging characteristics predict epidermal growth factor receptor amplification status in glioblastoma.** *Clin Cancer Res* 2005;11:8600–05 CrossRef Medline
 20. Gutman DA, Cooper LA, Hwang SN, et al. **MR imaging predictors of molecular profile and survival: multi-institutional study of the TCGA glioblastoma data set.** *Radiology* 2013;267:560–69 CrossRef Medline
 21. Hegi ME, Diserens AC, Gorlia T, et al. **MGMT gene silencing and benefit from temozolomide in glioblastoma.** *N Engl J Med* 2005;352:997–1003 CrossRef Medline
 22. Hartmann M, Jansen O, Egelhof T, et al. **Effect of brain edema on the recurrence pattern of malignant gliomas** [Article in German]. *Radiologie* 1998;38:948–53 CrossRef Medline
 23. Rios Velazquez E, Meier R, Dunn WD, Jr., et al. **Fully automatic GBM segmentation in the TCGA-GBM dataset: prognosis and correlation with VASARI features.** *Sci Rep* 2015;5:16822 CrossRef Medline
 24. Gevaert O, Mitchell LA, Achrol AS, et al. **Glioblastoma multiforme: exploratory radiogenomic analysis by using quantitative image features.** *Radiology* 2014;273:168–74 CrossRef Medline
 25. Henson JD, Hannay JA, McCarthy SW, et al. **A robust assay for alternative lengthening of telomeres in tumors shows the significance of alternative lengthening of telomeres in sarcomas and astrocytomas.** *Clin Cancer Res* 2005;11:217–25 Medline
 26. Capper D, Weissert S, Bals J, et al. **Characterization of R132H mutation-specific IDH1 antibody binding in brain tumors.** *Brain Pathol* 2010;20:245–54 CrossRef Medline
 27. Royds JA, Pilbrow AP, Ahn A, et al. **The rs11515 polymorphism is more frequent and associated with aggressive breast tumors with increased ANRIL and decreased p16 (INK4a) expression.** *Front Oncol* 2015;5:306 CrossRef Medline
 28. Palmisano WA, Divine KK, Saccomanno G, et al. **Predicting lung cancer by detecting aberrant promoter methylation in sputum.** *Cancer Res* 2000;60:5954–58 Medline
 29. McDonald KL, McDonnell J, Muntoni A, et al. **Presence of alternative lengthening of telomeres mechanism in patients with glioblastoma identifies a less aggressive tumor type with longer survival.** *J Neuropathol Exp Neurol* 2010;69:729–36 CrossRef Medline
 30. Ludwig HC, Feiz-Erfan I, Bockermann V, et al. **Expression of nitric oxide synthase isozymes (NOS I-III) by immunohistochemistry and DNA in situ hybridization. Correlation with macrophage presence, vascular endothelial growth factor (VEGF) and oedema volumetric data in 220 glioblastomas.** *Anticancer Res* 2000;20:299–304 Medline
 31. Senger DR, Galli SJ, Dvorak AM, et al. **Tumor cells secrete a vascular permeability factor that promotes accumulation of ascites fluid.** *Science* 1983;219:983–85 CrossRef Medline
 32. Carlson MR, Pope WB, Horvath S, et al. **Relationship between survival and edema in malignant gliomas: role of vascular endothelial growth factor and neuronal pentraxin 2.** *Clin Cancer Res* 2007;13:2592–98 CrossRef Medline
 33. Qiu XX, Wang CH, Lin ZX, et al. **Correlation of high delta-like ligand 4 expression with peritumoral brain edema and its prediction of poor prognosis in patients with primary high-grade gliomas.** *J Neurosurg* 2015;123:1578–85 CrossRef Medline
 34. Jain RK, Tong RT, Munn LL. **Effect of vascular normalization by antiangiogenic therapy on interstitial hypertension, peritumor edema, and lymphatic metastasis: insights from a mathematical model.** *Cancer Res* 2007;67:2729–35 CrossRef Medline
 35. Pierpaoli C, Jezzard P, Basser PJ, et al. **Diffusion tensor MR imaging of the human brain.** *Radiology* 1996;201:637–48 CrossRef Medline
 36. Mantovani A, Marchesi F, Malesci A, et al. **Tumour-associated macrophages as treatment targets in oncology.** *Nat Rev Clin Oncol* 2017;14:399–416 CrossRef Medline
 37. Royds JA, Al Nadaf S, Wiles AK, et al. **The CDKN2A G500 allele is more frequent in GBM patients with no defined telomere maintenance mechanism tumors and is associated with poorer survival.** *PloS One* 2011;6:e26737 CrossRef Medline
 38. Chen YJ, Hakin-Smith V, Teo M, et al. **Association of mutant TP53 with alternative lengthening of telomeres and favorable prognosis in glioma.** *Cancer Res* 2006;66:6473–76 CrossRef Medline
 39. Metellus P, Coulibaly B, Colin C, et al. **Absence of IDH mutation identifies a novel radiologic and molecular subtype of WHO grade II gliomas with dismal prognosis.** *Acta Neuropathol* 2010;120:719–29 CrossRef Medline
 40. Wang YY, Wang K, Li SW, et al. **Patterns of tumor contrast enhancement predict the prognosis of anaplastic gliomas with IDH1 mutation.** *AJNR Am J Neuroradiol* 2015;36:2023–29 CrossRef Medline

Diagnostic Accuracy of Centrally Restricted Diffusion in the Differentiation of Treatment-Related Necrosis from Tumor Recurrence in High-Grade Gliomas

N. Zakhari, M.S. Taccone, C. Torres, S. Chakraborty, J. Sinclair, J. Woulfe, G.H. Jansen, and T.B. Nguyen

ABSTRACT

BACKGROUND AND PURPOSE: Centrally restricted diffusion has been demonstrated in recurrent high-grade gliomas treated with bevacizumab. Our purpose was to assess the accuracy of centrally restricted diffusion in the diagnosis of radiation necrosis in high-grade gliomas not treated with bevacizumab.

MATERIALS AND METHODS: In this prospective study, we enrolled patients with high-grade gliomas who developed a new ring-enhancing necrotic lesion and who underwent re-resection. The presence of a centrally restricted diffusion within the ring-enhancing lesion was assessed visually on diffusion trace images and by ADC measurements on 3T preoperative diffusion tensor examination. The percentage of tumor recurrence and radiation necrosis in each surgical specimen was defined histopathologically. The association between centrally restricted diffusion and radiation necrosis was assessed using the Fisher exact test. Differences in ADC and the ADC ratio between the groups were assessed via the Mann-Whitney *U* test, and receiver operating characteristic curve analysis was performed.

RESULTS: Seventeen patients had re-resected ring-enhancing lesions: 8 cases of radiation necrosis and 9 cases of tumor recurrence. There was significant association between centrally restricted diffusion by visual assessment and radiation necrosis ($P = .015$) with a sensitivity of 75% and a specificity of 88.9%, a positive predictive value 85.7%, and a negative predictive value of 80% for the diagnosis of radiation necrosis. There was a statistically significant difference in the ADC and ADC ratio between radiation necrosis and tumor recurrence ($P = .027$).

CONCLUSIONS: The presence of centrally restricted diffusion in a new ring-enhancing lesion might indicate radiation necrosis rather than tumor recurrence in high-grade gliomas previously treated with standard chemoradiation without bevacizumab.

ABBREVIATIONS: HGG = high-grade glioma; RN = radiation necrosis

The appearance of a new ring-enhancing lesion after surgery and chemoradiation for high-grade glioma (HGG) can be seen in tumor recurrence and radiation necrosis (RN). A radiation-induced ring-enhancing lesion contains coagulative necrosis secondary to vascular endothelial injury and fibrinoid necrosis of small blood vessels.¹ On the other hand, the nonenhancing necrotic com-

ponent in recurrent glioblastoma contains liquefactive necrosis.² Differentiation between the 2 remains difficult on conventional MR imaging.³⁻⁶ Diffusion restriction has been reported in HGGs treated with bevacizumab² and in radiation necrosis of metastatic brain lesions.⁷ Our purpose was to assess the accuracy of centrally restricted diffusion in the diagnosis of RN in HGG not treated with bevacizumab.

Received April 20, 2017; accepted after revision October 17.

From the Department of Radiology (N.Z., C.T., S.C., T.B.N.), Division of Neuroradiology, University of Ottawa, The Ottawa Hospital Civic and General Campus, Ottawa, Ontario, Canada; and Division of Neurosurgery (M.S.T., J.S.) and Department of Pathology and Laboratory Medicine (J.W., G.H.J.), University of Ottawa, The Ottawa Hospital Civic Campus, Ottawa, Ontario, Canada.

This work was supported by the Brain Tumour Foundation of Canada (grant awarded in 2012).

Paper previously presented at: Annual Meeting of the American Society of Neuro-radiology and the Foundation of the ASNR Symposium, April 22–27, 2017; Long Beach, California.

Please address correspondence to Thanh B. Nguyen, MD, FRCPC, Department of Radiology, Division of Neuro-radiology, University of Ottawa, The Ottawa Hospital Civic and General Campus, 1053 Carling Ave, Ottawa, Ontario, Canada, K1Y 4E9; e-mail: thnguyen@toh.ca

<http://dx.doi.org/10.3174/ajnr.A5485>

MATERIALS AND METHODS

Patient Population

We consecutively enrolled patients with HGG who developed a new enhancing lesion on follow-up MR imaging after resection, radiation (60 Gy in 30 fractions of 2 Gy during 6 weeks), and temozolomide therapy, from December 2012 to December 2016. The patients were part of a prospective diagnostic accuracy study on dynamic contrast-enhanced and DSC MR imaging for glioma recurrence, approved by our institutional research ethics board. Written informed consent was obtained from all the patients. For the assessment of central diffusion restriction in newly developed necrotic enhancing lesions, the inclusion criteria were the presence of a central area of necrosis

within the newly enhancing lesion and surgical re-resection of this lesion. The exclusion criteria were an entirely solid newly enhancing lesion, bevacizumab therapy, and an operation >3 months after the study MR imaging. A short interval between the operation and the MR imaging was chosen to ensure that the pathology results were representative of the lesions visualized on the imaging study.

MR Imaging Acquisition Protocols

Each patient was scanned on a 3T MR imaging scanner (Magnetom Trio; Siemens, Erlangen, Germany) with the following parameters: conventional MR imaging protocol using axial T1 precontrast (TR = 280 ms, TE = 2.51 ms, flip angle = 90°, voxel size = 1.1 × 0.9 × 3 mm), axial FLAIR (TR = 9710 ms, TE = 93 ms, TI = 2580 ms, voxel size = 1.1 × 0.9 × 3 mm), axial T2 (TR = 6910 ms, TE = 97 ms, voxel size = 0.7 × 0.7 × 3 mm), and a postcontrast axial T1 volumetric interpolated brain examination (TR = 8.48 ms, TE = 3.21 ms, flip angle = 12°, voxel size = 1 × 1 × 1 mm). We used an IV injection of 0.1 mmol/kg of gadobutrol (Gadovist 1.0; Bayer Schering Pharma, Berlin, Germany). Diffusion tensor imaging was performed with the following parameters: TR = 3100 ms, TE = 106 ms, 20 directions, $b = 0/1000$, voxel size = 1.3 × 1.3 × 2.5 mm.

MR Image Interpretation and Data Collection

The ADC maps were coregistered to the axial T1-weighted post-contrast images using a commercially available software (Olea Sphere 1.3; Olea Medical, La Ciotat, France). Qualitative and quantitative assessments were performed by 1 neuroradiologist (N.Z.) blinded to the clinical information and histopathologic results. The presence of centrally restricted diffusion within part or all of the necrotic component was visually assessed in each ring-enhancing lesion and recorded as present or absent. Central diffusion restriction was defined as higher signal on trace images with lower signal on ADC compared with the rest of the lesion. For quantitative analysis, ADC values were calculated from DTI. Separate ROIs (Fig 1C) were manually placed within the necrotic component of each lesion excluding the enhancing wall, as well as within the enhancing component of the lesions, and the minimum ADC was recorded. The ROI size was kept between 20 and 30 mm². ROIs were placed in the contralateral normal-appearing white matter. We calculated the following ADC ratios: ADC Necrosis Ratio = ADC Central Necrosis/ADC White Matter; ADC Enhancement Ratio = ADC Enhancing Component/ADC White Matter; and ADC Necrosis/Enhancement Ratio = ADC Central Necrosis/ADC Enhancing Component.

Histopathologic Analysis

Following surgical resection, an experienced neuropathologist (J.W. or G.H.J.), blinded to the imaging findings, determined the presence or absence of viable tumor and/or radiation necrosis using the 2007 World Health Organization classification and estimated the percentage of viable tumor and radiation necrosis within the specimen. Visual assessment was performed under ×4 high-power-field microscopy to determine the approximate percentage area of radiation necrosis or tumor recurrence relative to the whole tissue area. The following criteria were used

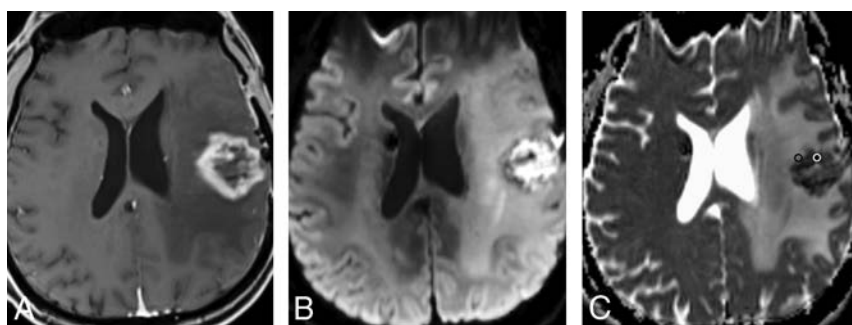


FIG 1. Radiation necrosis: *A*, Axial T1-weighted MR image shows a left frontal necrotic ring-enhancing lesion. *B* and *C*, Axial DWI and ADC map demonstrate diffusion restriction within the necrotic center of the lesion. Representative ROIs are placed on the ADC map corresponding to the enhancing rim (*black ROI*) and the necrotic component (*white ROI*).

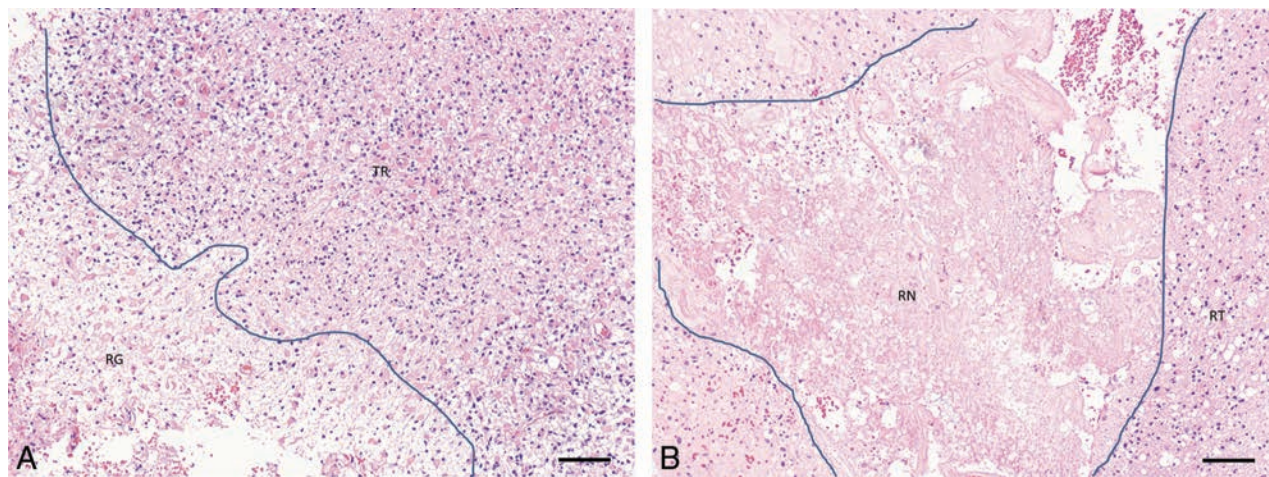


FIG 2. *A*, Specimen showing recurrent tumor (TR) adjacent to an area of brain tissue showing reactive gliosis (RG). *B*, Specimen showing predominantly radiation necrosis (RN, center) with a small amount of viable tumor peripherally containing residual glioma (RT). Lines in both images show interface between reactive brain and radiation necrosis, respectively, with recurrent tumor. Both sections stained with hematoxylin and eosin. Scale bars = 100 microns.

for the diagnosis of radiation necrosis: the presence of coagulative necrosis, hyalinized vessels, and microcalcifications. For the diagnosis of recurrent tumor, we used the following criteria: the presence of increased cellularity and nuclear pleomorphism. Given that most lesions consisted of a mixture of tumor- and treatment-related changes in different proportions, a lesion was categorized as predominantly tumor recurrence or predominantly RN based on the component with the higher proportion in the specimen (Fig 2).

Statistical Analysis

The association between the presence of centrally restricted diffusion and pathologically proved radiation necrosis was assessed

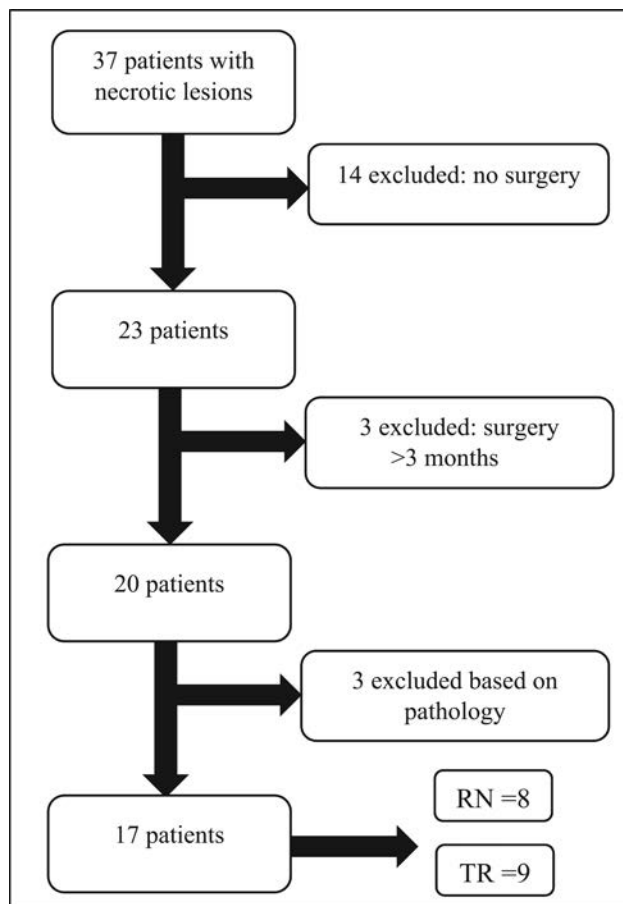


FIG 3. Flow chart illustrating patient selection. TR indicates tumor recurrence.

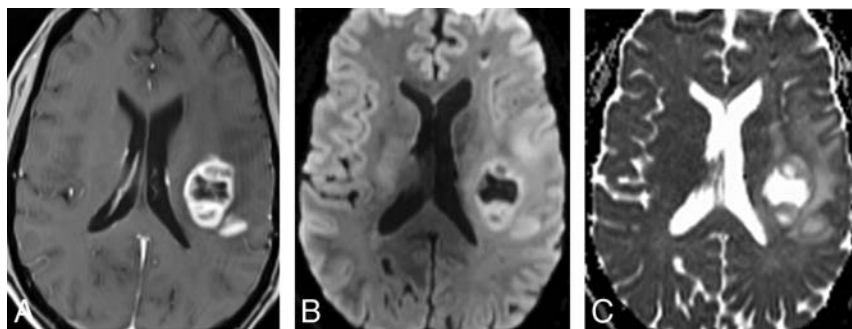


FIG 4. Tumor recurrence. A, Axial T1-weighted MR image shows a left frontal necrotic ring-enhancing lesion. B and C, Axial DWI and ADC map demonstrate facilitated diffusion within the necrotic center of the lesion.

using the Fisher exact test, and the diagnostic accuracy of this finding was calculated using receiver operating characteristic curve analysis. Differences in the minimum ADC and ADC ratio of the necrotic component as well as the enhancing rim between radiation necrosis and tumor recurrence were assessed via the Mann-Whitney *U* test. A *P* value of .05 indicated statistical significance. All data were analyzed with MedCalc for Windows (Version 12; MedCalc Software, Mariakerke, Belgium).

RESULTS

Thirty-seven patients with HGG with new necrotic peripherally enhancing lesions were identified. Twenty-three patients had re-resection of the identified lesions, and 14 had nonsurgical management. Three patients had an operation >3 months after the study MR imaging. Three patients were subsequently excluded on the basis of the pathology results: Two had equal proportions of necrosis and tumor, and 1 had hemorrhage and pus with no evidence of tumor recurrence or RN (Fig 3). Of note, the lesion excluded for presence of pus and blood product in the center of the lesion at the operation had central diffusion restriction on imaging.

There were 13 men and 4 women in the included patients. Average age was 55.9 ± 10.3 years (range, 33.3–77.6 years). The average duration between the operation and the MR imaging examination was 25.8 ± 23.99 days (range, 1–78 days).

Qualitative Assessment

Nine patients had predominant tumor recurrence, and 8 had predominant RN (Fig 3). The presence of centrally restricted diffusion in the necrotic lesions was significantly associated with the predominance of RN on histopathologic analysis ($P = .015$) (Figs 1 and 4 and Table 1). Central diffusion restriction was seen in 6 patients with RN. From the 9 patients with predominant tumor recurrence, only 1 patient had central diffusion restriction. On histopathologic analysis, radiation necrosis comprised approximately 30% of this patient's surgical specimen. The presence of central diffusion restriction had a sensitivity of 75% and a specificity of 88.9%, with a positive predictive value of 85.7% and a negative predictive value of 80% for the diagnosis of radiation necrosis in a newly developed necrotic lesion after treatment of HGG. From the 20 patients who were excluded, 9 patients had central diffusion restriction on visual inspection.

Quantitative Assessment

There was a significant difference in the minimum ADC and ADC ratio in the necrotic component of the tumor recurrence and RN lesions ($P = .027$) with a lower median ADC and ADC ratio in the RN group compared with the tumor recurrence group (Table 2). On the basis of the receiver operating characteristic curve analysis (area under the curve = 0.82; 95% CI, 0.5–0.96; $P = .002$), an ADC cutoff value of $\leq 1316 \times 10^{-6} \text{ mm}^2/\text{s}$ provides 100% specificity for RN but only 55.6% sensitivity. Using a cutoff of $\leq 1197.03 \times 10^{-6} \text{ mm}^2/\text{s}$ results in 80% specificity and 66.7% sensitivity for the identification of RN. Similarly, an ADC necrosis ratio cutoff value

of ≤ 1.78 provides 100% specificity and 55.6% sensitivity for the identification of RN (Fig 5).

No significant difference was found in the ADC and ADC ratio of the enhancing components between tumor recurrence and RN ($P = .63$ and $P = .85$) (Table 2). However, there was a significant difference in the necrotic-to-enhancing component ADC ratio ($P = .043$), with a lower ratio in the RN group (Table 2). On the basis of the receiver operating characteristic curve analysis (area under the curve = 0.79; 95% CI, 0.53–0.95; $P = .001$), a cutoff value of ≤ 0.95 provides 88.9% sensitivity and 62.5% specificity for RN (Fig 5).

DISCUSSION

The results of the current study suggest that evaluation of diffusion restriction in the nonenhancing necrotic center rather than the peripheral enhancing component of ring-enhancing lesions developing after treatment of HGG may be a useful tool in differentiating RN from tumor recurrence. Central diffusion restriction is associated with a predominance of radiation necrosis on pathology, with a lower minimum ADC in the lesion center in RN compared with tumor recurrence.

Most of the previously published studies assessing the diagnostic accuracy of DWI in differentiating tumor recurrence and RN focused on assessment of diffusion restriction and ADC values in the enhancing component of the lesion with the expectation that the increased cellularity in tumor recurrence and increased extracellular space associated with cell death in RN would result in diffusion restriction and lower ADC values with tumor recurrence.⁸⁻¹⁰ However, the results were not consistent.¹¹⁻¹⁵ A meta-analysis of the diagnostic accuracy of DWI showed moderate diagnostic performance and recommended against the use of DWI alone in differentiating RN and tumor recurrence.¹⁶

Like the results of the current study, evaluation of the central zone of radiation necrosis and malignant glioma in rat models

identified a pattern of central diffusion restriction in radiation necrosis with significantly lower ADC values compared with malignant glioma. The diffusion restriction in the central zone of radiation necrosis corresponded to coagulative necrosis on histopathology.¹²

Asao et al¹⁷ reported that most of the radiation necrosis lesions in their patient population, consisting predominantly of astrocytic neoplasms, had heterogeneous signal intensity on DWI with hyperintensities within the lesions. There are also a few reported cases in the literature with diffusion restriction in the center of radiation necrosis, simulating central diffusion restriction in the abscess.^{18,19} In fact, one of the cases that showed central diffusion restriction in our series was found to have infection and hemorrhage within the lesion center at the operation.

Nonenhancing diffusion restriction has also been reported in bevacizumab-treated HGG^{20,21} as well as bevacizumab-treated brain metastasis.²² Nguyen et al² demonstrated that progressively expanding diffusion restriction in HGG treated with bevacizumab pathologically represents coagulative necrosis surrounded by viable tumor cells. They also showed lower ADC in the diffusion-restricted necrosis compared with the hypercellular nonenhancing tumor.

In their series of treated metastatic lesions, Cha et al⁷ described a 3-layer pattern of radiation necrosis with a central core of lique-

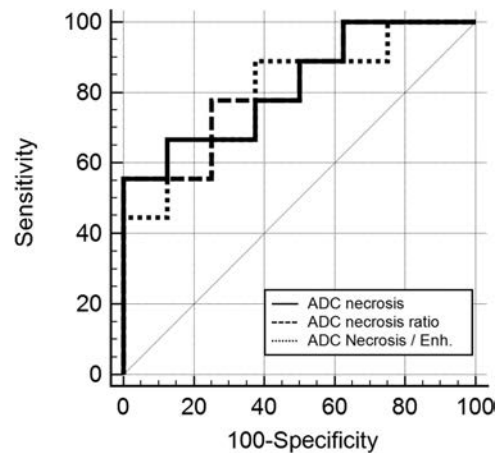


FIG 5. Graph displaying ADC central necrosis, the ADC necrosis ratio, and ADC necrosis/enhancement receiver operating characteristic curves.

Table 1: Results of qualitative assessment for the presence of centrally restricted diffusion

Diagnosis	Central Diffusion Restriction	
	Present	Absent
RN	6	2
TR	1	8

Note:—TR indicates tumor recurrence.

Table 2: Median ADC values and ADC ratios of the necrotic and enhancing components for radiation necrosis and tumor recurrence^a

ADC	RN		TR		P
	Median	95% CI	Median	95% CI	
Necrosis (10^{-6} mm ² /s)	992.15 (755.06–1197.29)	684.72–1220.80	1759.86 (1136.70–2401.44)	1054.80–2588.01	.027
Necrosis ratio ^b	1.24 (0.96–1.57)	0.91–1.74	2.21 (1.41–2.9)	1.31–3.32	.027
Enhancement (10^{-6} mm ² /s)	1044.37 (945.09–1229.65)	867.08–1245.53	1106.70 (958.53–1200.02)	955.86–1241.24	.63
Enhancement ratio ^c	1.38 (1.13–1.55)	1.02–1.59	1.39 (1.14–1.51)	1.12–1.60	.85
Necrosis/enhancement ^d	0.93 (0.74–1.07)	0.56–1.27	1.59 (0.98–2.3)	0.96–2.41	.043

Note:—TR indicates tumor recurrence.

^a Interquartile ranges are in parentheses.

^b Necrosis Ratio = ADC Central Necrosis/ADC White Matter.

^c Enhancement Ratio = ADC Enhancing Component/ADC White Matter.

^d Necrosis/Enhancement = ADC Central Necrosis/ADC Enhancing Component.

fied necrosis showing increased ADC, a nonenhancing middle layer of coagulative necrosis with low ADC, and an outer layer of elevated CBV representing a zone of active inflammation. Our findings of diffusion restriction centrally in the nonenhancing component along the inner aspect of the enhancing ring likely correspond to the middle layer in their 3-layer pattern. They also showed lower minimum ADC values in RN compared with tumor recurrence, comparable with the current study.⁷

In this study, we included only surgically proved cases, leading to the small number of patients in this series, which is the main limitation to the study. Although only surgically proved cases were included, the pathologic samples were not limited to the areas of diffusion restriction, another limitation to this study. While we classified the lesions into predominant tumor recurrence or RN on the basis of the component with the higher proportion in the surgical specimen, the proportion of tumor in the cases classified as predominant RN in this series ranged from 5% to 20%. However, it can still be argued from a pathologic point of view that the presence of any amount of tumor cells in the specimen should be considered evidence of tumor recurrence. Future studies with image-guided stereotactic biopsy of the regions of centrally restricted diffusion would be of great value in confirming the current findings. The results of this study cannot be generalized to patients treated with bevacizumab or lesions with no necrosis.

CONCLUSIONS

This study shows that the presence of central nonenhancing restricted diffusion in a newly necrotic ring-enhancing lesion might indicate RN rather than tumor recurrence in HGG previously treated with standard chemotherapy without bevacizumab.

Disclosures: Santanu Chakraborty—UNRELATED: Grants/Grants Pending: Bayer Healthcare Pharmaceuticals, GE Healthcare, John Woulfe—UNRELATED: Grants/Grants Pending: Parkinson Society Canada, Canadian Institutes of Health Research, Thanh B. Nguyen—RELATED: Grant: Brain Tumour Foundation of Canada*; UNRELATED: Grants/Grants Pending: Bayer Healthcare Pharmaceuticals, GE Healthcare, Radiological Society of North America. *Money paid to the institution.

REFERENCES

- Chao ST, Ahluwalia MS, Barnett GH, et al. **Challenges with the diagnosis and treatment of cerebral radiation necrosis.** *Int J Radiat Oncol Biol Phys* 2013;87:449–57 CrossRef Medline
- Nguyen HS, Milbach N, Hurrell SL, et al. **Progressing bevacizumab-induced diffusion restriction is associated with coagulative necrosis surrounded by viable tumor and decreased overall survival in patients with recurrent glioblastoma.** *AJNR Am J Neuroradiol* 2016;37:2201–08 CrossRef Medline
- Kumar AJ, Leeds NE, Fuller GN, et al. **Malignant gliomas: MR imaging spectrum of radiation therapy- and chemotherapy-induced necrosis of the brain after treatment.** *Radiology* 2000;217:377–84 CrossRef Medline
- Mullins ME, Barest GD, Schaefer PW, et al. **Radiation necrosis versus glioma recurrence: conventional MR imaging clues to diagnosis.** *AJNR Am J Neuroradiol* 2005;26:1967–72 Medline
- Hygino da Cruz LC Jr, Rodriguez I, Domingues RC, et al. **Pseudoprogression and pseudoresponse: imaging challenges in the assessment of posttreatment glioma.** *AJNR Am J Neuroradiol* 2011;32:1978–85 CrossRef Medline
- Fatterpekar GM, Galheigo D, Narayana A, et al. **Treatment-related change versus tumor recurrence in high-grade gliomas: a diagnostic conundrum—use of dynamic susceptibility contrast-enhanced (DSC) perfusion MRI.** *AJR Am J Roentgenol* 2012;198:19–26 CrossRef Medline
- Cha J, Kim ST, Kim HJ, et al. **Analysis of the layering pattern of the apparent diffusion coefficient (ADC) for differentiation of radiation necrosis from tumour progression.** *Eur Radiol* 2013;23:879–86 CrossRef Medline
- Shah R, Vattoth S, Jacob R, et al. **Radiation necrosis in the brain: imaging features and differentiation from tumor recurrence.** *Radiographics* 2012;32:1343–59 CrossRef Medline
- Chan YL, Yeung DK, Leung SF, et al. **Diffusion-weighted magnetic resonance imaging in radiation-induced cerebral necrosis: apparent diffusion coefficient in lesion components.** *J Comput Assist Tomogr* 2003;27:674–80 CrossRef Medline
- Hein PA, Eskey CJ, Dunn JF, et al. **Diffusion-weighted imaging in the follow-up of treated high-grade gliomas: tumor recurrence versus radiation injury.** *AJNR Am J Neuroradiol* 2004;25:201–09 Medline
- Rock JP, Scarpace L, Hearshen D, et al. **Associations among magnetic resonance spectroscopy, apparent diffusion coefficients, and image-guided histopathology with special attention to radiation necrosis.** *Neurosurgery* 2004;54:1111–17, discussion 1117–19 Medline
- Wang S, Chen Y, Lal B, et al. **Evaluation of radiation necrosis and malignant glioma in rat models using diffusion tensor MR imaging.** *J Neurooncol* 2012;107:51–60 CrossRef Medline
- Kazda T, Bulik M, Pospisil P, et al. **Advanced MRI increases the diagnostic accuracy of recurrent glioblastoma: single institution thresholds and validation of MR spectroscopy and diffusion weighted MR imaging.** *Neuroimage Clin* 2016;11:316–21 CrossRef Medline
- Lee WJ, Choi SH, Park CK, et al. **Diffusion-weighted MR imaging for the differentiation of true progression from pseudoprogression following concomitant radiotherapy with temozolomide in patients with newly diagnosed high-grade gliomas.** *Acad Radiol* 2012;19:1353–61 CrossRef Medline
- Song YS, Choi SH, Park CK, et al. **True progression versus pseudoprogression in the treatment of glioblastomas: a comparison study of normalized cerebral blood volume and apparent diffusion coefficient by histogram analysis.** *Korean J Radiol* 2013;14:662–72 CrossRef Medline
- Zhang H, Ma L, Shu C, et al. **Diagnostic accuracy of diffusion MRI with quantitative ADC measurements in differentiating glioma recurrence from radiation necrosis.** *J Neurol Sci* 2015;351:65–71 CrossRef Medline
- Asao C, Korogi Y, Kitajima M, et al. **Diffusion-weighted imaging of radiation-induced brain injury for differentiation from tumor recurrence.** *AJNR Am J Neuroradiol* 2005;26:1455–60 Medline
- Tung GA, Evangelista P, Rogg JM, et al. **Diffusion-weighted MR imaging of rim-enhancing brain masses: is markedly decreased water diffusion specific for brain abscess?** *AJR Am J Roentgenol* 2001;177:709–12 CrossRef Medline
- Biousse V, Newman NJ, Hunter SB, et al. **Diffusion weighted imaging in radiation necrosis.** *J Neurol Neurosurg Psychiatry* 2003;74:382–84 CrossRef Medline
- Farid N, Almeida-Freitas DB, White NS, et al. **Restriction-spectrum imaging of bevacizumab-related necrosis in a patient with GBM.** *Front Oncol* 2013;3:258 CrossRef Medline
- Rieger J, Bähr O, Müller K, et al. **Bevacizumab-induced diffusion-restricted lesions in malignant glioma patients.** *J Neurooncol* 2010;99:49–56 CrossRef Medline
- Sivasundaram L, Hazany S, Wagle N, et al. **Diffusion restriction in a non-enhancing metastatic brain tumor treated with bevacizumab: recurrent tumor or atypical necrosis?** *Clin Imaging* 2014;38:724–26 CrossRef Medline

Addition of Amide Proton Transfer Imaging to FDG-PET/CT Improves Diagnostic Accuracy in Glioma Grading: A Preliminary Study Using the Continuous Net Reclassification Analysis

A. Sakata, T. Okada, Y. Yamamoto, Y. Fushimi, T. Dodo, Y. Arakawa, Y. Mineharu, B. Schmitt, S. Miyamoto, and K. Togashi



ABSTRACT

BACKGROUND AND PURPOSE: Amide proton transfer imaging has been successfully applied to brain tumors, however, the relationships between amide proton transfer and other quantitative imaging values have yet to be investigated. The aim was to examine the additive value of amide proton transfer imaging alongside [¹⁸F] FDG-PET and DWI for preoperative grading of gliomas.

MATERIALS AND METHODS: Forty-nine patients with newly diagnosed gliomas were included in this retrospective study. All patients had undergone MR imaging, including DWI and amide proton transfer imaging on 3T scanners, and [¹⁸F] FDG-PET. Logistic regression analyses were conducted to examine the relationship between each imaging parameter and the presence of high-grade (grade III and/or IV) glioma. These parameters included the tumor-to-normal ratio of FDG uptake, minimum ADC, mean amide proton transfer value, and their combinations. In each model, the overall discriminative power for the detection of high-grade glioma was assessed with receiver operating characteristic curve analysis. Additive information from minimum ADC and mean amide proton transfer was also evaluated by continuous net reclassification improvement. $P < .05$ was considered significant.

RESULTS: Tumor-to-normal ratio, minimum ADC, and mean amide proton transfer demonstrated comparable diagnostic accuracy in differentiating high-grade from low-grade gliomas. When mean amide proton transfer was combined with the tumor-to-normal ratio, the continuous net reclassification improvement was 0.64 (95% CI, 0.036–1.24; $P = .04$) for diagnosing high-grade glioma and 0.95 (95% CI, 0.39–1.52; $P = .001$) for diagnosing glioblastoma. When minimum ADC was combined with the tumor-to-normal ratio, the continuous net reclassification improvement was 0.43 (95% CI, -0.17 – 1.04 ; $P = .16$) for diagnosing high-grade glioma, and 1.36 (95% CI, 0.79–1.92; $P < .001$) for diagnosing glioblastoma.

CONCLUSIONS: Addition of amide proton transfer imaging to FDG-PET/CT may improve the ability to differentiate high-grade from low-grade gliomas.

ABBREVIATIONS: ADC_{min} = minimum ADC; APT = amide proton transfer; AUC = area under the curve; NRI = net reclassification improvement; ROC = receiver operating characteristic; S0 image = reference dataset acquired without presaturation; SUV = standard uptake value; T/N = tumor-to-normal

MR imaging has an established role for the localization, characterization, and diagnosis of brain tumors, as well as for assessing the effects of treatment. Several studies have demonstrated the utility of various types of advanced sequences for grading brain tumors through the visualization of water diffusion,

tumor metabolites, or perfusion characteristics.^{1,2} For pre- and postoperative assessment of gliomas, DWI has been the most commonly used of these advanced sequences,² and the derived ADC is a quantitative parameter that is inversely correlated with tumor cellularity and hence glioma grade.^{3,4} However, its clinical impact has remained limited because of the substantial overlap in regional ADCs among gliomas of different grades.⁵

PET is another quantitative imaging technique used in neuro-oncology.² The standard uptake value (SUV) obtained with FDG-PET also plays an important role in the grading of brain tumors.² High-grade gliomas generally show a higher level of glucose metabolism than low-grade gliomas and therefore exhibit increased

Received May 19, 2017; accepted after revision October 20.

From the Department of Diagnostic Imaging and Nuclear Medicine (A.S., T.O., Y.F., T.D., K.T.), Brain Research Center (T.O.), Department of Neurosurgery (Y.A., Y.M., S.M.), and Department of Healthcare Epidemiology (Y.Y.), School of Public Health, Kyoto University Graduate School of Medicine, Kyoto, Japan; and Magnetic Resonance (B.S.), Siemens Healthcare, Bayswater, Australia.

This work was supported by a Grant-in-Aid for Scientific Research on Innovative Areas "Initiative for High-Dimensional Data-Driven Science through Deepening of Sparse Modeling" of Ministry of Education, Culture, Sports, Science and Technology, Japan, provided to K.T. (MEXT grant number 25120002).

Please address correspondence to T. Okada, MD, Human Brain Research Center, Kyoto University Graduate School of Medicine, 54 Shogoin Kawaharacho, Sakyo-ku, Kyoto 606-8507, Japan; e-mail: tomokada@kuhp.kyoto-u.ac.jp

Indicates open access to non-subscribers at www.ajnr.org

Indicates article with supplemental on-line photos.

<http://dx.doi.org/10.3174/ajnr.A5503>

SUV. However, physiologic FDG uptake by the brain may obscure tumor uptake. PET also has shortcomings in terms of the cost, exposure to radiation, and relatively low spatial resolution.

In addition to the aforementioned methods, chemical exchange–dependent saturation transfer imaging has recently emerged as a new contrast mechanism for MR imaging in the field of cellular and molecular imaging.^{6–8} This method of magnetization transfer imaging has several variants, one of which is amide proton transfer (APT) imaging, which focuses on endogenous cytosolic proteins and peptides with amide protons in the peptide bond.⁹ This technique has been successfully applied to human brain tumors.^{3,10–16} Some reports have shown that the APT asymmetry value is useful in tumor grading, allowing differentiation of pseudoprogression from recurrence¹⁷ and the assessment of treatment response.^{18,19} However, the relationship between APT and other quantitative imaging values has yet to be investigated.

The purposes of this study were the following: 1) to compare the diagnostic accuracy of APT imaging for preoperative grading of glial tumors with that of DWI and [¹⁸F] FDG-PET, and 2) to examine the additive value of APT imaging combined with [¹⁸F] FDG-PET and DWI for the preoperative grading of gliomas. To quantify the additive value of APT imaging, we used a statistical method called the net reclassification index (NRI), an index that shows how well a new model reclassifies subjects.²⁰ NRI is calculated as the difference in the proportion of subjects classified correctly as opposed to wrongly classified after application of a new model. This measure can demonstrate the superiority of a new model over a previous one.

MATERIALS AND METHODS

Our institutional review board approved this retrospective study (R0120), and the requirement to obtain informed consent was waived.

Patients

Eighty-three consecutive adult (older than 18 years of age) patients with suspected supratentorial gliomas who were treated at our hospital between December 2012 and April 2015 were reviewed. The inclusion criteria were the following: 1) pathologic diagnosis of grades II–IV diffuse glioma (2007 World Health Organization criteria)²¹; 2) the availability of results from preoperative MR imaging, including DWI and APT imaging, and FDG-PET obtained within the year before the operation. Twenty-four patients did not meet the inclusion criteria because of no histology or histology other than glioma ($n = 7$) or incomplete datasets ($n = 17$). Ten patients were also excluded because of major therapeutic intervention (such as an operation, radiation therapy, or chemotherapy including steroids) before imaging ($n = 5$) or severe artifacts ($n = 5$). Finally, we analyzed data from 49 patients who underwent [¹⁸F] FDG-PET/CT and MR imaging, including DWI and APT imaging. Subsets from this patient population ($n = 26$; 13 each) have been used in previous publications,^{15,22} though not with the research focus presented in the current study (Fig 1).

Imaging Acquisition

DWI. MR imaging was conducted by using two 3T scanners (Magnetom Trio; Siemens, Erlangen, Germany) with 32-channel head coils. In addition to the conventional FLAIR sequence

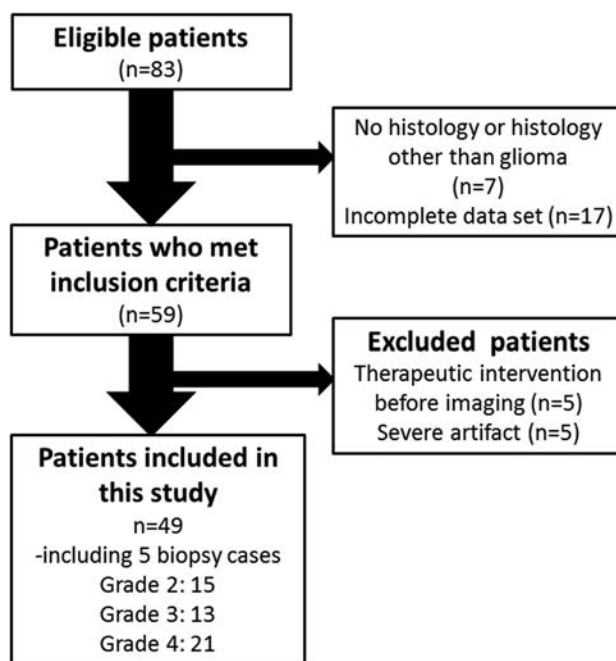


FIG 1. Flowchart showing the 83 eligible patients who received a histologic diagnosis of primary glioma after MR imaging and PET and subsequently underwent an operation during the 29-month period.

(TR/TE, 12,000/100 ms; TI, 2760 ms; flip angle, 120°; resolution, 0.69 × 0.69 mm), T2-weighted FSE (TR/TE, 3200/79 ms; flip angle, 120°; resolution, 0.49 × 0.49 mm) and pre- and postcontrast-enhanced T1-weighted imaging were acquired (using magnetization-prepared rapid acquisition of gradient echo with the following settings: TR/TE, 6/2.26 ms; flip angle, 15°; resolution, 0.9 × 0.9 × 0.9 mm). Contrast materials used were 0.1 mmol/kg of gadopentetate dimeglumine (Magnevist; Bayer HealthCare Pharmaceuticals, Wayne, New Jersey) or gadoteridol (ProHance; Bracco Diagnostics, Princeton, New Jersey). DWI (TR/TE, 5000/77 ms; resolution, 1.4 × 1.4 mm; slice thickness, 3 mm with a 1-mm gap) was performed with motion-probing gradients of $b = 1000 \text{ s/mm}^2$ applied in 3 orthogonal directions. Images without motion-probing gradients were also obtained, and ADC maps were calculated.

APT. APT imaging was conducted using a prototype 3D gradient-echo pulse sequence (TR/TE, 8.3/3.3 ms; flip angle, 12°; 24 slices; resolution, 1.72 × 1.72 × 4 mm). The presaturation pulses consisted of 3 consecutive radiofrequency pulses of 100-ms duration with 100-ms interpulse delays and a time-average amplitude of 2 μT . Eighteen consecutive datasets were acquired with different offset frequencies $\Delta\omega$ (0, ± 0.6 , ± 1.2 , ± 1.8 , ± 2.4 , ± 3.0 , ± 3.6 , ± 4.2 , and ± 4.8 ppm) from the bulk water resonance. Saturated images ($S[\Delta\omega]$) were normalized with a reference dataset acquired without presaturation (S_0 image). The APT effect was calculated as the asymmetry of the magnetization transfer rate using the following equation: $APT_{\text{asym}} = (S[-3.5 \text{ ppm}] - S[+3.5 \text{ ppm}]) / S_0 \times 100$ (%). The APT_{asym} at 3.5 ppm was obtained from linear interpolation between the originally sampled points using an offset resolution of 0.1 ppm and subsequent correction for inhomogeneity of the static magnetic field, as previously described.²³

[¹⁸F] FDG-PET. PET was performed with a PET/CT scanner (Discovery ST Elite; GE Healthcare, Milwaukee, Wisconsin). Each patient fasted for at least 4 hours before PET. After intravenous administration of FDG at 4 MBq/kg body weight, the patient rested in a waiting room for 30 minutes. After performing low-dose CT for attenuation correction, we performed emission scans of the brain for 15 minutes with a 128 × 128 matrix and 47 slices (resolution, 2.0 × 2.0 × 3.27 mm). The reconstructed PET data were converted to SUV data using the following equation: SUV = Count at a Pixel (kBq/cm³) / Injection Dose (MBq) / Weight (kg).

Imaging Analysis

All image processing was conducted by 2 neuroradiologists (A.S. and T.O., with 4 and 22 years of experience of imaging processing) in consensus to double-check the quality. Images were coregistered using SPM8 software (<http://www.fil.ion.ucl.ac.uk/spm/software/spm12>) implemented in Matlab (MathWorks, Natick, Massachusetts). All postcontrast T1-weighted, ADC, S0, and APT images were coregistered to the corresponding FLAIR images and resliced; S0 images were used for coregistration of APT images to anatomic images. Registrations were visually inspected and manually corrected if necessary. FDG-PET images were not coregistered to MR images because the image resolution and contrast were different.

Minimum ADC

Two board-certified neuroradiologists (A.S. and T.D., each with 7 years of experience in diagnostic neuroradiology) analyzed the ADC maps independently using ImageJ, Version 1.48 (National Institutes of Health, Bethesda, Maryland). All continuous sections that included tumor were evaluated by placing 3 circular ROIs over the low-intensity area corresponding to the solid portion of the tumor.²⁴ The area of the ROIs was predefined as 30 mm², and each ROI was carefully positioned to avoid contamination from adjacent tissues and estimation errors caused by necrosis, hemorrhage, or calcification.

APT_{mean}

For the APT images, board-certified neuroradiologists (A.S. and T.D.) independently placed an ROI over a representative slice of the tumor (1 ROI per patient). In case of tumors with an enhancing portion, ROIs were drawn on the enhanced area (viable tumor core) on the contrast-enhanced T1-weighted images. When such enhancement was absent, ROIs were drawn by selecting abnormal signal areas on the FLAIR images. Foci of necrosis, hemorrhage, or calcification were manually avoided. All ROIs were applied to the resliced APT images, and mean values (APT_{mean}) were calculated.

Tumor-to-Normal Ratio

For SUV_{maximum} measurement, 2 neuroradiologists with board certification in nuclear medicine (Y.F. and T.O., with 13 and 18 years of experience respectively) independently drew several oval ROIs (diameter = 10 mm) to include the area with the highest SUV. The number of ROIs varied, depending on the size of the tumor (median, 9; range, 1–25). Fifteen ROIs (5 ROIs on each of 3 axial slices) were also placed on the contralateral frontoparietal gray matter. When a tumor occupied the bilateral lobes, the hemi-

sphere with the largest part of the tumor was defined as the side of the tumor. Semiquantitative analysis was performed using the tumor-to-normal (T/N) ratio, defined as the SUV_{maximum} in the tumor divided by the average SUV of the normal gray matter.²⁵

Pathologic Analysis

Tumors were graded according to the 2007 World Health Organization classification of brain tumors by board-certified neuropathologists with >15 years of experience.²¹ The grade of glial tumor was determined on the basis of histologic characteristics such as nuclear atypia, mitosis, microvascular proliferation, and the presence of necrosis. Immunohistochemical analyses were used when necessary. Grade III and IV tumors were considered high-grade, and grade II tumors, as low-grade.

Statistical Analysis

To determine the interrater reliability for continuous data (T/N ratio, minimum ADC [ADC_{min}] and APT_{mean} measurements), the intraclass correlation coefficient was calculated with a 2-way random model with absolute agreement on average measures. Interpretation of the intraclass correlation coefficient followed methods described by Landis and Koch²⁶: <0, no reproducibility; 0.0–0.20, slight reproducibility; 0.21–0.40, fair reproducibility; 0.41–0.60, moderate reproducibility; 0.61–0.80, substantial reproducibility; and 0.81–1.00, almost perfect reproducibility.

To assess the ability to correctly differentiate high-grade gliomas, we conducted receiver operating characteristic (ROC) curve analysis for APT_{mean}, ADC_{min}, and the T/N ratio. We compared the areas under the curve (AUCs) using the method described by DeLong et al.²⁷

Clinical models were created for logistic regression analysis, combining 2 of the 3 parameters APT_{mean}, ADC_{min}, and the T/N ratio. The added value of the additional imaging beyond [¹⁸F] FDG-PET (which showed the highest AUC for the primary outcome) was quantified by consecutively extending the basic model and assessing the increase in AUC. Furthermore, the number of patients correctly reclassified after adding these parameters was expressed as the NRI. The continuous NRI generalizes a summary measure proposed for reclassification tables by eliminating risk categories and defining any increase in model-based probability resulting from the addition of a new marker as upward reclassification, and any decrease as downward reclassification. The continuous NRI index is equal to twice the difference in the probabilities of upward reclassification for the events minus the nonevents.²⁰ Internal validation for both logistic regression analysis and NRI was performed with 1000 bootstrapped samples. Furthermore, we conducted additional ROC and NRI analyses to evaluate the additive value of APT to ADC.

Statistical analysis was performed using STATA, Version 13 software (StataCorp, College Station, Texas). *P* < .05 was considered indicative of a significant difference.

RESULTS

Patient Characteristics

Forty-nine patients (32 men, 17 women) with a new histopathologic diagnosis of glioma and adequate image sets were included in this study. The mean age was 58.3 years (range, 21–90 years).

Grade II glioma was seen in 15 patients (9 diffuse astrocytomas, 4 oligodendrogliomas, 2 oligoastrocytomas); grade III glioma, in 13 patients (9 anaplastic astrocytomas, 1 anaplastic oligodendroglioma, 3 anaplastic oligoastrocytomas); and glioblastoma, in 21 patients. Five patients underwent surgical biopsy, and 44 patients underwent surgical resection. The characteristics of the patients with low- and high-grade gliomas are given in Table 1. Representative cases are shown in Figs 2 and 3.

Interrater Reliability

Interrater reliability showed almost perfect reproducibility for the T/N ratio, ADC_{min} , and APT measurements, with intraclass

Table 1: Patient characteristics

	Low-Grade Gliomas	High-Grade Gliomas
Patients (No.)	15	34
M/F	10/5	22/12
Age (yr)	51.5 ± 15.9	59.5 ± 15.6
Median (range) of interval between surgery and MRI (day)	45 (1–168)	13 (0–76)
Median (range) of interval between surgery and PET (day)	51 (15–306)	13 (1–218)
T/N	0.75 ± 0.26	1.19 ± 0.43
ADC_{min} ($\times 10^{-6}$ mm ² /s)	980 ± 179	757 ± 221
APT _{mean} (%)	0.87 ± 0.39	1.33 ± 0.46

correlation coefficients of 0.89 (95% confidence interval, 0.81–0.94) for T/N ratio, 0.90 (95% CI, 0.82–0.95) for ADC_{min} , and 0.97 (95% CI, 0.95–0.99) for APT. Given the high interrater reliability, the subsequent statistical evaluation of these measurements used the mean of the values measured by both raters for each patient.

ROC Curve for Each Single Method and Comparison of AUCs

Table 2 and On-line Fig 1 summarize the results of ROC curve analysis for each parameter. No significant differences were seen among T/N_{ratio}, APT_{mean}, and ADC_{min} in the differentiation of higher grade gliomas from lower grade ones (grades III and IV versus grade II, $P = .60$; grade IV versus grades II and III, $P = .68$).

Logistic Regression Analysis to Evaluate the Added Value of APT Imaging to [¹⁸F] FDG-PET for Differentiation of High- from Low-Grade Gliomas

Table 3 and On-line Fig 2 summarize the results for the AUCs of each combination of the 2 parameters. In comparison with the AUC for the T/N ratio alone, some tendencies toward improvement were seen with either combination of the T/N ratio and APT_{mean}, but the differences did not reach statistical significance.

Net Reclassification Improvement to Evaluate the Added Value of APT Imaging to [¹⁸F] FDG-PET for the Diagnosis of High-Grade Glioma

Table 4 summarizes the NRI results for each combination of the 2 parameters. When APT_{mean} was combined with the T/N ratio, the continuous NRI was 0.64 (95% CI, 0.036–1.24, $P = .04$) for diagnosis of high-grade glioma and 0.95 (95% CI, 0.39–1.52; $P = .001$) for the diagnosis of glioblastoma.

Validation

Results of the internal validation are summarized in Tables 5 and 6.

Additive Value of APT Imaging to DWI for Glioma Grading

Table 7 summarizes the results of the AUCs for a combination of ADC_{min} and APT_{mean}. In comparison with the AUC for ADC_{min} alone, some improvement was observed, though the difference did not reach statistical significance (grades III and IV versus grade II, $P = .36$; grade IV versus grades II and III, $P = .42$). The continuous NRI was 0.48 (95% CI, –0.13–1.09, $P = .12$) for the diagnosis of high-grade glioma and 1.14 (95% CI, 0.58–1.71; $P < .001$) for diagnosis of glioblastoma when the APT_{mean} was combined with the ADC_{min} .

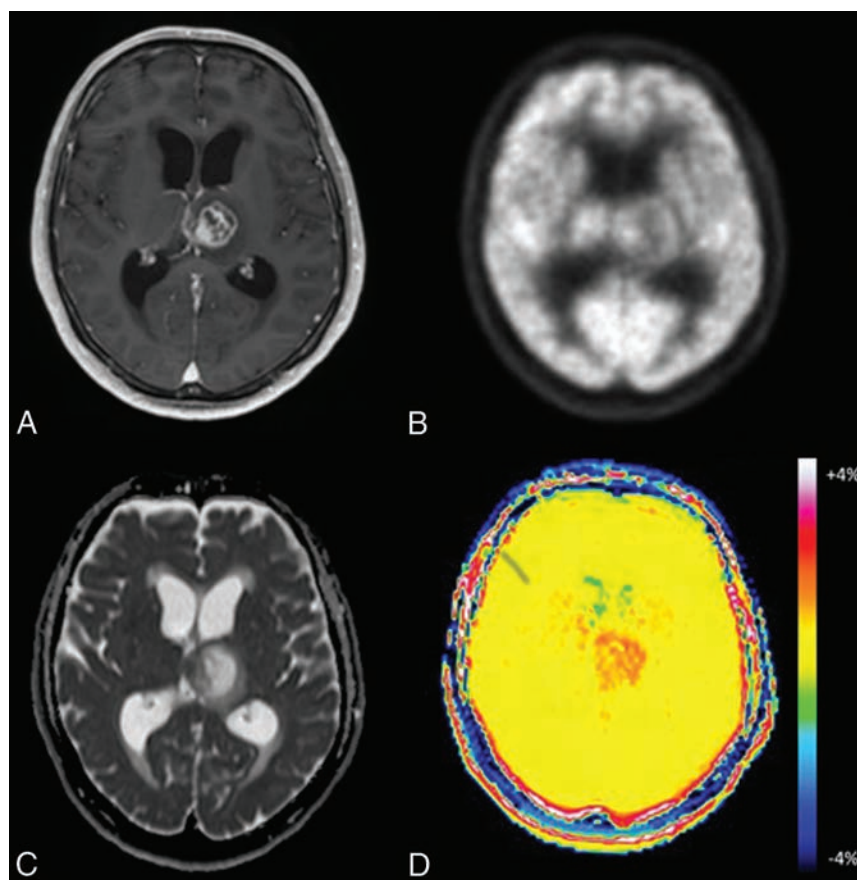


FIG 2. Glioblastoma in a 65-year-old man. A, Axial MR imaging shows a contrast-enhancing lesion in the left thalamus. B, FDG-PET shows less uptake by the lesion compared with gray matter. C, On the ADC map, the medial portion of the tumor demonstrates focal low-to-intermediate ADC values in comparison with normal brain. D, The APT image shows increased signal in both solid and necrotic portions of the tumor.

DISCUSSION

This study has 2 major findings. First, we demonstrated that APT_{mean} offered good diagnostic accuracy for high-grade glioma, comparable with that of other single imaging biomarkers such as ADC_{min} or the T/N ratio from [^{18}F] FDG-PET. Second, our results also indicated that multiparametric analysis including APT and FDG-PET can improve the classification of gliomas of differing aggressiveness.

By focusing on amide protons, APT imaging has been used to visualize endogenous mobile proteins and peptides, and tissue pH, without requiring administration of a contrast agent.^{9,28,29} The method involves a chemical exchange saturation transfer mechanism, with the signal changes observed being the result of a reduction in the bulk water signal intensity caused by chemical exchanges with magnetically labeled backbone amide protons on a resonance of around +3.5 ppm of that of free water.

Prior studies on APT imaging have been successfully applied to the assessment of human brain tumors.^{3,11-18} However, details

of the relationships between APT imaging and other clinical imaging parameters of malignancy have yet to be fully elucidated. This study confirmed that APT imaging can be used for grading glial tumors, with a diagnostic accuracy comparable with that of other imaging biomarkers derived from DWI and FDG-PET. Previous studies have shown the diagnostic accuracy of APT imaging to be comparable with DSC-PWI,^{13,16} and better than contrast-enhanced T1-weighted imaging.²² As in previous studies, our results also demonstrated excellent interrater reproducibility in the measurement of APT.^{3,11-16} We believe that for the preoperative grading of brain tumors, APT can be considered an alternative approach to PET and other MR imaging methods such as DWI.

Multiparametric analysis including APT has the potential to improve the diagnostic accuracy in glioma grading. Several researchers have argued that multiparametric MR imaging methods have the potential to improve the diagnostic performance of preoperative glioma grading.³⁰⁻³² Furthermore, Yoon et al¹ reported that adding FDG-PET to multiparametric MR imaging, including

DWI, PWI, and MR spectroscopy, can improve the diagnostic accuracy of glioma grading. However, few studies have examined glioma grading with multiparametric imaging that included APT imaging and PWI or DWI.^{10,16} To the best of our knowledge, our investigation represents the first study to show the utility of multiparametric analysis, including APT and PET, in the preoperative grading of gliomas.

To assess discrimination in the multiparametric logistic regression analysis, we applied 2 different statistical methods: ROC curve analysis and NRI. In ROC analysis, the AUC is commonly used to measure the discriminatory ability of a model to correctly classify subjects with or without a disease and has thus been a standard metric used to quantify improvement. However, this metric is known to have various limitations, including a lack of clinical relevance and difficulty in interpreting small-magnitude changes.¹⁶ We did not observe any significant gains to the AUCs with the addition of either APT_{mean} or ADC_{min} to the T/N ratio. This was partly due to the relatively high diagnostic accuracy of each single method. As an alternative, NRI allows

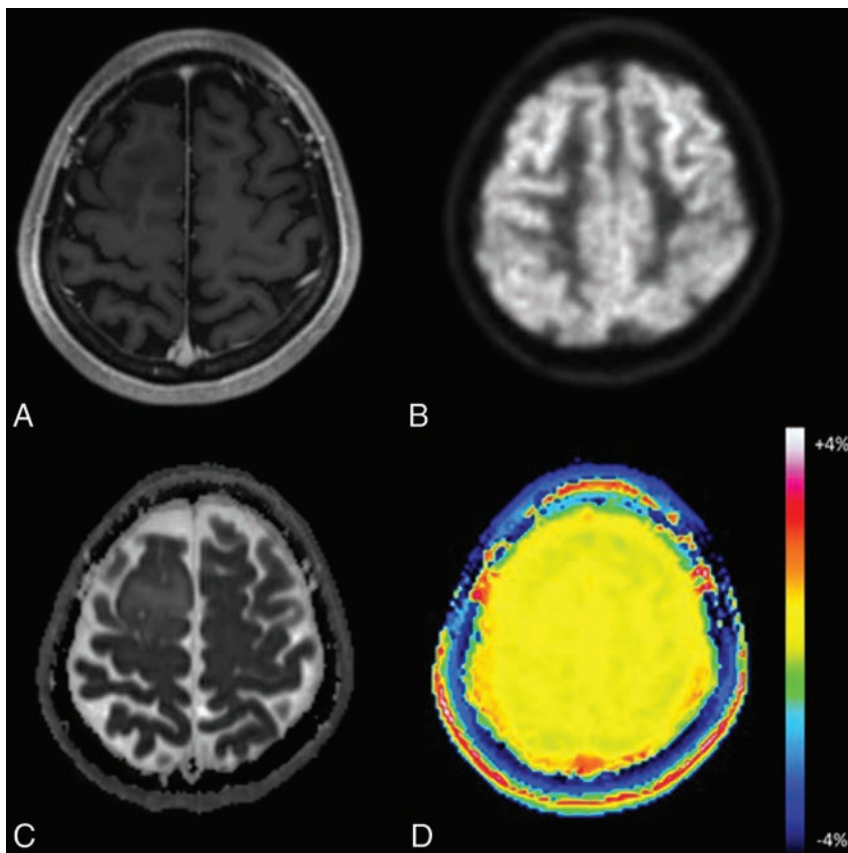


FIG 3. Oligodendroglioma in a 45-year-old woman. *A*, Axial MR imaging shows no contrast-enhancing lesion in the right frontal lobe. *B*, FDG-PET demonstrates little uptake by the lesion compared with gray matter. *C*, On the ADC map, the tumor shows foci with no diffusion restriction within the tumor. *D*, The APT image shows no increased signal in this lesion.

Table 2: AUCs of each single parameter for predicting glioma grading

	Grade II vs Grades III and IV			Grades II and III vs Grade IV		
	AUC	95% CI	Optimal Cutoff	AUC	95% CI	Optimal Cutoff
T/N	0.84	0.72–0.97	0.88	0.85	0.83–0.97	1.03
APT_{mean}	0.76	0.66–0.91	1.26%	0.86	0.76–0.97	1.28%
ADC_{min}	0.78	0.62–0.90	$792.5 \times 10^{-6} \text{ mm}^2/\text{s}$	0.92	0.82–1.00	$788 \times 10^{-6} \text{ mm}^2/\text{s}$

Table 3: AUCs of each combination of parameters for predicting glioma grading

	Grade II vs Grades III and IV			Grades II and III vs Grade IV		
	AUC	95% CI	P Value	AUC	95% CI	P Value
T/N+APT _{mean}	0.85	0.73–0.97	.75	0.9	0.82–0.99	.24
T/N+ADC _{min}	0.86	0.76–0.97	.58	0.94	0.86–1.00	.19
T/N	0.84	0.72–0.97	NA	0.85	0.73–0.98	NA

Note:—NA indicates not applicable.

Table 4: Continuous NRI results with the combination of 2 imaging parameters

	Grade II vs Grades III and IV			Grades II and III vs Grade IV		
	NRI	95% CI	P Value	NRI	95% CI	P Value
T/N+APT _{mean}	0.64	0.036–1.24	.04	0.95	0.39–1.52	.001
T/N+ADC _{min}	0.43	–0.17–1.04	.16	1.36	0.79–1.92	<.0001

Table 5: Validated logistic regression analysis results with the combination of 2 imaging parameters

	Grade II vs Grades III and IV		Grade IV vs Grades II and III	
	AUC	95% CI (Bias-Corrected)	AUC	95% CI (Bias-Corrected)
T/N+APT _{mean}	0.86	0.70–0.95	0.90	0.79–0.97
T/N+ADC _{min}	0.86	0.73–0.95	0.93	0.82–0.99

Table 6: Validated continuous NRI results with the combination of 2 imaging parameters

	Grade II vs Grades III and IV		Grades II and III vs Grade IV	
	NRI	95% CI (Bias-Corrected)	NRI	95% CI (Bias-Corrected)
T/N+APT _{mean}	0.64	–0.14–1.26	0.9	0.29–1.46
T/N+ADC _{min}	0.49	–0.36–1.28	1.33	0.88–1.76

Table 7: AUCs of ADC_{min} and APT_{mean} for predicting glioma grading using ROC curve analysis

	Grade II vs Grades III and IV			Grades II and III vs Grade IV		
	AUC	95%CI	P Value	AUC	95%CI	P Value
ADC _{min} +APT _{mean}	0.82	0.71–0.94	.36	0.94	0.86–1.00	.42
ADC _{min}	0.79	0.66–0.91	NA	0.92	0.82–1.00	NA

Note:—NA indicates not applicable.

quantification of the degree of correct reclassification.^{33,34} This measure is calculated as a change in the proportion of correct classifications minus incorrect ones, resulting from the new model in comparison with the former one.²⁰ Using this approach, we demonstrated that the addition of APT_{mean} to the first model with a T/N ratio achieved significant improvements, while the addition of ADC_{min} offered no significant improvement in the discrimination of high-grade gliomas. On the basis of our observations and prior reports that have shown moderate correlations between APT_{asym} values and histologic or other imaging biomarkers, we believe that APT shows potential as another useful and adjunctive biomarker of tumor aggressiveness in neuro-oncology.

We conducted further analysis to evaluate the additive value of APT imaging to DWI, and our results showed that a combination of APT and ADC did not significantly improve the primary outcome (ie, the diagnostic accuracy of high-grade glioma). This is different from a previous study that demonstrated a significant improvement.¹⁶ Differences in the acquisition parameters may explain the different findings of the 2 studies, but our results may indicate the importance of multitechnique imaging–based diagnosis.

Several limitations must be considered when interpreting the present results. This study was retrospective in design and included a relatively small cohort. We included approximately 20

patients with low-grade gliomas, which prevented us from conducting robust multivariate regression analyses with >2 variables. Second, we excluded patients with grade I glioma for 2 reasons: one being that adult cases with grade I glioma are relatively rare, with most patients with grade I glioma being diagnosed as having pilocytic astrocytoma in our hospital, in addition to being mostly younger than 18 years of age; and the second reason being that grade I glioma is known to be different from diffuse glioma in its pathologic, genetic, and even imaging characteristics.^{35,36} Third, the intervals between imaging and an operation were longer for low-grade gliomas than for high-grade gliomas. This difference was because elective operations were conducted for patients with suspected low-grade gliomas, with FDG-PET being performed in the initial assessment of the tumor in our institution. FDG-PET was usually not repeated before the operation, due to the high cost and radiation exposure. We found no size increases on conventional MR imaging during this interval, so we do not consider this delay as likely to have affected the results, especially considering the relatively low proliferative activity of low-grade glioma.

Fourth, we analyzed only a single representative slice from the APT imaging.

However, a previous study has shown that the difference of measurements on APT imaging has little effect on glioma grading.¹⁵ Fifth, we conducted this study using 2 scanners of the same type, with the same sequences and parameters. To our knowledge, there is no study assessing interscanner or intervender differences in APT imaging. There may well be some interscanner differences, even between scanners of the same type; however, our results showed that APT imaging has additive value, even when different scanners of the same type are used. Finally, we did not examine the relationship between the imaging parameters and the molecular profiles of tumors. Several recent studies have clarified the importance of the molecular status of the tumor, including the mutation of genes such as *IDH-1*, *ATRX*, and *TERT*.^{37,38} We should conduct further studies to investigate the potential associations between imaging parameters and such molecular or genetic profiles of gliomas.

CONCLUSIONS

Our findings indicate that APT, DWI, and FDG-PET are useful for predicting the malignant grade of cerebral glioma. In combination with FDG-PET, APT showed the potential to improve the diagnostic performance in the identification of high-grade glioma. To investigate the accuracy of our results, external validation using larger samples should be conducted in future clinical studies.

ACKNOWLEDGMENTS

We thank Karl Embleton, PhD, from Edanz Group (www.edanzediting.com/ac) for editing a draft of this article.

Disclosures: Tomohisa Okada—UNRELATED: Payment for Lectures Including Service on Speakers Bureaus: Siemens Healthcare Japan, Comments: honorarium for a talk; OTHER RELATIONSHIPS: I have a research collaboration with Siemens Healthcare, Japan. Benjamin Schmitt—UNRELATED: Employment: Siemens Healthcare, Comments: full-time employee. Kaori Togashi—RELATED: Grant: Ministry of Education, Culture, Sports, Science and Technology, Japan (No. 25120002), Comments: governmental research grant; OTHER RELATIONSHIPS: I am conducting collaborative work with Siemens Healthcare.

REFERENCES

1. Yoon JH, Kim JH, Kang WJ, et al. Grading of cerebral glioma with multiparametric MR imaging and 18F-FDG-PET: concordance and accuracy. *Eur Radiol* 2014;24:380–89 CrossRef Medline
2. Chung C, Metser U, Ménard C. Advances in magnetic resonance imaging and positron emission tomography imaging for grading and molecular characterization of glioma. *Semin Radiat Oncol* 2015; 25:164–71 CrossRef Medline
3. Bai Y, Lin Y, Zhang W, et al. Noninvasive amide proton transfer magnetic resonance imaging in evaluating the grading and cellularity of gliomas. *Oncotarget* 2017;8:5834–42 CrossRef Medline
4. Higano S, Yun X, Kumabe T, et al. Malignant astrocytic tumors: clinical importance of apparent diffusion coefficient in prediction of grade and prognosis. *Radiology* 2006;241:839–46 CrossRef Medline
5. Murakami R, Hirai T, Sugahara T, et al. Grading astrocytic tumors by using apparent diffusion coefficient parameters: superiority of a one- versus two-parameter pilot method. *Radiology* 2009;251:838–45 CrossRef Medline
6. van Zijl PC, Yadav NN. Chemical exchange saturation transfer (CEST): what is in a name and what isn't? *Magn Reson Med* 2011;65: 927–48 CrossRef Medline
7. Zaiss M, Bachert P. Chemical exchange saturation transfer (CEST) and MR Z-spectroscopy in vivo: a review of theoretical approaches and methods. *Phys Med Biol* 2013;58:R221–69 CrossRef Medline
8. Vinogradov E, Sherry AD, Lenkinski RE. CEST: from basic principles to applications, challenges and opportunities. *J Magn Reson* 2013;229:155–72 CrossRef Medline
9. Zhou J, Payen JF, Wilson DA, et al. Using the amide proton signals of intracellular proteins and peptides to detect pH effects in MRI. *Nat Med* 2003;9:1085–90 CrossRef Medline
10. Zhou J, Lal B, Wilson DA, et al. Amide proton transfer (APT) contrast for imaging of brain tumors. *Magn Reson Med* 2003;50: 1120–26 CrossRef Medline
11. Togao O, Yoshiura T, Keupp J, et al. Amide proton transfer imaging of adult diffuse gliomas: correlation with histopathological grades. *Neuro Oncol* 2014;16:441–48 CrossRef Medline
12. Park JE, Kim HS, Park KJ, et al. Histogram analysis of amide proton transfer imaging to identify contrast-enhancing low-grade brain tumor that mimics high-grade tumor: increased accuracy of MR perfusion. *Radiology* 2015;277:151–61 CrossRef Medline
13. Togao O, Hiwatashi A, Yamashita K, et al. Grading diffuse gliomas without intense contrast enhancement by amide proton transfer MR imaging: comparisons with diffusion- and perfusion-weighted imaging. *Eur Radiol* 2017;27:578–88 CrossRef Medline
14. Park JE, Kim HS, Park KJ, et al. Pre- and posttreatment glioma: comparison of amide proton transfer imaging with MR spectroscopy for biomarkers of tumor proliferation. *Radiology* 2016;278: 514–23 CrossRef Medline
15. Sakata A, Okada T, Yamamoto A, et al. Grading glial tumors with amide proton transfer MR imaging: different analytical approaches. *J Neurooncol* 2015;122:339–48 CrossRef Medline
16. Choi YS, Ahn SS, Lee SK, et al. Amide proton transfer imaging to discriminate between low- and high-grade gliomas: added value to apparent diffusion coefficient and relative cerebral blood volume. *Eur Radiol* 2017;27:3181–89 CrossRef Medline
17. Ma B, Blakeley JO, Hong X, et al. Applying amide proton transfer-weighted MRI to distinguish pseudoprogression from true progression in malignant gliomas. *J Magn Reson Imaging* 2016;44: 456–62 CrossRef Medline
18. Park KJ, Kim HS, Park JE, et al. Added value of amide proton transfer imaging to conventional and perfusion MR imaging for evaluating the treatment response of newly diagnosed glioblastoma. *Eur Radiol* 2016;26:4390–403 CrossRef Medline
19. Sagiyama K, Mashimo T, Togao O, et al. In vivo chemical exchange saturation transfer imaging allows early detection of a therapeutic response in glioblastoma. *Proc Natl Acad Sci U S A* 2014;111: 4542–47 CrossRef Medline
20. Pencina MJ, D'Agostino RB Sr, D'Agostino RB Jr, et al. Evaluating the added predictive ability of a new marker: from area under the ROC curve to reclassification and beyond. *Stat Med* 2008;27: 157–72; discussion 207–12 CrossRef Medline
21. Louis DN, Ohgaki H, Wiestler OD, et al. The 2007 WHO classification of tumours of the central nervous system. *Acta Neuropathol* 2007;114:97–109 CrossRef Medline
22. Sakata A, Fushimi Y, Okada T, et al. Diagnostic performance between contrast enhancement, proton MR spectroscopy, and amide proton transfer imaging in patients with brain tumors. *J Magn Reson Imaging* 2017;46:732–39 CrossRef Medline
23. Schmitt B, Zaiss M, Zhou J, et al. Optimization of pulse train pre-saturation for CEST imaging in clinical scanners. *Magn Reson Med* 2011;65:1620–29 CrossRef Medline
24. Yamashita K, Yoshiura T, Hiwatashi A, et al. Differentiating primary CNS lymphoma from glioblastoma multiforme: assessment using arterial spin labeling, diffusion-weighted imaging, and 18F-fluorodeoxyglucose positron emission tomography. *Neuroradiology* 2013; 55:135–43 CrossRef Medline
25. Manabe O, Hattori N, Yamaguchi S, et al. Oligodendroglial component complicates the prediction of tumour grading with metabolic imaging. *Eur J Nucl Med Mol Imaging* 2015;42:896–904 CrossRef Medline
26. Landis JR, Koch GG. The measurement of observer agreement for categorical data. *Biometrics* 1977;33:159–74 CrossRef Medline
27. DeLong ER, DeLong DM, Clarke-Pearson DL. Comparing the areas under two or more correlated receiver operating characteristic curves: a nonparametric approach. *Biometrics* 1988;44: 837–45 CrossRef Medline
28. Schmidt H, Schwenzer NF, Gatidis S, et al. Systematic evaluation of amide proton chemical exchange saturation transfer at 3T: effects of protein concentration, pH, and acquisition parameters. *Invest Radiol* 2016;51:635–46 CrossRef Medline
29. Sun PZ, Wang E, Cheung JS. Imaging acute ischemic tissue acidosis with pH-sensitive endogenous amide proton transfer (APT) MRI: correction of tissue relaxation and concomitant RF irradiation effects toward mapping quantitative cerebral tissue pH. *Neuroimage* 2012;60:1–6 CrossRef Medline
30. Fudaba H, Shimomura T, Abe T, et al. Comparison of multiple parameters obtained on 3T pulsed arterial spin-labeling, diffusion tensor imaging, and MRS and the Ki-67 labeling index in evaluating glioma grading. *AJNR Am J Neuroradiol* 2014;35:2091–98 CrossRef Medline
31. Server A, Kulle B, Gadmar ØB, et al. Measurements of diagnostic examination performance using quantitative apparent diffusion coefficient and proton MR spectroscopic imaging in the preoperative evaluation of tumor grade in cerebral gliomas. *Eur J Radiol* 2011;80:462–70 CrossRef Medline
32. Nguyen TB, Cron GO, Perdrizet K, et al. Comparison of the diagnostic accuracy of DSC- and dynamic contrast-enhanced MRI in the preoperative grading of astrocytomas. *AJNR Am J Neuroradiol* 2015; 36:2017–22 CrossRef Medline
33. Halligan S, Altman DG, Mallett S. Disadvantages of using the area under the receiver operating characteristic curve to assess imaging

- tests: a discussion and proposal for an alternative approach. *Eur Radiol* 2015;25:932–39 CrossRef Medline
34. Rutjes A, Reitsma J, Coomarasamy A, et al. **Evaluation of diagnostic tests when there is no gold standard: a review of methods.** *Health Technol Assess* 2007;11:iii, ix–51 Medline
35. Collins VP, Jones DT, Giannini C. **Pilocytic astrocytoma: pathology, molecular mechanisms and markers.** *Acta Neuropathol* 2015;129:775–88 CrossRef Medline
36. de Fatima Vasco Aragao M, Law M, Batista de Almeida D, et al. **Comparison of perfusion, diffusion, and MR spectroscopy between low-grade enhancing pilocytic astrocytomas and high-grade astrocytomas.** *AJNR Am J Neuroradiol* 2014;35:1495–502 CrossRef Medline
37. Eckel-Passow JE, Lachance DH, Molinaro AM, et al. **Glioma groups based on 1p/19q, IDH, and TERT promoter mutations in tumors.** *N Engl J Med* 2015;372:2499–508 CrossRef Medline
38. Koschmann C, Calinescu AA, Nunez FJ, et al. **ATRX loss promotes tumor growth and impairs nonhomologous end joining DNA repair in glioma.** *Sci Transl Med* 2016;8:328ra28 CrossRef Medline

Diffusion-Weighted Imaging of Brain Metastasis from Lung Cancer: Correlation of MRI Parameters with the Histologic Type and Gene Mutation Status

W.S. Jung, C.H. Park, C.-K. Hong, S.H. Suh, and S.J. Ahn

ABSTRACT

BACKGROUND AND PURPOSE: Development of noninvasive imaging biomarkers indicating the histology and the gene mutation status of brain metastasis from lung cancer is important. We aimed to investigate diffusion-weighted imaging parameters as predictors of the histology and gene mutations of brain metastasis from lung cancer.

MATERIALS AND METHODS: DWI data for 74 patients with brain metastasis from lung cancer were retrospectively reviewed. The patients were first grouped according to the primary tumor histology (adenocarcinoma, small-cell lung cancer, squamous cell carcinoma), and those with adenocarcinoma were further divided into *epidermal growth factor receptor (EGFR)* mutation–positive and wild type groups. Sex; age; number, size, and location of brain metastasis; DWI visual scores; the minimum ADC; and the normalized ADC ratio were compared among groups using χ^2 and ANOVA. Multiple logistic regression analysis was performed to determine independent predictors of the *EGFR* mutation.

RESULTS: The minimum ADC was lower in the small-cell lung cancer group than in the other 2 groups, though the difference was not significant. Furthermore, minimum ADC and the normalized ADC ratio were significantly lower in the *EGFR* mutation–positive group than in the wild type group ($P = .021$ and $.014$, respectively). Multivariate analysis revealed that minimum ADC and the normalized ADC ratio were independently associated with the *EGFR* mutation status ($P = .028$ and $.021$, respectively).

CONCLUSIONS: Our results suggest that DWI parameters (minimum ADC and normalized ADC ratio) for the solid components of brain metastasis from lung cancer are not correlated with their histology, whereas they can predict the *EGFR* mutation status in brain metastasis from lung adenocarcinoma.

ABBREVIATIONS: ADC_{min} = minimum ADC; BM = brain metastasis; *EGFR* = *epidermal growth factor receptor*; nADC = normalized ADC; NSCLC = non-small-cell lung cancer; TKI = tyrosine kinase inhibitor

Lung cancer is one of the leading causes of cancer-related deaths in East Asia and the most frequent site of origin for brain metastasis (BM).^{1–4} Despite advances in systemic therapy and improvement in survival rates for patients with advanced lung cancer, BM remains an important cause of morbidity and mortality.¹ Recently, many studies reported that compared with those with BM with wild type *epidermal*

growth factor receptor (EGFR), patients with lung cancer with BM having *EGFR* mutations, particularly those with non-small-cell lung cancer (NSCLC), had improved survival due to higher response rates to whole-brain radiation therapy and specific chemotherapy medications such as *EGFR*-associated tyrosine kinase inhibitors (TKIs).^{5–8}

Development of noninvasive imaging biomarkers indicating the gene mutation status of BM from lung cancer is important because they would provide clinicians with strong evidence for making clinical decisions, aid in the early initiation of specific chemotherapy for patients with gene mutations, and, consequently, contribute to an improved prognosis.⁸

Diffusion-weighted MR imaging of the brain is based on the differential diffusion rates or the Brownian motion of water. It is an essential technique for diagnosing acute infarction in the brain because of its ability to detect cytotoxic edema caused by altered water diffusion secondary to cellular damage. DWI is also widely used for the assessment of tumor pathology in the field of neuro-oncology.⁹ Specifically, apparent diffusion coefficient values derived from DWI have been shown to correlate with tumor cellularity, glioma grade,

Received June 26, 2017; accepted after revision September 7.

From the Departments of Radiology (W.S.J., C.H.P., S.H.S., S.J.A.) and Neurosurgery (C.-K.H.), Gangnam Severance Hospital, Yonsei University, College of Medicine, Seoul, Korea; and Department of Radiology (W.S.J.), Ajou University School of Medicine, Suwon, Korea.

This study was supported by a faculty research grant from Yonsei University College of Medicine (6-2016-0111) and by a National Research Foundation of Korea (NRF) grant funded by the Korea government (MSIP) (No.2017RIC1B5014927). The funder had no role in study design, data collection and analysis, decision to publish, or preparation of the manuscript.

Please address correspondence to Sung Jun Ahn, MD, PhD, Department of Radiology, Gangnam Severance Hospital, Yonsei University, College of Medicine, 211 Eonju-ro, Gangnam-gu, Seoul 135-720, Korea; e-mail: aahng77@yuhs.ac

<http://dx.doi.org/10.3174/ajnr.A5516>

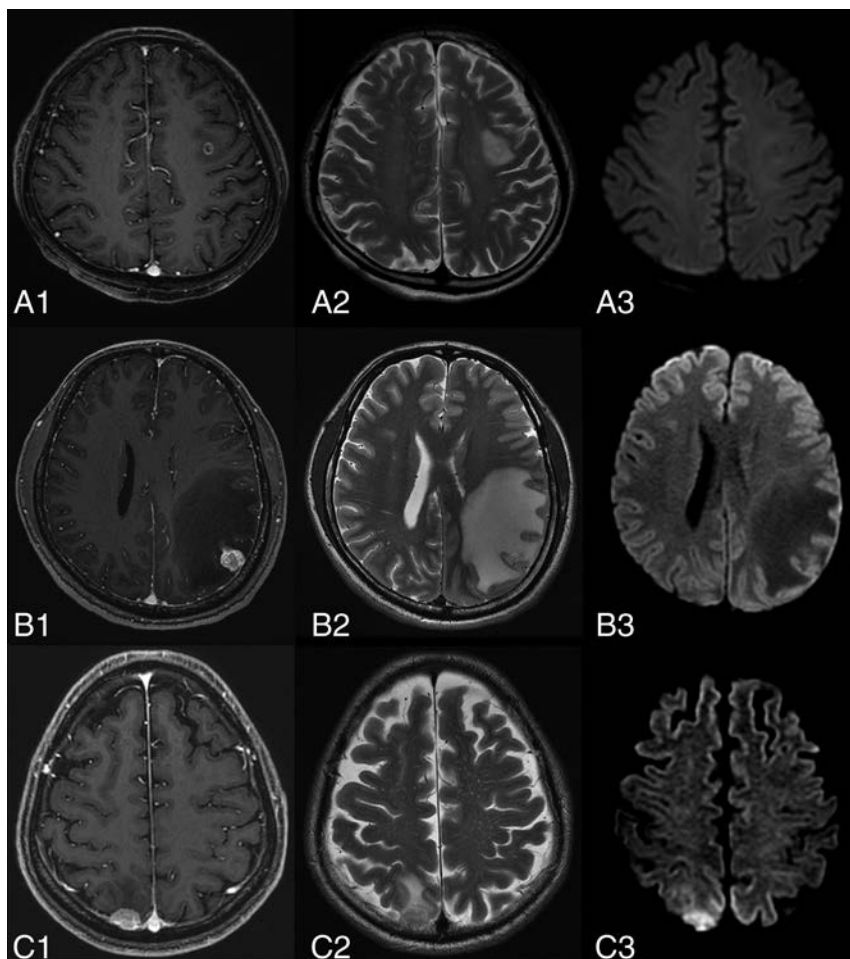


FIG 1. Representative MR images depicting visual scores based on diffusion-weighted imaging findings for brain metastasis from lung cancer. Contrast-enhanced T1-weighted images show an apparent enhanced tumor in the left frontal lobe (A1), left parietal lobe (B1), and right parietal lobe (C1). T2-weighted images (A2, B2, and C2) show varying degrees of peritumoral brain edema. A3, BM is not detectable on DWI (A3, score = 1). B3 and C3, DWI images show iso-signal intensity (score = 2) and high signal intensity (score = 3), respectively, relative to the normal-appearing cortical gray matter.

and treatment response.⁹⁻¹³ Moreover, recent studies have shown that DWI parameters may differentiate the histology of BM from lung cancer.^{14,15} However, the association between DWI parameters and the gene mutation status has not been assessed for BM from lung cancer, to our knowledge.

We hypothesized that the molecular and genetic backgrounds of tumors affect signal intensity and ADC values of lung cancer BM on DWI. Therefore, we aimed to investigate DWI parameters as imaging biomarkers for prediction of the histologic type and gene mutation status of BM from lung cancer.

MATERIALS AND METHODS

Patient Population

We retrospectively reviewed data for 100 patients diagnosed with BM from lung cancer between January 2012 and April 2016. All patients had received a histopathologic diagnosis of lung cancer based on bronchoscopic, percutaneous needle-guided, or surgical biopsies and had undergone gene mutation studies. Accordingly, they were stratified into groups based on the histopathology of the lung cancer. Furthermore, patients with lung adenocarcinoma were divided according to the gene mutation status.

We excluded patients with the following conditions: MR imaging evidence of intratumoral hemorrhage ($n = 5$), lesions that were too small for the measurement of ADC values ($n = 12$), leptomeningeal seeding metastasis ($n = 6$), and a history of chemotherapy or radiation therapy for BM ($n = 3$). Eventually, 74 patients were included in this study. Approval for the use of clinical data was obtained from the internal review board of our institution (Gangnam Severance Hospital).

Pathology and EGFR Mutation

Analysis of Lung Cancer

One experienced pathologist (Hee Surng Park, with 8 years of experience in pathology) evaluated the pathology and *EGFR* mutation status of the lung cancer. Genomic DNA was extracted from the lung cancer specimen, and *EGFR* tyrosine kinase exons 19, 20, and 21 and *V-Ki-ras2 Kirsten rat sarcoma viral oncogene homolog (Kras)* were amplified by a nested polymerase chain reaction using specific primers. Fluorescence in situ hybridization testing with *anaplastic lymphoma kinase (Alk)* break-apart probes was performed to detect rearrangements. The details of the sequencing procedure are described elsewhere.^{16,17} The presence of *EGFR* mutations was determined by the presence of deletions within exons 19 and 20 and L858R point mutations in exon 21.

MR Imaging Protocol

All patients were imaged with a 3T clinical MR imaging device (Discovery MR750, GE Healthcare, Milwaukee, Wisconsin; Achieva, Philips Healthcare, Best, the Netherlands). Our MR imaging protocol for BM included routine T2-weighted fast-spin-echo sequences (TR/TE, 5414/96 ms), axial fluid-attenuated inversion recovery sequences (TR/TE/TI, 4000/80/2000 ms), axial diffusion-weighted echo-planar sequences (TR/TE, 8000/65.6 ms; slice thickness/intersection gap, 4/1 mm; matrix size, 160×160 ; FOV, 240×240 mm; 3 directions; b-value = 0 and 1000 s/mm^2), and contrast-enhanced 3D T1 fast-spoiled gradient-recalled sequences (TR/TE, 8.2/3.2 ms; flip angle, 12° ; slice thickness, 1 mm; matrix size, 256×256 ; FOV, 220×220 mm). Intravenous gadolinium-based contrast agent was used at a dose of 0.1 mmol/kg body weight. ADC values were automatically calculated by the operating console of the MR imaging device and displayed as corresponding ADC maps.

Image Evaluation

Two experienced neuroradiologists (S.H.S., with 12 years of experience in neuroimaging, and S.J.A., with 6 years of experience in

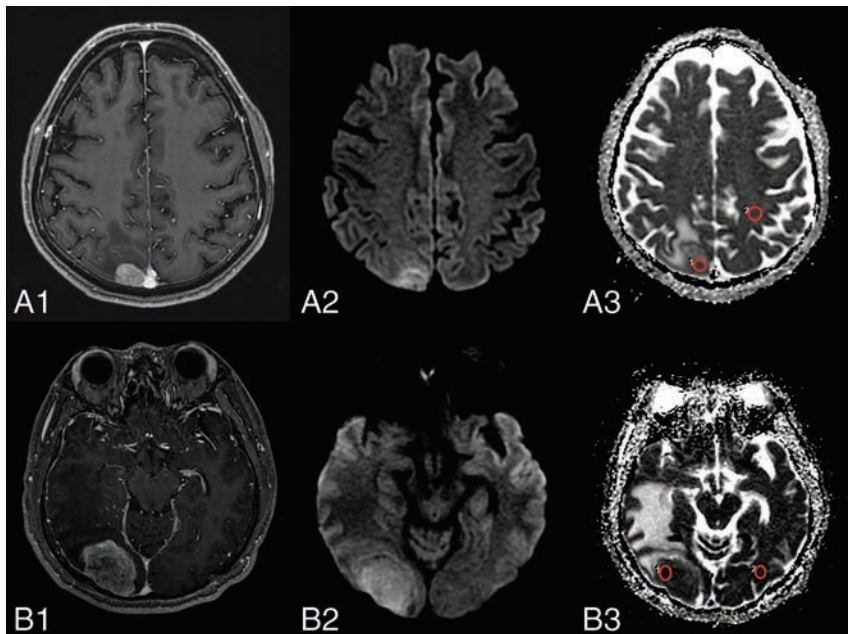


FIG 2. Representative images depicting the ROI within a tumor and the corresponding contralateral normal-appearing white matter for the calculation of apparent diffusion coefficient values for brain metastasis lesions stratified by the *EGFR* mutation status. *A1* and *B1*, Contrast-enhanced T1-weighted images show contrast enhancement of the metastasis. *A2* and *B2*, Diffusion-weighted images show mild-to-moderate high signal intensity in the contrast-enhanced areas. *A3* and *B3*, ADC map with ROIs within the tumor and corresponding contralateral normal-appearing white matter. *A1–A3*, Wild type *EGFR*. *B1–B3*, *EGFR* mutation–positive.

neuroimaging) visually assessed the signal intensity on DWI in areas corresponding to the enhanced portion of the lesions on contrast-enhanced T1-weighted images; both were blinded to the clinical and pathologic information. If there were multiple brain lesions, the largest one, which reflected DWI findings for most BM lesions, was selected as the target lesion to increase the accuracy of the measurement. The lesions on DWI were visually scored as follows: 1, negative findings on DWI; 2, isointense relative to the normal-appearing cortical gray matter; and 3, hyperintense relative to the normal-appearing cortical gray matter (Fig 1).

The study coordinator (W.S.J.) marked circular ROIs (each area, 20 mm²) over the target lesion on the ADC map, avoiding cystic or necrotic parts. The minimum ADC (ADC_{min}) value was calculated from these ROIs. The same method was applied to a corresponding site in the contralateral white matter judged as normal on both contrast-enhanced T1- and T2-weighted images. Then, to assess the objective difference between the ADC value for the tumor and for the contralateral normal area, the normalized ADC (nADC) ratio was calculated as the ratio of the ADC_{min} of the tumor divided by the ADC_{min} of the corresponding contralateral white matter area (Fig 2).

Statistical Analysis

All statistical analyses were performed with the statistical software SAS, Version 9.2 (SAS Institute, Cary, North Carolina), and MedCalc for Windows, Version 12.7.0 (MedCalc Software, Mariakerke, Belgium). The χ^2 test and ANOVA were used to compare DWI visual scores, ADC_{min} values, the nADC ratio, the number and size of the BMs, and the presence of intratumoral necrosis or

hemorrhage among the adenocarcinoma, squamous cell carcinoma, and small-cell lung carcinoma groups. Subgroup analysis according to the gene mutation status was also performed for the adenocarcinoma group. For multivariate analysis, a linear regression model was used to identify statistically significant variables. To investigate the interobserver reproducibility for DWI visual scores, we derived the intraclass correlation coefficient with a 2-way random model of absolute agreement.

RESULTS

Relationship between DWI Visual Scores and BM Histology and Mutation Status

In total, 74 patients (mean age, 64.19 ± 10.76 years; 50 men and 24 women) with BMs from lung cancer underwent DWI. Of these, 56 (75.67%) were diagnosed with adenocarcinoma (group 1); 11 (14.86%), with small-cell lung cancer (group 2); and 7 (9.45%), with squamous cell carcinoma (group 3). Of the 56 adenocarcinomas, 12 were poorly differentiated, 2 were well-differentiated, and 1 was moderately differentiated adenocarcinoma. For the remaining 41 cases of adenocarcinoma, detailed pathologic results were not available.

The 56 patients with adenocarcinoma were subdivided according to the status of mutations in *EGFR*, *Alk*, and *Kras*. In total, 55 patients had been examined for the *EGFR* mutation status, with 26 having *EGFR* mutations and 29 having wild type *EGFR*. Among the patients with *EGFR* mutations, 13, 4, and 9 had mutations in exons 19, 20, and 21, respectively. In addition, mutations were confirmed in 4 of 29 and 3 of 32 patients examined for *Alk* and *Kras* mutations, respectively.

Interobserver reproducibility for DWI visual scores was excellent (intraclass correlation coefficient, 0.972; 95% confidence interval, 0.955–0.982; $P < .001$). There was no significant difference in DWI visual scores among the 3 histology-based groups (Table 1) and between the 2 mutation-based groups (Table 2).

Relationship between ADC Values and Histologic Type
ADC_{min} and the nADC ratio were not significantly different among the small-cell lung cancer (531.18 ± 160.54 × 10⁻⁶ mm²/s and 0.88 ± 0.2, respectively), adenocarcinoma (623.38 ± 163.07 × 10⁻⁶ mm²/s and 1.04 ± 0.28, respectively), and squamous cell carcinoma (682.14 ± 182.07 × 10⁻⁶ mm²/s and 1.11 ± 0.28, respectively; $P = .131$ and 0.144) groups. Moreover, the location, size, and number of BMs and the presence of intratumoral hemorrhage or necrosis showed no significant differences among groups. The detailed patient characteristics are shown in Table 1.

Relationship between ADC Values and Histologic Type

ADC_{min} and the nADC ratio were not significantly different among the small-cell lung cancer (531.18 ± 160.54 × 10⁻⁶ mm²/s and 0.88 ± 0.2, respectively), adenocarcinoma (623.38 ± 163.07 × 10⁻⁶ mm²/s and 1.04 ± 0.28, respectively), and squamous cell carcinoma (682.14 ± 182.07 × 10⁻⁶ mm²/s and 1.11 ± 0.28, respectively; $P = .131$ and 0.144) groups. Moreover, the location, size, and number of BMs and the presence of intratumoral hemorrhage or necrosis showed no significant differences among groups. The detailed patient characteristics are shown in Table 1.

Table 1: Characteristics of BM among primary lung cancer groups

	Total (n = 74)	Adenocarcinoma (n = 56)	Small-Cell Lung Cancer (n = 11)	Squamous Cell Carcinoma (n = 7)	P Value
DWI visual score		1.87 ± 0.76	2.27 ± 0.90	1.85 ± 0.69	.298
ADC _{min} (×10 ⁻⁶ mm ² /s)	615.23 ± 166.83	623.38 ± 163.07	531.18 ± 160.54	682.14 ± 182.07	.131
nADC ratio	1.02 ± 0.28	1.04 ± 0.28	0.88 ± 0.2	1.11 ± 0.28	.144
Age (yr)	64.19 ± 10.76	63.63 ± 11.15	68.09 ± 9.14	62.57 ± 9.73	.420
Male sex	50 (67.57)	36 (64.29)	9 (81.82)	5 (71.43)	.587
Site of BM					.545
Anterior circulation—dominant ^a	25 (33.78)	21 (37.5)	2 (18.18)	2 (28.57)	
Posterior circulation—dominant ^b	11 (14.86)	7 (12.5)	2 (18.18)	2 (28.57)	
Even distribution	38 (51.35)	28 (50)	7 (63.64)	3 (42.86)	
No. of BMs					.051
1	18 (24.32)	16 (28.57)	0 (0)	2 (28.57)	
1 < BM < 10	43 (58.11)	32 (57.14)	6 (54.55)	5 (71.43)	
≥ 10	13 (17.57)	8 (14.29)	5 (45.45)	0 (0)	
Target lesion size of BM					.367
< 10 mm	31 (41.89)	22 (39.29)	7 (63.64)	2 (28.57)	
10 mm ≤ BM < 30 mm	32 (43.24)	24 (42.86)	3 (27.27)	5 (71.43)	
≥ 30 mm	11 (14.86)	10 (17.86)	1 (9.09)	0 (0)	
Intratumoral necrosis	32 (43.24)	21 (37.5)	6 (54.55)	5 (71.43)	.160
Intratumoral hemorrhage	15 (20.27)	11 (19.64)	3 (27.27)	1 (14.29)	.882

^a BMs mainly located in the frontal, parietal, and temporal lobes.

^b BMs mainly located in the occipital lobes, cerebellum, and brain stem.

Table 2: Comparison of ADC_{min} values and normalized ADC ratio according to gene mutation status in adenocarcinoma group

	Wild Type	Mutation	P Value
<i>EGFR</i>	29 (52.7)	26 (47.3)	
DWI visual score	1.92 ± 0.77	1.87 ± 0.76	.179
ADC _{min} (×10 ⁻⁶ mm ² /s)	674.55 ± 182.78	575.85 ± 115.01	.021
nADC ratio	1.13 ± 0.32	0.95 ± 0.19	.014
<i>Alk</i>	25 (86.2)	4 (13.8)	
DWI visual score	1.96 ± 0.79	2 ± 1.15	.930
ADC _{min} (×10 ⁻⁶ mm ² /s)	583.8 ± 183.84	562 ± 159.12	.825
nADC ratio	1 ± 0.34	0.83 ± 0.19	.328
<i>Kras</i>	29 (90.6)	3 (9.4)	
DWI visual score	1.82 ± 0.77	2.33 ± 0.57	.274
ADC _{min} (×10 ⁻⁶ mm ² /s)	641.31 ± 168.32	631.45 ± 161.74	.310
nADC ratio	1.08 ± 0.31	1.08 ± 0.32	.926

Relationship between ADC Values and Gene Mutation Status

ADC_{min} was significantly lower in the *EGFR* mutation-positive group than in the wild type group (575.85 ± 115.01 × 10⁻⁶ mm²/s versus 674.55 ± 182.78 × 10⁻⁶ mm²/s, *P* = .021); similar results were obtained for the nADC ratio (0.95 ± 0.19 versus 1.13 ± 0.32, *P* = .014). However, there were no significant differences in the location, size, and number of BMs and the presence of necrosis or hemorrhage between groups (Table 2).

ADC_{min} and the nADC ratio also showed significant differences according to the following *EGFR* genotypes: exon 19 and/or 21 mutations (*n* = 22; 564.14 ± 109.25 × 10⁻⁶ mm²/s and 0.93 ± 0.17, respectively), exon 20 mutations (*n* = 4; 640.25 ± 141.90 × 10⁻⁶ mm²/s and 1.05 ± 0.28, respectively), and wild type *EGFR* (*n* = 29; 674.55 ± 182.78 × 10⁻⁶ mm²/s and 1.13 ± 0.32, respectively; *P* = .049 and .038). A post hoc analysis showed that ADC_{min} and the nADC ratio were significantly lower in the exon 19 and/or 21 mutation group than in the wild type group (*P* = .039 and 0.029, respectively; Fig 3). There was no significant difference in the 2 parameters between the *Alk* mutation-positive

and wild type groups and between the *Kras* mutation-positive and wild type groups (Table 2).

Multivariate logistic regression analysis revealed that ADC_{min} and the nADC ratio were independently associated with the *EGFR* mutation status (OR, 0.996; 95% CI, 0.992–1.000; *P* = .028; and OR, 0.064; 95% CI, 0.006–0.666; *P* = .021, respectively) after adjustment for sex; age; size, location, and number of BMs; presence of intratumoral necrosis or hemorrhage; and DWI visual scores. Specifically, ADC_{min} and the nADC ratio were significantly associated with exon 19 and/or 21 mutations (OR, 0.995; 95% CI, 0.991–0.999; *P* = .020; and OR, 0.044; 95% CI, 0.004–0.563; *P* = .016, respectively; Table 3).

DISCUSSION

In the present study, we tested the hypothesis that the signal intensity of BM from lung cancer on DWI may be expressed differently according to the genetic background of the lesion. Our results indicated a significant association of ADC_{min} and the nADC ratio with the *EGFR* mutation status and the location of the mutation. However, there was no association between the ADC parameters and the histologic type of the tumor.

A few previous studies have demonstrated opposing results for the relationship between the histologic type and DWI parameters for BM from lung cancer. Hayashida et al¹⁴ evaluated 26 brain metastatic lesions in patients with primary lung cancer and reported that small- and large-cell neuroendocrine carcinomas showed high signal intensity on DWI. Thus, they concluded that signal intensity on DWI can predict the histology of metastases. However, Duygulu et al¹⁵ evaluated 37 patients with BM from lung cancer and reported the absence of a correlation between

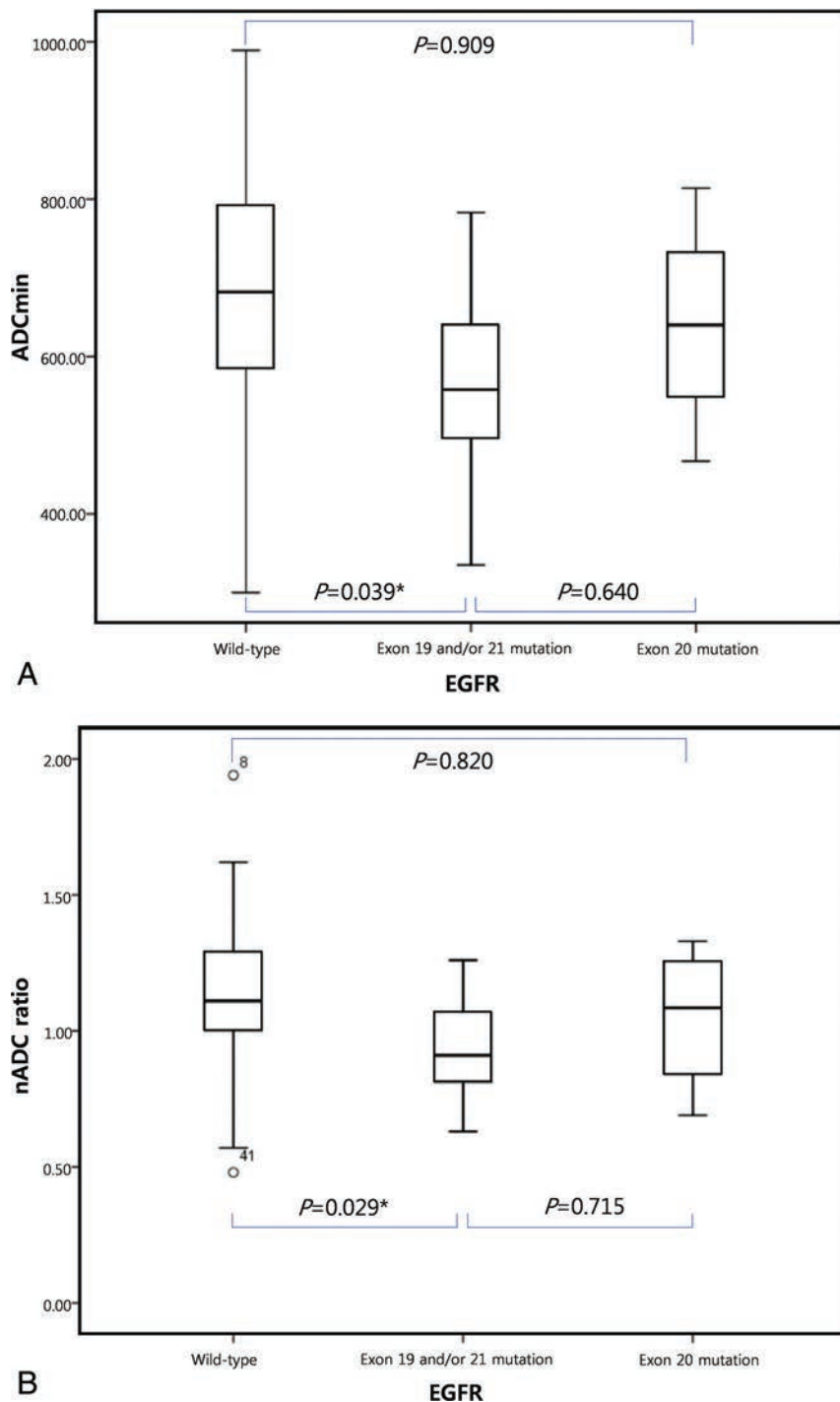


FIG 3. Boxplot for minimum apparent diffusion coefficient (A) and normalized ADC ratio (B) values for patients with lung adenocarcinoma with wild type *EGFR*, mutations in exon 19 and/or 21, and mutations in exon 20. Asterisk indicates statistically significant.

restricted diffusion on DWI and the primary pathology. In the present study, we also found no correlation between DWI parameters and BM histology; we believe our results are more reliable because of the large sample size compared with those in the previous studies. However, a nonsignificant trend existed for lower ADC_{min} and nADC in the small-cell lung cancer group, even compared with the adenocarcinoma *EGFR* mutation-positive group. In our results, most small-cell lung cancer cases (8/11) showed lower ADC values ($<600 \times 10^{-6} \text{ mm}^2/\text{s}$), while the mi-

nority (3/11) showed higher ADC values ($\geq 600 \times 10^{-6} \text{ mm}^2/\text{s}$). Two conflicting ADC values of small-cell lung cancer may explain the nonsignificant result of a lower ADC trend for small-cell lung cancer. We presume that there may be 2 different subtypes of small-cell lung cancer and would recommend further study.

EGFR is a transmembrane protein with cytoplasmic kinase activity that transduces important growth factor signaling from the extracellular milieu to the cell.¹⁸ For patients with advanced NSCLC, initial therapy with a TKI can lead to substantial therapeutic improvement and may be considered as an alternative treatment for BM in the future.^{8,17,19-21} Sensitive *EGFR* mutations are found in the first 4 exons (18–21) of the tyrosine kinase domain of *EGFR*, and the 2 major mutations are deletions in exon 19 and a single point mutation in exon 21 (L858R).²²⁻²⁴ Identification of exon 19 or 21 mutation is also a useful tool for the prediction of response to treatment with TKI.²⁵⁻²⁷ Also, several studies have demonstrated that the characteristics of BM are dependent on the *EGFR* genotype. The number of BM lesions was significantly higher in patients with *EGFR*-mutated NSCLC than in those with wild type NSCLC. Moreover, leptomeningeal metastases were more common in patients with *EGFR*-mutated NSCLC.⁸ Tumors with exon 19 deletions reportedly showed a higher incidence of BM compared with tumors with exon 21 mutations.²⁸

A previous study indicated that patients with NSCLC bearing exon 19 deletions exhibited a peculiar pattern of multiple, small brain metastases, similar to miliary BM.²⁹ Another study showed that brain metastases with exon 21 mutations were more common in the caudate, cerebellum, and temporal lobe compared with those with exon 19 deletions.³⁰ Other characteristic molecular changes of non-small-cell lung cancer are a *Kras* mutation and *Alk* rearrangement.^{31,32} Patients who were *Alk*-positive and treated with the *Alk* TKI crizotinib in the second-line setting experienced improved progression-free survival compared with standard chemotherapy.³³ Patients with NSCLC with *Alk* rearrangements have improved survival outcome after radiation therapy for BMs.³⁴ On the contrary, there are currently no target therapy options for patients with the *Kras* mutation.

Table 3: Independent predictors of EGFR mutation status

Predictors	EGFR Mutation (Exon 19 + 20 + 21)		EGFR Mutation (Exon 19 + 21)	
	OR (95% CI)	P Value	OR (95% CI)	P Value
Female sex	1.630 (0.539–4.927)	.387	1.538 (0.483–4.898)	.466
Age, per 1-yr increase	0.975 (0.928–1.024)	.307	0.972 (0.923–1.024)	.282
Site of BM				
Anterior circulation–dominant ^a	Reference		Reference	
Posterior circulation–dominant ^b	0.750 (0.132–4.250)	.745	0.833 (0.145–4.781)	.837
Even distribution	0.867 (0.275–2.734)	.807	0.741 (0.222–2.471)	.625
No. of BM				
1	Reference		Reference	
1 < BM < 10	1.765 (0.491–6.337)	.383	1.765 (0.446–6.979)	.418
≥ 10	6.000 (0.873–41.214)	.068	7.500 (1.039–54.116)	.045
Target lesion size of BM				
< 10 mm	Reference		Reference	
10 mm ≤ BM < 30 mm	1.015 (0.318–3.243)	.979	0.923 (0.275–3.102)	.897
≥ 30 mm	1.500 (0.315–7.135)	.61	1.333 (0.260–6.828)	.729
Intratumoral necrosis	1.188 (0.395–3.569)	.759	0.887 (0.273–2.884)	.841
Intratumoral hemorrhage	1.440 (0.382–5.428)	.59	1.412 (0.353–5.649)	.625
Diffusion visual scoring	1.630 (0.680–2.601)	.199	1.514 (0.722–2.974)	.274
ADC _{min}	0.996 (0.992–1.000)	.028	0.995 (0.991–0.999)	.020
nADC ratio	0.064 (0.006–0.666)	.021	0.044 (0.004–0.563)	.016

^a BMs mainly located in the frontal, parietal, and temporal lobes.

^b BMs mainly located in the occipital lobes, cerebellum, and brain stem.

Gene expression analysis is based on invasive tissue sampling and can be associated with sampling errors; therefore, the development of imaging markers that reflect the gene mutation status is important.³⁵ Our findings demonstrated that low ADC values for BM from lung adenocarcinoma are associated with a high possibility of an EGFR mutation, particularly in exons 19 and 21. Such patients are expected to respond well to noninvasive TKI treatment, and clinicians can plan this treatment accordingly if the mutation status is known. Moreover, Huang et al¹³ recently reported that ADC_{min} has the potential to predict and monitor the response of primary CNS lymphoma to chemotherapy. Therefore, through further study, we can apply serial ADC values to predict the response of BM from lung adenocarcinoma with EGFR mutations to TKI treatment.

Our study had several limitations. First, grades of lung cancer pathology (well, moderately, or poorly differentiated) in adenocarcinoma were not considered, which can affect the results of DWI parameters.¹⁴ Second, the genetic testing was performed with samples obtained from the lungs because brain metastases were diagnosed using brain MR imaging rather than histologic confirmation. Further study is necessary, in which tissues are obtained directly from the brain lesion, revealing the molecular biologic characteristics of the BMs more reliably.

CONCLUSIONS

We demonstrated that there is no correlation between ADC values (ADC_{min} or nADC ratio) of the solid components of the BM from lung cancer and their histologic type. However, the EGFR gene mutation status of BM from lung adenocarcinoma can be predicted using ADC values. A further prospective, large-scale cohort study is needed to demonstrate the relationship between gene mutation status and ADC values.

ACKNOWLEDGMENTS

All authors appreciate Heae Surng Park for her assistance in pathologic review of this study.

REFERENCES

- Nayak L, Lee EQ, Wen PY. **Epidemiology of brain metastases.** *Curr Oncol Rep* 2012;14:48–54 CrossRef Medline
- Jemal A, Tiwari RC, Murray T, et al; American Cancer Society. **Cancer statistics, 2004.** *CA Cancer J Clin* 2004;54:8–29 CrossRef Medline
- Shin HR, Ahn YO, Bae JM, et al. **Cancer incidence in Korea.** *Cancer Res Treat* 2002;34:405–08 CrossRef Medline
- Won YJ, Sung J, Jung KW, et al. **Nationwide cancer incidence in Korea, 2003–2005.** *Cancer Res Treat* 2009;41:122–31 CrossRef Medline
- Lynch TJ, Bell DW, Sordella R, et al. **Activating mutations in the epidermal growth factor receptor underlying responsiveness of non-small-cell lung cancer to gefitinib.** *N Engl J Med* 2004;350:2129–39 CrossRef Medline
- Mok TS, Wu YL, Thongprasert S, et al. **Gefitinib or carboplatin-paclitaxel in pulmonary adenocarcinoma.** *N Engl J Med* 2009;361:947–57 CrossRef Medline
- Johnson ML, Sima CS, Chaft J, et al. **Association of KRAS and EGFR mutations with survival in patients with advanced lung adenocarcinomas.** *Cancer* 2013;119:356–62 CrossRef Medline
- Eichler AF, Kahle KT, Wang DL, et al. **EGFR mutation status and survival after diagnosis of brain metastasis in nonsmall cell lung cancer.** *Neuro Oncol* 2010;12:1193–99 CrossRef Medline
- Wieduwilt MJ, Valles F, Issa S, et al. **Immunochemotherapy with intensive consolidation for primary CNS lymphoma: a pilot study and prognostic assessment by diffusion-weighted MRI.** *Cancer Res Treat* 2012;18:1146–55 CrossRef Medline
- Lee EJ, Lee SK, Agid R, et al. **Preoperative grading of presumptive low-grade astrocytomas on MR imaging: diagnostic value of minimum apparent diffusion coefficient.** *AJNR Am J Neuroradiol* 2008;29:1872–77 CrossRef Medline
- Guo AC, Cummings TJ, Dash RC, et al. **Lymphomas and high-grade astrocytomas: comparison of water diffusibility and histologic characteristics.** *Radiology* 2002;224:177–83 CrossRef Medline
- Lee KC, Moffat BA, Schott AF, et al. **Prospective early response im-**

- aging biomarker for neoadjuvant breast cancer chemotherapy. *Cancer Res Treat* 2007;13:443–50 Medline
13. Huang WY, Wen JB, Wu G, et al. Diffusion-weighted imaging for predicting and monitoring primary central nervous system lymphoma treatment response. *AJNR Am J Neuroradiol* 2016;37:2010–18 CrossRef Medline
 14. Hayashida Y, Hirai T, Morishita S, et al. Diffusion-weighted imaging of metastatic brain tumors: comparison with histologic type and tumor cellularity. *AJNR Am J Neuroradiol* 2006;27:1419–25 Medline
 15. Duygulu G, Ovali GY, Calli C, et al. Intracerebral metastasis showing restricted diffusion: correlation with histopathologic findings. *Eur J Radiol* 2010;74:117–20 CrossRef Medline
 16. Han SW, Kim TY, Hwang PG, et al. Predictive and prognostic impact of epidermal growth factor receptor mutation in non-small-cell lung cancer patients treated with gefitinib. *J Clin Oncol* 2005;23:2493–501 CrossRef Medline
 17. Cho BC, Im CK, Park MS, et al. Phase II study of erlotinib in advanced non-small-cell lung cancer after failure of gefitinib. *J Clin Oncol* 2007;25:2528–33 CrossRef Medline
 18. da Cunha Santos G, Shepherd FA, Tsao MS. EGFR mutations and lung cancer. *Annu Rev Pathol* 2011;6:49–69 CrossRef Medline
 19. Lee YJ, Choi HJ, Kim SK, et al. Frequent central nervous system failure after clinical benefit with epidermal growth factor receptor tyrosine kinase inhibitors in Korean patients with nonsmall-cell lung cancer. *Cancer* 2010;116:1336–43 CrossRef Medline
 20. Matsumoto S, Takahashi K, Iwakawa R, et al. Frequent EGFR mutations in brain metastases of lung adenocarcinoma. *Int J Cancer* 2006;119:1491–94 CrossRef Medline
 21. Omuro AM, Kris MG, Miller VA, et al. High incidence of disease recurrence in the brain and leptomeninges in patients with nonsmall cell lung carcinoma after response to gefitinib. *Cancer* 2005;103:2344–48 CrossRef Medline
 22. Gazdar AF. Activating and resistance mutations of EGFR in non-small-cell lung cancer: role in clinical response to EGFR tyrosine kinase inhibitors. *Oncogene* 2009;28(suppl 1):S24–31 CrossRef Medline
 23. Greulich H, Chen TH, Feng W, et al. Oncogenic transformation by inhibitor-sensitive and -resistant EGFR mutants. *PLoS Med* 2005;2:e313 CrossRef Medline
 24. Ichihara S, Toyooka S, Fujiwara Y, et al. The impact of epidermal growth factor receptor gene status on gefitinib-treated Japanese patients with non-small-cell lung cancer. *Int J Cancer* 2007;120:1239–47 CrossRef Medline
 25. Jackman DM, Yeap BY, Sequist LV, et al. Exon 19 deletion mutations of epidermal growth factor receptor are associated with prolonged survival in non-small cell lung cancer patients treated with gefitinib or erlotinib. *Clin Cancer Res* 2006;12:3908–14 CrossRef Medline
 26. Carey KD, Garton AJ, Romero MS, et al. Kinetic analysis of epidermal growth factor receptor somatic mutant proteins shows increased sensitivity to the epidermal growth factor receptor tyrosine kinase inhibitor, erlotinib. *Cancer Res* 2006;66:8163–71 CrossRef Medline
 27. Mulloy R, Ferrand A, Kim Y, et al. Epidermal growth factor receptor mutants from human lung cancers exhibit enhanced catalytic activity and increased sensitivity to gefitinib. *Cancer Res* 2007;67:2325–30 CrossRef Medline
 28. Heon S, Yeap BY, Britt GJ, et al. Development of central nervous system metastases in patients with advanced non-small cell lung cancer and somatic EGFR mutations treated with gefitinib or erlotinib. *Clin Cancer Res* 2010;16:5873–82 CrossRef Medline
 29. Sekine A, Kato T, Hagiwara E, et al. Metastatic brain tumors from non-small cell lung cancer with EGFR mutations: distinguishing influence of exon 19 deletion on radiographic features. *Lung Cancer* 2012;77:64–69 CrossRef Medline
 30. Takano K, Kinoshita M, Takagaki M, et al. Different spatial distributions of brain metastases from lung cancer by histological subtype and mutation status of epidermal growth factor receptor. *Neuro Oncol* 2016;18:716–24 CrossRef Medline
 31. Slebos RJ, Kibbelaar RE, Dalesio O, et al. K-ras oncogene activation as a prognostic marker in adenocarcinoma of the lung. *N Engl J Med* 1990;323:561–65 CrossRef Medline
 32. Soda M, Choi YL, Enomoto M, et al. Identification of the transforming EML4-ALK fusion gene in non-small-cell lung cancer. *Nature* 2007;448:561–66 CrossRef Medline
 33. Shaw AT, Kim DW, Nakagawa K, et al. Crizotinib versus chemotherapy in advanced ALK-positive lung cancer. *N Engl J Med* 2013;368:2385–94 CrossRef Medline
 34. Mak KS, Gainor JF, Niemierko A, et al. Significance of targeted therapy and genetic alterations in EGFR, ALK, or KRAS on survival in patients with non-small cell lung cancer treated with radiotherapy for brain metastases. *Neuro Oncol* 2015;17:296–302 CrossRef Medline
 35. Jamshidi N, Diehn M, Bredel M, et al. Illuminating radiogenomic characteristics of glioblastoma multiforme through integration of MR imaging, messenger RNA expression, and DNA copy number variation. *Radiology* 2014;270:1–2 CrossRef Medline

Diagnostic Accuracy of Amino Acid and FDG-PET in Differentiating Brain Metastasis Recurrence from Radionecrosis after Radiotherapy: A Systematic Review and Meta-Analysis

H. Li, L. Deng, H.X. Bai, J. Sun, Y. Cao, Y. Tao, L.J. States, M.D. Farwell, P. Zhang, B. Xiao, and L. Yang



ABSTRACT

BACKGROUND: Current studies that analyze the usefulness of amino acid and FDG-PET in distinguishing brain metastasis recurrence and radionecrosis after radiation therapy are limited by small cohort size.

PURPOSE: Our aim was to assess the diagnostic accuracy of amino acid and FDG-PET in differentiating brain metastasis recurrence from radionecrosis after radiation therapy.

DATA SOURCES: Studies were retrieved from PubMed, Embase, and the Cochrane Library.

STUDY SELECTION: Fifteen studies were included from the literature. Each study used PET to differentiate radiation necrosis from tumor recurrence in contrast-enhancing lesions on follow-up brain MR imaging after treating brain metastasis with radiation therapy.

DATA ANALYSIS: Data were analyzed with a bivariate random-effects model. Sensitivity, specificity, positive likelihood ratio, negative likelihood ratio, and diagnostic odds ratio were pooled, and a summary receiver operating characteristic curve was fit to the data.

DATA SYNTHESIS: The overall pooled sensitivity, specificity, positive likelihood ratio, negative likelihood ratio, and diagnostic odds ratio of PET were 0.85, 0.88, 7.0, 0.17, and 40, respectively. The area under the receiver operating characteristic curve was 0.93. On subgroup analysis of different tracers, amino acid and FDG-PET had similar diagnostic accuracy. Meta-regression analysis demonstrated that the method of quantification based on patient, lesion, or PET scan (based on lesion versus not, $P = .07$) contributed to the heterogeneity.

LIMITATIONS: Our study was limited by small sample size, and 60% of the included studies were of retrospective design.

CONCLUSIONS: Amino acid and FDG-PET had good diagnostic accuracy in differentiating brain metastasis recurrence from radionecrosis after radiation therapy.

ABBREVIATIONS: SRS = stereotactic radiosurgery; QUADAS = Quality Assessment of Diagnostic Accuracy Studies; ^{11}C -MET = [^{11}C]-methyl-L-methionine; ^{18}F -FET = O-(2-[^{18}F]fluoroethyl)-L-tyrosine; ^{18}F -FDOPA = L-3,4-dihydroxy-6-[^{18}F]-fluorophenylalanine

Metastatic brain tumors are the most common brain tumor in adults, with incidence estimates ranging from 200,000 to 300,000 patients per year.¹ The frequency of brain metastasis is

increasing, likely due to increased frequency of advanced imaging procedures performed.² Prognosis can vary widely and depends on age, performance status, number of lesions, extracranial disease status, and primary malignancy.³ More recently, radiation therapy, particularly stereotactic radiosurgery (SRS), has become an increasingly important treatment option for the initial management of patients with brain metastasis.⁴ The efficacy of SRS, when used alone or combined with whole-brain radiation therapy, has been demonstrated in Phase III studies and has shown a 12-month local control rate of 70%–90%.^{5–8}

One of the most common complications after SRS for brain metastasis is radiation injury. These injuries can either be reversible,

Received June 14, 2017; accepted after revision September 19.

From the Department of Neurology (H.L., L.D., L.Y.), Second Xiangya Hospital of Central South University, Changsha, Hunan Province, People's Republic of China; Departments of Radiology (H.X.B., J.S., M.D.F.) and Pathology (P.Z.), Hospital of the University of Pennsylvania, Philadelphia, Pennsylvania; Cancer Research Institute (Y.C., Y.T.), Central South University, Changsha, Hunan Province, People's Republic of China; Department of Radiology (L.J.S.), Children's Hospital of Philadelphia, Philadelphia, Pennsylvania; and Department of Neurology (B.X.), Xiangya Hospital of Central South University, Changsha, Hunan Province, People's Republic of China.

This study was supported by Shenghua Yuying Project of Central South University to Li Yang.

Please address correspondence to Li Yang, MD, Department of Neurology, Second Xiangya Hospital, Central South University, No. 139 Middle Renmin Rd, Changsha, Hunan Province, 410011, People's Republic of China; e-mail: yangli762@csu.edu.cn and Bo Xiao, MD, Department of Neurology, Xiangya Hospital, Central South

University, No. 87 Xiangya Rd, Changsha, Hunan Province, 410000, People's Republic of China; e-mail: xiaobo_xy@126.com

Indicates article with supplemental on-line tables.

<http://dx.doi.org/10.3174/ajnr.A5472>

such as swelling of the tumor or demyelination, or irreversible, such as liquefactive or coagulative necrosis.^{9,10} The irreversible injury, also called radionecrosis, can occur during the same period as tumor recurrence.¹¹ It occurs in approximately 25% of patients after radiation therapy.^{12,13} While conventional MR imaging remains the most accurate technique for detecting the presence of brain metastasis, the appearance of metastasis is similar to that of radionecrosis on contrast-enhanced T1-weighted and T2-weighted sequences.¹⁴⁻¹⁶ As a consequence, it is often impossible to distinguish radiation necrosis from tumor relapse either clinically or with MR imaging. In current practice, many imaging methods such as advanced MR imaging (eg, dynamic susceptibility contrast perfusion and susceptibility-weighted imaging, diffusion-weighted imaging), MRS, perfusion-weighted MR imaging, SPECT, and PET have been used empirically to address this problem.¹⁷

New postprocessing techniques such as textural analysis and MR fingerprinting hold great promise for differentiating radiation necrosis from tumor recurrence.¹⁸⁻²⁰ However, no relevant studies have been performed using these techniques because they are difficult to implement and data training requires a large number of patients, which are difficult to recruit from a single institution. Of these imaging methods, metabolic PET imaging is the most widely studied due to its availability and established clinical utility for other indications. 2-[¹⁸F]fluoro-2-deoxy-D-glucose (¹⁸F-FDG) was used as the PET radiotracer in some early studies, but the high physiologic glucose consumption of the brain and the variable glucose uptake of metastatic brain lesions limited its use.^{21,22} Recently, amino acid PET imaging using [¹¹C]-methyl-L-methionine (¹¹C-MET), O-(2-[¹⁸F]fluoroethyl)-L-tyrosine (¹⁸F-FET), and L-3,4-dihydroxy-6-[¹⁸F]-fluorophenylalanine (¹⁸F-FDOPA) have demonstrated more promising results.^{8,23,24}

However, current studies that analyze the usefulness of amino acid and FDG-PET in distinguishing brain metastasis recurrence and radionecrosis after radiation therapy are limited by a small cohort size. Thus, we conducted a meta-analysis to assess the diagnostic accuracy of amino acid and FDG-PET in differentiating brain metastasis recurrence from radionecrosis after radiation therapy.

MATERIALS AND METHODS

Search Strategy

We searched PubMed (1966–2017), Embase (1980–2017), and the Cochrane Library (1996–2017). The studies chosen were restricted to humans, but not restricted by date, language, or publication status. We used the following combined search terms: (Positron-Emission Tomography, PET) AND (recurrence, recurrence*, recurrent, relapse*, recrudescence*, neoplasm metastasis, metastas*, progression) AND (radionecrosis, radiation necrosis, radiation-induced necrosis, posttreatment necrosis, radiation injury, radionecrotic, postradiotherapy necrosis) AND (radiation therapy, radiotherap*, radiation therap*, radiation treatment, radiosurgery, radiosurger*). We combined the terms appropriately with Medical Subject Headings terms and used an appropriate adjustment for different data bases. Details of the search strategies can be found in the Appendix.

Selection Criteria

Studies were selected if they included the following: 1) subjects who underwent amino acid or FDG-PET for differentiating brain metas-

tasis recurrence from radionecrosis after radiation therapy; 2) follow-up data that enabled the building of a 2 × 2 contingency table to calculate sensitivity and specificity; and 3) at least 10 subjects who underwent both the experimental test (PET) and the reference standard test (histopathology or clinical and radiologic follow-up) for the final brain metastasis recurrence or radionecrosis diagnosis.

We excluded the following types of studies: 1) letters, case reports, editorials, review articles, and animal studies; 2) nonoriginal and unpublished studies; 3) those that used a patient cohort that overlapped the cohort of a previous study; and 4) those that included no detailed information about the diagnostic and quantitative accuracy of PET.

Data Extraction

After literature selection, studies in full text were reviewed by 2 authors (H.L. and L.D.). We retrieved data including first author, publication year, country, study design, the number of patients, the number of lesions, the method of quantification, age, sex, primary tumor, follow-up time, radiation therapy methods, tracer, standard references, and cutoff index. The number of true-positive, false-positive, false-negative, and true-negative was calculated. The method of quantification could be based on lesion, patient, or PET scan. If a study did not specify how many lesions each patient had and used each patient as the unit of measurement in reporting their results, the numbers were counted on the basis of the patient. If a study contained lesions from different PET scans of the same patient (eg, after repeat treatment), these lesions were counted separately and the method of quantification was defined on the basis of the PET scan. All discrepancies were resolved in consensus after discussion.

Quality Assessment

Two authors (H.L. and L.D.) assessed the methodologic quality of the selected studies by using Quality Assessment of Diagnostic Accuracy Studies (QUADAS)-2 (<http://annals.org/aim/article/474994/quadas-2-revised-tool-quality-assessment-diagnostic-accuracy-studies>).²⁵ Discrepancies were resolved in consensus meetings by a panel including a third author (H.X.B.). The risk of bias was analyzed in 4 domains: patient selection, index test, reference standard, and flow and timing. Applicability was assessed in the following 3 domains: patient selection, index test, and reference standard. Signaling questions were applied to determine the risk of bias and applicability.

Statistical Analysis

We used bivariate random-effects models described previously by Reitsma et al²⁶ to perform the meta-analysis. The pooled estimates of sensitivity, specificity, positive likelihood ratio, negative likelihood ratio, and diagnostic odds ratios and their corresponding 95% confidence intervals were calculated, and forest plots were drawn. In addition, a summary receiver operating characteristic curve was fit to the estimates of sensitivity, specificity, and corresponding variances, and the area under the receiver operating characteristic curve was calculated. The summary receiver operating characteristic curve and the area under the receiver operating characteristic curve were used to provide an overall summary of the test performance. This study considered that an area under the receiver operating characteristic curve of >0.90 indi-

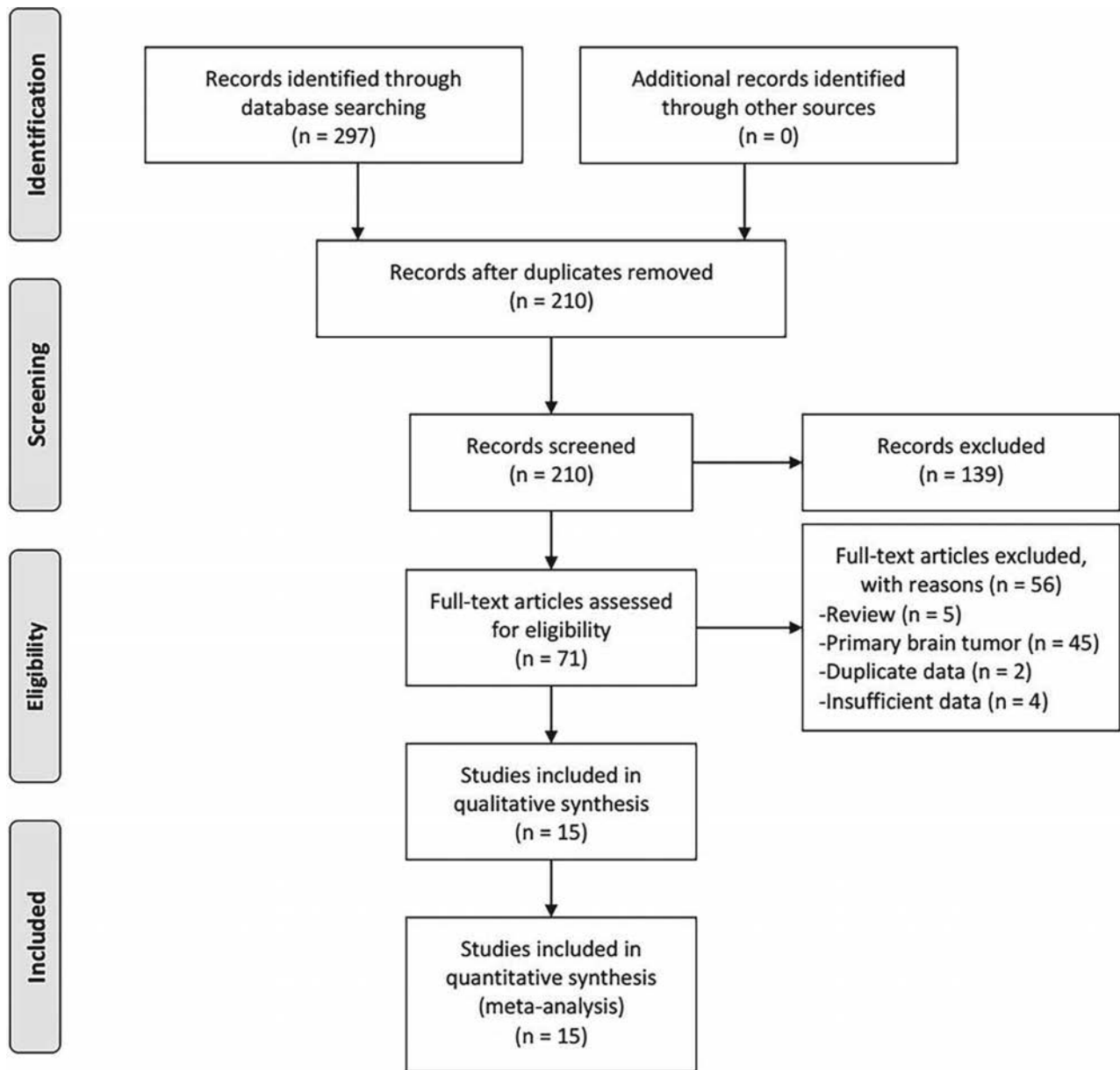


FIG 1. Preferred Reporting Items for Systematic Reviews and Meta-Analyses (PRISMA; <http://prisma-statement.org/>) 2009 flow diagram.

cated high accuracy and an area under the receiver operating characteristic curve near 0.50 indicated low accuracy.²⁷ Inter-study heterogeneity was assessed by calculating the I^2 and Cochran Q statistics for each forest plot, and the difference was considered statistically significant when the P value was $<.05$. The I^2 values were used to determine the proportion of the variation among the studies attributable to heterogeneity rather than chance. Heterogeneity was ranked low (25%), moderate (50%), and high (75%).²⁸ The posttest probability of tumor recurrence was computed on the basis of likelihood ratios, and pretest probability, by applying the Bayes theorem.^{29,30}

Additionally, sensitivity analysis was conducted using the leave-one-out approach by excluding studies one by one to evaluate the influences of individual studies on the final effects. Univariate meta-regression and subgroup analysis were used to explore the sources of heterogeneity. The covariates investigated

included study design, country, radiation therapy methods, tracer, cutoff index, analytic method used, sample size, median age, and male percentage. Finally, publication bias was evaluated by the Deeks test for funnel plot asymmetry. All analyses were performed by using STATA IC 14 (StataCorp, College Station, Texas).

RESULTS

Literature Search and Characteristics of the Included Studies

A total of 297 studies were identified, of which 87 were excluded because of duplication. After we read the titles and abstracts, a further 139 studies were excluded. The remaining 71 full-text studies were carefully reviewed, and we eliminated the following: review articles ($n = 5$), primary brain tumor ($n = 45$), duplicate data ($n = 2$), and insufficient data ($n = 4$). Finally, 15 studies^{8,13,22-24,31-40} were included for further analysis (Fig 1).

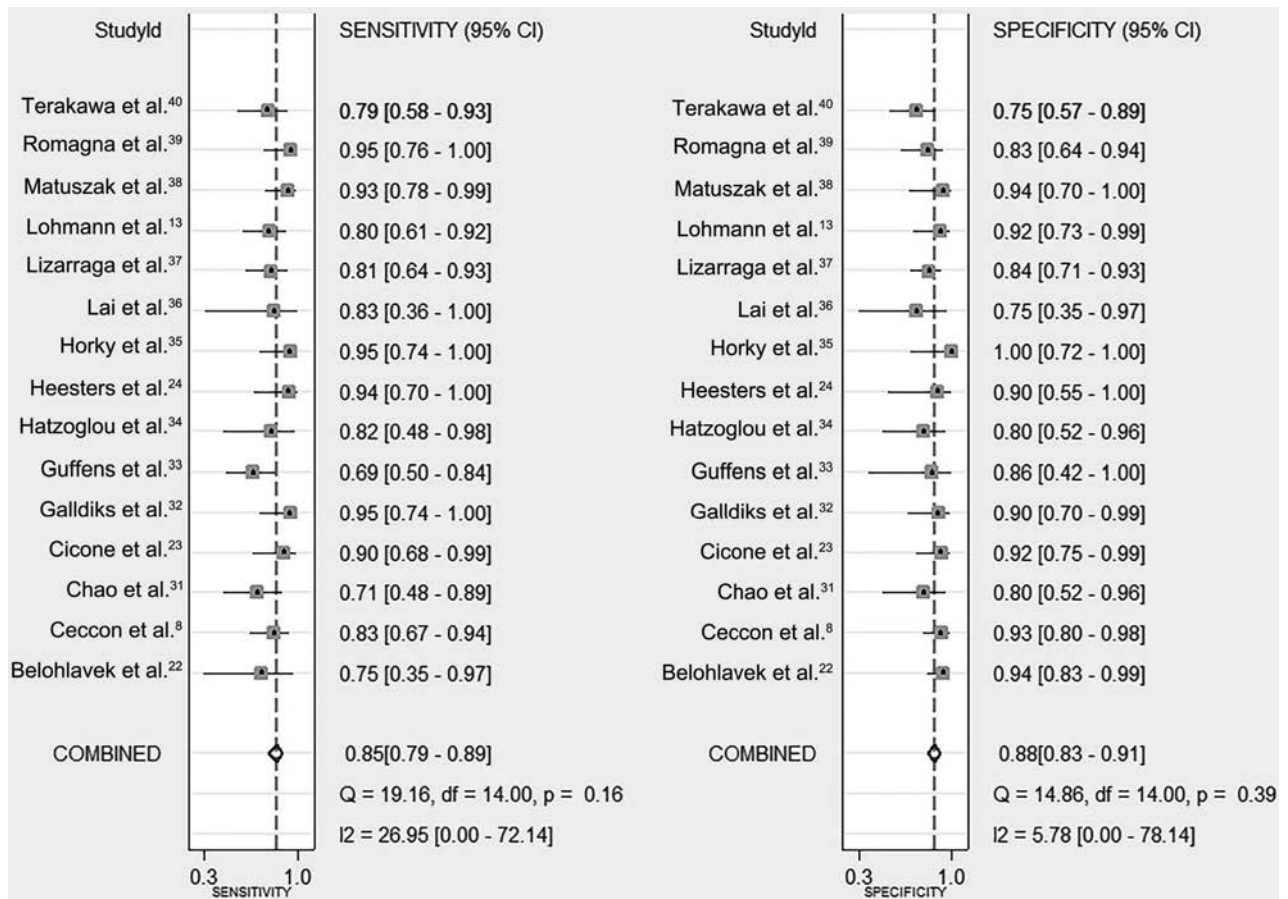


FIG 2. Pooled sensitivity and specificity of PET. The point estimates (□), pooled estimates (◇), and 95% CIs (error bars) from each study are shown.

The characteristics of these studies are summarized in On-line Table 1. The 15 studies encompassing 505 patients were published between 2001 and 2017. Six^{22,23,32,34,36,39} were prospective, and 9^{8,13,24,31,33,35,37,38,40} were retrospective. The age of patients ranged from 17 to 81 years. Five studies^{31,34-37} were conducted in the United States; and 4,^{8,13,32,39} in Germany. The rest of the studies were conducted in other countries including the Czech Republic,²² Italy,²³ Belgium,³³ the Netherlands,²⁴ France,³⁸ and Japan.⁴⁰ The primary tumors for the metastases were mainly from renal cell carcinoma, lung cancer, breast cancer, colorectal cancer, and melanoma. The radiation therapy methods were all SRS with or without other methods. Six studies^{22,31,34-36,38} used ¹⁸F-FDG as the tracer, 5 studies^{8,13,32,33,39} used ¹⁸F-FET, 2 studies^{24,40} used ¹¹C-MET, and 2 studies^{23,37} used ¹⁸F-FDOPA. The standard reference used for all studies except Lai et al³⁶ (only histopathology) was histopathology with clinical and/or radiologic follow-up.

Quality Assessment

Seven domains were assessed regarding bias and applicability for each article.²⁵ Of the total 105 domains from all articles, 18 domains were determined as high risk (17 for risk of bias and 1 for applicability concerns). Two domains were determined to be of unclear risk because of the incomplete reporting of the studies. Therefore, the overall quality was acceptable. We found that bias stemmed mainly from the patient selection ($n = 9$), index test

(high risk, $n = 5$; unclear risk, $n = 2$), and flow and timing ($n = 2$) domains. The quality assessment of the 15 included articles using QUADAS-2 is shown in On-line Table 2.

Pooled Measures of Diagnostic Accuracy and Clinical Utility

Our results showed that pooled sensitivity, specificity, positive likelihood ratio, negative likelihood ratio, and diagnostic odds ratio were 0.85 (95% CI, 0.79–0.89), 0.88 (95% CI, 0.83–0.91), 7.0 (95% CI, 5.0–9.9), 0.17 (95% CI, 0.12–0.24), and 40 (95% CI, 22–73), respectively (Fig 2). The area under the receiver operating characteristic curve was 0.93 (95% CI, 0.90–0.95), which suggested high diagnostic accuracy (Fig 3). Low heterogeneity was detected in these estimates (overall heterogeneity: $I^2 = 0\%$; 95% CI, 0%–100%, $P = .48$; sensitivity: $I^2 = 27.0\%$; 95% CI, 0%–72.1%; $P = .16$; specificity: $I^2 = 5.8\%$; 95% CI, 0%–78.1%; $P = .39$) (Fig 2).

To assess the clinical utility of our findings, we estimated the posttest probability of tumor recurrence after applying positive and negative likelihood ratios to contrast-enhancing lesions on MR imaging after radiation therapy with a range of pretest probabilities of tumor recurrence. These data are presented in Fig 4.

Meta-Regression and Subgroup Analysis

To explore the source of heterogeneity, we conducted univariate meta-regression. Of all the covariates, our results showed that the

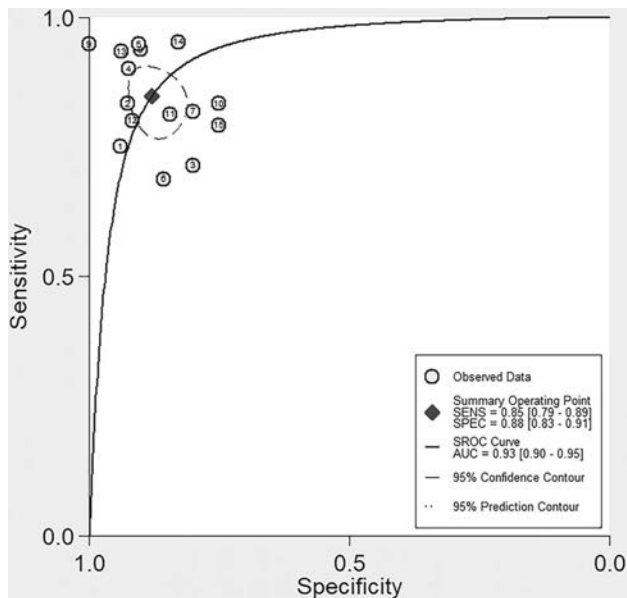


FIG 3. Summary receiver operating characteristic curve of PET. Each circle indicates 1 included study, and the size of the circle indicates the weight of that study. The summary point (◆) indicates an estimate of sensitivity and specificity, with the dashed line representing the 95% confidence region and the dotted line representing the 95% prediction region.

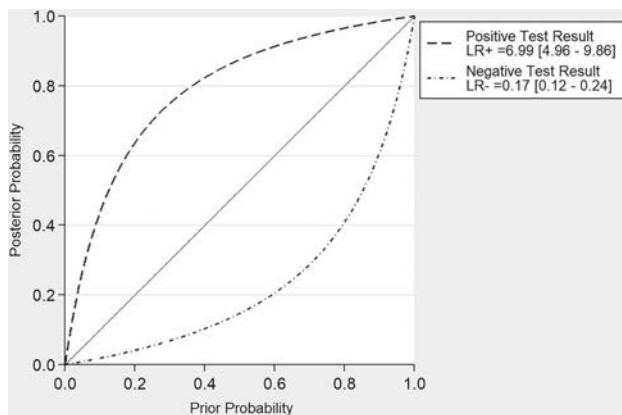


FIG 4. Bayesian plot of estimates of posttest probability of PET after applying pooled positive and negative likelihood ratios to donors with a range of pretest probabilities. LR+ indicates pooled positive likelihood ratio; LR-, pooled negative likelihood ratio.

method of quantification by the study (based on lesion versus not, $P = .07$; based on patient versus not, $P = .60$; based on scan versus not, $P = .11$) contributed to the heterogeneity. Studies analyzed on the basis of lesion^{8,13,22,23,31-34,37,38,40} showed a lower sensitivity (0.82; 95% CI, 0.77–0.87) than those based on patient^{24,36} (0.91; 95% CI, 0.78–1.00) or PET scan^{35,39} (0.95; 95% CI, 0.88–1.00). On subgroup analysis of different tracers, 6 studies of ¹⁸F-FDG returned a pooled sensitivity of 0.85 (95% CI, 0.77–0.94) and specificity of 0.90 (95% CI, 0.83–0.96); 5 studies of ¹⁸F-FET returned a pooled sensitivity of 0.83 (95% CI, 0.76–0.91) and specificity of 0.89 (95% CI, 0.83–0.95); 2 studies of ¹¹C-MET returned a pooled sensitivity of 0.86 (95% CI, 0.74, 0.98) and specificity of 0.79 (95% CI, 0.66–0.93); and 2 studies of ¹⁸F-FDOPA returned a pooled sensitivity of 0.86 (95% CI, 0.74–0.97)

and specificity of 0.88 (95% CI, 0.79–0.97). Details are shown in On-line Table 3.

Sensitivity and Publication Bias Analysis

Sensitivity analysis using the leave-one-out approach demonstrated that the direction and magnitude of estimates were not influenced by any study removed (On-line Table 4). After we excluded the 2 studies that were published as abstracts,^{24,33} the results did not change significantly (On-line Table 4). No publication bias was detected per Deeks funnel plot asymmetry test ($P = .85$) (Fig 5).

DISCUSSION

The brain is the most common site for central nervous system malignancy.⁴¹ Brain metastases, which commonly spread from lung, breast, melanoma, colon, and kidney cancers, are at least 10 times more frequent than primary brain tumor.⁴² Radiation therapy can be used therapeutically, prophylactically, or most commonly as palliative (noncurative) treatment for brain metastasis. Radionecrosis, a commonly observed complication that is impossible to eliminate, typically shows delayed occurrence and has been reported to occur in up to 25% of patients after the completion of radiation therapy. In fact, depending on the irradiated volume and radiation dose, the risk of radionecrosis may be as high as 50%.¹² Furthermore, clinical monitoring may also be challenging because both recurrent brain metastasis and radiation injury are characterized by similar neurologic symptoms and MR imaging signs.⁴³ Because tumor cells are hypermetabolic (with an increased rate of glycolysis) with elevated hexokinase activity and lower glucose-6-phosphatase activity while radiation necrosis is hypometabolic,⁴⁴ PET using tracers such as ¹⁸F-FDG, ¹¹C-MET, ¹⁸F-FET, and ¹⁸F-FDOPA has been introduced as a diagnostic tool for differentiation.

In our meta-analysis, we included 15 studies focusing on amino acid and FDG-PET in differentiating brain metastasis recurrence from radionecrosis after radiation therapy. The results showed that PET had an overall pooled sensitivity of 0.85, specificity of 0.88, positive likelihood ratio of 7.0, negative likelihood ratio of 0.17, and diagnostic odds ratio of 40. A summary receiver operating characteristic curve was developed with an area under the receiver operating characteristic curve of 0.93. Low heterogeneity was found, and further meta-regression analysis demonstrated that the analytic method used by the individual study may contribute to the heterogeneity. Most studies^{8,13,22,23,31-34,37,38,40} ($n = 11$) analyzed data based on contrast-enhancing lesions found on brain MR imaging. Only 2 studies^{24,36} analyzed data based on patients; and 2 others,^{35,39} based on each PET scan. Study design, country, radiation therapy methods, tracers, cutoff indexes, sample size, median age, and male percentage did not contribute to heterogeneity. Sensitivity analysis using a leave-one-out approach and publication bias detection showed that our results were stable and reliable. Furthermore, the Bayesian plot demonstrated that PET scans had clinical significance to some extent.

Among our included studies, Guffens et al³³ had the lowest diagnostic accuracy of 71.8% and sensitivity of 68.8%. This may be due to differences in baseline characteristics of the included

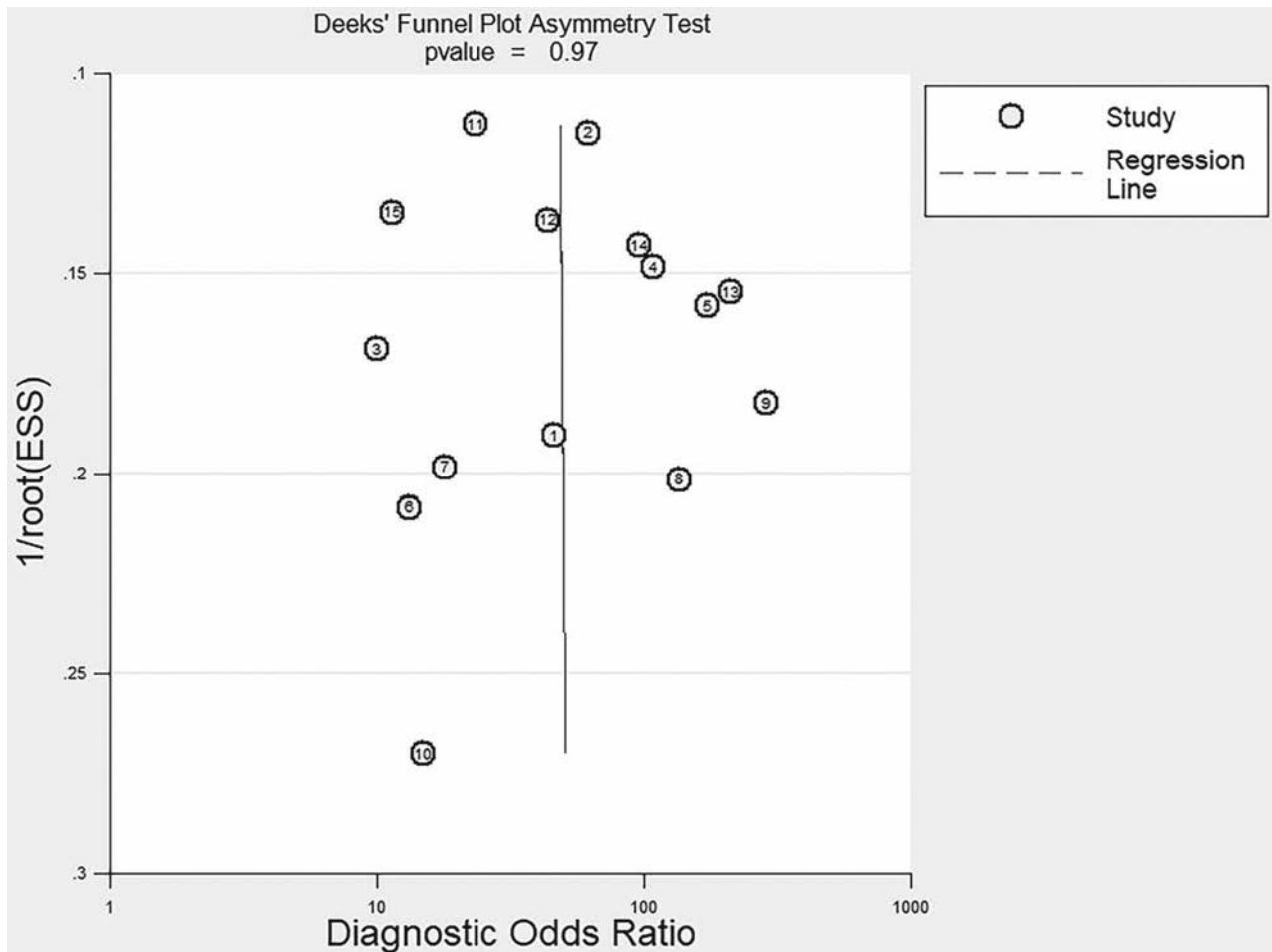


FIG 5. Funnel plot for Deeks' test based on the data of PET for differentiating brain metastasis recurrence from radionecrosis after radiation therapy.

cohort. For example, median age, sex proportion, and radiation therapy method were all unclear in this study. Furthermore, the origin of the brain metastasis was less varied than in other studies. Horkey et al³⁵ had a specificity of 100% with no false-positives. The small sample size (25 patients with 27 lesions) and the brain lesion size cutoff used (only lesions with volume at least 0.51 cm³ were evaluated with FDG-PET) may contribute to this result. The low specificity (75%) reported by Lai et al³⁶ may also have been affected by the small sample size.

Meta-regression and subgroup analyses did not find any difference in the cutoff index using quantitative methods with or without the time-activity curve and visual scale. However, we still question whether a threshold effect made a difference because each study used different indexes. Moreover, we did not find any difference in the various tracers used, which is contrary to some previous studies in the literature.^{8,13,39} This could be attributed to the small number of studies in our subgroup analysis. A recent study by Tomura et al⁴⁵ demonstrated that PET using ¹¹C-MET was superior to FDG-PET in differentiating radiation necrosis from recurrent tumor after gamma knife radiosurgery. The strength of the study by Tomura et al⁴⁵ is its direct comparison of FDG-PET and ¹¹C-MET PET by performing the 2 on the same patients. However, the study is limited by the small cohort size (15 patients with 18 lesions) as well as testing only 1 amino acid PET

tracer. Future larger studies directly comparing the different tracers on the same lesions are needed to prove the superiority of amino acid PET over FDG-PET.

Other imaging methods have also been used to differentiate brain metastasis recurrence from radionecrosis after radiation therapy, but the studies are few, and the results are inconsistent. Some researchers focused on the use of conventional MR imaging. Dequesada et al⁴⁶ showed a good diagnostic accuracy (sensitivity = 80%, specificity = 96%) in 32 patients using an MR imaging-based parameter called the “lesion quotient,” which was defined as the ratio of the nodule as seen on T2 imaging to the total enhancing area on T1 imaging. However, in a subsequent larger study of 51 patients by Stockham et al,¹⁵ the lesion quotient was inadequately sensitive (59%) and specific (41%) for discriminating tumor progression and radionecrosis. Leeman et al⁴⁷ calculated the edema/lesion volume ratio on preoperative MR imaging of 49 patients and reported a sensitivity of 63% and specificity of 85% in differentiating metastasis recurrence from radionecrosis. Using qualitative analysis of the time-dependent changes in lesion morphology on MR imaging of 31 patients treated with SRS for brain metastases, Wagner et al⁴⁸ showed that all radiation-induced injuries had a black interior area on the subtraction images for 15 to 55 minutes, whereas all malignant lesions had white components ($P < .001$). Although these studies based on conven-

tional MR imaging demonstrated promise, all were based on a small number of patients and were experimental in nature with insufficient evidence for clinical use.

Among our included studies, only 2 studies directly commented on the added value of PET over conventional or advanced MR imaging. Bělohávek et al²² demonstrated that a subsequent positive FDG-PET finding following a positive conventional MR imaging finding could increase the probability of correctly identifying metastasis recurrence by 68% (from 32% to 100%) and a negative FDG-PET finding could decrease this probability by 20.9% (from 32% to 11.1%). Chao et al³¹ showed a higher sensitivity of FDG-PET when coregistered with MR imaging (FDG-PET with MR imaging coregistration versus FDG-PET alone, 86% versus 65%). A recent cost-effectiveness analysis⁴⁹ on the use of FET-PET in addition to MR imaging compared with MR imaging alone for the diagnosis of recurrent brain metastases demonstrated that the additional use of FET-PET increased the rate of a correct diagnosis by 42% compared with MR imaging alone and suggests that it may be cost-effective. However, with the relatively low spatial resolution of PET and variable uptake of metastasis from tumors of different origins, the sensitivity of PET would not be expected to reach 100%. The specificity can also hardly reach 100% because of high background activity. Thus, the clinical application may be somewhat limited. Although we could show that amino acid or FDG-PET had high sensitivity and specificity in distinguishing radiation necrosis from tumor recurrence, the significant costs associated with the use of PET may not justify its use in the patient population with brain metastasis. To demonstrate its cost-effectiveness, future studies should set carefully selected inclusion criteria and attempt to link the diagnostic utility of PET in the selected cohort to changes in management or improvement in survival.⁵⁰ Potential cost savings include avoiding biopsies and futile treatment when diagnosis is uncertain.

In addition to ¹⁸F-FDG, ¹¹C-MET, ¹⁸F-FET, and ¹⁸F-FDOPA included in our analysis, other PET tracers such as ¹⁸F-fluorocholine,⁵¹ ¹⁸F-fluorothymidine (¹⁸F-FLT),^{52,53} and ¹¹C-choline^{54,55} can also be used in differentiating tumor recurrence and radiation necrosis. For example, Enslow et al⁵² compared FLT-PET with FDG-PET in differentiating radiation necrosis from recurrent glioma and demonstrated a higher diagnostic accuracy of FDG-PET (area under the receiver operating characteristic curve: FLT-PET versus FDG-PET = mean, 0.86; 95% CI, 0.67–1.00, versus mean, 0.93; 95% CI, 0.80–1.00). However, the study focused on primary gliomas and was limited by a small cohort size ($n = 15$).

Other studies in the literature focused on the use of advanced imaging techniques to distinguish brain metastasis recurrence from radionecrosis after radiation therapy. In a study of 14 patients with cerebral metastasis who had clinical or radiographic progression following SRS, Lai et al³⁶ reported the sensitivity and specificity of thallium SPECT to be only 50.0% and 62.5%, respectively. In the same study, arterial spin-labeling MR imaging had a sensitivity of 83.3% and specificity of 100.0%. Cicone et al²³ reported that the overall accuracy of MRP was lower than that of ¹⁸F-FDOPA PET (perfusion-weighted MR imaging versus PET: sensitivity, 86.7% versus 93.3%; specificity, 68.2% versus 90.9%; accuracy, 75.6% versus 91.9%) in 42 patients with 50 brain metastases, while Hatzoglou et al³⁴ reported a higher sensitivity of

perfusion-weighted MR imaging than ¹⁸F-FDG-PET (91% versus 82%) in 53 patients. However, in the study by Hatzoglou et al,³⁴ 29 patients received postoperative partial brain radiation therapy for gliomas and the study cohort was too small for subgroup analysis. Additionally, MR spectroscopy⁵⁶ (sensitivity, 36%; specificity, 55%), perfusion CT⁵⁷ (sensitivity, 85.7%; specificity, 100%), and chemical exchange saturation transfer⁵⁸ were also tested for differential diagnosis in a small number of patients with variable conclusions. Overall, there are insufficient data for analysis and comparison with PET.

To our knowledge, this meta-analysis is the first to assess the diagnostic accuracy of amino acid and FDG-PET in differentiating brain metastasis recurrence from radionecrosis after radiation therapy. There are other meta-analyses focusing on PET in differentiating radionecrosis from recurrence in gliomas and demonstrating good diagnostic value.^{59–61} However, the mechanism of tracer uptake can be different between primary brain tumor and metastasis recurrence because metastasis has vessels that resemble origin tissues, resulting in the lack of any discernible blood-brain barrier, while glioma vessels usually have some remaining blood-brain barrier structure.⁶²

Moreover, we acknowledge several limitations of our study. First, our total pooled sample size was still quite small. Second, we included many retrospective studies ($n = 9$), which reduced the quality of our study. Third, we did not include studies that investigated the diagnostic accuracy of amino acid or FDG-PET in distinguishing postsurgical changes from tumor recurrence. Fourth, further analysis based on cutoff indexes could not be performed due to the lack of studies and incomplete reporting. Finally, there is evidence that ¹⁸F-FDG can accumulate in abscesses and inflammatory lesions, which can increase false-positive rates and add some bias.⁶³

CONCLUSIONS

In this meta-analysis, we demonstrated that amino acid and FDG-PET had good diagnostic accuracy in differentiating brain metastasis recurrence from radionecrosis after radiation therapy. While amino acid and FDG-PET may not be the most effective method to differentiate recurrence from radionecrosis after radiation therapy, it is still superior to other methods that are currently in practice.

APPENDIX

PubMed ($n = 106$)

(Positron-Emission Tomography[MH] OR (“Positron Emission”[TIAB] OR “Positron-Emission”[TIAB]) AND tomography[TIAB]) OR PET[TIAB]) AND (radionecrosis[TIAB] OR “radiation necrosis”[TIAB] OR “radiation-induced necrosis”[TIAB] OR “posttreatment necrosis”[TIAB] OR “radiation injury”[TIAB] OR “radionecrotic”[TIAB] OR “Post-Radiation therapy Necrosis”[TIAB]) AND (recurrence[MH] OR recurrence*[TIAB] OR recurrent[TIAB] OR relapse*[TIAB] OR recrudescence*[TIAB] OR neoplasm metastasis[MH] OR metastas*[TIAB] OR progression[TIAB]) AND (radiosurgery[MH] OR radiosurger*[TIAB] OR radiation therapy[MH] OR radiotherap*[TIAB] OR “radiation therap*”[TIAB] OR “radiation treatment”[TIAB])

Cochrane Library (n = 6)

([mh "Positron-Emission Tomography"] OR ("Positron Emission":ti,ab OR "Positron-Emission":ti,ab) AND tomography:ti,ab) OR PET:ti,ab) AND (radionecrosis:ti,ab OR "radiation necrosis":ti,ab OR "radiation-induced necrosis":ti,ab OR "posttreatment necrosis":ti,ab OR "radiation injury":ti,ab OR "radionecrotic":ti,ab OR "Post-Radiation therapy Necrosis":ti,ab) AND ([mh recurrence] OR recurrence*:ti,ab OR recurrent:ti,ab OR relapse*:ti,ab OR recrudescence*:ti,ab OR [mh "neoplasm metastasis"] OR metastas*:ti,ab OR progression:ti,ab) AND ([mh radiosurgery] OR radiosurger*:ti,ab OR [mh radiation therapy] OR radiotherap*:ti,ab OR "radiation therap*":ti,ab OR "radiation treatment":ti,ab)

Embase (n = 185)

'positron emission tomography'/exp/mj OR ('positron emission':ti,ab OR 'positron-emission':ti,ab AND tomography:ti,ab) OR pet:ti,ab AND (radionecrosis:ti,ab OR 'radiation necrosis':ti,ab OR 'radiation-induced necrosis':ti,ab OR 'posttreatment necrosis':ti,ab OR 'radiation injury':ti,ab OR 'radionecrotic':ti,ab OR 'postradiotherapy necrosis':ti,ab) AND ('cancer recurrence'/exp/mj OR 'tumor recurrence'/exp/mj OR recurrence*:ti,ab OR recurrent:ti,ab OR relapse*:ti,ab OR recrudescence*:ti,ab OR 'metastasis'/exp/mj OR metastas*:ti,ab OR progression:ti,ab) AND ('radiosurgery'/exp/mj OR radiosurger*:ti,ab OR 'radiation therapy'/exp/mj OR radiotherap*:ti,ab OR 'radiation therap*':ti,ab OR 'radiation treatment':ti,ab) AND [embase]/lim.

Disclosures: Li Yang—RELATED: Grant: Shenghua Yuying Project of Central South University.

REFERENCES

1. American Brain Tumor Association. Metastatic brain tumors. <http://www.abta.org/secure/metastatic-brain-tumor.pdf>. Accessed May 10, 2017
2. Sperduto PW, Kased N, Roberge D, et al. **Summary report on the graded prognostic assessment: an accurate and facile diagnosis-specific tool to estimate survival for patients with brain metastases.** *J Clin Oncol* 2012;30:419–25 CrossRef Medline
3. Bai HX, Zou Y, Lee AM, et al. **Diagnostic value and safety of brain biopsy in patients with cryptogenic neurological disease: a systematic review and meta-analysis of 831 cases.** *Neurosurgery* 2015;77:283–95 CrossRef Medline
4. Wang J, Liu X, Ma F, et al. **Role of radiotherapy in the treatment of primary mediastinal large B-cell lymphoma.** *Oncol Lett* 2015;10:2925–30 CrossRef Medline
5. Kocher M, Soffietti R, Abacioglu U, et al. **Adjuvant whole-brain radiotherapy versus observation after radiosurgery or surgical resection of one to three cerebral metastases: results of the EORTC 22952–26001 study.** *J Clin Oncol* 2011;29:134–41 CrossRef Medline
6. Aoyama H, Shirato H, Tago M, et al. **Stereotactic radiosurgery plus whole-brain radiation therapy vs stereotactic radiosurgery alone for treatment of brain metastases a randomized controlled trial.** *JAMA* 2006;295:2483–91 CrossRef Medline
7. Andrews DW, Scott CB, Sperduto PW, et al. **Whole brain radiation therapy with or without stereotactic radiosurgery boost for patients with one to three brain metastases: phase III results of the RTOG 9508 randomised trial.** *Lancet* 2004;363:1665–72 CrossRef Medline
8. Ceccan G, Lohmann P, Stoffels G, et al. **Dynamic O-(2–18F-fluoroethyl)-L-tyrosine positron emission tomography differentiates brain metastasis recurrence from radiation injury after radiotherapy.** *Neuro Oncol* 2017;19:281–88 CrossRef Medline
9. Greene-Schloesser D, Robbins ME, Peiffer AM, et al. **Radiation-induced brain injury: a review.** *Front Oncol* 2012;2:73 CrossRef Medline
10. Narloch JL, Farber SH, Sammons S, et al. **Biopsy of enlarging lesions after stereotactic radiosurgery for brain metastases frequently reveals radiation necrosis.** *Neuro Oncol* 2017;19:1391–97 CrossRef Medline
11. Chen W. **Clinical applications of PET in brain tumors.** *J Nucl Med* 2007;48:1468–81 CrossRef Medline
12. Minniti G, Clarke E, Lanzetta G, et al. **Stereotactic radiosurgery for brain metastases: analysis of outcome and risk of brain radionecrosis.** *Radiat Oncol* 2011;6:48 CrossRef Medline
13. Lohmann P, Stoffels G, Ceccan G, et al. **Radiation injury vs. recurrent brain metastasis: combining textural feature radiomics analysis and standard parameters may increase 18F-FET PET accuracy without dynamic scans.** *Eur Radiol* 2017;27:2916–27 CrossRef Medline
14. Verma N, Cowperthwaite MC, Burnett MG, et al. **Differentiating tumor recurrence from treatment necrosis: a review of neuro-oncologic imaging strategies.** *Neuro Oncol* 2013;15:515–34 CrossRef Medline
15. Stockham AL, Tievsky AL, Koefman SA, et al. **Conventional MRI does not reliably distinguish radiation necrosis from tumor recurrence after stereotactic radiosurgery.** *J Neurooncol* 2012;109:149–58 CrossRef Medline
16. Tan Y, Zhang H, Xiao EH. **Perivascular epithelioid cell tumour: dynamic CT, MRI and clinicopathological characteristics—analysis of 32 cases and review of the literature.** *Clin Radiol* 2013;68:555–61 CrossRef Medline
17. Menoux I, Armspach JP, Noël G, et al. **Techniques d'imagerie utilisées dans le diagnostic différentiel entre radionécrose cérébrale et rechute tumorale après irradiation en conditions stéréotaxiques de métastases cérébrales: revue de la littérature.** *Cancer/Radiothérapie* 2016;20:837–45
18. Karaosmanoglu AD, Onur MR, Ozmen MN, et al. **Magnetic resonance imaging of liver metastasis.** *Semin Ultrasound CT MR* 2016;37:533–48 CrossRef Medline
19. Zhou H, Vallières M, Bai HX, et al. **MRI features predict survival and molecular markers in diffuse lower-grade gliomas.** *Neuro Oncol* 2017;19:862–70 CrossRef Medline
20. McGivney DF, Pierre E, Ma D, et al. **SVD compression for magnetic resonance fingerprinting in the time domain.** *IEEE Trans Med Imaging* 2014;33:2311–22 CrossRef Medline
21. Galldiks N, Langen KJ, Pope WB. **From the clinician's point of view: what is the status quo of positron emission tomography in patients with brain tumors?** *Neuro Oncol* 2015;17:1434–44 CrossRef Medline
22. Bělohávek O, Šimonová G, Kantorová I, et al. **Brain metastases after stereotactic radiosurgery using the Leksell gamma knife: can FDG PET help to differentiate radionecrosis from tumour progression?** *Eur J Nucl Med Mol Imaging* 2003;30:96–100 CrossRef Medline
23. Cicone F, Minniti G, Romano A, et al. **Accuracy of F-DOPA PET and perfusion-MRI for differentiating radionecrotic from progressive brain metastases after radiosurgery.** *Eur J Nucl Med Mol Imaging* 2015;42:103–11 CrossRef Medline
24. Heesters M, van der Weide HL, Bolt RA, et al. **C-11-Methionine PET and radiotherapy dose distribution in the differentiation of radionecrosis and tumour progression after radiosurgery of brain metastases.** *Neuro Oncol* 2012;14:i74
25. Whiting PF. **QUADAS-2: a revised tool for the quality assessment of diagnostic accuracy studies.** *Ann Intern Med* 2011;155:529–36 CrossRef Medline
26. Reitsma JB, Glas AS, Rutjes AW, et al. **Bivariate analysis of sensitivity and specificity produces informative summary measures in diagnostic reviews.** *J Clin Epidemiol* 2005;58:982–90 Medline
27. Swets JA. **Measuring the accuracy of diagnostic systems.** *Science* 1988;240:1285–93 Medline
28. Higgins JP, Thompson SG, Deeks JJ, et al. **Measuring inconsistency in meta-analyses.** *BMJ* 2003;327:557–60 Medline
29. Anzures-Cabrera J, Higgins JP. **Graphical displays for meta-analysis: an**

- overview with suggestions for practice. *Res Synth Methods* 2010;1:66–80 CrossRef Medline
30. Sutton AJ, Abrams KR. Bayesian methods in meta-analysis and evidence synthesis. *Stat Methods Med Res* 2001;10:277–303 CrossRef Medline
 31. Chao ST, Suh JH, Raja S, et al. The sensitivity and specificity of FDG PET in distinguishing recurrent brain tumor from radionecrosis in patients treated with stereotactic radiosurgery. *Int J Cancer* 2001;96:191–97 Medline
 32. Galldikis N, Stoffels G, Filss CP, et al. Role of O-(2-18F-fluoroethyl)-L-tyrosine PET for differentiation of local recurrent brain metastasis from radiation necrosis. *J Nucl Med* 2012;53:1367–74 CrossRef Medline
 33. Guffens F, Maes A, Van Laere K, et al. Dynamic O-(2-18F-fluoroethyl)-L-tyrosine PET improves differentiation of local recurrent brain metastasis from radiation necrosis. *J Nucl Med* 2015;56(suppl 3):628
 34. Hatzoglou V, Yang TJ, Omuro A, et al. A prospective trial of dynamic contrast-enhanced MRI perfusion and fluorine-18 FDG PET-CT in differentiating brain tumor progression from radiation injury after cranial irradiation. *Neuro Oncol* 2016;18:873–80 CrossRef Medline
 35. Horky LL, Hsiao EM, Weiss SE, et al. Dual phase FDG-PET imaging of brain metastases provides superior assessment of recurrence versus post-treatment necrosis. *J Neurooncol* 2011;103:137–46 CrossRef Medline
 36. Lai G, Mahadevan A, Hackney D, et al. Diagnostic accuracy of PET, SPECT, and arterial spin-labeling in differentiating tumor recurrence from necrosis in cerebral metastasis after stereotactic radiosurgery. *AJNR Am J Neuroradiol* 2015;36:2250–55 CrossRef Medline
 37. Lizarraga KJ, Allen-Auerbach M, Czernin J, et al. 18F-FDOPA PET for differentiating recurrent or progressive brain metastatic tumors from late or delayed radiation injury after radiation treatment. *J Nucl Med* 2014;55:30–36 CrossRef Medline
 38. Matuszak J, Waissi W, Clavier JB, et al. Métastases cérébrales: apport de l'acquisition tardive en TEP/TDM au 18F-FDG pour le diagnostic différentiel entre récurrence tumorale et radionécrose. *Médecine Nucléaire* 2016;40:129–41
 39. Romagna A, Unterrainer M, Schmid-Tannwald C, et al. Suspected recurrence of brain metastases after focused high dose radiotherapy: can [18F]FET-PET overcome diagnostic uncertainties? *Radiat Oncol* 2016;11:139 CrossRef Medline
 40. Terakawa Y, Tsuyuguchi N, Iwai Y, et al. Diagnostic accuracy of 11C-methionine PET for differentiation of recurrent brain tumors from radiation necrosis after radiotherapy. *J Nucl Med* 2008;49:694–99 Medline
 41. Lei D, Li K, Li L, et al. Disrupted functional brain connectome in patients with posttraumatic stress disorder. *Radiology* 2015;276:818–27 CrossRef Medline
 42. Vargo MM. Brain tumors and metastases. *Phys Med Rehabil Clin N Am* 2017;28:115–41 CrossRef Medline
 43. Chao ST, Ahluwalia MS, Barnett GH, et al. Challenges with the diagnosis and treatment of cerebral radiation necrosis. *Int J Radiat Oncol Biol Phys* 2013;87:449–57 CrossRef Medline
 44. Gao S, Li S, Yang X, et al. 18FDG PET-CT for distant metastases in patients with recurrent head and neck cancer after definitive treatment: a meta-analysis. *Oral Oncol* 2014;50:163–67 CrossRef Medline
 45. Tomura N, Kokubun M, Saginoya T, et al. Differentiation between treatment-induced necrosis and recurrent tumors in patients with metastatic brain tumors: comparison among 11C-methionine-PET, FDG-PET, MR permeability imaging, and MRI-ADC—preliminary results. *AJNR Am J Neuroradiol* 2017;38:1520–27 CrossRef Medline
 46. Dequesada IM, Quisling RG, Yachnis A, et al. Can standard magnetic resonance imaging reliably distinguish recurrent tumor from radiation necrosis after radiosurgery for brain metastases? A radiographic-pathological study. *Neurosurgery* 2008;63:898–903; discussion 904 CrossRef Medline
 47. Leeman JE, Clump DA, Flickinger JC, et al. Extent of perilesional edema differentiates radionecrosis from tumor recurrence following stereotactic radiosurgery for brain metastases. *Neuro Oncol* 2013;15:1732–38 CrossRef Medline
 48. Wagner S, Lanfermann H, Eichner G, et al. Radiation injury versus malignancy after stereotactic radiosurgery for brain metastases: impact of time-dependent changes in lesion morphology on MRI. *Neuro Oncol* 2017;19:586–94 CrossRef Medline
 49. Heinzel A, Müller D, Yekta-Michael SS, et al. O-(2-18F-fluoroethyl)-L-tyrosine PET for evaluation of brain metastasis recurrence after radiotherapy: an effectiveness and cost-effectiveness analysis. *Neuro Oncol* 2017;19:1271–78 CrossRef Medline
 50. Miles K, McQueen L, Ngai S, et al. Evidence-based medicine and clinical fluorodeoxyglucose PET/MRI in oncology. *Cancer Imaging* 2015;15:18 CrossRef Medline
 51. Spaeth N, Wyss MT, Weber B, et al. Uptake of 18F-fluorocholine, 18F-fluoroethyl-L-tyrosine, and 18F-FDG in acute cerebral radiation injury in the rat: implications for separation of radiation necrosis from tumor recurrence. *J Nucl Med* 2004;45:1931–38 Medline
 52. Enslow MS, Zollinger LV, Morton KA, et al. Comparison of 18F-fluorodeoxyglucose and 18F-fluorothymidine PET in differentiating radiation necrosis from recurrent glioma. *Clin Nucl Med* 2012;37:854–61 CrossRef Medline
 53. Spence AM, Muzi M, Link JM, et al. NCI-sponsored trial for the evaluation of safety and preliminary efficacy of 3'-deoxy-3'-[18F]fluorothymidine (FLT) as a marker of proliferation in patients with recurrent gliomas: preliminary efficacy studies. *Mol Imaging Biol* 2009;11:343–55 CrossRef Medline
 54. Takenaka S, Asano Y, Shinoda J, et al. Comparison of (11)C-methionine, (11)C-choline, and (18)F-fluorodeoxyglucose-PET for distinguishing glioma recurrence from radiation necrosis. *Neurol Med Chir (Tokyo)* 2014;54:280–89 CrossRef Medline
 55. Tan H, Chen L, Guan Y, et al. Comparison of MRI, F-18 FDG, and 11C-choline PET/CT for their potentials in differentiating brain tumor recurrence from brain tumor necrosis following radiotherapy. *Clin Nucl Med* 2011;36:978–81 CrossRef Medline
 56. Huang J, Wang AM, Shetty A, et al. Differentiation between intra-axial metastatic tumor progression and radiation injury following fractionated radiation therapy or stereotactic radiosurgery using MR spectroscopy, perfusion MR imaging or volume progression modeling. *Magn Reson Imaging* 2011;29:993–1001 CrossRef Medline
 57. Vidiri A, Guerrisi A, Pinzi V, et al. Perfusion computed tomography (PCT) adopting different perfusion metrics: recurrence of brain metastasis or radiation necrosis? *Eur J Radiol* 2012;81:1246–52 CrossRef Medline
 58. Mehrabian H, Desmond KL, Soliman H, et al. Differentiation between radiation necrosis and tumor progression using chemical exchange saturation transfer. *Clin Cancer Res* 2017;23:3667–75 CrossRef Medline
 59. Deng SM, Zhang B, Wu YW, et al. Detection of glioma recurrence by ¹¹C-methionine positron emission tomography and dynamic susceptibility contrast-enhanced magnetic resonance imaging: a meta-analysis. *Nucl Med Commun* 2013;34:758–66 CrossRef Medline
 60. Nihashi T, Dahabreh IJ, Terasawa T. Diagnostic accuracy of PET for recurrent glioma diagnosis: a meta-analysis. *AJNR Am J Neuroradiol* 2013;34:944–50, S1–11 CrossRef Medline
 61. Wang X, Hu X, Xie P, et al. Comparison of magnetic resonance spectroscopy and positron emission tomography in detection of tumor recurrence in posttreatment of glioma: a diagnostic meta-analysis. *Asia Pac J Clin Oncol* 2015;11:97–105 CrossRef Medline
 62. Cha S, Lupo JM, Chen M, et al. Differentiation of glioblastoma multiforme and single brain metastasis by peak height and percentage of signal intensity recovery derived from dynamic susceptibility-weighted contrast-enhanced perfusion MR imaging. *AJNR Am J Neuroradiol* 2007;28:1078–84 Medline
 63. Antinori A, De Rossi G, Ammassari A, et al. Value of combined approach with thallium-201 single-photon emission computed tomography and Epstein-Barr Virus DNA polymerase chain reaction in CSF for the diagnosis of AIDS-related primary CNS lymphoma. *J Clin Oncol* 1999;17:554–60 Medline

Feasibility of Brain Atrophy Measurement in Clinical Routine without Prior Standardization of the MRI Protocol: Results from MS-MRIUS, a Longitudinal Observational, Multicenter Real-World Outcome Study in Patients with Relapsing-Remitting MS

R. Zivadinov, N. Bergsland, J.R. Korn, M.G. Dwyer, N. Khan, J. Medin, J.C. Price, B. Weinstock-Guttman, and D. Silva; on behalf of the MS-MRIUS Study Group



ABSTRACT

BACKGROUND AND PURPOSE: Feasibility of brain atrophy measurement in patients with MS in clinical routine, without prior standardization of the MRI protocol, is unknown. Our aim was to investigate the feasibility of brain atrophy measurement in patients with MS in clinical routine.

MATERIALS AND METHODS: Multiple Sclerosis and Clinical Outcome and MR Imaging in the United States (MS-MRIUS) is a multicenter (33 sites), retrospective study that included patients with relapsing-remitting MS who began treatment with fingolimod. Brain MR imaging examinations previously acquired at the baseline and follow-up periods on 1.5T or 3T scanners with no prior standardization were used, to resemble a real-world situation. Brain atrophy outcomes included the percentage brain volume change measured by structural image evaluation with normalization of atrophy on 2D-T1-weighted imaging and 3D-T1WI and the percentage lateral ventricle volume change, measured by VIENA on 2D-T1WI and 3D-T1WI and NeuroSTREAM on T2-fluid-attenuated inversion recovery examinations.

RESULTS: A total of 590 patients, followed for 16 months, were included. There were 585 (99.2%) T2-FLAIR, 425 (72%) 2D-T1WI, and 166 (28.2%) 3D-T1WI longitudinal pairs of examinations available. Excluding MR imaging examinations with scanner changes, the analyses were available on 388 (65.8%) patients on T2-FLAIR for the percentage lateral ventricle volume change, 259 and 257 (43.9% and 43.6%, respectively) on 2D-T1WI for the percentage brain volume change and the percentage lateral ventricle volume change, and 110 (18.6%) on 3D-T1WI for the percentage brain volume change and percentage lateral ventricle volume change. The median annualized percentage brain volume change was -0.31% on 2D-T1WI and -0.38% on 3D-T1WI. The median annualized percentage lateral ventricle volume change was 0.95% on 2D-T1WI, 1.47% on 3D-T1WI, and 0.90% on T2-FLAIR.

CONCLUSIONS: Brain atrophy was more readily assessed by estimating the percentage lateral ventricle volume change on T2-FLAIR compared with the percentage brain volume change or percentage lateral ventricle volume change using 2D- or 3D-T1WI in this observational retrospective study. Although measurement of the percentage brain volume change on 3D-T1WI remains the criterion standard and should be encouraged in future prospective studies, T2-FLAIR–derived percentage lateral ventricle volume change may be a more feasible surrogate when historical or other practical constraints limit the availability of percentage brain volume change on 3D-T1WI.

ABBREVIATIONS: MS-MRIUS = Multiple Sclerosis and Clinical Outcome and MR Imaging in the United States; PBVC = percentage brain volume change; PLVVC = percentage lateral ventricle volume change; RRMS = relapsing-remitting MS; SIENA = structural image evaluation with normalization of atrophy

Multiple sclerosis is an inflammatory and neurodegenerative autoimmune disease of the central nervous system characterized by demyelination and axonal degeneration.¹ The mea-

surement of brain atrophy has become one of the most important biomarkers for assessing the extent of neurodegenerative pathology in patients with MS.²⁻⁴ Development of brain atrophy in patients with MS is 3–5 times accelerated compared with the healthy aging population,^{2,3,5,6} correlates with physical and cognitive disability from the earliest disease stages,^{7,8} and continues throughout the course of the disease.⁹⁻¹³

Received June 21, 2017; accepted after revision September 11.

From the Department of Neurology (R.Z., N.B., M.G.D.), Buffalo Neuroimaging Analysis Center, and Department of Neurology (B.W.-G.), Jacobs Multiple Sclerosis Center, Jacobs School of Medicine and Biomedical Sciences, University at Buffalo, State University of New York, Buffalo, New York; Translational Imaging Center at Clinical and Translational Science Institute (R.Z.), University of Buffalo, State University of New York, Buffalo, New York; QuintilesIMS (J.R.K.), Burlington, Massachusetts; QuintilesIMS (N.K., J.C.P.), Basel, Switzerland; and Novartis Pharmaceuticals AG (J.M., D.S.), Basel, Switzerland.

This work was supported by Novartis Pharmaceuticals AG, Switzerland.

Please address correspondence to Robert Zivadinov, MD, PhD, FAAN, FEAN, FANA, Translational Imaging Center at Clinical and Translational Science Institute, Buffalo

Neuroimaging Analysis Center, Jacobs School of Medicine and Biomedical Sciences, University at Buffalo, State University of New York, 100 High St, Buffalo, NY 14203; e-mail: rzivadinov@bnac.net

Indicates open access to non-subscribers at www.ajnr.org

Indicates article with supplemental on-line tables.

<http://dx.doi.org/10.3174/ajnr.A5442>

Evidence is mounting that the development of disability progression in patients with MS is partially independent of accumulation of active MR imaging lesions and substantially dependent on the development of brain atrophy.¹⁴ Hence, there is an increasing interest in evaluating the effect of disease-modifying therapy on decelerating brain volume loss in clinical trials and consequently making personalized, patient-centric treatment choices.^{2,4,15,16} Therefore, there is an urgent need for translation and incorporation of brain atrophy measurement into clinical routine and patient-level treatment monitoring.^{2,4}

While the need for assessment of brain atrophy on the individual patient level for the effectiveness of treatment monitoring has become a hot topic in the literature recently,¹⁵ there is little understanding of how major obstacles are to be overcome. The feasibility of brain atrophy measurement for the short term, mid-term, and long term,^{2-4,17} using MR imaging sequences available in a clinical routine is currently unknown.

Against this background, we aimed to determine whether it is feasible to measure brain atrophy in patients with MS in clinical routine without prior standardization of the MR imaging protocol, using a multicenter study design that included academic and nonacademic centers in the United States to resemble the real-world situation. The study evaluated MR imaging scanner strength, type, and the quality of pulse sequence characteristics and investigated whether MR imaging changes influence the measurement of brain atrophy on the most commonly used pulse sequences in a clinical routine on a group level over the midterm.

MATERIALS AND METHODS

The Multiple Sclerosis and Clinical Outcome and MR Imaging in the United States (MS-MRIUS) study is a multicenter, longitudinal, retrospective, observational chart review of patients with MS treated with fingolimod (Gilenya) in clinical routine practice. The methodologic approach and design of this retrospective study have been previously reported.¹⁸

Briefly, clinical information and digital brain MR imaging image data were retrospectively collected from 33 participating academic and nonacademic MS centers across the United States and integrated into a central research data base.

The inclusion criteria were the following: 1) adult patients younger than 65 years of age with relapsing-remitting MS (RRMS) able to walk 20 m with or without assistance at the index date (defined as the date the patient first received treatment with fingolimod), equivalent to an Expanded Disability Status Scale¹⁹ score of ≤ 6.5 ; 2) starting fingolimod at the index date and remaining on fingolimod for at least 28 days; 3) the availability of clinical data ± 12 months from baseline (index date); and 4) a minimum of index and follow-up (postindex date) MR imaging examinations performed from 6 months before to 1 month after the index date and 9–24 months after index, respectively. Key exclusion criteria were the following: 1) neurologic disease other than MS affecting CNS structure or function; 2) a history of alcohol or substance abuse; 3) participation in an interventional trial during the study period; 4) prior use of fingolimod or natalizumab; and 5) steroid treatment in the 30 days prior to the scan dates.

A subgroup of 184 patients had preindex scans performed 9–24 months before fingolimod initiation (median, 13.9 months), but

this was not a required inclusion criterion. This subgroup of patients was used only to investigate serial longitudinal changes (3 time points) of brain volume, measured for approximately 30 months.

All demographic and clinical data required for this study were collected from patient medical records into a study-specific electronic clinical research form. For each patient, clinical information was collected for a 48-month period, including 12–24 months' data in the pre- and postindex period.

MR imaging examinations should have been performed on 1.5T or 3T scanners, and no standardization was expected. Patients did not need to have study examinations performed on the same scanner type and strength to resemble a real-world situation. 2D- or 3D-T2 fluid-attenuated inversion recovery and 2D- or 3D-T1-weighted images were collected. The participating sites transferred digital images using the standard DICOM format. To ensure that patient privacy was protected and that we adhered to relevant regulations, the centralized imaging center followed guidance from DICOM PS3.15 2015b, Security and System Management Profiles, Annex E: Attribute Confidentiality Profiles (http://dicom.nema.org/medical/Dicom/2015b/output/html/part15.html#chapter_E).²⁰ Automatic de-identification via the on-line transfer portal was performed for all study scans. This pathway was the simplest and least burdensome for the sites, because all sites had digital transfer capability. DICOM images were automatically anonymized before transmission to the centralized imaging center via encrypted channels, and there was no “burned-in” information on the images.

All scans were inspected by an experienced rater at the centralized imaging center. We evaluated the following quality metrics: section thickness, excessive patient motion (“yes” or “no”), image contrast (“bad,” “acceptable,” or “good”), and overall quality (“bad,” “acceptable,” or “good”). The overall quality metric reflected anatomic coverage, the presence of imaging artifacts, noise level, and contrast. Examinations with excessive patient motion or bad image contrast automatically received a bad rating for overall quality. Additionally, for each MR imaging examination, differences in hardware model, scanner software, and the coil between index and postindex were evaluated. For each MR imaging sequence (2D- or 3D-T2-FLAIR, 2D-T1WI, and 3D-T1WI), differences in orientation, thickness, and protocol changes were examined. Then, overall hardware, software, coil, or protocol differences between time points were determined. Hardware change was defined as a change in the MR imaging scanner. Software was defined as an upgrade to a different software version using the same scanner. Coil change was defined as a change of the coil. Protocol change was defined as a meaningful change in TR/TE/TI/flip angle/geometry. When the hardware changes occurred, in almost all instances, software, coil, and protocol changes were noticed; therefore, we refer to those as the MR imaging scanner change. When software, coil, or protocol changes occurred without hardware change, we refer to those as software/coil/protocol MR imaging changes.

Longitudinal brain atrophy outcomes included percentage brain volume change (PBVC) measured by structural image evaluation, with normalization of atrophy (SIENA)²¹ on 2D-T1WI and 3D-T1WI and the percentage lateral ventricle volume change

Table 1: Demographic and clinical characteristics of the study subjects according to the MRI scanner changes between the index and postindex periods^a

Index Variables	Total Patients with RRMS (n = 590)	Patients with RRMS with MRI Scanner Changes (n = 309)	Patients with RRMS without MRI Scanner Changes (n = 281)	P Value ^b
Age at index in yr (median) (IQR)	42 (36; 49)	41 (35; 48)	44 (37; 51)	.007
Women (No.) (%)	464 (78.6)	247 (79.9)	217 (77.2)	.422
Race/ethnicity (No.) (%)				
Caucasian/white	494 (83.7)	252 (81.6)	242 (86.1)	.319
Non-Caucasian	63 (10.7)	37 (12.0)	26 (9.3)	
Unknown	33 (5.6)	20 (6.5)	13 (4.6)	
Body mass index at index (median) (IQR)	26.6 (23.2–30.6)	26.5 (23.3–30.4)	26.6 (23–30.9)	.895
Disease duration in yr (median) (IQR)	8 (4; 13)	7 (4; 12)	8 (4; 13)	.148
Number with relapse in 2 yr before index (No.) (%)	236 (40.0)	143 (46.3)	93 (33.1)	.003
EDSS at index (median) (IQR)	2.0 (1.0–3.0)	2.0 (1.0–3.0)	2.5 (1.5–3.5)	.002
Use of DMT 2 yr before index (No.) (%)				
Teriflunomide	5 (0.9)	3 (1)	2 (0.7)	.749
Glatiramer acetate	175 (30.8)	87 (28.9)	88 (32.8)	.310
Interferon- β	317 (55.7)	175 (58.1)	142 (53)	.217
Alemtuzumab	1 (0.2)	1 (0.3)	0 (0)	.345
Dimethyl fumarate	38 (6.7)	21 (7)	17 (6.3)	.763
No DMT	94 (15.9)	46 (14.9)	48 (17.1)	.467

Note:—EDSS indicates Expanded Disability Status Scale; IQR, interquartile range; DMT, disease-modifying treatment.

^a MRI changes include hardware/software/coil/protocol differences between the index and postindex.

^b P values represent group comparisons of patients with MS with and without MRI changes during the follow-up derived with the Student *t*, χ^2 , and Mann-Whitney rank sum tests as appropriate.

(PLVVC) measured by VIENA²² on 2D-T1WI and 3D-T1WI examinations and measured by NeuroSTREAM²³ on T2-FLAIR. Lesions were inpainted before segmentation to reduce the impact of T1 hypointensities.²⁴ All outcomes of brain atrophy analyses were assessed by an experienced rater. Because hardware changes can affect longitudinal measurements,^{25–27} SIENA PBVC and VIENA PLVVC analyses were considered invalid when a patient was imaged on different hardware. In addition, because NeuroSTREAM PLVVC was previously shown to be robust to hardware changes in a study that included 125 patients with MS and 76 healthy controls,²³ we explored the stability of this measure in patients with and without MR imaging hardware changes using the current real-world setting dataset.

The study adhered to the Health Insurance Portability and Accountability Act and received central and local institutional review board approvals.

Statistical Analyses

All statistical analyses were performed using the SAS statistical software systems (SAS Institute, Cary, North Carolina). All analyses were performed on the basis of a statistical analysis plan defined a priori. Summary statistics for continuous variables included the number of patients with valid/missing observations, mean, SD, median, interquartile ratio, minimum, and maximum. Summary statistics for categorical variables included frequencies and related percentages per class level. Demographic, clinical, and MR imaging characteristic differences were examined with the Student *t*, χ^2 , and Wilcoxon rank sum tests as appropriate. The MR imaging acquisition differences between academic and non-academic centers were examined using the χ^2 test. The influence of MR imaging changes during follow-up was investigated by analysis of covariance, adjusted for age, sex, days between time periods during the follow-up, and baseline volume, as appropriate. To investigate correlations between PLVVC on T2-FLAIR using NeuroSTREAM and PLVVC and PBVC on 2D-T1WI and

3D-T1WI using VIENA and SIENA, respectively, in patients with MS with and without software/coil/protocol MR imaging changes, we performed Spearman rank correlations. A nominal *P* value of $\leq .05$ was considered statistically significant, using 2-tailed tests.

RESULTS

Demographic and Clinical Characteristics at Index and Postindex

Table 1 outlines demographic and clinical characteristics of the study subjects, according to the MR imaging scanner changes between index and postindex. Of the 590 patients with RRMS included in the study, 464 (78.6%) were women. Of the 33 centers participating in the study, 25 (75.8%) centers were nonacademic specialty and community MS centers and 8 (24.2%) were academic; 398 (67.5%) patients with RRMS were collected in non-academic, and 192 (32.5%), in academic centers. Between index and postindex follow-ups, MR imaging scanner changes occurred in 284 (48.1%) patients with RRMS. The median follow-up between index and postindex was approximately 16 months.

The median age was somewhat lower in patients with RRMS with MR imaging scanner changes compared with those without (*P* = .007). The number of relapses in 2 years before index was significantly higher in patients with RRMS with MR imaging scanner changes compared with those without (*P* = .001). Patients with RRMS without MR imaging scanner changes had higher Expanded Disability Status Scale scores (*P* = .002). No significant differences between patients with RRMS with and without MR imaging scanner changes were detected for disease duration or previous type of disease-modifying treatment at index.

MR Imaging Acquisition Characteristics at Index and Postindex

At postindex, there was a higher proportion of patients examined on 3T scanners (34.1%) compared with the index (29.5%, Online Table 1). All except 3 patients at index (99.5%) and 4 patients

Table 2: Brain atrophy measures of the study subjects between index and postindex, according to MRI changes^a

	Total Patients with RRMS	Patients with RRMS with MRI Software/Coil/Protocol Changes	Patients with RRMS without MRI Software/Coil/Protocol Changes	P Value ^b
PBVC on 2D-T1WI	<i>n</i> = 259 −0.31 (−0.74–0.13)	<i>n</i> = 89 −0.35 (−0.97–0.11)	<i>n</i> = 170 −0.28 (−0.67–0.14)	.233
PBVC on 3D-T1WI	<i>n</i> = 110 −0.38 (−0.88 to −0.04)	<i>n</i> = 37 −0.38 (−0.93–0.02)	<i>n</i> = 73 −0.37 (−0.81 to −0.08)	.740
PLVVC on 2D-T1WI	<i>n</i> = 257 0.95 (−1.77–3.99)	<i>n</i> = 89 0.95 (−1.92–4.1)	<i>n</i> = 168 0.96 (−1.63–3.94)	.848
PLVVC on 3D-T1WI	<i>n</i> = 110 1.47 (−1.26–4.39)	<i>n</i> = 37 1.5 (−1.36–4.15)	<i>n</i> = 73 1.01 (−1.17–4.46)	.940
PLVVC on T2-FLAIR	<i>n</i> = 388 0.90 (−2.91–5.94)	<i>n</i> = 130 0.21 (−4.67–7.2)	<i>n</i> = 258 1.1 (−2.1–5.51)	.179
PLVVC on T2-FLAIR ^c	<i>n</i> = 554 0.51 (−3.95–6.01)	<i>n</i> = 291 −0.31 (−6.4–6.9)	<i>n</i> = 263 1.13 (−2.15–5.53)	.007

^a PBVC and PLVVC on 2D-, 3D-T1WI and T2-FLAIR were obtained in patients with software/coil/protocol scanner changes. All values in the table are presented as the number of patients for a particular analysis, median, and interquartile range. The longitudinal follow-up values are annualized.

^b *P* values represent patients with MS with and without MRI changes during the follow-up group comparisons and were derived using analysis of covariance adjusted for age, sex, days between index and postindex, and baseline volume as appropriate.

^c PLVVC on T2-FLAIR was performed in patients with hardware/software/coil/protocol changes.

at postindex (99.3%) had T2-FLAIR examinations, with most being 2D acquisitions, except for 9 examinations at index and 16 examinations at postindex, which were 3D. The use of 2D-T1WI decreased during follow-up from 79.7% at index to 75.6% at postindex, whereas the use of 3D-T1WI increased from 31.4% at index to 39.7% at postindex. Only 16.6% index and 20.7% postindex examinations had both 2D- and 3D-T1WI. A section thickness of ≤5 mm was present in 40%–50% of the T2-FLAIR and 35%–40% of the 2D-T1WI examinations. More than 85% of 3D-T1WI examinations were ≤2 mm thick. There was minimal-to-no excessive patient motion for all sequences, and scanner contrast and overall quality of the examinations were generally acceptable or good. 3D-T1WI examinations had superior quality to 2D-T1WI, with 80%–90% having good quality compared with 60%–70% on T2-FLAIR and 40%–45% on 2D-T1WI.

At index and postindex, there was a significantly higher proportion of 3T scanners (*P* < .001) and more 2D- and 3D-T1WI examinations in academic centers (On-line Table 2). The section thickness for various pulse sequences was lower in academic centers (≤5-mm section thickness for T2-FLAIR and 2D-T1WI and ≤2-mm section thickness for 3D-T1WI) (On-line Table 2). No differences in patient motion were found between academic and nonacademic centers, but scanner contrast and overall scan quality were better in the academic centers (On-line Table 2).

Eligibility of MR Imaging Examinations for Calculation of Brain Atrophy Outcomes

On-line Table 3 shows the eligibility of a longitudinal pair of examinations for calculation of PBVC and PLVVC measures between index and postindex. Among index-to-postindex examinations, hardware changes were identified in 29.5%; software, in 27.3%; and coil, in 31.9% of the longitudinal pairs. When pooled together, hardware/software/coil changes were identified in about 50% of the examinations, more frequently in the academic than in nonacademic centers (59.9% versus 42.2%, *P* = .002). A similar frequency of MR imaging protocol changes during the follow-up occurred on a pulse sequence basis for T2-FLAIR, 2D-T1WI, and

3D-T1WI, with higher rates of change in the academic than in nonacademic centers.

There were 585 (99.2%) T2-FLAIR, 425 (72%) 2D-T1WI, and 166 (28.1%) 3D-T1WI examinations eligible for calculation of brain atrophy outcomes. If we excluded longitudinal pairs of examinations that underwent hardware changes (174, 29.5%), analyses of brain atrophy outcomes were possible for 388 (65.8%) patients using PLVVC on T2-FLAIR, 259 and 257 (43.9% and 43.6%, respectively) patients using PBVC and PLVVC on 2D-T1WI, and 110 (18.6%) patients using PBVC and PLVVC on 3D-T1WI.

Changes in Brain Atrophy Measures during Follow-Up

At index (data not shown), no differences were seen in brain atrophy measures for any pulse sequence when stratified according to MR imaging software/coil/protocol changes occurring during the follow-up, except for the 3D-T1WI lateral ventricle volume, which was significantly higher in the group that underwent MR imaging changes (*P* = .05).

There were no significant differences in PBVC or PLVVC measures between patients with RRMS with and without software/coil/protocol MR imaging changes from index to postindex for any of the MR imaging sequence types explored. Median annualized PBVC was −0.31% on 2D-T1WI and −0.38% on 3D-T1WI. Median annualized PLVVC was 0.95% on 2D-T1WI, 1.47% on 3D-T1WI, and 0.90% on T2-FLAIR (Table 2).

In a subgroup of 91 patients with RRMS with available preindex, index, and postindex MR imaging examinations, no significant differences in brain atrophy measures were found between patients with RRMS with and without software/coil/protocol MR imaging changes (On-line Table 4).

Using all patients with RRMS, who had analysis for PLVVC on T2-FLAIR examination (*n* = 554) independent of hardware changes, we found a significant index-to-postindex difference when comparing those with and without MR imaging scanner changes (−0.31% versus 1.13%, *P* = .007, Table 2), but not in a subgroup of 184 patients with RRMS with available preindex,

index, and postindex MR imaging examinations (On-line Table 4).

When only MR imaging hardware change was considered, a significantly different PLVCC was observed for patients imaged with hardware changes between index and postindex ($n = 166$, 30%) compared with those who were not ($n = 388$, 70%) (-1.23% versus 0.9% , $P = .02$).

Correlation among Different Brain Atrophy Measures Using Different MR Imaging Pulse Sequences

On-line Table 5 shows the correlations between PLVCC on T2-FLAIR using NeuroSTREAM and PLVCC and PBVC on 2D-T1WI and 3D-T1WI using VIENA and SIENA, respectively, in patients with MS with and without software/coil/protocol MR imaging changes. PLVCC on 3D-T1WI, 2D-T1WI, and T2-FLAIR was significantly associated with PBVC on 3D-T1WI and 2D-T1WI when all patients with MS were considered. As expected, correlations were stronger in patients with MS who were not imaged with software/coil/protocol changes, compared with those who were. PBVC on 3D-T1WI was associated with PLVCC on 3D-T1WI ($r = -0.7$, $P < .0001$), PLVCC on T2-FLAIR ($r = -0.5$, $P < .0001$), and PLVCC on 2D-T1WI ($r = -0.39$, $P < .0001$) in patients with MS imaged without MR imaging software/coil/protocol changes during the follow-up.

DISCUSSION

This is one of the first multicenter, retrospective, real-world studies that investigated the feasibility of brain atrophy measurement in a clinical routine without prior standardization of the MR imaging protocol, using academic and nonacademic centers specialized in treatment and monitoring of MS in the United States. The main findings of the study can be summarized as follows: 1) The quality of the MR images used for brain atrophy analyses were mostly acceptable or good in all centers; 2) about 70% of the centers used 1.5T field strength, and there was a tendency for higher use of 3T scanners during the follow-up; 3) academic centers performed MR imaging examinations with thinner sections, better contrast, and overall scan quality; they also used 3T scanners more frequently, with $>50\%$ of postindex examinations being performed on 3T, and had a higher proportion of 3D-T1WI examinations; 4) T2-FLAIR examinations were used in $>99\%$ of patients, while the figures were 72% for 2D-T1WI and 28% for 3D-T1WI examinations longitudinally; 5) scanner changes occurred in $>50\%$ of the patients during the follow-up, and the changes occurred more frequently in the academic, compared with nonacademic centers; 6) measurement of PLVCC on T2-FLAIR was feasible in 66% of patients, making it the most suitable measure of brain atrophy for clinical routine, while PBVC was obtained in 44% of patients on 2D-T1WI and 18% on 3D-T1WI; 7) excluding MR imaging hardware changes, there were no significant differences of brain atrophy outcomes in patients with and without MR imaging software/coil/protocol changes from index to postindex; 8) hardware changes resulted in significant PLVCC differences on T2-FLAIR, though this was not evident in the subgroup of patients with 3 serial MR imaging examinations during 30 months; and 9) finally, PBVC changes on 2D- and 3D-T1WI in patients treated with fingolimod for 16 months were similar to

those reported in pivotal and/or open-label observational studies.²⁸

Clinical routine MR imaging examinations pose many unique challenges.^{2,16} They have a lower signal-to-noise ratio and/or spatial resolution due to trade-offs in scanning time. They lack standardization, which, in turn, is compounded by changes in MR imaging hardware and/or software upgrades. In the MS-MRIUS study, we confirmed that the spatial resolution was lower than that used in MS research clinical trials; however, most of the scans were of acceptable or good quality with negligible patient motion.

The MS-MRIUS study detected important differences in the type of MR imaging scanners used between academic and nonacademic centers in the United States. On the basis of some previous reports of the use of MR imaging in the referral of patients with MS to academic centers in the United States,²⁹ it could be expected that the adherence to the Consortium of MS Centers³⁰ and Magnetic Resonance Imaging in MS (MAGNIMS)³¹ MR imaging acquisition protocol guidelines for MS is somewhat lower in nonacademic compared with academic centers, which was exactly what we found in the current study. However, MR imaging scanner changes during the follow-up occurred even more frequently in academic than in nonacademic centers, which could be attributed to academic centers upgrading software more frequently or replacing their scanning technology more rapidly.

Image resolution and image contrast are important for a reliable and optimal segmentation of brain volume, and 3D pulse sequences are preferred for measurement of brain atrophy as the criterion standard for brain volumetric imaging because of the reduction of partial volume effects and more accurate coregistration, especially for serial imaging with time, compared with 2D-pulse sequences.^{2,3,16,17} Although 3D-T1WI is the recommended sequence for the calculation of brain volume measures, it is considered only as an optional sequence in the current MR imaging acquisition guidelines.^{30,31} The MS-MRIUS study showed that less than one-quarter of patients with MS had eligible 3D-T1WI for estimation of brain volume measures during the follow-up, which substantially impacted applicability for use in clinical routine. On the other hand, the MS-MRIUS study showed that T2-FLAIR was eligible in 99% of patients, allowing reliable PLVCC analysis in 66% of patients during the follow-up. Therefore, measurement of PLVCC on T2-FLAIR increased by 33% the proportion of patients who obtained reliable brain atrophy measurements compared with 2D-T1WI and by 73% compared with 3D-T1WI, respectively.

Given that more than half of the patients underwent changes in the MR imaging scanner during the follow-up, there is a strong need for a universally applicable panel of simple brain volume measures that are resistant to MR imaging scanner changes. For proper estimation of brain volume changes with time, patients should undergo an acquisition with the same hardware and without software/coil/protocol changes. However, this is very difficult to achieve in clinical routine because of a number of different logistic factors.² The MS-MRIUS study showed no significant impact of software/coil/protocol changes on the measurement of PBVC and PLVCC in the clinical routine during 16 months, as evaluated using 3 different types of software on 3 different types of sequences. In particular, PLVCC is of interest as a choice for brain

atrophy assessment in the clinical routine because it is relatively robust to the negative impact of imprecise positioning, gradient distortions, incomplete head coverage, and other motion and wraparound artifacts.¹² In addition, PLVVC occurs at a 5-fold greater rate compared with PBVC, and the effect size of PBVC and PLVVC for the estimation of disability progression from baseline to 10-year follow-up is similar.¹²

In a previous study, the correlation analysis between PLVVC on T2-FLAIR using NeuroSTREAM and PLVVC and PBVC on 3D-T1WI using VIENA and SIENA, respectively, was described.²³ The correlation analysis from the present study showed similar associations between PBVC on 3D-T1WI and PLVVC on T2-FLAIR in patients with MS who did not experience software/coil/protocol MR imaging changes during the follow-up, corroborating that PLVVC on T2-FLAIR can be used reliably in retrospective and prospective observational studies without prior standardization of the MR imaging protocol. However, measurement of brain atrophy on T2-FLAIR using PLVVC is still suboptimal compared with PBVC on 3D-T1WI, which should prompt clinicians in the more extensive use of the latter in clinical practice.

In line with other recent studies,^{23,25,26} the MS-MRIUS study showed that scanner changes had an impact on brain volume estimates. While it was previously shown that NeuroSTREAM-derived PLVVC is relatively robust to different field strengths when imaged during a short time (approximately 2% coefficient of variation in the 1.5T versus 3T scan-rescan test for 72 hours),²³ the current study showed that PLVVC on T2-FLAIR was significantly different in patients with RRMS with hardware changes, compared with those without. If the measurement of brain atrophy is to become an additional assessment tool for monitoring individual patients with MS, the annualized rate of pathologic cutoff⁵ will have to be lower than the error rate introduced by hardware changes or the analyses will be considered invalid for those patients. Although the MS-MRIUS study was not designed to answer this important question, it provides the first evidence of the feasibility of brain atrophy measurement in clinical routine without prior standardization of the MR imaging protocol. Future studies should investigate in greater detail the influence of individual components of scanner changes on a variety of brain atrophy measures, applicable to clinical routine, over the short term, midterm, and long term.

CONCLUSIONS

We showed, in this retrospective observational study, that T2-FLAIR was the most frequent sequence in the clinical routine. To increase general applicability of brain atrophy measurement in observational studies in the clinical routine, one can more feasibly estimate brain atrophy by assessing PLVVC on T2-FLAIR compared with PBVC or PLVVC using 2D- or 3D-T1WI. As the most accurate and well-established measurement of brain atrophy, PBVC assessment on 3D-T1WI is, and should remain, the criterion standard of brain volumetric imaging research. However, T2-FLAIR-derived PLVVC may be a more feasible surrogate when historical or other practical constraints limit the availability of PBVC on 3D-T1WI.

APPENDIX

MS-MRIUS study group:

Principal Investigator: R. Zivadinov.

Co-Principal Investigator: B. Weinstock-Guttman.

Study Steering Committee: R. Zivadinov, J. Medin, D. Silva, B. Weinstock-Guttman.

QuintilesIMS: N. Khan, J.R. Korn, J. Price.

Novartis: J. Medin, D. Silva.

MRI Analysis Center: R. Zivadinov, N. Bergsland, M.G. Dwyer, D.P. Ramasamy, E. Carl, Buffalo Neuroimaging Analysis Center, Department of Neurology, Jacobs School of Medicine and Biomedical Sciences, University at Buffalo, State University of New York, Buffalo, New York.

Study sites:

Advanced Neurosciences Institute, Franklin, Tennessee: S. Hunter; Allegheny-Singer Research Institute, Pittsburgh, Pennsylvania: T. Scott; Barnabas Health, Livingston, New Jersey: K. Pandey; Central Texas Neurology Consultants, Round Rock, Texas: E. Fox; Central State Medical Center, Freehold, New Jersey: A. Katz; Christiana Care Health Systems, Newark, Delaware: J. Silversteen; College Park Family Care Center, Overland Park, Kansas: J. Kaplan; Denver Health and Hospital Authority, Denver, Colorado: E. Maa; Evergreen Health, Kirkland, Washington: V. Simnad; Georgetown University, Washington, DC: R. Shin; Island Neurological Associates, Plainview, New Jersey: S. Newman; Kinkel Neurologic, Williamsville, New York: P. Kinkel; Mercy Clinic Neurology, Chesterfield, Missouri: B. Green; Minneapolis Clinic of Neurology, Golden Valley, Minnesota: J. Calkwood; MS Center of Northeastern NY, Latham, New York: K. Edwards; Neurological Services of Orlando, Orlando, Florida: D. Jacobs; Neurology & Neuroscience Associates, Akron, Ohio: D. Huang; Neurology Center of San Antonio, San Antonio, Texas: A. Bass; Neuroscience Group of Neenah, Neenah, Wisconsin: S. Hibbs; NYU Langone Medical Center, New York City, New York: I. Kister; Ohio Health, Columbus, Ohio: G. Eubank; OMRF MS Center of Excellence, Oklahoma City, Oklahoma: G. Pardo; Partners MS Center, Harvard, Boston, Massachusetts: C. Chitnis; Phoenix Neurological Associates, Phoenix, Arizona: B. Hendin; Providence St. Vincent Medical Center, Portland, Oregon: S. Cohan; Raleigh Neurology Associates, Raleigh, North Carolina: M. Freedman; South Shore Neurologic Associates, Patchogue, New York: M. Gudesblatt; SUNY University of Buffalo, Buffalo, New York: B. Weinstock-Guttman; The Elliot Lewis Center for MS Care, Boston, Massachusetts: E. Lathi; University of Colorado, Denver, Colorado: E. Alvarez; University of Rochester, Rochester, New York: A. Goodman; University of Tennessee, Knoxville, Tennessee: R. Trudell; Washington University, St Louis, Missouri: R. Naismith.

Disclosures: Robert Zivadinov—RELATED: Grant: QuintilesIMS*; UNRELATED: Consultancy: Novartis, Sanofi Genzyme, Celgene; Grants/Grants Pending: Novartis, Sanofi Genzyme, QuintilesIMS*; Payment for Lectures Including Service on Speakers Bureaus: Novartis, Sanofi Genzyme. Jonathan R. Korn—RELATED: Consulting Fee or Honorarium: QuintilesIMS, Comments: QuintilesIMS received funding from Novartis to perform this study.* Michael G. Dwyer—RELATED: Grant: Novartis*; UNRELATED: Consultancy: Claret Medical, EMD Serono. Nasreen Khan—RELATED: Consulting Fee or Honorarium: QuintilesIMS, Comments: The work performed was paid by QuintilesIMS. The QuintilesIMS study was supported by Novartis; UNRELATED: Employment: Real-World Economics Consultancy, Comments: I am the owner of the consultancy firm Real-World Economics Consultancy, which provides consulting services for pharmaceutical and other consulting companies. In the past, I have

worked with QuintilesIMS and Novartis. Jennie Medin—RELATED: *Support for Travel to Meetings for the Study or Other Purposes*: Novartis, *Comments*: I am a paid employee of Novartis; *Fees for Participation in Review Activities such as Data Monitoring Boards, Statistical Analysis, Endpoint Committees, and the Like*: Novartis, *Comments*: I am a paid employee of Novartis; *Other*: Novartis, *Comments*: I am a paid employee of Novartis Pharma AG; UNRELATED: *Employment*: Novartis, *Comments*: I am a paid employee of Novartis; *Payment for Manuscript Preparation*: Novartis, *Comments*: I am a paid employee of Novartis; *Stock/Stock Options*: Novartis, *Comments*: I am a paid employee of Novartis; *Travel/Accommodations/Meeting Expenses Unrelated to Activities Listed*: Novartis, *Comments*: I am a paid employee of Novartis; *Other*: Novartis, *Comments*: I am a paid employee of Novartis. Jennifer C. Price—RELATED: *Other*: QuintilesIMS, *Comments*: I am a paid employee of QuintilesIMS, which was paid by Novartis to perform this study; UNRELATED: *Employment*: QuintilesIMS, *Comments*: I am a paid employee of QuintilesIMS. Bianca Weinstock-Guttman—RELATED: *Grant*: Novartis*; UNRELATED: *Consultancy*: Biogen, TEVA, Novartis, Genzyme, Genentech, EMD Serono; *Payment for Lectures Including Service on Speakers Bureaus*: Biogen, TEVA, Novartis, Genentech. Diego Silva—RELATED: *Other*: Novartis, *Comments*: I am a Novartis employee; UNRELATED: *Employment*: Novartis; *Stock/Stock Options*: Novartis, *Comments*: I am a Novartis employee. *Money paid to the institution.

REFERENCES

- Vercellino M, Masera S, Lorenzatti M, et al. **Demyelination, inflammation, and neurodegeneration in multiple sclerosis deep gray matter.** *J Neuropathol Exp Neurol* 2009;68:489–502 CrossRef Medline
- Zivadinov R, Jakimovski D, Gandhi S, et al. **Clinical relevance of brain atrophy assessment in multiple sclerosis: implications for its use in a clinical routine.** *Expert Rev Neurother* 2016;16:777–93 CrossRef Medline
- Miller DH, Barkhof F, Frank JA, et al. **Measurement of atrophy in multiple sclerosis: pathological basis, methodological aspects and clinical relevance.** *Brain* 2002;125:1676–95 CrossRef Medline
- De Stefano N, Airas L, Grigoriadis N, et al. **Clinical relevance of brain volume measures in multiple sclerosis.** *CNS Drugs* 2014;28:147–56 CrossRef Medline
- De Stefano N, Stromillo ML, Giorgio A, et al. **Establishing pathological cut-offs of brain atrophy rates in multiple sclerosis.** *J Neurol Neurosurg Psychiatry* 2016;87:93–99 CrossRef Medline
- Schippling S, Ostwaldt AC, Suppa P, et al. **Global and regional annual brain volume loss rates in physiological aging.** *J Neurol* 2017; 264:520–28 CrossRef Medline
- Zivadinov R, Havrdová E, Bergsland N, et al. **Thalamic atrophy is associated with development of clinically definite multiple sclerosis.** *Radiology* 2013;268:831–41 CrossRef Medline
- Calabrese M, Rinaldi F, Mattisi I, et al. **The predictive value of gray matter atrophy in clinically isolated syndromes.** *Neurology* 2011;77: 257–63 CrossRef Medline
- Fisher E, Lee JC, Nakamura K, et al. **Gray matter atrophy in multiple sclerosis: a longitudinal study.** *Ann Neurol* 2008;64:255–65 CrossRef Medline
- Popescu V, Agosta F, Hulst HE, et al; MAGNIMS Study Group. **Brain atrophy and lesion load predict long term disability in multiple sclerosis.** *J Neurol Neurosurg Psychiatry* 2013;84:1082–91 CrossRef Medline
- Jacobsen C, Hagemer J, Myhr KM, et al. **Brain atrophy and disability progression in multiple sclerosis patients: a 10-year follow-up study.** *J Neurol Neurosurg Psychiatry* 2014;85:1109–15 CrossRef Medline
- Zivadinov R, Uher T, Hagemer J, et al. **A serial 10-year follow-up study of brain atrophy and disability progression in RRMS patients.** *Mult Scler* 2016;22:1709–18 CrossRef Medline
- Filippi M, Preziosa P, Copetti M, et al. **Gray matter damage predicts the accumulation of disability 13 years later in MS.** *Neurology* 2013; 81:1759–67 CrossRef Medline
- Sormani MP, Arnold DL, and De Stefano N. **Treatment effect on brain atrophy correlates with treatment effect on disability in multiple sclerosis.** *Ann Neurol* 2014;75:43–49 CrossRef Medline
- Zivadinov R, Dwyer MG, and Bergsland N. **Brain atrophy measurements should be used to guide therapy monitoring in MS: YES.** *Mult Scler* 2016;22:1522–24 CrossRef Medline
- Azevedo CJ, Pelletier D. **Whole-brain atrophy: ready for implementation into clinical decision-making in multiple sclerosis?** *Curr Opin Neurol* 2016;29:237–42 CrossRef Medline
- Rocca MA, Battaglini M, Benedict RH, et al. **Brain MRI atrophy quantification in MS: from methods to clinical application.** *Neurology* 2017;88:403–13 CrossRef Medline
- Zivadinov R, Khan N, Medin J, et al. **An observational study to assess brain MRI change and disease progression in multiple sclerosis clinical practice: the MS-MRIUS study.** *J Neuroimaging* 2017;27: 339–47 CrossRef Medline
- Kurtzke JF. **Rating neurologic impairment in multiple sclerosis: an expanded disability status scale (EDSS).** *Neurology* 1983;33:1444–52 CrossRef Medline
- Fetzer DT, West OC. **The HIPAA privacy rule and protected health information: implications in research involving DICOM image databases.** *Acad Radiol* 2008;15:390–95 CrossRef Medline
- Smith SM, Zhang Y, Jenkinson M, et al. **Accurate, robust, and automated longitudinal and cross-sectional brain change analysis.** *Neuroimage* 2002;17:479–89 CrossRef Medline
- Vrenken H, Vos EK, van der Flier WM, et al. **Validation of the automated method VIENA: an accurate, precise, and robust measure of ventricular enlargement.** *Hum Brain Mapp* 2014;35:1101–10 CrossRef Medline
- Dwyer MG, Silva D, Bergsland N, et al. **Neurological software tool for reliable atrophy measurement (NeuroSTREAM) of the lateral ventricles on clinical-quality T2-FLAIR MRI scans in multiple sclerosis.** *Neuroimage Clin* 2017;15:769–79 CrossRef Medline
- Gelineau-Morel R, Tomassini V, Jenkinson M, et al. **The effect of hypointense white matter lesions on automated gray matter segmentation in multiple sclerosis.** *Hum Brain Mapp* 2012;33:2802–14 CrossRef Medline
- Chu R, Tauhid S, Glanz BI, et al. **Whole brain volume measured from 1.5T versus 3T MRI in healthy subjects and patients with multiple sclerosis.** *J Neuroimaging* 2016;26:62–67 CrossRef Medline
- Lysandropoulos AP, Absil J, Metens T, et al. **Quantifying brain volumes for multiple sclerosis patients follow-up in clinical practice: comparison of 1.5 and 3 Tesla magnetic resonance imaging.** *Brain Behav* 2016;6:e00422 CrossRef Medline
- Biberacher V, Schmidt P, Keshavan A, et al. **Intra- and interscanner variability of magnetic resonance imaging based volumetry in multiple sclerosis.** *Neuroimage* 2016;142:188–97 CrossRef Medline
- De Stefano N, Silva DG, Barnett MH. **Effect of fingolimod on brain volume loss in patients with multiple sclerosis.** *CNS Drugs* 2017;31: 289–305 CrossRef Medline
- Carmosino MJ, Brousseau KM, Arciniegas DB, et al. **Initial evaluations for multiple sclerosis in a university multiple sclerosis center: outcomes and role of magnetic resonance imaging in referral.** *Arch Neurol* 2005;62:585–90 CrossRef Medline
- Traboulsee A, Simon JH, Stone L, et al. **Revised Recommendations of the Consortium of MS Centers Task Force for a Standardized MRI Protocol and Clinical Guidelines for the Diagnosis and Follow-Up of Multiple Sclerosis.** *AJNR Am J Neuroradiol* 2016;37:394–401 CrossRef Medline
- Rovira À, Wattjes MP, Tintoré M, et al; MAGNIMS study group. **Evidence-based guidelines: MAGNIMS consensus guidelines on the use of MRI in multiple sclerosis-clinical implementation in the diagnostic process.** *Nat Rev Neurol* 2015;11:471–82 CrossRef Medline

Improved Precision of Automatic Brain Volume Measurements in Patients with Clinically Isolated Syndrome and Multiple Sclerosis Using Edema Correction

J.B.M. Warntjes, A. Tisell, I. Håkansson, P. Lundberg, and J. Ernerudh

ABSTRACT

BACKGROUND AND PURPOSE: The presence of edema will result in increased brain volume, which may obscure progressing brain atrophy. Similarly, treatment-induced edema reduction may appear as accelerated brain tissue loss (pseudoatrophy). The purpose of this study was to correlate brain tissue properties to brain volume, to investigate the possibilities for edema correction and the resulting improvement of the precision of automated brain volume measurements.

MATERIALS AND METHODS: A group of 38 patients with clinically isolated syndrome or newly diagnosed MS were imaged at inclusion and after 1, 2, and 4 years using an MR quantification sequence. Brain volume, relaxation rates (R_1 and R_2), and proton density were measured by automated software.

RESULTS: The reduction of normalized brain volume with time after inclusion was 0.273%/year. The mean SDs were 0.508%, 0.526%, 0.454%, and 0.687% at baseline and 1, 2, and 4 years. Linear regression of the relative change of normalized brain volume and the relative change of R_1 , R_2 , and proton density showed slopes of -0.198 ($P < .001$), 0.156 ($P = .04$), and 0.488 ($P < .001$), respectively. After we applied the measured proton density as a correction factor, the mean SDs decreased to 24.2%, 4.8%, 33.3%, and 17.4%, respectively. The observed atrophy rate reduced from 0.273%/year to 0.238%/year.

CONCLUSIONS: Correlations between volume and R_1 , R_2 , and proton density were observed in the brain, suggesting that a change of brain tissue properties can affect brain volume. Correction using these parameters decreased the variation of brain volume measurements and may have reduced the effect of pseudoatrophy.

ABBREVIATIONS: BPF = brain parenchymal fraction; BPV = brain parenchymal volume; ICV = intracranial volume; NEDA = no evidence of disease activity; PD = proton density; R_1 and R_2 = relaxation rates; S_{R1} , S_{R2} , and S_{PD} = correlation slopes

Brain atrophy and accelerated brain volume loss are present early in the disease course of MS and correlate with the presence and development of physical disability and cognitive impairment.¹ When assessing disease activity in MS, the term “no evidence of disease activity” (NEDA) is increasingly used, where NEDA-3 is defined by the combination of the following: 1) no relapses, 2) no brain MR imaging activity (no new or enlarging T2 lesions or gadolinium-enhancing lesions), and 3) no sustained

disability worsening (Expanded Disability Status Scale progression). However, given the clinical importance of brain atrophy, it is desirable to expand the NEDA concept to NEDA-4, in which “no increased brain volume loss/brain atrophy rate” is added.² Disease-modifying immunomodulatory treatment options in MS vary in efficacy and adverse effect profile. Personalized treatment for a patient with MS requires clinically feasible and reliable assessment of disease activity status at treatment initiation and treatment follow-up. Although there is not yet enough evidence to support the use of brain volume measures to monitor treatment response or for making treatment decisions in individual patients, brain volume loss is now often incorporated in large clinical trials of potential new MS drugs.³ Monitoring brain volume and brain volume changes with time in clinical practice, however, is often hampered by the additional time and effort burden of brain segmentation methods and their inherent precision. Moreover, disease activity induces changes in the intra- or extracellular water content, which, in turn, can lead to changes in total brain volume. Therefore, resolution of inflammatory edema after

Received July 5, 2017; accepted after revision October 8.

From the Center for Medical Image Science and Visualization (J.B.M.W., A.T., P.L.); Division of Cardiovascular Medicine (J.B.M.W.) and Radiation Physics (A.T., P.L.), Department of Medical and Health Sciences; Department of Neurology (I.H.), Department of Clinical and Experimental Medicine; Department of Clinical Immunology and Transfusion Medicine (J.E.); and Department of Clinical and Experimental Medicine (J.E.), Linköping University, Sweden; and SyntheticMR AB (J.B.M.W.), Linköping, Sweden.

Please address correspondence to J.B.M. Warntjes, MD, Center for Medical Image Science and Visualization (CMIV), Linköping University, 58185 Linköping, Sweden; e-mail: marcel.warntjes@cmiv.liu.se

<http://dx.doi.org/10.3174/ajnr.A5476>

Table 1: Patient diagnoses, relapse status, and treatment status at baseline and at follow-up MRI

Clinical and Laboratory Data	Baseline	1 Year	2 Years	4 Years
Diagnosis (CIS/RRMS/PPMS)	16/19/3	10/25/3	7/28/3	5/30/3
Relapse within last 2 mo before MRI (yes/no)	13/25	3/35	1/37	2/36
Treatment ^a (No. of subjects)				
No DMT	38	17	18	18
Interferon- β 1b	0	16	12	5
Interferon- β 1a	0	1	1	1
Dimethyl fumarate	0	0	0	2
Fingolimod	0	1	1	3
Natalizumab	0	3	6	9

Note:—CIS indicates clinically isolated syndrome; RRMS, relapsing-remitting MS; PPMS, primary-progressive MS; DMT, disease modifying therapy.

^aIn addition, 1 patient received temporary relapse-controlling corticosteroid treatment within 2 months prior to baseline.

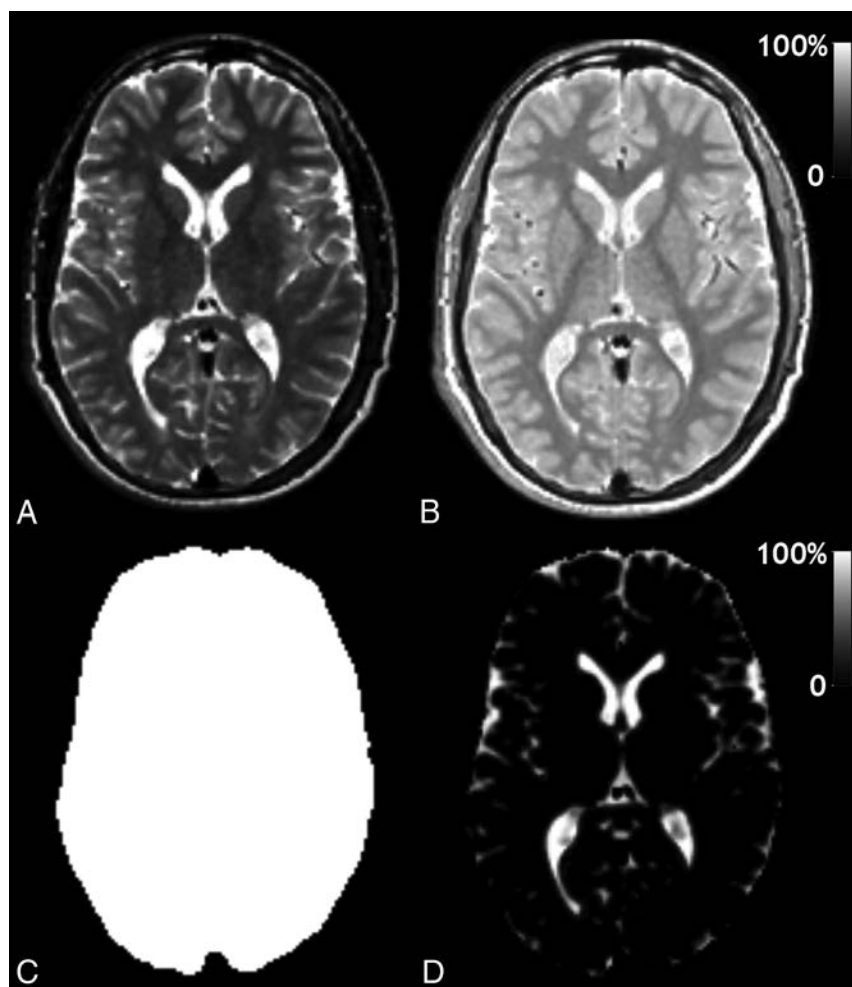


FIG 1. Typical output of the SyMRI software: A, Synthetic T2-weighted image of a section of the brain of one of the patients. This synthetic image was generated from the R_1 , R_2 , and PD maps in combination with a TE/TR = 100/4500 ms. B, PD map on a scale of 0%–100%, in which 100% corresponds to pure water at 37°C. C, Automatically generated intracranial mask (ICV). D, Automatically generated CSF partial volume map on a scale of 0%–100%. The brain parenchymal volume is calculated as the sum of all ICV minus the sum of all CSF. The brain parenchymal fraction is calculated as BPV/ICV.

a successful treatment may appear as atrophy, known as “pseudoatrophy,” as previously reported in patients with early-onset MS.^{4,5} Likewise, an increase in disease activity may increase the total edema, visible only as diffuse hyperenhancement on T2-

weighted or FLAIR images. This may lead to swelling of the brain, obscuring the progressing atrophy.

Recent progress in quantitative MR imaging permits measurement of physical properties of the brain, such as relaxation rates (R_1 and R_2) and proton density (PD) in a reasonable scan time.⁶ Axonal damage, gliosis, inflammation, and edema are related to changes in these values.^{7–12} Therefore, it can be expected that the mean values of R_1 , R_2 , and PD have a relationship with processes that may lead to global volume changes in the brain. SyntheticMR (SyMRI; SyntheticMR, Linköping, Sweden) is a brain segmentation tool with high precision,^{13–15} which is based on quantitative MR imaging. It therefore combines the ability to fully automatically measure brain volumes and simultaneously obtain values for mean R_1 , R_2 , and PD of brain tissue.

The aim of this study was to investigate the relation between brain volumes of patients with clinically isolated syndrome and those with MS using a fully automatic brain volume segmentation method and the mean R_1 , R_2 , and PD values in these brains. Provided that these 2 measures correlated, the second aim was to use R_1 , R_2 , and PD as a correction factor for brain volume and investigate whether the precision of the brain segmentation method would improve.

MATERIALS AND METHODS

Subject Group

The study included 44 patients (29 women) who were consecutively enrolled in a prospective longitudinal cohort study of patients with clinically isolated syndrome and those with newly diagnosed MS. All patients fulfilled the revised McDonald criteria for clinically isolated syndrome or MS at inclusion.¹⁶ Brain MR imaging was performed at baseline and at 1, 2, and 4 years. Retrospectively, 1 subject was excluded due to severe hydrocephalus; for 5 subjects, the study was prematurely terminated due to moving to another place or pregnancy.

The remaining 38 all had 4 time points (baseline, 1, 2, and 4 years), a total of 152 examinations. Examinations were performed during the daytime, between 8 AM and 4 PM. Of these, 104 (68%) were performed in the morning, and 48 (32%), in the afternoon. The included subjects had a mean age of

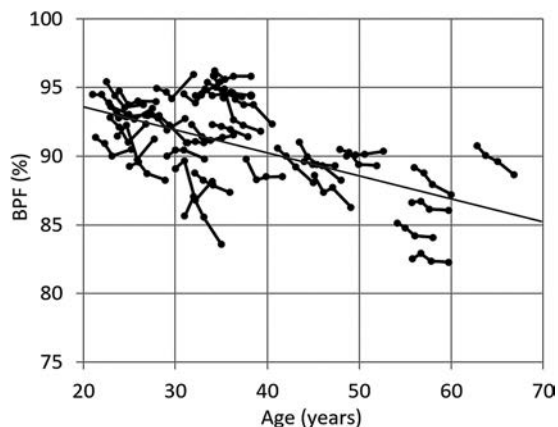


FIG 2. Brain parenchymal fraction of all subjects at all times. The 4 time points of each individual are connected with a line. The gray line indicates the linear regression slope.

35 ± 11 years (range, 21–67 years) and a median Expanded Disability Status Scale of 2.0 (interquartile range, 1.0–2.0) at baseline. Further patient characteristics are presented in Table 1.

Ethics Statement

The study was approved by the regional ethics committee, and written informed consent was obtained from all participants.

Acquisition

The MR imaging quantification method was a multiecho, multi-delay saturation recovery spin-echo sequence, which has been described previously.⁶ The multisection sequence consisted of section-selective saturation pulses, interleaved with a Carr-Purcell-Meiboom-Gill acquisition of 5 echoes at multiples of 14-ms TE. The saturation pulse acts on a section n , while the subsequent acquisition acts on a section m . By a variable shift between sections n and m , multiple effective delay times were created between the saturation and acquisition of each section. The sequence was repeated 4 times, resulting in a matrix of 20 images per section, at 5 different TEs and at 4 different saturation delay times. All these images had a different effect of R_1 and R_2 relaxation. The TR was 4280 ms with 43 sections of 3-mm thickness. The FOV was 230 mm with an in-plane resolution of 1.4 mm. The scan time was 6 minutes and 20 seconds on an Achieva 1.5T scanner (Philips Healthcare, Best, the Netherlands).

Postprocessing

The calculation of the intracranial volume (ICV), the brain parenchymal volume (BPV), and brain parenchymal fraction ($BPF = BPV / ICV$) is an automatic function of SyMRI 9.0. The same software also shows the R_1 , R_2 , and PD maps of the entire acquisition volume. Typical images and maps from this software in our patients are shown in Fig 1. An adjustment was made in the software to extract the average R_1 , R_2 , and PD values for the entire brain and gray and white matter. This was done by taking the ICV and removing all CSF (clipped at 50% partial volume) and subsequently eroding 1 pixel on all sides of the volume to remove the partial volume effects of CSF. The available GM and WM segmentation maps were used to retrieve the average R_1 , R_2 , and PD of GM and WM inside the eroded volume.

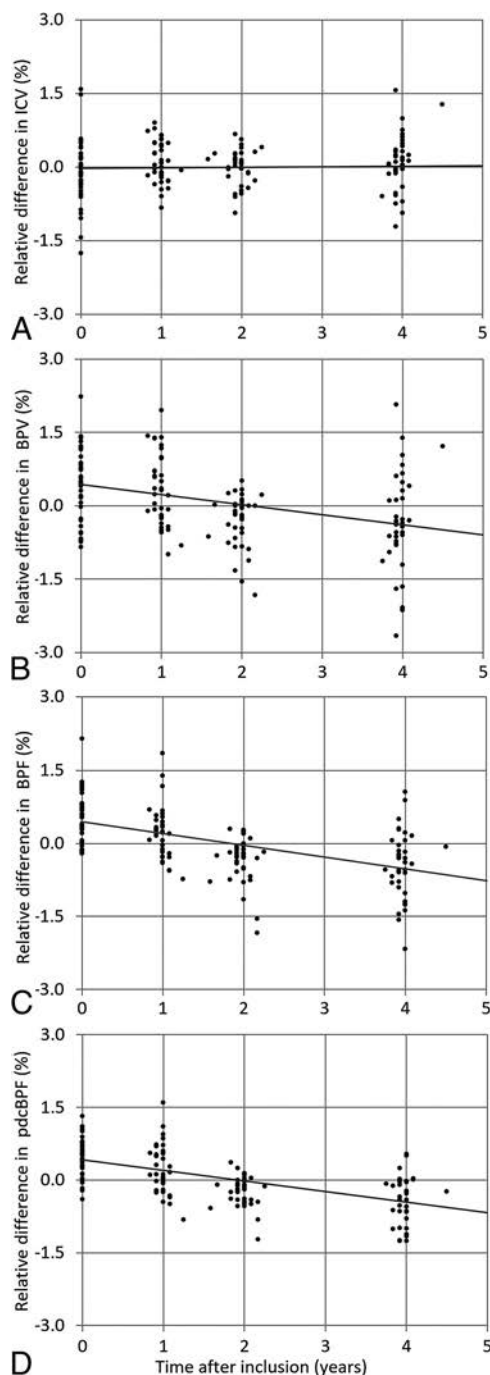


FIG 3. Relative difference of intracranial volume (A), brain parenchymal volume (B), and brain parenchymal fraction (C) of all subjects as a function of time after inclusion of the study. D, The relative difference in BPF of all subjects is shown again as a function of time after inclusion is shown, but corrected for PD. This figure is comparable with C, albeit with less variation in the data. The gray lines indicate the linear regression slopes.

Finding the Correlation of BPF with R_1 , R_2 , and PD

The average value and SD of ICV, BPV, BPF, R_1 , R_2 , and PD were calculated for each time point. In the relative change of BPF_i for all measurements, i was found by dividing each of these measurements by the average $\langle BPF \rangle_s$ of each subject s . This removed individual differences in BPF size. Subtraction by 1 centered the relative change of BPF around zero. The resulting data points

Table 2: Observed correlation slopes S_{R1} , S_{R2} , and S_{PD} of the relative change in BPF as a function of relative change in R_1 , R_2 , and PD of the entire brain and gray and white matter

	Brain	Gray Matter	White Matter
S_{R1} value (%/%)	-0.198	-0.133	-0.364
S_{R1} (95% CI) (%/%)	(-0.242 to -0.152)	(-0.222 to -0.044)	(-0.4376 to -0.290)
S_{R1} P value	<.001	.02	<.001
S_{R2} value (%/%)	0.156	0.303	0.090
S_{R2} (95% CI) (%/%)	(0.039-0.274)	(0.228-0.378)	(-0.016-0.196)
S_{R2} P value	.04	<.001	.2
S_{PD} value (%/%)	0.488	.396	.655
S_{PD} (95% CI) (%/%)	(0.382-0.594)	(0.146-0.645)	(0.535-0.776)
S_{PD} P value	<.001	.003	<.001

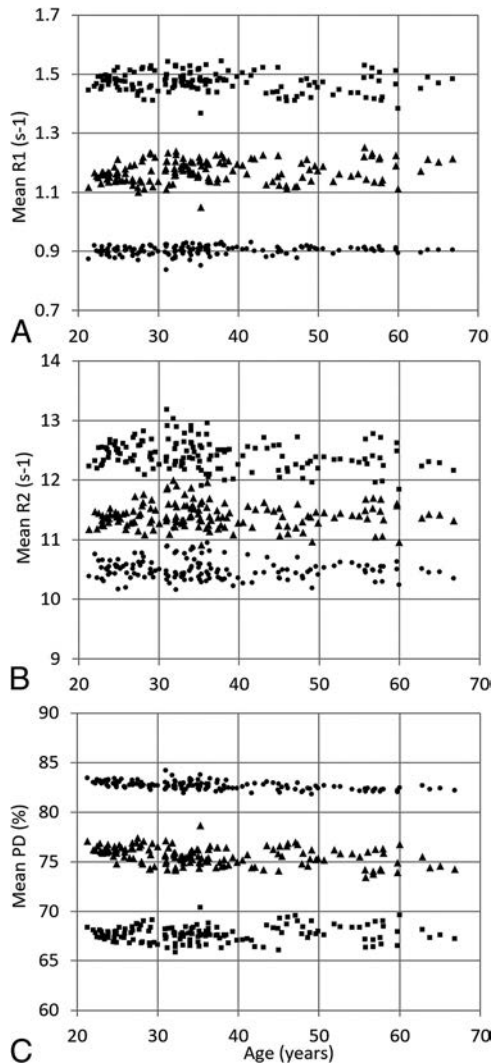


FIG 4. Observed mean R_1 (A), mean R_2 (B), and mean proton density (C) of the entire brain (triangles), gray matter (dots), and white matter (squares) as a function of age for all subjects.

were assumed to change linearly as a function of time after inclusion of t , expressed as an intercept and slope. A noise term ε accounts for the observed variation of the data.

$$1) \quad \frac{BPF_i}{\langle BPF \rangle_s} - 1 = Intercept + Slope \times t + \varepsilon.$$

We believe that the noise term ε does not only contain random noise but may have a correlation with the observed relative change

of R_1 , R_2 , and/or PD, independent of the time after inclusion. The relative change of R_1 , R_2 , and PD can be calculated in the same way as the relative change of BPF. Then, the correlation slopes S_{R1} , S_{R2} , and S_{PD} were found according to

$$2) \quad \varepsilon = \left(\frac{BPF_i}{\langle BPF \rangle_s} - 1 \right) - Intercept - Slope \times t = S_{R1} \left(\frac{R1_i}{\langle R1 \rangle_s} - 1 \right),$$

and equivalently for R_2 , and PD.

Correction of BPF

Once the slopes S_{R1} , S_{R2} , and S_{PD} are found, they can be used as correction terms for BPF to reduce ε . In other studies, it is unlikely that there is an average R_1 , R_2 , or PD per subject available; hence, the terms $\langle R_1 \rangle_s$, $\langle R_2 \rangle_s$, and $\langle PD \rangle_s$ must be replaced by an expected R_{1exp} , R_{2exp} , and PD_{exp} value, which can be taken from the average values of all our subjects. The corrected BPF is then calculated as the observed BPF multiplied by a factor $(1-\varepsilon)$.

RESULTS

Finding the Correlation of BPF with R_1 , R_2 , and PD

The average ICV of all subjects at all times was 1407 ± 151 mL; the average BPV was 1278 ± 129 mL, resulting in an average BPF of $90.9\% \pm 3.2\%$. The BPF of all subjects at all times is plotted in Fig 2. Linear regression on all data as a function of age showed a slope of BPF of $-0.167\%/year$ (95% confidence interval, -0.131 to -0.204 ; $P < .001$).

In Fig 3, the normalized ICV, BPV, and BPF are shown as a function of time after inclusion. For the separate time points, at 1, 2, and 4 years after the time of inclusion, the decrease of BPV and BPF was 2.2 mL ($P = .4$) and 0.37% ($P < .001$) after 1 year, 12.2 mL ($P < .001$) and 0.87% ($P < .001$) after 2 years, and 12.3 mL ($P = .007$) and 0.97% ($P < .001$) after 4 years. Linear regression as a function of all 4 years showed that the ICV had a nonsignificant slope of $0.02\%/year$ (95% confidence interval, -0.03 - 0.08 ; $P = .6$). The BPV showed a significant decrease with time after inclusion, with a slope of $-0.236\%/year$ (95% CI, -0.372 to -0.173 ; $P < .001$). Also, the BPF showed a significant decrease with time after inclusion, with a slope of $-0.273\%/year$ (95% CI, -0.211 to -0.335 ; $P < .001$). The intercept was 0.472%.

The relative changes in BPF were corrected for time using the observed slope of $-0.273\%/year$ and an intercept of 0.472% (Equation 2). Then, the resulting values for BPF were compared with the relative changes in the R_1 , R_2 , and PD to obtain the slopes S_{R1} , S_{R2} , and S_{PD} . For S_{R1} , a significant slope of -0.198 was observed ($P < .001$). For S_{R2} , this was 0.156 ($P = .04$); and for S_{PD} , a significant slope of 0.488 was observed ($P < .001$). Similar-but-weaker correlations were found when only GM or WM were taken into account. All data are summarized in Table 2. No correlation was found between relative BPF and time of day of the examination ($P = .7$).

Table 3: Observed mean values and slopes of R_1 , R_2 , and PD of the entire brain and gray and white matter as a function of subject age

	Brain	Gray Matter	White Matter
R_1 intercept (s^{-1})	1.151	0.897	1.495
R_1 slope (s^{-1}/y)	0.00054	0.00015	-0.00063
R_1 slope (95% CI) (s^{-1}/y)	(0.0002-0.0010)	(-0.0001-0.0002)	(-0.0011-0.0002)
R_1 slope P value	.04	.4	.2
R_2 intercept (s^{-1})	11.44	10.57	12.62
R_2 slope (s^{-1}/y)	-0.0001	-0.0018	-0.0056
R_2 slope (95% CI) (s^{-1}/y)	(-0.004-0.002)	(-0.004-0.001)	(-0.009-0.000)
R_2 slope P value	.5	.3	.05
PD intercept (%)	75.65	82.44	67.44
PD slope (%/y)	-0.026	-0.019	0.009
PD slope (95% CI) (%/y)	(-0.039-0.013)	(-0.025 to -0.013)	(-0.003-0.020)
PD slope P value	<.001	<.001	.2

Note:—y indicates year.

Table 4: Observed SDs of the relative changes in BPF at baseline and at 1, 2, and 4 years after inclusion^a

	Baseline (%)	1 Year (%)	2 Years (%)	4 Years (%)
Uncorrected	0.508	0.526	0.454	0.687
Corr. for brain R_1	0.362 (28.8%)	0.506 (3.7%)	0.327 (28.1%)	0.599 (12.8%)
Corr. for brain PD	0.385 (24.2%)	0.500 (4.9%)	0.303 (33.3%)	0.567 (17.4%)
Corr. for GM R_2	0.506 (0.4%)	0.465 (11.5%)	0.297 (34.7%)	0.561 (16.2%)
Corr. for GM PD	0.481 (5.3%)	0.539 (-2.4%)	0.398 (12.5%)	0.673 (1.9%)
Corr. for WM R_1	0.343 (32.6%)	0.463 (12.0%)	0.349 (23.2%)	0.568 (17.3%)
Corr. for WM PD	0.399 (21.5%)	0.474 (9.8%)	0.326 (28.3%)	0.492 (28.3%)

Note:—Corr. indicates corrected.

^a When BPF is corrected for average R_1 , R_2 , or PD values for brain, GM, or WM, the SDs of the observations decrease. The percentage reduction is given in parentheses. Corrections were only included when a high significance was found in Table 2.

Correction of BPF

The observed mean R_1 , R_2 , and PD of the entire brain as a function of subject age are shown in Fig 4 (triangles). Only minor changes as a function of subject age were observed; linear regression showed a slope in R_1 of 0.00054 seconds⁻¹/year. For R_2 , this was -0.0001 seconds⁻¹/year; and for PD, it was -0.026%/year. The R_1 intercept for all subjects was $1.151 \pm$ seconds⁻¹, the R_2 intercept was 11.44 seconds⁻¹, and the PD intercept was 75.65%. All data, including for whole brain and GM and WM only, are summarized in Table 3. Using these values, one can establish the expected R_1 value for the whole brain of each subject, $R_{1exp} = 1.151 + 0.00054 \times \text{age}$; the expected R_2 value for the brain of for each subject, $R_{2exp} = 11.44 - 0.0001 \times \text{age}$; and the expected PD value for the brain of each subject, $PD_{exp} = 75.65 - 0.026 \times \text{age}$.

On the basis of these expected values for R_1 , R_2 , and PD, a correction of the BPF values can be made using Equation 2. The PD-corrected BPF values, using S_{PD} , are shown in Fig 3D. In comparison with the uncorrected BPF values, as shown in Fig 3C, the variation of the data points was reduced. The SDs at baseline and at 1, 2, and 4 years after inclusion, when corrected for R_1 , R_2 , or PD, are given in Table 4. The highest reductions were achieved with R_1 and PD, for which SDs decreased, on average, more than 20%. The baseline values especially changed substantially. If one used the correction, the observed atrophy rate decreases slightly—for example, PD-corrected BPF shows a slope of -0.238%/year, and R_1 -corrected BPF shows a slope of -0.256%/year, decreases of 12.8% and 6.2%, respectively, in comparison with the original slope of -0.273%/year.

DISCUSSION

In this work, brain volume measurements were combined with measures reflecting the physical properties of the brain. Generally, the variation in brain volume measurements is high because it includes the normal variation in human head size. Thus, BPF is used for clinical follow-up because it normalizes brain volume with the intracranial volume, hence removing head size differences.¹⁷ An additional factor for brain volume variations is the placement of the MR imaging acquisition volume. The acquisition coverage in our case included 43 sections, with a total of 129 mm, which was not sufficient for all subjects to cover the entire cranium. Differences of the placement of the acquisition volume may therefore have resulted in differences of the included ICV and BPV. This is a second reason that BPF is more reliable to use, because it is a ratio of the included volumes and hence less sensitive to the exact positioning of the acquisition volume. The stability of BPF over BPV is confirmed by the higher significance of the observed atrophy rate in our data.

Yet an additional factor, which is generally ignored, is that brain tissue composition may be different at each examination. Brain volume may not be as invariant as one may expect and may change with, for example, hydration, dehydration, time of day, blood pressure, physical activity, eating habits, or drug and alcohol consumption. Previous studies have shown that brain volume can exhibit a diurnal variation on the order of 0.4%–0.7%,^{18,19} though this could not be verified in all studies.²⁰ In our data, no evidence of a relation with the time of day was found either ($P = .7$). Besides the general factors that can influence brain volume, patients with MS may exhibit additional effects. Starting treatment to suppress the inflammatory processes in the CNS is expected to reduce brain tissue edema, which hence may lead to an apparently accelerated brain atrophy directly after onset. The existence of the so-called pseudoatrophy has been described previously^{4,5} and is confirmed in, for example, natalizumab treatment, in which effective inflammation reduction leads to a higher initial brain volume loss, compared with the subsequent brain volume loss.^{21,22}

For our study, we hypothesized that the average R_1 and R_2 and proton density of the brain were associated with water content of brain tissue, including the component due to edema. Our MR quantification approach has the advantage of simultaneously measuring R_1 , R_2 , and PD and automatically calculating brain volume and BPF using the same single sequence. We found that the average R_1 , R_2 , and PD values are relatively stable over the investigated age range. The total change of the observed values was <2 SDs during a complete lifetime (Fig 4). The mean values of WM and GM and the observed slow decrease of PD were very similar to previously reported values.²³

A significant correlation was found between the relative change in observed BPF and the relative change in average R_1 and PD of the brain. No correlation was found for R_2 , in contrast to a previous study in which only R_2 (T2) was used in a study with substantial dehydration and rehydration.²⁴ The presence of these relations provides evidence that BPF is indeed affected by changes in brain tissue composition. The correlation is stronger in WM than in GM; this finding suggests that the average value for brain tissue is mainly affected by changes in WM for patients with MS. It means that when a subject exhibits a lower BPF, it is at least partly related to a higher R_1 and a lower PD. In our study, no relation with the time of day was found, suggesting that the effect of disease activity is a stronger factor than diurnal fluctuations.

The observation that the variation in measured BPF can be reduced by correction of the average PD of the entire brain or the average PD of WM suggests that the level of edema in patients with MS varies, leading both to changes in total water content of brain parenchyma and changes in brain volume. Especially, the reduction of variation in BPF at baseline indicates that correction for edema could play an important role in the interpretation of the atrophy rate after the time of inclusion. If the effect of pseudoatrophy can be reduced, there would be no need to exclude an initial period of time to avoid the observation of an exaggerated atrophy rate, as was proposed as an alternative strategy.²⁵ In our study, 13 patients had a clinical relapse within 2 months before MR imaging at baseline, compared with only 3, 1, and 2 at follow-up MR imaging. The higher proportion of patients in clinical relapse at baseline MR imaging was, in part, because the relapse was often the cause of neurologic evaluation and inclusion in the cohort study, in part because of a considerable number of patients receiving disease-modifying MS drugs during follow-up.

Limitations in our study were the low number of included patients, the specific selection of patients, and the inevitable differences in individual patient management, leading to additional factors that were treated as random variables in the analysis. The choice of a group of early-onset patients with MS precludes any general conclusions on patients with MS or other neurodegenerative diseases. No distinction was made using the Expanded Disability Status Scale because all patients had relatively low scores (interquartile Expanded Disability Status Scale range, 1.0–2.0). Also, no control group was included to assess the normal decrease of BPF or any correlation with R_1 , R_2 , or PD with the healthy brain, precluding a reference value for normal variation. The time between measurements was at least a year, which is too long to monitor the dynamic behavior of the disease activity. Because brain volume loss is a critical parameter in MS research and clinical management, however, this work must be seen as an indicator that brain volume measurements may be confounded by other factors and that the precision of such measurements may benefit from monitoring the brain tissue characteristics as well. Our study indicates that edema correction may improve the precision of monitoring brain volume loss for patients with MS. Possibly, other neurologic, psychiatric, and geriatric conditions could also benefit from such a correction, and we intend to include larger groups to investigate further possibilities. A

faster rate of probing would potentially show disease dynamics, which would be interesting to investigate, especially in the first 12 months after onset, when the effect of pseudoatrophy is expected to predominate.

CONCLUSIONS

Edema correction for brain volume using the mean R_1 and R_2 or proton density of the brain reduced the variation in brain volume measurement values in our cohort with up to 33% and may have reduced the effect of pseudoatrophy.

Disclosures: J.B. Marcel Warntjes—UNRELATED: Employment: SyntheticMR AB, Comments: part-time employee; Stock/Stock Options: SyntheticMR AB. Peter Lundberg—UNRELATED: Employment: University Hospital; Grants/Grants Pending: Conventional National Science Council funding*. *Money paid to the institution.

REFERENCES

1. Vågberg M, Lindqvist T, Ambarki K, et al. **Automated determination of brain parenchymal fraction in multiple sclerosis.** *AJNR Am J Neuroradiol* 2013;34:498–504 CrossRef Medline
2. Giovannoni G, Tomic D, Bright JR, et al. **“No evident disease activity”: the use of combined assessments in the management of patients with multiple sclerosis.** *Mult Scler* 2017;23:1179–87 CrossRef Medline
3. ClinicalTrials.gov Identifiers: NCT01412333, NCT01247324, NCT02792218, NCT01226745, NCT02425644. www.clinicaltrials.gov. Accessed June 1, 2017
4. De Stefano N, Airas L, Grigoriadis N, et al. **Clinical relevance of brain volume measures in multiple sclerosis.** *CNS Drugs* 2014;28:147–56 CrossRef Medline
5. Zivadinov R, Reder AT, Filippi M, et al. **Mechanisms of action of disease-modifying agents and brain volume changes in multiple sclerosis.** *Neurology* 2008;71:136–44 CrossRef Medline
6. Warntjes JB, Leinhard OD, West J, et al. **Rapid magnetic resonance quantification on the brain: optimization for clinical usage.** *Magn Reson Med* 2008;60:320–29 CrossRef Medline
7. Warntjes M, Engström M, Tisell A, et al. **Modeling the presence of myelin and edema in the brain based on multi-parametric quantitative MRI.** *Front Neurol* 2016;7:16 CrossRef Medline
8. Kumar R, Delshad S, Woo MA, et al. **Age-related regional brain T2-relaxation changes in healthy adults.** *J Magn Reson Imaging* 2012; 35:300–08 CrossRef Medline
9. Neema M, Stankiewicz J, Arora A, et al. **T1- and T2-based MRI measures of diffuse gray matter and white matter damage in patients with multiple sclerosis.** *J Neuroimaging* 2007;17:16S–21S CrossRef Medline
10. Larsson HB, Frederiksen J, Petersen J, et al. **Assessment of demyelination, edema, and gliosis by in-vivo determination of T1 and T2 in the brain of patients with acute attack of multiple sclerosis.** *J Magn Reson Med* 1989;11:337–38 CrossRef Medline
11. Vymazal J, Righini A, Brooks RA, et al. **T1 and T2 in the brain of healthy subjects, patients with Parkinson disease, and patients with multiple system atrophy: relation to iron content.** *Radiology* 1999; 211:489–95 CrossRef Medline
12. Warntjes JB, Engström M, Tisell A, et al. **Brain characterization using normalized quantitative magnetic resonance imaging.** *PLoS One* 2013;8:e70864 CrossRef Medline
13. Hagiwara A, Warntjes M, Hori M, et al. **SyMRI of the brain: rapid quantification of relaxation rates and proton density, with Synthetic MRI, automatic brain segmentation, and myelin measurement.** *Invest Radiol* 2017;52:647–57 CrossRef Medline
14. Vågberg M, Ambarki K, Lindqvist T, et al. **Brain parenchymal fraction in an age-stratified healthy population: determined by MRI using manual segmentation and three automated segmentation methods.** *J Neuroradiol* 2016;43:384–91 CrossRef Medline
15. Granberg T, Uppman M, Hashim F, et al. **Clinical feasibility of Syn-**

- thetic MRI in multiple sclerosis: a diagnostic and volumetric validation study. *AJNR Am J Neuroradiol* 2016;37:1023–29 CrossRef Medline
16. Polman CH, Reingold SC, Banwell B, et al. **Diagnostic criteria for multiple sclerosis: 2010 revisions to the McDonald criteria.** *Ann Neurol* 2011;69:292–302 CrossRef Medline
 17. Rudick RA, Fisher E, Lee JC, et al. **Use of the brain parenchymal fraction to measure whole brain atrophy in relapsing-remitting MS: Multiple Sclerosis Collaborative Research Group.** *Neurology* 1999;53:1698–704 CrossRef Medline
 18. Nakamura K, Brown RA, Narayanan S, et al. **Diurnal fluctuations in brain volume: statistical analyses of MRI from large populations.** *Neuroimage* 2015;118:126–32 CrossRef Medline
 19. Duning T, Kloska S, Steinträger, et al. **Dehydration confounds the assessment of brain atrophy.** *Neurology* 2005;64:548–50 CrossRef Medline
 20. Meyers SM, Tam R, Lee JS, et al. **Does hydration status affect MRI measures of brain volume or water content?** *J Magn Reson Imaging* 2016;44:296–304 CrossRef Medline
 21. Magraner M, Coret F, Casanova B. **The relationship between inflammatory activity and brain atrophy in natalizumab treated patients.** *Eur J Radiol* 2012;81:3485–90 CrossRef Medline
 22. Møllergård J, Tisell A, Blystad I, et al. **Cerebrospinal fluid levels of neurofilament and tau correlate with brain atrophy in natalizumab-treated multiple sclerosis.** *Eur J Neurol* 2017;24:112–21 CrossRef Medline
 23. Neeb H, Zilles K, Shah NJ. **Fully-automated detection of cerebral water content changes: study of age- and gender-related H₂O patterns with quantitative MRI.** *Neuroimage* 2006;29:910–22 CrossRef Medline
 24. Nakamura K, Brown RA, Araujo D, et al. **Correlation between brain volume change and T2 relaxation time induced by dehydration and rehydration: implications for monitoring atrophy in clinical studies.** *Neuroimage Clin* 2014;6:166–70 CrossRef Medline
 25. De Stefano N, Giorgio A, Battaglini M, et al. **Reduced brain atrophy rates are associated with lower risk of disability progression in patients with relapsing multiple sclerosis treated with cladribine tablets.** *Mult Scler* 2017 Jan 1. [Epub ahead of print] CrossRef Medline

Combining Quantitative Susceptibility Mapping with Automatic Zero Reference (QSM0) and Myelin Water Fraction Imaging to Quantify Iron-Related Myelin Damage in Chronic Active MS Lesions

Y. Yao, T.D. Nguyen, S. Pandya, Y. Zhang, S. Hurtado Rúa, I. Kovanlikaya, A. Kuceyeski, Z. Liu, Y. Wang, and S.A. Gauthier



ABSTRACT

BACKGROUND AND PURPOSE: A hyperintense rim on susceptibility in chronic MS lesions is consistent with iron deposition, and the purpose of this study was to quantify iron-related myelin damage within these lesions as compared with those without rim.

MATERIALS AND METHODS: Forty-six patients had 2 longitudinal quantitative susceptibility mapping with automatic zero reference scans with a mean interval of 28.9 ± 11.4 months. Myelin water fraction mapping by using fast acquisition with spiral trajectory and T2 prep was obtained at the second time point to measure myelin damage. Mixed-effects models were used to assess lesion quantitative susceptibility mapping and myelin water fraction values.

RESULTS: Quantitative susceptibility mapping scans were on average 6.8 parts per billion higher in 116 rim-positive lesions compared with 441 rim-negative lesions ($P < .001$). All rim-positive lesions retained a hyperintense rim over time, with increasing quantitative susceptibility mapping values of both the rim and core regions ($P < .001$). Quantitative susceptibility mapping scans and myelin water fraction in rim-positive lesions decreased from rim to core, which is consistent with rim iron deposition. Whole lesion myelin water fractions for rim-positive and rim-negative lesions were 0.055 ± 0.07 and 0.066 ± 0.04 , respectively. In the mixed-effects model, rim-positive lesions had on average 0.01 lower myelin water fraction compared with rim-negative lesions ($P < .001$). The volume of the rim at the initial quantitative susceptibility mapping scan was negatively associated with follow-up myelin water fraction ($P < .01$).

CONCLUSIONS: Quantitative susceptibility mapping rim-positive lesions maintained a hyperintense rim, increased in susceptibility, and had more myelin damage compared with rim-negative lesions. Our results are consistent with the identification of chronic active MS lesions and may provide a target for therapeutic interventions to reduce myelin damage.

ABBREVIATIONS: FAST-T2 = fast acquisition with spiral trajectory and T2-prep; GRE = gradient-echo; MWF = myelin water fraction; ppb = parts per billion; QSM = quantitative susceptibility mapping; QSM0 = QSM with automatic uniform CSF zero reference; rim- = rim-negative; rim+ = rim-positive

MS is an inflammatory demyelinating and neurodegenerative disease of the CNS. Differentiating MS lesions, especially chronic lesions, may provide a biomarker for disease progression and a therapeutic target to reduce ongoing tissue damage. A subset of chronic lesions, identified as chronic active or slowly expanding lesions, have been described as having a rim of iron-enriched proinflammatory activated microglia and macrophages.¹⁻⁴ Iron-enriched

proinflammatory microglia release cytotoxins to adjacent oligodendrocytes,⁵ limit remyelination, and contribute to further demyelination in chronic active lesions.³ Therefore, identifying MS lesions with iron accumulation may enable the prediction of tissue damage.

MR imaging with a gradient-echo (GRE) sequence is sensitive to iron^{1,6} and has been explored by many investigators to detect an iron rim in chronic active MS lesions.³ Iron may be detected as hypointensity on a T2⁻-weighted GRE magnitude image or its phase-enhanced version known as SWI.^{8,10} An R2^{*} ($= 1 \div T2^*$) map computed from a multiecho GRE magnitude image can be used to estimate iron content.¹¹ Unfortunately, precise mapping of iron location by these magnitude-based approaches is

Received June 16, 2017; accepted after revision October 13.

From the Department of Radiology (Y.Y., Y.Z.), Tongji Hospital, Tongji Medical College, Huazhong University of Science & Technology, Wuhan, China; Departments of Radiology (Y.Y., T.D.N., S.P., I.K., A.K., Z.L., Y.W.) and Neurology (S.A.G.), Weill Cornell Medicine, New York, New York; Department of Mathematics (S.H.R.), Cleveland State University, Cleveland, Ohio; and Department of Biomedical Engineering (Z.L., Y.W.), Cornell University, Ithaca, New York.

This work was supported by grant RG 4661-A-2 from the National Multiple Sclerosis Society, grant RO1 NS090464 from the National Institutes of Health, and grant ULI TR000456-06 from the Weill Cornell Clinical and Translational Science Center (CTSC).

Paper previously presented at: Annual Meeting and Exhibition of the International Society for Magnetic Resonance in Medicine, April 22–27, 2017; Honolulu, Hawaii.

Please address correspondence to Susan A. Gauthier, DO, MPH, Department of Neurology, Weill Cornell Medical College, 1305 York Ave, Suite Y217, New York, NY 10021; e-mail: sag2015@med.cornell.edu

Indicates open access to non-subscribers at www.ajnr.org

Indicates article with supplemental on-line photos.

<http://dx.doi.org/10.3174/ajnr.A5482>

hindered by blooming artifacts, particularly at high iron concentrations.¹² Alternatively, the local magnetic field derived from a GRE phase image has been studied to quantify iron.^{13,14} However, because the local phase is affected by magnetic sources in the surrounding tissue, the phase pattern may not represent the true magnetic susceptibility pattern.¹⁵ Quantitative susceptibility mapping (QSM)¹⁶ is a phase-based magnetic field deconvolution technique that overcomes the blooming artifacts and provides more accurate quantification and localization of the magnetic sources.^{17,18} QSM has been established as a more sensitive and quantitative technique for measuring brain iron compared with $T2^*$, $R2$, and $R2^*$.^{19,20} Studies have emerged combining QSM with additional MR tissue parameters, such as $R2^*$, to characterize the pattern of iron deposition and demyelination among various MS lesions.²¹⁻²³ However, the interpretation of iron accumulation and the associated tissue damage can be complicated because QSM and $R2^*$ are both sensitive to iron and myelin. Moreover, accurate tracking of lesion susceptibility changes over time is hindered by the lack of a reliable susceptibility reference, given that CSF can often appear highly heterogeneous on QSM and normal-appearing white matter may undergo pathologic iron or myelin changes.¹⁴

This study aimed to address these challenges by combining 2 recently developed techniques: myelin water fraction (MWF) imaging by using fast acquisition with spiral trajectory and T2-prep (FAST-T2)^{24,25} and QSM with automatic uniform CSF zero reference (QSM0). MWF is a well-validated quantitative MR imaging biomarker for myelin,^{26,27} which can be mapped efficiently and reproducibly with FAST-T2.^{25,28} The QSM0 algorithm improves QSM zero reference selection by enforcing the susceptibility homogeneity of CSF within the brain ventricles and eliminating the need for manual drawing of CSF ROIs. QSM0 and MWF were used to identify MS lesions with a hyperintense rim pattern consistent with iron deposition and to assess the extent of myelin damage found within these lesions.

MATERIALS AND METHODS

Patient Population

This was a retrospective study of a cohort of 46 patients with MS (14 men, 32 women; mean age, 43.6 ± 10.7 years) selected from a prospective, ongoing clinical MS MR imaging data base from October 2011 to April 2015. The only inclusion criteria consisted of having simultaneous QSM and FAST-T2 sequences and a prior QSM. This cohort consisted of 1 patient with clinically isolated syndrome, 44 with relapsing-remitting MS, and 1 with secondary-progressive MS (mean disease duration, 8.7 ± 7.5 years; mean Expanded Disability Status Scale score, 1.78 ± 1.84). Forty-three patients were on various disease-modifying therapies, and 3 were untreated. Patients identified for analysis had completed 2 longitudinal brain MR imaging examinations with a mean time interval of 28.9 ± 11.4 months. Approximately 45% of the patients changed to a different MS treatment between the 2 MR imaging time points. This study was approved by the Weill Cornell Medicine institutional review board.

MR Imaging Data Acquisition

Brain MR imaging was performed on a 3T MR scanner (Signa HDxt; GE Healthcare, Milwaukee, Wisconsin) with an 8-channel head coil. The scanning protocol consisted of standard T1-weighted and T2-weighted sequences for anatomy and multiecho GRE imaging for QSM, as well as gadolinium-enhanced T1-weighted imaging to detect blood-brain barrier disruption. In addition, a FAST-T2 sequence was run at the second time point to map lesion MWF as a quantitative biomarker of myelin damage. The typical imaging parameters for pertinent imaging sequences were as follows: 1) T2-weighted multisection 2D fast spin-echo: TR, 5250 ms; TE, 86 ms; axial field of view, 24 cm; phase field of view factor, 0.75; acquisition matrix, 416×256 interpolated to 512×512 ; section thickness, 3 mm without gap; flip angle, 90° ; echo-train length, 23; number of signal averages, 2; and readout bandwidth, ± 50 kHz; 2) multiecho GRE: TR, 57 ms; first TE, 4.3 ms; echo spacing, 4.8 ms; echo-train length, 11; axial field of view, 24 cm; phase field of view factor, 0.8; acquisition matrix, 416×320 interpolated to 512×512 ; section thickness, 3 mm; flip angle, 20° ; bandwidth, 244 kHz; number of signal averages, 0.75; and readout bandwidth, ± 62.5 kHz; 3) 3D stack-of-spirals FAST-T2: spiral TR, 7.8 ms; spiral TE, 0.5 ms; nominal T2-prep times, 0 ms (T2-prep turned off), 7.6, 17.6, 27.6, 67.6, 147.6, and 307.6 ms; number of spiral leaves per stack, 32; axial field of view, 24 cm; acquisition matrix, 192×192 interpolated to 256×256 ; section thickness, 5 mm; number of sections, 32; flip angle, 10° ; and readout bandwidth, ± 125 kHz.

MR Imaging Postprocessing

Brain QSM0 maps were reconstructed from multiecho GRE data by using the morphology-enabled dipole inversion method^{29,30} and incorporating automated segmentation and regularization specific to CSF. Briefly, CSF within the lateral ventricles was identified by thresholding of the $R2^*$ map ($R2^* < 5$ seconds⁻¹) and imposing voxel connectivity. A regularization term penalizing susceptibility variation within the CSF mask was incorporated into the morphology-enabled dipole inversion algorithm to search for a solution with homogeneous CSF susceptibility. MWF maps were reconstructed from FAST-T2 data by using a multivoxel non-linear least-squares data-fitting algorithm with spatial smoothness constraints.²⁵ The lower and upper T2 bounds for each of the 3 water pools (in milliseconds) were set to [5 20], [20 200], and [200 2000], respectively (corresponding to myelin water, intra- and extracellular water, and long-T2 water such as CSF). MWF was calculated as the ratio of the myelin water signal and the total water signal within a voxel. Anatomic images and MWF maps were co-registered to GRE magnitude images (and the associated QSM maps) by using the FMRIB Linear Image Registration Tool (FLIRT; <https://fsl.fmrib.ox.ac.uk/fsl/fslwiki/FLIRT>) algorithm.³¹

Image Analysis

Two neuroradiologists (Y.Z. and Y.Y) with 6 and 4 years of experience, respectively, independently reviewed all images. First, MS lesions were identified and manually traced on T2-weighted images. Only gadolinium-negative lesions were considered in the primary analysis. Lesions were identified as rim-positive (rim+) or rim-negative (rim-) based on the consensus of both reviewers regarding

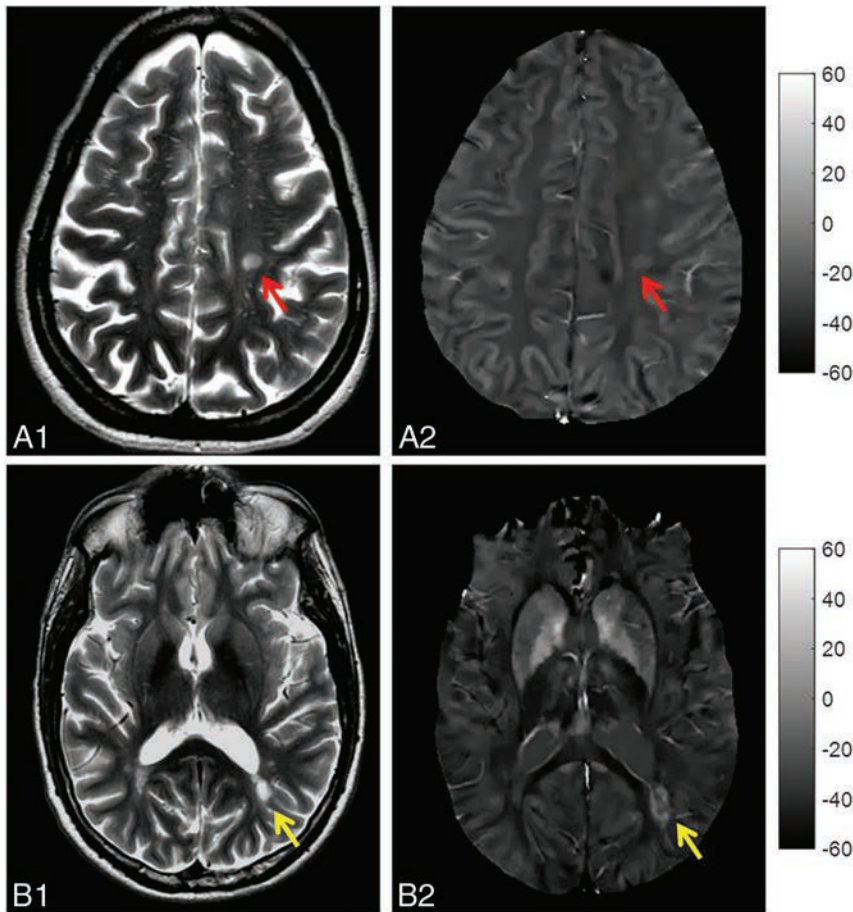


FIG 1. Top panel, Example of rim- lesion (red arrow): T2-weighted image (A1) and QSM (A2) in a patient with relapsing-remitting MS. Bottom panel, Example of rim+ lesion (yellow arrow): T2-weighted image (B1) and QSM (B2) in another patient with relapsing-remitting MS.

their visual appearance on QSM obtained at each time point (QSM1 and QSM2). In the case of a disagreement, a third neuroradiologist (I.K.) with 20 years of experience was called on to determine the lesion subtype. Next, ROI analysis was performed by using ITK-SNAP software (version 3.2; <http://www.itksnap.org/>) to obtain regional QSM measurements within the identified lesions. ROIs were traced on QSM and MWF for the whole lesion by using the T2-weighted lesion ROI as a starting point, with additional manual adjustments if needed. Central veins, identified as vessel-like structures with a hyperintense QSM appearance, were manually removed from QSM ROIs. In addition, for rim+ lesions, the lesion core (defined as the part of the lesion that extends from the center to the inner boundary of the hyperintense QSM rim) was traced on QSM and then transferred to MWF maps and manually edited if necessary. Lesion rim ROI was defined as the ROI difference between the whole lesion and the lesion core.

Statistical Analysis

Mixed-effects models were implemented to assess the variables of interest (lesion QSM and MWF values) among rim+ and rim- lesions. The modeling strategy accounts for multiple lesions per patient and repeated measurements (longitudinal analysis), and the following covariates were always considered: patient age, sex, T2-weighted lesion volume, and time interval between MRIs. The final model is reported after using a back-fitting procedure set at $\alpha = 0.10$ for in-

clusion. The mean QSM and MWF values within the lesion core and rim areas of rim+ lesions were compared by a paired *t* test.

RESULTS

Identification of QSM Rim+ and Rim- Lesions

All T2-weighted hyperintense lesions that were present at both time points were reviewed and considered chronic if they were not enhancing with gadolinium. Two lesions were excluded because of a subthreshold volume ($<14 \text{ mm}^3$), and 15 lesions were excluded because of image artifacts and poor QSM quality. The remaining lesions included 116 rim+ lesions from 35 of 46 patients with MS (34 relapsing-remitting and 1 secondary-progressive) and 441 rim- lesions from 42 of 46 patients with MS (1 clinically isolated syndrome, 40 relapsing-remitting, and 1 secondary-progressive). Most patients (31 of 46) were found to have both rim+ and rim- lesions. Of the patients having 1 lesion subtype, 4 of 15 had only rim+ lesions and the remaining patients (11 of 15) had only rim- lesions. Ten patients had gadolinium-enhancing lesions at any time point (12 lesions). The clinical characteristics (ie, disease duration or Expanded Disability Status Scale score) between the 2 groups of patients having only

1 lesion subtype were similar. Among all the patients, there was no significant correlation between the number of rim+ lesions and disease duration ($P = .43$).

Comparison of QSM Rim+ and Rim- Lesions

Figure 1 shows an example of T2-weighted images and corresponding QSM from 2 patients with relapsing-remitting MS, illustrating the appearance of rim+ and rim- lesions on QSM (4 additional patient examples are shown in On-line Fig 1). For whole lesion ROI, QSM1 of rim+ lesions and rim- lesions were 6.0 ± 14.4 parts per billion (ppb) and -7.0 ± 17.1 ppb, respectively (On-line Fig 2). There was no significant difference between the patient age among the rim+ and rim- lesion subgroups (44.1 ± 10.6 versus 43.5 ± 10.7 ; $P = .82$), and the Expanded Disability Status Scale score was similar among the lesion subtype groups ($P = .80$). After accounting for patient variability as a random effect (mixed-effects model), the QSM1 values in rim+ lesions were on average 6.8 ppb higher than those in rim- lesions ($P < .001$). There was no significant association found with T2-weighted lesion volume, sex, or patient age.

Longitudinal Assessment of QSM Classification

QSM classification at follow-up MR imaging predominantly remained the same. All rim+ lesions retained the hyperintense rim

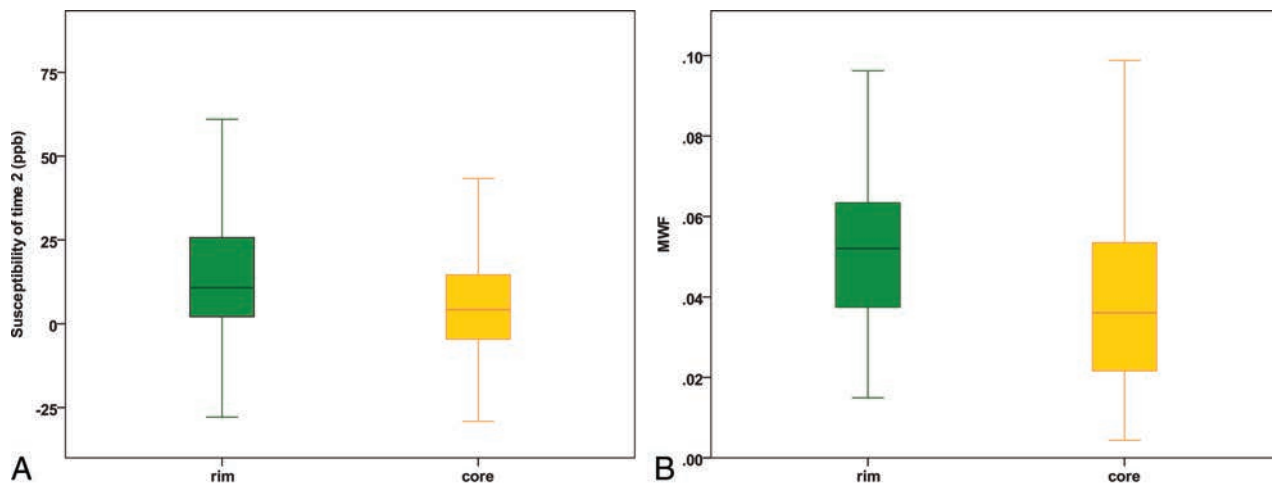


FIG 2. Comparison of susceptibility (A) and MWF (B) differences within the rim and core of QSM hyperintense rim+ lesions. Rim ROIs (green) have significantly higher susceptibility and higher MWF compared with core ROIs (yellow).

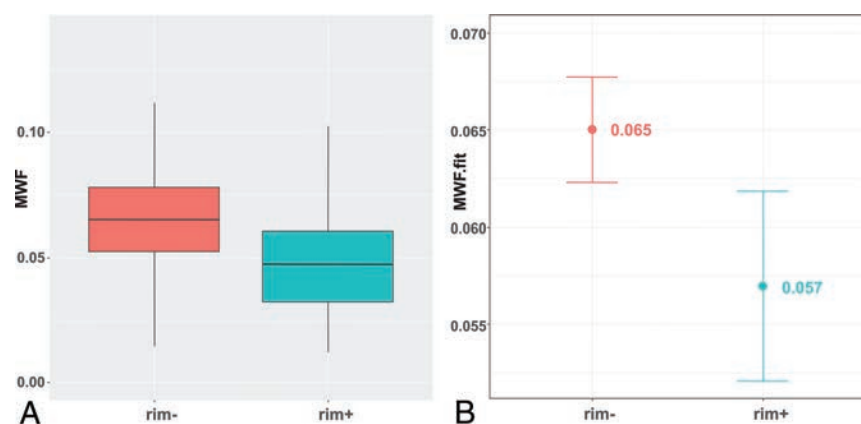


FIG 3. A, Boxplot of rim- (pink) and rim+ (blue) lesions, which demonstrates lower MWF in rim+ compared with rim- lesions. B, Confidence interval plot of rim- (pink) and rim+ (blue) lesions derived from a mixed-effects model, which demonstrates lower MWF mean effect in rim+ lesions compared with rim- lesions after controlling for multiple lesions per patient and T2 lesion size ($P < .001$).

at both time points (QSM1 and QSM2). Three lesions were initially identified as rim- at QSM1 and demonstrated a positive hyperintense rim at QSM2. T2 lesion volume remained stable between the 2 longitudinal MR imagings for both rim+ ($P = .94$) and rim- ($P = .07$) lesions. Rim+ lesions demonstrated an increase in whole-lesion QSM (4.8 ± 10.3 ppb) over time, with both the core and rim ROI values increasing by 4.0 ± 11.6 ppb and 5.3 ± 11.0 ppb, respectively. QSM values for rim- lesions also increased over time, but with smaller differences (2.3 ± 10.8 ppb). A mixed-effects model confirmed a significant change in QSM values within the rim ($P < .001$) and core ($P < .001$) regions of rim+ lesions.

QSM and MWF Assessment of Lesions

At the second time point, QSM and MWF values within the rim and core regions of rim+ lesions were examined to support the premise that iron is present at the lesion edge. The volumes of the rim and core area were 271.4 ± 200.9 mm³ and 116.6 ± 113.7 mm³, respectively. There was a centripetal pattern of reduction observed in both QSM and MWF. In rim+ lesions, the mean QSM value significantly decreased from the rim (13.3 ± 16.3 ppb) to the core

(5.9 ± 15.2 ppb; $P < .01$; Fig 2). As with QSM, the rim+ lesions demonstrated a significant decrease of MWF from the rim (0.052 ± 0.022) to the core (0.039 ± 0.022 ; $P < .01$; Fig 2).

MWF whole-lesion values for rim+ lesions were lower compared with rim- lesions (0.055 ± 0.070 and 0.066 ± 0.040 , respectively; Fig 3) and found to be consistently lower with the exclusion of patients with gadolinium-enhancing lesions (0.044 ± 0.021 and 0.068 ± 0.040 , respectively; On-line Fig 3). This difference became more obvious in the mixed-effects model, which showed that whole-lesion MWF in rim+ lesions was on average 0.01 (Fig 3) lower compared with rim- ($P < .001$). A similar difference in MWF (0.011; $P < .001$) was

found with the exclusion of patients with gadolinium-enhancing lesions (On-line Fig 3). T2-weighted lesion volume remained a significant covariate in the final model ($P < .001$). For every cubic millimeter increase in T2-weighted volume, MWF decreased by 0.000013. The MWF differences among rim+ and rim- lesions can be appreciated on the MWF map shown in Fig 4. In rim+ lesions, we further expanded our analysis to explore the specific relationship of the hyperintense rim at the first time point (susceptibility value and volume on QSM1) and subsequent MWF. In the mixed-effects model, the volume of the rim at QSM1 ($P < .01$) was the only significant covariate; for every cubic millimeter increase in QSM1 rim volume, lesion MWF decreased by 0.00002. Figure 5 highlights the MWF differences between thick rim and thin rim lesions.

DISCUSSION

Our study is one of many demonstrating that GRE MR imaging can identify a discrete subset of chronic MS lesions,^{1,3,4,7-9} and as with other studies, we demonstrate the retention of the iron rim and more tissue damage in these selected lesions. There are 3

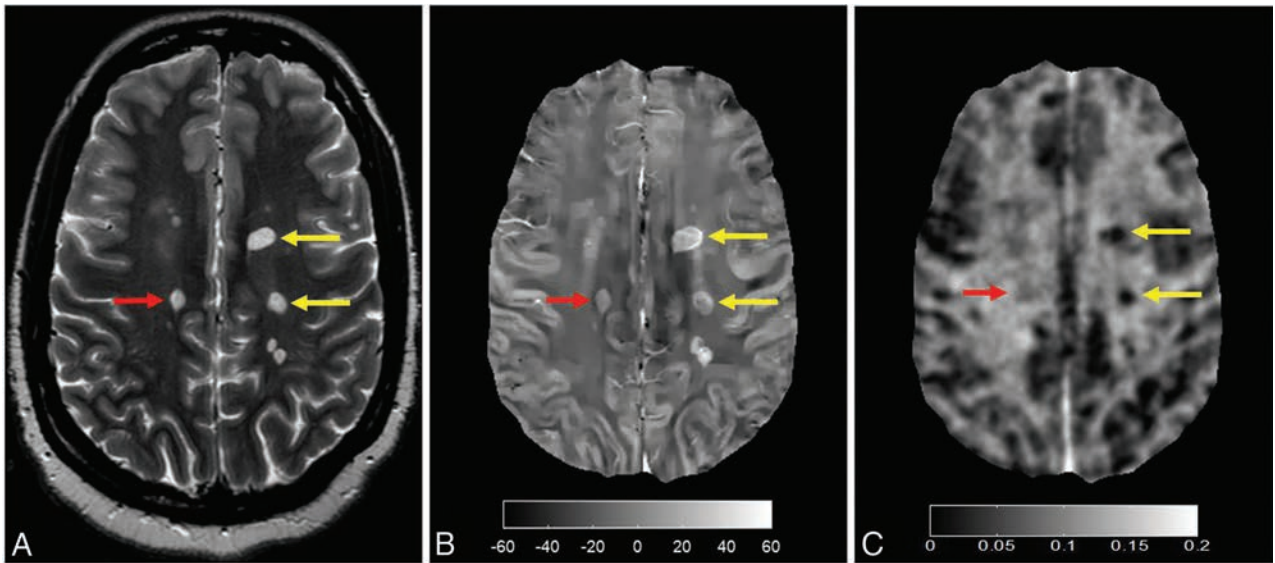


FIG 4. T2-weighted (A), QSM (B), and MWF map (C) images of a patient with relapsing-remitting MS are shown. The hypointense appearance of rim+ lesions (yellow arrows) on the MWF map is consistent with a lower MWF compared with the more isointense appearance of a rim- lesion (red arrow).

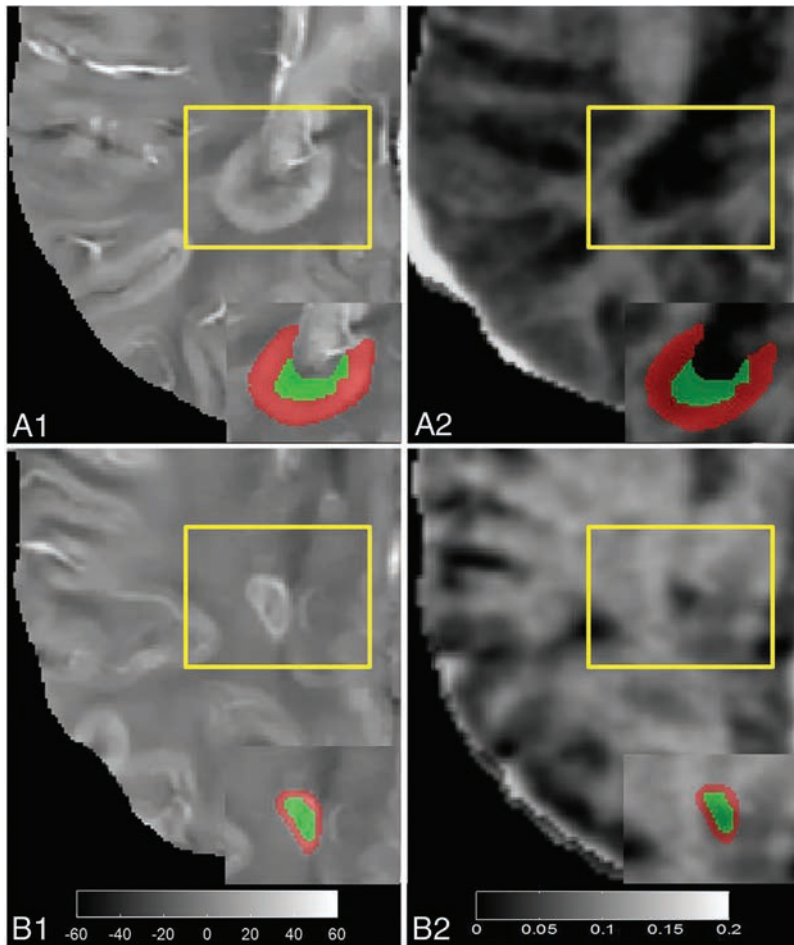


FIG 5. *Top panel*, An example of thick rim lesion (yellow rectangle); QSM (A1) and MWF (A2) in a patient with relapsing-remitting MS. The QSM and MWF values in the core and rim are as follows: -5.2827 ± 14.3945 ppb and 2.2262 ± 17.7374 ppb; $1.5204\% \pm 1.3975\%$ and $4.2542\% \pm 2.5327\%$. *Bottom panel*, An example of thin rim lesion (yellow rectangle); QSM (B1) and MWF (B2) in another patient with relapsing-remitting MS. The QSM and MWF values in the core and rim are as follows: -3.0355 ± 10.271 ppb and 0.9208 ± 13.5405 ppb; $7.4161\% \pm 1.5726\%$ and $8.4678\% \pm 1.3358\%$. The hypointense appearance of a thick rim lesion on the MWF map is lower compared with the thin rim lesions.

unique components to our study: 1) the application of QSM0 for a more accurate identification and quantification of iron rim lesions in a longitudinal study, compared with conventional QSM, SWI, or MR phase; 2) a multitechnique approach of combining QSM with a myelin-specific MR imaging acquisition (MWF); and 3) quantitatively examining the susceptibility and myelin content within the individual components of QSM hyperintense rim+ lesions (rim and core regions). Our work provides further *in vivo* evidence that GRE MR imaging can identify chronic lesions with more demyelination, which is consistent with the known histopathologic classification of a chronic active MS lesion.

QSM studies of MS lesions have uncovered interesting dynamics wherein lesion susceptibility substantially increases shortly after gadolinium enhancement and remains high for the first few years.^{32,33} The susceptibility increase in MS lesions can come from demyelination and/or iron accumulation.¹⁷ The integrated multitechnique QSM+MWF approach described in this study allows for a novel quantitative investigation of the connection between iron-associated inflammation and tissue damage in the brains of patients with MS. Recent patient studies demonstrated increased tissue damage on T1-weighted images for MS lesions with a persistent rim on phase images⁴ and a

higher occurrence of lesions with a QSM rim in patients with progressive MS and increasing disability.²³ However, it is difficult to quantify tissue damage on T1-weighted hypointensity. In addition, studies using QSM and R2* described QSM hyperintense rim lesions as having minor myelin loss compared with other lesion subtypes,²² which is inconsistent with the histopathologic description of chronic active lesions as having extensive demyelination³⁴; this discrepancy may be the consequence of R2* being influenced by iron. For a quantitative assessment of tissue damage in white matter MS lesions, MWF is regarded as an indirect measure of myelin with a relatively high specificity given the strong pathologic correlation.²⁶⁻²⁸ We recognize that an increase of susceptibility within a chronic lesion can be due to demyelination or iron deposition, which limits direct iron quantification by QSM.¹⁷ We identify QSM rim+ lesions as having a rim of iron based upon the susceptibility gradient between the rim and core regions. Support of this approach is based upon 3 factors: 1) a known pattern of demyelination found within chronic active MS lesions (attenuated loss of myelin in core)^{3,6,12}; 2) histologic studies demonstrating that GRE can detect iron within activated microglia and macrophages at the edge of chronic active MS lesions^{1,3,4,11,14,15}; and 3) our own data, demonstrating a decrease in both susceptibility and MWF from rim to core, which can only be explained by iron deposition. Thus, we conclude that iron is contributing, at least in part, to the signal at the rim, but importantly, we are not quantifying the absolute extent that iron or myelin is contributing to the QSM signal.

This QSM+MWF study helps highlight the clinical importance of chronic active lesions, which have been largely ignored in current clinical practice, but may potentially be treated to reduce tissue damage and possibly slow disease progression as suggested by clinical and immunohistologic data. After the acute stage, a significant increase in both QSM and R2* occurs in lesions that are no longer enhancing, yet under 1 year of age, suggesting that iron release occurs during the early stages after myelin destruction.²¹ These findings are consistent with the release of iron secondary to myelin and oligodendrocyte destruction^{9,35} and provide a source for iron-laden proinflammatory microglia and for iron-driven amplification of oxidative stress within the acute MS lesion.^{2,36} Studies have shown evidence for oxidative stress damage to oligodendrocytes and mitochondrial and dystrophic axons in acute MS lesions,³⁷ which consequently inhibit endogenous remyelination. Correspondingly, we found that lesions having a QSM hyperintense rim had a significantly lower MWF throughout the whole lesion compared with those identified as without rim. Interestingly, we found an association with rim volume and lesion MWF, which is consistent with thicker-rimmed chronic lesions demonstrating more active demyelination.³⁴

Chronic active MS lesions have been found to be more prominent in progressive disease compared with the relapsing stage of the disease, and their continued expansion may play an essential role in the pathogenesis of progressive disease.³⁸ In vivo imaging studies of phase or QSM have revealed conflicting results regarding the prevalence of rim+ lesions among patients with MS.³⁹ One previous study demonstrated a vast difference among QSM and phase results, wherein the authors concluded that QSM was superior to the depiction of spatial susceptibility patterns in MS

lesions.¹⁵ Similarly, we found wide-ranging differences in lesion classification based upon QSM versus phase images (data not shown). A major contributing factor to the difficulty of identifying and quantifying rim+ lesions has been the choice of susceptibility reference tissue. Wiggerman et al³⁵ have recently demonstrated in postmortem samples that lesion phase and QSM contrast can be highly influenced by pathologic alterations in myelin and iron in normal-appearing white matter, a typical choice of QSM reference in MS lesion studies. CSF being 99% pure water is another common choice of susceptibility reference; however, current QSM reconstruction algorithms often produce a highly inhomogeneous CSF appearance in the brain ventricles, most likely due to the susceptibility anisotropy effect of the adjacent brain white matter. Consequently, the zero reference in previous studies often depends on the manual selection of ROI, making it less suited for longitudinal studies. A unique component of our study was the use of QSM0, a recently developed QSM inversion method that automatically selects a CSF mask based on R2* derived from a GRE magnitude image and enforces uniformity within the CSF region. This improvement could lead to better detection and quantification of QSM lesions. Interestingly, the current study population is predominantly relapsing patients with minimal disability and differs significantly from postmortem studies, which generally lack the inclusion of younger patients. Therefore, to determine the true prevalence and incidence of these lesions among patients with MS, future studies will require a consistent imaging protocol, for which we favor QSM0, on a larger cohort of patients that includes both relapsing and progressive stages of the disease. In addition, QSM and MWF provides an opportunity to further explore the range of myelin damage of these particular lesions, especially those found in younger MS patients.

This study has several limitations. First, our analysis is limited by the incomplete longitudinal design due to MWF only being acquired at the second time point. Further studies evaluating the longitudinal relationship of QSM and MWF in acute MS lesions will improve our understanding of the complex association of lesion iron deposition and myelin damage. Although our results of combining the data from QSM and MWF provide support for iron deposition, we lack histologic validation that lesions demonstrating a hyperintense rim on QSM truly have iron deposition; however, a number of mentioned studies have validated GRE imaging to identify these lesions. Further highlighting the necessity of histopathologic validation is that paramagnetic iron is generally expected to shorten the T2 relaxation time of brain tissue, and the resulting effect on the accuracy of MWF quantification is currently not well understood. Therefore, MWF measurements in QSM rim+ lesions in the presence of elevated iron should be interpreted with caution. Last, clinical factors, such as specific treatments or medication changes, were not considered as variables of interest in our analysis. Treatment duration was the only "treatment-related" variable included in the mixed-effects models because of the complexity of individual patient management decisions. Our analysis presumes that specific MS treatments have no influence on the lesions' iron or myelin content, and we recognize that this may be a limitation; however, there is no current evidence to contradict this assumption. Furthermore, larger stud-

ies would be required to properly assess the influence of specific treatments on QSM and MWF. In addition, in a separate analysis, we assessed the potential influence of enhancing lesions and the remote effect of inflammation related to breakdown of the blood-brain barrier. We found that after removing patients with enhancing lesions, a significant difference in MWF remained among rim+ and rim- lesions.

CONCLUSIONS

Our study demonstrated that differences exist among individual lesions based upon the QSM hyperintensity pattern. QSM rim+ lesions maintained a hyperintense rim and demonstrated an increase in susceptibility over time. Centripetal decrease in QSM and MWF identified a subset of MS lesions with excess iron deposition at the rim and more myelin damage. These results raise the possibility that QSM may provide insight into pathologic mechanisms of injury, such as iron release and chronic inflammation, within individual lesions. Furthermore, a hyperintense rim on QSM may provide a biomarker to target and study myelin injury within chronic active MS lesions. Treatments targeting the modulation of chronic CNS inflammation would provide a novel therapeutic strategy to prevent ongoing myelin damage as well as enhance remyelination and decrease disease progression.

Disclosures: Thanh Nguyen—RELATED: Grants/Grants Pending: National Institutes of Health; UNRELATED: Grants/Grants Pending: National Institutes of Health, National Multiple Sclerosis Society*. Yi Wang—RELATED: Grants/Grants Pending: National Institutes of Health, Comments: grant R01 NS090464*; UNRELATED: Grants/Grants Pending: National Institutes of Health, Comments: we are actively seeking National Institutes of Health grants to translate our work into clinical practice*; Patents (Planned, Pending, or Issued): Cornell University, Comments: I am one of the inventors named on the QSM patents*; Stock/Stock Options: Medimagetric, Comments: Medimagetric is working with Cornell to commercialize QSM technology. Susan Gauthier—RELATED: Grants/Grants Pending: National Institutes of Health, Comments: grant R01NS090464, focused on multiple sclerosis lesion magnetic susceptibility activity*; UNRELATED: Grants/Grants Pending: Genzyme*, Mallinckrodt*, Novartis*. *Money paid to the institution.

REFERENCES

- Bagnato F, Hametner S, Yao B, et al. **Tracking iron in multiple sclerosis: a combined imaging and histopathological study at 7 Tesla.** *Brain* 2011;134:3602–15 CrossRef Medline
- Stephenson E, Nathoo N, Mahjoub Y, et al. **Iron in multiple sclerosis: roles in neurodegeneration and repair.** *Nat Rev Neurol* 2014;10:459–68 CrossRef Medline
- Dal-Bianco A, Grabner G, Kronnerwetter C, et al. **Slow expansion of multiple sclerosis iron rim lesions: pathology and 7 T magnetic resonance imaging.** *Acta Neuropathol* 2017;133:25–42 CrossRef Medline
- Absinta M, Sati P, Schindler M, et al. **Persistent 7-Tesla phase rim predicts poor outcome in new multiple sclerosis patient lesions.** *J Clin Invest* 2016;126:2597–609 CrossRef Medline
- Cairo G, Recalcati S, Mantovani A, et al. **Iron trafficking and metabolism in macrophages: contribution to the polarized phenotype.** *Trends Immunol* 2011;32:241–47 CrossRef Medline
- Langkammer C, Schweser F, Krebs N, et al. **Quantitative susceptibility mapping (QSM) as a means to measure brain iron? A post mortem validation study.** *Neuroimage* 2012;62:1593–99 CrossRef Medline
- Hammond KE, Metcalf M, Carvajal L, et al. **Quantitative in vivo magnetic resonance imaging of multiple sclerosis at 7 Tesla with sensitivity to iron.** *Ann Neurol* 2008;64:707–13 CrossRef Medline
- Yao B, Ikonomidou VN, Cantor FK, et al. **Heterogeneity of multiple sclerosis white matter lesions detected with T2*-weighted imaging at 7.0 Tesla.** *J Neuroimaging* 2015;25:799–806 CrossRef Medline
- Mehta V, Pei W, Yang G, et al. **Iron is a sensitive biomarker for inflammation in multiple sclerosis lesions.** *PLoS One* 2013;8:e57573 CrossRef Medline
- Haacke EM, Makki M, Ge Y, et al. **Characterizing iron deposition in multiple sclerosis lesions using susceptibility weighted imaging.** *J Magn Reson Imaging* 2009;29:537–44 CrossRef Medline
- Langkammer C, Krebs N, Goessler W, et al. **Quantitative MR imaging of brain iron: a postmortem validation study.** *Radiology* 2010;257:455–62 CrossRef Medline
- Li J, Chang S, Liu T, et al. **Reducing the object orientation dependence of susceptibility effects in gradient echo MRI through quantitative susceptibility mapping.** *Magn Reson Med* 2012;68:1563–69 CrossRef Medline
- Hopp K, Popescu BF, McCrea RP, et al. **Brain iron detected by SWI high pass filtered phase calibrated with synchrotron X-ray fluorescence.** *J Magn Reson Imaging* 2010;31:1346–54 CrossRef Medline
- Wiggermann V, Hametner S, Hernandez-Torres E, et al. **Susceptibility-sensitive MRI of multiple sclerosis lesions and the impact of normal-appearing white matter changes.** *NMR Biomed* 2017;30 CrossRef Medline
- Eskreis-Winkler S, Deh K, Gupta A, et al. **Multiple sclerosis lesion geometry in quantitative susceptibility mapping (QSM) and phase imaging.** *J Magn Reson Imaging* 2015;42:224–29 CrossRef Medline
- Wang Y, Liu T. **Quantitative susceptibility mapping (QSM): decoding MRI data for a tissue magnetic biomarker.** *Magn Reson Med* 2015;73:82–101 CrossRef Medline
- Wisnieff C, Ramanan S, Olesik J, et al. **Quantitative susceptibility mapping (QSM) of white matter multiple sclerosis lesions: interpreting positive susceptibility and the presence of iron.** *Magn Reson Med* 2015;74:564–70 CrossRef Medline
- Stuber C, Pitt D, Wang Y. **Iron in multiple sclerosis and its non-invasive imaging with quantitative susceptibility mapping.** *Int J Mol Sci* 2016;17:E100 CrossRef Medline
- Deistung A, Schäfer A, Schweser F, et al. **Toward in vivo histology: a comparison of quantitative susceptibility mapping (QSM) with magnitude-, phase-, and R2*-imaging at ultra-high magnetic field strength.** *Neuroimage* 2013;65:299–314 CrossRef Medline
- Langkammer C, Liu T, Khalil M, et al. **Quantitative susceptibility mapping in multiple sclerosis.** *Radiology* 2013;267:551–59 CrossRef Medline
- Zhang Y, Gauthier SA, Gupta A, et al. **Quantitative susceptibility mapping and R2* measured changes during white matter lesion development in multiple sclerosis: myelin breakdown, myelin debris degradation and removal, and iron accumulation.** *AJNR Am J Neuroradiol* 2016;37:1629–35 CrossRef Medline
- Li X, Harrison DM, Liu H, et al. **Magnetic susceptibility contrast variations in multiple sclerosis lesions.** *J Magn Reson Imaging* 2016;43:463–73 CrossRef Medline
- Harrison DM, Li X, Liu H, et al. **Lesion heterogeneity on high-field susceptibility MRI is associated with multiple sclerosis severity.** *AJNR Am J Neuroradiol* 2016;37:1447–53 CrossRef Medline
- Nguyen TD, Wisnieff C, Cooper MA, et al. **T2 prep three-dimensional spiral imaging with efficient whole brain coverage for myelin water quantification at 1.5 Tesla.** *Magn Reson Med* 2012;67:614–21 CrossRef Medline
- Nguyen TD, Deh K, Monohan E, et al. **Feasibility and reproducibility of whole brain myelin water mapping in 4 minutes using fast acquisition with spiral trajectory and adiabatic T2prep (FAST-T2) at 3T.** *Magn Reson Med* 2016;76:456–65 CrossRef Medline
- Laule C, Kozlowski P, Leung E, et al. **Myelin water imaging of multiple sclerosis at 7 T: correlations with histopathology.** *Neuroimage* 2008;40:1575–80 CrossRef Medline
- McCreary CR, Bjarnason TA, Skihar V, et al. **Multiexponential T2 and magnetization transfer MRI of demyelination and remyelination in murine spinal cord.** *Neuroimage* 2009;45:1173–82 CrossRef Medline
- Vargas WS, Monohan E, Pandya S, et al. **Measuring longitudinal**

- myelin water fraction in new multiple sclerosis lesions. *Neuroimage Clin* 2015;9:369–75 CrossRef Medline
29. de Rochefort L, Liu T, Kressler B, et al. **Quantitative susceptibility map reconstruction from MR phase data using Bayesian regularization: validation and application to brain imaging.** *Magn Reson Med* 2010;63:194–206 CrossRef Medline
 30. Liu J, Liu T, de Rochefort L, et al. **Morphology enabled dipole inversion for quantitative susceptibility mapping using structural consistency between the magnitude image and the susceptibility map.** *Neuroimage* 2012;59:2560–68 CrossRef Medline
 31. Jenkinson M, Bannister P, Brady M, et al. **Improved optimization for the robust and accurate linear registration and motion correction of brain images.** *Neuroimage* 2002;17:825–41 CrossRef Medline
 32. Chen W, Gauthier SA, Gupta A, et al. **Quantitative susceptibility mapping of multiple sclerosis lesions at various ages.** *Radiology* 2014;271:183–92 CrossRef Medline
 33. Zhang Y, Gauthier SA, Gupta A, et al. **Longitudinal change in magnetic susceptibility of new enhanced multiple sclerosis (MS) lesions measured on serial quantitative susceptibility mapping (QSM).** *J Magn Reson Imaging* 2016;44:426–32 CrossRef Medline
 34. Kuhlmann T, Ludwin S, Prat A, et al. **An updated histological classification system for multiple sclerosis lesions.** *Acta Neuropathol* 2017;133:13–24 CrossRef Medline
 35. Wiggermann V, Hernández Torres E, Vavasour IM, et al. **Magnetic resonance frequency shifts during acute MS lesion formation.** *Neurology* 2013;81:211–18 CrossRef Medline
 36. Haider L. **Inflammation, iron, energy failure, and oxidative stress in the pathogenesis of multiple sclerosis.** *Oxid Med Cell Longev* 2015; 2015:725370 CrossRef Medline
 37. Haider L, Fischer MT, Frischer JM, et al. **Oxidative damage in multiple sclerosis lesions.** *Brain* 2011;134:1914–24 CrossRef Medline
 38. Prineas JW, Kwon EE, Cho ES, et al. **Immunopathology of secondary-progressive multiple sclerosis.** *Ann Neurol* 2001;50:646–57 CrossRef Medline
 39. Cronin MJ, Wharton S, Al-Radaideh A, et al. **A comparison of phase imaging and quantitative susceptibility mapping in the imaging of multiple sclerosis lesions at ultrahigh field.** *MAGMA* 2016;29: 543–57 CrossRef Medline

Noninvasive Assessment of Intracranial Pressure Status in Idiopathic Intracranial Hypertension Using Displacement Encoding with Stimulated Echoes (DENSE) MRI: A Prospective Patient Study with Contemporaneous CSF Pressure Correlation

A.M. Saindane, D. Qiu, J.N. Oshinski, N.J. Newman, V. Biousse, B.B. Bruce, J.F. Holbrook, B.M. Dale, and X. Zhong



ABSTRACT

BACKGROUND AND PURPOSE: Intracranial pressure is estimated invasively by using lumbar puncture with CSF opening pressure measurement. This study evaluated displacement encoding with stimulated echoes (DENSE), an MR imaging technique highly sensitive to brain motion, as a noninvasive means of assessing intracranial pressure status.

MATERIALS AND METHODS: Nine patients with suspected elevated intracranial pressure and 9 healthy control subjects were included in this prospective study. Controls underwent DENSE MR imaging through the midsagittal brain. Patients underwent DENSE MR imaging followed immediately by lumbar puncture with opening pressure measurement, CSF removal, closing pressure measurement, and immediate repeat DENSE MR imaging. Phase-reconstructed images were processed producing displacement maps, and pontine displacement was calculated. Patient data were analyzed to determine the effects of measured pressure on pontine displacement. Patient and control data were analyzed to assess the effects of clinical status (pre-lumbar puncture, post-lumbar puncture, or control) on pontine displacement.

RESULTS: Patients demonstrated imaging findings suggesting chronically elevated intracranial pressure, whereas healthy control volunteers demonstrated no imaging abnormalities. All patients had elevated opening pressure (median, 36.0 cm water), decreased by the removal of CSF to a median closing pressure of 17.0 cm water. Patients pre-lumbar puncture had significantly smaller pontine displacement than they did post-lumbar puncture after CSF pressure reduction ($P = .001$) and compared with controls ($P = .01$). Post-lumbar puncture patients had statistically similar pontine displacements to controls. Measured CSF pressure in patients pre- and post-lumbar puncture correlated significantly with pontine displacement ($r = 0.49$; $P = .04$).

CONCLUSIONS: This study establishes a relationship between pontine displacement from DENSE MR imaging and measured pressure obtained contemporaneously by lumbar puncture, providing a method to noninvasively assess intracranial pressure status in idiopathic intracranial hypertension.

ABBREVIATIONS: DENSE = displacement encoding with stimulated echoes; ICP = intracranial pressure; IIH = idiopathic intracranial hypertension; IQR = interquartile range; LP = lumbar puncture

Intracranial pressure (ICP) reflects the pressure of the brain parenchyma and CSF. Many clinical disorders can abnormally elevate ICP through a variety of mechanisms, resulting in important clinical manifestations and findings on imaging.¹ Idiopathic intracranial hypertension (IIH) is a condition of unknown etiol-

ogy with elevated ICP unrelated to an intracranial mass lesion, meningeal process, or cerebral venous thrombosis.^{2,3} Patients with IIH are usually female, obese, and typically present with headaches, transient visual obscurations, and/or papilledema; treatment includes medication to decrease CSF production, weight loss, and/or CSF diversion.⁴ Measurement of ICP is essential for the diagnosis and management of IIH and many other neurologic and neurosurgical conditions and is typically estimated by lumbar puncture (LP) and CSF manometry. Because LP is invasive with small but definite risks and may be required at multiple time points for suspected treatment failure, it would be highly desirable to have a noninvasive and clinically practical technique to assess ICP status in IIH and other ICP disorders.⁵

Displacement encoding with stimulated echoes (DENSE) is an MR imaging technique that encodes pixel-wise tissue displace-

Received June 24, 2017; accepted after revision October 22.

From the Departments of Radiology and Imaging Sciences (A.M.S., D.Q., J.N.O., J.F.H.) and Ophthalmology (N.J.N., V.B., B.B.B.), Emory University, Atlanta, Georgia; Department of Biomedical Engineering (J.N.O.), Georgia Institute of Technology, Atlanta, Georgia; MR R&D Collaborations (B.M.D.), Siemens Healthineers, Apex, North Carolina; and MR R&D Collaborations (X.Z.), Siemens Healthineers, Atlanta, Georgia.

Please address correspondence to Amit M. Saindane, MD, Division of Neuroradiology, Emory University School of Medicine, Emory University Hospital, D112, 1364 Clifton Road, Atlanta, GA 30322; e-mail: asainda@emory.edu

<http://dx.doi.org/10.3174/ajnr.A5486>

ments into the phase of the stimulated echoes. DENSE is well-suited for measuring small displacements and has been shown to measure brain motion as small as 0.01 mm⁶ with good reproducibility.⁷ This study evaluates the ability of DENSE MR imaging to measure dynamic brain displacements in patients with IIH by using a tightly controlled protocol before and after LP and CSF removal with pressure reduction and compares these brain displacements to that of healthy control subjects. The hypothesis for this study is that high ICP constrains brain motion, but this brain motion can be normalized by the reduction of ICP through the removal of CSF. The validation of such a relationship would provide the basis for the use of DENSE brain displacement as a non-invasive means of assessing ICP status.

MATERIALS AND METHODS

Patients and Control Subjects

Approval for this prospective study was obtained from the Emory University institutional review board, and informed written consent was obtained from each participant. Nine patients, evaluated by a neuro-ophthalmologist between April 2015 and March 2017 at Emory University Hospital, with signs and symptoms of elevated ICP (eg, headaches, transient visual obscurations, and papilledema) were recruited and completed this study. Patients were excluded if they had standard contraindications to MR imaging or to gadolinium-based contrast agents. Exclusion criteria also included presence of an intracranial mass, hydrocephalus, or venous sinus thrombosis on MR imaging. Four additional suspected patients with IIH who were recruited and met the inclusion criteria were excluded from analysis because of excessive motion artifact on DENSE. Nine healthy nonobese volunteers were recruited as a comparison group. Although performance of LP on healthy volunteers was not considered ethically possible, each volunteer was questioned about history of headaches and visual disturbances.

MRI Technique and Study Protocol

All patients and healthy control subjects underwent MR imaging at 3T (Tim Trio; Siemens, Erlangen, Germany) in the supine position. A single midsagittal section through the brain was imaged by using a peripheral pulse unit-gated, segmented EPI, cine DENSE sequence.⁶ The pulse wave from the peripheral pulse unit was used for triggering the DENSE sequence. The image parameters were displacement encoding frequency (k_c), 1.0 or 1.5 cycle/mm; through-plane dephasing frequency (k_d), 0.08 cycle/mm; TE, 8.9–10.4 ms; TR, 55–59 ms; EPI factor, 8; segments, 16; pixel size, 1.2 × 1.2 mm²; section thickness, 7 mm; averages, 4; and frames, 10–20 (depending on the pulse duration). Different displacement frequencies were used in some subjects to acquire displacement information across a larger dynamic range. Displacement was encoded in the foot-to-head and anterior-to-posterior directions. The acquisition time for DENSE was approximately 2 minutes.

Control subjects underwent MPRAGE for planning and sagittal DENSE. Patients with IIH underwent the following tightly controlled protocol consisting of brain MR imaging and fluoroscopically guided LP: 1) The patient had MR imaging with sagittal T2 sampling perfection with application-optimized contrasts by using different flip angle evolution (SPACE; Siemens, Erlangen,

Germany), sagittal DENSE, axial DWI, axial T2*-weighted imaging, and axial T1-weighted imaging sequences; 2) The patient was then taken immediately to the fluoroscopy suite and an LP performed in the prone position with a 22-gauge spinal needle and opening pressure measured by using CSF manometry; 3) CSF was withdrawn and the closing pressure measured; and 4) The patient was then taken immediately back for MR imaging with sagittal T2 SPACE, sagittal DENSE, contrast-enhanced MRV, axial fat-saturated T2-weighted imaging, axial postcontrast T1-weighted imaging, and sagittal postcontrast MPRAGE sequences.

Image Analysis

A subspecialty-certified neuroradiologist with 9 years of experience (A.M.S.) evaluated MR imaging and MRV images for intracranial abnormalities. DENSE images were exported for off-line processing in ImageJ (National Institutes of Health, Bethesda, Maryland). Phase-reconstructed images were divided by $2\pi k_c$ to convert to displacement in millimeters. A single identical ROI was placed in the central pons on the magnitude images and then copied to the corresponding motion-encoded (foot-to-head) phase images (Fig 1A, -B). Mean displacement values in the ROIs were plotted over the phases of the cardiac cycle and the minimum value of displacement was subtracted from the maximum displacement to yield the maximum change in displacement across the cardiac cycle (Fig 1C). Postprocessing took 2–3 minutes per subject.

Statistical Analysis

Statistical analysis was performed by using SPSS version 22.0 (IBM, Armonk, New York). Patient and control demographics were compared by using the Fisher exact test and the Mann-Whitney *U* test. Group differences in DENSE displacement between control subjects, pre-LP patients with IIH, and post-LP patients with IIH were evaluated by using a paired samples *t* test for patients with IIH pre- and post-LP and an independent samples *t* test for patients with IIH and control subjects. The relationship between measured pressure and DENSE displacement was assessed by using the Pearson correlation.

RESULTS

Patients and Controls

A total of 9 female patients with IIH were included in this study (Table 1). The median age for these patients was 28.1 years (interquartile range [IQR], 22.5–32.1 years), and the median body mass index was 38.9 (IQR, 28.1–41.8). All patients had an elevated opening pressure of 36.0 cm water (IQR, 32.5–41.0 cm water), a median of 15.0 mL CSF removed (IQR, 13–16 mL), and a resultant median closing pressure of 17.0 cm water (IQR, 15.5–19.0 cm water). The median change in pressure was 20.0 cm water (IQR, 15.0–23.0 cm water), representing a median 53% reduction of pressure (IQR, 47%–58%). The median time from pre-LP DENSE imaging to opening pressure measurement was 56.0 minutes (IQR, 40–72 minutes), and the median time from the closing pressure to the post-LP DENSE was 26.0 minutes (IQR, 17.5–34.0 minutes). None of the patients had unexpected structural intracranial abnormalities (eg, intracranial mass, hydrocephalus, ve-

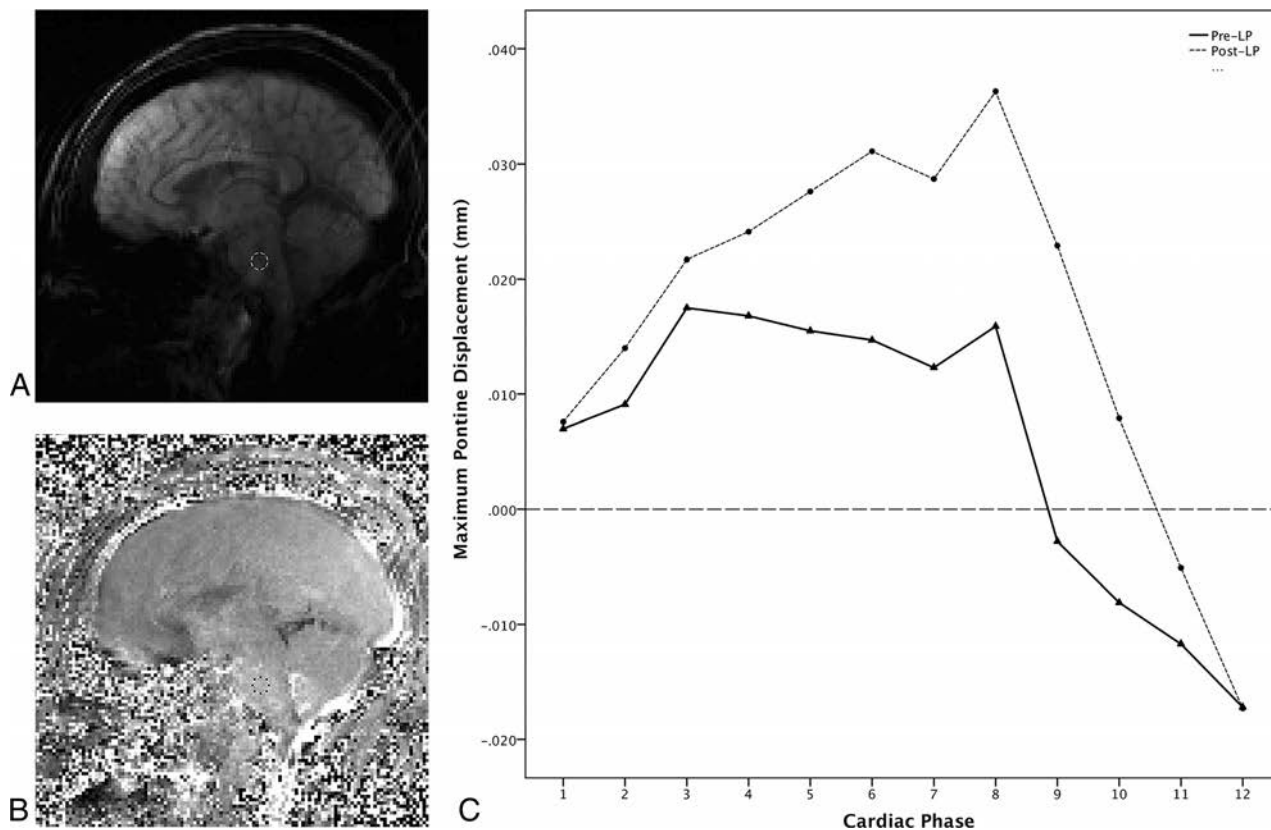


FIG 1. DENSE imaging with ROI placement and measured displacement across the cardiac cycle from a 44-year-old woman with IIH (Patient 9). *A*, Sagittal magnitude image from pre-LP DENSE encoded for motion in the foot-to-head direction. An ROI has been placed in the midpons to avoid partial volume effects from CSF flow. *B*, Corresponding phase image from the pre-LP DENSE encoded for motion in the foot-to-head direction with ROI transferred from the magnitude image into the midpons for measurement to be propagated to all 12 images acquired across the cardiac cycle. *C*, Graph showing DENSE displacement in the foot-to-head direction across the cardiac cycle divided into 12 phases. The *solid line* shows the pre-LP displacements across the cardiac cycle, and the *dotted line* shows post-LP displacements across the cardiac cycle. Maximum displacement is calculated by subtracting the lowest value from the highest across the cardiac cycle for both the pre-LP and post-LP states. Note the increased displacement in the post-LP state.

Table 1: Pressure measurements, DENSE pontine displacements, and times between measurements in patients with IIH pre-LP and post-LP

Patient No.	OP, cm H ₂ O	CP, cm H ₂ O	OP to CP Pressure Change, cm H ₂ O	OP to CP Pressure Change, %	CSF Removed, cc	Pre-LP DENSE, mm	Post-LP DENSE, mm	% Change	Pre-LP DENSE to OP Time, min	CP to Post-LP DENSE Time, min
1	26	15	11	-42	11	0.124	0.134	8	56	17
2	41	18	23	-56	16	0.022	0.059	164	95	48
3	36	17	19	-53	20	0.071	0.097	36	67	18
4	46	19	27	-59	22	0.047	0.087	86	204	35
5	40	16	24	-60	15	0.105	0.119	14	51	34
6	33	16	17	-52	15	0.037	0.051	39	39	21
7	35	15	20	-57	15	0.024	0.052	113	72	10
8	32	19	13	-41	14	0.078	0.085	8	41	30
9	49	26	23	-47	12	0.035	0.054	54	35	26

Note:—CP indicates closing pressure; OP, opening pressure.

nous sinus thrombosis, etc) to explain elevated ICP, though previously described imaging findings associated with elevated ICP were found in all patients involving the orbits (distension of the perioptic nerve subarachnoid space, flattening of the posterior sclera, intraocular protrusion of the prelaminar optic nerve, enhancement of the prelaminar optic nerve, and vertical tortuosity of the orbital optic nerve),⁸ skull base (“empty” sella turcica and prominent Meckel caves),^{9,10} cerebellar tonsils,¹¹ and venous sinuses (transverse venous sinus stenosis).¹² All patients had papill-

edema and met the formal diagnostic criteria for IIH. Seven of 9 patients are followed regularly by neuro-ophthalmology, received standard medical treatment including acetazolamide and weight loss, and have experienced no visual loss. Follow-up is not available for 2 patients to assess their clinical outcomes.

A total of 9 healthy control subjects were included in the study (7 men and 2 women). The median age for control subjects was 34.0 years (IQR, 23.5–40.0 years). No control subject reported a history of chronic headaches or visual disturbances.

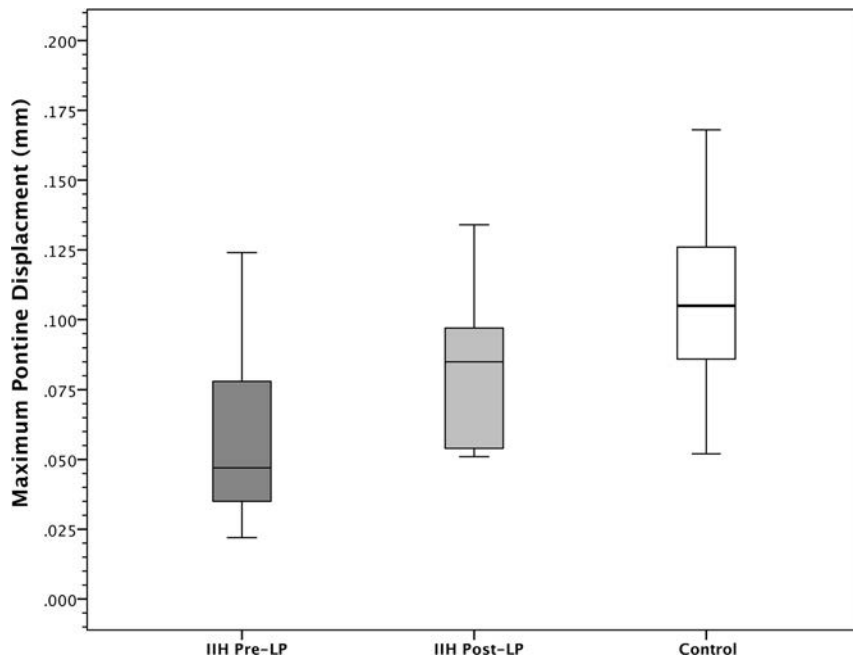


FIG 2. Comparison of maximum pontine displacement in pre-LP, post-LP, and control groups. The maximum pontine displacement of an ROI in the central pons in the pre-LP IIH group was significantly lower than in the post-LP state within subjects ($P < .001$) and significantly lower than the control group ($P = .01$). The maximum pontine displacement in post-LP patients with IIH did not significantly differ from control subjects ($P = .10$). Values are shown in mean \pm SD.

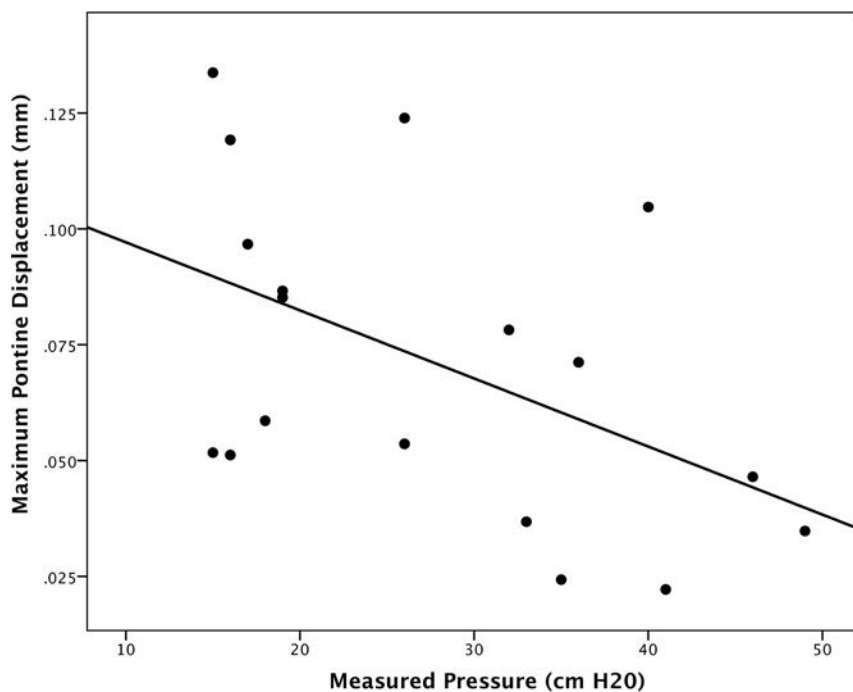


FIG 3. Correlation of measured CSF pressure and pontine displacement by DENSE. The maximum pontine displacement measured by DENSE correlates moderately with measured pressure (opening pressure or closing pressure) by CSF manometry ($r = 0.49$; $P = .04$).

All healthy control subjects had normal brain imaging, including no findings to suggest chronically elevated ICP. Patients and healthy control subjects did not significantly differ in age ($P = .35$), though there were significant sex differences ($P = .002$).

Reducing CSF pressure through CSF removal resulted in within-subject increase in pontine displacement for all patients with IIH, with mean post-LP pontine displacement similar to that of healthy control subjects. Establishing this relationship between pressure and pontine displacement by using DENSE raises the

DENSE Analysis

For patients with IIH, the mean pre-LP pontine displacement was 0.060 mm (SD = 0.036 mm), which was increased to a mean of 0.082 mm (SD = 0.031 mm) post-LP, representing a range of 8% to 164% increase in pontine displacement (mean of 58%; $P = .001$). Control subjects demonstrated a mean pontine displacement of 0.109 mm (SD = 0.034 mm), which was significantly higher than the pre-LP patients with IIH ($P = .01$), but not significantly different from the post-LP patients with IIH ($P = .10$; Fig 2). Across patients using both pre-LP and post-LP measured CSF pressures and DENSE measurements, there was a significant moderate correlation between pressure and pontine displacement by using DENSE ($r = -0.49$; $P = .04$; Fig 3).

DISCUSSION

This study prospectively used a protocol that tightly coupled DENSE MR imaging with the CSF opening pressure and closing pressure measured by LP and CSF manometry. We chose IIH as a model for elevated ICP because there is no intracranial abnormality such as a mass lesion that would vary in size or effect between patients. We hypothesized that elevated ICP would constrain peak brain motion because vascular pulsations may be less able to drive brain motion in a high-pressure state. We specifically evaluated the foot-to-head direction of motion and the brain stem because this had previously been the direction and location of the highest brain motion in healthy volunteers⁶ (compared with the anteroposterior direction, presumably related to increased compliance of the spinal canal from the presence of neural foramina openings and epidural fat). The midpons was chosen as an easily identifiable landmark for ROI placement where there would not be partial volume effects with CSF flow. In comparison with healthy control subjects, patients with IIH had significantly decreased pontine displacement. Re-

potential for its use for noninvasive assessment of ICP status. Merits to the technique include a very short acquisition time and simple postprocessing, which could easily be automated for inline real-time clinical use. Specifically, the technique could be used to noninvasively track patients after a baseline DENSE measurement to assess for therapy failure in IIH and potentially other conditions (eg, CSF shunt failure as a cause of recurrent headache).

The reference standard for ICP measurement is direct ICP monitoring, which is highly invasive and not practical or necessary for most patients because CSF pressure by LP generally agrees with ICP.¹³ Orbital, skull base, dural venous sinus, and other imaging findings^{8–12} have been described in IIH, but are not of sufficient accuracy to be diagnostic of elevated ICP^{14,15} and may persist after pressure reduction.¹⁶ Clinical examination of papilledema by using the Frisén scale varies among medical specialists,¹⁷ and the absence of papilledema does not exclude ICP elevation. Transcranial Doppler sonography and optic nerve ultrasonography have shown variable results for the assessment of ICP.^{18,19} An MR imaging approach derived from transcranial CSF flow and blood volumetric flow rates has been used to differentiate between normal and elevated ICP^{20,21}; however, this approach is complex for clinical use and requires further investigation in a larger cohort.

There are several limitations to this study, including the relatively small number of patients evaluated. We attempted to minimize time lags between pressure and DENSE measurements; however, transport and procedural time precluded tighter coupling of the steps. Because CSF is regenerated over time, it could increase pressure post-LP above the measured closing pressure, introducing systematic error into the post-LP DENSE. Variability in the timing interval between DENSE and pressure measurement across patients could introduce additional error. Patients and control subjects differed in demographic features, so it is difficult to exclude the contributions of these and other variables to the comparisons between IIH and control groups. Next, there is substantial variability between patients in baseline pontine displacement and in their extent of change after LP and CSF removal. A variety of factors, including the extent and duration of elevated ICP and variations in potential adaptive responses related to the elevated ICP, could be responsible for this finding; therefore, the degree of change in pontine displacement through CSF pressure reduction may vary by patient-specific factors. We did not use a head immobilization device or correct in postprocessing for any bulk head motion, and this would perhaps further improve the robustness of the results in terms of interpatient differences and differences pre- to post-LP. An LP was not performed on healthy control subjects, so their exact ICP status is not known; however, the selection of nonobese control subjects without self-reported symptoms of elevated ICP makes it extremely unlikely that they have undiagnosed IIH. Finally, it is unclear how DENSE would perform in the setting of an intracranial mass, hydrocephalus, or other important brain abnormality or in circumstances where there is only mild elevation of ICP. Future extension to a larger cohort with normal and abnormally elevated ICP, as well as to other scanner systems and patients with other etiologies of abnor-

mal ICP, will be required to determine the broader applicability of the DENSE technique.

CONCLUSIONS

This study establishes a relationship between pontine displacement obtained by DENSE MR imaging and CSF pressure obtained contemporaneously by LP in patients with IIH, providing a potential method for noninvasively assessing ICP status.

Disclosures: Deqiang Qiu—UNRELATED: Grants/Grants Pending: Siemens Medical Solutions*. John N. Oshinski—UNRELATED: Grants/Grants Pending: Siemens Medical Solutions, Comments: we (Emory) received a grant on the development of DENSE MRI applications. The grant work did not directly relate to this project, but is on a similar topic*. Nancy J. Newman—UNRELATED: Consultancy: GenSight Biologics, Santhera Pharmaceuticals, Quark Pharmaceuticals, Comments: consultant for GenSight Biologics and Santhera Pharmaceuticals, Data Safety Monitoring Board for Quark; Expert Testimony: Medical-legal firms, Comments: medical-legal expert for law firms on topics of papilledema and idiopathic intracranial hypertension. Valérie Biousse—UNRELATED: Consultancy: GenSight Biologics. Beau B. Bruce—UNRELATED: Consultancy: MedImmune, Comments: Data Safety Monitoring Board; Expert Testimony: Bayer, Comments: individual litigants; Grants/Grants Pending: National Institutes of Health*. Brian M. Dale—UNRELATED: Employment: Siemens Healthcare. Xiaodong Zhong—UNRELATED: Employment: Siemens Medical Solutions USA. *Money paid to the institution.

REFERENCES

1. Holbrook J, Saindane AM. **Imaging of intracranial pressure disorders.** *Neurosurgery* 2017;80:341–54 CrossRef Medline
2. Friedman DI, Jacobson DM. **Diagnostic criteria for idiopathic intracranial hypertension.** *Neurology* 2002;59:1492–95 CrossRef Medline
3. Friedman DI, Liu GT, Digre KB. **Revised diagnostic criteria for the pseudotumor cerebri syndrome in adults and children.** *Neurology* 2013;81:1159–65 CrossRef Medline
4. Friedman DI, Jacobson DM. **Idiopathic intracranial hypertension.** *J Neuroophthalmol* 2004;24:138–45 CrossRef Medline
5. Bruce BB. **Noninvasive assessment of cerebrospinal fluid pressure.** *J Neuroophthalmol* 2014;34:288–94 CrossRef Medline
6. Zhong X, Meyer CH, Schlesinger DJ, et al. **Tracking brain motion during the cardiac cycle using spiral cine-DENSE MRI.** *Med Phys* 2009;36:3413–19 CrossRef Medline
7. Soellinger M, Rutz AK, Kozerke S, et al. **3D cine displacement-encoded MRI of pulsatile brain motion.** *Magn Reson Med* 2009;61:153–62 CrossRef Medline
8. Brodsky MC, Vaphiades M. **Magnetic resonance imaging in pseudotumor cerebri.** *Ophthalmology* 1998;105:1686–93 CrossRef Medline
9. Saindane AM, Lim PP, Aiken A, et al. **Factors determining the clinical significance of an “empty” sella turcica.** *AJR Am J Roentgenol* 2013;200:1125–31 CrossRef Medline
10. Bialer OY, Rueda MP, Bruce BB, et al. **Meningoceles in idiopathic intracranial hypertension.** *AJR Am J Roentgenol* 2014;202:608–13 CrossRef Medline
11. Aiken AH, Hoots JA, Saindane AM, et al. **Incidence of cerebellar tonsillar ectopia in idiopathic intracranial hypertension: a mimic of the Chiari I malformation.** *AJNR Am J Neuroradiol* 2012;33:1901–06 CrossRef Medline
12. Farb RI, Vanek I, Scott JN, et al. **Idiopathic intracranial hypertension: the prevalence and morphology of sinovenous stenosis.** *Neurology* 2003;60:1418–24 CrossRef Medline
13. Lenfeldt N, Koskinen LO, Bergenheim AT, et al. **CSF pressure assessed by lumbar puncture agrees with intracranial pressure.** *Neurology* 2007;68:155–58 CrossRef Medline
14. Bidot S, Saindane AM, Peragallo JH, et al. **Brain imaging in idiopathic intracranial hypertension.** *J Neuroophthalmol* 2015;35:400–11 CrossRef Medline
15. Agid R, Farb RI. **Neuroimaging in the diagnosis of idiopathic intracranial hypertension.** *Minerva Med* 2006;97:365–70 Medline
16. Bono F, Giliberto C, Mastrandrea C, et al. **Transverse sinus stenoses**

- persist after normalization of the CSF pressure in IIIH.** *Neurology* 2005;65:1090–93 CrossRef Medline
17. Johnson LN, Hepler RS, Bartholomew MJ. **Accuracy of papilledema and pseudopapilledema detection: a multispecialty study.** *J Fam Pract* 1991;33:381–86 Medline
18. Ballantyne SA, O'Neill G, Hamilton R, et al. **Observer variation in the sonographic measurement of optic nerve sheath diameter in normal adults.** *Eur J Ultrasound* 2002;15:145–49 CrossRef Medline
19. Ragauskas A, Bartusis L, Piper I, et al. **Improved diagnostic value of a TCD-based non-invasive ICP measurement method compared with the sonographic ONSD method for detecting elevated intracranial pressure.** *Neurol Res* 2014;36:607–14 CrossRef Medline
20. Tain RW, Bagci AM, Lam BL, et al. **Determination of cranio-spinal canal compliance distribution by MRI: methodology and early application in idiopathic intracranial hypertension.** *J Magn Reson Imaging* 2011;34:1397–404 CrossRef Medline
21. Alperin NJ, Lee SH, Loth F, et al. **MR-intracranial pressure (ICP): a method to measure intracranial elastance and pressure noninvasively by means of MR imaging: baboon and human study.** *Radiology* 2000;217:877–85 CrossRef Medline

Leukoaraiosis Attenuates Diagnostic Accuracy of Large-Vessel Occlusion Scales

 Y. Mayasi,  R.P. Goddeau Jr,  M. Moonis,  B. Silver,  A.H. Jun-O'Connell,  A.S. Puri, and  N. Henninger



ABSTRACT

BACKGROUND AND PURPOSE: Prehospital stroke scales may help identify patients likely to have large-vessel occlusion to facilitate rapid triage to thrombectomy-capable stroke centers. Scale misclassification may result in inaccurate decisions and possible harm. Pre-existing leukoaraiosis has been shown to attenuate the association between deficit type and stroke severity. We sought to determine whether leukoaraiosis affects the predictive ability of 5 commonly used large-vessel occlusion scales.

MATERIALS AND METHODS: We retrospectively analyzed 274 consecutive patients with stroke with available brain MR imaging and vessel imaging. We used the following large-vessel occlusion scales: the 3-Item Stroke Scale; Field Assessment Stroke Triage for Emergency Destination; Rapid Arterial Occlusion Evaluation; Vision, Aphasia, Neglect score; and Cincinnati Prehospital Stroke Severity Scale. For diagnostic scale accuracy, we assessed sensitivity, specificity, positive predictive value, negative predictive value, and κ . Multivariable logistic regression was used to determine the predictive ability of the scales after adjustment for leukoaraiosis and potential confounders.

RESULTS: In unadjusted analyses, all scales predicted the presence of large-vessel occlusion ($n = 46$, $P < .01$ each), though diagnostic accuracy was attenuated among patients with moderate-to-severe leukoaraiosis. After adjustment, the Field Assessment Stroke Triage for Emergency Destination (OR = 3.2; 95% CI, 1.1–9.5; $P = .033$) and Rapid Arterial Occlusion Evaluation (OR = 3.7; 95% CI, 1.3–10.8; $P = .015$), but not the 3-Item Stroke Scale (OR = 5.4; 95% CI, 0.86–33.9; $P = .073$), Vision, Aphasia, Neglect score (OR = 2.5; 95% CI, 0.8–7.2), and Cincinnati Prehospital Stroke Severity Scale (OR = 2.8; 95% CI, 1.0–8.0), predicted large-vessel occlusion.

CONCLUSIONS: The diagnostic accuracy of the tested large-vessel occlusion scales was attenuated in the presence of moderate-to-severe leukoaraiosis. This information that may aid the design of future studies that require large-vessel occlusion scale screening of patients who are likely to have concomitant leukoaraiosis.

ABBREVIATIONS: CPSSS = Cincinnati Prehospital Stroke Severity Scale; EST = endovascular stroke therapy; FAST-ED = Field Assessment Stroke Triage for Emergency Destination; LVO = large-vessel occlusion; RACE = Rapid Arterial Occlusion Evaluation; 3I/SS = 3-Item Stroke Scale; VAN = Vision, Aphasia, Neglect

Recent endovascular stroke therapy (EST) trials have shown significantly improved outcomes among patients with large-vessel occlusion (LVO).¹ Reliable prehospital identification of pa-

tients with LVO and transfer to an EST-capable center are critical because earlier treatment is associated with more favorable outcome.^{2–5}

Although the ideal prehospital triage of patients with potential LVO remains uncertain, several clinical scales have been developed to aid identification of patients likely to have an LVO before vascular imaging is available, such as in the prehospital setting or during telestroke consultations.^{6–10} However, these scales have the potential to misclassify patients.¹¹ Several factors may attenuate diagnostic accuracy of stroke scales, including stroke location in the posterior circulation, atypical presentation, and the presence of stroke mimics.^{2,12} Inaccurate LVO prediction may delay patient transfer to an endovascular center (false-negatives) with an increased risk for a worse outcome.¹³ Conversely, unwarranted patient transfer to an EST-capable hospital (false-positives) may overburden the relatively few available EST-capable centers. It is important to understand factors that

Received July 7, 2017; accepted after revision October 2.

From the Department of Neurology (Y.M., R.P.G., M.M., B.S., A.H.J.-O., N.H.), Department of Radiology, Division of Neurointerventional Radiology (A.S.P.), and Department of Psychiatry (N.H.), University of Massachusetts Medical School, Worcester, Massachusetts.

Dr Henninger is supported by K08NS091499 from the National Institute of Neurological Disorders and Stroke of the National Institutes of Health. The content is solely the responsibility of the authors and does not necessarily represent the official views of the National Institutes of Health.

Please address correspondence to Nils Henninger, MD, PhD, Departments of Neurology and Psychiatry, University of Massachusetts Medical School, 55 Lake Ave, North, Worcester, MA 01655; e-mail: nils.henninger@umassmed.edu

 Indicates open access to non-subscribers at www.ajnr.org

 Indicates article with supplemental on-line photos.

<http://dx.doi.org/10.3174/ajnr.A5473>

may increase the risk for misclassification to improve prediction accuracy.

Pre-existing leukoaraiosis is identified in most patients with stroke on brain MR imaging as white matter hyperintensities.¹⁴ Prior studies have shown that leukoaraiosis alters the classic association between the NIHSS deficit and hemispheric lateralization, relates to greater-than-expected NIHSS scores in relation to the acute infarct extent, and worsens outcome after EST.¹⁴⁻¹⁷ Because most available LVO scales are based on the NIHSS,⁶⁻¹⁰ we sought to determine whether leukoaraiosis severity affects the diagnostic accuracy of several previously developed prehospital stroke scales.⁶⁻¹⁰ We hypothesized that the diagnostic scale performance is reduced among patients with stroke with moderate-to-severe pre-existing leukoaraiosis. Clarifying this issue may aid clinical study design and choice of LVO scales to more reliably identify patients with stroke with LVO in the prehospital setting when neuroimaging data are unavailable, and it is expected that a substantial proportion of screened patients will have advanced leukoaraiosis.

MATERIALS AND METHODS

Study Cohort

We retrospectively analyzed 274 consecutive patients with acute ischemic stroke shown on brain MR imaging who were included in the University of Massachusetts Memorial Medical Center Stroke Registry between January 2013 and January 2014.^{15,18} Patient demographics, laboratory data, comorbidities, preadmission medications, and stroke pathogenesis (using the Causative Classification System for Ischemic Stroke as previously described^{15,18}) after completion of diagnostic evaluation were collected on all patients. NIHSS scores were assessed at the time of presentation by members of the stroke team certified in the NIHSS. Only patients with complete details on all NIHSS subcategories were included (On-line Fig 1). All patients underwent head CT and either CTA ($n = 249$) or MRA ($n = 25$) at admission. Ten patients underwent both CTA and MRA. To reliably determine the white matter lesion burden (leukoaraiosis), we only included patients with available brain MR imaging. Our investigation was approved by our Institutional Review Board (No. H00006964), and a Health Insurance Portability and Accountability Act waiver of informed consent was granted. We adhere to the Strengthening the Reporting of Observational Studies in Epidemiology (www.strobe-statement.org) and Standards for Reporting of Diagnostic Accuracy Studies (www.stard-statement.org) guidelines.

Neuroimaging Protocol

All MR imaging and MRA sequences were acquired on a 1.5T whole-body MR imaging scanner (Signa HD; GE Healthcare, Milwaukee, Wisconsin) between 1 and 7 days after stroke. Brain MR imaging sequences included T1, T2, FLAIR, and DWI. DWI was performed with echo-planar imaging with a TR of 8000 ms, TE of 102 ms, FOV of 22×22 cm, image matrix of 128×128 , slice thickness of 5 mm with a 1-mm interslice gap, and b-values of 0 and 1000 s/mm^2 . FLAIR was performed with a TR of 9002 ms, TE of 143 ms, FOV of 22×22 cm, image matrix of 256×224 , and slice thickness of 6 mm with a 1-mm interslice gap. All MRA was

performed with TOF-echo-spoiled gradient-echo pulse sequences. Head MRA was performed with a TR of 25 ms, flip angle of 20° , FOV of 20 cm, matrix of 256×224 , and slice thickness of 1.4 mm. Neck MRA performed with contrast used a TE of 1.8, flip angle of 45° , FOV of 33, slice thickness of 1 mm, and matrix of 28.4×22.4 cm. Patients received 20 mL of gadobenate dimeglumine (MultiHance; Bracco Diagnostics, Princeton, New Jersey). Neck MRA was performed without contrast with a TR of 24 ms, TE of 5.1 ms, flip angle of 60° , FOV of 20, slice thickness of 1.5 mm, and matrix of 512×160 .

All CT sequences were obtained on a 64-detector row scanner (Brilliance; Philips Healthcare, Best, the Netherlands).^{17,19} CT was performed in a nonhelical mode at 120 kV(peak) and 200 mA, with data reconstruction at 5-mm axial sections. CTA was performed using a 64×0.625 mm detector configuration with a pitch of 0.673 from the arch of the aorta to the vertex using 120 kV(p), 300 mA, and 0.5-second rotation time. Patients received 60–80 mL of iopamidol (Isovue 370; Bracco Diagnostics) in the antecubital vein at a rate of 4 mL/s through a power injector, followed by 40 mL of saline. 3D orthogonal MIP images were created in 3 planes.

Leukoaraiosis Grading

In all patients, leukoaraiosis was defined on MR imaging as supratentorial white matter FLAIR hyperintensity lesions according to the Standards for Reporting Vascular Changes on Neuroimaging²⁰ criteria and graded according to the Fazekas scale as previously described in detail.^{14,15} The total Fazekas scale score was calculated by adding the periventricular and subcortical scores.¹⁴ We have previously shown substantial interrater reliability with an intraclass correlation coefficient of 0.969 (95% CI, 0.943–0.983).¹⁴ In addition, we dichotomized the degree of leukoaraiosis according to the median Fazekas scale score to 0–2 ($n = 145$, absent-to-mild leukoaraiosis) versus 3–6 ($n = 129$, moderate-to-severe leukoaraiosis) for statistical purposes.

Definition of Large-Vessel Occlusion

Large-vessel occlusion was defined on the admission CTA or MRA as the presence of an apparent occlusion of the intracranial internal carotid artery and proximal middle cerebral artery (M1). The included prehospital stroke scales were not designed to assess the presence of occlusion in the distal MCA (M2), basilar, and intracranial vertebral arteries. Therefore, occlusion in these vessels was considered non-LVO for this study, and only considered in the exploratory analyses. All images were reviewed by a neuro-radiologist as part of the routine clinical work-up. The site of the LVO was abstracted from the radiologic report and by cross-validating with the original scans by one of the authors (Y.M.), who was masked to clinical data. Discrepant interpretations were resolved by consensus after review by a second neurologist (N.H.).

Prehospital Stroke Scales

To determine the impact of pre-existing leukoaraiosis on LVO prediction, we examined 5 previously published scales that could be reliably reconstructed by abstraction from the admission NIHSS score sheet and the detailed neurologic examination documented in our medical records. We used the following addi-

Table 1: Baseline characteristics (unadjusted) of the studied patient population as stratified by the presence-versus-absence of proximal LVO^a

Characteristics	All Patients (n = 274)	LVO (n = 46)	No LVO (n = 228)	P Value
Age (yr)	69 (60–80)	68 (58–77)	70 (60–81)	.347
Female sex	126 (46%)	24 (52%)	102 (45%)	.418
Admission NIHSS score	5 (2–10)	14 (4–17)	4 (2–9)	<.001
Prestroke mRS	0 (0–1)	0 (0–1)	0 (0–1)	.774
LVO stroke scale scores				
3I/SS	1 (0–2)	2 (1–3)	1 (0–2)	<.001
VAN	0 (1–2)	3 (0–4)	0 (0–2)	<.001
CPSSS	0 (0–1)	1 (0–3)	0 (0–1)	.001
FAST-ED	2 (0–4)	4 (2–6)	1 (0–3)	<.001
RACE	2 (0–4)	5 (1–7)	1 (0–3)	<.001
Laboratory data				
Admission glucose level (mg/dL)	119 (100–142)	120 (105–143)	119 (99–142)	.515
Admission creatinine level (mg/dL)	0.95 (0.78–1.20)	0.90 (0.73–1.0)	0.97 (0.79–1.20)	.090
HbA1c level (%) (n = 161)	5.9 (5.7–6.5)	6.0 (5.6–6.3)	5.9 (5.7–6.6)	.794
LDLc level (mg/dL) (n = 171)	93 (72–123)	89 (65–111)	94 (74–123)	.274
Neuroimaging				
Fazekas scale score (0–2)	129 (48%)	30 (65%)	99 (43%)	.009
Pre-existing risk factors				
Hypertension	210 (77%)	34 (74%)	176 (77%)	.703
Hyperlipidemia	152 (56%)	26 (57%)	132 (58%)	.076
Diabetes	75 (27%)	11 (24%)	64 (28%)	.594
Prior stroke or TIA	59 (22%)	6 (13%)	53 (23%)	.168
Atrial fibrillation	42 (15%)	8 (17%)	34 (15%)	.823
Coronary artery disease	58 (21%)	4 (9%)	54 (24%)	.028
Congestive heart failure	20 (7%)	1 (2%)	19 (8%)	.215
Peripheral arterial disease	18 (7%)	1 (2%)	17 (8%)	.221
Preadmission medications				
Statin	124 (45%)	19 (41%)	105 (46%)	.689
Antihypertensive	185 (67%)	32 (70%)	153 (67%)	.863
Antiglycemic	53 (19%)	9 (20%)	44 (19%)	1.000
Antiplatelets	145 (53%)	24 (52%)	121 (53%)	1.000
Oral anticoagulant	19 (7%)	4 (9%)	15 (7%)	.749

Note:—HbA1c indicates glycated hemoglobin A1c; LDLc, low-density lipoprotein cholesterol.

^a Proximal LVO is defined as an occlusion of the internal carotid artery or middle cerebral artery M1 segment. Data are No. (%) or median (25th–75th percentile).

tional prespecified rules for derivation of the scores because we previously found that severe leukoaraiosis substantially attenuates the classic hemispheric lateralization of the NIHSS deficit¹⁵: If both sides were weak, the weaker side determined the sign scored; and if both sides were equally weak, the presence of the sign was scored.

The Field Assessment Stroke Triage for Emergency Destination (FAST-ED) was calculated on the basis of the presence of facial palsy (scored 0–1), arm weakness (0–2), speech changes (0–2), eye deviation (0–2), and denial/neglect (0–2). A score of ≥ 4 was considered suggestive of LVO.⁹ The Rapid Arterial Occlusion Evaluation (RACE) was calculated on the basis of the presence of facial palsy (0–2), arm motor function (0–2), leg motor function (0–2), gaze (0–1), and aphasia or agnosia (0–2). A score ≥ 5 was considered indicative of LVO.⁸ The Vision, Aphasia, Neglect (VAN) score was calculated on the basis of the presence of arm motor weakness (0–1) plus the presence of visual disturbance (blindness, field cut, diplopia [0–1]), aphasia (0–1), and neglect (including forced gaze deviation [0–1]). In the absence of arm weakness, the patient received a score of zero. A score ≥ 2 was considered indicative of LVO.⁶ The Cincinnati Prehospital Stroke Severity Scale (CPSSS) was calculated on the basis of the presence of conjugate gaze deviation, (0–2), arm weakness (0–1), and impaired consciousness (0–1). A score of ≥ 2 was considered indic-

ative of LVO.¹⁰ The 3-Item Stroke Scale (3I/SS) was calculated on the basis of the level of consciousness (0–2), gaze deviation (0–2), and hemiparesis (0–2). A score ≥ 4 was considered indicative of LVO.⁷

Statistics

Unless otherwise stated, continuous variables are reported as mean \pm SD or median (25th–75th percentile). Categorical variables are reported as proportions. Between-group comparisons for continuous and ordinal variables were performed with the Mann-Whitney *U* test. Categorical variables were compared using the χ^2 test or Fisher exact test as appropriate. To determine the diagnostic accuracy of the LVO scales, we calculated the area under receiver operating curves (C statistics, ordinal scales) as well as sensitivity, specificity, positive predictive value, negative predictive value, and κ (dichotomized scales each) with corresponding 95% CIs.

We created multivariable logistic regression models to determine whether the tested LVO scale cutoffs predicted large-artery occlusion (dependent variable) independent of leukoaraiosis (as determined by the Fazekas scale score). All models were adjusted for factors known to be associated with leukoaraiosis, including age, sex, and preadmission

mRS and a history of hypertension, stroke/TIA, and atrial fibrillation. In addition, models were adjusted for the Fazekas scale score \times LVO Scale Interaction to determine whether the leukoaraiosis burden differentially modified the predictive ability of the tested scales. Variables were sequentially removed (likelihood ratio) from the models at a significance level of 0.1 to avoid model overfitting. Collinearity diagnostics were performed (and its presence rejected) for all multivariable regression models. The Hosmer-Lemeshow goodness-of-fit statistic was used to assess model fit.

Two-sided significance tests were used throughout; unless stated otherwise, a 2-sided $P < .05$ was considered statistically significant. All statistical analyses were performed with SPSS, Version 22 (IBM, Armonk, New York).

RESULTS

Of 502 patients with ischemic stroke, 274 fulfilled the study criteria and were included in the analysis (On-line Fig 1).

Baseline characteristics of included patients stratified by the presence of LVO are summarized in Table 1. Overall, 46 patients had a proximal LVO (17%), and 228 (83%) patients had no LVO. Baseline characteristics of the included patients were well-balanced except for a higher NIHSS ($P < .001$) and Fazekas scale score ($P = .009$) among patients with LVO. The relative distribu-

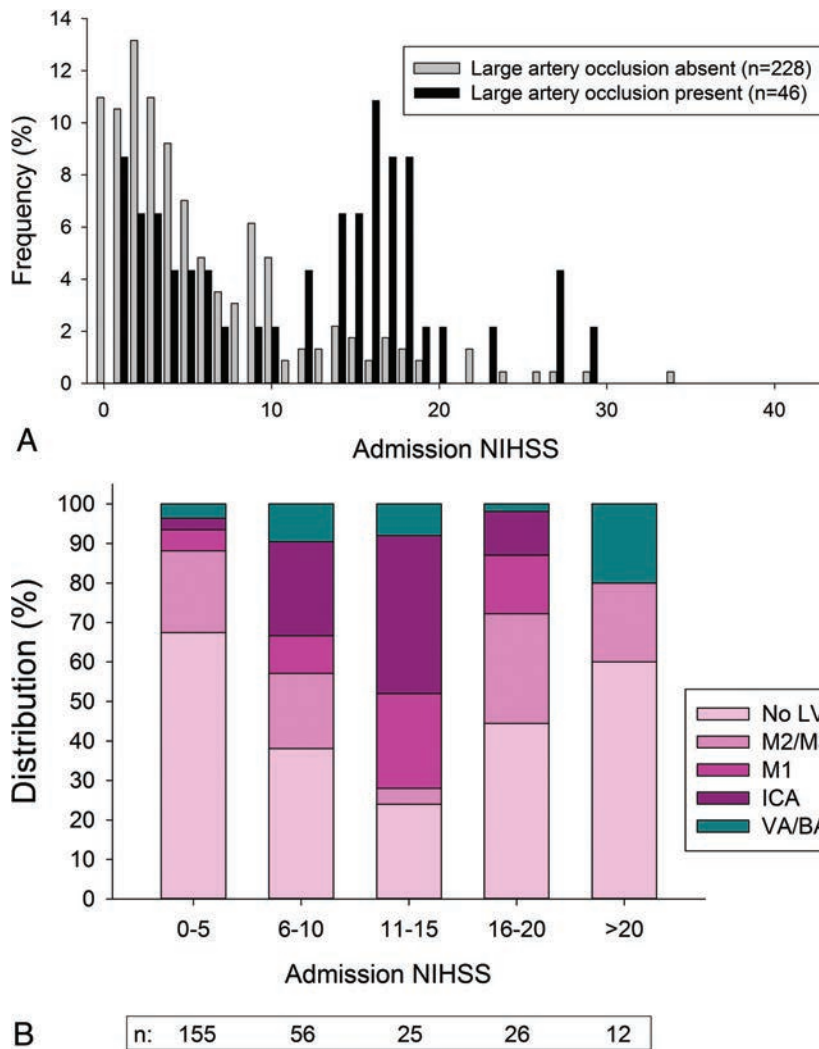


FIGURE. NIHSS and LVO distribution in the tested cohort. *A*, Relative frequency of NIHSS scores as stratified by the presence-versus-absence of large-artery occlusion. *B*, Distribution of NIHSS scores according to large-artery occlusion status. There was no difference in the distribution of NIHSS scores (bins) between subjects with absent-to-mild versus moderate-to-severe leukoaraiosis ($P = .319$, χ^2 test).

tion of the NIHSS scores and types of arterial occlusion in the included patients are summarized in the Figure.

On-line Fig 2 shows the percentage of LVO cases that would have gone unidentified across different LVO score thresholds. On average, more cases would have gone unnoticed in patients with moderate-to-severe leukoaraiosis compared with those with only absent-to-mild leukoaraiosis.

Table 2 summarizes the diagnostic accuracy of the established LVO scale cutoffs both in the entire cohort and when stratified by leukoaraiosis. Overall, the diagnostic accuracy was modest in the entire cohort and further attenuated among patients with moderate-to-severe leukoaraiosis.

We calculated the area under receiver operating curve to examine the diagnostic performance of the 5 tested prehospital LVO scales for the presence of a proximal LVO as an ordinal variable in the entire cohort as well as stratified by leukoaraiosis burden (On-line Fig 3A–C). All scales predicted LVO in the entire cohort ($P < .01$ each, Table 3) and in patients with absent-to-mild leukoaraiosis ($P < .001$ each). However, none

predicted LVO among patients with moderate-to-severe leukoaraiosis ($P > .05$ each). Results did not meaningfully change when the definition of LVO was liberalized to include MCA-M2, vertebral artery, and basilar artery occlusions (On-line Fig 3D–F). Last, results were similar in exploratory analyses excluding patients with small subcortical infarcts as well as those with posterior circulation infarcts (not shown).

Finally, on multivariable logistic regression with adjustment for leukoaraiosis and potential confounders, we found that despite an overall similar direction of association of all scales, only the FAST-ED and RACE scales predicted LVO (Table 3). In all models, leukoaraiosis severity was independently associated with the presence of LVO ($P < .05$, each). No Leukoaraiosis \times LVO Scale Interaction was found in the examined models.

DISCUSSION

The goal of our study was to determine whether the diagnostic accuracy of previously validated prehospital LVO stroke scales is affected by the presence of leukoaraiosis—knowledge that may aid investigators in choosing scales that allow more reliable patient screening in the prehospital setting. Using a hospital-based acute ischemic stroke cohort, we found that the diagnostic accuracy of several LVO scales was attenuated among patients with severe leukoaraiosis. After we adjusted for leukoaraiosis

severity and potential confounders, only 2 of the 5 tested scales (FAST-ED and RACE) predicted LVO.

Prehospital stroke scales have been developed to aid stroke recognition and prediction of LVO by non-stroke specialists when neuroimaging information is unavailable. Our results may aid the clinical study design when prehospital patient screening involves LVO scales, and it is expected that a substantial proportion of patients are likely to have leukoaraiosis. If confirmed, our data suggest that in such a setting, scales like the FAST-ED and RACE may be advantageous because they appeared less impervious to leukoaraiosis-related misclassification. Furthermore, LVO scales are increasingly used to render decisions regarding immediate patient transfer to EST-capable hospitals when LVO is suspected,^{13,21–23} including in the setting of telemedicine consultations.²⁴ In this setting, our results may be impactful when a plain head CT is reviewed (and provides information on leukoaraiosis severity) but no CTA was obtained due to lack of resources or immedi-

Table 2: Diagnostic accuracy of prehospital stroke scales in predicting LVO stratified by leukoaraiosis severity^a

Scale	Sensitivity (%)	Specificity (%)	PPV (%)	NPV (%)	κ
Total cohort (n = 274)					
3I/SS \geq 4	22 (11–36)	90 (86–94)	31 (19–47)	85 (83–87)	0.14 (0–0.28)
VAN \geq 2	70 (54–82)	63 (57–69)	28 (23–33)	91 (87–94)	0.20 (0.10–0.30)
CPSSS \geq 2	41 (27–57)	79 (74–84)	29 (19–47)	87 (84–90)	0.18 (0.05–0.31)
RACE \geq 5	50 (35–65)	85 (80–89)	40 (31–51)	89 (86–92)	0.32 (0.18–0.46)
FAST-ED \geq 4	57 (41–71)	79 (73–84)	35 (27–43)	90 (83–87)	0.28 (0.15–0.41)
Absent-to-mild leukoaraiosis (Fazekas scale score, 0–2; n = 129)					
3I/SS \geq 4	50 (21–79)	88 (80–94)	33 (18–52)	94 (89–96)	0.09 (0–0.27)
VAN \geq 2	73 (54–88)	68 (58–77)	41 (32–50)	89 (82–94)	0.32 (0.16–0.48)
CPSSS \geq 2	37 (20–56)	87 (79–93)	46 (30–63)	82 (77–86)	0.25 (0.06–0.45)
RACE \geq 5	53 (34–72)	91 (83–96)	64 (46–78)	87 (81–90)	0.47 (0.29–0.65)
FAST-ED \geq 4	57 (37–75)	84 (75–90)	52 (38–65)	86 (81–91)	0.39 (0.09–0.57)
Moderate-to-severe leukoaraiosis (Fazekas scale score, 3–6; n = 145)					
3I/SS \geq 4	25 (7–52)	92 (86–96)	29 (12–53)	91 (88–93)	0.18 (0–0.41)
VAN \geq 2	63 (35–85)	60 (51–68)	16 (11–23)	93 (87–96)	0.10 (0–0.22)
CPSSS \geq 2	50 (25–75)	74 (65–81)	19 (12–29)	92 (88–95)	0.14 (0–0.29)
RACE \geq 5	44 (20–70)	81 (73–87)	22 (13–35)	92 (88–94)	0.17 (0–0.35)
FAST-ED \geq 4	56 (30–80)	74 (66–82)	21 (14–32)	93 (89–96)	0.11 (0–0.27)

Note:—NPV indicates negative predictive value; PPV, positive predictive value.

^aData in parentheses are 95% CI.

Table 3: Multivariable logistic regression analysis for the ability of previously defined clinical stroke scale cutoffs to predict large-vessel occlusion in the examined cohort

Stroke Scale	Crude OR (95% CI)	P Value	Adjusted OR (95% CI) ^a	P Value
3I/SS \geq 4	4.736 (1.513–14.826)	.008	5.389 (0.856–33.908)	.073
VAN \geq 2	3.918 (1.979–7.760)	<.001	2.468 (0.845–7.206)	.098
CPSSS \geq 2	2.710 (1.388–5.290)	.003	2.794 (0.973–8.028)	.056
RACE \geq 5	5.706 (2.881–11.299)	<.001	3.236 (1.099–9.527)	.033
FAST-ED \geq 4	4.749 (2.447–9.217)	<.001	3.740 (1.291–10.839)	.015

^aEach model was adjusted for leukoaraiosis burden (as determined by the Fazekas scale score) as well as Leukoaraiosis \times Stroke Scale Interaction. When additionally entered into the model, the prestroke modified Rankin Scale, age, sex, hypertension, history of stroke/transient ischemic attack, and atrial fibrillation were not retained in the final step of the analysis. In all analyses, leukoaraiosis and stroke scales were entered as dichotomized variables. When all analyses were repeated by entering the Fazekas scale score and stroke scale scores as ordinal variables, the VAN ($P = .029$), CPSSS ($P = .024$), FAST-ED ($P = .003$), RACE ($P = .002$), and 3I/SS ($P = .006$) scores predicted LVO independent of the leukoaraiosis burden (not shown). There was no Leukoaraiosis \times Stroke Scale Interaction in any of the examined models ($P > .05$, each).

ate availability or because repeat CTA is not desirable to avoid repeat imaging at the EST-capable hub hospital.^{25,26} Leukoaraiosis has been repeatedly shown to confer an increased risk of poor outcome in patients with LVO, including those undergoing EST.^{17,19} Arguably, the presence of severe leukoaraiosis could thus prompt CTA at an outside hospital (versus transfer without CTA) to minimize the cost associated with unnecessary transfers.²⁷ However, to date, no study has shown that patients with severe leukoaraiosis do not benefit from EST. Accordingly, our data should not direct medical decision-making. Nevertheless, one could envision that the presence of specific, yet-to-be-defined, clinical patient characteristics trigger “prescreening” of patients with CTA to aid transfer decisions. Such factors may be very old age, pre-stroke functional status, and cognitive impairment, which have been associated with leukoaraiosis and limited benefit from EST.²⁸

The strengths of our study relate to inclusion of consecutive patients with available MR imaging, imaging assessment by experienced examiners, and adjustment for important factors associated with leukoaraiosis and stroke severity. Limitations relate to the retrospective and observational nature of the study, as well as the inclusion of a moderately sized single-

center cohort. In this respect, the overall diagnostic accuracy of the tested scales was only modest in our cohort. This result may be partially explained by our hospital-based study, which only included patients with proved stroke and who had available vessel imaging because the diagnostic accuracy is sensitive to the characteristics (disease prevalence and spectrum) of the tested population. Nevertheless, our results are in line with observations from other hospital-based studies suggesting generalizability of our results.^{29,30} Last, due to our study design,

we only examined LVO stroke scales based on the NIHSS. Accordingly, our results may not translate to other scales and should be interpreted cautiously.

CONCLUSIONS

Our results indicate that the presence of moderate-to-severe leukoaraiosis attenuates the diagnostic accuracy of available LVO scales and that the RACE and FAST-ED scales appeared more resilient to the confounding effects of leukoaraiosis. If confirmed in a larger cohort, this information may aid the design of studies that require prehospital LVO scale screening of patients likely to have concomitant leukoaraiosis.

Disclosures: Brian Silver—UNRELATED: Consultancy: Women’s Health Initiative, National Institutes of Health; Employment: Joint Commission; Expert Testimony, Comments: medicolegal malpractice; Patents (Planned, Pending or Issued): transcranial magnetic stimulation; Payment for Development of Educational Presentations: Ebix, MedLink, Medscape. Ajit Puri—UNRELATED: Consultancy: Stryker, Codman; Grants/Grants Pending: Stryker, Medtronic, Comments: research grants*; Payment for Lectures Including Service on Speakers Bureaus: Stryker; Stock/Stock Options: InNeuroCo. Nils Henninger—RELATED: Grant: National Institute of Neurological Disorders and Stroke, Comments: K08*; UNRELATED: Board Membership: OmnioX, Comments: Advisory Board member; Other: Oak Ridge Associated Universities, Comments: ad hoc reviewer. *Money paid to the institution.

REFERENCES

1. Goyal M, Hill MD, Saver JL, et al. **Challenges and opportunities of endovascular stroke therapy.** *Ann Neurol* 2016;79:11–17 CrossRef Medline
2. Zhao H, Coote S, Pesavento L, et al. **Large vessel occlusion scales increase delivery to endovascular centers without excessive harm from misclassifications.** *Stroke* 2017;48:568–73 CrossRef Medline
3. Skagen K, Skjelland M, Russell D, et al. **Large-vessel occlusion stroke: effect of recanalization on outcome depends on the National Institutes of Health Stroke Scale score.** *J Stroke Cerebrovasc Dis* 2015;24:1532–39 CrossRef Medline
4. Saver JL, Goyal M, van der Lugt A, et al; HERMES Collaborators. **Time to treatment with endovascular thrombectomy and outcomes from ischemic stroke: a meta-analysis.** *JAMA* 2016;316:1279–88 CrossRef Medline
5. Chen CJ, Ding D, Starke RM, et al. **Endovascular vs medical management of acute ischemic stroke.** *Neurology* 2015;85:1980–90 CrossRef Medline
6. Teles MS, Ver Hage A, Carter J, et al. **Stroke vision, aphasia, neglect (VAN) assessment—a novel emergent large vessel occlusion screening tool: pilot study and comparison with current clinical severity indices.** *J Neurointerv Surg* 2017;9:122–26 CrossRef Medline
7. Singer OC, Dvorak F, du Mesnil de Rochemont R, et al. **A simple 3-item stroke scale: comparison with the National Institutes of Health Stroke Scale and prediction of middle cerebral artery occlusion.** *Stroke* 2005;36:773–76 CrossRef Medline
8. Pérez de la Ossa N, Carrera D, Gorchs M, et al. **Design and validation of a prehospital stroke scale to predict large arterial occlusion: the rapid arterial occlusion evaluation scale.** *Stroke* 2014;45:87–91 CrossRef Medline
9. Lima FO, Silva GS, Furie KL, et al. **Field assessment stroke triage for emergency destination: a simple and accurate prehospital scale to detect large vessel occlusion strokes.** *Stroke* 2016;47:1997–2002 CrossRef Medline
10. Katz BS, McMullan JT, Sucharew H, et al. **Design and validation of a pre-hospital scale to predict stroke severity: Cincinnati Prehospital Stroke Severity Scale.** *Stroke* 2015;46:1508–12 CrossRef Medline
11. Scheitz JF, Abdul-Rahim AH, MacIsaac RL, et al. **Clinical selection strategies to identify ischemic stroke patients with large anterior vessel occlusion: results from SITS-ISTR (Safe Implementation of Thrombolysis in Stroke International Stroke Thrombolysis Registry).** *Stroke* 2017;48:290–97 CrossRef Medline
12. Kasner SE. **Clinical interpretation and use of stroke scales.** *Lancet Neurol* 2006;5:603–12 CrossRef Medline
13. Mohamad NF, Hastrup S, Rasmussen M, et al. **Bypassing primary stroke centre reduces delay and improves outcomes for patients with large vessel occlusion.** *Eur Stroke J* 2016;1:85–92 CrossRef
14. Helenius J, Henninger N. **Leukoaraiosis burden significantly modulates the association between infarct volume and National Institutes of Health Stroke Scale in ischemic stroke.** *Stroke* 2015;46:1857–63 CrossRef Medline
15. Helenius J, Goddeau RP Jr, Moonis M, et al. **Impact of leukoaraiosis burden on hemispheric lateralization of the National Institutes of Health Stroke Scale deficit in acute ischemic stroke.** *Stroke* 2016;47:24–30 CrossRef Medline
16. Onteddu SR, Goddeau RP Jr, Minaeian A, et al. **Clinical impact of leukoaraiosis burden and chronological age on neurological deficit recovery and 90-day outcome after minor ischemic stroke.** *J Neurol Sci* 2015;359:418–23 CrossRef Medline
17. Zhang J, Puri AS, Khan MA, et al. **Leukoaraiosis predicts a poor 90-day outcome after endovascular stroke therapy.** *AJNR Am J Neuroradiol* 2014;35:2070–75 CrossRef Medline
18. Henninger N, Goddeau RP Jr, Karmarkar A, et al. **Atrial fibrillation is associated with a worse 90-day outcome than other cardioembolic stroke subtypes.** *Stroke* 2016;47:1486–92 CrossRef Medline
19. Henninger N, Lin E, Baker SP, et al. **Leukoaraiosis predicts poor 90-day outcome after acute large cerebral artery occlusion.** *Cerebrovasc Dis* 2012;33:525–31 CrossRef Medline
20. Wardlaw JM, Smith EE, Biessels GJ, et al; Standards for Reporting Vascular changes on nEuroimaging (STRIVE v1). **Neuroimaging standards for research into small vessel disease and its contribution to ageing and neurodegeneration.** *Lancet Neurol* 2013;12:822–38 CrossRef Medline
21. Rinaldo L, Brinjikji W, Rabinstein AA. **Transfer to high-volume centers associated with reduced mortality after endovascular treatment of acute stroke.** *Stroke* 2017;48:1316–21 CrossRef Medline
22. Southerland AM, Johnston KC, Molina CA, et al. **Suspected large vessel occlusion: should emergency medical services transport to the nearest primary stroke center or bypass to a comprehensive stroke center with endovascular capabilities?** *Stroke* 2016;47:1965–67 CrossRef Medline
23. Nogueira RG, Silva GS, Lima FO, et al. **The FAST-ED App: a smartphone platform for the field triage of patients with stroke.** *Stroke* 2017;48:1278–84 CrossRef Medline
24. Akbik F, Hirsch JA, Chandra RV, et al. **Telestroke—the promise and the challenge, Part one: growth and current practice.** *J Neurointerv Surg* 2017;9:357–60 CrossRef Medline
25. Srivastava PV, Sudhan P, Khurana D, et al. **Telestroke a viable option to improve stroke care in India.** *Int J Stroke* 2014;9(suppl A100):133–34 CrossRef Medline
26. Schwamm LH, Rosenthal ES, Hirshberg A, et al. **Virtual TeleStroke support for the emergency department evaluation of acute stroke.** *Acad Emerg Med* 2004;11:1193–97 CrossRef Medline
27. Liang JW, Stein L, Wilson N, et al. **Timing of vessel imaging for suspected large vessel occlusions does not affect groin puncture time in transfer patients with stroke.** *J Neurointerv Surg* 2017 Jan 24. [Epub ahead of print] CrossRef Medline
28. Khan MA, Baird GL, Miller D, et al. **Endovascular treatment of acute ischemic stroke in nonagenarians compared with younger patients in a multicenter cohort.** *J Neurointerv Surg* 2017;9:727–31 CrossRef Medline
29. Heldner MR, Hsieh K, Broeg-Morway A, et al. **Clinical prediction of large vessel occlusion in anterior circulation stroke: mission impossible?** *J Neurol* 2016;263:1633–40 CrossRef Medline
30. Hastrup S, Damgaard D, Johnsen SP, et al. **Prehospital acute stroke severity scale to predict large artery occlusion: design and comparison with other scales.** *Stroke* 2016;47:1772–76 CrossRef Medline

The Role of Hemodynamics in Intracranial Bifurcation Arteries after Aneurysm Treatment with Flow-Diverter Stents

 A.P. Narata,  F.S. de Moura,  I. Larrabide,  C.M. Perrault,  F. Patat,  R. Bibi,  S. Velasco,  A.-C. Januel,  C. Cognard,  R. Chapot,  A. Bouakaz,  C.A. Sennoga, and  A. Marzo



ABSTRACT

BACKGROUND AND PURPOSE: Treatment of intracranial bifurcation aneurysms with flow-diverter stents can lead to caliber changes of the distal vessels in a subacute phase. This study aims to evaluate whether local anatomy and flow disruption induced by flow-diverter stents are associated with vessel caliber changes in intracranial bifurcations.

MATERIALS AND METHODS: Radiologic images and demographic data were acquired for 25 patients with bifurcation aneurysms treated with flow-diverter stents. Whisker plots and Mann-Whitney rank sum tests were used to evaluate if anatomic data and caliber changes could be linked. Symmetry/asymmetry were defined as diameter ratio ≥ 1 = symmetric and diameter ratio < 1 = asymmetric. Computational fluid dynamics was performed on idealized and patient-specific anatomies to evaluate flow changes induced by flow-diverter stents in the jailed vessel.

RESULTS: Statistical analysis identified a marked correspondence between asymmetric bifurcation and caliber change. Symmetry ratios were lower for cases showing narrowing or subacute occlusion (medium daughter vessel diameter ratio = 0.59) compared with cases with posttreatment caliber conservation (medium daughter vessel diameter ratio = 0.95). Computational fluid dynamics analysis in idealized and patient-specific anatomies showed that wall shear stress in the jailed vessel was more affected when flow-diverter stents were deployed in asymmetric bifurcations (diameter ratio < 0.65) and less affected when deployed in symmetric anatomies (diameter ratio ~ 1.00).

CONCLUSIONS: Anatomic data analysis showed statistically significant correspondence between caliber changes and bifurcation asymmetry characterized by diameter ratio < 0.7 ($P < .001$). Similarly, computational fluid dynamics results showed the highest impact on hemodynamics when flow-diverter stents are deployed in asymmetric bifurcations (diameter ratio < 0.65) with noticeable changes on wall shear stress fields. Further research and clinical validation are necessary to identify all elements involved in vessel caliber changes after flow-diverter stent procedures.

ABBREVIATIONS: DR = daughter vessel diameter ratio; FDS = flow-diverter stent; WSS = wall shear stress

Endovascular treatment of intracranial aneurysms by using a flow-diverter stent (FDS) is a widely accepted technique for complex proximal aneurysms. The successful use of FDSs in voluminous carotid aneurysms was the motivation for extending this treatment to complex lesions like hemorrhagic vertebral artery dissections, blister aneurysms, and complex MCA aneu-

rysms.^{1,2} From a review of 106 reported cases in which bifurcation aneurysms were treated with FDSs, it was found that the bifurcating branch “jailed” by the stent remained unchanged in 30%–57% of cases, narrowing occurred in 29%–60.8% of cases, and occlusion occurred in 8.27%–25% of cases.^{3–8} Although the sample size is relatively small, it is worth noting that nearly two-thirds of jailed arteries were narrower after FDS treatment, which can lead to severe consequences. Depending on collateralization, permanent neurologic impairment can appear after FDS treatment, affecting 0%–27% of patients. MR imaging–positive ischemic lesions were detected in 43%–64% of the patients.^{4,6}

Please address correspondence to Ana Paula Narata, MD, Service of Neuroradiology, University Hospital of Tours, 2 Blvd Tonnelles, 37000 Tours, France; e-mail: ana-paula.narata@chu-tours.fr

 Indicates article with supplemental on-line table.

 Indicates article with supplemental on-line photo.

<http://dx.doi.org/10.3174/ajnr.A5471>

Received June 20, 2017; accepted after revision October 2.

From the University Hospital of Tours (A.P.N., R.B.), Tours, France; Engineering, Modeling, and Applied Social Sciences Center (F.S.d.M.), Federal University of ABC, Santo André, Brazil; PLADEMA-CONICET (I.L.), Universidad Nacional del Centro de la Provincia de Buenos Aires, Tandil, Argentina; Mechanical Engineering Department, INSIGNEO Institute for in Silico Medicine (C.M.P., A.M.), University of Sheffield, Sheffield, United Kingdom; UMR “Imagerie et Cerveau,” Inserm U930 (F.P., A.B., C.A.S.), Université François Rabelais, Tours, France; University Hospital of Poitiers (S.V.), Poitiers, France; University Hospital of Toulouse (A.-C.J., C.C.), Toulouse, France; and Alfried Krupp Krankenhaus (R.C.), Essen, Germany.

This work was supported by the Newton Programme Fund from the Royal Academy of Engineering, London, United Kingdom.

The reason some branches remain unchanged and others are affected by a narrowing process is unknown. Iosif and colleagues^{6,9} have linked episodes of FDS-induced vessel occlusions with the presence of collateral branches that would increase blood supply to the target tissues when resistance to flow increases in the occluding vessel. This would ultimately lead to the occlusion of the jailed vessel. Supported by animal-model data, this theory proposes collateral blood supply and endothelial cell coverage of the stent at the ostium (where the stent jails the daughter vessel) as a mechanism leading to complete vessel occlusion. However, this would only explain some but not the entire cohort of cases reporting vessel subacute occlusion or narrowing. For instance, the same theory cannot explain why FDS treatment of intracranial aneurysms near the anterior choroidal artery, ophthalmic artery, and some MCA bifurcations, all benefiting from collateral supply, often lead to the successful conservation of patency of the jailed artery.^{5,10} It thus seems that other factors are at play in those cases. Because it is well known that hemodynamics is a key element in endothelial flow-mediated vasodilation and vasoconstriction, we explored hemodynamic disturbance after FDS procedures in idealized and patient-specific anatomies.

MATERIALS AND METHODS

The research hypothesis is that pretreatment hemodynamics are perturbed in those cases showing partial or complete occlusion of the unstented daughter vessel. The methodology of the study was developed to test this hypothesis and structured within 3 different phases: radiologic data analysis to identify possible associations with clinical outcome in our patient datasets (phase I), idealized geometry computational fluid dynamics study (phase II), and patient-specific computational fluid dynamics study to characterize the influence of FDS on hemodynamics at bifurcations of different types (phase III).

Phase I: Radiologic Data Analysis

Clinical data were collected cooperatively between the University Hospitals of Tours, Toulouse, and Poitiers, France, and Alfried Krupp Krankenhaus, Germany. A total of 25 patients with bifurcation aneurysms treated with FDSs between December 2010 and December 2015 were identified retrospectively and followed prospectively upon appropriate ethical approval and patient consent. Only anterior communicating artery aneurysms with agenesis of the contralateral anterior cerebral artery, basilar artery aneurysms with bilateral hypoplasia of the posterior communicating arteries, and MCA aneurysms were included.

Radiologic imaging data and clinical outcome at baseline and at 3-month follow-up were obtained from the patient medical records. The On-line Table shows the demographic constitution of the study population along with anatomic information and clinical outcome. Anatomic data represent the average values of measurements performed on the pre-FDS imaging data, which were assessed independently by 3 senior neuroradiologists who were kept unaware of the study outcomes. Three vessel diameter and angle measurements were taken along the initial part of each bifurcating branch, reporting only its arithmetic average value and their standard deviation to quantify interobserver variability. Vessel diameters and angles were measured from 2D acquisitions

by digital subtraction angiography and 3D rotational angiography images by using OsiriX (<http://www.osirix-viewer.com>). The reliability of these measures was assessed with 2-way, mixed intraclass correlation coefficients showing high reliability (intraclass correlation coefficients [$3, \kappa$] = 0.971).

Statistical analysis included the comparison of the daughter vessel diameter ratios (DRs; ratios between smaller and larger diameters) and bifurcating angles for 2 groups: Group A ($n = 14$) included cases where narrowing or subacute occlusion of the jailed artery was observed at 3-month follow-up, and Group B ($n = 11$) included cases showing no caliber changes of the jailed artery at baseline or 3-month follow-up. Because data were not normally distributed, a Mann-Whitney rank sum test was performed to quantify statistical differences between DR and angle distributions in the 2 groups.

Phase II: Idealized Computational Fluid Dynamics Study

We created a number of idealized 3D geometries representative of patient-specific anatomies to allow a controlled analysis of the sensitivity to factors influencing hemodynamics. For all idealized cases, parent vessel diameter was set to 2.51 mm to represent the average size of the population in the On-line Table. Inlet and outlet lengths were set to 10 and 4 times the parent vessel diameter, respectively.

DR was varied between 0.4 and 1 (DR = 1 = symmetrical). Mutual bifurcation diameters were defined in accordance with Murray's law, an established theory in biomechanics regulating the relationship of bifurcating vessel diameters and based on minimal energy consumption.¹¹

Daughter vessel angles were fixed at 120°, except for some of the symmetric bifurcation cases (DR = 1), in which the angle for only 1 of the bifurcating vessels was set at 60°, 90°, 120°, and 150° to capture their effect of the angles on flow distribution across the bifurcation (Fig 1, line iv).

Stents were virtually deployed in the idealized geometries by using an approach previously described by Larrabide et al,¹² leading to a total of 3 configurations for each bifurcation type (unstented, stented along smaller daughter vessel d_1 , and stented along larger daughter vessel d_2). FDS models represent typical geometries available on the market. In particular, these represent 48 wires (24 braids on each direction) and a wire thickness of 0.04 mm. The deployed stent diameter was set to fit the diameter of the parent vessel, ensuring a proper apposition of the FDS to the vessel wall.

Governing equations for steady flow were solved by using ANSYS CFX (ANSYS, Canonsburg, Pennsylvania). Blood was assumed incompressible, with attenuation $\rho = 1050 \text{ kg} \times \text{m}^{-3}$, and Newtonian, with viscosity $\mu = 0.0035 \text{ Pa} \times \text{s}$. The appropriateness of the modeling approach and computational accuracy were verified based on computational methodologies reported in the literature.^{13,14} Fully developed parabolic velocity profiles were imposed at inlet boundaries, resulting in typical volumetric flow rates at peak systole and end diastole ($Q_{\text{sys}} = 3.71 \text{ mL/s}$; $Q_{\text{dia}} = 0.98 \text{ mL/s}$).¹⁵ Outlet boundaries were set to mimic typical resistance to flow from the peripheral beds, and their values were derived from predicted values of pressure and volumetric flow data obtained with the 1D model developed and validated by Rey-

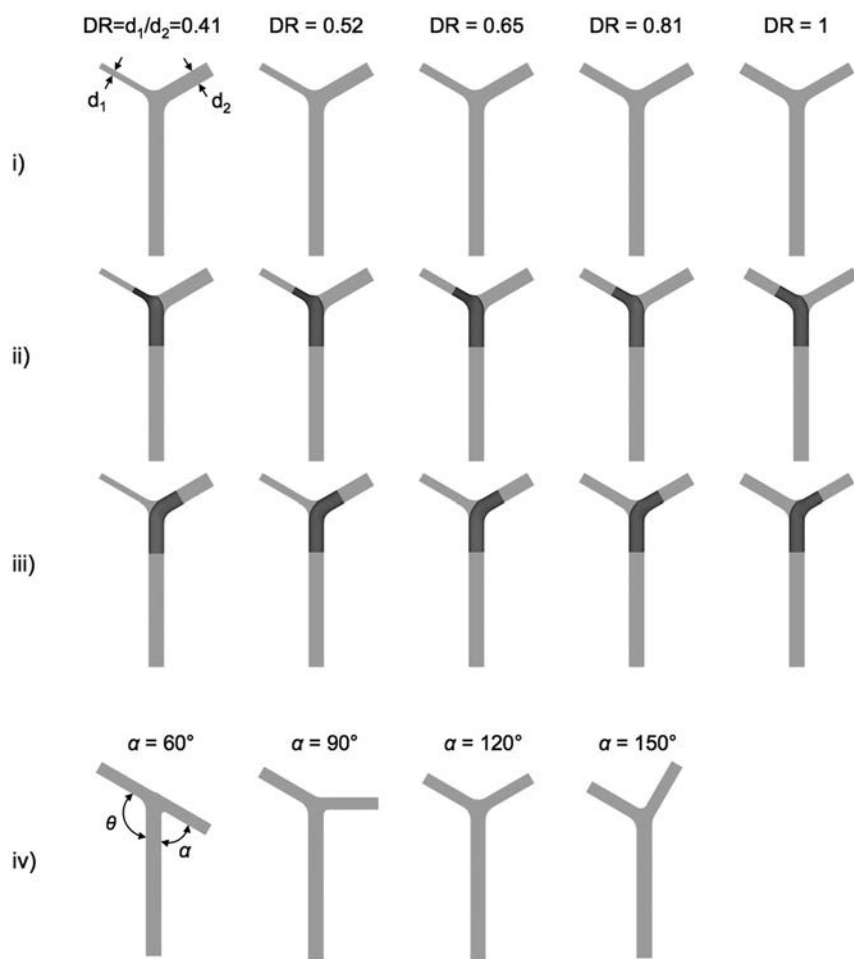


FIG 1. Idealized 3D geometries used for study phase II. Line i indicates unstenched geometries; line ii, geometries with stent deployed along smaller daughter vessel; line iii, geometries with FDS deployed along larger daughter vessel; line iv, geometries used to study the effect of bifurcation angles, where α was varied while θ was kept constant at 120° .

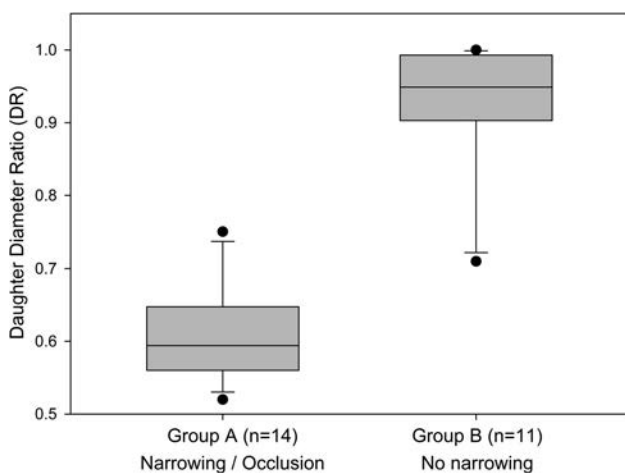


FIG 2. Whisker plot showing DR distribution within Group A (mean = 0.59; SD = 0.0766), including datasets with events of partial (narrowing) or complete occlusion, and Group B (mean = 0.935, SD = 0.0823), including datasets reporting no constriction (patency). Each boxplot describes first quartile values (bottom black line), median values (middle black line), and third quartile values (top black line). Error bars show minimum (bottom black bar) and maximum (top black bar) values. Solid circles denote outliers identified by using the maximum normed residual test.

mond et al.¹⁵ These were set as resistance to flow rather than any a priori pressure or velocity value that might adversely affect, and overconstrain, posttreatment flow redistribution across the bifurcation. For the symmetrical bifurcation case (DR = 1), peripheral resistances were varied within typical physiologic ranges (50–60 mm Hg s/mL) encountered at MCA bifurcations as previously described by Raymond et al.¹⁵ to study their influence on pre- and posttreatment hemodynamics.

Phase III: Patient-Specific Computational Fluid Dynamics Study

Six patient datasets were selected for the patient-specific computational fluid dynamics analyses, all representing cerebral bifurcations but with different levels of bifurcation asymmetry; these are cases 6, 7, and 22–25 in the On-line Table. The @neurIST computational tool chain was used for medical image segmentation and surface reconstruction.^{14,16} Blender was used for further surface mesh manipulation and refinement. Finally, surface meshes were superimposed on the original images for final check and validation.

Stents were virtually deployed by using the process described above along the same bifurcating vessel in accordance with clinical procedures. Computa-

tional analyses were performed following the same steady-state computational approach described for phase II, but with inlet boundary conditions set as average volumetric flow rate values (rather than diastolic and systolic flow rates as in phase II) to simulate the most representative flow condition at the bifurcation locations¹⁵ ($Q_{avg} = 1.25$ mL/s for patients 6 and 24; $Q_{avg} = 2.3$ mL/s for patients 7, 22, 23, and 25).

RESULTS

Phase I

Fig 2 shows a box-and-whisker plot for the 25 datasets categorized as cases where FDS treatment had no vessel caliber change (Group B, $n = 11$) and cases where narrowing or sub-acute occlusion was observed either at baseline or at follow-up (Group A, $n = 14$) and their correlation with daughter vessel DR. These distributions already show a marked correspondence between nonsymmetrical anatomies and vessel changes (Group A), with DR values between the first and third quartile centered on the nonsymmetrical region ($DR_{median} = 0.59$; $DR_{1st\ quartile} = 0.52$; $DR_{3rd\ quartile} = 0.65$). Conversely, a marked correspondence was observed between symmetrical anatomies and lumen conservation, with DR values centered on the symmetrical region of DR = 1 ($DR_{median} = 0.95$;

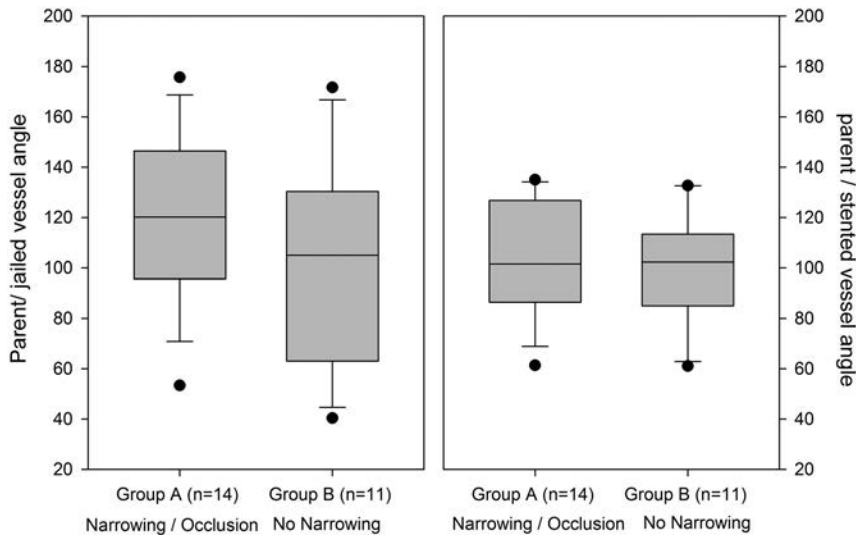


FIG 3. Whisker plots correlating DR with angles between parent and jailed vessel (*left*) and with angles between parent and stented vessel (*right*). Each boxplot describes first quartile values (*bottom black line*), median values (*middle black line*), and third quartile values (*top black line*). Error bars show minimum (*bottom black bar*) and maximum (*top black bar*) values. *Solid circles* denote outliers identified by using the maximum normed residual test.

$DR_{1st\ quartile} = 0.91$; $DR_{3rd\ quartile} = 0.99$). A maximum normed residual test identified 1 outlier in each group. These outliers are represented in Fig 2. The *t* test confirmed a statistically significant difference between the 2 groups' mean values, with *P* values $\leq .001$. No correspondence of statistical significance was observed between angle measurements and artery diameter changes (Fig 3). The On-line Figure shows a percentage decrease in the diameter of the jailed daughter branch mostly distributed around 50%.

Phase II

Computational results obtained for idealized anatomies are reported in Figs 4 and 5. Fig 4 shows space-averaged wall shear stress (WSS) forces exerted by the flow of blood on the endothelial layer over the nonstented region of both daughter vessels at diastolic flow rates.

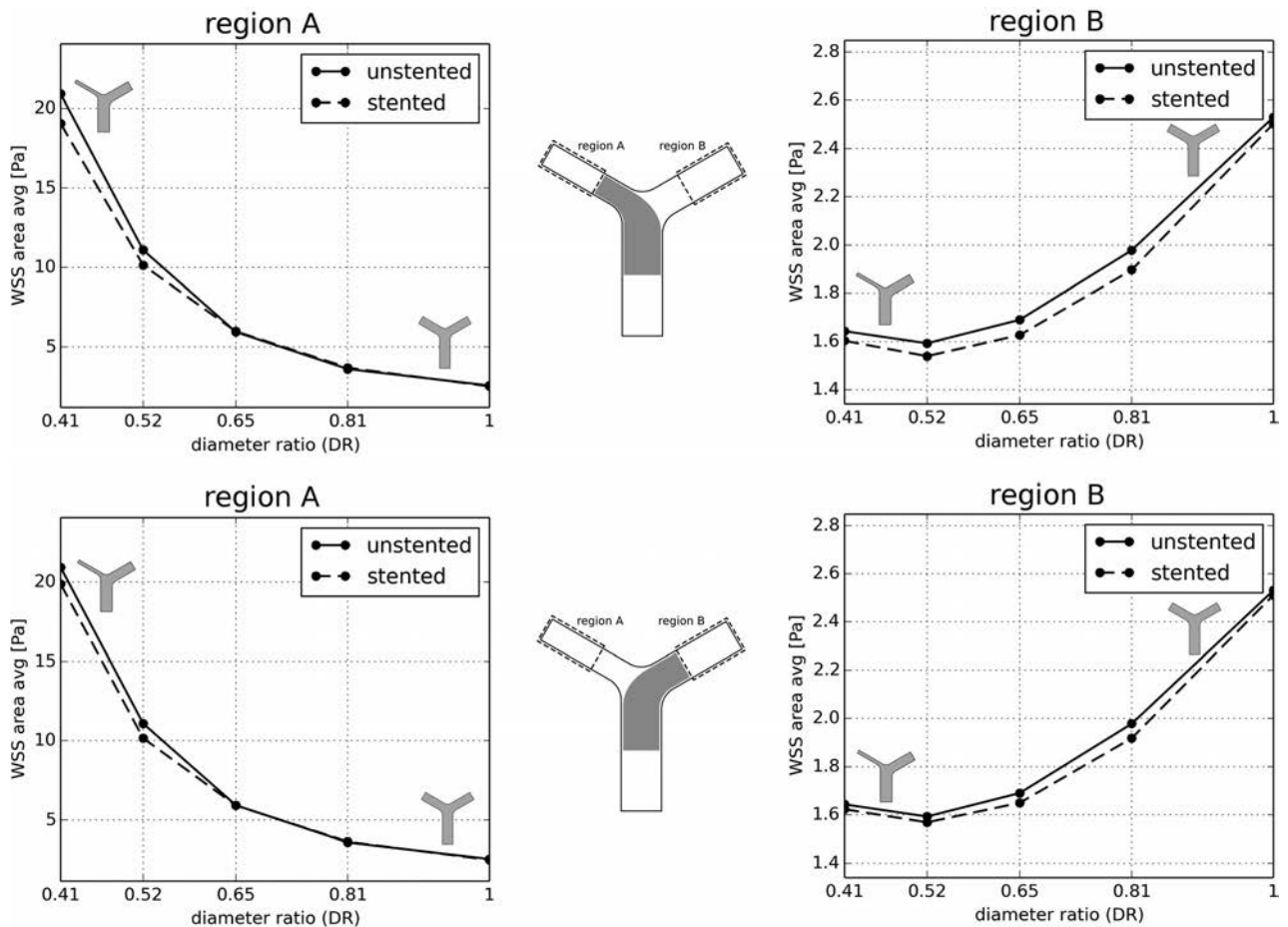


FIG 4. Space-average WSS calculated along the smaller daughter vessel (*region A, left graphs*) and larger daughter vessel (*region B, right graphs*) for diastolic volumetric flow rates (0.98 mL/s) and 3 different configurations (*solid lines, no stent; top graphs, dotted lines, stent along smaller vessel d1; bottom graphs, dotted lines, stent along larger vessel d2*).

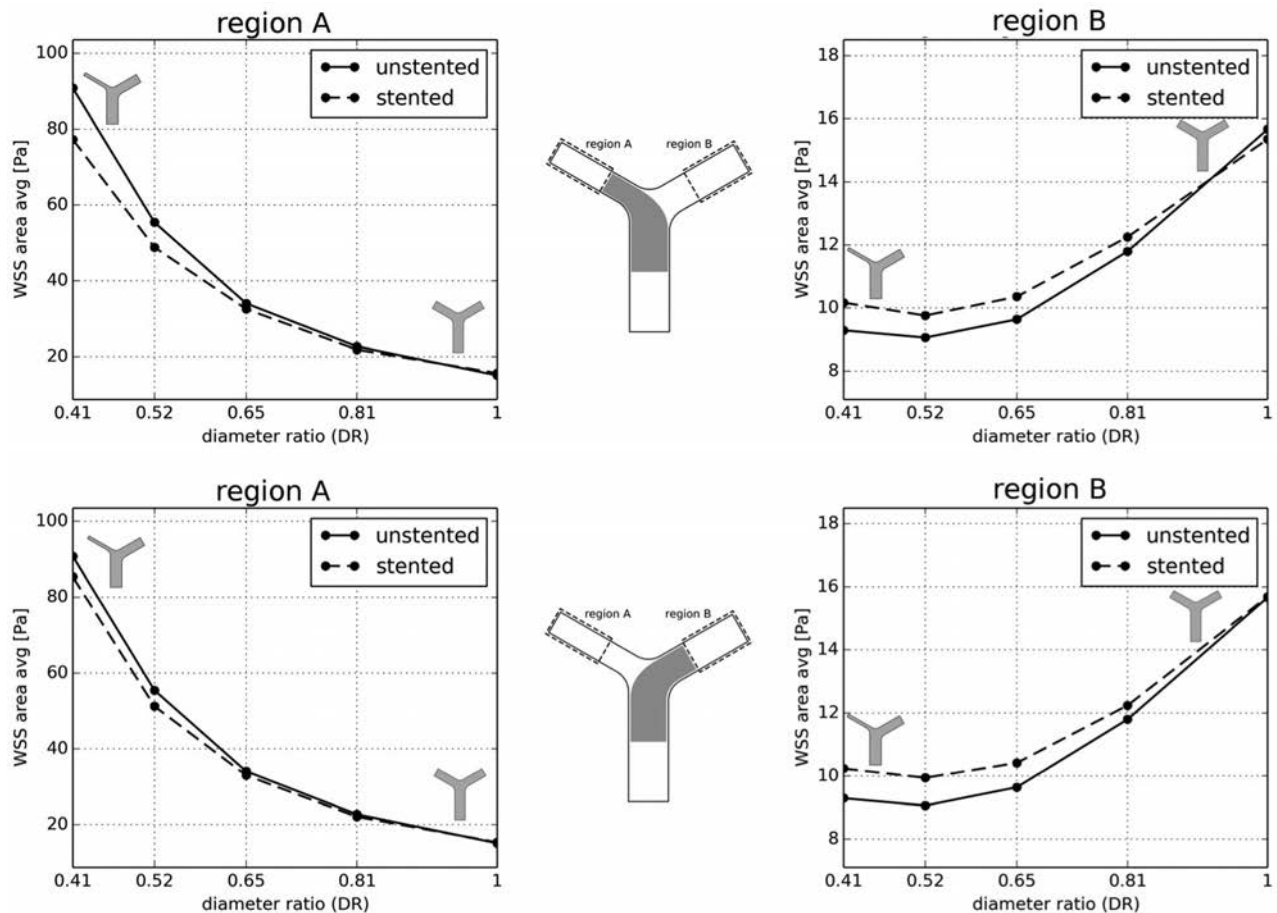


FIG 5. Space-averaged WSS calculated along the smaller daughter vessel (region A, left graphs) and larger daughter vessel (region B, right graphs) for peak systolic volumetric flow rates (3.71 mL/s) and 3 different stent deployment configurations (solid lines, no stent; top graphs, dotted lines, stent along smaller vessel d1; bottom graphs, dotted lines, stent along larger vessel d2).

WSS values computed over the smaller daughter vessel (Fig 4, region A) for both stent configurations show a 2 Pa (10%) decrease in WSS after stent deployment in nonsymmetrical bifurcations ($DR = 0.41$) and less pronounced changes when DRs approach symmetric values ($0.65 < DR < 1$). WSS calculated along the larger daughter vessel (Fig 4, region B) is less affected by the flow diverter, with changes in WSS values confined to less than 0.1 Pa (4%) across all ranges of DR values. Results for peak systolic flow rates (Fig 5) showed similar trends, with WSS fields mostly affected in nonsymmetrical bifurcations in both regions. Volumetric flow rates predicted at the daughter vessel outlets and pressures computed along the same vessels showed that stent deployment only marginally affects flow redistribution and pressure fields across the bifurcation, with maximum FDS-induced changes in flow rates of approximately 0.01 mL/s and pressures of approximately 2 mm Hg at peak systole. When we analyzed the influence of varying peripheral resistance within physiologic ranges and angles, we did not find any noticeable effect.

Phase III

Computational fluid dynamics results for patient-specific analysis are reported in the Table and Fig 6. In accordance with phase II observations, the patient-specific analysis showed how hemodynamic effects become larger when flow diverters are deployed in a

Space-averaged WSS values computed over the unstented (jailed) daughter vessel before and after stent deployment

Patient	DR	SP-AVG WSS (Pa)		% Difference	Outcome
		No Stent	Stent		
6	0.71	16.8	16.8	0.0	No narrowing
7	0.90	15.4	15.2	-1.3	No narrowing
22	0.47	7.2	6.8	-5.6	Narrowing
23	0.52	8.9	8.7	-2.2	Narrowing
24	0.90	1.9	1.9	0.0	No narrowing
25	0.50	11.5	11.2	-2.6	Narrowing

Note:—SP-AVG indicates space-averaged.

nonsymmetrical configuration. Contour plots of WSS show some hemodynamic effect along the unstented daughter vessels for patients 22 and 25, where a decrease in WSS is qualitatively perceivable compared with the unstented configuration. A more quantitative analysis of the WSS space-averaged values over the same vessels is reported in the Table, with higher hemodynamic changes (decreased WSS) for the nonsymmetrical bifurcation and a comparatively smaller hemodynamic effect for the symmetrical ones. The only exception is represented by patient 6 (Table), in whom a bifurcation with $DR = 0.7$ showed no hemodynamic differences between stented and unstented configurations. Patient 6 presented acute occlusion (the only case) and jailed vessel complete recanalization with preserved diameter at 3-month follow-up.

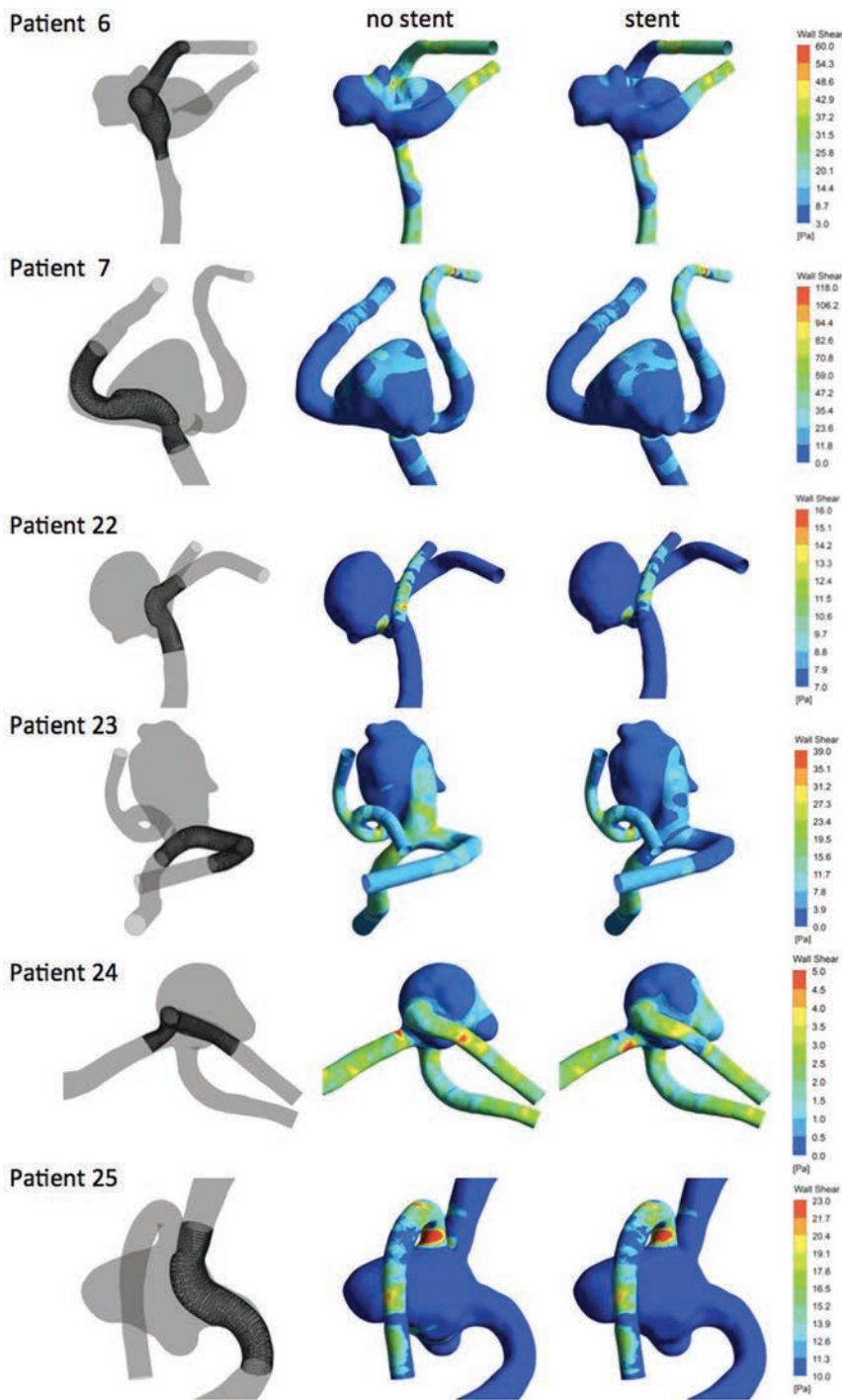


FIG 6. Computational fluid dynamics results for patient-specific analyses (phase III). WSS contours and anatomies were investigated.

DISCUSSION

Wide-neck bifurcation aneurysms present an unfavorable configuration for endovascular treatment. Balloon remodeling, stent-assisted coiling, and other complex procedures such as double-stent placement are often applied to provide more support to coil packing, with permanent neurologic impairment estimated in approximately 10% of cases.⁵ A number of bifurcation aneurysms have been treated by using FDS procedures, and results are worse than in proximal aneurysms, with lower occlusion rates (33%–97%) and higher permanent neurologic impairment (0%–27%).

In the published series of bifurcation aneurysms treated with FDSs, approximately two-thirds of the arteries jailed by the FDS were affected by a narrowing process or complete subacute occlusion.^{3–8} In the 25-aneurysm dataset reported in this study, narrowing or complete subacute occlusion was observed in 56% of cases. Only 1 patient (patient 6) presented acute arterial occlusion and complete artery recanalization at 3-month follow-up, keeping a normal diameter. The main hypothesis is that acute occlusion was caused by a thrombotic process because occlusion was immediate (during the procedure) and completely reversible. Occlusion and narrowing processes by permanent flow changes seem to be subacute events and not reversible.

Causes and mechanisms underlying FDS-induced artery caliber changes have not been elucidated. An analysis of anatomic and radiologic data for the study cohort reported here found a statistically significant correspondence between levels of bifurcation asymmetry and narrowing or subacute occlusion of the jailed artery. These correspondences were found for a 25-dataset cohort; a larger cohort size would be needed to enhance the significance of these findings.

Insertion of an FDS in asymmetric idealized bifurcations led to more changes in daughter vessel hemodynamics, in particular a reduction in WSS, compared with symmetric cases, regardless of whether the FDS was deployed along the larger or smaller branch. Deploying the FDS along the smaller bifurcating vessel led to more pronounced alterations in the hemodynamic parameters investigated. Patient-specific simulations confirmed previous results from the idealized geometry study, with observable hemodynamic changes in the asymmetric group. Although changes in WSS values seem

modest to definitely suggest a role played by hemodynamics, our findings have to be taken in a qualitative way and in view of the limitations of our approach. The computational fluid dynamics analysis was performed by using typical boundary conditions (eg, inlet flow rates). A more patient-specific approach would be necessary to fully understand in a quantitative way the significance of WSS alterations with respect to caliber changes and endothelial behavior. Nonetheless, the study identified an important trend demonstrating that hemodynamics is mostly perturbed by an FDS

when deployed in a nonsymmetrical bifurcation. It seems that changes in the forces to which endothelial cells are exposed may lead to vasomotor reaction in cerebral arteries.¹⁷⁻¹⁹ Considering that this study does not include biologic events analysis (eg, thrombosis) and in view of current knowledge, it is audacious to link small WSS changes to vasoconstriction as the main explanation. The role played by hemodynamics in the endothelial-mediated constrictive mechanisms needs further investigations.

The study of idealized cases identified a symmetry ratio threshold (DR = 0.65) below which hemodynamic changes were noticeable. This threshold is similar to the value found in our 25-patient dataset that encompasses most cases within the group with narrowing or subacute occluding vessels (DR < 0.7). Further research and a statistically relevant number of datasets are necessary to fully validate and handle confidence in this association. However, this study affirmed the possibility that the phenomenon of FDS-induced vasoconstriction may be explained not only through the presence or absence of collateral vasculature,^{6,9} but also through changes induced on the local bifurcation hemodynamics.

As previously stated by Peach et al,²⁰ successful use of an FDS in the treatment of intracranial aneurysms can only be achieved when the FDS creates sufficient resistance to flow entering the aneurysm so as to promote thrombosis while minimizing any alteration of the pre-existing hemodynamic stability and vessel homeostasis in the extra-aneurysm regions. We have found that hemodynamic changes were minimal when FDSs were deployed in symmetrical bifurcations and became progressively more significant as the level of asymmetry increased.

FDS-induced changes to flow and pressure were not significant, though alterations to local distributions of flow velocities were observed and justified changes in WSS. We only observed minor changes to pressure and flow redistribution upon stent deployment. This is somewhat in disagreement with other computational studies reported in the literature,^{21,22} where more significant alterations in flow and pressure data were observed between the unstented and stented configurations. This can be explained by the fact that in our approach, where we coupled the fluid solver to a 1D resistance model effectively imposing outlet pressure as a function of flow rate, we could impose, and keep constant, physiologically realistic values of peripheral resistance across our bifurcations. This guaranteed consistency on the imposition of peripheral resistance, which cannot be guaranteed by the imposition of constant pressure outlet boundary conditions because a different redistribution of flow, caused for example by the presence of a flow-diverting device, would lead to a different value of outlet resistance if pressure is maintained constant. The same findings are also somehow in disagreement with previously published data from experimental studies, where arguably peripheral resistance would have been kept constant. However, these studies do not provide any information on the peripheral resistances set for the experiment and only vaguely refer to the experimental model being connected to a "flow loop with flexible chloride tubing."^{23,24} In these studies, the significant changes in pressure caused by the presence of low-porosity FDSs might have been affected by much lower than physiologic values of peripheral resistance, in the presence of which the local resistance of the FDS might be much greater and inevitably expected to induce large

changes in flow redistribution and, therefore, pressure. We believe that our multidimensional resistance-based approach could offer a viable boundary condition option, other than pressure-based approaches, for the type of studies presented in this study, as also elegantly elucidated by Vignon-Clementel et al.²⁵ However, a deeper understanding of the different physiologic conditions modeled by the 2 approaches and their suitability to investigate flow through stented bifurcation would require further research.

To evaluate the change in bifurcation angles that may have been induced by the deployment of a relatively stiff device, we studied the influence of angle changes on symmetrical idealized bifurcations without stents. This study did not produce noticeable changes in distal vessel hemodynamics to justify a subsequent study on the influence of angles on stented bifurcations. This is also confirmed by other studies reported in the literature.^{26,27}

One might question the applicability of the theory identified by this study to sidewall arteries. Indeed, asymmetric bifurcations present similar anatomies to sidewall arteries, albeit with much higher percentages of parent arteries in the follow-up because ophthalmic and anterior choroidal arteries do not seem to suffer the same clinical fate when covered by FDSs.^{28,29} This could be explained by a different influence that peripheral vascular resistance has on local hemodynamics at different locations in the vascular network. Vascular resistance can be described as the impediment to blood flow in a vessel and is well described by the Hagen-Poiseuille relationship. This equation shows that resistance, or impediment to flow, increases with higher values of blood viscosity (hematocrit), vessel length, and smaller vessel radius. It should also be noted that, by far, the most important influence on resistance to flow is given by vessel radius, which appears to the power of 4 in this relationship. This strong influence of vessel radius on flow was one of the main reasons we decided to focus our study on reciprocal vessel diameters at bifurcations. In the systemic circulation, resistance to flow exerted by small peripheral vessels is known to have a significant influence on overall systemic blood flow.³⁰ When we have studied the influence of peripheral resistance and varied it within physiologic ranges reported for MCA bifurcations, we have noticed little influence compared with the changes induced by FDS. This might not be the case at other vascular locations where the level of peripheral resistance is different. In fact, Raymond et al¹⁵ reported 2- to 3-fold higher values of peripheral resistance distal to the ophthalmic and choroidal arteries compared with known peripheral resistance after MCA bifurcations. It is therefore possible that the presence of an FDS in proximal vessels, which can also be considered as an impediment to flow, would not affect a flow that is predominantly dominated and influenced by a much higher peripheral resistance at these locations. This aspect requires further research to fully explain why FDS treatment at these locations does not seem to lead to vessel caliber changes.

CONCLUSIONS

This study identified a statistically significant correlation between nonsymmetrical bifurcations and narrowing or subacute occlusion in a patient dataset, showing that bifurcation anatomies below a certain level of symmetry (DR < 0.65) are more likely to

become narrower or occluded. A FDS induced modest hemodynamic changes (decreased WSS) when bifurcations were not symmetrical, but these were comparatively higher than those observed in symmetric bifurcations. Upon further research and clinical validation, this knowledge has the potential to guide and motivate further studies to reduce risk in complex aneurysm endovascular treatment, with the prospect of extending minimally invasive procedures to vascular regions that are currently deemed unsafe for FDS treatment.

Disclosures: Ignacio Larrabide—UNRELATED: Consultancy: Galgo Medical, Comments: development and validation of intracranial aneurysm treatment algorithms; Employment: CONICET, Comments: research fellow; Grants/Grants Pending: MINCYT, Comments: grant PICT 2015–0006*; Payment for Lectures Including Service on Speakers Bureaus: UNICEN, Comments: currently hold a position as lecturer at UNICEN. Christophe Cognard—UNRELATED: Consultancy: Stryker, Medtronic, Microvention. René Chapot—UNRELATED: Consultancy: Microvention, Medtronic, Stryker; Payment for Lectures Including Service on Speakers Bureaus: Microvention, Balt, Stryker, Medtronic, Siemens, Neuravi. Alberto Marzo—RELATED: Grant: Newton Fund Royal Academy of Engineering, Comments: grant funded traveling expenses to interact with researchers in Brazil on aspects of this grant*. *Money paid to the institution.

REFERENCES

- Gonzalez AM, Narata AP, Yilmaz H, et al. **Blood blister-like aneurysms: single center experience and systematic literature review.** *Eur J Radiol* 2014;83:197–205 CrossRef Medline
- Narata AP, Yilmaz H, Schaller K, et al. **Flow-diverting stent for ruptured intracranial dissecting aneurysm of vertebral artery.** *Neurosurgery* 2012;70:982–88; discussion 988–89 CrossRef Medline
- Briganti F, Delehaye L, Leone G, et al. **Flow diverter device for the treatment of small middle cerebral artery aneurysms.** *J Neurointerv Surg* 2016;8:287–94 CrossRef Medline
- Caroff J, Neki H, Mihalea C, et al. **Flow diverter stents for the treatment of saccular middle cerebral artery bifurcation aneurysms.** *AJNR Am J Neuroradiol* 2016;37:279–84 CrossRef Medline
- Gawlitza M, Januel AC, Tall P, et al. **Flow diversion treatment of complex bifurcation aneurysms beyond the circle of Willis: a single-center series with special emphasis on covered cortical branches and perforating arteries.** *J Neurointerv Surg* 2016;8:481–87 CrossRef Medline
- Saleme S, Iosif C, Ponomarjova S, et al. **Flow-diverting stents for intracranial bifurcation aneurysm treatment.** *Neurosurgery* 2014; 75:623–31 CrossRef Medline
- Topcuoglu OM, Akgul E, Daglioglu E, et al. **Flow diversion in middle cerebral artery aneurysms: is it really an all-purpose treatment?** *World Neurosurg* 2016;87:317–27 CrossRef Medline
- Yavuz K, Geyik S, Saatci I, et al. **Endovascular treatment of middle cerebral artery aneurysms with flow modification with the use of the Pipeline embolization device.** *AJNR Am J Neuroradiol* 2014;35: 529–35 CrossRef Medline
- Iosif C, Berg P, Ponnsonard S, et al. **Role of terminal and anastomotic circulation in the patency of arteries jailed by flow-diverting stents: animal flow model evaluation and preliminary results.** *J Neurosurg* 2016;125:898–908 CrossRef Medline
- Kallmes D, Hanel R, Lopes D, et al. **International retrospective study of the Pipeline embolization device: a multicenter aneurysm treatment study.** *AJNR Am J Neuroradiol* 2015;36:108–15 CrossRef Medline
- Fung YC. **Optimum design of blood vessel bifurcation.** In: *Biomechanics: Circulation.* New York: Springer-Verlag; 1997:118–25
- Larrabide I, Kim M, Augsburg L, et al. **Fast virtual deployment of self-expandable stents: method and in vitro evaluation for intracranial aneurysmal stenting.** *Med Image Anal* 2012;16:721–30 CrossRef Medline
- Bernardini A, Larrabide I, Morales HG, et al. **Influence of different computational approaches for stent deployment on cerebral aneurysm haemodynamics.** *Interface Focus* 2011;1:338–48 CrossRef Medline
- Villa-Urriol MC, Berti G, Hose DR, et al. **@neurIST complex information processing toolchain for the integrated management of cerebral aneurysms.** *Interface Focus* 2011;1:308–19 CrossRef Medline
- Reymond P, Bohraus Y, Perren F, et al. **Validation of a patient-specific one-dimensional model of the systemic arterial tree.** *Am J Physiol Heart Circ Physiol* 2011;301:H1173–82 CrossRef Medline
- Marzo A, Singh P, Reymond P, et al. **Influence of inlet boundary conditions on the local haemodynamics of intracranial aneurysms.** *Comput Methods Biomech Biomed Engin* 2009;12:431–44 CrossRef Medline
- Bryan RM Jr., Marrelli SP, Steenberg ML, et al. **Effects of luminal shear stress on cerebral arteries and arterioles.** *Am J Physiol Heart Circ Physiol* 2001;280:H2011–22 Medline
- Heistad DD. **What's new in the cerebral microcirculation? Landis Award lecture.** *Microcirculation* 2001;8:365–75 CrossRef Medline
- Koller A, Toth P. **Contribution of flow-dependent vasomotor mechanisms to the autoregulation of cerebral blood flow.** *J Vasc Res* 2012; 49:375–89 CrossRef Medline
- Peach TW, Spranger K, Ventikos Y. **Towards predicting patient-specific flow-diverter treatment outcomes for bifurcation aneurysms: from implantation rehearsal to virtual angiograms.** *Ann Biomed Eng* 2016;44:99–111 CrossRef Medline
- Tang AY, Chung WC, Liu ET, et al. **Computational fluid dynamics study of bifurcation aneurysms treated with Pipeline embolization device: side branch diameter study.** *J Med Biol Eng* 2015;35:293–304 CrossRef Medline
- Kono K, Terada T. **Hemodynamics of 8 different configurations of stenting for bifurcation aneurysms.** *AJNR Am J Neuroradiol* 2013; 34:1980–86 CrossRef Medline
- Roszelle BN, Babiker MH, Hafner W, et al. **In vitro and in silico study of intracranial stent treatment for cerebral aneurysms: effects on perforating vessel flows.** *J NeuroInterv Surg* 2013;5:354–60 CrossRef Medline
- Roszelle BN, Gonzalez LF, Babiker MH, et al. **Flow diverter effect on cerebral aneurysm hemodynamics: an in vitro comparison of telescoping stents and the Pipeline.** *Neuroradiology* 2013;55:751–58 CrossRef Medline
- Vignon-Clementel IE, Figueroa CA, Jansen KE, et al. **Outflow boundary conditions for three-dimensional finite element modeling of blood flow and pressure in arteries.** *Comput Methods Appl Mech Eng* 2006;195:3776–96 CrossRef
- Beier S, Ormiston J, Webster M, et al. **Impact of bifurcation angle and other anatomical characteristics on blood flow - a computational study of non-stented and stented coronary arteries.** *J Biomech* 2016;49:1570–82 CrossRef Medline
- Farnoush A, Avolio A, Qian Y. **Effect of bifurcation angle configuration and ratio of daughter diameters on hemodynamics of bifurcation aneurysms.** *AJNR Am J Neuroradiol* 2013;34:391–96 CrossRef Medline
- Kühn AL, Hou SY, Perras M, et al. **Flow diverter stents for unruptured saccular anterior circulation perforating artery aneurysms: safety, efficacy, and short-term follow-up.** *J Neurointerv Surg* 2015; 7:634–40 CrossRef Medline
- Neki H, Caroff J, Jittapiromsak P, et al. **Patency of the anterior choroidal artery covered with a flow-diverter stent.** *J Neurosurg* 2015; 123:1540–45 CrossRef Medline
- Guyton A, Hall J. *Textbook of Medical Physiology.* 13th ed. Philadelphia: Sanders Elsevier; 2011:195–96

Feasibility of Permanent Stenting with Solitaire FR as a Rescue Treatment for the Reperfusion of Acute Intracranial Artery Occlusion

H.G. Woo, L. Sunwoo, C. Jung, B.J. Kim, M.-K. Han, H.-J. Bae, Y.J. Bae, B.S. Choi, and J.H. Kim



ABSTRACT

BACKGROUND AND PURPOSE: The Solitaire FR can be used not only as a tool for mechanical thrombectomy but also as a detachable permanent stent. Our aim was to assess the feasibility and safety of permanent stent placement with the Solitaire FR compared with other self-expanding stents for intracranial artery recanalization for acute ischemic stroke.

MATERIALS AND METHODS: From January 2011 through January 2016, we retrospectively selected 2979 patients with acute ischemic stroke. Among them, 27 patients who underwent permanent stent placement (13 patients with the Solitaire FR [Solitaire group] and 14 patients with other self-expanding stents [other stent group]) were enrolled. The postprocedural modified TIC1 grade and angiographic and clinical outcomes were assessed. The safety and efficacy of permanent stent placement of the Solitaire FR for acute large-artery occlusion were evaluated.

RESULTS: Stent placement was successful in all cases. Modified TIC1 2b–3 reperfusion was noted in 84.6% of the Solitaire group and in 78.6% of the other stent group. Procedural time was significantly shorter in the Solitaire group than in the other stent group ($P = .022$). Shorter procedural time was correlated with favorable outcome ($\rho = 0.46$, $P = .035$). No significant differences were found in the modified TIC1 grade, NIHSS score, mRS, and hemorrhagic transformation rate between the 2 groups. The acute in-stent thrombosis rate at discharge was significantly lower when a glycoprotein IIb/IIIa inhibitor was injected during the procedure ($P = .013$).

CONCLUSIONS: Permanent stent placement with the Solitaire FR compared with other self-expanding stents appears to be feasible and safe as a rescue tool for refractory intra-arterial therapy.

ABBREVIATIONS: ISR = in-stent restenosis; mTIC1 = modified TIC1

Acute ischemic stroke is a high-burden disease and one of the leading causes of death and neurologic disability. In 2012, the US FDA approved the Solitaire FR (Covidien, Irvine, California) after the Solitaire With the Intention For Thrombectomy (SWIFT) trial, which demonstrated that stent retriever devices had substantially high rates of recanalization.¹ Five randomized trials of endovascular treatment found improvements in clinical outcomes over medical therapy and indicated that 71% of patients treated with mechanical thrombectomy had successful reperfusion.^{2–7}

These trials have proved that the stent retriever is a safe and reliable tool for endovascular reperfusion therapy. Thereafter, endovascular reperfusion therapy using the stent retriever has become the standard treatment for acute large-artery occlusion in the anterior circulation within 6 hours from onset in addition to IV tPA.

In the era of stent retriever thrombectomy, it is important to determine the appropriate strategy for acute intracranial artery occlusions refractory to conventional mechanical thrombectomy, considering the rate of unsuccessful reperfusion ranging from 14% to 41% in 5 randomized clinical trials.^{2–7} To that end, some case series reported outstanding procedural and clinical outcomes using self-expanding stents such as the Neuroform (Stryker Neurovascular, Kalamazoo, Michigan), Wingspan (Stryker), or Enterprise self-expanding stent (Codman & Shurtleff, Raynham, Massachusetts) as a rescue treatment.^{8–12} Moreover, because acute large-artery occlusion with underlying intracranial atherosclerotic disease is more common in Asian populations than in Western populations,¹³

Received July 22, 2017; accepted after revision October 4.

From the Departments of Radiology (H.G.W., L.S., C.J., Y.J.B., B.S.C., J.H.K.) and Neurology (B.J.K., M.-K.H., H.-J.B.), Seoul National University Bundang Hospital, Bundang, Seongnam, Korea.

This work was supported by a grant from the Seoul National University Bundang Hospital Research Fund (No. 14-2016-019).

Please address correspondence to Leonard Sunwoo, MD, Department of Radiology, Seoul National University Bundang Hospital, 82 Gumi-ro 173 Beon-Gil, Seongnam, Gyeonggi-do, 13620, Republic of Korea; e-mail: leonard.sunwoo@gmail.com

 Indicates article with supplemental on-line table.

<http://dx.doi.org/10.3174/ajnr.A5477>

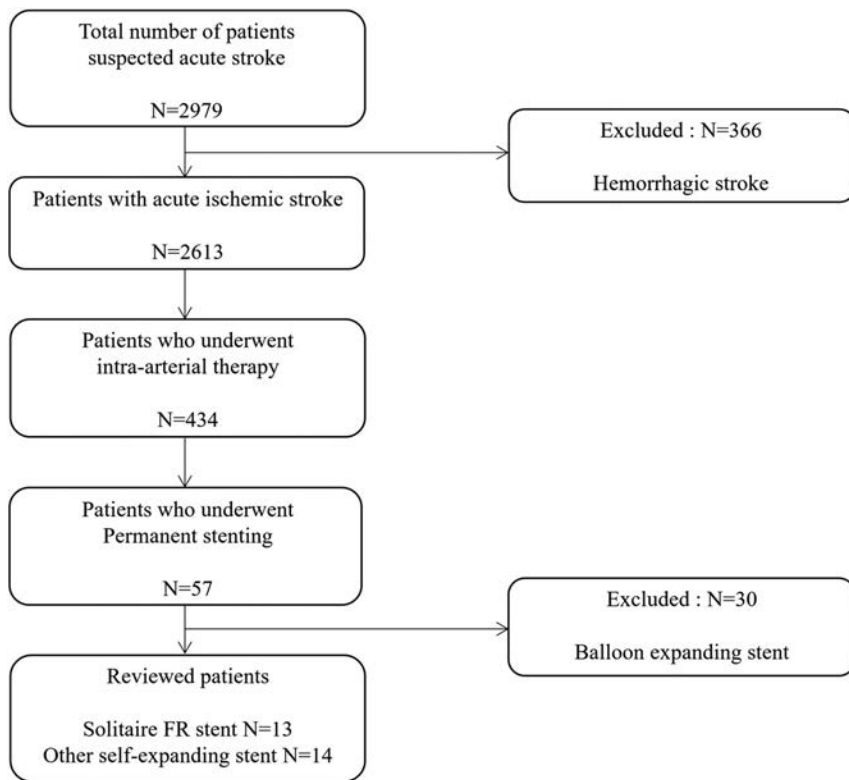


FIG 1. Flowchart of patient inclusion.

stent implantation for restoring blood flow could be particularly useful to Asian patients with atherosclerosis-related in situ stenosis or occlusion.

The Solitaire FR can be used not only as a tool for mechanical thrombectomy but also as a tool for permanent stent placement after detachment. However, to our knowledge, no study has yet been performed to assess the feasibility of permanent stent placement of the Solitaire FR to restore blood flow. At our center, Solitaire FR stent implantation is often used to treat ischemic stroke in case of unsuccessful recanalization with the Solitaire stent retriever and/or other endovascular interventions. We hypothesized that permanent stent placement with the Solitaire FR compared with other self-expanding stents may be a feasible and safe rescue treatment for intracranial artery recanalization in acute ischemic stroke.

MATERIALS AND METHODS

The institutional review board approved this retrospective study, and informed consent was waived.

Subjects

Initially, 2979 consecutive patients with acute ischemic stroke from January 2011 through January 2016 were retrospectively selected from the data base in our institution. Among them, 434 patients with suspected cerebrovascular occlusion on CTA or MRA underwent further diagnostic cerebral angiography and intra-arterial therapy. Of these, 57 patients were treated with stent insertion as a rescue treatment for recanalization of an occluded intracranial vessel. Finally, 27 patients who met the following inclusion criteria were enrolled in this study: 1) occlusion of the

basilar artery, intracranial segment of vertebral artery, or MCA (M1 or M2 segment) confirmed with CTA, MRA, or DSA; and 2) permanent stent implantation as a rescue procedure. These included 13 patients who underwent permanent stent placement with the Solitaire FR (Solitaire group) and 14 patients who underwent permanent stent placement with other self-expanding stents (other stent group) (Fig 1).

Procedures

All procedures were performed on a biplane angiography machine (Integris Allura; Philips Healthcare, Best, the Netherlands). For the anterior circulation, a 9F balloon-tipped guiding catheter was guided by a 5F diagnostic catheter and was placed in the distal common carotid artery or ICA. For posterior circulation, a 6F shuttle and 5F or 6F coaxial guiding systems were placed in the extracranial vertebral artery. Initial angiography was performed to assess the occlusion level and preprocedural modified TICI (mTICI) grade. Next, mechanical thrombectomy using the Soli-

taire FR was performed for the occluded segment. An angiogram was obtained to thoroughly evaluate the re-establishment of flow. If the occlusion remained, the procedure was repeated immediately. For patients who had refractory occlusion or who had residual flow-compromising degree of stenosis after 3–7 attempts of mechanical thrombectomy, suction thrombectomy, or chemical thrombolysis, permanent stent placement was considered as a final bailout option. Timing of when to perform permanent stent placement and deciding what kind of stent would be used were at the discretion of the neurointerventionalist. A glycoprotein IIb/IIIa inhibitor (tirofiban) was administered intravenously if the patient was about to undergo permanent stent insertion and had not taken proper antithrombotic medication before the procedure.¹⁴ The glycoprotein IIb/IIIa inhibitor was initially injected as a loading dose (0.4 mcg/kg) for 30 minutes, followed by continuous infusion for prevention of acute in-stent thrombosis (0.1 mcg/kg/min). The patients immediately received additional oral acetylsalicylic acid (300 mg) and clopidogrel (75 mg) to protect the stent after excluding symptomatic hemorrhagic transformation and/or brain edema with significant mass effect with brain CT on the following day.

Evaluation of Outcomes and Clinical and Angiographic Follow-Up

The mTICI reperfusion grade and change of neurologic deficit were assessed at the end of the procedure. Successful recanalization was defined as mTICI 2b–3 recanalization on a delayed angiogram obtained after at least 10 minutes. The procedural success of permanent stent placement was defined as accurate

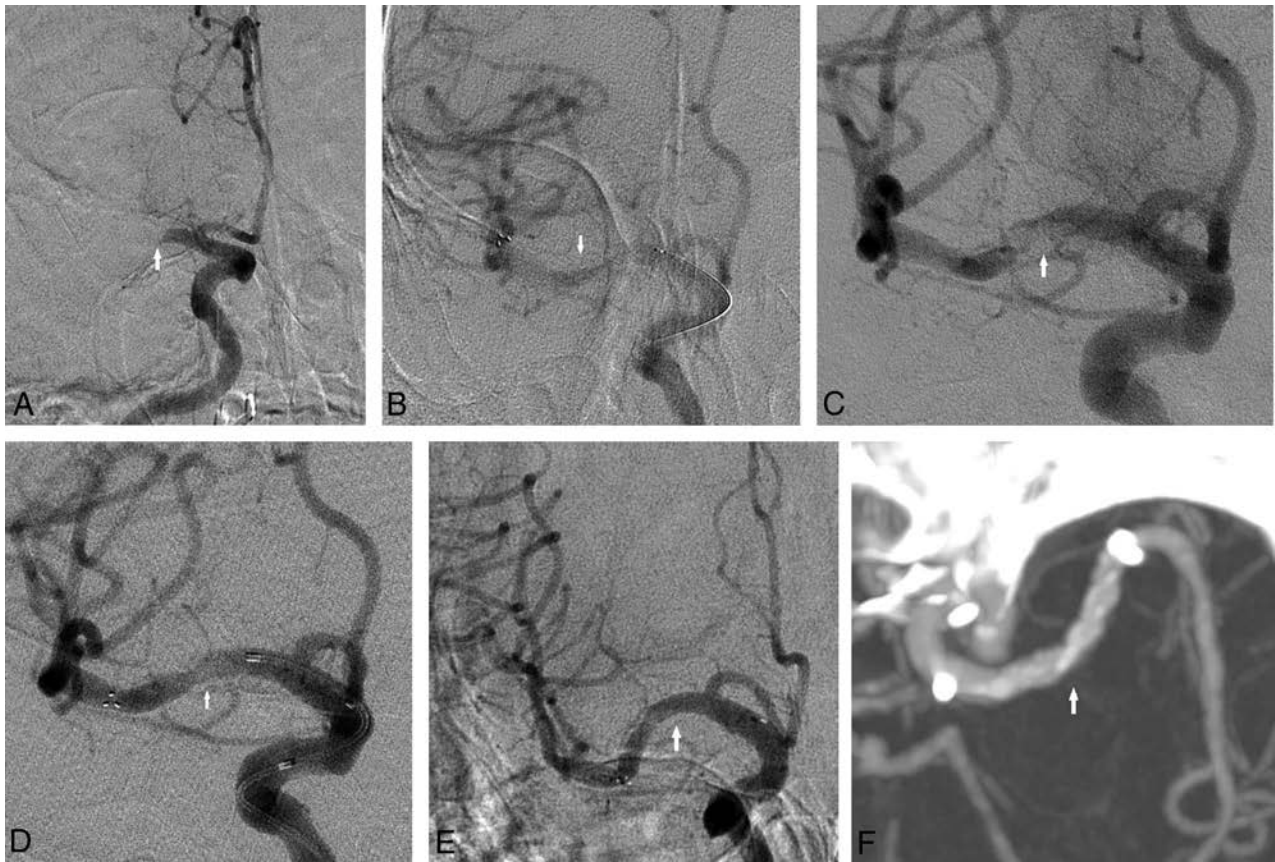


FIG 2. A 55-year-old man with acute ischemic stroke, presenting with an initial NIHSS score of 22. *A*, A right internal carotid angiogram shows occlusion of the right middle cerebral artery M1 portion. *B*, Initial placement of the Solitaire stent. A right internal carotid angiogram shows visible anterograde flow in the right middle cerebral artery M1 portion. *C*, A 5-minute delayed right internal carotid angiogram after thrombectomy using the Solitaire stent shows repeat buildup of thrombus and reocclusion. *D*, After 3 passages of the Solitaire stent with recurrent reocclusion, the decision for a permanent stent was made. A right internal carotid angiogram during the intravenous infusion of glycoprotein IIb/IIIa inhibitor shows a patent lumen of a temporarily deployed Solitaire stent. *E*, A 30-minute delayed angiogram after detachment of the Solitaire stent reveals complete recanalization. *F*, A follow-up angiogram at 3 months reveals a patent right middle cerebral artery with no evidence of in-stent restenosis at the M1 portion. The patient had an mRS score of 1 at 3 months.

delivery and deployment of the stent completely covering the target lesion and resulting in a residual stenosis of <50%. Angiographic follow-up was scheduled at discharge and 3 months after discharge, with DSA or CTA to assess in-stent restenosis (ISR). ISR was defined as absolute stenosis of >50% within the stent, including its margin, or $\geq 20\%$ reduction of the lumen size relative to the residual stenosis.

Clinical outcomes were evaluated according to the NIHSS score at admission, after intra-arterial therapy, and at discharge and according to the mRS at discharge and 3, 6, and 12 months. The initial and follow-up clinical evaluations were performed by 3 experienced stroke neurologists. Good functional outcome was defined as an mRS of 0–2, whereas poor outcome was defined as an mRS of 3–6. We defined symptomatic brain hemorrhage as parenchymal, subarachnoid, or intraventricular hemorrhage detected by CT or MR imaging that was associated with new neurologic signs or symptoms lasting ≥ 24 hours or a seizure.^{15,16} In addition, we evaluated mortality at 3, 6, and 12 months (Fig 2).

Statistical Methods

Statistical analysis was performed using SPSS 22.0 for Windows (IBM, Armonk, New York). Clinical and laboratory findings and

outcomes between the Solitaire group and the other stent group were compared. The Mann-Whitney *U* test, χ^2 test, or Fisher exact test was used to analyze categorical variables. A Spearman correlation coefficient was used to assess the correlation between the variables. Frequency, median, and interquartile ranges were used for descriptive statistics.

RESULTS

The On-line Table summarizes the clinical characteristics, treatment, and outcome in the Solitaire group and the other stent group. No significant differences were found in demographic information, lesion location, comorbidities, Trial of Org 10172 in Acute Stroke Treatment (TOAST) classification,¹⁷ NIHSS score at admission, and outcome between the 2 groups.

Stent placement was successful in all procedures, and mTICI 2b–3 recanalization was obtained in 11 patients (84.6%) in the Solitaire group and 11 patients (78.6%) in the other stent group ($P > .9$). Total procedural time was significantly shorter in the Solitaire group compared with the other stent group (69 versus 115 minutes, $P = .022$). There were no significant differences in onset-to-emergency department time, onset-to-angiography

Comparison of in-stent restenosis and postprocedural mTICI grade between administration of GP IIb/IIIa inhibitors and no administration of GP IIb/IIIa inhibitors

	GP IIb/IIIa Inhibitors		P Value
	Yes	No	
ISR at discharge (yes) (%)	0/16 (0)	3/3 (50.0)	.013 ^a
ISR at 3 mo (yes) (%)	2/9 (18.2)	4/1 (80.0)	.036 ^a
Postprocedural mTICI grade (0–2a/2b–3) (%)	2/16 (11.1/88.9)	3/6 (33.3/66.7)	.295
Overall hemorrhagic transformation (yes) (%)	3/15 (16.7)	4/5 (44.4)	.175
Symptomatic ICH (yes) (%)	1/17 (5.6)	2/7 (22.2)	.250
mRS at 3 mo 0–2 (%)	8/18 (44.4)	0/9 (0)	.026 ^a
mRS at 6 mo 0–2 (%)	9/18 (50.0)	2/9 (22.2)	.231
mRS at 12 mo 0–2 (%)	9/18 (50.0)	2/9 (22.2)	.231
Mortality at 3 mo (%)	3/15 (16.7)	4/5 (44.4)	.175
Mortality at 6 mo (%)	4/14 (22.2)	4/5 (44.4)	.375
Mortality at 12 mo (%)	4/14 (22.2)	4/5 (44.4)	.375

Note:—GP indicates glycoprotein.

^a Significant.

time, and onset-to-reperfusion time between the 2 groups. The postprocedural NIHSS score and mRS at discharge and at 3, 6, and 12 months were also not statistically different between the 2 groups (On-line Table).

Procedural time showed a moderate positive correlation with mRS at 3 months and mRS at 6 months, respectively ($\rho = 0.47$, $P = .030$ and $\rho = 0.46$, $P = .035$, respectively). However, no significant correlation was found between the time from onset to reperfusion and clinical outcome.

During the procedure, a glycoprotein IIb/IIIa inhibitor was administered in 7 of 13 patients (53.8%) in the Solitaire group and 11 of 14 patients (78.6%) in the other stent group ($P = .236$) (On-line Table). There was a trend toward a higher rate of mTICI 2b–3 recanalization when the glycoprotein IIb/IIIa inhibitor was used than when it was not used (88.9% versus 66.7%), but statistical significance was not reached ($P = .295$) (Table).

There were no significant differences in ISR at discharge and at 3 months between the 2 groups (On-line Table). However, both ISR at discharge and ISR at 3 months were significantly lower when a glycoprotein IIb/IIIa inhibitor was administered during the procedure ($P = .013$ and $P = .036$, respectively). Also, the proportion of favorable mRS (0–2) at 3 months was significantly higher in the patients who were administered a glycoprotein IIb/IIIa inhibitor during the procedure compared with those who were not ($P = .026$) (Table). No significant difference was noted in ISR at discharge between patients with cancer and those without cancer.

Rates of overall hemorrhagic transformation and symptomatic intracerebral hemorrhage in the Solitaire group (15.4% and 0%, respectively) were not significantly different from those in the other stent group (35.7% and 21.4%, respectively) (On-line Table). Also, mortalities at 3, 6, and 12 months in the Solitaire group (23.1%, 30.8%, and 30.8%, respectively) were not significantly different from those in the other stent group (28.6%, 28.6%, and 28.6%, respectively) (On-line Table).

Three patients in the Solitaire group died of respiratory failure with underlying metastatic cancer (bronchial bleeding due to disseminated intravascular coagulation, sepsis and pneumonia, and malignant pleural effusion and pneumonia) at 3 months, and 1 patient in the Solitaire group died of respiratory failure with underlying cancer (sepsis and pancytopenia) at 6 months. Three

patients in the other stent group died of cerebral herniation caused by malignant cerebral edema or intracerebral hemorrhage at discharge, and 1 patient in the other stent group died of pneumonia and sepsis at 3 months.

DISCUSSION

We have shown that permanent detachment of the Solitaire FR achieved mTICI 2b–3 recanalization in 84.6% of patient with acute ischemic stroke in whom mechanical thrombectomy had failed. Total procedural time was significantly shorter in the Solitaire group than in the other stent group ($P = .022$). Shorter procedural time was correlated with favorable outcome ($\rho = 0.46$, $P = .035$). There were no significant differences in discharge NIHSS score; mRS at 3, 6, and 12 months; complication rates such as symptomatic intracerebral hemorrhage; and mortality between the 2 groups. This finding suggests that permanent stent placement with the Solitaire FR might be considered a rescue therapy in preference to other self-expanding stents for failed mechanical thrombectomy in patients with acute intracranial artery occlusion. The efficacy and safety of permanent stent placement using other self-expanding stents for recanalization of acute intracranial vessel occlusion have been evaluated in several previous studies.^{8–12} However, to our knowledge, there has been no study that compares the outcome of the Solitaire FR stent with that of other self-expanding stents for rescue treatment.

For the prevention of recurrent stroke, intracranial artery stent placement is not recommended as the first-line treatment of intracranial atherosclerosis according to the Stenting vs Aggressive Medical Management for Preventing Recurrent Stroke in Intracranial Stenosis (SAMMPRIS)¹⁸ trial, which reported early morbidity as high as 14.7% in the stent placement group. However, in the acute setting, several case series demonstrated high recanalization rates of 74.5%–92% for intracranial stent placement when other endovascular methods had failed.^{8–10,19,20} Self-expanding stents (eg, Neuroform, Wingspan, or Enterprise) have been used in most patients in these series.

Intracranial atherosclerotic disease is more common in Asian populations than in Western populations,¹³ though the reason remains unclear. Possible explanations include the inherited susceptibility of intracranial vessels to atherosclerosis, acquired differences in the prevalence of risk factors, and differential responses to the same risk factors.¹³ Thrombus lodged in segments of underlying intracranial atherosclerotic stenosis may become refractory to mechanical disruption or clot retrieval. Therefore, intracranial artery stent placement might be considered a feasible option in the treatment of Asian patients with acute large-artery occlusion. Recently, Baek et al²⁰ demonstrated more favorable outcomes in the stent group than in the nonstent group in Korean populations. In addition, studies from East Asia have shown lower rates of periprocedural complications and morbidities in patients with intracranial stent placement when other endovascular procedures failed to achieve recanalization.^{13,21–26}

In addition to a tool for mechanical thrombectomy, the Solitaire FR can also be used as a permanent stent because it is detachable.²⁷ In this study, we achieved an mTICI of 2b–3 in 84.6% of the cases in Solitaire group, comparable with 78.6% in the other

stent group. Moreover, because permanent stent placement using the Solitaire FR does not require the insertion of another device, the use of the Solitaire FR can significantly reduce the procedural time as well as cost. Consequently, this might reduce the time interval from stroke onset to reperfusion and hence might potentially reduce the risk of periprocedural complications. In this study, shorter procedural time was correlated with favorable outcome. In addition, although no statistical significance was found, there were trends toward lower rates of symptomatic intracerebral hemorrhage and overall hemorrhagic transformation in the Solitaire group compared with the other stent group. Another advantage of the Solitaire FR in relation to other self-expandable stents is that the Solitaire FR enables the assessment of vessel patency during its temporary placement. When antegrade flow is restored and the target vessel lumen is patent during the temporary deployment of the Solitaire stent but recurrent occlusion after stent retrieval occurs, permanent detachment of the Solitaire FR can be an option.

The combination of thrombolytics and the glycoprotein IIb/IIIa antagonist has been shown to have a synergistic effect on the recanalization efficiency in other studies.^{14,28} In this study, the use of glycoprotein IIb/IIIa antagonists was based on the likely mechanism of stroke. When underlying intracranial atherosclerotic stenosis was suspected and when recurrent buildup of thrombus was noted during the temporary placement of the stent, then the glycoprotein IIb/IIIa inhibitor was particularly considered. Although the immediate postprocedural success rate (mTICI grade 2b–3) regarding glycoprotein IIb/IIIa inhibitor usage was not significantly different (88.9% versus 66.7%, $P = .295$), we observed better angiographic outcomes at discharge and at 3 months and better clinical outcomes at 3 months when a glycoprotein IIb/IIIa antagonist was used during the procedure ($P = .013$, $P = .036$, and $P = .026$, respectively). Because a glycoprotein IIb/IIIa antagonist prevents acute thrombus formation and subsequent distal embolization by inhibiting the final common pathway of platelet aggregation, its effect may be seen more often during the early phase after the onset of stroke. No significant difference was found in overall complication rates based on the use of a glycoprotein IIb/IIIa antagonist.

As with any other intracranial stents, dual antithrombotic therapy is recommended to prevent delayed thrombosis within the stent.^{19,29} Patients in our study were routinely given aspirin in combination with clopidogrel. However, initiating these drugs may be difficult in an acute setting when IV tPA has been administered. In this situation, delayed initiation of antiplatelet medication by at least 24 hours is recommended to reduce the risk of symptomatic intracranial hemorrhage.³⁰

In addition to the retrospective nature of this study, our study has a few limitations. First, although most clinical characteristics and outcome variables were comparable between the Solitaire group and the other stent group, a noninferiority test could not be performed due to the small sample size. A follow-up study with a larger study population and a longer follow-up period would be desirable. Second, the inclusion of patients with underlying cancer might have led to difficulties in interpreting clinical outcomes.

CONCLUSIONS

Compared with other self-expandable stents, the permanent deployment of the Solitaire FR as a rescue therapy for reperfusion of intracranial artery occlusion appears to be feasible and safe and requires a shorter procedural time.

Disclosures: Leonard Sunwoo—RELATED: Grant: Seoul National University Bundang Hospital Research Fund (No. 14-2016-019).

REFERENCES

1. Saver JL, Jahan R, Levy EI, et al; SWIFT Trialists. **Solitaire flow restoration device versus the Merci Retriever in patients with acute ischaemic stroke (SWIFT): a randomised, parallel-group, non-inferiority trial.** *Lancet* 2012;380:1241–49 CrossRef Medline
2. Berkhemer OA, Fransen PS, Beumer D, et al. **A randomized trial of intraarterial treatment for acute ischemic stroke.** *N Engl J Med* 2015; 372:11–20 CrossRef Medline
3. Campbell BC, Mitchell PJ, Kleinig TJ, et al; EXTEND-IA Investigators. **Endovascular therapy for ischemic stroke with perfusion-imaging selection.** *N Engl J Med* 2015;372:1009–18 CrossRef Medline
4. Goyal M, Demchuk AM, Menon BK, et al; ESCAPE Trial Investigators. **Randomized assessment of rapid endovascular treatment of ischemic stroke.** *N Engl J Med* 2015;372:1019–30 CrossRef Medline
5. Jovin TG, Chamorro A, Cobo E, et al; REVASCAT Trial Investigators. **Thrombectomy within 8 hours after symptom onset in ischemic stroke.** *N Engl J Med* 2015;372:2296–306 CrossRef Medline
6. Saver JL, Goyal M, Bonafe A, et al; SWIFT PRIME Investigators. **Stent-retriever thrombectomy after intravenous t-PA vs. t-PA alone in stroke.** *N Engl J Med* 2015;372:2285–95 CrossRef Medline
7. Goyal M, Menon BK, van Zwam WH, et al; HERMES collaborators. **Endovascular thrombectomy after large-vessel ischaemic stroke: a meta-analysis of individual patient data from five randomised trials.** *Lancet* 2016;387:1723–31 CrossRef Medline
8. Brekenfeld C, Schroth G, Mattle HP, et al. **Stent placement in acute cerebral artery occlusion: use of a self-expandable intracranial stent for acute stroke treatment.** *Stroke* 2009;40:847–52 CrossRef Medline
9. Levy EI, Mehta R, Gupta R, et al. **Self-expanding stents for recanalization of acute cerebrovascular occlusions.** *AJNR Am J Neuroradiol* 2007;28:816–22 Medline
10. Zaidat OO, Wolfe T, Hussain SI, et al. **Interventional acute ischemic stroke therapy with intracranial self-expanding stent.** *Stroke* 2008; 39:2392–95 CrossRef Medline
11. Levy EI, Siddiqui AH, Crumlish A, et al. **First Food and Drug Administration-approved prospective trial of primary intracranial stenting for acute stroke: SARIS (stent-assisted recanalization in acute ischemic stroke).** *Stroke* 2009;40:3552–56 CrossRef Medline
12. Levy EI, Rahman M, Khalessi AA, et al. **Midterm clinical and angiographic follow-up for the first Food and Drug Administration-approved prospective, single-arm trial of primary stenting for stroke: SARIS (Stent-Assisted Recanalization for Acute Ischemic Stroke).** *Neurosurgery* 2011;69:915–20; discussion 920 CrossRef Medline
13. Kim JS, Bonovich D. **Research on intracranial atherosclerosis from the East and West: why are the results different?** *J Stroke* 2014;16: 105–13 CrossRef Medline
14. Abou-Chebl A, Bajzer CT, Krieger DW, et al. **Multimodal therapy for the treatment of severe ischemic stroke combining GPIIb/IIIa antagonists and angioplasty after failure of thrombolysis.** *Stroke* 2005; 36:2286–88 CrossRef Medline
15. Hacke W, Kaste M, Fieschi C, et al. **Randomised double-blind placebo-controlled trial of thrombolytic therapy with intravenous alteplase in acute ischaemic stroke (ECASS II): Second European-Australasian Acute Stroke Study Investigators.** *Lancet* 1998;352: 1245–51 CrossRef Medline
16. Hacke W, Kaste M, Bluhmki E, et al; ECASS Investigators. **Thrombolysis with alteplase 3 to 4.5 hours after acute ischemic stroke.** *N Engl J Med* 2008;359:1317–29 CrossRef Medline

17. Adams HP Jr, Bendixen BH, Kappelle LJ, et al; TOAST Investigators. **Classification of subtype of acute ischemic stroke: definitions for use in a multicenter clinical trial.** *Stroke* 1993;24:35–41 Medline
18. Chimowitz MI, Lynn MJ, Derdeyn CP, et al; SAMMPRIS Trial Investigators. **Stenting versus aggressive medical therapy for intracranial arterial stenosis.** *N Engl J Med* 2011;365:993–1003 CrossRef Medline
19. Levy EI, Ecker RD, Horowitz MB, et al. **Stent-assisted intracranial recanalization for acute stroke: early results.** *Neurosurgery* 2006;58:458–63; discussion 458–63 CrossRef Medline
20. Baek JH, Kim BM, Kim DJ, et al. **Stenting as a rescue treatment after failure of mechanical thrombectomy for anterior circulation large artery occlusion.** *Stroke* 2016;47:2360–63 CrossRef Medline
21. Ramee SR, Subramanian R, Felberg RA, et al. **Catheter-based treatment for patients with acute ischemic stroke ineligible for intravenous thrombolysis.** *Stroke* 2004;35:e109–111 CrossRef Medline
22. Gupta R, Vora NA, Horowitz MB, et al. **Multimodal reperfusion therapy for acute ischemic stroke: factors predicting vessel recanalization.** *Stroke* 2006;37:986–90 CrossRef Medline
23. Sauvageau E, Samuelson RM, Levy EI, et al. **Middle cerebral artery stenting for acute ischemic stroke after unsuccessful Merci retrieval.** *Neurosurgery* 2007;60:701–06; discussion 706 CrossRef Medline
24. Sauvageau E, Levy EI. **Self-expanding stent-assisted middle cerebral artery recanalization: technical note.** *Neuroradiology* 2006;48:405–08 CrossRef Medline
25. Fitzsimmons BF, Becske T, Nelson PK. **Rapid stent-supported revascularization in acute ischemic stroke.** *AJNR Am J Neuroradiol* 2006;27:1132–34 Medline
26. Jeon P, Kim BM, Kim DI, et al. **Emergent self-expanding stent placement for acute intracranial or extracranial internal carotid artery dissection with significant hemodynamic insufficiency.** *AJNR Am J Neuroradiol* 2010;31:1529–32 CrossRef Medline
27. Stampfl S, Hartmann M, Ringleb PA, et al. **Stent placement for flow restoration in acute ischemic stroke: a single-center experience with the Solitaire stent system.** *AJNR Am J Neuroradiol* 2011;32:1245–48 CrossRef Medline
28. Seo JH, Jeong HW, Kim ST, et al. **Adjuvant tirofiban injection through deployed Solitaire stent as a rescue technique after failed mechanical thrombectomy in acute stroke.** *Neurointervention* 2015;10:22–27 CrossRef Medline
29. Bose A, Hartmann M, Henkes H, et al. **A novel, self-expanding, nitinol stent in medically refractory intracranial atherosclerotic stenoses: the Wingspan study.** *Stroke* 2007;38:1531–37 CrossRef Medline
30. Adams HP Jr, Adams RJ, Brott T, et al; Stroke Council of the American Stroke Association. **Guidelines for the early management of patients with ischemic stroke: a scientific statement from the Stroke Council of the American Stroke Association.** *Stroke* 2003;34:1056–83 CrossRef Medline

Better Than Nothing: A Rational Approach for Minimizing the Impact of Outflow Strategy on Cerebrovascular Simulations

C. Chnafa, O. Brina, V.M. Pereira, and D.A. Steinman



ABSTRACT

BACKGROUND AND PURPOSE: Computational fluid dynamics simulations of neurovascular diseases are impacted by various modeling assumptions and uncertainties, including outlet boundary conditions. Many studies of intracranial aneurysms, for example, assume zero pressure at all outlets, often the default (“do-nothing”) strategy, with no physiological basis. Others divide outflow according to the outlet diameters cubed, nominally based on the more physiological Murray’s law but still susceptible to subjective choices about the segmented model extent. Here we demonstrate the limitations and impact of these outflow strategies, against a novel “splitting” method introduced here.

MATERIALS AND METHODS: With our method, the segmented lumen is split into its constituent bifurcations, where flow divisions are estimated locally using a power law. Together these provide the global outflow rate boundary conditions. The impact of outflow strategy on flow rates was tested for 70 cases of MCA aneurysm with 0D simulations. The impact on hemodynamic indices used for rupture status assessment was tested for 10 cases with 3D simulations.

RESULTS: Differences in flow rates among the various strategies were up to 70%, with a non-negligible impact on average and oscillatory wall shear stresses in some cases. Murray-law and splitting methods gave flow rates closest to physiological values reported in the literature; however, only the splitting method was insensitive to arbitrary truncation of the model extent.

CONCLUSIONS: Cerebrovascular simulations can depend strongly on the outflow strategy. The default zero-pressure method should be avoided in favor of Murray-law or splitting methods, the latter being released as an open-source tool to encourage the standardization of outflow strategies.

ABBREVIATIONS: ACA = anterior cerebral artery; CFD = computational fluid dynamics; OA = ophthalmic artery; OSI = oscillatory shear index; PcomA = posterior communicating artery; TAWSS = time-averaged wall shear stress

Simulating blood flows by image-based computational fluid dynamics (CFD) has become a prevalent technique for studying the natural history and treatment options for cerebrovascular

disorders, notably intracranial aneurysms.¹ The accuracy of these nominally patient-specific simulations is subject to not only the CFD methodology² but also numerous approximations and assumptions. For example, while patient-specific lumen geometries are readily available from routine clinical angiography and used to create the 3D model, properties of blood and the vessel wall are rarely acquired for each patient. Most of the time, rigid walls are assumed and population-averaged constants are used for blood viscosity. When patient-specific flow rates are available, it is typically only at the model inlet.³ More often, inlet flow rates are assumed from literature values, sometimes coupled to a scaling law to account for interindividual differences in flow.⁴ On the other hand, an assumption that remains particularly latent is that of the outlet flow rates.

Inspection of articles published in the *American Journal of Neuroradiology* and other clinical and biomedical engineering research journals reveals that the outflow strategy is rarely or only superficially reported. When information is provided, most stud-

Received July 24, 2017; accepted after revision October 13.

From the Biomedical Simulation Laboratory (C.C., D.A.S.), Department of Mechanical and Industrial Engineering, University of Toronto, Toronto, Ontario, Canada; and Joint Division of Medical Imaging (O.B., V.M.P.), Department of Medical Imaging and Division of Neurosurgery, Department of Surgery, Toronto Western Hospital, University Health Network, and University of Toronto, Toronto, Ontario, Canada.

This work was supported by grants from the Heart & Stroke Foundation (G-13-0001830, to D.A.S.) and the University Health Network (AMO AFP 410004349, to V.M.P.). D.A.S. also acknowledges the support of a Mid-Career Investigator Award (MC7455) from the Heart & Stroke Foundation of Canada.

Please address correspondence to David A. Steinman, PhD, Department of Mechanical & Industrial Engineering, University of Toronto, 5 King’s College Rd, Toronto, ON M5S 3G8 Canada; e-mail: steinman@mie.utoronto.ca

 Indicates article with supplemental on-line appendix and tables.

 Indicates article with supplemental on-line photos.

<http://dx.doi.org/10.3174/ajnr.A5484>

ies focusing on multi-outlet CFD models report using “zero pressure” or “traction-free” outlet boundary conditions to determine the division of flow among the outlets, a trend also noted by Marzo et al.⁵ This outflow strategy is often the default (“do nothing”) setting for CFD solvers, and implicit is the assumption that the necessarily truncated cerebrovascular model has all of its outlets connected to the same artery distally, which is rarely the case. (That assumption should not be confused with the more physiological assumption that outlets feed microvascular beds having the same resistance; see the On-line Appendix). As also detailed in the On-line Appendix, subjective—and rarely documented—choices about the CFD models, such as truncation of downstream branches or addition of flow extensions, may therefore play a role in determining the division of outflow rates, which, incidentally, is typically known only after the CFD simulation is completed.⁶

Another popular outflow strategy is to explicitly apportion the flow rates among the outlets according to their diameters cubed.⁷ This “Murray law” strategy derives from the eponymous principle that pumping versus metabolic power is optimized for the circulatory system⁸ and reflects conduit vessels adapting their calibers to the flow rate demanded by the downstream microvascular beds. Murray’s law hinges on the simplifying assumption of Poiseuille flow, which does not necessarily hold for larger, conduit arteries⁹; thus, like the zero-pressure strategy, the predicted flow rates, and hence the CFD simulations, may also be sensitive to the number and extent of outlets retained in the model. (A third, less common approach is to impose microvascular resistances directly at the outlets; however, absent patient-specific flow rates, population-average resistances must be imposed, resulting in population-average flow divisions.)

Therefore, the aim of the present study was 2-fold: 1) to present a novel and more robust alternative, hereafter referred to as the “splitting” method, which uses vessel diameters to estimate patient-specific outflow divisions that are more grounded in physiology and less sensitive to the subjective extent of the CFD model; and 2) to quantify the uncertainty of cerebrovascular CFD models to outflow strategy.

MATERIALS AND METHODS

Study Cohort

We evaluated outflow strategies for 70 patients with MCA aneurysms (55 ± 11 years of age, 73% women) from a broader cohort of 244 consecutive patients with 358 aneurysms, included from March 2011 to March 2014. These cases were segmented from 3D rotational angiography, from the cervical ICA to at least the M2 branches, using either a threshold segmentation method (Aneufuse; @neurIST, <http://www.aneurist.org/>) or a gradient-based watershed technique (Matlab; MathWorks, Natick, Massachusetts). Arteries below a threshold diameter of 0.6 mm were not segmented; thus, the ophthalmic artery (OA) was excluded for roughly 25% of the models. The posterior communicating artery (PcomA) was also typically excluded, except for cases with evident fetal posterior cerebral arteries. Detailed morphologic characteristics of this cohort can be found elsewhere.⁶

These 3D segmentations were used to construct 0D models, on which the various outflow strategies were tested for their impact on branch flow rates. 3D CFD simulations were performed on a

subset of 10 representative cases to determine the impact of outflow conditions on derived hemodynamic indices.

Splitting Method

Murray’s law is a specific case of a more general principle that the flow rate in a vessel is proportional to the diameter of that vessel raised to some power (ie, $Q \propto D^n$, with $n = 3$ for Murray’s law). As commonly practiced in CFD, the Murray-law strategy is to simply prescribe the flow rate for outlet i as

$$1) \quad \frac{Q_i}{\sum Q_i} = \frac{D_i^n}{\sum D_i^n}$$

where Q_i is the flow rate of the outlet, D_i is the diameter of the outlet, and, customarily, $n = 3$. The summations are over all outlets, and by conservation of mass, the sum of outflows must equal the inflows. Note that all outlets are treated the same according to their diameters, irrespective of the branch generation to which they belong—that is, no attention is paid to branching within the model.

Our proposed outflow splitting method is based on the same power law relationship between diameter and flow rate, but in the spirit of Murray’s original derivation, it is used locally for each bifurcation within the model (eg, see Fig 1, case A). In other words, starting from the inlets, at each bifurcation encountered, we assume the flow divides according to a power law:

$$2) \quad \frac{Q_1}{Q_2} = \left(\frac{D_1}{D_2} \right)^n$$

where D_1 and D_2 are the diameters of the 2 daughter branches at the given bifurcation, and Q_1/Q_2 is the bifurcation flow division. These outflows then serve as the inflows for subsequent bifurcations, until the CFD model outlets are reached, at which point the proportion of the original inlet flow to each outlet is known. A more detailed derivation, with examples, is given in the On-line Appendix. It is important to note that our splitting method does not impose these individual internal flow divisions on the CFD model. Rather, they are used, as detailed below, to compute outlet flow rates that, imposed on the CFD model, will give rise to the expected internal flow divisions.

0D Modeling for the Impact of Outflow Strategy on Flow Rate Distribution

Recently, we developed a novel lumped parameter approach for fast and accurate prediction of flow divisions in 3D CFD models when outflow pressures are prescribed.⁶ Briefly, given a 3D lumen geometry model, a 0D (electrical circuit) model is derived in 2 steps: 1) The centerlines of the model are computed with the Vascular Modeling Toolkit (VMTK; www.vmtk.org); and 2) these centerlines are decomposed in a network of straight, rigid segments parameterized by their mean radius, length, and bifurcation angles. In these reduced-order networks, we assume fully developed, steady, Poiseuille flow so that for each segment, the flow rate is proportional to the pressure gradient along the vessel and the inverse of its resistance. Equations for all segments are assembled and solved iteratively by applying an analog of the Kirchhoff current law to satisfy segment-to-segment mass conser-

vation.¹⁰ The method was previously validated for this MCA aneurysm cohort via pulsatile 3D CFD simulations that had prescribed only ICA inflow but used different pressures for each outlet.⁶ By setting all outlet pressures to zero, this 0D approach was used to calculate the outflow rates for the zero-pressure method.

To determine the outflow rates for the splitting method, we took advantage of the fact that the above-described 3D to 0D process includes the automated identification of bifurcations and measurement of inflow/outflow branch diameters. It was therefore straightforward to adapt this to our proposed splitting method using, for each bifurcation, the power law equation (Equation 2) relating the outflow division to daughter branch diameters and solving simultaneously to obtain the desired outlet flow rates. A power law exponent $n = 2$ was used at all bifurcation levels. Finally, for the Murray-law method, we simply applied Equation 1, based on the outlet diameters and with a power law exponent $n = 3$, reflecting common practice.

The 0D models were solved for each case assuming steady flow, with a cross-sectional mean velocity of 0.27 m/s applied to the ICA inlet, under the assumption that inflow rate scales with cross-sectional area⁴ (ie, a power law with $n = 2$). The resulting inflow rates are plotted in On-line Fig 1. Outlet flow rates were then calculated according to the 3 different methods (zero-pressure, Murray-law, splitting) and used to calculate the MCA, anterior cerebral artery (ACA), OA, and PcomA flow rates. It is important to remember that, for these MCA aneurysm cases, the parent artery (ie, the MCA) flow rate is effectively determined by the outflow method in addition to the prescribed ICA inflow.

3D CFD Modeling for Impact of Outflow Strategy on Hemodynamic Indices

As shown in Fig 1, a subset of 10 representative cases was selected for 3D CFD to determine the impact of the outflow strategy on

nominal hemodynamic predictors of rupture status. Of these, 3 were chosen to exemplify the impact of model extent. Specifically, as also shown in Fig 1, the alterations were either drastic, with branches clipped immediately distal to the aneurysm (case A) or mild, with shortened M2 segments (case B) or a change of the number of outlets and length of the M2 segments (case C).

For these 10 cases and their 3 variants, we performed CFD simulations using a minimally dissipative solver developed and validated within the Open-Source Finite-Element Method Library, FEniCS (<https://fenicsproject.org/>).¹¹ The segmented lumens were meshed using VMTK, with 4 layers of boundary elements and the mesh density chosen to be highest in the vicinity of the aneurysm sac, where the tetrahedron side length was 0.12 mm on average.¹² The number of tetrahedral elements per case was 3.8 million on average, ranging from 2.3 to 4.7 million, reflecting the variability of the aneurysm sizes and extents of the CFD model domains.

We assumed rigid walls, blood kinematic viscosity of 0.0035 m²/s, and blood density of 1060 kg/m³. Like the 0D models, a cycle-averaged cross-sectional mean velocity of 0.27 m/s was applied to the ICA inlet in all cases and was used to scale a representative older adult ICA flow waveform shape¹³ to impose fully developed Womersley velocity profiles at the ICA inlet. To account for possible dampening along the ICA and MCA,¹⁴ we reduced the harmonics of this inflow waveform in amplitude by 10%. The number of time-steps per cardiac cycle was set to 10,000,¹² and all simulations were run for at least 3 cardiac cycles to wash away any initial transients. The analysis was based on the output from 1000 uniformly spaced time-steps from the last cycle.

For the zero-pressure CFD simulations, the pressure was set to zero at all CFD model outlets via traction-free boundary conditions. For the splitting method, outlet flow rates were imposed as mass flux conditions to the outlets of the CFD model, which amounts to traction-free boundary conditions (see “Discus-

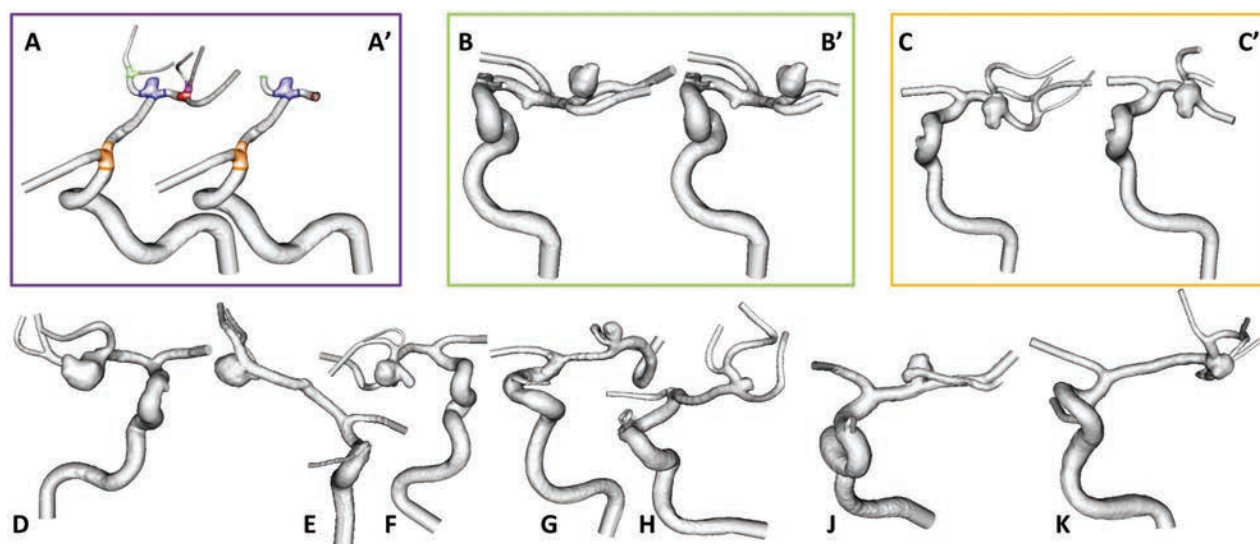


FIG 1. The 10 representative cases of MCA aneurysms used for 3D CFD. A subset of 3 cases (A–C) was truncated differently, as depicted by A', B', C'. These are color-coded to identify their data in subsequent figures. Cases A and A' highlight their individual bifurcations, as used by the splitting method.

Table 1: For the 70 patients with MCA aneurysms, mean \pm SD flow rates (mL/min) in the major arteries and mean flow divisions at the ICA terminus^a

Outflow Method	ACA	MCA	OA	PcomA	ACA:MCA
Zero-pressure	103 \pm 50	137 \pm 53	15 \pm 10	71 \pm 42	43:57
Murray-law	89 \pm 47	152 \pm 57	14 \pm 11	65 \pm 46	37:63
Splitting	86 \pm 38	154 \pm 46	16 \pm 8	60 \pm 30	36:64
Literature values	84 \pm 24	142 \pm 31	11 \pm 5	59 \pm 14 ^b	37:63

^a Enriched tables are provided in On-line Tables 1 and 2.

^b Literature values measured at the posterior cerebral artery.

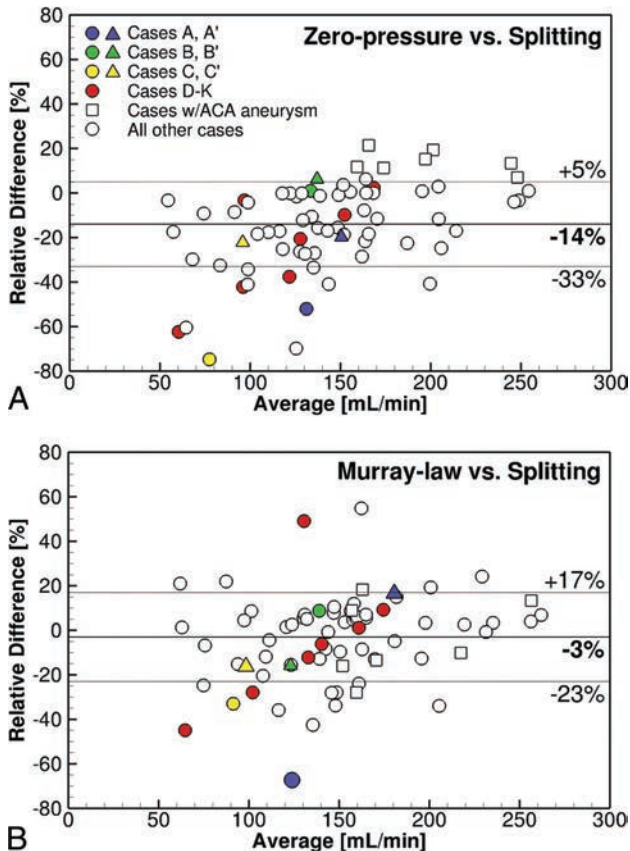


FIG 2. Bland-Altman plots reveal non-negligible limits of agreement (upper and lower dotted lines) for cycle-averaged MCA flow rates computed via the different outflow strategies. Colored circles represent the 10 cases subsequently selected for 3D CFD. Note that the modified extents (cases A', B', C') show non-negligible changes in flow rates for both zero-pressure and Murray-law methods. The y-axis is defined as the considered outflow method minus the splitting method flow rate, divided by the average of flow rates obtained with the 2 methods.

Table 2: Impact of model extent on predicted MCA flow rates (mL/min) for the 3 cases with modified outflow extents

Outflow Method	A	A'	B	B'	C	C'
Zero-pressure	97	136	134	141	49	85
Murray-law	82	195	145	113	76	90
Splitting	166	166	133	133	106	106

sion”). CFD simulations for the Murray-law method were not performed.

For each CFD model, the time-averaged wall shear stress (TAWSS) magnitude and oscillatory shear index (OSI) were determined from the time-varying velocity data. The aneurysm sac was digitally isolated,¹⁵ and for each permutation of case and outflow method, we computed the following hemodynamic indices

often used for rupture status assessment¹²: sac-averaged TAWSS and sac-maximum TAWSS, both normalized to the parent artery TAWSS; and sac-averaged OSI.

RESULTS

Impact of Outflow Strategy on Flow Rate Distribution

Table 1 demonstrates the overall impact of outflow strategy on flow rates in the major arteries and their accuracy relative to in vivo measurements averaged from the literature. Although all 3 methods predicted MCA flow rates to within <10% on average, the zero-pressure method overestimated ACA flow rates by 23%, causing an imbalance of flow at the ICA terminus. On the other hand, the Murray-law and splitting methods also predicted ACA flow rates to within <10% on average and thus had ACA/MCA flow divisions nearly identical to the in vivo average. For those cases with a PcomA, the zero-pressure method had the largest overestimation relative to in vivo values, while the small OA flow rates were overpredicted by all outflow strategies. SDs (ie, inter-individual variances) were largest for the zero-pressure method, followed by the Murray-law method, while the splitting method was closest to, albeit still higher than, the in vivo variances.

Figure 2 shows the marked impact of outflow strategy on flow rates at the MCA, which is the parent artery for these aneurysm cases. Notably, Fig 2A reveals that relative to the more physiological splitting method, the zero-pressure method underestimates MCA flow rates by 14% on average, but >50% for some cases. Figure 2B shows that the Murray-law and splitting methods give closer results on average, but the limits of agreement still have a wide range and thus large differences for individual cases, from +50% to -70%.

Impact of Model Extent on Flow Rate Distribution

Figure 2 also shows that the modified extents for cases A–C resulted in non-negligible changes in MCA flow rates. This impact of modified extents is further highlighted in Table 2, where removal of the M3 branches for case A resulted in 40% and 138% increases in MCA flow for the zero-pressure and Murray-law methods, respectively. Even the mild modifications to cases B and C resulted in non-negligible changes in MCA flow rates: a 22% decrease with the Murray-law method for case B versus B' and a 73% increase with the zero-pressure method for case C versus C'. With the splitting method, model extent had no impact on flow rates as designed.

Such impact of model extent can also be inferred from cases that had an ACA aneurysm in addition to the MCA aneurysm (squares in Fig 2). These models extended at least to the A2 branches, whereas those with only MCA aneurysms were truncated at the A1 branch. Per Fig 2A, such imbalance in the number and size of MCA-versus-ACA outlets—more flow resistance is offered by the M1+M2 branches versus the single A1 stub—led to the marked underestimation of MCA flow rates by the zero-pressure method, whereas the ACA aneurysm cases (having more balanced ACA and MCA flow resistances) had flow rates closer to the splitting method. Per Fig 2B, the Murray-law method was less susceptible to such frank imbalances.

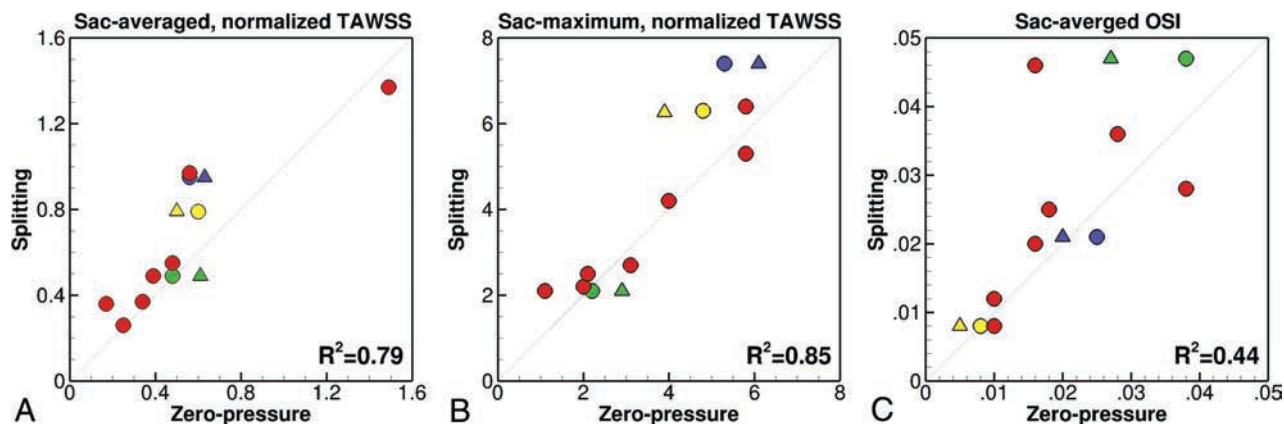


FIG 3. Comparison of 3 normalized hemodynamic indices (see “Materials and Methods”) determined from 3D CFD simulations, computed using zero-pressure-versus-splitting methods. The *lower right* of each panel shows the coefficients of determination (R^2) as measures of correlation and agreement. The *dotted line* is perfect agreement. Note the *triangles* and different colors used to highlight the different truncations for cases A, B, and C (see symbol legend in Fig 2). These data points are translated only horizontally because the splitting method is, by design, not sensitive to model extent.

Impact on Hemodynamic Indices

Quantitative differences between zero-pressure and splitting methods for nominal metrics of rupture status are shown in Fig 3, to appreciate the practical impact of outflow strategy. (Qualitative differences in the surface distributions from which these sac-integrated values were derived can be seen in On-line Figs 2 and 3.) Normalized TAWSS was affected by the outflow method, showing absolute differences of $21\% \pm 18\%$, reflecting differences in the CFD-computed wall shear stress patterns. Without the parent artery normalization, differences in aneurysm TAWSS were $40\% \pm 25\%$, reflecting the compounding effect of differences in parent artery (MCA) inflow rates on wall shear stress magnitudes.

For the zero-pressure method, changes in the extent of models A, B, and C resulted in TAWSS differences of -12% , $+22\%$, and -22% , respectively. It is important to note that these differences are observed for the same cases with the same outflow strategy, with the only difference being an alternative but equally plausible choice of 3D model extent. Sac-maximum TAWSS showed absolute differences of $17\% \pm 13\%$ between the outflow methods and the comparable effect of model extent. Larger differences were observed for the sac-averaged OSI, showing more pronounced changes in the rank ordering of cases from low-to-high OSI. The absolute difference for OSI was $24\% \pm 17\%$, and modified extent had a greater impact than for sac-average and sac-maximum TAWSS, with differences from 24% to 63% relative to the OSI from the splitting method.

DISCUSSION

Relationship to Previous Studies: Impact of Outflow or Not?

Previous studies reporting the impact of the outflow rates on aneurysm CFD have shown mixed conclusions but typically relied on single cases and hemodynamic indices not commonly used in large-scale studies. Ramalho et al¹⁶ concluded that the choice of outflow strategy “highly influence[d] the hemodynamics inside the aneurysm [and] should be chosen with special caution.” Venugopal et al¹⁷ varied the outflow distribution by factors 2–12 times greater than what we reported, yet seeing its impact on TAWSS maps, they concluded that it was “difficult to draw any conclusions regarding the role of shear stress in the aneurysm’s

growth.” Grinberg and Karniadakis¹⁸ showed that using zero-pressure versus lumped parameter outflow conditions led to a “300% difference in flow rates through the outlets” for their patient-specific cerebrovasculature model. On the other hand, Cebal et al¹⁹ reported that outflow rate variations of $\pm 25\%$ “did not alter the main characteristics of the intra-aneurysmal flow patterns.” These disparate conclusions have given mixed messages to the CFD and clinical communities and, as noted by Ramalho et al,¹⁶ called for “stud[ies] with larger number of geometries.”

The present study, based on 70 cases (10 with CFD), demonstrates that the choice of outflow strategy can alter the physiological plausibility and results of aneurysm CFD, with non-negligible impact on both flow rate distributions and nominal hemodynamic predictors of rupture status. The 2 most popular outflow strategies—zero-pressure and Murray-law—were also sensitive to subjective choices about CFD model extent, which are rarely documented and can vary widely among the CFD community. For example, in the most recent aneurysm CFD Challenge, which focused on MCA aneurysm cases, the presence and extent of proximal ICA, side branches, or distal bifurcations varied dramatically.²⁰ The splitting method we propose is minimally sensitive to such uncertainties and demonstrably offers robust and realistic flow distributions.

The differences we report in hemodynamic indices due to outflow strategy, as shown in Fig 3, are comparable with those reported due to CFD solution strategy,² which were, in turn, far greater than those due to non-Newtonian viscosity.²¹ Similarly, the divergent conclusions of Ramalho et al¹⁶ and Venugopal et al¹⁷ were drawn from TAWSS patterns that appear, qualitatively at least, to be comparable with those presented in studies of geometric^{22–24} or inflow³ uncertainties. Together these suggest that the outflow strategy should be considered at least as important as other assumptions or uncertainties in aneurysm CFD.

Implications for Clinical CFD: Does Outflow Really Matter?

It could be argued that our findings are exaggerated by our use of extensive models that include the cervical ICA with side (OA, PcomA) and terminal ACA branches, meaning that the aneurysm

(ie, MCA) inflow is also effectively determined by the outflow method. Indeed, CFD studies of MCA aneurysms often comprise just the single (M1/M2) bifurcation.^{2,25,26} Setting aside the thorny question of whether flow in the MCA can be considered fully developed in such studies considering complex flow patterns almost certainly present upstream of the ICA siphon and terminus,^{24,27} for these cases, the Murray-law and splitting methods would, assuming the same power law exponent, indeed give the same results. Consider, however, our case J, for which all 3 outflow methods predicted the M1 inflow to within <5%. The difference in M2 outflows predicted by the zero-pressure and splitting methods was a modest 15%, yet this resulted in a 50% difference in the normalized sac-averaged TAWSS (0.17 versus 0.36, respectively). This would seem to suggest that our findings about the zero-pressure strategy would hold even for less extensive aneurysm CFD models.

To appreciate the potential implications of this, consider that Takao et al²⁵ and Miura et al²⁶ used a zero-pressure strategy for their large (50 and 106 cases, respectively) studies of (truncated) MCA aneurysm CFD models and reported differences in sac-averaged TAWSS of -13% and -25%, respectively, between ruptured and unruptured cases. Note that these differences are comparable with differences we observed for the zero-pressure method just by changing the 3D model extent. Such differences would only be exacerbated for smaller studies, and emphasize the need for consistency, both between and within studies, regarding the extent of the 3D models.

Recommendations for Clinical CFD: Stop Doing Nothing

The zero-pressure outflow strategy remains popular because it places fewer constraints on the outlet velocity profile. A traction-free boundary condition is used by default, which requires only that the velocity vectors are approximately parallel to the vessel axis. On the other hand, prescribing outflow divisions as in the Murray-law or splitting methods often requires the velocity profile itself to be prescribed, which, in turn, usually necessitates the addition of long flow extensions to avoid errors or instabilities engendered by this more explicit approach.

Some solvers, like ours, offer outlet flux boundary conditions, which allow the user to specify outflow rates without having to prescribe a velocity profile. In our case, outlet flux is implemented by iterating the outlet pressures (which appear in the traction-free outlet equations) until the desired flow split is achieved.²⁸ For solvers without such capability, we note that our splitting method, when coupled with a 0D solver as described in the “Materials and Methods,” can provide an accurate estimate of the outflow pressures required to achieve a given outflow division.⁶ That therefore makes it possible for any CFD solver to achieve a desired outflow division using more relaxed traction-free (versus restrictive velocity profile) boundary conditions, simply by prescribing those estimated outlet pressures.

Notes of Caution

In this study, we compared the splitting method using $n = 2$ with the Murray-law method using its customary $n = 3$. The impact of the choice of the power law exponent on outflow strategy is summarized in On-line Table 1. Average flow rates from the Murray-

law method were relatively insensitive to n ; however, intraindividual variations were larger with $n = 3$, as expected.⁴ The splitting method was more sensitive to the power law exponent, with $n = 3$ underestimating flow to smaller branches (OA, Pcoma) and biasing flow to the larger MCA. This dependence on n , however, underscores the accuracy of the flexibility of the splitting method: Flow division at the crucial ICA terminus is demonstrably closer to a square law^{29,30}; n can be increased toward a cube law for more distal branches, if desired.

The way diameters are measured from the 3D models could also introduce some variability in the calculation of outflow rates. Owing to our use of a 0D model as the basis for the splitting method, our diameters were averaged over each vessel segment. For the Murray-law method, we used the mean diameter of each outlet face, as is customary, which can create a dependency on where the artery segment is truncated.²⁷ For cases B and B', for example, the number of outlets was the same, just the branch length was reduced, yet there was a 22% change in the MCA flow rates. This difference would undoubtedly have been less had we based the Murray-law outflows on vessel-average diameter rather than the (customary) single-point outflow face. On the other hand, our use of a 0D model makes it possible to account, a priori, for the hemodynamic impact of vascular abnormalities, such as a stenosis, on the outflow rates, in a way that would be more difficult using standard zero-pressure or Murray-law methods.

CONCLUSIONS

Outflow strategy is at least as important as other assumptions made for cerebrovascular CFD. The prevalent zero-pressure or do-nothing strategy should be avoided because it is both unphysiological and operator-dependent. The Murray-law strategy is better than nothing, but here we present our more physiological and robust splitting method as an open source tool (www.github.com/ChrisChnafa/aneuTools) to encourage standardization of cerebrovascular CFD. Irrespective of their outflow strategy, CFD studies should always report, or at least demonstrate, the physiological plausibility of the actual outflow (and inflow) rates experienced by their models.

REFERENCES

1. Chung B, Cebal JR. **CFD for evaluation and treatment planning of aneurysms: review of proposed clinical uses and their challenges.** *Ann Biomed Eng* 2015;43:122–38 [CrossRef Medline](#)
2. Valen-Sendstad K, Steinman DA. **Mind the gap: impact of computational fluid dynamics solution strategy on prediction of intracranial aneurysm hemodynamics and rupture status indicators.** *AJNR Am J Neuroradiol* 2014;35:536–43 [CrossRef Medline](#)
3. Jansen IG, Schneiders JJ, Potters WV, et al. **Generalized versus patient-specific inflow boundary conditions in computational fluid dynamics simulations of cerebral aneurysmal hemodynamics.** *AJNR Am J Neuroradiol* 2014;35:1543–48 [CrossRef Medline](#)
4. Valen-Sendstad K, Piccinelli M, Krishnankutty Rema R, et al. **Estimation of inlet flow rates for image-based aneurysm CFD models: where and how to begin?** *Ann Biomed Eng* 2015;43:1422–31 [CrossRef Medline](#)
5. Marzo A, Singh P, Larrabide I, et al. **Computational hemodynamics in cerebral aneurysms: the effects of modeled versus measured boundary conditions.** *Ann Biomed Eng* 2011;39:884–96 [CrossRef Medline](#)
6. Chnafa C, Valen-Sendstad K, Brina O, et al. **Improved reduced-order**

- modelling of cerebrovascular flow distribution by accounting for arterial bifurcation pressure drops. *J Biomech* 2017;51:83–88 CrossRef Medline**
7. Janiga G, Berg P, Sugiyama S, et al. **The Computational Fluid Dynamics Rupture Challenge 2013, Phase I: prediction of rupture status in intracranial aneurysms.** *AJNR Am J Neuroradiol* 2015;36:530–36 CrossRef Medline
 8. Murray CD. **The physiological principle of minimum work, I: the vascular system and the cost of blood volume.** *Proc Natl Acad Sci U S A* 1926;12:207–14 CrossRef Medline
 9. Zamir M, Sinclair P, Wonnacott TH. **Relation between diameter and flow in major branches of the arch of the aorta.** *J Biomech* 1992;25:1303–10 CrossRef Medline
 10. Manini S, Antiga L, Botti L, et al. **pyNS: an open-source framework for 0D haemodynamic modelling.** *Ann Biomed Eng* 2015;43:1461–73 CrossRef Medline
 11. Mortensen M, Valen-Sendstad K. **Oasis: a high-level/high-performance open source Navier-Stokes solver.** *Computer Physics Communications* 2015;188:177–88 CrossRef
 12. Khan MO, Valen-Sendstad K, Steinman DA. **Narrowing the expertise gap for predicting intracranial aneurysm hemodynamics: impact of solver numerics versus mesh and time-step resolution.** *AJNR Am J Neuroradiol* 2015;36:1310–16 CrossRef Medline
 13. Hoi Y, Wasserman BA, Xie YJ, et al. **Characterization of volumetric flow rate waveforms at the carotid bifurcations of older adults.** *Physiol Meas* 2010;31:291–302 CrossRef Medline
 14. Zarrinkoob L, Ambarki K, Wahlin A, et al. **Aging alters the dampening of pulsatile blood flow in cerebral arteries.** *J Cereb Blood Flow Metab* 2016;36:1519–27 CrossRef Medline
 15. Piccinelli M, Steinman DA, Hoi Y, et al. **Automatic neck plane detection and 3D geometric characterization of aneurysmal sacs.** *Ann Biomed Eng* 2012;40:2188–211 CrossRef Medline
 16. Ramalho S, Moura A, Gambaruto AM, et al. **Sensitivity to outflow boundary conditions and level of geometry description for a cerebral aneurysm.** *Int J Numer Meth Biomed Eng* 2012;28:697–713 CrossRef Medline
 17. Venugopal P, Valentino D, Schmitt H, et al. **Sensitivity of patient-specific numerical simulation of cerebral aneurysm hemodynamics to inflow boundary conditions.** *J Neurosurg* 2007;106:1051–60 CrossRef Medline
 18. Grinberg L, Karniadakis GE. **Outflow boundary conditions for arterial networks with multiple outlets.** *Ann Biomed Eng* 2008;36:1496–514 CrossRef Medline
 19. Cebral JR, Castro MA, Appanaboyina S, et al. **Efficient pipeline for image-based patient-specific analysis of cerebral aneurysm hemodynamics: technique and sensitivity.** *IEEE Trans Med Imaging* 2005;24:457–67 CrossRef Medline
 20. Valen-Sendstad K. **Consistent prediction of intracranial aneurysm hemodynamics: challenging or not?** In: *Proceedings of the 14th Interdisciplinary Cerebrovascular Symposium*. Montpellier, France; June 28–30, 2017
 21. Khan MO, Steinman DA, Valen-Sendstad K. **Non-Newtonian versus numerical rheology: practical impact of shear-thinning on the prediction of stable and unstable flows in intracranial aneurysms.** *Int J Numer Method Biomed Eng* 2017;33 Epub ahead of print 2016 Nov 9 CrossRef Medline
 22. Schneiders JJ, Marquering HA, Antiga L, et al. **Intracranial aneurysm neck size overestimation with 3D rotational angiography: the impact on intra-aneurysmal hemodynamics simulated with computational fluid dynamics.** *AJNR Am J Neuroradiol* 2013;34:121–28 CrossRef Medline
 23. Sen Y, Qian Y, Avolio A, et al. **Image segmentation methods for intracranial aneurysm haemodynamic research.** *J Biomech* 2014;47:1014–19 CrossRef Medline
 24. Hodis S, Kargar S, Kallmes DF, et al. **Artery length sensitivity in patient-specific cerebral aneurysm simulations.** *AJNR Am J Neuroradiol* 2015;36:737–43 CrossRef Medline
 25. Takao H, Murayama Y, Otsuka S, et al. **Hemodynamic differences between unruptured and ruptured intracranial aneurysms during observation.** *Stroke* 2012;43:1436–39 CrossRef Medline
 26. Miura Y, Ishida F, Umeda Y, et al. **Low wall shear stress is independently associated with the rupture status of middle cerebral artery aneurysms.** *Stroke* 2013;44:519–21 CrossRef Medline
 27. Valen-Sendstad K, Piccinelli M, Steinman DA. **High-resolution computational fluid dynamics detects flow instabilities in the carotid siphon: implications for aneurysm initiation and rupture?** *J Biomech* 2014;47:3210–16 CrossRef Medline
 28. Gin R, Straatman AG, Steinman DA. **A dual-pressure boundary condition for use in simulations of bifurcating conduits.** *J Biomech Eng* 2002;124:617–19 CrossRef Medline
 29. Ingebrigtsen T, Morgan MK, Faulder K, et al. **Bifurcation geometry and the presence of cerebral artery aneurysms.** *J Neurosurg* 2004;101:108–13 CrossRef Medline
 30. Chnafa C, Bouillot P, Brina O, et al. **Vessel calibre and flow splitting relationships at the internal carotid artery terminal bifurcation.** *Physiol Meas* 2017;38:2044–57 CrossRef Medline

Intranasal Esthesioneuroblastoma: CT Patterns Aid in Preventing Routine Nasal Polypectomy

M.E. Peckham, R.H. Wiggins III, R.R. Orlandi, Y. Anzai, W. Finke, and H.R. Harnsberger



ABSTRACT

BACKGROUND AND PURPOSE: Esthesioneuroblastoma is a neuroectodermal tumor that commonly arises in the nasal cavity olfactory recess and, when isolated to the intranasal cavity, can be indistinguishable from benign processes. Because lesional aggressiveness requires a more invasive operation for resection than polypectomy, patients with isolated intranasal lesions were studied to define distinguishing CT characteristics.

MATERIALS AND METHODS: Patients with intranasal esthesioneuroblastoma and controls without esthesioneuroblastoma with olfactory recess involvement were identified by using a report search tool. Studies demonstrating skull base invasion and/or intracranial extension were excluded. The imaging spectrum of these lesions was reviewed on both CT and MR imaging, and CT findings were compared with those of controls without esthesioneuroblastoma. Two blinded readers assessed subjects with esthesioneuroblastomas and controls without esthesioneuroblastoma and, using only CT criteria, rated their level of suspicion for esthesioneuroblastoma in each case.

RESULTS: Eight histologically proved cases of intranasal esthesioneuroblastoma were reviewed. All cases had CT demonstrating 3 main findings: 1) an intranasal polypoid lesion with its epicenter in a unilateral olfactory recess, 2) causing asymmetric olfactory recess widening, and 3) extending to the cribriform plate. Twelve patients with non-esthesioneuroblastoma diseases involving the olfactory recess were used as controls. Using these 3 esthesioneuroblastoma CT criteria, 2 blinded readers evaluating patients with esthesioneuroblastoma and controls had good diagnostic accuracy (area under the curve = 0.85 for reader one, 0.81 for reader 2) for predicting esthesioneuroblastoma.

CONCLUSIONS: Esthesioneuroblastoma can present as a well-margined intranasal lesion that unilaterally widens the olfactory recess. CT patterns can help predict esthesioneuroblastoma, potentially preventing multiple operations by instigating the correct initial operative management.

ABBREVIATIONS: ENB = esthesioneuroblastoma; OR = olfactory recess

Esthesioneuroblastoma (ENB) is a rare malignant neuroectodermal neoplasm arising from the neuroepithelium, most commonly within the nasal cavity olfactory recess, which makes up approximately 3% of intranasal tumors (Fig 1).^{1,2} This enhancing lesion, which is most often isodense to soft tissue on CT and frequently isointense to gray matter on T2, is most commonly characterized by intracranial extension through the skull base,

creating a “dumbbell” shape, with the waist of the lesion located at the cribriform plate.³⁻⁵ Symptoms of this lesion are nonspecific, mirroring those of benign intranasal masses such as polyps, which can lead to delay in diagnosis, with the lesion often extending intracranially on delayed pathologic confirmation.^{4,6}

Esthesioneuroblastoma most commonly originates in the nasal cavity olfactory recess (OR), which is a space defined by the insertion of the vertical aspect of the middle turbinate laterally, anterior skull base superiorly, and the nasal septum medially (Fig 1).⁷ Rare exceptions reported in the literature include lesions originating in the inferior meatus of the nasal cavity, maxillary sinus, pterygopalatine fossa, sphenoid sinus, ethmoid sinuses, and sphenoclivar region.^{2,8-13} In contradistinction, common benign inflammatory polyps most often arise in relation to sinus outlets, most commonly in the middle or superior meatus.¹⁴ Other malignant lesions that can arise in the nasal cavity include sinonasal undifferentiated carcinoma, neuroendocrine carcinoma, and

Received June 9, 2017; accepted after revision September 18.

From the Departments of Radiology and Imaging Sciences (M.E.P., R.H.W., Y.A., W.F., H.R.H.), Division of Otolaryngology–Head and Neck Surgery (R.H.W., R.R.O.), and BioMedical Informatics (R.H.W.), University of Utah Health Sciences Center, Salt Lake City, Utah.

Please address correspondence to Miriam E. Peckham, MD, Departments of Radiology and Imaging Sciences, University of Utah Health Sciences Center, 30 North, 1900 East, 1A071, Salt Lake City, UT 84132-2140; e-mail: Miriam.Peckham@hsc.utah.edu; @Miriam_Peckham

Indicates article with supplemental on-line table.

<http://dx.doi.org/10.3174/ajnr.A5464>



FIG 1. Coronal bone algorithm CT of the sinuses in a healthy subject demonstrates normal thin and symmetric olfactory recesses (*asterisks*) between the midline nasal septum and the shared superior attachments of the middle and superior turbinates laterally.

small-cell undifferentiated carcinoma, each of which can originate along the sinonasal tract.¹⁵

The most common route of spread for ENB is into the paranasal sinuses, followed by intracranial spread. These local routes of spread are most commonly staged by the Kadish staging system.⁴ Cervical nodal metastases have also been found up to a rate of 44%, with spread most commonly seen to level II lymph nodes.^{16,17} Spread to retropharyngeal lymph nodes has also been reported.¹⁸ Much rarer is distant spread to the thorax and skeleton.¹⁹ Positron-emission tomography has been found helpful in evaluating nodal metastases as well as distant spread and local recurrence.²⁰

Treatment of ENB requires complete tumor resection, usually involving anterior skull base reconstruction and primary dural closure.²¹ Surgical management of ENB has more recently evolved from external-approach craniofacial resection toward an endonasal approach, which has fewer postoperative complications.²²⁻²⁴ An expanded endonasal approach, paired with radiation therapy and/or chemotherapy, has been found to have a high rate of local control and significantly improved survival outcomes.^{24,25}

Small ENBs isolated to the nasal cavity can have a clinical presentation and imaging appearance like that of benign lesions such as inflammatory polyps, with smooth well-circumscribed margins rendering them indistinguishable. Location is a key differentiating factor for ENB, which characteristically originates in the olfactory recess in most cases. A prior study recommended further imaging evaluation whenever patients were found to have an opacified OR on CT; however, this study did not go into detail

regarding additional CT findings more specific to ENB.⁷ We aimed to show that looking for additional clues, specifically osseous changes of the olfactory recess, can allow the radiologist to raise the suspicion for ENB, potentially allowing preoperative detection. Although ENB is relatively uncommon compared with other intranasal lesions, its propensity for aggressive local spread and the potential for distal metastases make it an important lesion to exclude before surgical intervention.

MATERIALS AND METHODS

The institutional review board approved this study, and it was compliant with the Health Insurance Portability and Accountability Act. Cases of extracranial ENB seen at our quaternary care center from 2009 to 2016 were identified retrospectively through a search of our picture archiving and communication system, with histologic confirmation from the institutional electronic medical record. Cases demonstrating skull base invasion or intracranial extension were excluded. The clinical presentation and imaging spectrum on preoperative CT studies were then reviewed and documented. The postoperative pathologic reports were reviewed, as well as postoperative follow-up and care. Non-ENB cases of sinus conditions involving the OR were also identified retrospectively through a search of our picture archiving and communication system. Histologic confirmation of these lesions was present in 4/12 patients, with the remaining 8 showing diagnostic findings matching a specific non-ENB clinical history on initial CT, non-ENB diagnostic findings on follow-up MR imaging, or resolution of findings on subsequent imaging.

In cases of ENB, CT images were reviewed by a senior neuro-radiologist with expertise in head and neck imaging and a neuro-radiology fellow to characterize the location of the lesion and whether there was opacification/involvement or widening of the OR. When available, MR imaging was reviewed for the following features: T2 signal differentiation of the lesion from inflammatory disease, diffusion characteristics, enhancement characteristics, and evidence of sinus involvement. Sensitivity and specificity calculations were performed comparing these findings with histology.

Two blinded readers assessed patients with ENB and controls without ENB and, using only CT criteria, rated their level of suspicion for ENB in each case using a standard rating scale from 1 to 5 (1 = definitely not, 2 = probably not, 3 = equivocal, 4 = probably yes, 5 = definitely yes). Receiver operating characteristic curves were generated for individual readers to evaluate diagnostic accuracy. Statistical analyses were performed using commercial statistical analysis software (STATA, Release 14; StataCorp, College Station, Texas).

RESULTS

Thirty cases of possible ENB on imaging were reported at our quaternary care institution from 2009 to 2016. Of these cases, 20 were histology-proved ENB, and the 10 remaining cases had varying diagnoses, including inflammatory polyp, squamous cell carcinoma, metastatic disease, sinonasal undifferentiated carcinoma, and epithelial adenomatoid hamartoma. Of the 20 pathologically proved cases of ENB, 12 showed intracranial extension and/or imaging evidence of skull base invasion and were therefore excluded from this study. Eight cases (3 women) were completely

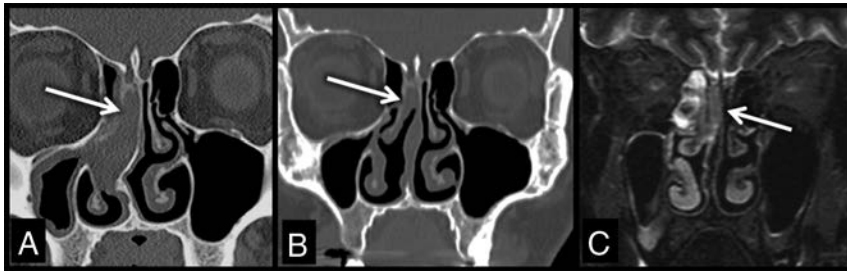


FIG 2. Coronal bone algorithm CT (A and B) and coronal T2-weighted MR image (C) obtained prepolypectomy (A), and postpolypectomy (B and C) demonstrate a soft-tissue-density lesion (arrows) that extends to the cribriform plate and widens the right olfactory recess. Opacification of the paranasal sinuses cannot be differentiated from the lesion on CT; however, paranasal sinus T2 bright secretions are readily discerned on MR imaging from the lesion (arrow), which is isointense to gray matter (C). This patient required an additional anterior skull base resection once ENB was diagnosed after routine polypectomy.

extracranial, showing no evidence of skull base invasion, with an age range of 40–74 years (mean age, 58 years). Of these extracranial cases, imaging and histologic studies demonstrated that 3 of the lesions were completely isolated to the nasal cavity and 5 were intranasal with variable adjacent sinus involvement (On-line Table). Initial CT scans were available for review in all cases. MR imaging was available for 5 patients, in 2 performed preoperatively, in 2 performed after initial polypectomy, and in 1 performed after recurrence (On-line Table).

Twelve non-ENB cases of sinus conditions (7 women) with OR involvement between 2009 and 2017 were obtained with an age range of 16–81 years (mean age, 48 years). These cases had varying diagnoses including CSF leak, encephalocele, allergic rhinitis, chronic sinusitis, antrochoanal/inflammatory polyp, mycetoma, and glomus tumor.

Clinical Features of Intranasal Esthesioneuroblastoma

Difficulty breathing due to nasal stuffiness and fullness was the most common presenting symptom in patients with intranasal ENB. Other symptoms included anosmia and rhinorrhea. Five patients had presurgical biopsies before resection. Three patients required an additional operation after referral to our institution for skull base resection after ENB was found incidentally during routine nasal polypectomy. On presentation, there was no clinical or imaging evidence in these patients of nodal involvement.

CT Features of Intranasal Esthesioneuroblastoma

All cases had CT demonstrating a circumscribed intranasal polypoid lesion with the following features: 1) its epicenter in a unilateral OR, 2) causing asymmetric osseous remodeling/widening of the OR, and 3) extending to the cribriform plate. All except 1 patient had additional opacification of several paranasal sinuses; however, extension versus fluid entrapment could not be discerned by CT (Fig 2).

Six original preoperative CT reports were available. In 2 cases, the radiologist suspected a malignant lesion and recommended follow-up imaging. The 4 remaining cases had been referred from outside facilities and the patients had already undergone biopsy; however, the biopsy results appeared to be available to the radiologist in only half of those patients because the chance of malignancy was dismissed in 2 patients and, in the remaining 2 patients, the results were described as consistent with prior ENB biopsy. The

preoperative imaging diagnosis of ENB was never specifically stated as a possibility in any cases without prior biopsy.

MR Imaging Features of Intranasal Esthesioneuroblastoma

In the 5 cases with MR imaging, all lesions were T2 isointense to gray matter and showed diffuse enhancement to a lesser degree than the adjacent nasal mucosa. When available (3 subjects), diffusion-weighted imaging demonstrated hyperintense DWI signal intensity and hypointense ADC signal intensity within the mass. Entrapped fluid within the paranasal sinuses was differentiated from tumor extension by its T2 hyperintensity, greater than the intrinsic T2 signal within the ENB mass (Fig 2C). All MR imaging cases that had imaging evidence of paranasal sinus tumor extension (3 subjects) were confirmed histologically.

Histologic Findings

Following surgical resection, 3 of these cases were proved histologically to be isolated to the nasal cavity, while the 5 remaining cases showed additional sinus involvement. Dural margins were negative in 7/8 subjects, with this information not available in 1 subject.

Histologic grading of these lesions showed 1 case with grade 1, three cases with grade 2, and 2 cases with grade 3 morphology. These grades did not correspond with sinus involvement. Two patients with grade 3 lesions had local recurrence, with 1 of the patients also showing nodal recurrence 3 years after the initial resection. No recurrence was found in the patients with grade 1 or 2 lesions (On-line Table).

Comparison with Controls

Among the 12 patients without ENB with sinus conditions involving the OR, only 3/12, all of which were masses (glomus tumor, inflammatory polyp, and epithelial adenomatoid hamartoma), showed unilateral and asymmetric widening/remodeling of the OR. The remaining 9 cases consisted mostly of non-mass-like infectious/inflammatory processes that opacified but did not asymmetrically widen/remodel the OR (Fig 3). The 3 CT criteria of a mass with its epicenter in the OR, causing asymmetric osseous widening/remodeling of the OR, and extending to the cribriform plate, were demonstrated in all ENB cases (sensitivity of 100% compared with histology) and in 3 cases without ENB (specificity of 75% compared with histology).

Performance of Blinded Readers

Blinded readers demonstrated strong individual accuracy in predicting ENB using the 3 CT criteria, with reader 1 having an area under the curve of 0.85 ± 0.087 and reader 2 having an area under the curve of 0.81 ± 0.089 (Fig 4). When results were dichotomized between ENB absence and presence, the sensitivity for reader 1 was 87.5% with a specificity of 58.3% and sensitivity for reader 2 was 50.0% with a specificity of 83.3%.



FIG 3. Coronal bone algorithm CT (A and B) images obtained in a control subject with chronic sinusitis (A) and a subject with ENB (B). While there is asymmetric opacification of the right OR with extension to the cribriform plate in the subject with chronic sinusitis (A), the OR is not widened. This finding contrasts with that in the subject with ENB who demonstrates additional asymmetric widening/remodeling of the OR. Both subjects have opacification of the adjacent paranasal sinuses, which, in the subject with ENB, was found to represent tumor extension. The subject with ENB underwent additional anterior skull base resection surgery when ENB was found after routine polypectomy.

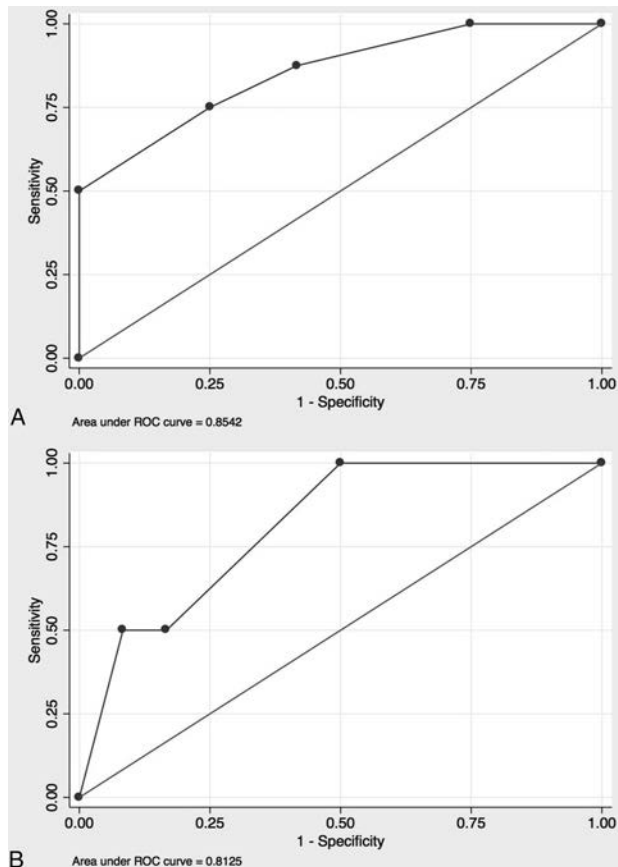


FIG 4. Receiver operating characteristic curves for reader 1 (A) and reader 2 (B). Sensitivity and specificity varied between both readers; however, the overall diagnostic accuracy was strong, with reader 1 showing an area under the curve of 0.85, and reader two, 0.81.

DISCUSSION

Esthesioneuroblastoma is a rare neuroendocrine mass that, when isolated to the nasal cavity, can appear very similar to benign

sinonasal masses on CT. Because this lesion is malignant and requires a more invasive operation for resection than a standard polypectomy, patients with intranasal lesions without intracranial involvement were studied to define distinguishing imaging characteristics. On the basis of these characteristics, CT imaging findings are established to recommend further work-up with MR imaging and/or biopsy before complete surgical resection.

Patients presenting with intranasal ENB were of a similar age range and had presenting symptoms of nasal stuffiness and fullness like those seen with benign entities. Reflecting this nonspecific presentation, malignancy was not initially suspected in almost half of the patients and a standard nasal polypectomy was performed without obtaining a presurgical biopsy or performing further imaging. This resulted in the necessity to perform a second more extensive operation for anterior skull base resection when postoperative pathology results showed ENB.

The margins of the intranasal ENB mass did not significantly differ from those in benign inflammatory lesions, with both entities appearing smooth and well-circumscribed with homogeneous soft-tissue density. Although these findings were overall similar, the 3 characteristics of a mass epicenter in a unilateral OR causing widening/osseous remodeling and extending to the cribriform plate showed high sensitivity and moderate specificity for ENB. Of the 9 controls with nonmass lesions opacifying the OR, none demonstrated all 3 of these characteristics. These 3 characteristics had strong diagnostic accuracy when used by blinded readers to identify ENB.

A consistent finding in patients with ENB was adjacent paranasal sinus opacification, which was seen in 7/8 patients, representing tumor in 5 cases. The sinus opacification in the 2 patients with isolated intranasal ENB was found to represent entrapped fluid related to sinus blockage from the intranasal mass, a finding that was readily discernible on MR imaging but not on CT. Because fluid and tumor within the paranasal sinuses had similar density on CT, that sequence alone was not reliable for evaluating local disease spread. These cases demonstrated that the presence of an intranasal mass can create a confusing picture of paranasal sinus opacification and that the 3 CT criteria regarding the OR were the most important imaging findings for predicting ENB.

The T2-weighted and STIR MR imaging sequences were readily able to differentiate tumor from paranasal sinus inflammatory disease. The coronal plane was the most helpful because it clearly showed involvement and widening of the OR and extension of the lesions to the cribriform plate. The T2 sequence aided differentiation of the ENB mass from other common benign polyps, with ENB lesions demonstrating T2 isointensity and hypointense ADC signal, both of which correlate with increased cellularity.⁵ The MR imaging T2-weighted sequences were also helpful for evaluating local disease spread into the paranasal sinuses because hyperintense entrapped paranasal sinus fluid could be readily differentiated from the more T2 isointense signal of the ENB tumor. The ability to differentiate ENB from inflammatory entities by signal characteristics further supports the importance of obtaining preoperative MR imaging when ENB is suspected by CT.

The importance of prompting further work-up when there is OR opacification and widening on CT is demonstrated because

almost half of the patients with intranasal ENB required a second more extensive operation for complete resection. Two cases that necessitated repeat surgery had outside radiology reports that were not available for review; however, this lesion was clearly not initially suspected by the managing physicians in reviewing the electronic medical record. Most interesting, in 2 cases in which a presurgical biopsy was performed at an outside institution, the radiologist apparently did not have access to these results and therefore did not suspect or prompt any further work-up for malignancy based on the original CT findings. Also, ENB was never specifically mentioned as a possibility in any of the CT reports in which biopsy results were unavailable. These results strengthen the concept that in CT sinus studies, evaluation for opacification/widening of the OR must be included on the imaging checklist.

Management of ENB requires complete surgical resection with clear margins whenever anatomically feasible. Adjuvant therapy is often necessary, due to higher grade lesions or close/positive margins. Extracranial ENB is almost always amenable to complete surgical resection, due to rare involvement with the orbits and lack of cerebral involvement. Because the tumor arises from nasal olfactory epithelium near the skull base, resection of the dura as a superior margin is nearly always necessary. This procedure is readily performed endonasally in a number of skull base centers, without the need for a formal craniotomy. In a rare lesion with a radiographically clear area between the lesion and the skull base, the surgeon may choose to spare the dura. Knowledge of the histology of olfactory lesions is critical because the management of an ENB differs considerably from that of a benign neoplasm and from inflammatory polyps. Benign lesions typically do not require skull base/dural resection and inflammatory polyps often are treated even less aggressively, with surgery focused on improving access for topical anti-inflammatory therapy.²⁶ With the otolaryngologist having the correct diagnosis of an extracranial ENB, the correct definitive operation is performed initially and the patient is spared multiple trips to the operating room.

The greatest limitations in this case-control study were low power because of the rarity of extracranial ENB, as well as the subtle imaging changes associated with extracranial ENB in comparison with cases without ENB involving the OR, which made blinded reads challenging. However, even with the limited number of cases and subtle imaging characteristics, blinded readers demonstrated strong individual accuracy for predicting ENB using this method, with reader 1 demonstrating high sensitivity and reader 2 demonstrating high specificity. Although extracranial ENB is rare, the consistency of its CT imaging findings does provide helpful information for guiding care.

CONCLUSIONS

Esthesioneuroblastoma can present as a well-marginated polypoid mass lesion isolated to the nasal cavity. Because this lesion is managed differently from more common benign nasal entities, this important diagnosis should be included in the differential whenever a mass follows 3 important CT criteria: epicenter within a unilateral OR, widening/osseous remodeling of the OR, and extension of the lesion to the cribriform plate. These criteria were sensitive for ENB and provided strong diagnostic accuracy when used by blinded readers. The presence of these findings should elicit preoperative MR imaging and/or biopsy, which can aid the

surgeon in operative planning and prevent routine nasal polypectomy for resection of these aggressive lesions.

REFERENCES

- Berger L, Luc R. L'esthesioneuroepitheliome olfactif. *Bull Assoc Fr Etude Cancer* 1924;13:410–21
- Lee JY, Kim HK. Primary olfactory neuroblastoma originating from the inferior meatus of the nasal cavity. *Am J Otolaryngol* 2007; 28:196–200 CrossRef Medline
- Yu T, Xu YK, Li L, et al. Esthesioneuroblastoma methods of intracranial extension: CT and MR imaging findings. *Neuroradiology* 2009;51:841–50 CrossRef Medline
- Dias FL, Sa GM, Lima RA, et al. Patterns of failure and outcome in esthesioneuroblastoma. *Arch Otolaryngol Head Neck Surg* 2003;129: 1186–92 CrossRef Medline
- Dublin AB, Bobinski M. Imaging characteristics of olfactory neuroblastoma (esthesioneuroblastoma). *J Neurol Surg B Skull Base* 2016; 77:1–5 CrossRef Medline
- London NR Jr, Reh DD. Differential diagnosis of chronic rhinosinusitis with nasal polyps. *Adv Otorhinolaryngol* 2016;79:1–12 CrossRef Medline
- Hoxworth JM, Glastonbury CM, Fischbein NJ, et al. Focal opacification of the olfactory recess on sinus CT: just an incidental finding? *AJNR Am J Neuroradiol* 2008;29:895–97 CrossRef Medline
- Jiang ZY, Katz A, Francis C. Hyponatremia and right maxillary sinus mass. *JAMA Otolaryngol Head Neck Surg* 2015;141:1021–22 CrossRef Medline
- Unal A, Ozluedik S, Tezer MS, et al. An atypical esthesioneuroblastoma of the inferior nasal cavity and maxillary sinus: report of a case. *Tumori* 2006;92:440–43 Medline
- Matsunaga M, Nakagawa T, Sakamoto T, et al. Sphenoid esthesioneuroblastoma arising from the hindmost olfactory filament. *Auris Nasus Larynx* 2015;42:170–72 CrossRef Medline
- Leon-Soriano E, Alfonso C, Yebenes L, et al. Bilateral synchronous ectopic ethmoid sinus olfactory neuroblastoma: a case report. *Am J Case Rep* 2016;17:268–73 CrossRef Medline
- Seccia V, Lenzi R, Casani AP, et al. Ectopic olfactory neuroblastoma arising in the pterygopalatine fossa. *Otolaryngol Head Neck Surg* 2010;142:460–61 CrossRef Medline
- Purohit B, Winder T, Maggio EM, et al. Aggressive primary olfactory neuroblastoma of the sphenoclivar region: a case report and literature review. *Laryngoscope* 2015;125:822–25 CrossRef Medline
- Larsen PL, Tos M. Origin of nasal polyps: an endoscopic autopsy study. *Laryngoscope* 2004;114:710–19 CrossRef Medline
- Hofer MJ, Rohlf J, Teymoortash A, et al. A 62-year-old female with an intranasal mass extending into the lamina cribrosa. *Brain Pathol* 2013;23:105–08 CrossRef Medline
- Rinaldo R, Ferlito A, Shaha AR, et al. Esthesioneuroblastoma and cervical lymph node metastases: clinical and therapeutic implications. *Acta Otolaryngol* 2002;122:215–21 CrossRef Medline
- Howell MC, Branstetter BF 4th, Snyderman CH. Patterns of regional spread for esthesioneuroblastoma. *AJNR Am J Neuroradiol* 2011;32: 929–33 CrossRef Medline
- Zollinger LV, Wiggins RH, Cornelius RS, et al. Retropharyngeal lymph node metastasis from esthesioneuroblastoma: a review of the therapeutic and prognostic implications. *AJNR Am J Neuroradiol* 2008;29:1561–63 CrossRef Medline
- Pickuth D, Heywang-Kobrunner S, Spielman RP. Computed tomography and magnetic resonance imaging features of olfactory neuroblastoma: an analysis of 22 cases. *Clin Otolaryngol Allied Sci* 1999;24:457–61 CrossRef Medline
- Broski SM, Hunt CH, Johnson GB, et al. The added value of 18F-FDG PET/CT for evaluation of patients with esthesioneuroblastoma. *J Nucl Med* 2012;53:1200–06 CrossRef Medline
- Tomio R, Toda M, Tomita T, et al. Primary dural closure and anterior cranial base reconstruction using pericranial and nasoseptal

- multi-layered flaps in endoscopic-assisted skull base surgery.** *Acta Neurochir (Wien)* 2014;156:1911–15 CrossRef Medline
22. Lund VJ, Howard D, Wei W, et al. **Olfactory neuroblastoma: past, present, and future?** *Laryngoscope* 2003;113:502–07 CrossRef Medline
23. Smee RI, Broadley K, Williams JR, et al. **Retained role of surgery for olfactory neuroblastoma.** *Head Neck* 2011;33:1486–92 CrossRef Medline
24. Hwang CS, Seo YW, Park SC, et al. **Role of surgical treatment for esthesioneuroblastomas: 31-year experience at a single institution.** *J Craniomaxillofac Surg* 2017;45:120–26 CrossRef Medline
25. Roxbury CR, Ishii M, Gallia GL, et al. **Endoscopic management of esthesioneuroblastoma.** *Otolaryngol Clin North Am* 2016;49:153–65 CrossRef Medline
26. Orlandi RR, Kingdom TT, Hwang PH, et al. **International Consensus Statement on Allergy and Rhinology: Rhinosinusitis.** *Int Forum Allergy Rhinol* 2016;(suppl 1):S22–209 CrossRef Medline

Lymphographic-Like Technique for the Treatment of Microcystic Lymphatic Malformation Components of <3 mm

V. Da Ros, M. Iacobucci, F. Puccinelli, L. Spelle, and G. Saliou



ABSTRACT

BACKGROUND AND PURPOSE: The treatment of microcystic lymphatic malformations remains challenging. Our aim was to describe the lymphographic-like technique, a new technique of slow bleomycin infusion for the treatment of microcyst components of <3 mm, performed at our institution.

MATERIALS AND METHODS: A retrospective analysis of a prospectively collected lymphatic malformation data base was performed. Patients with at least 1 microcystic lymphatic malformation component demonstrated on MR imaging treated by lymphographic-like technique bleomycin infusion were included in the study. Patient interviews and MR imaging were performed to assess subjective and objective (microcystic lymphatic malformation size decrease of >30%) clinical improvement, respectively. Patients were reviewed 3 months after each sclerotherapy session. Lymphographic-like technique safety and efficacy were assessed.

RESULTS: Between January 2012 and July 2016, sixteen patients (5 males, 11 females; mean age, 15 years; range, 1–47 years) underwent the bleomycin lymphographic-like technique for microcystic lymphatic malformations. Sixty sclerotherapy sessions were performed, with a mean of 4 sessions per patient (range, 1–8 sessions) and a mean follow-up of 26 months (range, 5–58 months). We observed no major and 3 minor complications: 1 eyelid infection, 1 case of severe postprocedural nausea and vomiting, and 1 case of skin discoloration. One patient was lost to follow-up. Overall MR imaging objective improvement was observed in 5/16 (31%) patients; overall improvement of clinical symptoms was obtained in 93% of treated patients.

CONCLUSIONS: The bleomycin lymphographic-like technique for microcystic lymphatic malformations is safe and feasible with objective improvement in about one-third of patients. MR signal intensity changes after the lymphographic-like technique are associated with subjective improvement of the patient's symptoms.

ABBREVIATIONS: LM = lymphatic malformation; mLM = microcystic lymphatic malformation; LL-T = lymphographic-like technique

Lymphatic malformations (LMs) are congenital slow-flow vascular anomalies resulting from abnormal development of lymphatic vessels.¹ LMs can be solitary or multifocal and can be classified as macrocystic, microcystic (<1 cm), or combined lesions based on the size of the cysts. Some of the microcystic component is often characterized by multiple smaller cysts (<3 mm), in which direct puncture and selective hand injection cannot be attempted due to the size of the lesion. The bleomycin² sclerother-

apy technique is essentially reserved for macrocystic LMs, but in selected cases, successful results have also been observed for the treatment of the microcystic component.^{3,4}

We describe the bleomycin administration procedure used in our institution for the microcystic lymphatic malformation (mLM) component and the bleomycin safety profile. Preprocedural and postprocedural clinical data and MR imaging were used to objectively and subjectively demonstrate the efficacy of this procedure.

MATERIALS AND METHODS

This study was approved the Clinical Investigation Committee of Bicêtre Hospital, and patient informed consent was waived by this committee due to the retrospective observational nature of the study.

Diagnosis

The mLM component of LMs was diagnosed on the basis of clinical and imaging features by an interventional neuroradiologist

Received May 26, 2017; accepted after revision September 12.

From the Department of Neuroradiology (V.D.R., M.I., L.S., G.S.), Bicêtre Hospital, Le Kremlin Bicêtre Cedex, France; Department of Diagnostic Imaging and Interventional Radiology, Molecular Imaging and Radiotherapy (V.D.R.), Policlinico Tor Vergata, Rome, Italy; Department of Bioimaging and Radiological Sciences (M.I.), Policlinico "A. Gemelli," Rome, Italy; and Department of Neuroradiology (F.P., G.S.), Centre Hospitalier Universitaire Vaudois, Lausanne, Switzerland.

Please address correspondence to Guillaume Saliou, MD, Department of Radiology, Centre Hospitalier Universitaire Vaudois, Rue du Bugnon 46, CH-1011 Lausanne, Switzerland; e-mail: guillaume.saliou@chuv.ch

<http://dx.doi.org/10.3174/ajnr.A5449>

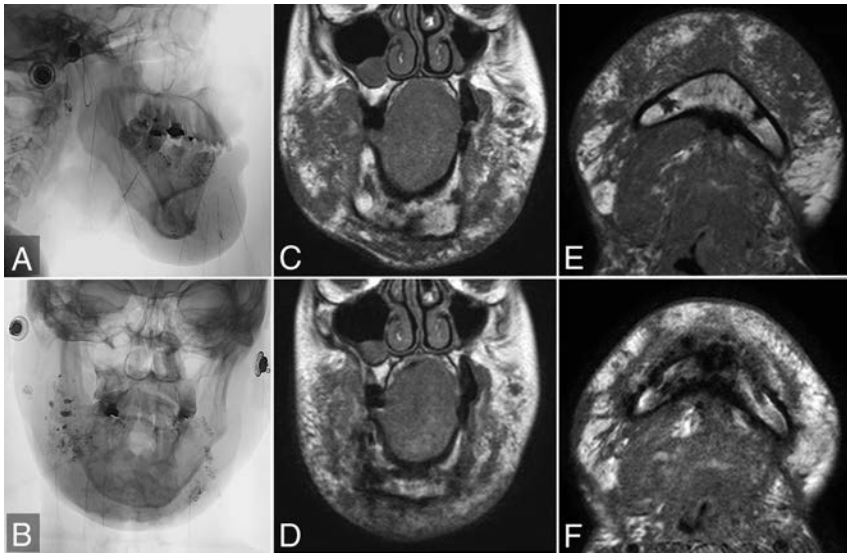


FIG 1. Lateral (A) and anteroposterior (B) plain radiography during a sclerotherapy session in a patient with a diffuse maxillofacial microcystic lymphatic malformation. She had been previously treated by an operation. Before sclerotherapy, on the T1-weighted coronal (C) and axial (E) views, the lymphatic malformation extended into the maxillofacial soft tissues, with multiple small diffuse hypointense microcystic lesions measuring <3 mm. No macrocyst was identified. After 7 sclerotherapy sessions and a cumulative dose of 90 mg of bleomycin, T1-weighted coronal (D) and axial (F) views demonstrate dramatic reduction in the size of the lymphatic malformation. However, soft tissues of the face remain thickened due to fat transformation (hyperintense) of the cysts.

and maxillofacial surgeon, in our weekly multidisciplinary clinic. The diagnostic criteria were clinical (including vesicular maculopapular lesions on the skin surface, a soft-tissue mass with a rubbery hard texture, oozing of lymphatic fluid and/or hemorrhagic fluid, and/or pain and tenderness) and MR imaging was used to assess the extent of the lesions and the dimensions of the cysts. When imaging and clinical features were not conclusive, surgical biopsy was planned to confirm the diagnosis. However, no pre-treatment surgical biopsy was required in this patient series.

Lymphographic-Like Technique

All procedures were performed by the same operator (G.S.) under aseptic conditions with the patients under general anesthesia. The position of the 22-ga needles inserted into the lymphatic malformation was checked by fluoroscopic and sonographic guidance, especially in deep or small lesions. When blood reflux was observed in the needle, the position of the needle was modified. Because the microcysts in this series were very small (<3 mm), we did not wait for lymphatic fluid reflux in the needle. Four-to-8 needles inserted into the microcystic component of the lymphatic malformations were used in each session, depending on the volume of mixture available based on the patient's weight. Each needle was connected to a pump with a line comprising a dead space of about 1.8 mL. Bleomycin was diluted as follows: 15 mg of bleomycin in 5 mL of saline and 3 mL of contrast to obtain 8 mL of mixture. This total volume of 8 mL was injected at each session in adults. Because a dose of 0.5 mg/kg per session was injected in children weighing <35 kg, the volume of mixture was determined as follows: 8 mL of mixture every 30 kg of weight. Each line was then filled with 1 mL of mixture, and the remaining line dead space was filled with saline. In low-weight babies, when the total

volume of mixture was <4 mL, contrast medium diluted with saline (50%/50%) was added to obtain a volume of 4 mL to fill 4 syringes. A 10-cm-long gas bubble between the bleomycin mixture and the saline was used to avoid mixing the 2 solutions. Finally, the line was connected to a 10-mL electronic syringe pump filled with 1 mL of saline, and the infusion was administered at a flow rate of 0.7 mL/h. At the end of the injection, a low-dose CT scan was obtained to check diffusion of the mixture in the lymphatic malformation.

Posttreatment Care and Follow-Up

No compressive dressing was applied after completion of the sclerosant infusion. An intravenous infusion of 5 mg of dexamethasone sodium phosphate was routinely performed during the first hour after sclerotherapy to prevent excessive inflammation and its complications. The patient or family was instructed to evaluate sclerotherapy-related complications such as dermal discoloration, bleb formation, lymphedema, or necrosis occurring after discharge. Patients re-

turned to the radiology outpatient clinic 1 month later for assessment of any sclerotherapy-related complications. When no complications were observed, a 1-month interval was observed between the 2 bleomycin injection sessions; at 3 months from the first sclerotherapy, patients were asked to undergo a follow-up MR imaging.

The result of infusion sclerotherapy was initially assessed by 3-month follow-up T2- and T1-weighted sequences in axial and coronal views. On the initial MR images, retrieved from the PACS, anatomic landmarks were used to measure the target microcystic lesion. Soft-tissue thickness was measured from the dermal surface to an interface between the lesion and underlying structures such as the muscular fascia or bony cortex (Fig 1). Posttreatment objective MR imaging evaluations were classified as no change ($<10\%$ decrease in size), minor improvement (10% – 30% decrease in size), and objective improvement ($>30\%$ decrease). Clinical results were based on both the physician's physical examination and patient interview. Clinical results were graded as follows: poor subjective response to treatment, good response (reduction of subjective symptoms without decrease in lesion size), and excellent results (reduction of subjective symptoms with a clinically evident decrease in lesion size). Moreover, evaluation of the clinical response was based on the physician's examination at 12 months and was designed to assess cosmetic improvement (decrease in lesion size $<10\%$, 10% – 30% , and $>30\%$ on the physician's physical examination). Dysphagia was evaluated by the water test, and relief of pain and skin tension were assessed by the Faces Pain Scale. The decision to continue or discontinue treatment was based on this assessment.

We assessed the final result of infusion sclerotherapy at the

Objective and subjective clinical results

Patient No.	Sex	Age (yr)	Site	No. of Sessions	MRI Findings		Subjective Clinical Symptom Findings ^c
					% Decrease ^a	% Fat Transformations ^b	
1	M	5	Orbital	1	+	+	1
2	F	12	Maxillofacial	4	+	+	1
3	F	22	Tongue	7	+++	+++	2
4	F	8	Maxillofacial	2	+	+	1
5	F	24	Maxillofacial	8	+	+	1
6	F	32	Orbital	6	++	++	1
7	F	6	Orbital	2	++	No	0
8	F	23	Maxillofacial	1	NA	NA	NA
9	F	47	Tongue	7	++	++	1
10	M	5	Orbital	3	+++	+++	2
11	F	23	Orbital	2	+++	+++	2
12	M	1	Maxillofacial	4	+	+	1
13	F	2	Tongue	3	+++	+++	2
14	M	4	Orbital	2	+++	+++	2
15	F	8	Orbital	6	++	++	1
16	M	20	Maxillofacial	2	+	+	1

Note:—NA indicates not available.

^a% Decrease: + = 0–10, ++ = 10–30, +++ = >30.

^b% Fat transformation on T1WI and T2WI MRI: + = 0–10, ++ = 10–30, +++ = >30.

^cClinical evaluation: 0 = no improvement or progression, 1 = clinical improvement, 2 = resolution of symptoms.

vascular anomaly clinic on the basis of a multidisciplinary consensus during the patient's follow-up visits, considering the objective and subjective results at each visit.

No further sclerotherapy was recommended by multidisciplinary consensus in cases with signs of deterioration, indicating ineffective treatment.

The initial and last clinical and MR imaging findings were compared to validate the infusion sclerotherapy.

RESULTS

Between January 2012 and July 2016, sixteen consecutive patients (male/female ratio: 5:11; mean age, 15 years; range, 1–47 years) presented with at least 1 microcystic component of an LM and were treated by the lymphographic-like technique (LL-T). The anatomic sites of mLM were maxillofacial ($n = 6$), orbital ($n = 7$), and tongue ($n = 3$). The patients' symptoms comprised dermal lesions such as vesicular maculopapular lesions ($n = 7$), swelling ($n = 12$), pain ($n = 8$), and swallowing disorders ($n = 3$). Demographic and clinical data of all subjects are summarized in the Table.

Six of the 16 patients (38%) included in this study presented with multiple LMs with both macrocystic and microcystic components. Twelve microcystic components were classified as small/focal, and 4, as large/diffuse. The sites of these lesions were as follows: 6 lesions on the face, 3 intraoral lesions, and 7 orbital lesions.

Three lesions (19%) were treated to obtain cosmetic improvement, 6 (38%) were treated for swelling leading to oral obstruction and dysphagia, 9 (56%) were treated for swelling causing a mass effect, and 4 (25%) were treated because of pain and skin tension. Three (50%) of the lesions causing oral obstruction were also responsible for orthodontic problems secondary to LM enlargement. Five of the 16 patients (31%) had been treated for an LM before the review period: Two patients had undergone a previous operation, 2 patients had undergone previous alcohol sclerotherapy, and 1 patient had been previously treated by both an oper-

ation and alcohol sclerotherapy. These previous treatments had been performed a minimum of 2 years earlier.

Treatment Details and Complications

Sixty bleomycin LL-T sessions were performed in 16 patients. Each patient received a mean of 4 sclerotherapy sessions (range, 1–8). The microcystic component was accessible in every case, and a small "pop" experienced when crossing the microcyst was a marker of penetration of the target lesion.

The dose of bleomycin administered per session ranged from 2 to 15 U, with a mean dose of 10.5 U. The mean injection time was 90 minutes (range, 80–120 minutes). The mean follow-up was 26 months (range, 5–58 months). One patient was lost to follow-up after the first LL-T session.

Three of the 16 patients (19%) developed transient complications secondary to LL-T: One patient developed an orbital infection during hospitalization that resolved in response to oral antibiotics, 1 patient experienced severe nausea and vomiting that resolved with intravenous fluid administration, and 1 patient developed temporary skin discoloration over the injection site that lasted for 1 month and resolved without treatment.

Subjective End Points

At last follow-up, an excellent subjective clinical result was obtained in 5 (31%) of the 16 patients, a good clinical response was obtained in 9 (56%) of the 16 patients, and no response was obtained in 1 patient, though the lesions were improved.

Objective End Points

Objective improvement was observed on MR imaging for 5 (33%) of the 15 lesions (Fig 1), a minor decrease in size was observed for 4/15 lesions (27%), and no change in size was observed for 6/15 lesions (40%). No cases of deterioration were observed, but none of the mLMs were completely cured.

Although 14/15 patients (93%) reported subjective improvement at last follow-up, this improvement was associated with a significant reduction in the size of the mLM on MR imaging in only 5/15 cases (33%). An MR signal intensity change corresponding to fat transformation (T1- and T2-weighted hyperintensity) of the mLM treated by LL-T was observed in all 14 patients (100%) who reported a subjective clinical improvement at last follow-up (Table).

DISCUSSION

mLMs are less responsive to conventional percutaneous sclerotherapy techniques,⁵ mostly because the contractile lymphatic cisterns are situated more deeply in the subcutaneous tissue⁶ and due to the small dimensions of the cysts or channels (<2 cm).⁷ We describe a new bleomycin administration tech-

nique that provided encouraging results in safety and efficacy for the difficult treatment of the smaller (<3 mm) cystic components of mLMs.

The lymphographic-like technique, based on very slow bleomycin infusion, is designed to ensure uniform drug delivery to the lesion, to avoid early rupture or occlusion of small lymphatic channels. The slower infusion rate is achieved with an electronic syringe pump. The constant and slower infusion rate compared with manual injection allows deeper progression of the sclerosant through microchannels with a decreased risk of extravasation into the surrounding soft tissues. Compared with conventional manual injections, the lymphographic-like technique achieves higher concentrations and increased residence time of the sclerosant in the microcystic component, ensuring more efficient tissue inflammation.

A similar technique was recently described by Lee et al,⁸ with good results in safety and efficacy for the treatment of mLMs. However, picibanil (OK-432) was used in this study, and this agent is not currently available on the European market. Several other drugs or chemicals have been proposed for the treatment of mLMs.^{9–11} Doxycycline is the sclerosant most commonly used for the treatment of both macrocystic and microcystic LMs.¹² Doxycycline has demonstrated excellent results in macrocystic LMs but with significantly higher overall complication rates in the case of mLM lesions due to the higher doses of doxycycline required to achieve good results.¹ Very early trials of bleomycin sclerotherapy for LMs have been reported.¹³ Fatal complications such as pulmonary interstitial fibrosis or hypersensitivity^{14,15} have been described. However, no complications were observed when no more than 15 U in adults or 0.5 U/kg per session in children and a cumulative dose <90 U in adults or 6 sessions of 0.5 U/Kg in children were administered,^{4,16} confirming that bleomycin is a safe sclerosant agent.¹⁶ Because a considerable proportion (>60%) of the lesions treated in this series were localized in sensitive regions (ie, orbit and tongue), where even minimal lymphedema can cause a functional deficit, bleomycin was the best sclerosant for the lymphographic-like technique in view of its safety profile.

A few published studies have evaluated the objective response in the treatment of mLMs.¹⁷ Our results show that with an objective moderate decrease in lesion size, a subjective patient symptom improvement, described as a loss of skin tension sensation, was observed when mML fat transformation (T1- and T2- weighted hyperintensity) after LL-T was observed on MR imaging.

Our study has several limitations. First, it was a retrospective study based on a small cohort of patients and was not adequately powered because only patients with microcystic disease were included. Second, because clinical outcomes are commonly classified into relatively arbitrary categories, it is difficult to compare our results with this new bleomycin infusion technique with those of previously published studies. We did not use a specific imaging protocol; however, T1- and T2-weighted imaging was sufficient to demonstrate mLM fat transformation. The infusion technique and the sclerosant agent were adapted to the characteristics and sites of the lesions. This decision was primarily based on the operator's clinical experience. However, our findings confirm the

value of percutaneous bleomycin sclerotherapy for alleviation of the symptoms of craniofacial mLMs, with complication rates similar to those reported in previous studies.⁸ Nonetheless, a prospective study comparing bleomycin infusion with the lymphographic-like technique with other treatment modalities should be considered to provide more reliable data.

CONCLUSIONS

mLMs remain the most challenging form of lymphatic malformation, and new approaches to the management of these lesions must be developed. A new sclerotherapy technique for mLMs is proposed. The lymphographic-like technique was feasible and safe and effective for the treatment of small (<3 mm) microcystic components of LMs, with a favorable subjective outcome. More detailed guidelines must be established to ensure more extensive and safe application of this sclerosant administration technique. In addition, a prospective randomized trial should compare conventional treatment with this new sclerotherapy technique.

Disclosures: Laurent Spelle—UNRELATED: Consultancy: Stryker, Medtronic, MicroVention, Balt.

REFERENCES

1. Burrows PE, Mitri RK, Alomari A, et al. **Percutaneous sclerotherapy of lymphatic malformations with doxycycline.** *Lymphat Res Biol* 2008;6:209–16 Medline
2. Chaudry G, Burrows PE, Padua HM, et al. **Sclerotherapy of abdominal lymphatic malformations with doxycycline.** *J Vasc Interv Radiol* 2011;22:1431–35 CrossRef Medline
3. Bai Y, Jia J, Huang XX, et al. **Sclerotherapy of microcystic lymphatic malformations in oral and facial regions.** *J Oral Maxillofac Surg* 2009;67:251–56 CrossRef Medline
4. Chaudry G, Guevara CJ, Rialon KL, et al. **Safety and efficacy of bleomycin sclerotherapy for microcystic lymphatic malformation.** *Cardiovasc Intervent Radiol* 2014;37:1476–81 CrossRef Medline
5. Hogeling M, Adams S, Law J, et al. **Lymphatic malformations: clinical course and management in 64 cases.** *Australas J Dermatol* 2011; 52:186–90 CrossRef Medline
6. Whimster I. **The pathology of lymphangioma circumscriptum.** *Br J Dermatol* 1976;94:473–86 CrossRef Medline
7. Giguère CM, Bauman NM, Sato Y, et al. **Treatment of lymphangiomas with OK-432 (Picibanil) sclerotherapy: a prospective multi-institutional trial.** *Arch Otolaryngol Head Neck Surg* 2002;128: 1137–44 CrossRef Medline
8. Lee J, Lee SJ, Chung HY, et al. **Infusion sclerotherapy of microcystic lymphatic malformation: clinico-radiological mid-term results.** *J Korean Soc Radiol* 2016;74:26–36 CrossRef
9. Mathur NN, Rana I, Bothra R, et al. **Bleomycin sclerotherapy in congenital lymphatic and vascular malformations of head and neck.** *Int J Pediatr Otorhinolaryngol* 2005;69:75–80 CrossRef Medline
10. Nehra D, Jacobson L, Barnes P, et al. **Doxycycline sclerotherapy as primary treatment of head and neck lymphatic malformations in children.** *J Pediatr Surg* 2008;43:451–60 CrossRef Medline
11. Herbreteau D, Riche MC, Enjolras O, et al. **Percutaneous embolization with Ethibloc of lymphatic cystic malformations with a review of the experience in 70 patients.** *Int Angiol* 1993;12:34–39 Medline
12. Shergill A, John P, Amaral JG. **Doxycycline sclerotherapy in children with lymphatic malformations: outcomes, complications and clinical efficacy.** *Pediatr Radiol* 2012;42:1080–88 CrossRef Medline

13. Yura J, Hashimoto T, Tsuruga N, et al. **Bleomycin treatment for cystic hygroma in children.** *Nihon Geka Hokan* 1977;46:607–14 Medline
14. Levy RL, Chiarillo S. **Hyperpyrexia, allergic-type response and death occurring with low-dose bleomycin administration.** *Oncology* 1980;37:316–17 Medline
15. Sung MW, Chang SO, Choi JH, et al. **Bleomycin sclerotherapy in patients with congenital lymphatic malformation in the head and neck.** *Am J Otolaryngol* 1995;16:236–41 CrossRef Medline
16. Sainsbury DC, Kessell G, Fall AJ, et al. **Intralesional bleomycin injection treatment for vascular birthmarks: a 5-year experience at a single United Kingdom unit.** *Plast Reconstr Surg* 2011;127:2031–44 CrossRef Medline
17. Spence J, Krings T, terBrugge KG, et al. **Percutaneous sclerotherapy for facial venous malformations: subjective clinical and objective MR imaging follow-up results.** *AJNR Am J Neuroradiol* 2010;31:955–60 CrossRef Medline

Semiautomated Middle Ear Volume Measurement as a Predictor of Postsurgical Outcomes for Congenital Aural Atresia

S.J. Kabadi, D.S. Ruhl, S. Mukherjee, and B.W. Kesser

ABSTRACT

BACKGROUND AND PURPOSE: Middle ear space is one of the most important components of the Jahrsdoerfer grading system (J-score), which is used to determine surgical candidacy for congenital aural atresia. The purpose of this study was to introduce a semiautomated method for measuring middle ear volume and determine whether middle ear volume, either alone or in combination with the J-score, can be used to predict early postoperative audiometric outcomes.

MATERIALS AND METHODS: A retrospective analysis was conducted of 18 patients who underwent an operation for unilateral congenital aural atresia at our institution. Using the Livewire Segmentation tool in the Carestream Vue PACS, we segmented middle ear volumes using a semiautomated method for all atretic and contralateral normal ears on preoperative high-resolution CT imaging. Postsurgical audiometric outcome data were then analyzed in the context of these middle ear volumes.

RESULTS: Atretic middle ear volumes were significantly smaller than those in contralateral normal ears ($P < .001$). Patients with atretic middle ear volumes of $>305 \text{ mm}^3$ had significantly better postoperative pure tone average and speech reception thresholds than those with atretic ears below this threshold volume ($P = .01$ and $P = .006$, respectively). Atretic middle ear volume incorporated into the J-score offered the best association with normal postoperative hearing (speech reception threshold $\leq 30 \text{ dB}$; OR = 37.8, $P = .01$).

CONCLUSIONS: Middle ear volume, calculated in a semiautomated fashion, is predictive of postsurgical audiometric outcomes, both independently and in combination with the conventional J-score.

ABBREVIATIONS: CAA = congenital aural atresia; J+ = modified J-score; J-score = Jahrsdoerfer grading system; PTA = pure tone average; SRT = speech reception threshold

Congenital aural atresia (CAA) comprises a spectrum of otologic abnormalities characterized by hypoplasia of the external auditory canal, malformations of the middle ear, and, less commonly, abnormalities of the inner ear. The anomalies occur in varying combinations and severity, with the rate of occurrence of 1 in 10,000 to 1 in 20,000 live births.¹ Unilateral atresia is 3–5 times more common than bilateral atresia. It more commonly occurs on the right side and more commonly affects males.²

CAA is more consistently associated with conductive hearing loss, with sensorineural hearing loss seen in a minority of patients.

In appropriate patients, surgical restoration of conductive hearing can be achieved through atresioplasty, which attempts to establish the normal sound-conducting mechanism of the external and middle ear by opening an ear canal into the middle ear space, freeing the ossicular chain, constructing a tympanic membrane using the temporalis fascia, and using a skin graft to create a clean, well-epithelialized, patent external auditory canal (Fig 1).³ Two absolute criteria for surgical candidacy include audiometric or evoked-response evidence of cochlear function and imaging evidence of normal inner ear structures.⁴ However, surgical correction of CAA is not without potential complications, the most serious of which is facial nerve paralysis. The most common complications of surgery are chronic myringitis, sensorineural hearing loss, soft-tissue external auditory canal stenosis, lateralization of the tympanic membrane, bony regrowth, ossicular chain reflexation, and acquired cholesteatoma.^{2,5} These complications necessitate revision surgery in 25%–33% of patients.^{5,6}

These potential complications of atresioplasty underscore the importance of judicious patient selection for surgery. Preoperative high-resolution CT of the temporal bone plays a pivotal role

Received July 12, 2017; accepted after revision October 3.

From the Departments of Radiology and Medical Imaging (S.J.K., S.M.) and Otolaryngology–Head and Neck Surgery (D.S.R., B.W.K.), University of Virginia, Charlottesville, Virginia.

Paper previously present as an abstract at: Annual Meeting of the American Society of Neuroradiology and the Foundation of the ASNR Symposium, April 22–27, 2017; Long Beach, California.

Please address correspondence to Suraj J. Kabadi, MD, Department of Radiology and Medical Imaging, University of Virginia, PO Box 800170, 1215 Lee St, Charlottesville, VA 22908; e-mail: sjk4g@virginia.edu; @sjk_doc

<http://dx.doi.org/10.3174/ajnr.A5475>

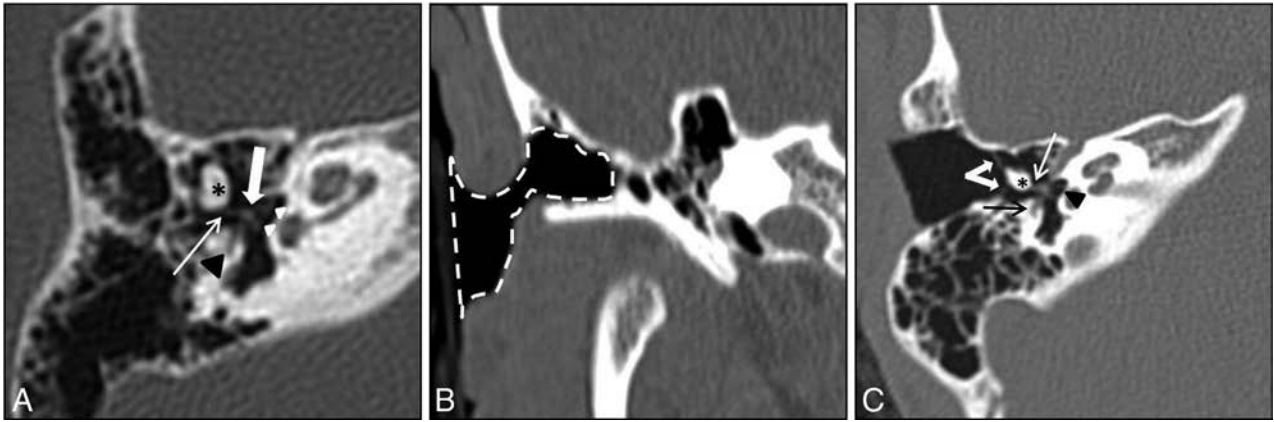


FIG 1. A, Preoperative axial CT image demonstrates a deformed, fused malleus-incus complex (*asterisk*). The incudostapedial joint is intact (*thin arrow*). The stapes (*thick arrow*) and footplate (*white arrowheads*) are normal. Note the tympanic segment of the facial nerve (*black arrowhead*) in the normal position. B, Postoperative coronal CT image demonstrates postsurgical changes of canaloplasty and meatoplasty (*dashed line*). C, Postoperative axial CT image demonstrates postsurgical changes of tympanoplasty (*thick white arrows*). Note again the fused malleus-incus complex (*asterisk*), intact incudostapedial joint (*thin white arrow*), normal oval window (*black arrowhead*), and tympanic segment of the facial nerve (*black arrow*).

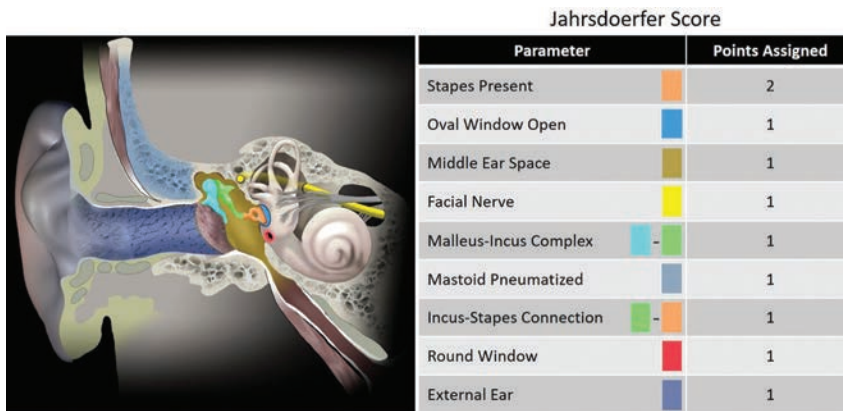


FIG 2. Schematic diagram of the ear (*left*) with corresponding color-coded structures used in the calculation of the Jahrsdoerfer score (*right*), which is used in evaluating a patient's surgical candidacy preoperatively for congenital aural atresia.

in evaluating surgical candidates and planning the operation.⁷ While different methods for determining surgical candidacy exist in the literature, the most widely accepted is the Jahrsdoerfer grading system (J-score). The J-score is a 10-point surgical rating scale based on 8 critical areas of temporal bone anatomy on high-resolution CT and the outward appearance of the external ear.⁴ Each area receives 1 rating scale point, except for the presence of a stapes, which receives 2 points (Fig 2). A J-score of ≤ 5 disqualifies a patient from surgery; a J-score of ≥ 7 is most often the threshold used to establish suitable candidacy for surgical repair of CAA. In fact, a patient with favorable anatomy scoring ≥ 7 has an approximately 85%–90% chance of achieving normal or near-normal hearing postoperatively.⁸

However, certain individual components of the J-score are themselves indispensable for successful surgery and often supersede the overall J-score. One such component is the middle ear space, because reduced middle ear space has been correlated independently with unfavorable postsurgical outcomes.^{8,9} Most surgeons will not perform atresioplasty without a well-aerated middle ear. Yet, the exact definitions of middle ear space and surgically appropriate middle ear aeration remain quite subjective.

The purpose of this study was to evaluate the efficacy of a semiautomated method of measuring middle ear space, which allows a more objective and reproducible method of ascertaining this space. In addition, we assessed whether middle ear volume derived with this method can be used, either independently or in combination with the J-score, to more accurately predict early postoperative audiometric outcomes compared with the J-score alone.

MATERIALS AND METHODS

This study was a retrospective institutional review board–approved review of patients who had primary repair of their

unilateral CAA by a single surgeon from January 2012 to December 2015. Patients were selected if they had adequate preoperative temporal bone high-resolution CT imaging and presurgical and postsurgical audiometric testing to include pure tone average (PTA), speech reception threshold (SRT), air-bone gap, and the speech discrimination score on both the atretic and contralateral normal ears. High-resolution CT bone windows, comprising 0.63- to 1.0-mm-thickness axial sections, were used for analysis. Coronal and sagittal multiplanar reconstructions were performed at the workstation as necessary.

J-scores were determined by the operating surgeon before the start of this study for each of the atretic ears in conventional fashion as previously detailed in the literature.¹⁰ This included assigning a single point for middle ear space based on a single linear measurement from the cochlear promontory medially to the atretic plate laterally. All patients in this study had a J-score of ≥ 7 .

Middle ear volumes were measured in a semiautomated fashion for all atretic ears and contralateral normal ears. The boundaries of the middle ear space were defined according to conventional anatomy as follows: roof, tegmen tympani; floor, jugular

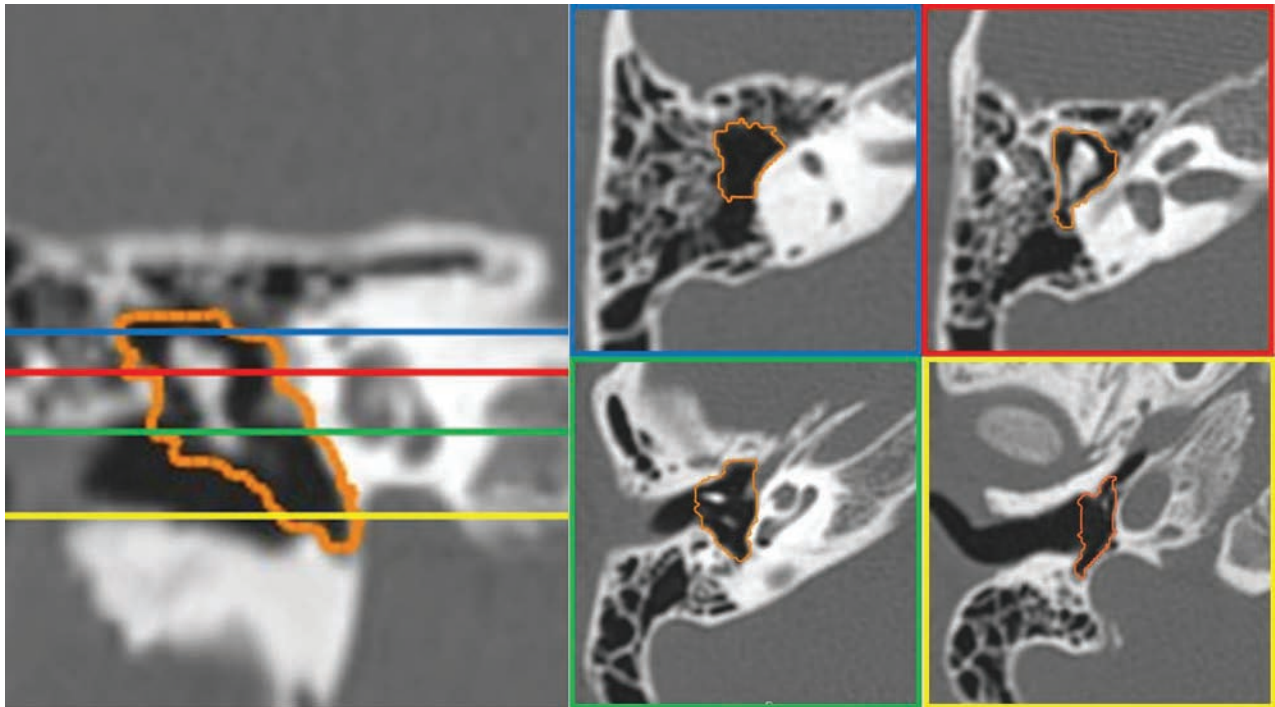


FIG 3. A normal ear with middle ear volume of 592 mm³. Coronal CT reconstruction (*left*) and corresponding axial CT images (*right*) in different regions of the middle ear demonstrate accurate semiautomated segmentation of the middle ear space.

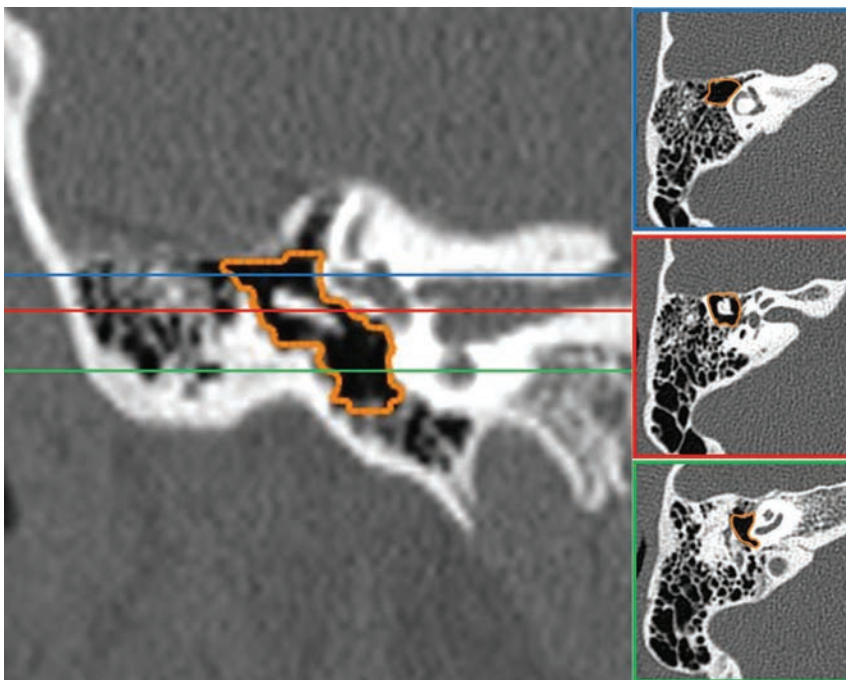


FIG 4. An atretic ear with middle ear volume of 362 mm³ and a J-score of 8. Coronal CT reconstruction (*left*) and corresponding axial CT images (*right*) in different regions of the middle ear demonstrate accurate semiautomated segmentation of the middle ear space.

fossa; medial, bony labyrinth; lateral, tympanic membrane (normal ear) or atretic plate (atretic ear); anterior, carotid wall; and posterior, mastoid antrum.

For each ear, semiautomated volumetric measurements of the middle ear were performed using the Livewire Segmentation tool in Carestream Vue PACS (Carestream Health, Rochester, New

York), with all measurements performed by a single board-certified radiologist. First, manual segmentation of the middle ear space was performed on every second axial section through the volume of interest by drawing an outline around the desired space, including on the superiormost and inferiormost sections, to establish the craniocaudal boundaries of the volume. On completion of manual segmentation, the imaging tool interpolated the segmentations on the remaining intervening axial sections in an automated fashion. Manual corrections were made to the interpolated sections as necessary if the interpolated outlines veered too far from the true outline of the middle ear space as determined by the performing radiologist. Once the segmentations on each continuous axial section in the desired volume were deemed appropriate, the tool constructed a 3D space from the outlined area of interest and reported the volume of the space in cubic millimeters (Figs 3–5). All segmentations

and volumes were finally reviewed by a board-certified neuroradiologist and otologic surgeon for accuracy.

Comparison among independent group means was performed using a Student *t* test; and among dependent data, using paired *t* testing. The Pearson correlation coefficient (*r*) and linear regression (*R*²) were used to assess association among variables. The Fisher

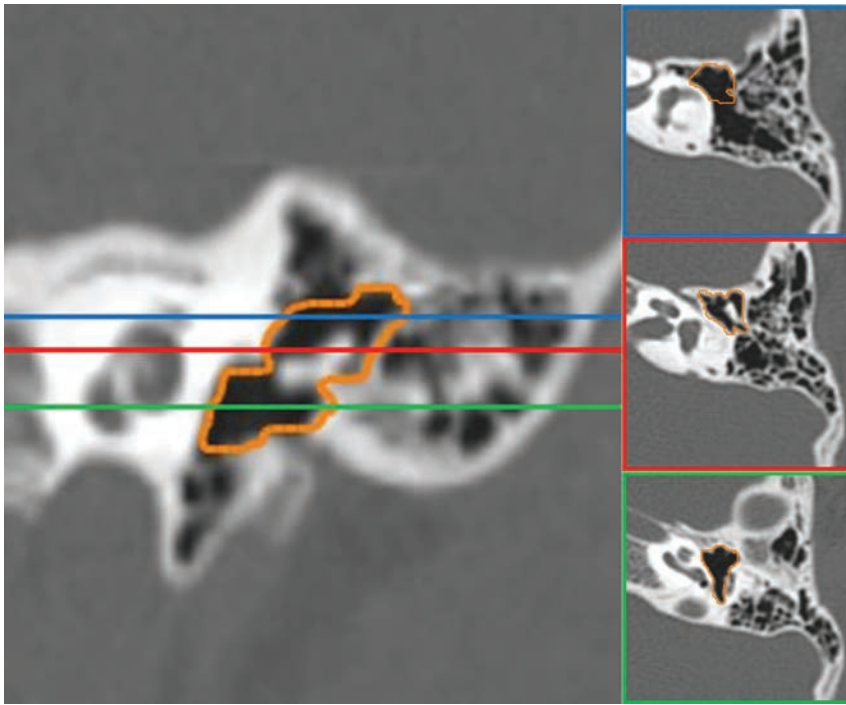


FIG 5. An atretic ear with middle ear volume of 251 mm³ and a J-score of 7. Coronal CT reconstruction (left) and corresponding axial CT images (right) in different regions of the middle ear demonstrate accurate semiautomated segmentation of the middle ear space.

Table 1: Patient demographics

Demographics		SD	P Value
Average age at operation	13 y	10.98	
Average J-score	7.86	0.51	
PTA (mean)			
Preop atresia ear	62.44 dB	5.62	<.0001 ^a
Postop atresia ear	30.56 dB	11.66	
SRT (mean)			
Preop atresia ear	57.50 dB	4.41	<.0001 ^a
Postop atresia ear	29.17 dB	11.52	
Middle ear volume (mean)			
Atretic ear	345.89 mm ³	63.16	<.0001 ^a
Nonatretic ear	627.06 mm ³	94.59	
Sex (No.)			
Male	12 (66.67%)		
Female	6 (33.33%)		
Laterality (No.)			
Left	2 (11.11%)		
Right	16 (88.89%)		

Note:—Preop indicates preoperative; Postop, postoperative.
^a Significant.

exact test was used to compare postoperative auditory outcomes among groups, and statistical significance was set at a *P* value < .05. Postoperative normal audiometric thresholds were defined as <30-dB sound pressure level. Calculations were performed on GraphPad Prism software (GraphPad Software, San Diego, California).

RESULTS

Eighteen patients with unilateral CAA met the inclusion criteria and were used in our data analysis. Thus, 18 atretic ears and 18 contralateral normal ears were used for comparative analysis. There were more males than females, and most atretic ears af-

fected the right side in our data. Audiometric follow-up testing occurred at least 6 weeks after surgery (average, 9 weeks; range, 6–35 weeks). All patients had improved PTA and SRT thresholds after primary atresia repair. Eight of the atretic ears (44.4%) achieved normal postoperative PTA, and 13 (72.2%) achieved normal postoperative SRT levels. Complete demographics of our patient population may be found in Table 1.

Traditional Jahrsdoerfer Score

Although there was a positive trend, traditional J-scores did not significantly correlate with atretic middle ear volume (Pearson *r* = 0.4122, *R*² = 0.1699, *P* = .0892). Thus, higher J-scores were not associated with larger middle ear volumes. However, higher J-scores correlated with better postoperative PTA and SRT (Pearson *r* = -0.4759, *R*² = 0.2265, *P* = .04637; and Pearson *r* = -0.5024, *R*² = 0.2524, *P* = .0336, respectively). J-scores of ≥8 were not significantly associated with normal postoperative PTA (*P* = .2174) or with normal postoperative SRT thresholds (*P* = .0770).

Middle Ear Volume

Atretic middle ear volumes were significantly smaller than contralateral normal ears (346 versus 627 mm³, *P* < .0001). Middle ear volume alone did not correlate with postoperative PTA or SRT (Pearson *r* = -0.2816, *R*² = 0.0793, *P* = .2577; and Pearson *r* = -0.4242, *R*² = 0.18, *P* = .0793, respectively). Using regression analysis to maximize sensitivity and specificity, we found that patients with atretic middle ear volumes of >305 mm³ had significantly better postoperative PTA and SRT thresholds compared with patients with smaller volumes (*P* = .0098 and *P* = .0062, respectively) (Fig 6). Middle ear volume above 305 mm³ was not significantly associated with normal postoperative PTA (*P* = .1185) but was significantly associated with normal postoperative SRT thresholds (*P* = .0368).

Modified J-Score

The calculated middle ear volume was incorporated into the traditional J-score as an objective measure. A volume of ≥305 mm³ was given 1 point, and a volume of less than this was not given a point in the middle ear space category. Using this objective measure, we assessed the modified J-score (henceforth referred to as the J+ score) for its correlation to postoperative hearing outcomes in the atretic ears. Higher J+ scores were associated with better postoperative PTA and SRT (Pearson *r* = -0.6327, *R*² = 0.43, *P* = .0048; and Pearson *r* = -0.6784, *R*² = 0.4602, *P* = .002, respectively) (Fig 7). Atretic ears with a J+ score of ≥8 were found to have better postoperative PTA and SRT thresholds than those

below this score ($P = .0042$ and $P = .0017$, respectively) (Fig 8). A J+ score of ≥ 8 was not significantly associated with normal postoperative PTA ($P = .2451$) but was significantly associated with normal postoperative hearing ($SRT \leq 30$ dB, $P = .0123$). Table 2 demonstrates the number of patients with normal postoperative PTA and SRT stratified by the traditional J-score, middle ear volume, and J+ score.

DISCUSSION

Middle ear aeration is regarded by many as the most important component of the J-score when determining surgical candidacy. Specifically, reduced middle ear space has been independently associated with unfavorable postsurgical outcomes.^{8,11} Lack of middle ear aeration may result in difficulty identifying a middle ear space and ossicular chain during drilling, re-fixation of the ossicular chain postoperatively, and postoperative stenosis with a constricted middle ear space and smaller tympanic membrane.⁸ However, the definition of middle ear space remains vague and subject to individual interpretation. In most cases of CAA, the middle ear space is indeed small, and a threshold for discriminating surgical adequacy is not well-established in the literature.

As part of the J-score, middle ear space is defined as a single linear measurement from the cochlear promontory medially to the atretic plate laterally, with a measurement of < 3 mm receiving no point on the scale.¹⁰ This region of the tympanic cavity is likely chosen due to its surgical relevance because smaller sizes may be associated with ossicular fixation and poorer hearing outcomes. However, using a single linear measurement within the middle ear space has the adverse potential of mischaracterizing the totality of the middle ear space and ultimately mischaracterizing surgical candidacy.

Attempts at more comprehensive measurement of the middle ear space have been described more recently in the literature. Specifically, middle ear space has been defined using 6 CT linear dimensions of the middle ear that have surgical relevance and are key indicators of topographic anatomy.¹¹ These linear measurements were used to derive mesotympanic volume, modeled as a rectangular prism as the product of mesotympanic length, width, and height. However, modeling the middle ear space as a rectangular prism is not anatomically sound because the irregular shape and contours of the middle ear prohibit simple geometric modeling and inevitably result in imprecise volume determinations. In addition, the process of measuring 6 different dimensions at specific landmarks is relatively cumbersome for routine clinical practice and is more prone to interobserver variability.

In our experience, the semiautomated method proposed in this study not only measures the entire middle ear volume more efficiently than any method in existing literature but does so more accurately by conforming to the abrupt contour changes of the tympanic cavity by outlining the desired space on each continuous axial section (either manually or through interpolation). Using this method, we demonstrate that middle ear volumes of > 305 mm³ had significantly better postoperative PTA and SRT compared with atretic ears below this threshold volume. When this threshold volume of 305 mm³ is used as part of the new J+ score as described above, a J+ score of ≥ 8 is predictive of better postoperative PTA and SRT. Furthermore, the J+ score correlates with better postoperative audiometric outcomes than the classic J-score. Thus, semiautomated derivation of middle ear volume is predictive of postsurgical audiometric outcomes both independently and in combination with the classic J-score.

Our numeric volume measurement of a normal middle ear volume of 627 mm³ is in agreement with existing literature, which describes a normal adult middle ear cavity volume of 640 mm³.¹² Our results are also in concordance with existing literature, which describes middle ear volume calculation by full manual segmentation.¹³ In their study, using the same anatomic boundaries of the middle ear space as in our study, Osborn et al¹³ demonstrated a statistically significant difference in mean volume between surgical candi-

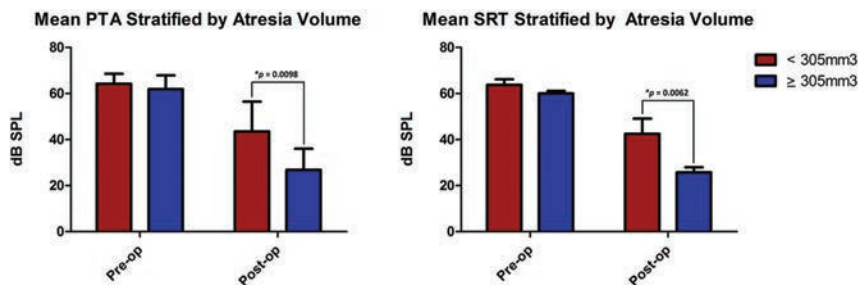


FIG 6. Atretic middle ear volumes of > 305 mm³ had significantly better postoperative pure tone average and speech reception threshold than atretic ears below this threshold volume.

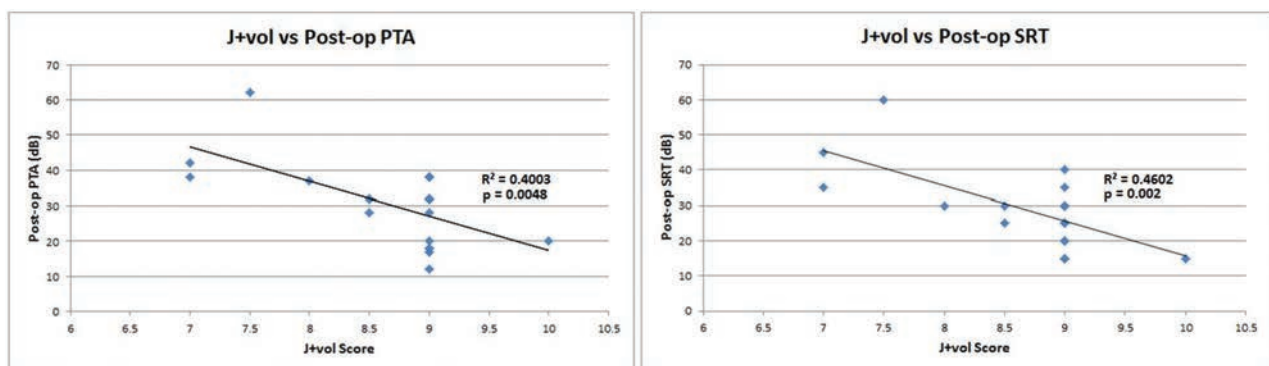


FIG 7. Higher J+ scores were associated with better postoperative pure tone average and speech reception threshold.

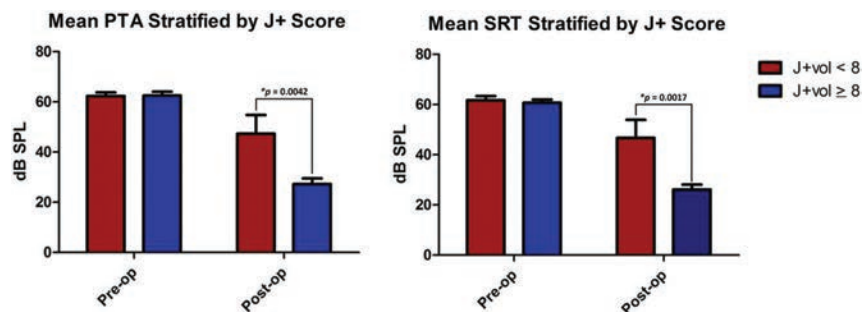


FIG 8. Atretic ears with a J+ score of ≥ 8 had significantly better postoperative pure tone average and speech reception threshold than those below this threshold score.

Table 2: Number of patients who achieved normal postoperative audiometric outcomes

	Normal Postop	
	PTA	SRT
All atretic ears	8	13
J-score < 8	1	2
J-score ≥ 8	7	11
Volume < 305 mm ³	0	1
Volume ≥ 305 mm ³	8	12
J+ score < 8	0	0
J+ score ≥ 8	8	13

Note:—Postop indicates postoperative.

date ears versus those of noncandidates and concluded that volumes derived through manual segmentation can serve as independent predictors of overall surgical candidacy. We believe our study improves on the methodology by using semiautomated segmentation instead of full manual segmentation and correlates middle ear volumes with postsurgical audiometric data rather than just discriminating between candidate and noncandidate ears.

The importance of judicious patient selection for atresiaplasty has become more significant due to recent literature suggesting suboptimal audiometric outcomes after atresiaplasty for CAA. Specifically, in a large systematic review, audiometric outcomes of patients undergoing atresiaplasty were shown to be poorer in comparison with audiometric outcomes of patients receiving an osseointegrated bone-conduction device.¹⁴ Certainly much of this finding is attributable to the considerable difficulty in performing atresiaplasty, which is considered one of the more difficult otologic operations due to intricate anatomic considerations and a high risk of complications. However, patient selection for atresiaplasty may also play a considerable role. This makes the results of our study more engaging because our demonstration of the improved association of the J+ score with normal postoperative hearing may provide an opportunity for more appropriate selection of patients who would benefit most from atresiaplasty.

However, there are several limitations to this study, specifically regarding the semiautomated methodology of segmentation. First, while the boundaries of the tympanic cavity are well-defined anatomically, their identification on high-resolution CT images is often inexact and subject to individual interpretation, resulting in the possibility of significant interobserver variability. Future work in implementing this method should include interobserver data validation to confirm the precision of middle ear volume measurement. Second, manual corrections to the interpolated out-

lines were required in most cases due to the abrupt irregular contour changes of the middle ear space on serial sections, which can only be negotiated by computer software to a limited extent. However, the manual corrections required can be performed rather quickly with the segmentation tool; thus, they still result in substantial overall time savings compared with complete manual segmentation. Finally, only patients with a J-score of ≥ 7 were included in our analysis. This is a limitation inherent with

any study that includes atresia repair outcomes because patients with a J-score of < 7 are unlikely to undergo surgery.

While we show a statistically significant correlation between middle ear volume and postsurgical outcomes, questions remain as to the intuitive importance of the entire middle ear space surgically. The epitympanum is known to be important surgically because it serves as the entry point into the middle ear during atresiaplasty. Similarly, the surgical relevance of the mesotympanum lies in its housing of critical middle ear components, including the stapes and oval window. However, the hypotympanum is rarely visualized during atresiaplasty and is not particularly relevant for surgery.¹¹ Therefore, in future work, it may be prudent to exclude the hypotympanum in middle ear volume calculations and evaluate whether similar, or perhaps stronger, correlation is found with postsurgical audiometric outcomes.

Further work may also focus on long-term postsurgical audiometric outcomes and whether improved outcomes persist several years after the operation if such data are available. Additional investigation may also be needed into the appropriateness of using a universal cutoff value for middle ear volume in determining surgical candidacy for atresiaplasty, regardless of age, because one can reasonably assume that middle ear volumes may increase during childhood. However, no normalized values for middle ear volumes as a function of age are currently available to aid in developing potential age-specific middle ear volume thresholds.

CONCLUSIONS

Middle ear aeration may be the most important predictor of surgical success for CAA. Yet, the characterization of adequate middle ear space in the context of surgical candidacy for CAA remains ambiguous. Current definitions of middle ear space are predominantly composed of linear measurements at arbitrarily chosen landmarks, which fail to adequately encompass the totality of the middle ear cavity. This study introduces a semiautomated method of measuring the entire volume of the middle ear using segmentation software, which the authors believe is a more useful representation of middle ear space in a surgical context. Middle ear volumes derived in this fashion are associated with better postsurgical audiometric outcomes, both independently and in combination with the J-score (J+ score) when a threshold value of 305 mm³ is used to assign a point on the scale. The J+ score correlates with postoperative hearing outcomes better than either the classic J-score or middle ear volume alone and may be used preoperatively to better determine surgical candidacy.

Disclosures: Bradley W. Kesser—UNRELATED: Payment for Lectures Including Service on Speakers Bureaus: DePuy Synthes. Comments: I received a single honorarium for a lecture and taught a temporal bone course*; Royalties: Nasco. Comments: I received royalties for an ear simulator that I and my colleagues patented and licensed to Nasco*. *Money paid to the institution.

REFERENCES

1. Kelley PE, Scholes MA. **Microtia and congenital aural atresia.** *Otolaryngol Clin North Am* 2007;40:61–80, vi CrossRef Medline
2. Chandrasekhar SS, De la Cruz A, Garrido E. **Surgery of congenital aural atresia.** *Am J Otol* 1995;16:713–17 Medline
3. Oliver ER, Hughley BB, Shonka DC, et al. **Revision aural atresia surgery: indications and outcomes.** *Otol Neurotol* 2011;32:252–58 CrossRef Medline
4. Jahrsdoerfer RA, Yeakley JW, Aquilar EA, et al. **Grading system for the selection of patients with congenital aural atresia.** *Am J Otol* 1992;13:6–12 Medline
5. Moss WJ, Lin HW, Cueva RA. **Surgical and audiometric outcomes for repair of congenital aural atresia and hypoplasia.** *JAMA Otolaryngol Head Neck Surg* 2016;142:52–57 CrossRef Medline
6. Digoy GP, Cueva RA. **Congenital aural atresia: review of short- and long-term surgical results.** *Otol Neurotol* 2007;28:54–60 CrossRef Medline
7. Gassner EM, Mallouhi A, Jaschke WR. **Preoperative evaluation of external auditory canal atresia on high-resolution CT.** *AJR Am J Roentgenol* 2004;182:1305–12 CrossRef Medline
8. Shonka DC Jr, Livingston WJ 3rd, Kesser BW. **The Jahrsdoerfer grading scale in surgery to repair congenital aural atresia.** *Arch Otolaryngol Head Neck Surg* 2008;134:873–77 CrossRef Medline
9. Lambert PR. **Major congenital ear malformations: surgical management and results.** *Ann Otol Rhinol Laryngol* 1988;97:641–49 CrossRef Medline
10. Yeakley JW, Jahrsdoerfer RA. **CT evaluation of congenital aural atresia: what the radiologist and the surgeon need to know.** *J Comput Assist Tomogr* 1996;20:724–31 Medline
11. Oliver ER, Lambert PR, Rumboldt Z, et al. **Middle ear dimensions in congenital aural atresia and hearing outcomes after atresiaplasty.** *Otol Neurotol* 2010;31:946–53 CrossRef Medline
12. Ikui A, Sando I, Haginomori S, et al. **Postnatal development of the tympanic cavity: a computer-aided reconstruction and measurement study.** *Acta Otolaryngol* 2000;120:375–79 CrossRef Medline
13. Osborn AJ, Oghalai JS, Vrabec JT. **Middle ear volume as an adjunct measure in congenital aural atresia.** *Int J Pediatr Otorhinolaryngol* 2011;75:910–14 CrossRef Medline
14. Nadaraja GS, Gurgel RK, Kim J, et al. **Hearing outcomes of atresia surgery versus osseointegrated bone conduction device in patients with congenital aural atresia: a systematic review.** *Otol Neurotol* 2013;34:1394–99 CrossRef Medline

Optimal Fat Suppression in Head and Neck MRI: Comparison of Multipoint Dixon with 2 Different Fat-Suppression Techniques, Spectral Presaturation and Inversion Recovery, and STIR

 S. Gaddikeri,  M. Mossa-Basha,  J.B. Andre,  D.S. Hippe, and  Y. Anzai



ABSTRACT

BACKGROUND AND PURPOSE: Uniform complete fat suppression is essential for identification and characterization of most head and neck pathology. Our aim was to compare the multipoint Dixon turbo spin-echo fat-suppression technique with 2 different fat-suppression techniques, including a hybrid spectral presaturation with inversion recovery technique and an inversion recovery STIR technique, in head and neck fat-suppression MR imaging.

MATERIALS AND METHODS: Head and neck MR imaging datasets of 72 consecutive patients were retrospectively reviewed. All patients were divided into 2 groups based on the type of fat-suppression techniques used (group A: STIR and spectral presaturation with inversion recovery gadolinium-T1WI; group B: multipoint Dixon T2 TSE and multipoint Dixon gadolinium-T1WI TSE). Objective and subjective image quality and scan acquisition times were assessed and compared between multipoint Dixon T2 TSE versus STIR and multipoint Dixon gadolinium-T1WI TSE versus spectral presaturation with inversion recovery gadolinium-T1WI using the Mann-Whitney *U* test.

RESULTS: A total of 64 patients were enrolled in the study (group A, $n = 33$ and group B, $n = 31$). Signal intensity ratios were significantly higher for multipoint Dixon T2 and gadolinium-T1WI techniques compared with STIR ($P < .001$) and spectral presaturation with inversion recovery gadolinium-T1WI ($P < .001$), respectively. Two independent blinded readers revealed that multipoint Dixon T2 and gadolinium-T1WI techniques had significantly higher overall image quality ($P = .022$ and $P < .001$) and fat-suppression grades ($P < .013$ and $P < .001$ across 3 different regions) than STIR and spectral presaturation with inversion recovery gadolinium-T1WI, respectively. The scan acquisition time was relatively short for the multipoint Dixon technique (2 minutes versus 4 minutes 56 seconds for the T2-weighted sequence and 2 minutes versus 3 minutes for the gadolinium-T1WI sequence).

CONCLUSIONS: The multipoint Dixon technique offers better image quality and uniform fat suppression at a shorter scan time compared with STIR and spectral presaturation with inversion recovery gadolinium-T1WI techniques.

ABBREVIATIONS: AP = anteroposterior; CHESS = chemical shift selective suppression; FS = fat suppression; Gad-T1WI = gadolinium-T1WI; mDixon = multipoint Dixon; SPIR = spectral presaturation with inversion recovery

Uniform and complete fat suppression (FS) is indispensable for accurate diagnosis and characterization of head and neck pathologies. Various FS MR imaging techniques are avail-

able clinically, each with its own advantages and disadvantages. Commonly used FS MR imaging techniques include STIR, chemical shift selective suppression (CHESS), hybrid methods such as spectral presaturation with inversion recovery (SPIR; Phillips Healthcare, Best, the Netherlands), spectral attenuated inversion recovery, and a more recent chemical shift method, the multipoint Dixon (mDixon Technique; Phillips Healthcare).

The STIR technique nulls the fat signal using a 180° inversion pulse as an initial excitation pulse, followed by a subsequent 90° pulse at a specified inversion time (approximately 160–180 ms for a 1.5T magnet). The CHESS technique uses a radiofrequency pulse tuned to the fat-resonance frequency together with a spoiler gradient, which saturates fat signal and thus leaves only water protons to produce signal. SPIR is a hybrid FS technique that combines the fat selectivity of CHESS and uses an inversion radiofrequency pulse like that in the STIR technique. Never-

Received March 3, 2017; accepted after revision October 16.

From the Departments of Neuroradiology (S.G.) and Radiology (S.G.), Rush University Medical Center, Chicago, Illinois; Departments of Neuroradiology (M.M.-B.) and Radiology (D.S.H.), University of Washington, Seattle, Washington; Department of Neuroradiology (J.B.A.), University of Washington Medical Center, Seattle, Washington; and Department of Radiology (Y.A.), University of Utah Health Center, Salt Lake City, Utah.

Paper previously presented at: Annual Meeting of the American Society of Neuroradiology and the Foundation of the ASNR Symposium, April 22–27, 2017; Long Beach, California.

Please address correspondence Santhosh Gaddikeri, MD, Department of Radiology, Rush University Medical Center, 1653 W Congress Parkway, Chicago, IL 60612; e-mail: Santhosh_Gaddikeri@rush.edu

 Indicates article with supplemental on-line table.

<http://dx.doi.org/10.3174/ajnr.A5483>

Table 1: Parameters used for different fat-suppression sequences on a 3T scanner^a

	Axial STIR	Axial T2WI	Axial Gad-T1WI	Axial Gad-T1WI
	TSE	mDixon TSE	SPIR TSE	mDixon TSE
Coil	16 Channel SENSE NV	16 Channel SENSE NV	16 Channel SENSE NV	16 Channel SENSE NV
TR/TE	3000/15 ms	3000/80 ms	600/9.2 ms	500/10 ms
Section thickness/ intersection gap	3/1 mm	3/1 mm	3/1 mm	3/1 mm
No. of axial images	40	40	40	40
FS technique	Inversion recovery (T1 = 200 ms)	mDixon	SPIR	mDixon
Acquisition matrix	200 × 141	232 × 232	288 × 196	204 × 199
NEX	2	1	1	1
Acquisition time	4 min, 56 sec	2 min, 2 sec	3 min, 2 sec	2 min, 8 sec
Parallel imaging	Yes	Yes	Yes	Yes
Gadolinium contrast	N/A	N/A	0.1 mmol/kg gadodiamide (Gd-DTPA) (ProHance)	0.1 mmol/kg gadodiamide (Gd-DTPA) (ProHance)

Note:—SENSE indicates sensitivity encoding; N/A, not applicable; NV, NeuroVascular.

^a Achieva; Philips Healthcare.

theless, SPIR differs from CHES in that the radiofrequency pulse used is an inversion pulse and is different from STIR in that the inversion pulse used is selective for fat spin excitation only.¹ The more recently developed mDixon technique is insensitive to magnetic field (both B0 and B1) inhomogeneity while preserving the desired image contrast at reduced scan acquisition times.²

In this retrospective study, we compared 3-point mDixon T2 TSE and mDixon gadolinium-T1WI (Gad-T1WI) TSE techniques with the commonly used T2 (STIR) and post-Gad-T1WI (SPIR) FS techniques, respectively, for assessing subjective and objective image quality while considering image-acquisition times.

MATERIALS AND METHODS

The ethics committee of our institution (University of Washington) approved this Health Insurance Portability and Accountability Act–compliant study. We retrospectively reviewed the imaging records of 72 consecutive patients who had undergone head and neck MR imaging without and with gadolinium administration for various clinical indications, between July 1, 2014, and September 30, 2014. Another inclusion criterion was that these patients also have a CT examination of the neck within 3 months before or after the MR imaging study. The CT data were used to quantify body habitus. Patients with poor renal function (glomerular filtration rate of <30) and suboptimal image quality secondary to patient motion artifacts were excluded from the study. None of the enrolled patients had cervical spine fusion hardware. Systematic changes were made in the institutional head and neck MR imaging protocol during the study time period so that the previously obtained STIR/SPIR combination of FS techniques was gradually switched to the evaluated mDixon FS techniques. The enrolled subjects were divided into 2 groups (group A and group B) based on the combination of FS techniques used for the corresponding T2-weighted sequence and Gad-T1WI sequence. In group A subjects, STIR images were acquired as a T2-weighted sequence and SPIR images were acquired as the post Gad-T1WI FS technique. In group B subjects, a 2D mDixon spin-echo (2D-3-point mDixon TSE) technique was

used to suppress fat signal in both T2-weighted and post-Gad-T1WI sequences.

Data Acquisition

All MR imaging scans were obtained on a 3T scanner (Achieva; Philips Healthcare). As per our institution protocol, we obtained the following MR imaging sequences: axial, sagittal, and coronal T1WI; and axial and coronal fluid-sensitive sequences with fat suppression (axial STIR and coronal CHES FS T2WI or axial and coronal mDixon FS T2WI), followed by gadolinium-enhanced (gadoteridol, ProHance, 279.3 mg/mL; Bracco Diagnostics, Princeton, New Jersey) axial and coronal T1WI with FS sequences (SPIR or mDixon). Parameters used for STIR, SPIR FS Gad-T1WI, mDixon FS T2WI, and mDixon FS Gad-T1WI are summarized in Table 1.

Data Analysis

Objective Analysis. All objective measurements were performed by a fellowship-trained neuroradiologist with 10 years of cumulative experience in head and neck imaging. As the surrogate measure of a patient's body size, the maximum anteroposterior (AP) neck diameter at the level of mandible (parallel to the C2–3 intervertebral disc), minimum AP diameter at the midneck level (parallel to the C4–5 intervertebral disc), and maximum transverse shoulder width (Fig 1) were measured on the neck CT topogram. The ratios of AP neck diameter at the level of the mandible to the AP diameter at the midneck level and shoulder width to AP diameter of the midneck were calculated for each subject and were compared between the 2 groups (groups A and B).

Signal intensity of the spinal cord and subcutaneous fat was measured (Fig 2) by placing a circular ROI measuring 5–10 mm in diameter on an axial image at 2 different levels (submandibular region and supraclavicular region) on all sequences. To normalize the relative fat signal intensity, we calculated the signal intensity ratio between the spinal cord and subcutaneous fat at both levels for each sequence. The ratios were compared between STIR and mDixon FS T2 TSE and between SPIR FS Gad-T1WI and mDixon FS Gad-T1WI TSE, respectively.

Subjective Analysis. Two fellowship-trained and board-certified neuroradiologists, each with 12 years of experience in in-

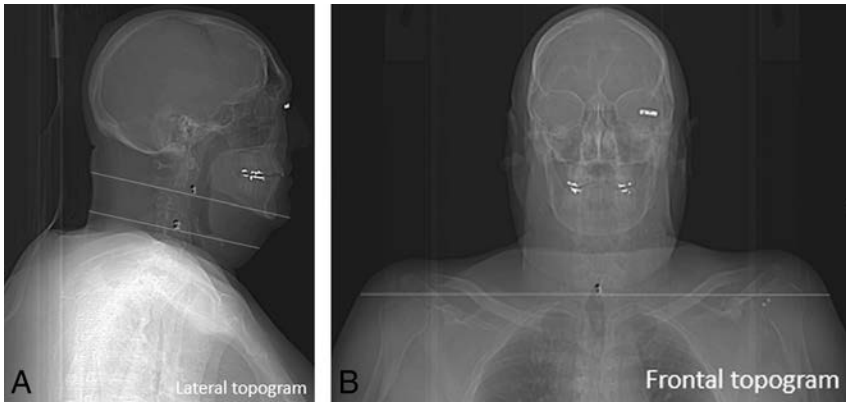


FIG 1. Lateral (A) and frontal (B) projections of CT topogram images with measurements of anteroposterior diameter at the level of C2–3 and C4–5 and transverse diameters at the shoulder.

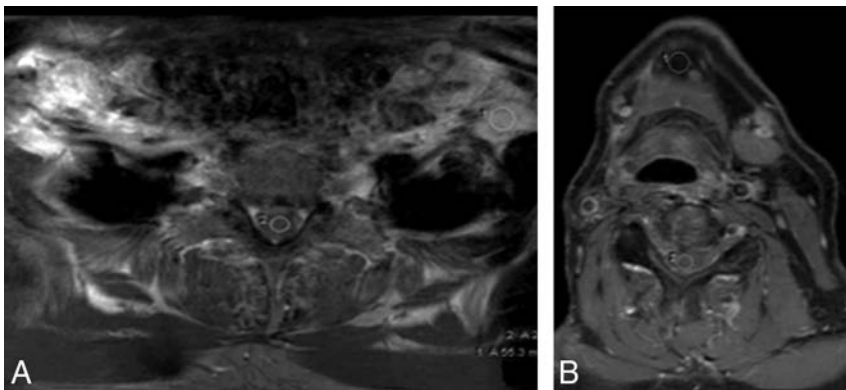


FIG 2. Gadolinium-enhanced T1-weighted MR images with SPIR (A) and mDixon (B) techniques for fat suppression. ROIs are placed on the spinal cord and fat to obtain a signal intensity ratio.

terpreting head and neck MR imaging, independently assessed the image quality. Readers were blinded to all FS techniques used. On a per-subject basis, the stack of axial images of each sequence (FS T2 sequence and FS Gad-T1WI sequence) was displayed and analyzed on a random basis on a PACS monitor. No preset window width or level was provided. The readers were free to vary both at their discretion. The 2 readers were asked to evaluate the following: 1) uniformity of fat suppression with emphasis on 3 areas that are prone to incomplete fat suppression (the maxillary, submandibular, and supraclavicular regions, respectively), 2) overall image quality for each fat-suppression technique, and 3) the presence of susceptibility artifacts from dental amalgam. Uniformity of fat suppression and overall image quality assessment were graded on a 5-point Likert-like scale (1 = poor, 2 = suboptimal, 3 = acceptable, 4 = good, and 5 = excellent).

Direct comparison of objective and subjective image-quality measurements between groups A and B (STIR versus mDixon T2 TSE and Gad-T1WI SPIR versus mDixon Gad-T1WI TSE) were performed. Sequence-specific acquisition times were collected and compared between the 2 groups.

Statistical Analysis

Variables were summarized as mean \pm SD or count (percentage). The sequence groups were compared using the Mann-Whitney *U* test. For the analysis of subjective image-quality ratings, the

ratings of 2 readers were averaged to compare the groups. A permutation test, clustered by patient, was used to compare the presence of dental amalgam susceptibility artifacts as rated by both readers separately between sequence groups. Interreader agreement of the subjective ratings was summarized using the Cohen κ (linearly weighted for 5-point scales and unweighted for binary variables) and percentage agreement. Percentage agreement for the 5-point scales was calculated after combining the ratings into a 3-point scale: 1–2, 3, and 4–5. Bias in ratings between the readers was assessed using the Wilcoxon signed rank test. A *P* value of $< .05$ was considered statistically significant. All statistical calculations were conducted with the statistical computing language R (Version 3.1.1; <http://www.r-project.org/>).

RESULTS

Patient Demographics

Group-based patient demographics are summarized in Table 2. A total of 64 patients met the inclusion criteria, following exclusion of 8 patients (due to suboptimal MR imaging due to motion artifacts [$n = 5$] and lack of intravenous gadolinium-based contrast agent administration [$n = 3$]).

Group A comprised 33 patients (10 women), while group B comprised 31 patients (11 women).

There was no statistically significant difference in the age (mean, 61 ± 15 years versus 55 ± 17 years; $P = .15$) or sex ($P = .79$) distribution, between the groups. There was no significant difference in body habitus, represented by the ratio between groups, of shoulder width-to-mandibular region AP neck diameter at the C2–3 level (1.53 ± 0.16 versus 1.48 ± 0.15 for groups A and B, respectively; $P = .35$); and the ratio of shoulder width-to-midneck AP diameter at the C4–5 level (3.21 ± 0.36 versus 3.16 ± 0.40 , for groups A and B, respectively; $P = .88$).

Objective Assessment

Objective image-quality measurements are summarized in Table 3. Signal intensity ratios measured between the spinal cord and subcutaneous fat at the submandibular and supraclavicular levels were significantly higher for the mDixon technique. For T2-weighted sequences (STIR versus mDixon T2-weighted TSE), the ratios measured 3.5 ± 3.4 versus 5.7 ± 1.6 , respectively ($P < .001$) at the submandibular level and 3.3 ± 3.4 versus 7.4 ± 2.4 , respectively ($P < .001$) at the supraclavicular level. Similarly, in the post-gadolinium-enhanced FS T1-weighted sequence (SPIR Gad-T1WI versus mDixon Gad-T1WI TSE), the ratios measured 0.9 ± 0.7 versus 3.7 ± 1.4 , respectively ($P < .001$) at submandibular level and 0.5 ± 0.3 versus 4.3 ± 2.0 , respectively ($P < .001$) at supraclavicular level.

Table 2: Demographics and body habitus^a

Variable	Sequence Group		P Value ^b
	Group B (n = 31)	Group A (n = 33)	
Sex			
Male	20 (64.5)	23 (69.7)	.79
Female	11 (35.5)	10 (30.3)	
Age (yr)	61 ± 15	55 ± 17	.15
Body habitus			
AP neck diameter at the level of mandible (C2–3) (mm)	185 ± 21	188 ± 21	.28
AP diameter of midneck (C4–5) (mm)	127 ± 22	124 ± 19	.90
Shoulder width (mm)	394 ± 35	394 ± 45	.84
AP neck diameter at the level of mandible-to-shoulder width ratio	1.48 ± 0.15	1.53 ± 0.16	.35
Shoulder width-to midneck AP diameter ratio	3.16 ± 0.40	3.21 ± 0.36	.88

^a Values are No. (%) or mean ± SD unless otherwise specified.

^b Mann-Whitney *U* test.

Table 3: Objective signal intensity ratios^a

Variable	Sequence Group		P Value ^b
	Group B (n = 31)	Group A (n = 33)	
T2WI spinal cord-to-fat ratio			
Submandibular level	5.7 ± 1.6	3.5 ± 3.4	<.001
Supraclavicular level	7.4 ± 2.4	3.3 ± 3.4	<.001
Post-Gad-T1WI spinal cord-to-fat ratio			
Submandibular level	3.7 ± 1.4	0.9 ± 0.7	<.001
Supraclavicular level	4.3 ± 2.0	0.5 ± 0.3	<.001

^a Values are mean ± SD unless otherwise specified.

^b Mann-Whitney *U* test.

Table 4: Subjective assessment of image quality, fat suppression, and susceptibility artifacts^a

Variable	Sequence Group		P Value ^b
	Group B (n = 31)	Group A (n = 33)	
T2WI/STIR images			
Overall image-quality grade	3.9 ± 0.5	3.6 ± 0.7	.022
Fat-saturation grade			
Maxillary region	4.6 ± 0.4	4.3 ± 0.5	.013
Mandibular region	4.4 ± 0.5	4.0 ± 0.6	.007
Lower neck region	4.7 ± 0.4	4.3 ± 0.4	.001
Dental amalgam susceptibility artifacts (%)	38.7%	22.7%	.056
Post-Gad-T1WIs			
Overall image-quality grade	4.0 ± 0.4	2.6 ± 0.6	<.001
Fat-saturation grade			
Maxillary region	4.8 ± 0.3	3.8 ± 0.7	<.001
Mandibular region	4.7 ± 0.3	2.8 ± 0.5	<.001
Lower neck region	4.8 ± 0.3	1.4 ± 0.7	<.001
Dental amalgam susceptibility artifacts (%)	37.1%	31.8%	.50

^a Two readers averaged. Values are mean ± SD unless otherwise specified.

^b Mann-Whitney *U* test comparing average ratings or permutation test (clustered by patient) for susceptibility artifacts.

Subjective Assessment

The averages of the 2 readers' subjective assessments of the uniformity of fat suppression and overall image quality for groups A and B are summarized in Table 4.

Fat Suppression. The average scores from both the readers for fat suppression at all 3 levels (maxillary, mandibular, and lower neck region) were significantly higher for mDixon T2-weighted FS TSE (mean, 4.4–4.7) compared with STIR (mean, 4.0–4.3; $P < .013$ for all regions) (Fig 3) and mDixon Gad-T1WI FS TSE sequences (mean, 4.7–4.8) compared with SPIR Gad-T1WI (mean, 1.4–3.8, $P < .001$ for all regions) (Figs 4 and 5).

Overall Image Quality. Similarly, the 2 readers' average scores for overall image quality were significantly higher for mDixon T2-weighted FS TSE than for STIR (mean, 3.9 versus 3.6; $P = .022$) and mDixon Gad-T1WI FS TSE sequences (mean, 4.0 versus 2.6; $P < .001$).

Susceptibility Artifacts Related to Dental Amalgam. There was no significant difference in the percentage of subjects with susceptibility artifacts related to dental amalgam between the 2 groups for both fluid-sensitive sequences (38.7% versus 22.7%, $P = .056$) and post-Gad-T1WI sequences (37.1% versus 31.8%, $P = .5$).

Interreader Agreement

The percentage agreement for the uniformity of fat suppression between the readers was >87% for group B patients (On-line Table), though the corresponding κ values ranged from 0.05 to 0.15. Across all 3 stations, readers gave ratings of only 4–5 for 87%–100% of cases, so there was a limited range of ratings for the κ assessment. Group A interreader agreement varied between 25% and 91% (On-line Table), with corresponding κ values from –0.07 to 0.58.

Across the 3 stations, readers used only 2 different levels 67%–99% of the time.

Scan Acquisition Times. The acquisition times were shorter for the mDixon techniques compared with STIR (2 minutes versus 4 minutes 56 seconds) and SPIR (2 minutes versus 3 minutes).

DISCUSSION

In this retrospective study, we enrolled 33 subjects who underwent MR imaging with a STIR and SPIR combination of fat-suppression techniques and 31 subjects with mDixon as the fat-sup-

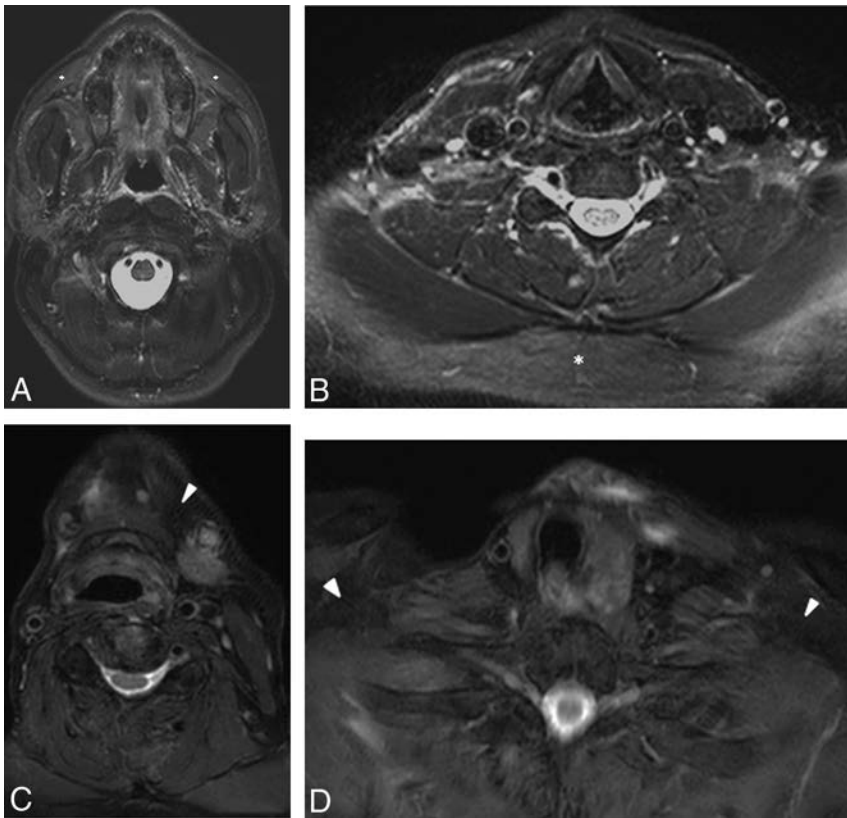


FIG 3. Axial STIR (A and B) and mDixon T2-weighted (C and D) MR images. Note incomplete fat suppression (*asterisks*) in the maxillary and supraclavicular regions on the STIR technique and complete uniform fat suppression (*arrowheads*) in the submandibular and supraclavicular regions on the mDixon technique.

pression technique. The subjects were matched for age, sex, and surrogate imaging markers of body habitus in the area of interest. In this study group, we demonstrate that the objective image quality measured for signal intensity ratios (spinal cord to subcutaneous fat signal) was significantly higher for the Dixon technique compared with STIR and SPIR. This finding clearly indicates that the mDixon technique provides better fat suppression, even in the areas where other fat-suppression techniques failed due to technical reasons. In the subjective assessment, readers scored the mDixon technique significantly higher for uniformity of fat suppression and overall image quality. An additional minor advantage with the mDixon technique is relatively shorter scan acquisition times. Our study results are in concordance with previous studies comparing the 3-point mDixon with the CHESSE fat-suppression technique in spine, neck, and orbit imaging.³⁻⁵

The main disadvantages associated with STIR include suppression of signals from tissues with similar T1 values (such as subacute hematoma and gadolinium-enhanced tissues). In addition, fewer sections were obtained for a given TR compared with the spin-echo technique because a certain portion of the time is consumed by the TI and TE of STIR. STIR is considered sensitive to spatial nonuniformity of the applied radiofrequency pulse (unless an adiabatic pulse is used). If the strength of the radiofrequency pulse varies from one position to another within the subject, then the tip angle of the inversion pulse, and hence the quality of fat suppression, will also vary with position. Finally, the uniformity of fat suppression may depend on selection of an appropriate

TI.⁶⁻⁹ In addition, STIR alters signal from all tissues and thus decreases the contrast as well as the signal-to-noise ratio.² CHESSE and its derivative SPIR hybrid techniques require a homogeneous magnetic field for uniform fat suppression. They fail to suppress fat signal around susceptibility distortions due to metallic hardware, sinuses, and skull base or in the regions far from the isocenter. They also increase the specific absorption rate to the patient and scan times due to use of an extra presaturation pulse and dephasing gradient. Uniformity of FS by CHESSE/SPIR techniques is heavily dependent on homogeneity of the main magnetic field (B₀) and radiofrequency magnetic field (B₁); hence, nonuniform fat suppression occurs farther away from the isocenter of B₀. Another important factor described to explain the nonuniformity of FS in the CHESSE/SPIR technique in areas with a sharp variation of the shape of anatomic structures such as the floor of the mouth and the supraclavicular region is the so-called bulk susceptibility phenomenon.⁶

The mDixon technique for FS was first described by Dixon in 1984.¹⁰ This

is a spectroscopic imaging technique that relies on water and fat chemical shift differences. The original technique was designed to acquire 2 sets of images, one with water and fat signal being in-phase and the other acquired when water and fat signals are at 180° out-of-phase (referred to as the “2-point Dixon technique”). Using these 2 sets of images, one can generate water-only and fat-only images.¹¹ The water-only images serve as effective fat suppression.^{3,4,12} The main advantage of this technique is that it is relatively insensitive to B₀ inhomogeneity but not completely immune to it because sometimes the B₀ inhomogeneity can manifest as phase errors. The fundamental assumption of the mDixon technique is that water and fat are the only 2 signal-contributing chemical species in the object to be imaged. Under this assumption, it is believed that water or fat each has only a single spectral peak. This assumption may be true for water but not for fat because fat is known to contain many spectral components. The B₀ inhomogeneity and other system imperfections contribute to phase error results in signal contributions to both water-only and fat-only images, even from the pixels containing only fat tissue.²

Failure of phase correction usually leads to swapping of water and fat assignments for the affected pixels, which can sometimes present a “pseudomass” appearance or incomplete fat suppression. Correlating with both water-only and fat-only images may help reduce this misinterpretation. A more recent technical advance, the 3-point Dixon technique, acquires an addi-

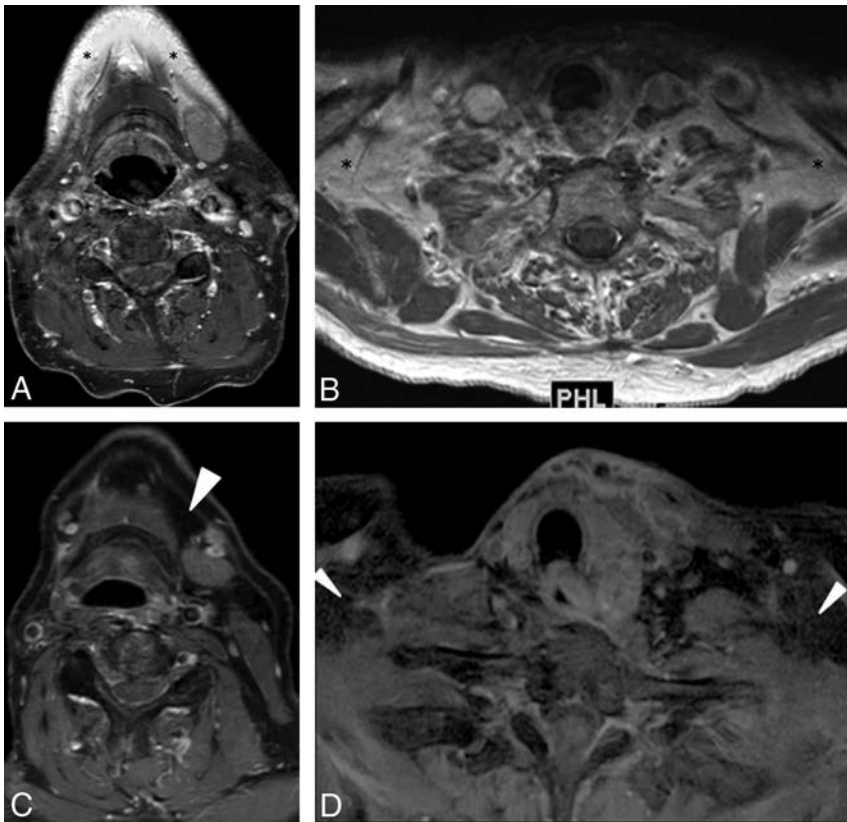


FIG 4. Gadolinium-enhanced axial T1-weighted MR images with SPIR (A and B) and mDixon (C and D) techniques for fat suppression. Note incomplete fat suppression (asterisks) in the submandibular and supraclavicular regions on the SPIR technique and complete uniform fat suppression (arrowheads) in similar regions on the mDixon technique.

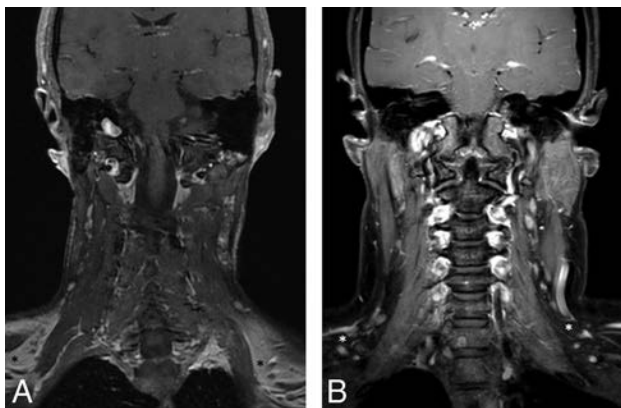


FIG 5. Gadolinium-enhanced coronal T1-weighted MR images with SPIR (A) and mDixon (B) techniques for fat suppression. Note incomplete fat suppression (dark asterisk) in the supraclavicular regions on the SPIR technique and complete uniform fat suppression (white asterisk) in similar regions on the mDixon technique.

tional third set of images along with the traditionally acquired 0° and 180°; it can be either -180°, 0, 180° or 0, 180°, 360°. This additional image set helps determine and correct the phase error.¹³⁻¹⁷ The 3-point Dixon technique is considered less prone to phase error, though it is not completely immune to it. This technique can be applied for both 2D and 3D imaging with different types of pulse sequences, including spin-echo and gradient-based echo sequences.²

Study Limitations

There are several limitations to this study: 1) It is a retrospective study and hence has a limitation of selection bias; 2) it is a relatively small cohort of patients, particularly when considering comparison for 3 different techniques; and 3) a combination of different FS techniques was used in 2 separate populations (groups A and B). This is particularly important because uniformity of FS in certain techniques such as CHES and its modifications (SPIR) depend heavily on the patient's body habitus and on patient position in the magnet. In our study, we think the contribution of patient-related factors was not significant, considering that there was no statistically significant difference in the demographics and patient body habitus (in the area of interest) between the groups. Fourth, lesion detectability and conspicuity were not assessed due to heterogeneity in the scan indications. Not all patients had a focal lesion, and when a focal lesion was present, no 2 lesions were comparable due to heterogeneity in the type of disease, location, and stage of treatment. Fifth, there was some disagreement between readers during the subjective assessment; however, rat-

ings by both readers showed similar trends between groups A and B, and the readers typically used only 2 different adjacent rating levels at each station. Therefore, while readers may have disagreed on individual ratings, they usually agreed that ratings were high (4-5), low (1-2), or moderate (2-3 or 3-4).

CONCLUSIONS

The mDixon technique provides more uniform fat suppression and improved image quality compared with other commonly used FS techniques such as STIR and SPIR, while reducing sequence acquisition times in head and neck MR imaging.

Disclosures: Daniel S. Hippe—UNRELATED: Grants/Grants Pending: GE Healthcare, Philips Healthcare, Toshiba America Medical Systems, Comments: for statistical work on other studies.

REFERENCES

1. Del Grande FD, Santini F, Herzka DA, et al. Fat-suppression techniques for 3-T MR imaging of the musculoskeletal system. *RadioGraphics* 2014;34:217-33 CrossRef Medline
2. Ma J. Dixon techniques for water and fat imaging. *J Magn Reson Imaging* 2008;28:543-58 CrossRef Medline
3. Ma J, Singh SK, Kumar AJ, et al. T2-weighted spine imaging with a fast three-point Dixon technique: comparison with chemical shift selective fat suppression. *J Magn Reson Imaging* 2004;20:1025-29 CrossRef Medline
4. Ma J, Jackson EF, Kumar AJ, et al. Improving fat-suppressed T2-weighted imaging of the head and neck with 2 fast spin-echo Dixon

- techniques: initial experiences.** *AJNR Am J Neuroradiol* 2009;30:42–45 Medline
5. Rybicki FJ, Mulkern RV, Robertson RL, et al. **Fast three-point Dixon MR imaging of the retrobulbar space with low-resolution images for phase correction: comparison with fast spin-echo inversion recovery imaging.** *AJNR Am J Neuroradiol* 2001;22:1798–802
 6. Tien RD. **Fat-suppression MR imaging in neuroradiology: techniques and clinical application.** *AJR Am J Roentgenol* 1992;158:369–79 CrossRef Medline
 7. Bydder GM, Steiner RE, Blumgart LH, et al. **MR imaging of the liver using short TI inversion recovery sequences.** *J Comp Assist Tomogr* 1985;9:1084–89 CrossRef Medline
 8. Bydder GM, Young IR. **MR imaging: clinical use of the inversion recovery sequence.** *J Comp Assist Tomogr* 1985;9:659–75 CrossRef Medline
 9. Shuman WP, Baron RL, Peters MJ, et al. **Comparison of STIR and spin-echo MR imaging at 1.5 T in 90 lesions of the chest, liver, and pelvis.** *AJR Am J Roentgenol* 1989;152:853–59 CrossRef Medline
 10. Dixon WT. **Simple proton spectroscopic imaging.** *Radiology* 1984;153:189–94 CrossRef Medline
 11. Hardy PA, Hinks RS, Tkach JA. **Separation of fat and water in fast spin-echo MR imaging with the three-point Dixon technique.** *J Magn Reson Imaging* 1995;5:181–85 CrossRef Medline
 12. Low RN, Austin MJ, Ma J. **Fast spin-echo triple echo Dixon: initial clinical experience with a novel pulse sequence for simultaneous fat-suppressed and nonfat-suppressed T2-weighted spine magnetic resonance imaging.** *J Magn Reson Imaging* 2011;33:390–400 CrossRef Medline
 13. Yeung HN, Kormos DW. **Separation of true fat and water images by correcting magnetic field inhomogeneity in situ.** *Radiology* 1986;159:783–86 CrossRef Medline
 14. Glover GH, Schneider E. **Three-point Dixon technique for true water/fat decomposition with B₀ inhomogeneity correction.** *Magn Reson Med* 1991;18:371–83 CrossRef Medline
 15. Glover GH. **Multipoint Dixon technique for water and fat proton and susceptibility imaging.** *J Magn Reson Imaging* 1991;1:521–30 CrossRef Medline
 16. Maas M, Hollak CE, Akkerman EM, et al. **Quantification of skeletal involvement in adults with type I Gaucher's disease: fat fraction measured by Dixon quantitative chemical shift imaging as a valid parameter.** *AJR Am J Roentgenol* 2002;179:961–65 CrossRef Medline
 17. Wang Y, Li D, Haacke EM, et al. **A three-point Dixon method for water and fat separation using 2D and 3D gradient-echo techniques.** *J Magn Reson Imaging* 1998;8:703–10 CrossRef Medline

Optic Nerve Measurement on MRI in the Pediatric Population: Normative Values and Correlations

C.E. Al-Haddad, M.G. Sebaaly, R.N. Tutunji, C.J. Mehanna, S.R. Saaybi, A.M. Khamis, and R.G. Hourani

ABSTRACT

BACKGROUND AND PURPOSE: Few articles in the literature have looked at the diameter of the optic nerve on MR imaging, especially in children, in whom observations are subjective and no normative data exist. The aim of this study was to establish a data base for optic nerve diameter measurements on MR imaging in the pediatric population.

MATERIALS AND METHODS: This was a retrospective study on the MR imaging of pediatric subjects (younger than 18 years of age) at the Department of Diagnostic Radiology at the American University of Beirut Medical Center, Beirut, Lebanon. The optic nerve measurements were obtained by 3 raters on axial and coronal sections at 3 mm (retrobulbar) and 7 mm (intraorbital) posterior to the lamina cribrosa.

RESULTS: Of 211 scans of patients (422 optic nerves), 377 optic nerves were measured and included. Ninety-four patients were female (45%) and the median age at MR imaging was 8.6 years (interquartile range, 3.9–13.3 years). Optic nerves were divided into 5 age groups: 0–6 months ($n = 18$), 6 months–2 years ($n = 44$), 2–6 years ($n = 86$), 6–12 years ($n = 120$), and 12–18 years ($n = 109$). An increase in optic nerve diameter was observed with age, especially in the first 2 years of life. Measurements did not differ with eye laterality or sex.

CONCLUSIONS: We report normative values of optic nerve diameter measured on MR imaging in children from birth to 18 years of age. A rapid increase in optic nerve diameter was demonstrated during the first 2 years of life, followed by a slower increase. This was independent of sex or eye laterality.

The optic nerve anatomically starts from the optic disc and ends in the optic chiasm and comprises 4 distinct parts: the optic nerve head, the intraorbital portion, the intracanalicular portion, and the intracranial portion.^{1–3} Just posterior to the sclera, the nerve acquires arachnoid membranes continuous with those of the brain,⁴ composing the optic nerve sheath complex. While funduscopy and optical coherence tomography can study the disc portion with high resolution, the remaining 3 portions are less accessible and require imaging studies, including MR imaging, sonography, and CT.^{5,6} In fact, MR imaging is superior due to its high soft-tissue resolution, the absence of ionizing radiation, and its high diagnostic accuracy as demonstrated by several studies evaluating the sensitivity of MR imaging compared with histopathologic examination in the detection of tumor invasion.^{7–9} According to Chawla et al⁷ and Schueler et al,⁸ the MR imaging

sensitivity in detecting optic nerve abnormality is 60%–75%, while its specificity is up to 90%. Indeed, the optic nerve has been studied in healthy individuals and in pathologic states using MR imaging, CT, sonography, and cross-sectional anatomy.^{10–14} These studies, however, have reported either qualitative parameters^{5,15} or normative values of both the optic nerve and sheath as a complex.^{16–19}

Ample literature exists on the use of MR imaging to classically describe the optic nerve sheath diameter, which has been associated with increased intracranial pressure from various causes like trauma, brain tumors, and idiopathic intracranial hypertension. Such studies are not sensitive to the optic nerve itself because measurements include the sheath, CSF, and optic nerve. Measurements of the optic nerve diameter have historically been difficult, due to problems in the methodology to be adopted, such as the differing appearance of the nerve sheath in the various MR imaging sequences and the width, which differs from anterior to posterior. With the use of new volumetric methods, thin-cut images, and the availability of fat-suppression sequences, such measurements can be accurately performed. Few articles in the literature have looked at the diameter of the optic nerve proper on MR imaging, especially in children, in whom observations are subjective and no normative data exist. Pathologic changes in the diam-

Received May 23, 2017; accepted after revision September 13.

From the Departments of Ophthalmology (C.E.A.-H., C.J.M.), Diagnostic Radiology (M.G.S., R.N.T., A.M.K., R.G.H.), and Pediatrics (S.R.S.), American University of Beirut Medical Center, Beirut, Lebanon.

Please address correspondence to Roula Hourani, MD, Department of Diagnostic Radiology, American University of Beirut Medical Center, Cairo St, Hamra, Beirut, Lebanon; PO Box 11-0236, Riad El Solh, Beirut, Lebanon; e-mail: rh64@aub.edu.lb

<http://dx.doi.org/10.3174/ajnr.A5456>

eter of the optic nerve itself are not uncommonly encountered in different disease entities affecting the pediatric population, including optic nerve hypoplasia or atrophy, Leber optic neuropathy, multiple sclerosis, and optic nerve enlargement, such as from gliomas in neurofibromatosis type 1.^{4,10,20-23} Measuring the optic nerve proper is essential to the diagnosis of such entities.

Our study aimed to report normative values for the optic nerve diameter on MR imaging in the pediatric population and examine its development across different age groups to generate a set of objective measurements for use by radiologists and ophthalmologists.

MATERIALS AND METHODS

Patient Selection

This was a retrospective review conducted at the Department of Diagnostic Radiology at the American University of Beirut Medical Center in Beirut, Beirut, Lebanon. The study was approved by the institutional review board, and informed consent was waived. We performed a thorough search on the institutional PACS for scans of patients younger than 18 years of age at the time of acquisition who underwent any MR imaging of the head and/or orbit with or without contrast enhancement between January 2010 and December 2015. Patients were divided into 5 age groups: younger than 6 months, 6 months to 2 years, 2–6 years, 6–12 years, and 12–18 years. We then reviewed patient charts and applied the following exclusion criteria: history of any brain or orbit tumor, enucleation of 1 eye, optic nerve lesions, enlargement or atrophy of the optic nerve, raised intracranial pressure (treated or not), and ischemia, hemorrhage, or atrophy along the optic pathway. We included patients who had indications for MR imaging other than optic nerve lesions, such as seizures and epilepsy, neck mass investigation, temporal bone abnormality, developmental

delay, recurrent headaches, and others. Scans with poor visualization of the optic nerve were excluded.

MR Imaging Measurements

All MR images were performed on the Ingenia 3T or 1.5T systems (Philips Healthcare, Best, the Netherlands). The brain and orbit MRIs were performed with a 16-channel head coil. The sequences analyzed consisted of 2-mm sections. A T1-weighted inversion recovery sequence in the axial and coronal plane was performed with the following parameters: TR range = 5000–7000 ms, TE range = 15–30 ms, TI = 400 ms, matrix size range = 168 × 100 to 212 × 130, FOV range = 180 × 180 mm to 230 × 230 mm, section thickness/spacing range = 2–0.3 to 2–0.5 mm, acquisition time = 5 minutes 16 seconds; and an orbit-dedicated STIR sequence in the axial and coronal planes was performed with the following parameters: TR range = 2240–2650 ms, TE range = 80–90 ms, TI = 200 ms, matrix size range = 256 × 195 to 320 × 255, FOV range = 200 × 200 mm to 250 × 250 mm, section thickness/spacing range = 2–0.3 mm to 3–0.3 mm, acquisition time = 2–3 minutes. The axial images were obtained parallel to the intraorbital portion of the optic nerve, and the coronal images were placed on the sagittal cuts perpendicular to the optic nerves.

Image analysis and measurements were performed by a trained cognitive neuroscientist (R.N.T.), a senior radiology resident (M.G.S.), and a neuroradiologist (R.G.H.) using OsiriX Imaging Software (<http://www.osirix-viewer.com>) on a high-resolution monitor. The measurements were obtained on axial and coronal sections at 3 and 7 mm posterior to the lamina cribrosa. Measurements at 3 mm were retrobulbar, and measurements at 7 mm were at the midaspect of the intraorbital segment of the optic nerve (Fig 1). These 2 loci were chosen to examine whether the midaspect is smaller than the retrobulbar portion of the optic nerve. For every patient, each eye was

treated individually. In some cases, on the axial or coronal cuts, 1 optic nerve was used for measurements, while the second one was not clearly delineated.

Statistical Analysis

All statistical analyses were performed with STATA 13 (StataCorp, College Station, Texas). The results were reported as mean ± SD. Interrater agreement was evaluated with intraclass correlation coefficients and corresponding 95% confidence intervals to ensure reliability and reproducibility of the results. After confirming agreement among the 3 raters,

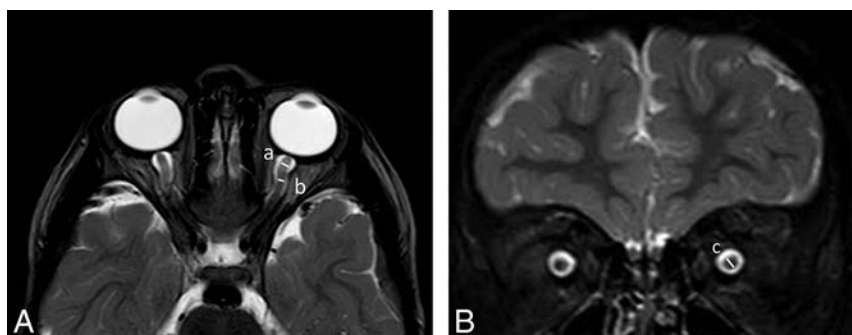


FIG 1. Axial (A) and coronal STIR (B) images of the orbits. An example of our measurement method. The optic nerve is measured without the nerve sheath, 3 (a) and 7 (b) mm posterior to the lamina cribrosa. It is also measured on the coronal plane (c) at the same 2 locations: retrobulbar and midaspect.

Table 1: Optic nerve diameter at each of the retrobulbar and midaspect locations on axial and coronal MRI sections

	Sex					Laterality				
	Male		Female		P Value	Right		Left		P Value
	No.	Mean (mm)	No.	Mean (mm)		No.	Mean (mm)	No.	Mean (mm)	
Axial										
Retrobulbar	203	2.22 ± 0.44	158	2.20 ± 0.41	.663	180	2.21 ± 0.43	181	2.22 ± 0.43	.925
Midaspect	176	1.53 ± 0.40	149	1.59 ± 0.43	.223	160	1.56 ± 0.43	165	1.56 ± 0.40	.923
Coronal										
Retrobulbar	182	2.28 ± 0.58	154	2.22 ± 0.40	.270	168	2.25 ± 0.50	168	2.26 ± 0.51	.820
Midaspect	184	1.73 ± 0.44	149	1.76 ± 0.42	.473	164	1.75 ± 0.42	169	1.74 ± 0.45	.892

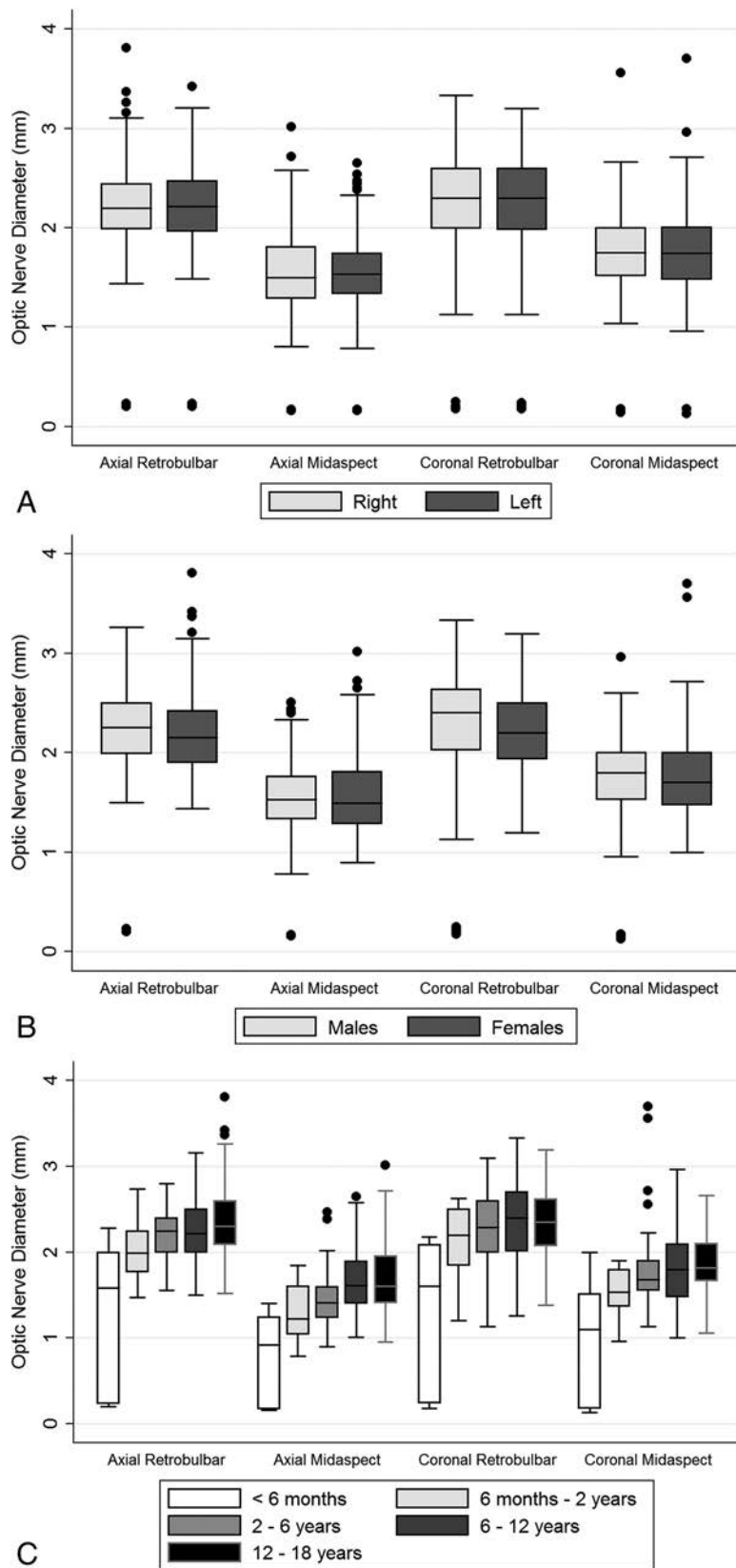


FIG 2. Optic nerve diameter measurements (millimeters) at each of the retrobulbar and midaspect locations on the axial and coronal MR imaging sections, according to eye laterality (A), sex (B), and age group (C).

we averaged the measurements. Data normality was assessed by the Shapiro-Wilk test for normality coupled with visual inspection of the data via histograms. Accordingly, differences between

up to 1.67 ± 0.36 mm for patients between 6 and 12 years of age and between 12 and 18 years of age and to 1.67 ± 0.40 mm between 12 and 18 years of age on the midaspect level.

the right and left eyes were evaluated using the paired Student *t* test or Wilcoxon signed rank test, and between-sex differences, with the unpaired *t* test or Mann-Whitney *U* test. ANOVA testing was performed to reveal between-group differences with a Šidák correction for multiple comparisons for more detailed results on confidence intervals and significances between each age group. Finally, measurement results were plotted versus age, and Pearson or Spearman correlation coefficients were calculated.

RESULTS

Two hundred eleven scans of patients were collected for measurement. The median age at MR imaging acquisition was 8.6 years (interquartile range, 3.9–13.3 years), and 94 (45%) patients were females. Interrater agreement was excellent, with an intraclass correlation coefficient of 0.842 (95% CI, 0.821–0.861; $P < .001$). The agreement between the readers for the patients younger than 6 months of age and children between 6 months and 2 years was good as well (intraclass correlation coefficient = 0.82; 95% CI, 0.579–0.931; $P < .001$; and intraclass correlation coefficient = 0.766; 95% CI, 0.693–0.823; $P < .001$, respectively).

Table 1 shows the optic nerve measurements on MR imaging at the retrobulbar and midaspect levels for each of the axial and coronal cuts. Optic nerve diameter measurements did not differ between the right and left eyes (Fig 2A) or between males and females (Fig 2B), regardless of the section and location of the measurement. However, the optic nerve significantly increased in diameter across age groups, which was also observed in all measurements (Fig 2C). At the axial cut, the mean diameter steadily increased with the age from 1.35 ± 0.82 mm among patients younger than 6 months up to 2.26 ± 0.38 mm and 2.35 ± 0.40 mm for patients between 6 and 12 years of age and between 12 and 18 years, respectively on the retrobulbar level (Table 2). Similarly, in the axial cuts, the mean diameter of the optic nerve increased with age from 0.73 ± 0.55 mm among patients younger than 6 months

Table 2: Optic nerve diameter measurements at each of the retrobulbar and midaspect locations on axial and coronal MRI sections

	Age Group										P Value ^a
	<6 mo		6 mo–2 yr		2–6 yr		6–12 yr		12–18 yr		
	No.	Mean (mm)	No.	Mean (mm)	No.	Mean (mm)	No.	Mean (mm)	No.	Mean (mm)	
Axial											
Retrobulbar	13	1.35 ± 0.82	44	2.03 ± 0.30	86	2.20 ± 0.30	109	2.26 ± 0.38	109	2.35 ± 0.40	<.001
Midaspect	9	0.73 ± 0.55	31	1.30 ± 0.33	73	1.46 ± 0.31	114	1.67 ± 0.36	98	1.67 ± 0.40	<.001
Coronal											
Retrobulbar	18	1.30 ± 0.83	29	2.08 ± 0.44	72	2.27 ± 0.41	113	2.37 ± 0.44	104	2.33 ± 0.39	<.001
Midaspect	18	0.99 ± 0.66	26	1.53 ± 0.27	69	1.79 ± 0.43	120	1.78 ± 0.38	100	1.87 ± 0.32	<.001

^a P value assessing the significance of the between-group comparisons using ANOVA.

Table 3: Two by 2 group comparisons of the optic nerve diameter measurements on different scans

	<6 mo	6 mo–2 yr	2–6 yr	6–12 yr
6 mo–2 yr				
Axial				
RB	.196	–	–	–
MA	.225	–	–	–
Coronal				
RB	.026 ^a	–	–	–
MA	.453	–	–	–
2–6 yr				
Axial				
RB	<.001 ^a	.035 ^a	–	–
MA	.010 ^a	.626	–	–
Coronal				
RB	<.001 ^a	.499	–	–
MA	<.001 ^a	.049 ^a	–	–
6–12 yr				
Axial				
RB	<.001 ^a	.003 ^a	.999	–
MA	<.001 ^a	<.001 ^a	.001 ^a	–
Coronal				
RB	<.001 ^a	.032 ^a	.870	–
MA	<.001 ^a	.007 ^a	.999	–
12–18 yr				
Axial				
RB	<.001 ^a	<.001 ^a	.085	.445
MA	<.001 ^a	<.001 ^a	.002 ^a	.999
Coronal				
RB	<.001 ^a	.094	.999	.999
MA	<.001 ^a	<.001 ^a	.127	.324

Note:—RB indicates retrobulbar; MA, midaspect.

^a P value significant at .05.

Significant between-group differences for all 4 measures were observed on 2 by 2 comparisons (Table 3). The results were then plotted in a measurement-versus-age comparison. The graphs show a steep increase in diameter in the first 2 years, after which the curve plateaus; this finding applied to both axial and coronal measurements and at the 2 loci, retrobulbar and midaspect. The most representative graph, obtained from midaspect measurements on the coronal cut plotted against age, is shown in Fig 3.

Most interestingly, there was a consistent difference in optic nerve diameters between the midaspect and retrobulbar portions, which was observed on both axial and coronal images and in most age groups.

DISCUSSION

In this study, we report normative values of optic nerve diameter measured on MR imaging in children from birth to 18 years of age, dividing them into 5 age groups: 0–6 months, 6 months–2 years, 2–6 years, 6–12 years, and 12–18 years. Our results showed

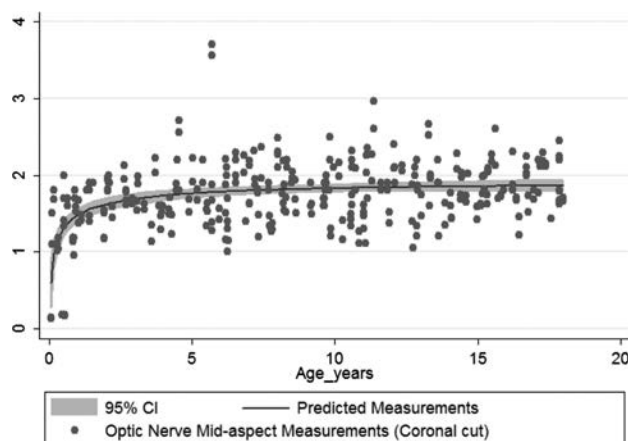


FIG 3. Optic nerve midaspect diameter growth with age on a coronal cut.

significant between-group differences in measurements, with a rapid increase in optic nerve diameter demonstrated during the first 2 years of life, followed by a slower increase to the 6 years of age with no significant change later. This was independent of sex or eye laterality.

Despite the technical challenges in the pediatric population, MR imaging was reliable in quantitatively assessing the size of the optic nerve proper. Multiple other studies have confirmed this finding with MR imaging for the diagnosis and early detection of optic nerve hypoplasia in children.^{18,22,24–27} However, there was no standardized method to obtain these measurements; thus, cross-study comparisons could not be performed accurately. Also, while there are reports on MR imaging measurements in healthy children, they focused on the optic nerve sheath complex as a whole and not the optic nerve itself.^{19,28} Therefore, there is a need to establish a standardized method for the measurement of the optic nerve on MR imaging in the pediatric population. These patients are at risk of multiple disease entities affecting the optic nerve,²⁹ such as optic nerve hypoplasia or atrophy, optic neuritis,^{30,31} optic neuropathies,³² and other associated optic nerve pathology with failure to thrive.³³ Objective assessment by MR imaging will aid in earlier and more accurate diagnoses of these various disorders in this vulnerable population.

Several studies have assessed the optic nerve sheath using various imaging modalities. This was mainly done to establish a normative data base in adults,^{5,10–14,27,28} or to use the optic nerve sheath complex as a surrogate to diagnose increased intracranial pressure. The latter outcome was studied both in children and using sonography, CT, or MR imaging and in different clinical

settings.^{19,34–36} In fact, MR imaging proved to be superior to high-resolution ultrasonography and CT in demonstrating optic nerve measurements without the risks of exposure to ionizing radiation.^{11,27,37}

Our results show that most of the optic nerve growth occurs in the first 2 years of life, which is in accordance with other published data regarding the early development of the optic nerve. In fact, the optic nerve increases in size in utero to reach normal neonate size at 36 weeks of gestation³⁸; then, it continues to grow up to 2 years of age and less rapidly thereafter according to histologic studies.^{39,40} Ophthalmologists and radiologists ought to be aware of this finding while interpreting MR imaging scans in various clinical scenarios in infants with early signs of cerebral palsy, developmental delays, delayed visual maturation, and poor visual behavior/fixation. Hence, it is important to obtain normative measurements of the optic nerve diameter in the pediatric population; these measurements are very sensitive to age, especially in the first 2 years of life. Our data are also in agreement with other literature in that there was no laterality or sex differences in optic nerve thickness on MR imaging.⁴¹ The midaspect portion of the optic nerve would be expected to be thinner than the retrobulbar portion on both axial and coronal cuts, consistent with our reported results. This is a consequence of the optic nerve itself becoming more organized as it acquires its sheath traveling posteriorly through the narrow bony orbit.^{1,2}

There are some limitations to this study. The relatively small sample size, particularly in the group of subjects younger than 2 years of age, could potentially affect the measurements. Moreover, these patients often require the administration of sedatives or general anesthesia, which may deviate their eyes from the primary position and may induce motion artifacts, which could explain the differences in measurement seen with changes in eye position and axial-versus-coronal cuts. The coronal cuts of the orbits were not obtained perpendicular to the axis of each optic nerve separately; this feature partly explains the difference in the measurements between the axial and coronal sections. Last, a prospective study with thorough general medical, neurologic, and ophthalmologic assessment of pediatric subjects before undergoing a standardized MR imaging examination of the orbit using the measurement criteria presented in this article is needed to confirm our findings.

CONCLUSIONS

We report normative values of the optic nerve diameter measured on MR imaging in children from birth to 18 years of age. A rapid increase in optic nerve diameter was demonstrated during the first 2 years of life followed by a slower increase. Our measurements can give radiologists and neuroscientists a reliable reference to diagnose optic nerve abnormalities in children.

REFERENCES

1. Duke-Elder S. *System of Ophthalmology: The Anatomy of the Visual System*. London: H. Kimpton; 1961
2. Rimmer S, Keating C, Chou T, et al. **Growth of the human optic disk and nerve during gestation, childhood, and early adulthood.** *Am J Ophthalmol* 1993;116:748–53 CrossRef Medline
3. Selhorst JB, Chen Y. **The optic nerve.** *Semin Neurol* 2009;29:29–35 CrossRef Medline
4. Hayreh SS. **Structure of the optic nerve.** In: Hayreh SS. *Ischemic Optic Neuropathies*. Berlin: Springer-Verlag; 2011
5. Atta H. **Imaging of the optic nerve with standardised echography.** *Eye* 1988;2:358–66 CrossRef Medline
6. Smith MM, Strottmann JM. **Imaging of the optic nerve and visual pathways.** *Semin Ultrasound CT MR* 2001;22:473–87 CrossRef Medline
7. Chawla B, Sharma S, Sen S, et al. **Correlation between clinical features, magnetic resonance imaging, and histopathologic findings in retinoblastoma: a prospective study.** *Ophthalmology* 2012; 119:850–56 CrossRef Medline
8. Schueler A, Hosten N, Bechrakis N, et al. **High resolution magnetic resonance imaging of retinoblastoma.** *Br J Ophthalmol* 2003;87: 330–35 CrossRef Medline
9. Sirin S, Schlamann M, Metz KA, et al. **High-resolution MRI using orbit surface coils for the evaluation of metastatic risk factors in 143 children with retinoblastoma, part 1: MRI vs. histopathology.** *Neuroradiology* 2015;57:805–14 CrossRef Medline
10. Parravano JG, Toledo A, Kucharczyk W. **Dimensions of the optic nerves, chiasm, and tracts: MR quantitative comparison between patients with optic atrophy and normals.** *J Comp Assis Tomogr* 1993; 17:688–90 CrossRef Medline
11. Hesselink J, Karampekios S. **Normal computed tomography and magnetic resonance imaging anatomy of the globe, orbit, and visual pathways.** *Neuroimaging Clin N Am* 1996;6:15–27 Medline
12. Ozgen A, Aydingöz U. **Normative measurements of orbital structures using MRI.** *J Comp Assis Tomogr* 2000;24:493–96 Medline
13. Ozgen A, Ariyurek M. **Normative measurements of orbital structures using CT.** *AJR Am J Roentgenol* 1998;170:1093–96 CrossRef Medline
14. Goeres P, Zeiler FA, Unger B, et al. **Ultrasound assessment of optic nerve sheath diameter in healthy volunteers.** *J Crit Care* 2016;31: 168–71 CrossRef Medline
15. Ossoinig K, Cennamo G, Frazier-Byrne S. **Echographic differential diagnosis of optic-nerve lesions.** In: Thijssen JM, Verbeek AM, eds. *Ultrasonography in Ophthalmology. Documenta Ophthalmologica Proceedings Series*. Vol 29. Dordrech: Springer; 1981
16. Miller DH, Newton MR, Van der Poel J, et al. **Magnetic resonance imaging of the optic nerve in optic neuritis.** *Neurology* 1988;38: 175–75 CrossRef
17. Wilejto M, Shroff M, Buncic J, et al. **The clinical features, MRI findings, and outcome of optic neuritis in children.** *Neurology* 2006;67: 258–62 CrossRef Medline
18. Hickman SJ, Toosy AT, Jones SJ, et al. **A serial MRI study following optic nerve mean area in acute optic neuritis.** *Brain* 2004;127:2498–505 CrossRef Medline
19. Shofty B, Ben-Sira L, Constantini S, et al. **Optic nerve sheath diameter on MR imaging: establishment of norms and comparison of pediatric patients with idiopathic intracranial hypertension with healthy controls.** *AJNR Am J Neuroradiol* 2012;33:366–69 CrossRef Medline
20. Trip SA, Schlottmann PG, Jones SJ, et al. **Optic nerve atrophy and retinal nerve fibre layer thinning following optic neuritis: evidence that axonal loss is a substrate of MRI-detected atrophy.** *Neuroimage* 2006;31:286–93 CrossRef Medline
21. Skarf B, Hoyt CS. **Optic nerve hypoplasia in children: association with anomalies of the endocrine and CNS.** *Arch Ophthalmol* 1984; 102:62–67 CrossRef Medline
22. Hellström A, Wiklund L-M, Svensson E. **Diagnostic value of magnetic resonance imaging and planimetric measurement of optic disc size in confirming optic nerve hypoplasia.** *J AAPOS* 1999;3: 104–08 CrossRef Medline
23. Avery RA, Mansoor A, Idrees R, et al. **Optic pathway glioma volume predicts retinal axon degeneration in neurofibromatosis type 1.** *Neurology*. 2016;87:2403–07 CrossRef Medline
24. Lenhart PD, Desai NK, Bruce BB, et al. **The role of magnetic resonance imaging in diagnosing optic nerve hypoplasia.** *Am J Ophthalmol* 2014;158:1164–71.e2 CrossRef Medline
25. Yiannakas MC, Wheeler-Kingshott CA, Berry AM, et al. **A method**

- for measuring the cross sectional area of the anterior portion of the optic nerve in vivo using a fast 3D MRI sequence. *J Magn Reson Imaging* 2010;31:1486–91 CrossRef Medline
26. Kalantari H, Jaiswal R, Bruck I, et al. **Correlation of optic nerve sheath diameter measurements by computed tomography and magnetic resonance imaging.** *Am J Emerg Med* 2013;31:1595–97 CrossRef Medline
 27. Steinborn M, Fiegler J, Kraus V, et al. **High-resolution ultrasound and magnetic resonance imaging of the optic nerve and the optic nerve sheath: anatomic correlation and clinical importance.** *Ultraschall Med* 2011;32:608–13 CrossRef Medline
 28. Steinborn M, Friedmann M, Hahn H, et al. **Normal values for transbulbar sonography and magnetic resonance imaging of the optic nerve sheath diameter (ONSD) in children and adolescents.** *Ultraschall Med* 2015;36:54–58 CrossRef Medline
 29. Taylor D. **Developmental abnormalities of the optic nerve and chiasm.** *Eye* 2007;21:1271–84 CrossRef Medline
 30. Manogaran P, Vavasour IM, Lange AP, et al. **Quantifying visual pathway axonal and myelin loss in multiple sclerosis and neuromyelitis optica.** *Neuroimage Clin* 2016;11:743–50 CrossRef Medline
 31. Buch D, Savatovsky J, Gout O, et al. **Combined brain and anterior visual pathways' MRIs assist in early identification of neuromyelitis optica spectrum disorder at onset of optic neuritis.** *Acta Neurologica Belg* 2017;117:67–74 CrossRef Medline
 32. Bansal NK, Hagiwara M, Borja MJ, et al. **Influence of clinical history on MRI interpretation of optic neuropathy.** *Heliyon* 2016;2:e00162 CrossRef Medline
 33. Birkebæk NH, Patel L, Wright NB, et al. **Optic nerve size evaluated by magnetic resonance imaging in children with optic nerve hypoplasia, multiple pituitary hormone deficiency, isolated growth hormone deficiency, and idiopathic short stature.** *J Pediatr* 2004;145:536–41 CrossRef Medline
 34. Geeraerts T. **Noninvasive surrogates of intracranial pressure: another piece added with magnetic resonance imaging of the cerebrospinal fluid thickness surrounding the optic nerve.** *Crit Care* 2013;17:187 CrossRef Medline
 35. Geeraerts T, Newcombe VF, Coles JP, et al. **Use of T2-weighted magnetic resonance imaging of the optic nerve sheath to detect raised intracranial pressure.** *Crit Care* 2008;12:R114 CrossRef Medline
 36. Le A, Hoehn ME, Smith ME, et al. **Bedside sonographic measurement of optic nerve sheath diameter as a predictor of increased intracranial pressure in children.** *Ann Emerg Med* 2009;53:785–91 CrossRef Medline
 37. Giger-Tobler C, Eisenack J, Holzmann D, et al. **Measurement of optic nerve sheath diameter: differences between methods? A pilot study.** *Klin Monbl Augenheilkd* 2015;232:467–70 CrossRef Medline
 38. Haratz K, Viñals F, Lev D, et al. **Fetal optic nerve sheath measurement as a non-invasive tool for assessment of increased intracranial pressure.** *Ultrasound Obstet Gynecol* 2011;38:646–51 CrossRef Medline
 39. Dolman CL, McCormick AQ, Drance SM. **Aging of the optic nerve.** *Arch Ophthalmol* 1980;98:2053–58 CrossRef Medline
 40. Magoon EH, Robb RM. **Development of myelin in human optic nerve and tract: a light and electron microscopic study.** *Arch Ophthalmol* 1981;99:655–59 CrossRef Medline
 41. Oyama J, Mori K, Imamura M, et al. **Size of the intracranial optic nerve and optic tract in neonates at term-equivalent age at magnetic resonance imaging.** *Pediatr Radiol* 2016;46:527–33 CrossRef Medline

Measuring Cerebral and Cerebellar Glutathione in Children Using ^1H MEGA-PRESS MRS

 F. Raschke,  R. Noeske,  R.A. Dineen, and  D.P. Auer



ABSTRACT

BACKGROUND AND PURPOSE: Glutathione is an important antioxidant in the human brain and therefore of interest in neurodegenerative disorders. The purpose of this study was to investigate the feasibility of measuring glutathione in healthy nonsedated children by using the ^1H Mescher-Garwood point-resolved spectroscopy (MEGA-PRESS) sequence at 3T and to compare glutathione levels between the medial parietal gray matter and the cerebellum.

MATERIALS AND METHODS: Glutathione was measured using MEGA-PRESS MRS (TR = 1.8 seconds, TE = 131 ms) in the parietal gray matter ($35 \times 25 \times 20 \text{ mm}^3$) of 6 healthy children (10.0 ± 2.4 years of age; range, 7–14 years; 3 males) and in the cerebellum of 11 healthy children (12.0 ± 2.7 years of age; range, 7–16 years; 6 males). A postprocessing pipeline was developed to account for frequency and phase variations in the edited ON and nonedited OFF spectra. Metabolites were quantified with LCModel and reported both as ratios and water-scaled values. Glutathione was quantified in the ON-OFF spectra, whereas total NAA, total Cho, total Cr, mIns, Glx, and taurine were quantified in the OFF spectra.

RESULTS: We found significantly higher glutathione, total Cho, total Cr, mIns, and taurine in the cerebellum ($P < .01$). Glx and total NAA were significantly higher in the parietal gray matter ($P < .01$). There was no significant difference in glutathione/total Cr ($P = .93$) between parietal gray matter and cerebellum.

CONCLUSIONS: We demonstrated that glutathione measurement in nonsedated children is feasible. We found significantly higher glutathione in the cerebellum compared with the parietal gray matter. Metabolite differences between the parietal gray matter and cerebellum agree with published MRS data in adults.

ABBREVIATIONS: GSH = glutathione; MEGA-PRESS = Mescher-Garwood point-resolved spectroscopy; PGM = parietal gray matter; Tau = taurine; t- = total

Glutathione (GSH) is an important antioxidant in the human brain^{1,2} and has been shown to be altered in a number of pathologies.^{3–7} Measuring GSH is of interest in neurodegenerative

disorders⁸ and may be a potential mechanistic biomarker for oxidative stress–related diseases and the efficacy of antioxidative treatments. Our specific interest is the quantification of GSH in the brains of children affected by neurodegenerative diseases such as ataxia telangiectasia, requiring a robust method to measure GSH levels in nonsedated children.

GSH can, in principle, be measured *in vivo* with ^1H -MRS. However, due to the low concentration of GSH in the healthy human brain and in particular its overlap with higher concentration metabolites, quantification of GSH at 3T with conventional MRS sequences is controversial.^{9–11} Spectral editing allows the removal of overlapping resonances for a direct and robust quantification of GSH.^{12–14} While spectral editing can be used to specifically measure GSH, it is more susceptible to subject motion than conventional single-voxel MRS sequences due to longer scan times and because spectral editing is a subtraction technique that relies on consistent data acquisition.

Few studies have reported *in vivo* GSH values in healthy children,^{15,16} and, to our knowledge, there is no study that specifically

Received June 22, 2017; accepted after revision September 13.

From the National Center for Tumor Diseases (F.R.), Partner Site Dresden, Dresden, Germany; German Cancer Research Center (F.R.), Heidelberg, Germany; Medical Faculty and University Hospital Carl Gustav Carus (F.R.), Technische Universität Dresden, Dresden, Germany; and Helmholtz Association/Helmholtz Zentrum Dresden Rossendorf (F.R.), Dresden, Germany; GE Healthcare (R.N.), Applied Science Lab Europe, Berlin, Germany; Sir Peter Mansfield Imaging Centre (R.A.D., D.P.A.), University of Nottingham, Nottingham, UK; Radiological Sciences, (R.A.D., D.P.A.), Division of Clinical Neuroscience, School of Medicine, University of Nottingham, Nottingham, UK; and National Institute for Health Research (R.A.D., D.P.A.), Nottingham Biomedical Research Centre, Nottingham, UK.

F.R. and the cost of the pediatric MRI scans were funded by the A-T Children's Project and Action for A-T.

Please address correspondence to: Rob Dineen, PhD, Radiological Sciences, University of Nottingham, Room B1435, Queen's Medical Centre, Nottingham, NG7 2UH, United Kingdom; e-mail: rob.dineen@nottingham.ac.uk

 Indicates article with supplemental on-line appendix.

 Indicates article with supplemental on-line photos.

<http://dx.doi.org/10.3174/ajnr.A5457>

measured GSH in children using spectral editing techniques or that reported GSH in the cerebellum. Therefore, the goal of this study was to investigate the feasibility of measuring GSH in healthy nonsedated children with the Mescher-Garwood point-resolved spectroscopy (MEGA-PRESS)^{13,17} sequence and to compare GSH levels obtained in the medial parietal gray matter (PGM) with those measured in the cerebellum. To minimize subtraction errors caused by phase and frequency variations, we adapted a MEGA-PRESS postprocessing technique published by An et al¹⁷ and modified it to work with our data.

MATERIALS AND METHODS

Subjects

Healthy children were recruited as part of an ongoing study, approved by the UK National Research Ethics Service East Midlands–Derby Committee (Reference 14/EM/1175). Informed consent was obtained from parents or guardians of participants. MRS data in the PGM were acquired in 6 children (10.0 ± 2.4 years of age; range, 7–14 years; 3 males). MR spectroscopic data in the cerebellum were acquired in 11 children (12.0 ± 2.7 years of age; range, 7–16 years; 6 males). There was no significant difference in age between the 2 groups (t test, $P = .14$). Structural MRI was checked by a neuroradiologist (R.A.D.) to ensure that children were neuroradiologically healthy.

Data Acquisition

Data were acquired on a 3T MR scanner (Discovery MR750; GE Healthcare, Milwaukee, Wisconsin) equipped with a 32-channel head coil, without sedation. In addition to standard pediatric MRI preparation, younger participants were shown an animation to help prepare them for the MRI,¹⁸ and participants could watch videos on an MRI-compatible monitor during the scan to improve tolerance. The MRI protocol included a 3D fast-spoiled gradient recalled T1-weighted structural MRI with 1-mm isotropic resolution for MRS planning (TR = 8.15 ms, TE = 3.172 ms, TI = 900 ms, FOV = $256 \times 256 \times 156$ mm). Single-voxel MEGA-PRESS GSH editing was performed using TR = 2 seconds, TE = 131 ms, and 128 ON and 128 OFF acquisitions. Spectral editing was achieved with sinc-weighted Gaussian pulses with a pulse length of 20 ms (bandwidth, 64 Hz) applied at 7.5 ppm (OFF) and 4.54 ppm (ON) for editing GSH.^{13,17} A nonedited, water-unsuppressed reference scan of 16 averages was acquired at identical acquisition parameters. MRS voxel sizes were $35 \times 25 \times 20$ mm in the PGM and $50 \times 22 \times 22$ mm in the cerebellum. Typical voxel locations are illustrated in Fig 1. Total acquisition time for MEGA-PRESS MRS was 9 minutes 30 seconds.

MRS Processing

MEGA-PRESS data were processed off-line with Matlab (MathWorks, Natick, Massachusetts). The workflow steps A–H are illustrated in On-line Fig 1. The phase angles between the 32 coil elements were calculated from the average unsuppressed water signal (A). All ON and OFF spectra were subsequently phased using the water phase angles and coil-combined by using the maximum peak height of the unsuppressed water signal as weighting factors (B). The resulting coil-combined 128 ON and 128 OFF spectra were potentially out of phase relative to each other due to

subject motion and frequency drift. To correct for this, we phased individual ON and OFF spectra by maximizing the correlation of the NAA peak between the real and absolute part of the spectrum in the range of 1.87 and 2.21 ppm (C). Next, a reference ON spectrum for phase and frequency correction was created, like that described by An et al¹⁷ by pair-wise aligning the 128 ON spectra in the spectral range of 1.3 and 3.3 ppm and iterative pair-wise averaging of the spectra with the smallest root mean square error (D). All 128 ON and 128 OFF spectra were subsequently aligned to this ON reference spectrum by time domain phase and frequency correction using the `fminsearch` function (<https://de.mathworks.com/help/matlab/ref/fminsearch.html>) (E) in Matlab. For the alignment, the correlation coefficient of the real part of the NAA peak (1.87–2.21 ppm) between the ON reference spectrum and the individual ON and OFF spectra was maximized. The 128 aligned ON and OFF spectra were then averaged to 1 ON and 1 OFF spectrum each (F). Individual poor-quality ON and OFF spectra were detected by calculating the correlation coefficient of the NAA peak (1.87–2.21 ppm) between the 128 ON/OFF spectra and the averaged ON/OFF spectrum, respectively (G). In our data, a correlation coefficient threshold of 0.8 (1 indicating perfect correlation) was used to pair-wise exclude individual ON and OFF spectra. Finally, the new ON and OFF average spectra were recalculated (H) and subtracted to obtain the final edited ON-OFF spectrum.

Metabolite Quantification

Unedited MEGA-PRESS OFF spectra were analyzed between 4 and 0.2 ppm with LCModel (Version 6.3-1H; <http://www.lcmodel.com/lcmodel.shtml>)¹⁹ using a basis set simulated with TARQUIN (<http://tarquin.sourceforge.net/>).²⁰ The OFF spectra were used to quantify total NAA (tNAA = NAA + *N*-acetyl aspartylglutamate), total Creatine (tCr = Cr + phosphocreatine), total Choline (tCho = glycerophosphorylcholine + phosphorylcholine), mIns, Glx, and Taurine (Tau). The edited ON-OFF MEGA-PRESS spectra were analyzed in the range of 3.6–0.2 ppm with LCModel, using a measured basis set from GSH and NAA solutions. LCModel parameters for the ON-OFF analysis are given in the On-line Appendix.

Metabolite values are reported as ratios to tCr and as water-scaled values using the unsuppressed OFF water signal. For the latter, corresponding structural T1WI was segmented via SPM software (<http://www.fil.ion.ucl.ac.uk/spm/software/spm12>) into gray matter, white matter, and CSF and aligned with the MRS volume with in-house software. Water-scaled metabolite values were corrected for CSF contamination by dividing them by $1 - \text{CSF}\%$. Because the complex anatomic structure in the cerebellum would not allow an accurate separation of gray and white matter, we did not take their differences in water content into account. T1 and T2 correction was not performed; thus, water-scaled and CSF-corrected metabolite values are reported as institutional units.

A 2-sample t test assuming unequal variances was used to determine significant differences in metabolite values and ratios between the PGM and the cerebellum.

RESULTS

The proposed GSH processing gave robust results in all spectra. On-line Fig 2 shows the edited ON-OFF spectra and correspond-

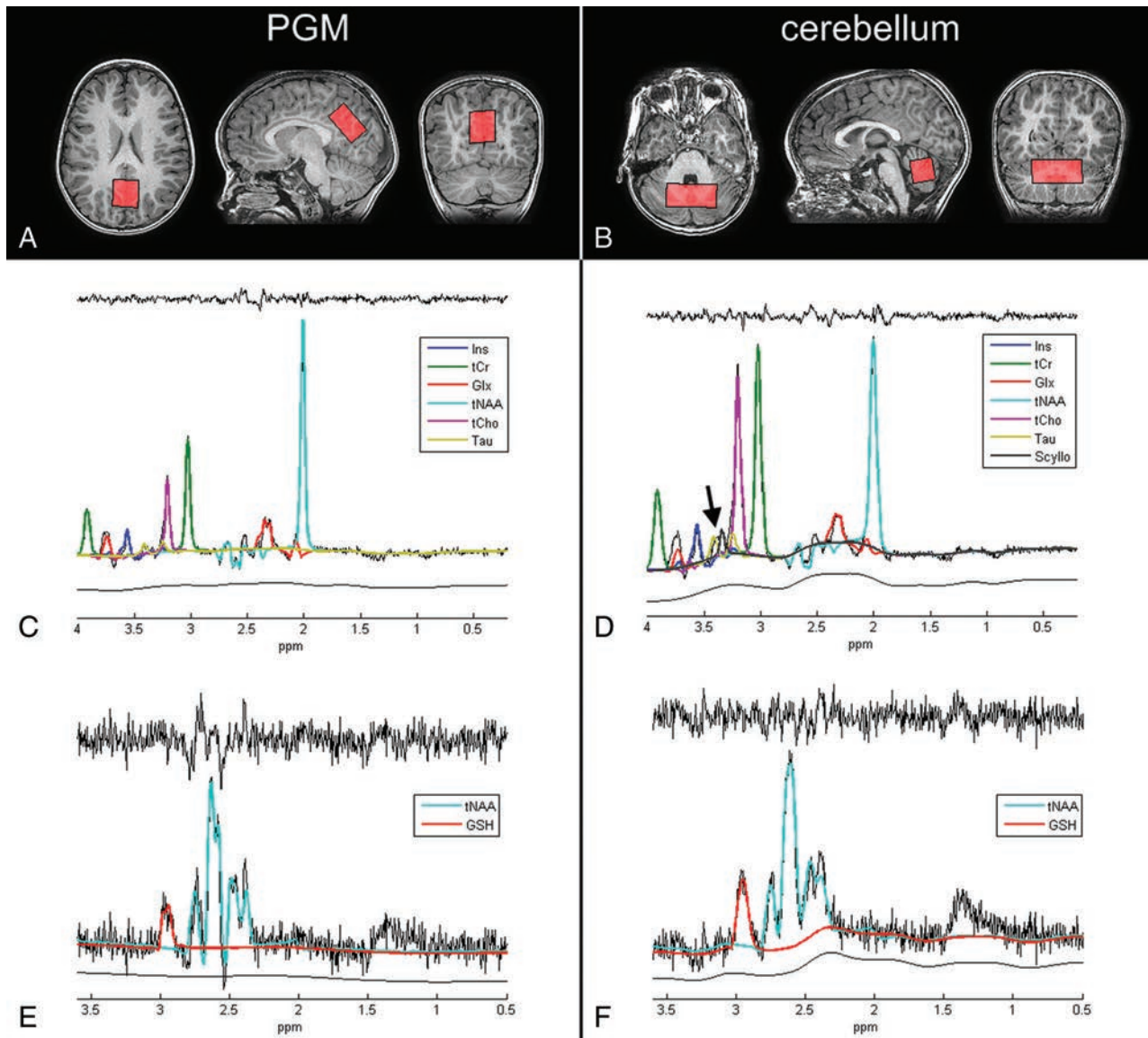


FIG 1. Examples of the MRS voxel placement in the PGM (A) and cerebellum (B) in two 7-year-old children. Corresponding OFF (C and D) and ON-OFF (E and F) spectra are shown below. Individual metabolite spectra fitted by LCModel are highlighted in different colors. D, The arrow highlights visible resonances that are particularly large in the cerebellum and likely belong to taurine and scyllo-inositol. Residuals of the fits (black, upper row) and estimated LCModel baselines (black, lower row) are shown for each spectrum.

ing GSH fits determined by LCModel for all subjects. An example in On-line Fig 1 illustrates the correction for phase and frequency shifts in a PGM spectrum acquired in an 11-year-old girl.

Figure 1 shows sample spectra from the PGM and cerebellum and corresponding metabolite fits for two 7-year-old children. The OFF spectra from the cerebellum show visible resonances between 3.3 and 3.5 ppm (see the arrow in Fig 1D). LCModel assigned these resonances to taurine (around 3.4 ppm) and scyllo-inositol (around 3.34 ppm), but the fitted scyllo-inositol signals were too small for reliable quantification in both the cerebellum (Cramer-Rao lower bounds, $21\% \pm 22\%$) and PGM (Cramer-Rao lower bounds, $33\% \pm 27\%$). We therefore only report the apparent taurine signal for the cerebellum (Cramer-Rao lower bounds, $9\% \pm 1\%$) and PGM (Cramer-Rao lower bounds, $14\% \pm 2\%$). However, the combined sum of Tau + scyllo-inositol showed the same trends as taurine using either water scaling or ratios (results not shown).

We found significantly higher GSH in the cerebellum compared with the PGM ($P < .01$). Additionally, we found higher tCho ($P < .01$), tCr ($P < .01$), mIns ($P < .01$), and Tau ($P < .01$) in the cerebellum, whereas NAA ($P < .01$) and Glx ($P < .01$) were significantly higher in the PGM. Boxplots are shown in Fig 2.

Figure 3 shows the results of the metabolite ratios between the PGM and cerebellum. There was no significant difference in GSH/tCr ($P = .93$). However, tNAA/tCr ($P < .01$), tNAA/tCho ($P < .01$), mIns/tCr ($P = .01$), and Glx/tCr ($P < .01$) were significantly higher in the PGM. Both tCho/tCr ($P < .01$) and Tau/tCr ($P = .02$) were lower in the PGM.

DISCUSSION

We demonstrate reliable detection of glutathione levels in the parietal gray matter and cerebellum of nonsedated children using a dedicated proton MRS protocol for acquisition and postprocessing. Postpro-

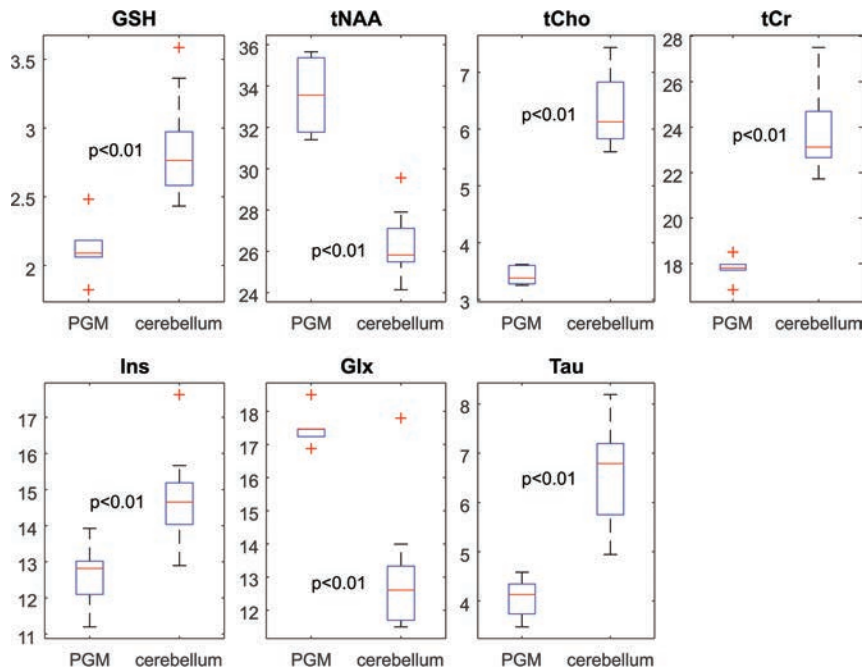


FIG 2. Boxplots showing the water-scaled metabolite values in institutional units in the PGM and cerebellum.

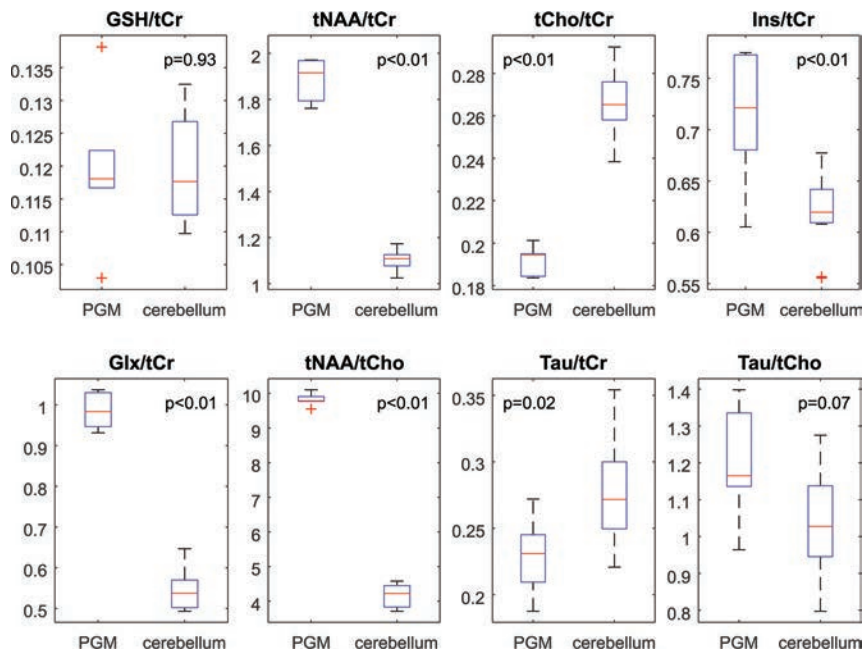


FIG 3. Boxplots showing the metabolite ratios in the PGM and cerebellum.

cessing of GSH MEGA-PRESS MRS was challenging, mainly because the editing pulse at 4.54 ppm also eliminates most of the residual water signal in the ON spectrum; this feature makes it difficult to precisely match its phase to the OFF spectrum. This difficulty can lead to subtraction artifacts, which are most often visible around the 2-ppm area and could severely bias GSH quantification due to residual overlapping Cr signal at 3 ppm. We therefore adapted and modified a previously published postprocessing approach.¹⁷ Whereas An et al¹⁷ focused on the complex spectral values from the Cr, Cho, and NAA peaks for alignment of individual spectra, our processing was simplified by focusing the alignment on the real part of the NAA and

omitting zero and first-order baseline adjustments. This was performed to reduce the number of fitted parameters for a more robust parameter determination in our lower SNR spectra caused by a smaller voxel size.

To the best of our knowledge, this is the first study to compare GSH levels in the cerebrum with those found in the cerebellum in children. Few studies compared GSH levels between the cerebellum and the cerebrum in adults. In agreement with our findings, Emir et al²¹ found higher GSH and tCr in the vermis compared with the occipital cortex and posterior cingulate in healthy adults using a short-echo STEAM sequence at 7T, albeit without T1, T2, and CSF correction. An extensive postmortem study in humans by Tong et al²² showed no significant difference in GSH between the occipital and cerebellar cortices in the 1- to 18-year age group. A histologic study in mice by Kang et al²³ revealed slightly lower GSH in the cerebellum compared with the cortex.

Previous studies reported higher Cho and Cr levels in the cerebellum compared with the cerebrum in healthy adults,^{24,25} in agreement with the results in our cohort of children, whereas an MR spectroscopic imaging study by Lecocq et al²⁶ found only reduced NAA in the cerebellum. Looking at metabolite ratios, several studies found lower tNAA/tCr in the cerebellum compared with the cerebrum in children²⁷ and adults,²⁸⁻³⁰ in agreement with our findings. Additionally, Goryawala et al³¹ showed lower Glx/tCr in the cerebellum in adults, in agreement with our results in children. Another noteworthy finding in this study was higher apparent Tau/tCr in the cerebellum compared with the PGM. Taurine is particularly high in infants and children in the cerebellar cortex.^{32,33} Additionally, elevated taurine is characteristic of medulloblastomas,³⁴ mainly originating in the cerebellum of children.

A limitation of this study is the relatively small sample size and the use of different subjects to scan the PGM and the cerebellum. Scanning the PGM and cerebellum in each subject would have allowed a pair-wise statistical analysis and likely reduced variability. We were, however, limited by time constraints in the MRI protocol due to the long acquisition time of GSH MEGA-PRESS MRS. Additionally, the MRS voxel in the cerebellum was relatively large, to ensure high-enough SNR for GSH quantification, thus having a relatively heterogeneous tissue composition, including the cerebellar gray matter (vermis and cortex) and the underlying cerebellar white matter.

CONCLUSIONS

We demonstrated that GSH measurement in nonsedated children is feasible. We found higher GSH in the cerebellum compared with the PGM. Differences in the other metabolites agree with published MRS data in adults; this finding suggests no major metabolic maturation effect from 7 years of age and older in our dataset.

Disclosures: Felix Raschke—RELATED: Grant: A-T Children's Project and Action for A-T, Comments: This work was supported by a research grant awarded by the 2 named charities*; UNRELATED: Support for Travel to Meetings for the Study or Other Purposes: Guarantors of Brain, Comments: travel grant to support travel to the International Society for Magnetic Resonance in Medicine meeting in 2015. Ralph Noeske—UNRELATED: Employment: GE Healthcare. Robert A. Dineen—RELATED: Grant: A-T Children's Project and Action for A-T.* Dorothee P. Auer—RELATED: Grant: A-T Children's Project and Action for A-T*; UNRELATED: Grants/Grants Pending: UK charities, UK research councils, National Institute for Health Research, UK funding.* *Money paid to the institution.

REFERENCES

1. Dringen R. **Metabolism and functions of glutathione in brain.** *Prog Neurobiol* 2000;62:649–71 CrossRef Medline
2. Mazzetti AP, Fiorile MC, Primavera A, et al. **Glutathione transferases and neurodegenerative diseases.** *Neurochem Int* 2015;82:10–18 CrossRef Medline
3. An L, Dani KA, Shen J, et al; Natural History of Stroke Investigators. **Pilot results of in vivo brain glutathione measurements in stroke patients.** *J Cereb Blood Flow Metab* 2012;32:2118–21 CrossRef Medline
4. Choi IY, Lee SP, Denney DR, et al. **Lower levels of glutathione in the brains of secondary progressive multiple sclerosis patients measured by 1H magnetic resonance chemical shift imaging at 3 T.** *Mult Scler* 2011;17:289–96 CrossRef Medline
5. Do KQ, Trabesinger AH, Kirsten-Krüger M, et al. **Schizophrenia: glutathione deficit in cerebrospinal fluid and prefrontal cortex in vivo.** *Eur J Neurosci* 2000;12:3721–28 CrossRef Medline
6. Matsuzawa D, Obata T, Shirayama Y, et al. **Negative correlation between brain glutathione level and negative symptoms in schizophrenia: a 3T 1H-MRS study.** *PLoS One* 2008;3:e1944 CrossRef Medline
7. Srinivasan R, Ratiney KH, Hammond-Rosenbluth KE, et al. **MR spectroscopic imaging of glutathione in the white and gray matter at 7 T with an application to multiple sclerosis.** *Magn Reson Imaging* 2010;28:163–70 CrossRef Medline
8. Aoyama K, Nakaki T. **Impaired glutathione synthesis in neurodegeneration.** *Int J Mol Sci* 2013;14:21021–44 CrossRef Medline
9. Sanaei Nezhad F, Anton A, Parkes LM, et al. **Quantification of glutathione in the human brain by MR spectroscopy at 3 Tesla: comparison of PRESS and MEGA-PRESS.** *Magn Reson Med* 2017;78:1257–66 CrossRef Medline
10. Oz G, Tkáč I. **Short-echo, single-shot, full-intensity proton magnetic resonance spectroscopy for neurochemical profiling at 4 T: validation in the cerebellum and brainstem.** *Magn Reson Med* 2011;65:901–10 CrossRef Medline
11. Mekle R, Mlynárik V, Gambarota G, et al. **MR spectroscopy of the human brain with enhanced signal intensity at ultrashort echo times on a clinical platform at 3T and 7T.** *Magn Reson Med* 2009;61:1279–85 CrossRef Medline
12. Mescher M, Merkle H, Kirsch J, et al. **Simultaneous in vivo spectral editing and water suppression.** *NMR Biomed* 1998;11:266–72 Medline
13. Terpstra M, Henry PG, Gruetter R. **Measurement of reduced glutathione (GSH) in human brain using LCModel analysis of difference-edited spectra.** *Magn Reson Med* 2003;50:19–23 CrossRef Medline
14. Trabesinger AH, Weber OH, Duc CO, et al. **Detection of glutathione in the human brain in vivo by means of double quantum coherence filtering.** *Magn Reson Med* 1999;42:283–89 Medline
15. Degnan AJ, Ceschin R, Lee V, et al. **Early metabolic development of posteromedial cortex and thalamus in humans analyzed via in vivo quantitative magnetic resonance spectroscopy.** *J Comp Neurol* 2014;522:3717–32 CrossRef Medline
16. Kreis R, Hofmann L, Kuhlmann B, et al. **Brain metabolite composition during early human brain development as measured by quantitative in vivo 1H magnetic resonance spectroscopy.** *Magn Reson Med* 2002;48:949–58 CrossRef Medline
17. An L, Zhang Y, Thomasson DM, et al. **Measurement of glutathione in normal volunteers and stroke patients at 3T using J-difference spectroscopy with minimized subtraction errors.** *J Magn Reson Imaging* 2009;30:263–70 CrossRef Medline
18. Szeszak S, Man R, Love A, et al. **Animated educational video to prepare children for MRI without sedation: evaluation of the appeal and value.** *Pediatr Radiol* 2016;46:1744–50 CrossRef Medline
19. Provencher SW. **Estimation of metabolite concentrations from localized in vivo proton NMR spectra.** *Magn Reson Med* 1993;30:672–79 CrossRef Medline
20. Wilson M, Reynolds G, Kauppinen RA, et al. **A constrained least-squares approach to the automated quantitation of in vivo 1H magnetic resonance spectroscopy data.** *Magn Reson Med* 2011;65:1–12 CrossRef Medline
21. Emir UE, Auerbach EJ, Van De Moortele PF, et al. **Regional neurochemical profiles in the human brain measured by 1H MRS at 7 T using local B1 shimming.** *NMR Biomed* 2012;25:152–60 CrossRef Medline
22. Tong J, Fitzmaurice PS, Moszczynska A, et al. **Do glutathione levels decline in aging human brain?** *Free Radic Biol Med* 2016;93:110–17 CrossRef Medline
23. Kang Y, Viswanath V, Jha N, et al. **Brain gamma-glutamyl cysteine synthetase (GCS) mRNA expression patterns correlate with regional-specific enzyme activities and glutathione levels.** *J Neurosci Res* 1999;58:436–41 Medline
24. Pouwels PJ, Frahm J. **Regional metabolite concentrations in human brain as determined by quantitative localized proton MRS.** *Magn Reson Med* 1998;39:53–60 CrossRef Medline
25. Jacobs MA, Horská A, van Zijl PC, et al. **Quantitative proton MR spectroscopic imaging of normal human cerebellum and brain stem.** *Magn Reson Med* 2001;46:699–705 Medline
26. Lecocq A, Le Fur Y, Maudsley AA, et al. **Whole-brain quantitative mapping of metabolites using short echo three-dimensional proton MRSI.** *J Magn Reson Imaging* 2015;42:280–89 CrossRef Medline
27. Cichočka M, Kozub J, Karcz P, et al. **Regional differences in the concentrations of metabolites in the brain of healthy children: a proton magnetic resonance spectroscopy ((1)HMRS) study.** *Polish J Radiol* 2016;81:473–77 CrossRef Medline
28. Granata F, Pandolfo G, Vinci S, et al. **Proton magnetic resonance spectroscopy (H-MRS) in chronic schizophrenia: a single-voxel study in three regions involved in a pathogenetic theory.** *Neuroradiol J* 2013;26:277–83 CrossRef Medline
29. Safriel Y, Pol-Rodriguez M, Novotny EJ, et al. **Reference values for long echo time MR spectroscopy in healthy adults.** *AJNR Am J Neuroradiol* 2005;26:1439–45 Medline
30. Sabati M, Sheriff S, Gu M, et al. **Multivendor implementation and comparison of volumetric whole-brain echo-planar MR spectroscopic imaging.** *Magn Reson Med* 2015;74:1209–20 CrossRef Medline
31. Goryawala MZ, Sheriff S, Maudsley A. **Regional distributions of brain glutamate and glutamine in normal subjects.** *NMR Biomed* 2016;29:1108–16 CrossRef Medline
32. Pouwels PJ, Brockmann K, Kruse B, et al. **Regional age dependence of human brain metabolites from infancy to adulthood as detected by quantitative localized proton MRS.** *Pediatr Res* 1999;46:474–85 CrossRef Medline
33. Blüml S, Wisnowski JL, Nelson MD Jr, et al. **Metabolic maturation of the human brain from birth through adolescence: insights from in vivo magnetic resonance spectroscopy.** *Cereb Cortex* 2013;23:2944–55 CrossRef Medline
34. Davies NP, Wilson M, Harris LM, et al. **Identification and characterisation of childhood cerebellar tumours by in vivo proton MRS.** *NMR Biomed* 2008;21:908–18 CrossRef Medline

Temporal Lobe Malformations in Achondroplasia: Expanding the Brain Imaging Phenotype Associated with *FGFR3*-Related Skeletal Dysplasias

S.A. Manikkam, K. Chetcuti, K.B. Howell, R. Savarirayan, A.M. Fink, and S.A. Mandelstam



ABSTRACT

SUMMARY: Thanatophoric dysplasia, achondroplasia, and hypochondroplasia belong to the *fibroblast growth factor receptor 3* (*FGFR3*) group of genetic skeletal disorders. Temporal lobe abnormalities have been documented in thanatophoric dysplasia and hypochondroplasia, and in 1 case of achondroplasia. We retrospectively identified 13 children with achondroplasia who underwent MR imaging of the brain between 2002 and 2015. All children demonstrated a deep transverse temporal sulcus on MR imaging. Further common neuroimaging findings were incomplete hippocampal rotation (12 children), oversulcation of the mesial temporal lobe (11 children), loss of gray-white matter differentiation of the mesial temporal lobe (5 children), and a triangular shape of the temporal horn (6 children). These appearances are very similar to those described in hypochondroplasia, strengthening the association of temporal lobe malformations in *FGFR3*-associated skeletal dysplasias.

ABBREVIATION: *FGFR3* = fibroblast growth factor receptor 3

Achondroplasia is the most frequent form of short-limb dwarfism, affecting more than 250,000 people worldwide,¹ with an incidence of 0.36–0.60 per 10,000 live births.² Achondroplasia is inherited as an autosomal dominant condition, in which most cases result from a glycine-to-arginine substitution at codon 380 in the transmembrane domain of the *fibroblast growth factor receptor 3* (*FGFR3*) gene.³ Thanatophoric dysplasia (a perinatal lethal skeletal dysplasia), achondroplasia, and hypochondroplasia belong to the *FGFR3* group of genetic skeletal disorders; different allelic mutations result in the variable severity of expression.^{4,5}

Temporal lobe abnormalities have been documented in thanatophoric dysplasia and hypochondroplasia.^{6–8} These changes were first reported in 1 case of an achondroplastic fetus in 2014⁹ but are not commonly described findings in the postnatal brain imaging of affected individuals, despite relatively frequent neuro-

imaging of the brain and craniocervical junction in infants and children with achondroplasia.^{10,11} Well-documented features of MR imaging of the brain in children with achondroplasia are narrowing of the subarachnoid space at the level of the foramen magnum, ventriculomegaly, and bifrontal widening of the subarachnoid space.¹²

Abnormal gyration of the temporal lobes has been described in thanatophoric dysplasia on prenatal sonography^{13–15} and prenatal MR imaging, which showed abnormal gyration of the temporal and occipital lobes and deep sulci on the medial aspects of both temporal and occipital lobes.¹⁴ One case of prenatal MR imaging in an achondroplastic fetus was published in 2014 by Pugash et al,⁹ describing temporal and occipital lobe abnormalities characteristic of hypochondroplasia in addition to the finding of short bones. Achondroplasia was subsequently confirmed on postnatal clinical and genetic testing.

In a review of postmortem neuropathologic changes in cases of confirmed thanatophoric dysplasia, megalencephaly and hippocampal dysplasia were found in all patients. Other very common findings were the following: polymicrogyria, enlarged temporal lobes, deep transverse temporal sulci, and neuroglial heterotopia. The combination of megalencephaly, an enlarged temporal lobe, and aberrant deep sulci was suggested to be specific for thanatophoric dysplasia.⁶

We hypothesized that the association of temporo-occipital developmental brain malformations with *FGFR3* osteochondrodysplasias extends to include individuals with achondroplasia, the most common nonlethal skeletal dysplasia.

Received February 21, 2017; accepted after revision September 13.

From the Departments of Medical Imaging (S.A. Manikkam, A.M.F., S.A. Mandelstam) and Neurology (K.B.H.), Royal Children's Hospital, Melbourne, Australia; Department of Radiology (K.C.), Alder Hey Children's Hospital, Liverpool, UK; Departments of Paediatrics (K.B.H., S.A. Mandelstam) and Radiology (A.M.F., S.A. Mandelstam), University of Melbourne, Melbourne, Australia; Murdoch Children's Research Institute (K.B.H., R.S., A.M.F., S.A. Mandelstam), Melbourne, Australia; Victorian Clinical Genetics Services (R.S.), Melbourne, Australia; and Florey Institute of Neuroscience and Mental Health (S.A. Mandelstam), Melbourne, Australia.

Please address correspondence to Samuel A. Manikkam, Department of Medical Imaging, Royal Children's Hospital, 50 Flemington Rd, Parkville, 3052, Victoria, Australia; e-mail: samuel.manikkam@gmail.com

Indicates article with supplemental on-line table.

<http://dx.doi.org/10.3174/ajnr.A5468>

Case Series

Approval for the study was obtained from the Royal Children's Hospital Melbourne Human Research Ethics Committee. A retrospective search was conducted of the Radiology Information System to identify children (from birth to 18 years of age) with a diagnosis of achondroplasia (determined by clinical, radiologic, or genetic evaluation) who had MR imaging of the brain performed between January 1, 2002, and December 31, 2015, for any clinical indication. Seventeen children with achondroplasia were

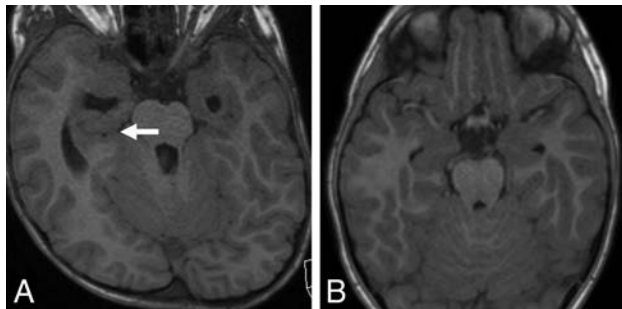


FIG 1. A, Axial T1-weighted MR image in a 5-year-old boy with achondroplasia shows a deep transverse sulcus within the temporal lobe (arrow) and abnormal configuration of the temporal horns of the lateral ventricles. B, Axial T1-weighted MR image in a 5-year-old male control shows the normal configuration of the mesial temporal lobes and temporal horns.

retrospectively identified from the Radiology Information System; ranging in age from 3 months to 12 years, with a median age of 2.5 years at the time of MR imaging. Four patients were excluded due to inadequate sequences for evaluation of the specific imaging criteria. Thirteen subjects were, therefore, included in the study (On-line Table). In the 9 children who underwent genetic testing, a common G-to-A transition at nucleotide 1138 (c.1138G>A G380R mutation) in the *FGFR3* gene was confirmed. In the remaining 4 children who did not undergo genetic testing, the diagnosis of achondroplasia was confirmed clinically and radiographically by a clinical geneticist.

The MR imaging studies were performed with 1 of three 1.5T imaging systems. The slice thickness of the T2WI sequences ranged from 1.5 to 4 mm. The T1WI was either reconstructed from 3D-T1WI or acquired with a slice thickness of 1.5–3 mm. Two pediatric neuroradiologists (S.A. Mandelstam, A.M.F.) and a pediatric neurologist (K.B.H.) reviewed the imaging for the presence of malformations of cortical development.

The MR images were assessed for the presence of the following: temporal lobe enlargement (defined as bulging of the surface of the temporal lobe beyond the contour of the adjacent frontal and parietal lobes), loss of gray-white matter differentiation of the mesial temporal lobe, incomplete hippocampal inversion, oversulcation of the mesial temporal lobe (assessed on coronal T2WI and 3D-T1WI), extension of oversulcation to the calcar avis, a

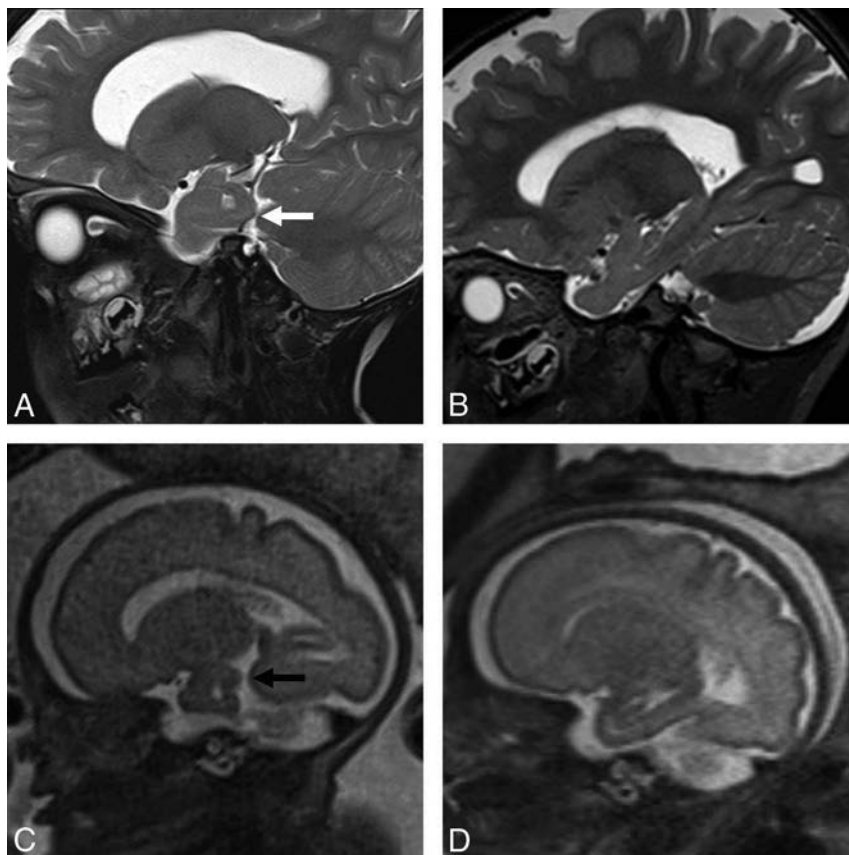


FIG 2. A, Sagittal T2-weighted MR image in a 2-year-old boy with achondroplasia shows a sagittal cleft within the temporal lobe (white arrow). B, Sagittal T2-weighted MR image of the child with achondroplasia in A demonstrates the prenatal appearance of the sagittal clefting within the temporal lobe at 30 weeks (black arrow). D, Antenatal sagittal T2-weighted MR image of a control fetus shows the normal appearance of the temporal lobe at the same gestation.

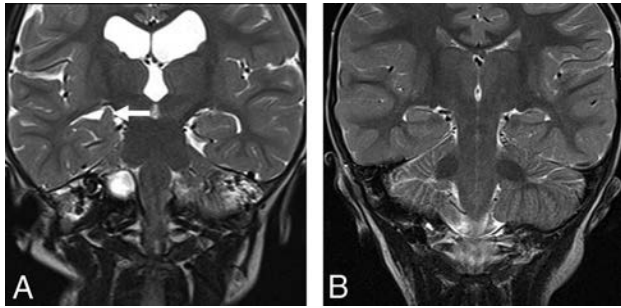


FIG 3. A, Coronal T2-weighted MR image in a 30-month-old boy with achondroplasia shows incomplete hippocampal inversion (*arrow*) and ventriculomegaly. B, Coronal T2-weighted MR image in a 30-month-old male control shows the normal appearance of the hippocampi.

Prevalence of MRI findings in children with achondroplasia

MRI Finding	Prevalence
Deep transverse temporal sulcus (axial T1WI)	13/13 (100%)
Sagittal clefting in the medial temporal lobe (sagittal T2WI)	13/13 (100%)
Incomplete hippocampal inversion	12/13 (92%)
Ventriculomegaly	12/13 (92%)
Oversulcation of the mesial temporal lobe	11/13 (85%)
Extension of oversulcation to the calcar avis	9/13 (69%)
Loss of gray-white matter differentiation of the mesial temporal lobe	5/7 ^a (71%)
Abnormal triangular shape of the temporal horn	6/13 (46%)
Megalencephaly	5/13 (38%)
Temporal lobe enlargement	1/13 (8%)

^a In the 6 children younger than 36 months of age, loss of gray-white matter differentiation of the mesial temporal lobe could not be accurately assessed on available sequences due to the incomplete myelination.

deep transverse temporal sulcus (assessed separately on axial T1WI and sagittal T2WI), triangular shape of the temporal horn, ventriculomegaly (defined as frontal horns of the lateral ventricles measuring >10 mm), megalencephaly, polymicrogyria, and subependymal heterotopia. The results were consensus-based.

MR imaging studies in all children showed the presence of a deep transverse temporal sulcus, visible on axial T1WI (Fig 1) and sagittal T2WI (Fig 2). Incomplete hippocampal inversion (Fig 3) and ventriculomegaly were found in 12 children (92%) (Table). The next most prevalent finding was oversulcation of the mesial temporal lobe in 11 (85%) (Fig 4), with extension of oversulcation to involve the calcar avis in 9 (69%) (Fig 5). Further common findings were loss of gray-white matter differentiation of the mesial temporal lobe in 5 children (71% of the children older than 36 months of age in whom this could be accurately assessed), a triangular shape of the temporal horn in 6 (46%) (Fig 1), and megalencephaly in 5 (38%). In our cohort, all children with megalencephaly also exhibited ventriculomegaly. Subependymal heterotopia and polymicrogyria were not demonstrated in any children. In one of the children, the temporal lobe changes were also recognized antenatally at 30 weeks' gestation, after the detection of short limbs and mild ventriculomegaly in the fetus on sonography. Comparison of the postnatal with the fetal imaging (Figs 2C and 4C) illustrates the evolution of the findings with brain maturation.

Seizures were reported in only 1 child who had focal seizures between 3 and 12 months of age. Seizures occurred in clusters and were characterized by behavioral arrest, apnea, facial suffusion,

and tachycardia. Electroencephalography recorded seizures arising independently in the left and right temporal regions.

DISCUSSION

Temporal lobe malformations have been previously described in other conditions composing the *FGFR3* family of skeletal dysplasias and were first reported in 2014 by Pugash et al⁹ in 1 case of an achondroplastic fetus with prenatal and subsequent postnatal imaging. In 2012, Linnankivi et al⁷ described 8 patients with hypochondroplasia and an *FGFR3* N540K mutation in whom brain MR imaging demonstrated bilateral temporal lobe dysgenesis, with abnormally shaped temporal horns and an aberrant hippocampal configuration. In a further cohort of children with hypochondroplasia, Philpott et al,⁸ in 2013, additionally described temporal lobe enlargement, deep transverse temporal sulci, overly sulcated mesial temporal lobes, megalencephaly, and mild ventriculomegaly. Correlating our findings with those of previous studies evaluating brain appearances in thanatophoric dysplasia and hypochondroplasia revealed common findings of temporal lobe sulcation abnormalities, incomplete hippocampal inversion, and ventriculomegaly.^{6,8} Polymicrogyria and subependymal heterotopia have been described in postmortem cases of thanatophoric dysplasia on neuropathology⁶ and in imaging of a case with hypochondroplasia,⁸ but these were not seen in our study. It may be that these are less common features that our sample size was not large enough to detect, or it may reflect differential effects of the different *FGFR3* mutations on the brain. It is also possible that subtle cases of polymicrogyria or subependymal heterotopia may be present pathologically, however, not visible on the MR images assessed.

There is a growing body of literature elucidating the role of *FGFR3* mutations in neural and skeletal development. FGFR is a membrane tyrosine kinase encoded by 4 genes (*FGFR 1–4*). In embryonic tissues in mice, *FGFR3* expression is limited principally to neural tube derivatives (developing brain and spinal cord), cartilage rudiments of developing bone, the cochlea, and the lens.¹⁶ All 4 fibroblast growth factor receptors are expressed in the developing brain and contribute to its development.⁶ The *FGFR3* gene in mice is expressed in a gradient in the developing cortex, with the highest levels adjacent to the hippocampal primordia and cortical hem.⁶ Mice with constitutive activation of *FGFR3* in the forebrain demonstrated selective promotion of growth of the caudolateral (occipitotemporal) cortex, which is highly correlated with the gradient of *FGFR3* expression in the ventricular zone at early stages of neurogenesis.¹⁷

Seizures are reported in *FGFR3* disorders, but rarely in achondroplasia. Our patient had temporal lobe seizures in infancy, similar to that reported in hypochondroplasia⁷ and Muenke syndrome,¹⁸ raising the possibility that *FGFR3*-associated temporal lobe dysgenesis predisposes to seizures. It is of clinical importance, however, to note that in our series, most children did not have seizures despite having temporal lobe malformations. It is not clear whether this is the case in the other *FGFR3* disorders.

Similar temporal lobe malformations are described in Apert syndrome, which is the result of localized gain-of-function mutations of *fibroblast growth factor receptor 2* (*FGFR2*) and characterized by craniosynostosis and syndactyly of the hands and feet.¹⁹

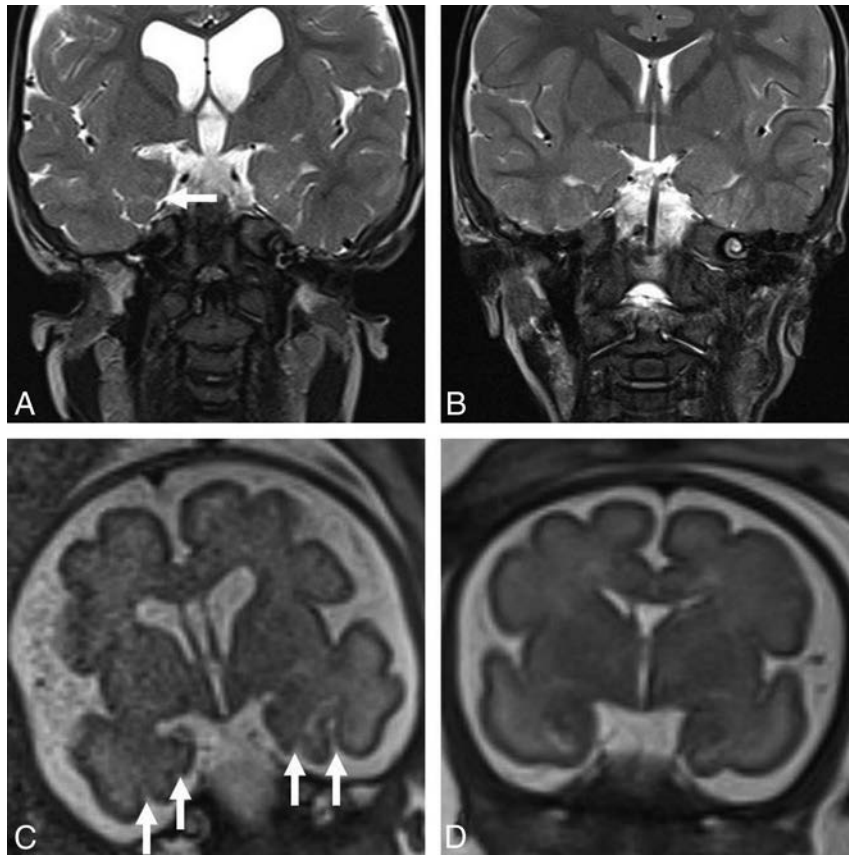


FIG 4. A, Coronal T2-weighted MR image in a 30-month-old boy with achondroplasia shows oversulcation and loss of gray-white matter differentiation of the mesial temporal lobes (*arrow*) and ventriculomegaly. B, Coronal T2-weighted MR image in a 30-month-old male control shows the normal sulcation and gray-white matter differentiation of the temporal lobes. C, Antenatal coronal T2-weighted fetal MR image of the child with achondroplasia in A obtained at 30 weeks shows oversulcation of the mesial temporal lobes (*white arrows*) and mild ventriculomegaly. D, Antenatal coronal T2-weighted MR image of a control fetus shows the normal appearance of the temporal lobes at the same gestation.

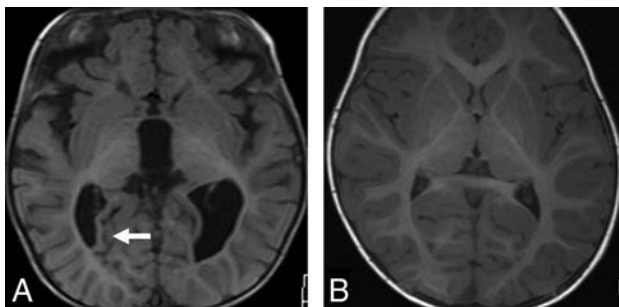


FIG 5. A, Axial T1-weighted MR image in a 1-year-old girl with achondroplasia shows oversulcation of the calcar avis (*arrow*) and moderate ventriculomegaly. B, Axial T1-weighted MR image in a 1-year-old female control shows the normal sulcation pattern of the calcar avis.

The findings described in prenatal and postnatal imaging include expansion and overconvolution of the temporal lobes and temporal lobe clefts.^{20–22}

The major limitations of our study are that it is retrospective, with a small sample size. It is not possible to determine what proportion of patients with achondroplasia have temporal lobe changes on the basis of such small numbers or to clarify the clinical and radiologic correlations. A further limitation is the qualitative rather than quantitative assessment of these cortical malformations on conventional MR imaging sequences.

In conclusion, this case series demonstrates the frequent presence of temporal lobe malformations in children with achondroplasia, the most common nonlethal skeletal dysplasia. The findings herein strengthen the association of temporal lobe malformations and skeletal dysplasias due to different mutations in the *FGFR3* gene.

REFERENCES

- Horton WA, Hall JG, Hecht JT. Achondroplasia. *Lancet* 2007;370:162–72 CrossRef Medline
- Waller DK, Correa A, Vo TM, et al. The population-based prevalence of achondroplasia and thanatophoric dysplasia in selected regions of the US. *Am J Med Genet A* 2008;146A:2385–89 CrossRef Medline
- Bellus GA, Hefferon TW, Ortiz de Luna RI, et al. Achondroplasia is defined by recurrent G380R mutations of FGFR3. *Am J Hum Genet* 1995;56:368–73 Medline
- Naski MC, Wang Q, Xu J, et al. Graded activation of fibroblast growth factor receptor 3 by mutations causing achondroplasia and thanatophoric dysplasia. *Nat Genet* 1996;13:233–37 CrossRef Medline
- Vajo Z, Francomano CA, Wilkin DJ. The molecular and genetic basis of fibroblast growth factor receptor 3 disorders: the achondroplasia family of skeletal dysplasias, Muenke craniosynostosis, and Crouzon syndrome with acanthosis nigricans. *Endocr Rev* 2000;21:23–39 Medline
- Hevner RF. The cerebral cortex malformation in thanatophoric

- dysplasia: neuropathology and pathogenesis.** *Acta Neuropathol* 2005;110:208–21 CrossRef Medline
7. Linnankivi T, Mäkitie O, Valanne L, et al. **Neuroimaging and neurological findings in patients with hypochondroplasia and FGFR3 N540K mutation.** *Am J Med Genet A* 2012;158A:3119–25 CrossRef Medline
 8. Philpott C, Widjaja E, Raybaud C, et al. **Temporal and occipital lobe features in children with hypochondroplasia/FGFR3 gene mutation.** *Pediatr Radiol* 2013;43:1190–95 CrossRef Medline
 9. Pugash D, Lehman AM, Langlois S. **Prenatal ultrasound and MRI findings of temporal and occipital lobe dysplasia in a twin with achondroplasia.** *Ultrasound Obstet Gynecol* 2014;44:365–68 CrossRef Medline
 10. Richette P, Bardin T, Stheneur C. **Achondroplasia: from genotype to phenotype.** *Joint Bone Spine* 2008;75:125–30 CrossRef Medline
 11. Trotter TL, Hall JG. **Health supervision for children with achondroplasia.** *Pediatrics* 2005;116:771–83 CrossRef Medline
 12. Kao SC, Waziri MH, Smith WL, et al. **MR imaging of the craniovertebral junction, cranium, and brain in children with achondroplasia.** *AJR Am J Roentgenol* 1989;153:565–69 CrossRef Medline
 13. Miller E, Blaser S, Shannon P, et al. **Brain and bone abnormalities of thanatophoric dwarfism.** *AJR Am J Roentgenol* 2009;192:48–51 CrossRef Medline
 14. Fink AM, Hingston T, Sampson A, et al. **Malformation of the fetal brain in thanatophoric dysplasia: US and MRI findings.** *Pediatr Radiol* 2010;40(suppl 1):S134–37 CrossRef Medline
 15. Blaas HG, Vogt C, Eik-Nes SH. **Abnormal gyration of the temporal lobe and megalencephaly are typical features of thanatophoric dysplasia and can be visualized prenatally by ultrasound.** *Ultrasound Obstet Gynecol* 2012;40:230–34 CrossRef Medline
 16. Peters K, Ornitz D, Werner S, et al. **Unique expression pattern of the FGF receptor 3 gene during mouse organogenesis.** *Dev Biol* 1993;155:423–30 CrossRef Medline
 17. Thomson RE, Kind PC, Graham NA, et al. **FGF receptor 3 activation promotes selective growth and expansion of occipitotemporal cortex.** *Neural Dev* 2009;4:4 CrossRef Medline
 18. Grosso S, Farnetani M, Berardi R, et al. **Medial temporal lobe dysgenesis in Muenke syndrome and hypochondroplasia.** *Am J Med Genet A* 2003;120A:88–91 CrossRef Medline
 19. Anderson J, Burns HD, Enriquez-Harris P, et al. **Apert syndrome mutations in fibroblast growth factor receptor 2 exhibit increased affinity for FGF ligand.** *Hum Mol Genet* 1998;7:1475–83 CrossRef Medline
 20. Tokumaru AM, Barkovich AJ, Ciricillo SF, et al. **Skull base and calvarial deformities: association with intracranial changes in craniofacial syndromes.** *AJNR Am J Neuroradiol* 1996;17:619–30 Medline
 21. Raybaud C, Di Rocco C. **Brain malformation in syndromic craniosynostoses, a primary disorder of white matter: a review.** *Childs Nerv Syst* 2007;23:1379–88 CrossRef Medline
 22. Stark Z, McGillivray G, Sampson A, et al. **Apert syndrome: temporal lobe abnormalities on fetal brain imaging.** *Prenat Diagn* 2015;35:179–82 CrossRef Medline

Systematic Radiation Dose Reduction in Cervical Spine CT of Human Cadaveric Specimens: How Low Can We Go?

 M. Tozakidou,  C. Reisinger,  D. Harder,  J. Lieb,  Z. Szucs-Farkas,  M. Müller-Gerbl,  U. Studler,  S. Schindera, and  A. Hirschmann



ABSTRACT

BACKGROUND AND PURPOSE: While the use of cervical spine CT in trauma settings has increased, the balance between image quality and dose reduction remains a concern. The purpose of our study was to compare the image quality of CT of the cervical spine of cadaveric specimens at different radiation dose levels.

MATERIALS AND METHODS: The cervical spine of 4 human cadavers (mean body mass index; 30.5 ± 5.2 kg/m²; range, 24–36 kg/m²) was examined using different reference tube current–time products (45, 75, 105, 135, 150, 165, 195, 275, 355 mAs) and a tube voltage of 120 kV(peak). Data were reconstructed with filtered back-projection and iterative reconstruction. Qualitative image noise and morphologic characteristics of bony structures were quantified on a Likert scale. Quantitative image noise was measured. Statistics included analysis of variance and the Tukey test.

RESULTS: Compared with filtered back-projection, iterative reconstruction provided significantly lower qualitative (mean noise score: iterative reconstruction = 2.10/filtered back-projection = 2.18; $P = .003$) and quantitative (mean SD of Hounsfield units in air: iterative reconstruction = 30.2/filtered back-projection = 51.8; $P < .001$) image noise. Image noise increased as the radiation dose decreased. Qualitative image noise at levels C1–4 was rated as either “no noise” or as “acceptable noise.” Any shoulder position was at level C5 and caused more artifacts at lower levels. When we analyzed all spinal levels, scores for morphologic characteristics revealed no significant differences between 105 and 355 mAs ($P = .555$), but they were worse in scans at 75 mAs ($P = .025$).

CONCLUSIONS: Clinically acceptable image quality of cervical spine CTs for evaluation of bony structures of cadaveric specimens with different body habitus can be achieved with a reference mAs of 105 at 120 kVp with iterative reconstruction. Pull-down of shoulders during acquisition could improve image quality but may not be feasible in trauma patients with unknown injuries.

ABBREVIATIONS: DLP = dose-length product; FBP = filtered back-projection; IR = iterative reconstruction

Cervical spine CT is routinely used in trauma settings due to its wide availability around the clock and ease of use.^{1,2} Furthermore, it is known to be superior to plain radiographs, which have been reported to fail in the detection of injuries in a substantial number of patients. In a study performed by Mower et al,³ injuries were missed on plain radiographs in 320 of 818 patients, most of which were in the lamina or posterior elements. Thus, CT is applied currently in a wide range of patients, even in young ones.^{1,2}

The ongoing discussion concerning radiation protection in terms of the as low as reasonably achievable principle demands reduction of the radiation dose down to a level at which image quality is still diagnostically sufficient.⁴ However, the clinically applied dose often relies on manufacturer’s recommendations and is not necessarily the lowest possible dose that can be achieved in clinical routine. One important and well-examined role in dose-reduction strategies is using mathematic models such as iterative reconstruction (IR) to reduce image noise and thus allow a lower radiation dose.⁵ The radiation dose for cervical spine CT may vary from one institution to another, depending on the CT scanner and its protocol. The mean radiation dose of the cervical spine in patients of a Canadian emergency department was reported to be 5.7 mSv.⁶ To the best of our knowledge, the lowest possible radiation dose for CT of the cervical spine with sufficient diagnostic value has not been investigated by a systematic stepwise dose reduction. For ethical reasons, a stepwise dose reduc-

Received May 30, 2017; accepted after revision October 23.

From the Clinic of Radiology and Nuclear Medicine (M.T., C.R., D.H., J.L., U.S., S.S., A.H.), University of Basel Hospital, Basel, Switzerland; Department of Diagnostic Radiology (Z.S.-F.), Hospital Centre of Biel, Biel, Switzerland; and Institute of Anatomy (M.M.-G.), University of Basel, Basel, Switzerland.

Please address correspondence to Magdalini Tozakidou, Clinic of Radiology and Nuclear Medicine, University of Basel Hospital, Petersgraben 4, 4031 Basel, Switzerland; e-mail: magdalini.tozakidou@gmail.com

 Indicates article with supplemental on-line tables.

<http://dx.doi.org/10.3174/ajnr.A5490>

Table 1: Characteristics of cadaveric specimens^a

Cadaveric Specimen	Body				Body Width (cm) at Level		
	Weight (kg)	Height (m)	BMI (kg/m ²)	Shoulder Level	C7	C5	C3
1	63	1.63	23.7	C5	38.3	34.8	15.7
2	93	1.68	33.0	C5	43.4	36.0	19.0
3	62	1.48	28.3	C5	37.3	32.3	15.4
4	94	1.62	35.6	C5	46.4	39.4	16.3

Note:—BMI indicates body mass index.

^a Cadavers' body weights included approximately 10–15 L formalin fixation.

tion cannot be performed in a clinical setting. Therefore, we decided to use cadaveric specimens in the present study.

The aim of the current study was to assess the image quality and diagnostic accuracy of cervical spine CT of cadaveric specimens at different radiation dose levels reconstructed with filtered back-projection (FBP) and an IR algorithm.

MATERIALS AND METHODS

Specimens and CT Protocol

Institutional review board approval was waived. Four human cadaveric specimens (2 women, 2 men; age at death, older than 50 years) were prospectively included. The demographics of each specimen are shown in Table 1.

Unenhanced CT scans of the cervical spine were performed on a 128–detector row multidetector CT scanner (Somatom Definition AS+; Siemens, Erlangen, Germany). Cadaveric specimens were in a supine position. Lateral and anteroposterior topograms served as references for the scan range from vertebrae C1 to T1. We used the following scan parameters: tube voltage, 120 kVp (peak); detector configuration, 128 × 0.6 mm; pitch factor, 0.8. The reference tube current–time product ranged from 45 to 355 mAs (45, 75, 105, 135, 150, 165, 195, 275, 355 mAs) by applying automatic tube current modulation (CARE Dose4D; Siemens). The protocol of the tube current–time product was set in steps of 30 mAs between 45 and 195 mAs and in steps of 80 mAs for higher values between 195 and 355 mAs because the difference in image quality is only minor in this range, to our knowledge. Our initial plan was to obtain only scans up to 275 mAs. However, scans at that dose seemed unacceptable for the lower C-spine at first glance; thus, we added another 80 mAs to the dose and scanned at 355 mAs. Additionally, we included 150 mAs in our protocol to compare our findings with the previously published results of Becce et al.⁷

Images were reconstructed using both a conventional FBP and an IR (sinogram-affirmed iterative reconstruction, strength 3) algorithm as described elsewhere in bone convolution kernels (B70 hours for FBP and I70 hours for IR algorithms, respectively).^{7–9} We used the following image reconstruction parameters: FOV, 15 × 15 cm to 21 × 21 cm according to the specimen constitution; section thickness/increment, 0.75/ 0.75 mm. Lateral body width was measured on anteroposterior topograms at 3 different heights: C3, C5, and C7 (Fig 1). Shoulder level was defined as the level of the cervical spine, on which the bony shoulder girdle is superimposed on the lateral topogram (Fig 1). For comparison of the height of the shoulder girdle in a clinical setting, topograms of cervical spine CTs of 30 nonintubated patients (15 women, 15 men; mean age, 66.9 ± 22.7 years) at the emergency department

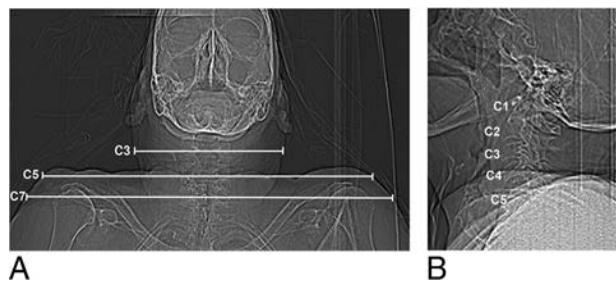


FIG 1. Lateral body width was measured on each anteroposterior topogram of the cadaveric specimens at 3 different heights: C3, C5, and C7 (A). On the lateral topogram, the shoulder level of this cadaveric specimen was C5 (B).

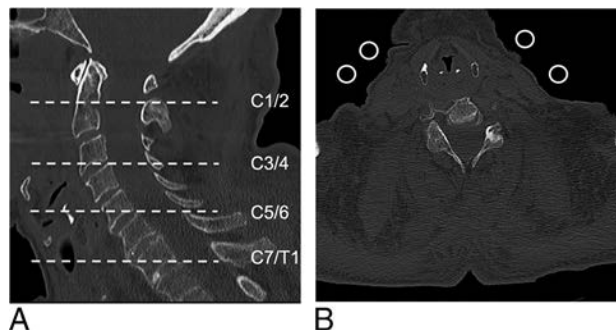


FIG 2. Quantitative and qualitative image noise were evaluated on 4 different cervical spine levels (A, dashed lines). Axial image (B) at level C5–6 shows 4 ROIs of 100 mm² each in the extracorporeal air for quantitative noise measurements.

in 1 week were reviewed by 1 reader. The height of the shoulder girdle was assessed on the lateral topogram and recorded.

Analysis of Radiation Exposure

The volume CT dose index and the dose-length product (DLP) were automatically generated by the CT unit. The effective dose was estimated by multiplying the DLP by an organ-specific conversion coefficient of 0.0051 mSv/mGy × cm for an adult neck region at 120 kVp.¹⁰

Analysis of Quantitative Image Noise

Four circular ROIs of 100 mm² each at the cervical spine levels (C1–2, C3–4, C5–6, and C7–T1) served for noise measurements. They were placed in the extracorporeal air on axial images at exactly the same level in each scan of the same cadaver by 1 reader with 2 years of experience in spine imaging (Fig 2). Image noise was defined as the SD of the mean CT numbers measured in Hounsfield units within an ROI.

Analysis of Qualitative Image Noise and Morphologic Characteristics

All CT scans were randomized and independently evaluated by 4 musculoskeletal fellowship-trained radiologists with 2, 3, 4, and 7 years of experience in spine imaging, respectively. Each reader was blinded to the scan parameters and image reconstruction algorithms. Ratings given by the 4 readers were averaged for statistical analysis.

All CT images were displayed with the window level/width set to 600/2000. A total of 72 datasets were assessed using axial and

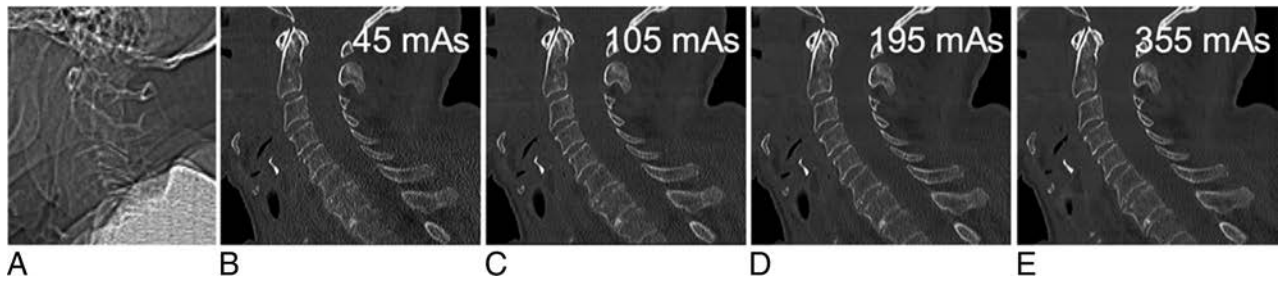


FIG 3. Lateral topogram (A) of this cadaveric specimen reveals shoulder height at the C5 level. Sagittal reformatted CT images (B–E; window level/width, 600/2000) of the cervical spine at 45, 105, 195, and 355 mAs reconstructed with sonogram-affirmed iterative reconstruction (strength level, 3) using bone convolution kernels show a decreasing image noise with increasing tube currents, but still sufficient image quality at 105 mAs compared with 355 mAs.

Table 2: Analysis of morphologic characteristics of bony cervical spine structures^a

Assessment, Localization	Score	Criteria
Cortex		
Vertebral body (sag/ax)	0	Not visible
	1	Visible, but not analyzable
	2	Clearly visible
Facet joint (sag)	0	Not visible
	1	Visible, but not analyzable
	2	Clearly visible
Trabeculae		
Vertebral body (sag)	0	Not visible
	1	Clearly visible
Integrity		
Anterior vertebral body line (sag)	0	Not visible
	1	Clearly visible
Posterior vertebral body line (sag)	0	Not visible
	1	Clearly visible
Alignment		
Vertebral body (sag)	0	Not visible
	1	Clearly visible
Facet joint (sag)	0	Not visible
	1	Clearly visible
Maximal sum	9	

Note:—sag indicates sagittal reformations; ax, axial reformations.

^a Cortex, trabeculae, and integrity were assessed on each cervical vertebral segment (eg, C3); alignment was assessed on each cervical level (eg, C3–4). The least visible cortices of each vertebral body and facet joint were used for this analysis.

sagittal reformations in OsiriX, Version 4.1.2 (<http://www.osirix-viewer.com>). Qualitative image noise was graded on a 3-point scale (1 = no noise, 2 = acceptable minor noise, 3 = unacceptable major noise) on 4 levels: C1–2, C3–4, C5–6, and C7–T1 using sagittal reformations (Figs 2A and 3). Morphologic characteristics of the bony structures were analyzed on a Likert scale. On each cervical segment (eg, C3), the cortex, trabeculae, and integrity of the anterior and posterior vertebral body lines were assessed; on each cervical level (eg, C3–4), alignment was assessed on either a 2- or a 3-point scale as shown in Table 2.

Statistical Analysis

Quantitative and qualitative parameters were compared using analysis of variance for repetitive measurements and the Tukey test. Statistical tests were performed using appropriate statistical software (Statistica 7, StatSoft, Tulsa, Oklahoma; MedCalc for Windows, MedCalc Software, Mariakerke, Belgium). A *P* value <

Table 3: Effective tube current at different cervical spine levels^a

Applied Tube Current (mAs)	Effective Tube Current (mAs)			
	C1–2	C3–4	C5–6	C7–T1
45	37 ± 4	46 ± 3	45 ± 3	43 ± 2
75	62 ± 7	78 ± 4	76 ± 2	70 ± 3
105	88 ± 8	110 ± 6	106 ± 5	99 ± 3
135	113 ± 13	139 ± 8	133 ± 9	127 ± 6
150	126 ± 13	155 ± 10	149 ± 6	142 ± 6
165	138 ± 14	170 ± 9	160 ± 6	157 ± 5
195	163 ± 16	204 ± 11	190 ± 6	186 ± 7
275	234 ± 23	280 ± 18	270 ± 19	257 ± 12
355	331 ± 27	344 ± 49	343 ± 14	336 ± 13

^a Data represent mean ± SD at the respective cervical spine levels.

.05 was considered statistically significant. Because a high shoulder position in the cadaveric specimens led to remarkably higher image noise and lower image quality at the levels C5–T1, upper cervical levels (C1–4) with no shoulder girdle superimposition were additionally separately analyzed. Interobserver agreement was assessed by calculating the Kendall coefficient of concordance.

RESULTS

Analysis of Radiation Exposure

The radiation dose output given by the volume CT dose index and DLP showed a linear relation to the applied tube current. The mean volume CT dose index, DLP, and effective dose were 26.5 mGy, 530 mGy × cm, and 2.7 mSv for the highest applied reference mAs value at 355 mAs and 3.3 mGy, 65 mGy × cm, and 0.3 mSv for the lowest applied reference mAs value at 45 mAs, respectively. The effective mAs ranged from 46 mAs (for reference mAs of 45) to 408 mAs (for reference mAs of 355). Detailed ranges of effective mAs for the 4 different cadavers were the following (reference mAs in parentheses): 46–51 mAs (45), 77–86 mAs (75), 105–121 mAs (105), 131–157 mAs (135), 146–172 mAs (150), 161–192 mAs (165), 195–225 mAs (195), 267–321 mAs (275), and 347–408 mAs (355). For details see Table 3.

Analysis of Quantitative Image Noise

Comparison of quantitative noise measurements in images with IR and FBP reconstructions showed significantly less noise in images with IR than in images with FBP (mean noise in air C1–T1: IR, 30 HU; FBP, 52 HU; *P* < .001). As expected, image noise decreased as tube current increased in both IR and FBP reconstructions. With iterative reconstructions, only images with a tube

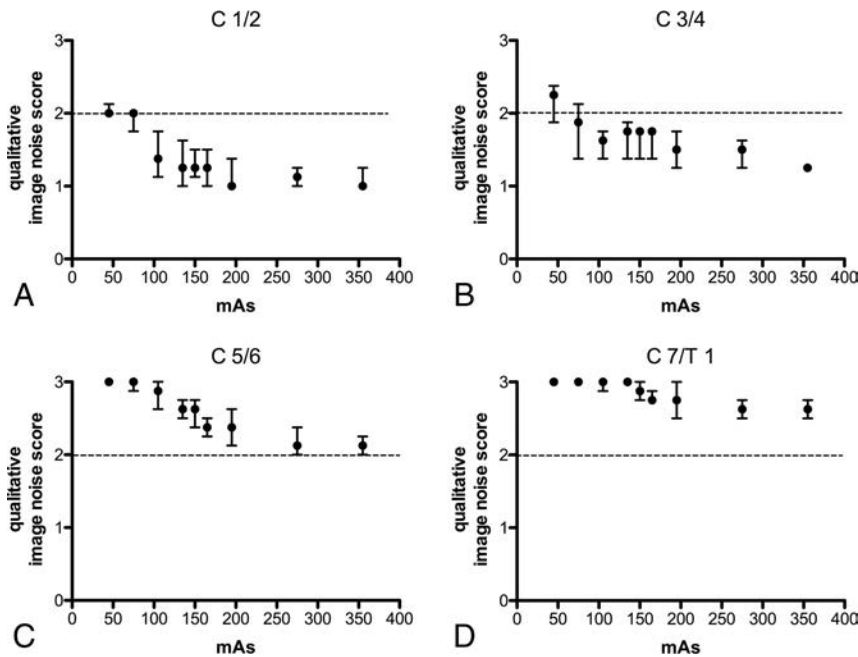


FIG 4. Qualitative image noise for iterative reconstructed images was evaluated on each cervical spine level using a noise score scale (1, no noise; 2, minor noise acceptable [dashed line, A–D]; 3, major noise, unacceptable). The median image noise was at least acceptable at levels C1–2 (A) with each tube current and at 75 mAs at levels C3–4 (B), but unacceptable at levels C5–T1 (C and D), except for 355 mAs at C5–6 (C). Data are median and 25th to 75th percentiles.

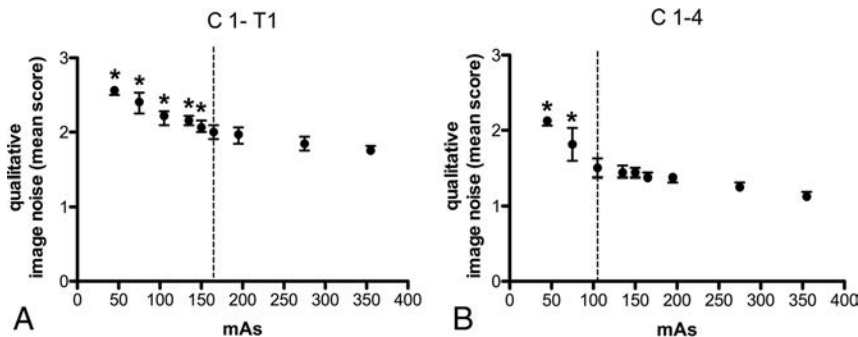


FIG 5. Grouped analysis of qualitative image noise shows significant differences at ≤ 150 mAs with 355 mAs for all cervical spine levels (45 mAs, $P < .001$; 75 mAs, $P < .001$; 105 mAs, $P = .0006$; 135 mAs, $P = .0019$; 150 mAs, $P = .039$) (A). Significant differences in image quality for levels C1–4, which were not superimposed by the shoulder girdle, were found for scans with ≤ 75 mAs (45 mAs, $P < .001$; 75 mAs, $P < .001$) compared with 355 mAs (B). The dashed lines in A and B represent the lowest tube currents (165 mAs for C1–T1 and 105 mAs for C1–4) that are not significantly different with respect to qualitative image noise compared with 355 mAs. Asterisks indicate values that are significantly different compared with 355 mAs ($P < .05$). Dots and bars indicate median and 25th to 75th percentiles.

current of 45 mAs showed a significant decrease in quantitative image noise compared with the highest applied tube current of 355 mAs at levels C1–4 when analyzing each cervical segment independently. When we summarized all cervical spine levels, no statistically significant difference of image noise was noted between IR images in scans at 75 and 355 mAs, whereas scans at 45 mAs showed higher image noise compared with scans at 355 mAs ($P = .010$). Analysis of the upper cervical spine (C1–4) revealed no significant difference in image noise in IR images in scans at 105 and 355 mAs, whereas scans at 75 mAs ($P = .004$) and 45 mAs ($P < .001$) showed significantly higher image noise compared with scans at 355 mAs.

Analysis of Qualitative Image Noise and Morphologic Characteristics

Overall, qualitative image quality was significantly better with IR than with FBP (noise score, $P = .03$; morphologic score, $P < .001$), even though morphologic characteristics only showed slight differences between IR and FBP (mean: IR, 44.6 ± 5.0 ; FBP, 43.3 ± 5.3 ; median: [25th to 75th percentile] IR, 44.8 [42.1/48.4]; FBP, 44.3 [39.8/47.6]).

Detailed results for iterative reconstructions are illustrated in Figs 4–6. In comparison with FBP reconstruction, IR images allow a higher reduction of the radiation dose (Table 4).

Regarding qualitative image noise, all scans with any reference tube current–time product for IR images at 105 mAs or higher were rated as acceptable or better at levels C1–2 and C3–4. In contrast, more than half of the scans at levels C5–6 and almost all scans at level C7–T1 were rated as not acceptable for all tube current–time products, even with the highest reference mAs value of 355 (median: C5–6 = 2.1 and C7–T1 = 2.6; Fig 4). When we grouped all cervical spine levels together, statistical analysis revealed a significant difference for qualitative image noise with the IR of scans at ≤ 150 mAs compared with scans at 355 mAs (45 mAs, $P < .001$; 75 mAs, $P < .001$; 105 mAs, $P = .0006$; 135 mAs, $P = .002$; 150 mAs, $P = .04$; Fig 5A). FBP analyses of qualitative image noise showed significant differences at ≤ 195 mAs (FBP) compared with 355 mAs (IR; $P = .012$). The Kendall coefficient of interobserver agreement for image noise was good with 0.67.

The height of the shoulders was at the C5 level in all cadavers. Hence, body width was larger at lower spine levels compared with the upper levels (Table 1). For comparison, in a clinical setting at the emergency department, the shoulder height of 30 patients was only slightly lower (C5–T1) than in the cadaveric specimens with 4 shoulders at C5, 12 at C6, and 7 each at C7 and T1, respectively.

Morphologic characteristics of images with IR were rated slightly better than with FBP reconstructions ($P = .001$). For IR images, grouped scores for all levels revealed no statistically significant difference between 105 and 355 mAs, but significantly lower scores at 75 mAs ($P = .03$) and 45 mAs ($P < .001$). Morphologic characteristics of the upper spine (C1–4) showed no significant difference between 45 and 355 mAs. Single analysis of

cortex visibility showed no significant difference for the upper cervical spine (C1–4), but significantly lower scores at 45 mAs ($P = .001$) when examining the entire cervical spine. Scores for trabeculae were significantly different at 45 mAs for the upper ($P = .03$) and the entire cervical spine ($P = .003$; On-line Table 1). Analysis of morphologic scores with FBP reconstructions are shown in On-line Tables 1 and 2. Interobserver agreement for morphologic characteristics was excellent with a Kendall coefficient of 0.848.

If we take the results of qualitative image noise and morphologic score analysis together, the image quality proved to be sufficient with a tube current of 105 mAs and iterative reconstructions for cervical spine levels, which are not superimposed by the shoulders.

DISCUSSION

CT image quality of the cervical spine in cadaveric specimens was superior with the IR compared with the FBP algorithm; this finding implies that the CT dose may be reduced when applying IR protocols in clinical practice. This result is in accordance with the literature and pertains to not only musculoskeletal imaging but also thoracic and abdominal imaging.^{7,11–13} FBP algorithms may lead to noisy images in low-dose protocols or obese patients.^{14,15} Reported benefits of IR algorithms include a reduced noise level with enhanced subjective and objective image quality as well as reduction of the radiation dose with preserved image quality.¹² However, Becce et al⁷ emphasized the restricted benefit of the IR

algorithm in analyzing trabecular bone structures in contrast to the discs or ligaments in cervical spine imaging, though overall image quality was superior using IR. This finding is in line with our results of morphologic characteristics on bony structures, which showed only subtle differences between IR- and FBP-reconstructed images and might be because spatial resolution depends on several factors, including image thickness, image matrix, voxel size, and FOV. The IR technique is not capable of compensating for image noise in very low tube currents due to photon starvation, which explains the unacceptable image quality at lower cervical spine levels.

Qualitative noise analysis revealed sufficient image quality for CT of the cervical spine by applying a reference tube current–time product of 165 mAs and 120 kVp with the IR algorithm. If we focused on the upper cervical spine (C1–4), which was not superimposed by the shoulder girdle, all scans at 105 mAs showed a sufficient image quality. Considering morphologic criteria, such as trabecular and cortical structures, even a reference tube current–time product as low as 105 mAs was satisfying. Our findings are in accordance with previously published results from Becce et al,⁷ who demonstrated that the low-dose protocol of the cervical spine is feasible at a reference level of 150 mAs. They compared a standard dose protocol at 275 mAs with a low-dose protocol of 150 mAs, each at a fixed tube current of 120 kVp.⁷ Several studies compared protocols at different tube current–time products^{7,16,17}; however, no tube current–time product lower than 150 mAs for CT of the cervical spine has been published so far, to our knowledge.

If we excluded cervical spine levels that are superimposed by shoulders, a further reduction of the tube current–time product to 105 mAs still revealed sufficient image quality in the analysis of the cervical spine.

Our results show that even very low dose protocols with 105 mAs do not impair image quality of the cervical spine. However, superimposition of the shoulder girdle proved to be a limitation of a further reduction of the dose. We demonstrated that image quality of the cervical spine at levels above the shoulder girdle is sufficient with a tube current of 45 mAs at level C1–2 and with a tube current of 75 mAs at level C3–4. This

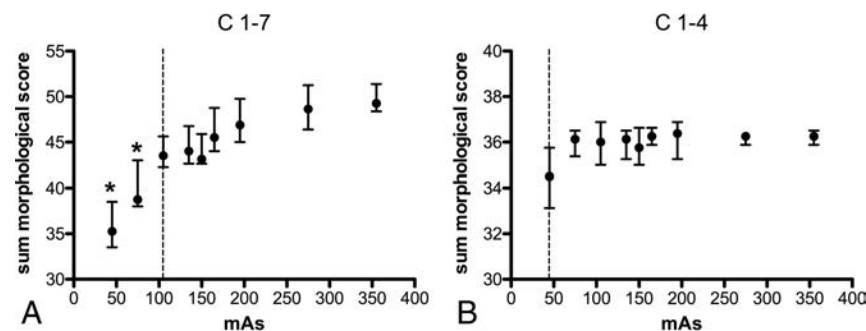


FIG 6. Analysis of morphologic characteristics for iterative reconstructed images shows significant impaired image quality with 75 mAs ($P = .0249$) and 45 mAs ($P = .0002$) compared with 355 mAs for all cervical spine levels (A). The dashed line (A) at 105 mAs represents the lowest value that is not significantly different in image quality compared with 355 mAs and can be recommended as the lowest tube current value with sufficient image quality. Analysis of cervical spine levels 1–4, which are not superimposed by the shoulders, shows no significant difference in image quality with any tube current compared with 355 mAs (B). Asterisks indicate values that are significantly different compared with 355 mAs ($P < .05$). Dots and bars indicate median and 25th to 75th percentiles.

Table 4: Minimum required dose for at least sufficient qualitative image quality of the cervical spine in IR and FBP images compared with 355 mAs (IR)^a

	Levels C1–T1		Levels C1–4	
	IR	FBP	IR	FBP
Image noise score	165 mAs DLP = 250 mGy × cm ED = 1.3 mSv	275 mAs DLP = 412 mGy × cm ED = 2.1 mSv	105 mAs DLP = 160 mGy × cm ED = 0.8 mSv	150 mAs DLP = 225 mGy × cm ED = 1.1 mSv
Morphologic characteristics score	105 mAs DLP = 160 mGy × cm ED = 0.8 mSv	105 mAs DLP = 160 mGy × cm ED = 0.8 mSv	45 mAs DLP = 65 mGy × cm ED = 0.3 mSv	45 mAs DLP = 65 mGy × cm ED = 0.3 mSv

Note:—ED indicates effective dose.

^a Data presented are the lowest applied tube current–time product at which scans showed no statistically significant differences in image quality compared with scans at the highest applied tube current–time product (355 mAs IR). Dose-length product and estimated effective dose are shown for each applied tube current–time product.

result is in line with a study performed by Kranz et al,¹⁸ who reported the importance of lowering both shoulders during CT of the cervical spine in patients with and without the use of CT table straps. At lower cervical spine levels, the radiation absorption was high due to superimposing the shoulder girdle, and image quality proved to be insufficient for most scans at these specific levels, even at the highest applied dose. Even in our small sample size of 30 patients who had a CT of the cervical spine in an emergency setting without attention being paid to the shoulder position during the scan, the shoulder girdle was at the level of C5–T1. Pull-down of the shoulders can be simple and efficient for low-dose CT of the cervical spine and should be performed whenever feasible. We believe the shoulder position is more relevant than the body mass index because the body mass index of our cadaveric specimens varied and ranged from 24 to 36 kg/m².

Reducing the reference tube current–time product of 275 mAs, which is recommended by the manufacturer for cervical spine imaging, to 105 mAs at 120 kVp reduces the effective dose by 62% from 2.1 to 0.8 mSv. With this low-dose CT protocol of the cervical spine, the effective dose is as low as the effective dose of 2 plain radiographs, which have been reported to be between 0.1 and 1 mSv.¹⁹ Geyer et al¹⁹ compared FBP images with adaptive statistical iterative reconstructions on 2 different 64-row multidetector CT systems (Light Speed VCT XT and Discovery CT 750HD; GE Healthcare, Milwaukee, Wisconsin) using a tube voltage of 120 kVp and automatic tube current modulation. Similarly, they could show that scanning with adaptive statistical iterative reconstructions at an estimated effective dose of 1.1 mSv is possible.¹⁹ It is well-known that fractures of the cervical spine can be missed on radiographs.^{20,21} Therefore, low-dose CT may be preferred over radiographs in settings of the cervical spine trauma.

The effects of changes of tube voltage on cervical spine CT were examined in a phantom study of Hoang et al.²² Their study revealed that reducing the voltage from 120 to 80 kVp for neck CT can result in a 50% reduction in the absorbed organ dose to the bone marrow of the cervical spine and mandible, without impairment in subjective image quality.²² However, in clinical settings, reduction of tube voltage down to 70 kVp seems to be diagnostic for soft-tissue evaluation but not necessarily for the cervical spine.²³ On the other hand, a lesser reduction of tube voltage to 100 kV showed a substantial reduction of the radiation dose with a small increase in objective image noise, but without differences in subjective image quality.¹⁷ In another study, Gleeson et al²⁴ used a higher kilovolt peak of 140 in a whole-body skeletal CT and reported dose reduction as a result of consecutive reduction of the tube current. Thus, additional dose reduction may be applicable with changes of tube voltage in addition to our applied tube current changes. We focused on bony structures in an emergency trauma setting without the use of intravenous contrast media; therefore, the beneficial effect of low kilovolt peak levels are negligible. High kilovolt peak levels have been suggested to be less susceptible to variations in body mass²⁴ and might improve image quality of the lower cervical spine, which is impaired by the shoulders. However, further studies are needed to support this hypothesis.

Our study has several limitations. First, formalin fixation of our cadaveric specimens hampered a low shoulder position. Thus,

cervical spine levels C5–T1 were superimposed by the shoulder girdle in all cadaveric specimens. We addressed this limitation in analyzing levels C1–4 separately. Second, formalin fixation might cause a change in radiation attenuation due to bone demineralization.²⁵ Third, because we applied automatic tube current modulation in the current study, the technical parameters could not be transferred automatically to the protocols of other CT machines. Fourth, we measured only noise in air, which might not be representative of noise in bone. However, measurements in soft tissue or the spinal cord were performed but were widely scattered; we attributed this feature to formalin fixation and insufficient distinguishability of the spinal cord from CSF. Fifth, no measurement of spatial resolution was performed. Sixth, the number of examined cadavers was small, hampering a meaningful comparison with respect to noise measurements. However, the published CT dose index values of our study can also be used to optimize the protocols of our vendor by using automatic tube current modulation.

CONCLUSIONS

Taking results from morphologic scores and image quality together, we conclude that clinically acceptable image quality of cervical spine CT for evaluation of bony structures of cadaveric specimens with variable body habitus can be achieved with a reference mAs as low as 105 at 120 kVp with IR. The high position of the shoulders is a limiting factor, even with high radiation doses. Pull-down of both shoulders during acquisition could improve image quality but may not be feasible in the trauma patient with unknown injuries.

ACKNOWLEDGMENTS

The authors thank our CT technician Geraldine Stadelmann for her excellent assistance in CT data acquisition.

REFERENCES

1. Daffner RH, Hackney DB. **ACR Appropriateness Criteria on suspected spine trauma.** *J Am Coll Radiol* 2007;4:762–75 CrossRef Medline
2. Saketkhoo DD, Bhargavan M, Sunshine JH, et al. **Emergency department image interpretation services at private community hospitals.** *Radiology* 2004;231:190–97 CrossRef Medline
3. Mower WR, Hoffman JR, Pollack CV Jr, et al; NEXUS Group. **Use of plain radiography to screen for cervical spine injuries.** *Ann Emerg Med* 2001;38:1–7 CrossRef Medline
4. Jaju A, Shaw HL, Don S, et al. **ALARA: impact of practice quality improvement initiative on dose reduction in pediatric voiding cystourethrogram.** *AJR Am J Roentgenol* 2015;205:886–93 CrossRef Medline
5. Ghetti C, Palleri F, Serreli G, et al. **Physical characterization of a new CT iterative reconstruction method operating in sinogram space.** *J Appl Clin Med Phys* 2013;14:4347 CrossRef Medline
6. Worrall JC, Jama S, Stiell IG. **Radiation doses to emergency department patients undergoing computed tomography.** *CJEM* 2014;16:477–84 CrossRef Medline
7. Becce F, Ben Salah Y, Verdun FR, et al. **Computed tomography of the cervical spine: comparison of image quality between a standard-dose and a low-dose protocol using filtered back-projection and iterative reconstruction.** *Skeletal Radiol* 2013;42:937–45 CrossRef Medline
8. Moscariello A, Takx RA, Schoepf UJ, et al. **Coronary CT angiography: image quality, diagnostic accuracy, and potential for**

- radiation dose reduction using a novel iterative image reconstruction technique-comparison with traditional filtered back-projection. *Eur Radiol* 2011;21:2130–38 CrossRef Medline
9. Winklehner A, Karlo C, Puipe G, et al. **Raw data-based iterative reconstruction in body CTA: evaluation of radiation dose saving potential.** *Eur Radiol* 2011;21:2521–26 CrossRef Medline
 10. Deak PD, Smal Y, Kalender WA. **Multisection CT protocols: sex- and age-specific conversion factors used to determine effective dose from dose-length product.** *Radiology* 2010;257:158–66 CrossRef Medline
 11. Schindera ST, Diedrichsen L, Müller HC, et al. **Iterative reconstruction algorithm for abdominal multidetector CT at different tube voltages: assessment of diagnostic accuracy, image quality, and radiation dose in a phantom study.** *Radiology* 2011;260:454–62 CrossRef Medline
 12. Willemink MJ, Leiner T, de Jong PA, et al. **Iterative reconstruction techniques for computed tomography part 2: initial results in dose reduction and image quality.** *Eur Radiol* 2013;23:1632–42 CrossRef Medline
 13. Gervaise A, Osemont B, Lecocq S, et al. **CT image quality improvement using Adaptive Iterative Dose Reduction with wide-volume acquisition on 320-detector CT.** *Eur Radiol* 2012;22:295–301 CrossRef Medline
 14. Pan X, Sidky EY, Vannier M. **Why do commercial CT scanners still employ traditional, filtered back-projection for image reconstruction?** *Inverse Probl* 2009;25:1230009 Medline
 15. Nelson RC, Feuerlein S, Boll DT. **New iterative reconstruction techniques for cardiovascular computed tomography: how do they work, and what are the advantages and disadvantages?** *J Cardiovasc Comput Tomogr* 2011;5:286–92 CrossRef Medline
 16. Wirth S, Meindl T, Treitl M, et al. **Comparison of different patient positioning strategies to minimize shoulder girdle artifacts in head and neck CT.** *Eur Radiol* 2006;16:1757–62 CrossRef Medline
 17. Mulkens TH, Marchal P, Daineffe S, et al. **Comparison of low-dose with standard-dose multidetector CT in cervical spine trauma.** *AJNR Am J Neuroradiol* 2007;28:1444–50 CrossRef Medline
 18. Kranz PG, Wylie JD, Hoang JK, et al. **Effect of the CT table strap on radiation exposure and image quality during cervical spine CT.** *AJNR Am J Neuroradiol* 2014;35:1870–76 CrossRef Medline
 19. Geyer LL, Körner M, Hempel R, et al. **Evaluation of a dedicated MDCT protocol using iterative image reconstruction after cervical spine trauma.** *Clin Radiol* 2013;68:e391–396 CrossRef Medline
 20. Woodring JH, Lee C. **Limitations of cervical radiography in the evaluation of acute cervical trauma.** *J Trauma* 1993;34:32–39 CrossRef Medline
 21. Acheson MB, Livingston RR, Richardson ML, et al. **High-resolution CT scanning in the evaluation of cervical spine fractures: comparison with plain film examinations.** *AJR Am J Roentgenol* 1987;148:1179–85 CrossRef Medline
 22. Hoang JK, Yoshizumi TT, Nguyen G, et al. **Variation in tube voltage for adult neck MDCT: effect on radiation dose and image quality.** *AJR Am J Roentgenol* 2012;198:621–27 CrossRef Medline
 23. Gnannt R, Winklehner A, Goetti R, et al. **Low kilovoltage CT of the neck with 70 kVp: comparison with a standard protocol.** *AJNR Am J Neuroradiol* 2012;33:1014–19 CrossRef Medline
 24. Gleeson TG, Byrne B, Kenny P, et al. **Image quality in low-dose multidetector computed tomography: a pilot study to assess feasibility and dose optimization in whole-body bone imaging.** *Can Assoc Radiol J* 2010;61:258–64 CrossRef Medline
 25. Fonseca AA, Cherubini K, Veeck EB, et al. **Effect of 10% formalin on radiographic optical density of bone specimens.** *Dentomaxillofac Radiol* 2008;37:137–41 CrossRef Medline

Clinical and Radiologic Characteristics of Deep Lumbosacral Dural Arteriovenous Fistulas

F. Jablawi, O. Nikoubashman, G.A. Schubert, M. Dafotakis, F.-J. Hans, and M. Mull



ABSTRACT

BACKGROUND AND PURPOSE: Spinal dural arteriovenous fistulas located in the deep lumbosacral region are rare and the most difficult to diagnose among spinal dural arteriovenous fistulas located elsewhere in the spinal dura. Specific clinical and radiologic features of these fistulas are still inadequately reported and are the subject of this study.

MATERIALS AND METHODS: We retrospectively evaluated all data of patients with spinal dural arteriovenous fistulas treated and/or diagnosed in our institution between 1990 and 2017. Twenty patients with deep lumbosacral spinal dural arteriovenous fistulas were included in this study.

RESULTS: The most common neurologic findings at the time of admission were paraparesis (85%), sphincter dysfunction (70%), and sensory disturbances (20%). Medullary T2 hyperintensity and contrast enhancement were present in most cases. The filum vein and/or lumbar veins were dilated in 19/20 (95%) patients. Time-resolved contrast-enhanced dynamic MRA indicated a spinal dural arteriovenous fistula at or below the L5 vertebral level in 7/8 (88%) patients who received time-resolved contrast-enhanced dynamic MRA before DSA. A bilateral arterial supply of the fistula was detected via DSA in 5 (25%) patients.

CONCLUSIONS: Clinical symptoms caused by deep lumbosacral spinal dural arteriovenous fistulas are comparable with those of spinal dural arteriovenous fistulas at other locations. Medullary congestion in association with an enlargement of the filum vein or other lumbar radicular veins is a characteristic finding in these patients. Spinal time-resolved contrast-enhanced dynamic MRA facilitates the detection of the drainage vein and helps to localize deep lumbosacral-located fistulas with a high sensitivity before DSA. Definite detection of these fistulas remains challenging and requires sufficient visualization of the fistula-supplying arteries and draining veins by conventional spinal angiography.

ABBREVIATIONS: AV = arteriovenous; CE-MRA = time-resolved contrast-enhanced dynamic MRA; FV = filum terminale vein; lsSDAVF = deep lumbosacral spinal dural arteriovenous fistula; SDAVF = spinal dural arteriovenous fistula

Despite being the most common spinal vascular malformation, spinal dural arteriovenous fistulas (SDAVFs) are rare and still underdiagnosed entities.^{1,2} The incidence of SDAVF in the general population is 5–10/million/year.^{3–5}

A recent meta-analysis of all case series that included >5 patients concluded that men were affected 5 times more often than women and that the mean age at the time of diagnosis was

55–60 years.⁶ If not treated properly, SDAVFs are associated with a considerable morbidity with progressive spinal cord symptoms.^{1,7,8} The clinical presentation of an SDAVF can be ascribed to venous congestion due to pathologic arteriovenous (AV) shunts in most cases.⁹ Initial symptoms are often non-specific.³ They include gait difficulties, symmetric or asymmetric sensory symptoms such as paraesthesia in 1 or both feet, diffuse or patchy sensory loss, and radicular pain.⁶ More than 80% of all SDAVFs are located between T6 and L2, but SDAVFs can occur anywhere along the dura of the spinal canal.⁷ According to various reports, fistulas in the sacral region occur in approximately 4% of patients with SDAVFs.^{6,10} However, larger series dealing with SDAVFs located in the deep lumbosacral region (lsSDAVF) are still lacking in the literature. The purpose of our study was to evaluate the clinical and radiologic data of 20 patients with lsSDAVFs presenting to our center between 1990 and 2017.

Received June 5, 2017; accepted after revision October 2.

From the Departments of Diagnostic and Interventional Neuroradiology (F.J., O.N., M.M.), Neurosurgery (G.A.S.), Diagnostic and Interventional Radiology (O.N.), and Neurology (M.D.), RWTH Aachen University Hospital, Aachen, Germany; and Department of Neurosurgery (F.-J.H.), Paracelsus Kliniken, Osnabrück, Germany.

Please address correspondence to Michael Mull, MD, Department of Diagnostic and Interventional Neuroradiology, RWTH Aachen University Hospital, Pauwelsstr 30, 52074 Aachen, Germany; e-mail: mmull@ukaachen.de



Indicates article with supplemental on-line photo.

<http://dx.doi.org/10.3174/ajnr.A5497>

MATERIALS AND METHODS

After obtaining permission from our local ethics board, we retrospectively evaluated the medical and radiologic reports of the RWTH Aachen University Hospital for patients diagnosed with SDAVF between January 1990 and March 2017. SDAVFs located above the L5 vertebral level and arteriovenous malformations of the filum terminale were excluded from our analysis.

Two experienced physicians analyzed the radiologic data blinded to all clinical data. A reference standard for statistical analysis was established in a consensus reading.

The extension of the T2 signal hyperintensity and the medullary contrast enhancement were qualified by the number of vertebral levels shown to be affected on T1 and T2 MR images. The appearance of the perimedullary veins was rated subjectively as absent, mild, or prominent due to their tortuous and dilated appearance on the T1 and T2 images.

The neurologic status was assessed according to the Aminoff-Logue disability score (AL-score). We re-evaluated the documented neurologic status at the time of admission (AL-score), the duration of symptoms from onset until diagnosis, as well as previous misdiagnosis and treatment.

Diagnostic Tools

MR Imaging/MRA. Before admission to our center, all 20 patients underwent extensive spinal DSA and/or MR imaging (0.5T and/or 1.5T). Two experienced physicians analyzed the radiologic data blinded to all clinical data. A reference standard for statistical analysis was established in a consensus reading.

The extension of the T2 signal hyperintensity and the medullary contrast enhancement was qualified by the number of vertebral levels shown to be affected on T1 and T2 MR images. The appearance of the perimedullary veins was rated subjectively as absent, mild, or prominent due to their tortuous and dilated appearance in the T1 and T2 images.

Moreover, 8/19 patients who were admitted after time-resolved contrast-enhanced MR angiography (CE-MRA) in our institution underwent additional spinal CE-MRA (1.5T) before DSA. MRA was performed on a clinical 1.5T MR imaging system with a phased array spine coil. The MR imaging protocol included 3 different pulse sequences: First, T2-weighted survey images were acquired to depict the course of the spinal cord as an anatomic reference. Second, MR fluoroscopy, performed with administration of a 2-mL test bolus of gadolinium-based contrast agent (gadopentetate dimeglumine; vial concentration, 0.5 mol/L), was used to determine the optimal scan delay between contrast injection and the start of the MRA acquisition. Finally, we performed a dynamic 2-phase 3D fast-spoiled gradient-echo pulse sequence with 45 mL of contrast agent. These 2 phases served to distinguish relatively early contrast enhancement, which mainly involves (normal and/or pathologic) arteries and arterialized veins, from later enhancement in which arteries and arterialized veins but also normal veins are visualized together. The number of sections was individually adjusted (range, 75–85 mm; 45–51 mm) to include the vertebral column, usually from T3 to S5. The precise evaluation was then achieved by MPR and maximum intensity projection. If initial CE-MRA findings were suspicious for a fistula zone, we performed additional coronal and axial contrast-

enhanced T1-weighted images focused on the suspected fistula region. Further details about our spinal CE-MRA technique have been previously described.^{1,11}

DSA. After re-evaluation of all previous spinal angiographic examinations performed elsewhere before admission to our center, we finally focused our further DSA examinations on the lumbosacral region.

DSA was performed with a femoral approach in a dedicated biplanar neuroangiographic suite. Standardized angiography included selective manual injections of 4–5 mL of 300 mg/mL of iodinated nonionic contrast medium into the lumbar and intercostal arteries. Furthermore, injections into both vertebral arteries, the costocervical arteries, the thyrocervical trunks, and the arterial feeders of the sacral region were added. Imaging was in the anteroposterior direction with 2 frames per second. Oblique and lateral views were added to elucidate the morphology of the AV shunt as well as the intradural course of the draining veins. Film sequences of at least 5–20 seconds were obtained. In 2 patients, in whom lsSDAVF was previously diagnosed elsewhere before referral to our center, our DSA examinations included solely the deep lumbosacral region.

Statistics

Pearson χ^2 tests and Fisher exact tests were used when applicable. Student *t* tests and Mann-Whitney *U* tests were used when applicable after testing for data distribution with a Shapiro-Wilk test. *P* values with an α level of $\leq .05$ were significant. All statistical analyses were performed with SPSS 23 software (IBM, Armonk, New York).

RESULTS

We identified 194 patients with SDAVFs located anywhere along the spine. Twenty (10.3%) of these patients had lsSDAVFs and were included in our study.

Clinical Features

Table 1 provides an overview of clinical findings in all 20 patients included in this study. Seventeen of 20 (85%) patients were men. The mean age was 63 ± 5 years (median, 63.5 years; range, 53–78 years). Overall, 16 (80%) patients experienced a gradual onset and progressive deterioration of neurologic function. The remaining 4 (20%) patients had a rapid deterioration of their motor function in the lower extremities within a mean period of 2.5 months (range, 1–4 months) and presented with a severe motor disability at time of admission.

However, the most common neurologic finding at time of admission at our institution was subjective and objective gait disturbances of the lower extremities. Paresis in the lower extremities was present in 17 (85%) patients. The remaining 3 patients (15%) had a slowly progressive ataxia and hypesthesia without manifest motor deficits. Sensory symptoms in various severities were documented in 18 (90%) patients and comprised diffuse loss of sensation and/or paresthesia in the lower extremities. One (case 15) of these 18 patients had dysesthesia from the T12 level downward. Fourteen (70%) patients presented with a sphincter dysfunction at time of admission to our institution.

The mean time between clinical onset and diagnosis in all 20 patients was 15 ± 12 months (median, 15 months; range, 1–36

Table 1: Clinical presentation of patients with deep lumbosacral spinal dural arteriovenous fistulas

Case No.	Age (yr)/Sex	Duration of Symptoms (mo)	Symptoms at Time of Diagnosis	AL-Score	Previous Diagnosis and Treatment
1	66, M	24	Paraparesis 3/5 ^a , sensory transverse lesion L5, sphincter dysfunction	3	Lumbar disc prolapse: discectomy L4–5
2	56, M	36	Paraparesis 3/5, sensory transverse lesion L2	3	
3	63, M	24	Paraparesis 2–3/5, sensory transverse lesion L1, sphincter dysfunction	4	
4	60, M	30	Paraparesis 4/5, sensory transverse lesion L4, sphincter dysfunction	3	Lumbar disc prolapse: discectomy L3–4, L4–5
5	71, M	14	Distal accentuated paraparesis 3/5, mild hypesthesia of the right leg	3	
6	66, M	18	Paraparesis 3/5, sensory transverse lesion L5, sphincter dysfunction	4	Lumbar spinal stenosis: dorsal decompression L1–2
7	55, M	2	Paraplegia and anesthesia below T8, sphincter dysfunction	5	
8	67, M	26	Paraparesis 4/5, sensory transverse lesion T12, sphincter dysfunction	2	Intramedullary tumor: biopsy
9	73, M	9	Paraparesis 3/5, sensory transverse lesion T5, sphincter dysfunction	4	Intramedullary tumor: biopsy
10	70, M	3	Paraparesis 3/5, sensory transverse lesion S1, sphincter dysfunction	4	
11	69, M	6	Paraparesis 1–2/5, sensory transverse lesion L4, sphincter dysfunction	5	
12	67, F	12	No paresis, hypesthesia below T11, ataxia	1	
13	63, M	1	Paraparesis 3/5, sphincter dysfunction	3	
14	61, M	11	Distal accentuated paraparesis 3/5, hypesthesia of the right leg, ataxia, sphincter dysfunction	3	Lumbar spinal stenosis: dorsal decompression and discectomies L4–5, L5–S1
15	67, F	9	Paraparesis 4/5, dysesthesia below T12, paresthesia on the dorsum of the left foot	2	Lumbar disc prolapse: discectomy L5–S1
16	63, M	ND	No paresis, sensory transverse lesion L1, ataxia, sphincter dysfunction	1	Repeat insufficient embolizations of lsSDAVF
17	55, M	10	Monoparesis left foot	1	Lumbar stenosis: dorsal decompression
18	78, M	4	Spastic paraparesis 3/5, paresthesia in both feet, sphincter dysfunction	4	
19	74, M	24	Paresis of the left leg 4/5, diffuse paresthesia of the lower extremities	2	
20	53, F	6	No paresis, diffuse paresthesia of the lower extremities, mild ataxia, mild sphincter dysfunction	1	

Note:—AL-Score indicates Aminoff-Logue disability score; ND, no data.

^aMuscle strength grade.

Table 2: Radiologic features of deep lumbosacral spinal dural arteriovenous fistulas

Case No.	MRI/MRA						DSA	
	Shunt Location	T2/T1 Hyperintensity (Extension)	Contrast Enhancement (Extension)	Perimedullary Vein Enlargement (Extension)	Prominent FV	Prominent Lumbar Vein	DSA until Diagnosis	Arterial Feeder
1	S1 R	T7-conus	T9–T10	Mild, T7–T8	No	No	4	Iliolumbar artery R
2	L5 R	T9–T11	T5–T11	Mild, T5–T11	No	Yes	4	Iliolumbar artery R
3	S1 L	T8-conus	Absent	Absent	Yes	No	4	Middle sacral artery L
4	S1 R	T9-conus	Absent	Mild, T10–T12	Yes	No	3	Iliolumbar artery R
5	S1 R	T3-conus	ND	ND	Yes	No	3	Iliolumbar artery R
6	L5 L	T8-conus	T9-conus	Mild, T10–T12	No	Yes	2	L5 L
7	S1 R	T6-conus	T8–T12	Mild, T7–T11	No	Yes	2	Lateral sacral artery L
8	S2 R	T10–T12	T11–T12	Mild, T11–T12	Yes	No	3	Lateral sacral artery R
9	L5 L	T4-conus	T9–T12	Absent	No	Yes	3	L4 L
10	S1 R	T4-conus	Absent	Severe, T6-conus	Yes	No	2	Lateral sacral artery R
11	S1 R	T6-conus	T12–L1	Mild, T6-conus	No	Yes	5	Iliolumbar artery bilateral
12	S3 R	T10-conus	T12	Severe, T7-conus	Yes	No	3	Lateral sacral artery bilateral
13	S1 R	T2-conus	T12-conus	Mild, T8-conus	Yes	No	4	Iliolumbar artery R
14	S2 L	T5-conus	T7-conus	Mild, T8–L3	Yes	No	4	Iliolumbar artery bilateral
15	S1 L	T5-conus	Absent	Severe, T7-conus	Yes	No	2	Lateral sacral artery L
16	S2 L	Absent	T10–11	Absent	Yes	No	2	Iliolumbar artery L
17	S1 L	T5-conus	T4–L1	Mild, T3–T4	Yes	No	2	Iliolumbar artery bilateral
18	S2 L	T8–T12	T8–T11	Mild, T9–T12	Yes	No	5	Iliolumbar artery bilateral
19	L5 R	T8-conus	T8-conus	Severe, T6–T12	No	Yes	2	Iliolumbar artery R
20	S2 R	T12-conus	T9-conus	Mild, T7–T11	No	Yes	1	Lateral sacral artery

Note:—R indicates right; L, left; ND, no data.

months). The mean Aminoff-Logue disability score at time of admission was 3 ± 1.5 (median, 3; range, 1–5).

Overall, 9 of 20 (45%) patients had undergone other treatments before admission to our institution. Six of these 9 patients underwent microsurgical lumbar dorsal decompression and/or discectomy due to the assumption of a spinal degenerative disease. Two other patients underwent a biopsy with the assumption of an intramedullary tumor. The remaining patient was admitted to our center due to recurrence of the lsSDAVF after repeat endovascular treatment performed elsewhere.

Radiologic Findings

Table 2 provides an overview of radiologic findings in all 20 patients.

On preoperative MR imaging, there was a medullary T2-weighted hyperintense signal in all except 1 patient (95%) (mean, 7 vertebral levels; range, 0–13 vertebral levels). The signal alteration involved the conus medullaris in 16 (80%) patients. There was intramedullary contrast enhancement in 15 (75%) patients (mean, 3 vertebral levels; range, 1–10 vertebral levels). Another 16 (85%) patients presented with an enlargement of the perimedul-

lary veins in the upper thoracic and/or thoracolumbar region in various extensions (mean, 4 vertebral levels; range, 0–7 vertebral levels). The filum terminale vein (FV) was dilated in 12 (60%) patients; in another 7 (35%) patients, other dilated lumbar veins were detected. In the remaining patient, no pathologic changes of the FV or the lumbar radicular veins were obvious in the presence of dilated perimedullary veins.

All 20 patients underwent repeat spinal DSA until a definite diagnosis was established (mean, 3 DSAs; range, 2–5 DSAs).

Overall, 8 (40%) patients received preoperative spinal CE-MRA, which revealed no evidence of an SDAVF in the upper thoracic or thoracolumbar region. However, in 7 of these 8 (88%) patients, CE-MRA demonstrated a prominent FV or lumbar radicular vein in the MIP, and MPR images suggested fistula localization in the deep lumbosacral region.

In 4 (20%) patients, the dilated perimedullary veins in the thoracolumbar region were microsurgically exposed and the direction of flow was assessed via Doppler sonography. The subsequent DSA was focused on the lumbosacral region, and a lsSDAVF could be identified in all 4 patients.

DSA revealed, in 17 (85%) patients, an arterial supply via the arches of the internal iliac arteries, namely the iliolumbar ($n = 11$) and the lateral sacral arteries ($n = 6$). The remaining 3 patients presented with an arterial supply via the middle sacral artery and the L4 and L5 segmental arteries, respectively.

In 5 (25%) of these 20 patients, DSA demonstrated a bilateral arterial supply via both the iliolumbar arteries ($n = 4$) and lateral sacral arteries ($n = 1$). There were no major complications related to angiography.

DISCUSSION

Because most studies that deal with lsSDAVFs are case reports and smaller case series, more comprehensive studies are lacking.¹² Thus, it was our aim to describe the clinical and radiologic features of lsSDAVFs in a series of 20 consecutive patients who presented to our institution. In the literature, the sacral region was considered a rare location for SDAVFs (4%).^{10,13} However, the incidence of lsSDAVF in our recent series accounts for up to 10.3% of patients with SDAVF. This higher rate of lsSDAVFs in our series is explained by the large number of patients with suspected SDAVFs who were referred to our institution as a tertiary referral center for spinal vascular diseases. Moreover, our current study also included SDAVFs localized at the L5 vertebral level ($n = 4$).

Nonetheless, to the best of our knowledge, our study represents, at the time of this writing, the largest single-center series dealing with clinical and radiologic features of lsSDAVF.

Clinical Features

The clinical presentations of SDAVFs of various locations are often nonspecific and may mimic a variety of conditions.^{14–16} Initial symptoms reported in the literature range from low back pain to complete spastic paraplegia.^{4,15,17} Comparing our recent findings with a previous analysis of SDAVFs presented to our center between 1989 and 2002, we observed no essential differentiations between clinical symptoms caused by lsSDAVFs and those caused by SDAVFs in other locations.¹⁸ Similar to patients with SDAVFs

in other locations, most patients in our recent study had a slightly progressive paraparesis, sensory abnormalities, and sphincter dysfunctions at time of admission.¹⁸

Moreover, the relatively high rate of misdiagnosis in patients with lsSDAVFs (40%) demonstrates the difficulties in detecting the suspected fistula and the broad spectrum of probable differential diagnoses.

These difficulties, in turn, may lead to clinically relevant delays until the correct diagnosis is established. It has been hypothesized that clinical symptoms become more severe the longer the correct diagnosis and treatment are delayed and the venous congestion persists.^{4,10,19} We could not identify a significant correlation between symptom duration and the severity of morbidity for all 20 patients ($P = .41$). Nevertheless, intraindividual progressive deterioration of symptoms was present in all our patients.

Radiologic Findings

Consistent with findings of fistulas in other locations, typical MR imaging findings in our series were a combination of intramedullary edema and dilated perimedullary vessels.^{9,20} In most cases, the spinal cord demonstrated contrast enhancement reflecting a disturbance of the blood-cord barrier in the presence of venous congestion.^{1,21,22}

Nevertheless, the enlargement of the perimedullary veins was absent and mild in 14 (70%) patients and prominent in only 4 (20%) patients. Additionally, dilated FV or radicular veins in the deep lumbosacral region were the hallmark of lsSDAVFs in our MR images and were present in 95% of patients.

In all 7 of 8 (88%) patients who underwent CE-MRA, the arterialized FV and lumbar veins appeared even more prominent than the enlarged perimedullary veins in the respective cases. Moreover, the multiplanar reconstruction of CE-MRA images in our series allowed a sufficient differentiation between FV and other lumbar veins. At least 3-mm sagittal sections in T1/T2 MR images are necessary to identify these veins.

The prominent appearance of the FV in patients with lsSDAVF has been previously discussed in a few reports.^{20,23} However, our recent findings demonstrate that the deep lumbosacral course of either a prominent arterialized FV or other lumbar radicular veins combined with typical medullary congestion should always evoke the differential diagnosis of an AV shunt in this region, even in the absence of prominent perimedullary veins (Figure).

One of the milestones in the diagnostic evaluation of spinal vascular malformations was the development of time-resolved contrast-enhanced MR angiography.^{1,11} In a series reported by Mull et al,¹ the MRA-derived level of the feeding artery in SDAVFs agreed with DSA findings in 14 of 19 cases, including 2 patients with lsSDAVF at the S1–2 level. In the remaining 5 cases, a mismatch of only 1 vertebral level (not side) was noted for the feeding artery.

CE-MRA facilitates localizing the AV shunt by focusing the DSA on the assumed fistula region, resulting in a shorter intervention time, less contrast agent application, and a lower exposure dose.^{1,11}

In fact, the need for microsurgical exploration to identify the blood flow in the arterialized veins in the thoracolumbar region

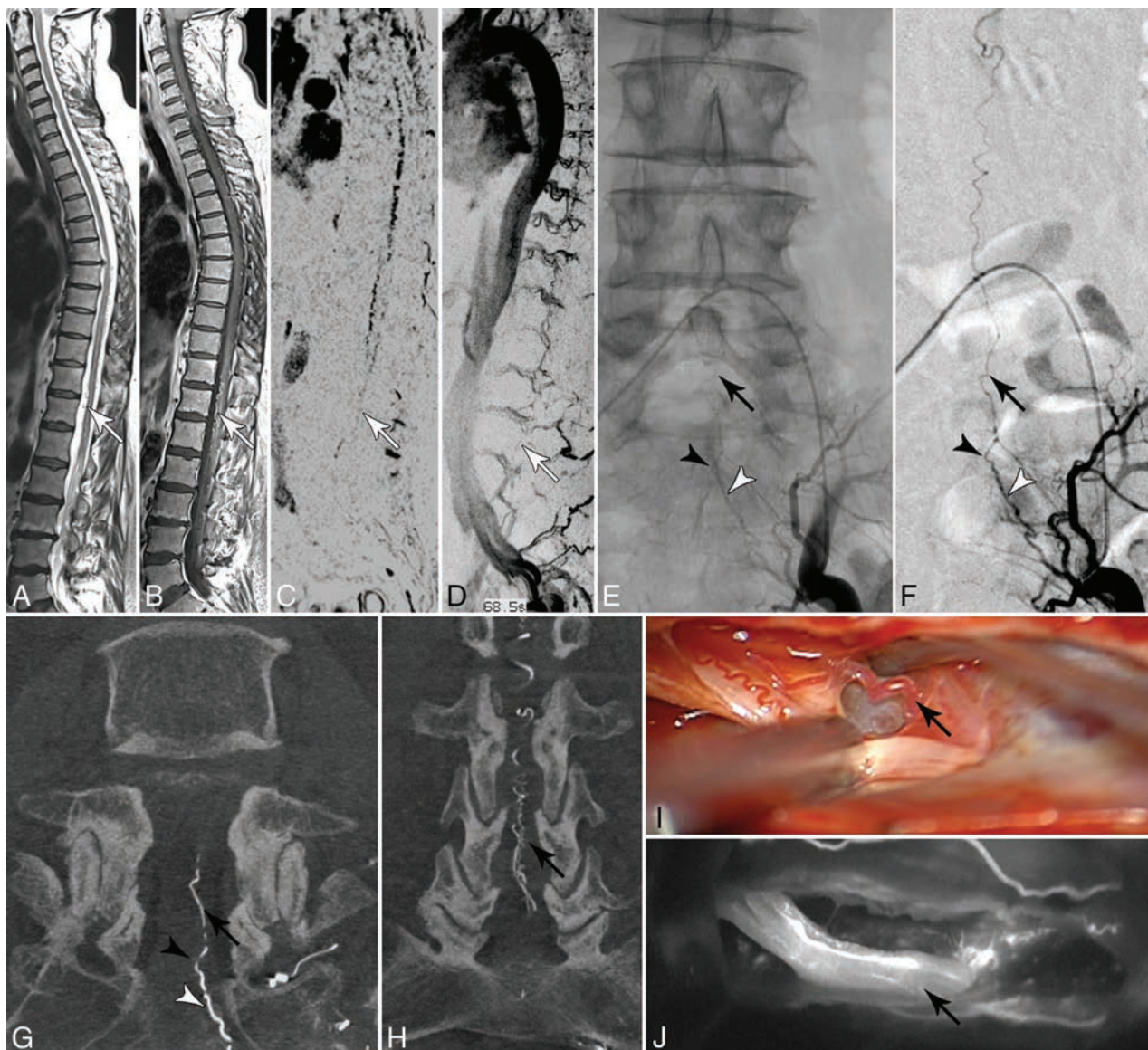


FIGURE. A and B, Sagittal T2- and contrast-enhanced T1-weighted images reveal congestive myelopathy and dilated perimedullary veins (white arrows). C and D, Spinal CE-MRA shows dilated radicular veins in the lumbar region suspicious for an SDAVF in the lumbosacral region (white arrows). E–H, DSA examinations identify the fistula in the dural sleeve of the left S2 root (black arrowhead) supplied via the lateral sacral artery (white arrowhead). Note the upward draining sacral radicular vein (black arrow). I and J, Intraoperative indocyanine green angiography confirms the intradural course of the arterialized draining vein (black arrow) embedded at the ventral side of the S2 nerve root.

decreased in our series after establishment of the CE-MRA technique in our center.

Due to our recent experience, we found that more advanced 4D-MRA techniques with better time resolution may provide additional information about the flow direction in the intradural arterialized veins.

DSA remains the criterion standard for the definite diagnosis of SDAVF.^{1,3,14,21} Whenever a spinal AV shunt is suspected, an angiography of all thoracic and lumbar segmental arteries is required. In nonconclusive cases, further examination of cervical and pelvic arterial feeders is required.²⁰

However, despite technologic advances, DSA of the pelvic region remains technically challenging. A trivial-but-common problem that resulted in an impaired DSA image quality was bowel dysfunction, present in most patients in our series. We

could overcome these difficulties by the prophylactic administration of spasmolytic medication 1 day before or during the DSA.

Moreover, due to the low-flow character of these fistulas and the long drainage up to the conus medullaris, lsSDAVFs could be easily missed by inexperienced readers during DSA. Thus, prolonged DSA series with additional oblique and lateral projections are recommended in these patients.

The fistula locations in our series ranged from L5 to S3 level. Sixteen of 20 (85%) demonstrated an arterial supply via arches of the internal iliac arteries. The arterial supply of the remaining 3 fistulas was unusual: Case 3 presented with an lsSDAVF localized at the S1 level, with an arterial supply via the middle sacral artery; cases 6 and 9 presented with a fistula localized at the L5 level with an arterial supply via an atypical L5 segmental artery arising from the abdominal aorta and a descending L4 segmental artery, re-

spectively. Most interesting, fistulas localized at the L5 level ($n = 4$) presented with a broad variety of arterial feeders comprising the iliolumbar arteries and L4 and L5 segmental arteries.

Moreover, 5 (25%) of 20 patients in our series presented with a bilateral arterial supply via the arches of both internal iliac arteries (On-line Figure).

The detection of a bilateral arterial supply of an lsSDAVF was significantly higher in patients who were diagnosed after establishment of CE-MRA in 2003 in our center ($P < .05$). This finding reflects growth in our own experience in diagnosing these fistulas and the development of multimodal diagnostic tools.

The complex angioarchitecture in the deep lumbosacral region with a variant and frequently bilateral arterial supply may contribute to difficulties in identifying the fistula. Thus, an optimal DSA examination for the sacral region requires selective and long visualization of all lumbar segmental arteries, the middle sacral artery, and both internal iliac arteries and their arches. If these examinations remain nonconclusive, super selective catheterization of potential feeding arteries in the pelvic and lumbar region may be indicated. Moreover, the bilateral arterial supply in these patients could be sufficiently visualized in series with super-selective distal microcatheter injection, resulting in a better opacification of the feeding arteries.

Whenever the AV shunt is identified, the ipsilateral and contralateral feeding arteries above and below the fistula should be examined to exclude the possibility of multiple arterial feeders to the fistula zone from the adjacent arteries.^{1,2,4}

Nonetheless, once an AV shunt in the deep lumbosacral region is suspected, the most probable differential diagnosis for an SDAVF is an arteriovenous malformation of the filum terminale. In both cases, namely SDAVF and filum terminale-AVM, symptoms are caused by medullary venous congestion resulting in comparable myelopathic disorders and a progressive clinical course. In contrast to lsSDAVFs, the filum terminale artery arising from the anterior spinal artery predominantly feeds a filum terminale-AVM.

Even though the filum terminale-AVM is an extremely rare disease, one should be aware of this differential diagnosis in every suspected AV shunt located in the deep lumbosacral region.

In inconclusive repeat DSAs, the search for the exact fistula localization should not be discontinued in patients with a high probability of an SDAVF.^{2,5} In certain cases, a surgical exploration of the arterialized perimedullary veins might be helpful; to facilitate the detection of the fistula localization in subsequent DSA in 4 patients with repeat nonconclusive DSA examinations, we microsurgically exposed the arterialized perimedullary veins in the thoracolumbar region at the level with the greatest vein enlargement. We then assessed the direction of blood flow in these veins via intraoperative Doppler sonography. In all 4 cases, a caudocranial blood flow was detected. Thus, subsequent DSA examinations were focused on the thus assumed deep lumbosacral origin of the fistula. This strategy was successful in all 4 cases.

In summary, we note that lsSDAVFs remain diagnostically challenging, even in experienced hands. Spinal CE-MRA provides, in most the cases, a sufficient visualization of the perimedullary and lumbar draining veins and facilitates the subsequent DSA examinations. However, for a precise fistula localization,

DSA remains the criterion standard diagnostic tool. The low-flow characteristics of these fistulas with a frequently variant arterial supply and problems of optimal visualization may cause serious difficulties in localizing the fistula via DSA. Thus, optimized DSA examinations require a sufficient visualization of all potential feeding arteries and draining veins in the pelvic and lumbar regions.

In practice, prolonged series as well as additional oblique and special lateral projections help visualize the intradural course of the draining vein up to the conus.

CONCLUSIONS

Clinical symptoms caused by lsSDAVFs are often nonspecific and may mimic a variety of conditions. The presence of a dilated FV and/or lumbar radicular vein on MR imaging/CE-MRA combined with typical congestive medullary changes should always evoke the differential diagnosis of an arteriovenous shunt in the deep lumbosacral region, even in the absence of perimedullary dilated veins. However, identifying lsSDAVF via DSA remains challenging due to the complex and variant spinal arterial supply in this region and the difficulties in the optimal visualization of the lumbosacral region.

REFERENCES

1. Mull M, Nijenhuis RJ, Backes WH, et al. **Value and limitations of contrast-enhanced MR angiography in spinal arteriovenous malformations and dural arteriovenous fistulas.** *AJNR Am J Neuroradiol* 2007;28:1249–58 CrossRef Medline
2. Jablawi F, Nikoubashman O, Mull M. **Arterial hypertension is associated with symptomatic spinal dural arteriovenous fistulas.** *World Neurosurg* 2017;103:360–63 CrossRef Medline
3. Thron A. **Spinal dural arteriovenous fistulas** [in German]. *Radiologe* 2001;41:955–60 CrossRef Medline
4. Behrens S, Thron A. **Long-term follow-up and outcome in patients treated for spinal dural arteriovenous fistula.** *J Neurol* 1999;246:181–85 CrossRef Medline
5. Thron A, Krings T, Otto J, et al. **The transdural course of radicular spinal cord veins: a microangiographical and microscopical study.** *Clin Neuroradiol* 2015;25:361–69 CrossRef Medline
6. Jellema K, Tijssen CC, van Gijn J. **Spinal dural arteriovenous fistulas: a congestive myelopathy that initially mimics a peripheral nerve disorder.** *Brain* 2006;129:3150–64 CrossRef Medline
7. Krings T, Geibprasert S. **Spinal dural arteriovenous fistulas.** *AJNR Am J Neuroradiol* 2009;30:639–48 CrossRef Medline
8. Koch C. **Spinal dural arteriovenous fistula.** *Curr Opin Neurol* 2006;19:69–75 CrossRef Medline
9. Krings T, Mull M, Gilsbach JM, et al. **Spinal vascular malformations.** *Eur Radiol* 2005;15:267–78 CrossRef Medline
10. Schaat TJ, Salzman KL, Stevens EA. **Sacral origin of a spinal dural arteriovenous fistula: case report and review.** *Spine (Phila Pa 1976)* 2002;27:893–97 CrossRef Medline
11. Nijenhuis RJ, Mull M, Wilmsink JT, et al. **MR angiography of the great anterior radiculomedullary artery (Adamkiewicz artery) validated by digital subtraction angiography.** *AJNR Am J Neuroradiol* 2006;27:1565–72 Medline
12. Nishio A, Ohata K, Takami T, et al. **Atypical spinal dural arteriovenous fistula with supply from the lateral sacral artery.** *J Clin Neurosci* 2007;14:65–68 CrossRef Medline
13. Jellema K, Canta LR, Tijssen CC, et al. **Spinal dural arteriovenous fistulas: clinical features in 80 patients.** *J Neurol Neurosurg Psychiatry* 2003;74:1438–40 CrossRef Medline
14. Gilbertson JR, Miller GM, Goldman MS, et al. **Spinal dural arterio-**

- venous fistulas: MR and myelographic findings.** *AJNR Am J Neuro-radiol* 1995;16:2049–57 Medline
15. Koenig E, Thron A, Schrader V, et al. **Spinal arteriovenous malformations and fistulae: clinical, neuroradiological and neurophysiological findings.** *J Neurol* 1989;236:260–66 CrossRef Medline
 16. Atkinson JL, Miller GM, Krauss WE, et al. **Clinical and radiographic features of dural arteriovenous fistula, a treatable cause of myelopathy.** *Mayo Clin Proc* 2001;76:1120–30 CrossRef Medline
 17. Schrader V, Koenig E, Thron A, et al. **Neurophysiological characteristics of spinal arteriovenous malformations.** *Electromyogr Clin Neurophysiol* 1989;29:169–77 Medline
 18. Mull M. **Durchblutungsstörungen des Rückenmarks: neurologische Untersuchungen zur Pathogenese und Strategien der Diagnosesicherung.** Department of Diagnostic and Interventional Neuroradiology, University Hospital Aachen. 2004. https://www.researchgate.net/publication/33987973_Durchblutungsstorungen_des_Ruckenmarks_neuroradiologische_Untersuchungen_zur_Pathogenese_und_Strategien_der_Diagnosesicherung. Accessed 2003
 19. Larsen DW, Halbach VV, Teitelbaum GP, et al. **Spinal dural arteriovenous fistulas supplied by branches of the internal iliac arteries.** *Surg Neurol* 1995;43:35–40; discussion 40–41 CrossRef Medline
 20. Burguet JL, Dietemann JL, Wackenheim A, et al. **Sacral meningeal arteriovenous fistula fed by branches of the hypogastric arteries and drained through medullary veins.** *Neuroradiology* 1985;27:232–37 CrossRef Medline
 21. Thron A, Mull M, Reith W. **Spinal arteriovenous malformations** [in German]. *Radiologe* 2001;41:949–54 CrossRef Medline
 22. Hetts SW, Moftakhar P, English JD, et al. **Spinal dural arteriovenous fistulas and intrathecal venous drainage: correlation between digital subtraction angiography, magnetic resonance imaging, and clinical findings.** *J Neurosurg Spine* 2012;16:433–40 CrossRef Medline
 23. Chen CJ, Hsu HL. **Engorged and tortuous intradural filum terminale vein as a sign of a sacral dural arteriovenous malformation.** *Eur J Radiol* 2002;44:152–55 CrossRef Medline
 24. Thron AK. **Applications in spinal dural AV fistulas.** In: *Vascular Anatomy of the Spinal Cord: Radioanatomy as the Key to Diagnosis and Treatment*. 2nd ed. Cham: Springer-Verlag; 2016
 25. Huffmann BC, Gilsbach JM, Thron A. **Spinal dural arteriovenous fistulas: a plea for neurosurgical treatment.** *Acta Neurochir (Wien)* 1995;135:44–51 CrossRef Medline

Cervical Cord Atrophy and Long-Term Disease Progression in Patients with Primary-Progressive Multiple Sclerosis

¹F.X. Aymerich, ²C. Auger, ³J. Alonso, ⁴M. Alberich, ⁵J. Sastre-Garriga, ⁶M. Tintoré, ⁷X. Montalban, and ⁸A. Rovira

ABSTRACT

BACKGROUND AND PURPOSE: Cervical cord atrophy has been associated with clinical disability in multiple sclerosis and is proposed as an outcome measure of neurodegeneration. The aim of this study was to quantify the development of cervical cord atrophy and to evaluate its association with disability progression in patients with primary-progressive multiple sclerosis.

MATERIALS AND METHODS: Thirty-one patients with primary-progressive multiple sclerosis underwent 1.5T brain and spinal cord MR imaging at baseline and 6–7 years later. The cervical spinal cord from C1 to C5 was segmented to evaluate the normalized overall cross-sectional area and the cross-sectional area of C2–C3, C3–C4, and C4–C5. The annualized rates of normalized cross-sectional area loss were also evaluated. To estimate clinical progression, we determined the Expanded Disability Status Scale score at baseline and at 2 and 14 years after baseline to compute the normalized area under the curve of the Expanded Disability Status Scale and the Expanded Disability Status Scale changes from baseline to the follow-up time points. Associations between the cord cross-sectional area and brain MR imaging and clinical measures were also investigated. Finally, the value of all these measures for predicting long-term disability was evaluated.

RESULTS: Some normalized cross-sectional area measurements showed moderate correlations with the normalized area under the curve of the Expanded Disability Status Scale, ranging from -0.439 to -0.359 ($P < .05$). Moreover, the annualized rate of the normalized mean cross-sectional area loss and the baseline Expanded Disability Status Scale were independent predictors of long-term disability progression.

CONCLUSIONS: These data indicate that development of cervical cord atrophy is associated with progression of disability and is predictive of this event in patients with primary-progressive MS.

ABBREVIATIONS: aNMCSA = annualized normalized mean cross-sectional area loss rate between the baseline and follow-up examination; BPF = brain parenchymal fraction; CSA = cross-sectional area; EDSS = Expanded Disability Status Scale; NMCSA = normalized mean CSA; NCSA23 = normalized CSA at the C2–C3 level; NCSA34 = normalized CSA at the C3–C4 level; NCSA45 = normalized CSA at the C4–C5 level; PPMS = primary-progressive multiple sclerosis; T1LV = T1 lesion volume; T2LV = T2 lesion volume

Primary-progressive multiple sclerosis (PPMS) is characterized by sustained progression of disability from disease onset and is typically associated with severe motor impairment.^{1,2} The rate at which disability progresses is highly variable, but impairment

occurs faster early in the disease course and reflects, in part, neuroaxonal loss and spinal cord dysfunction.³

The spinal cord is a clinically relevant site of the central nervous system and is often affected in multiple sclerosis. Focal and diffuse cord abnormalities, particularly in the cervical cord segment, have been described in up to 90% of patients with MS.⁴ MR imaging measurement of cervical cord atrophy in patients with this disease provides valuable additional information related to disability that cannot be obtained from brain metrics.⁵ A progressive reduction of the cervical cord cross-sectional area (CSA) occurs in PPMS,^{6–9} and spinal cord atrophy has been shown to correlate with the severity of clinical disability.^{10–12} Moreover, some cross-sectional studies have reported that spinal cord atrophy is an independent predictor of disability progression.^{11,12}

Nonetheless, the relationship between spinal cord area changes and worsening of disability has not been consistent among studies: Some authors describe an association,^{6,9} whereas others do

Received August 8, 2017; accepted after revision October 16.

From the Magnetic Resonance Unit (F.X.A., C.A., J.A., M.A., A.R.), Department of Radiology, and Centre d'Esclerosi Múltiple de Catalunya (J.S.-G., M.T., X.M.), Department of Neurology/Neuroimmunology, Hospital Universitari Vall d'Hebron, Universitat Autònoma de Barcelona, Barcelona, Spain; and Department of Automatic Control (F.X.A.), Universitat Politècnica de Catalunya–Barcelona Tech, Barcelona, Spain.

Paper previously presented, in part, at: Annual Meeting of the European Committee for Treatment and Research in Multiple Sclerosis, October 7–10, 2015; Barcelona, Spain.

Please address correspondence to F. Xavier Aymerich, PhD, Magnetic Resonance Unit, Hospital Universitari Vall d'Hebron, P. Vall d'Hebron 119–129, 08035 Barcelona, Spain; e-mail: xavier.aymerich@idi.gencat.cat

<http://dx.doi.org/10.3174/ajnr.A5495>

not.^{7,8} This discrepancy may be explained by several factors, such as differing sample sizes, follow-up periods, and methods used to measure the cord CSA.^{7,13-15}

Although some cross-sectional studies^{11,12} have demonstrated the value of spinal cord atrophy as an independent predictor of clinical outcome, only a few longitudinal studies^{9,16,17} have specifically focused on analyzing the clinical relevance of this finding in patients with MS, and these include a short follow-up or were not focused on PPMS.

Another factor to be taken into account is the method used for measuring the cervical cord CSA, because the optimal approach has not yet been identified. One of the most recently used is the proposed method of Horsfield et al,¹⁸ based on application of active surface models and known as the active surface method. With this approach, the CSA can be measured at specific levels and along extended portions of the cord with lower variability than other methods used in this region, such as the one proposed by Losseff et al.¹⁰ Some recent studies^{11,17,19} have used the active surface method for this purpose.

The aim of this study was to quantify the development of cervical cord atrophy and evaluate its association with the progression of clinical disability long term in patients with PPMS.

MATERIALS AND METHODS

Subjects

Thirty-one patients with PPMS were included in the study. These patients had been initially enrolled in a 2-year, double-blind, placebo-controlled, Phase II pilot study, in which patients with PPMS or “transitional” forms of MS received either interferon β -1b at doses of 8 MIU or a placebo for 24 months.²⁰

This study was approved by the Vall d’Hebron Clinical Research Ethics Committee, who waived the requirement of written informed consent.

Clinical Measures

The Expanded Disability Status Scale (EDSS) score and disease duration were the clinical measures included. The EDSS was assessed at 3 time points: baseline and 2 years and approximately 14 years after baseline (14.12 ± 2.88 years). Because EDSS values were not uniformly distributed across time, we used an averaged EDSS across time. To determine this value, we calculated the area under the curve of the EDSS. The area under the curve of the EDSS values was normalized to the maximum area under the curve of the EDSS in the time interval measured to obtain the normalized area under the curve of the EDSS (NAUCEDSS) value according to the following expression:

$$NAUCEDSS = \frac{\sum_{k=0}^1 [(t_{k+1} - t_k)[EDSS_{k+1} + EDSS_k]]}{10(t_2 - t_0)},$$

where t_k is the number of months from baseline (t_0) in the time point $k = (0, 1, 2)$, and $EDSS_k$ is the EDSS measurement at the time point k .

Moreover, to obtain a prediction of long-term EDSS change, the differences between the last measurement and the baseline EDSS measurement were computed for each patient.

MR Imaging Acquisition

Two MRIs were analyzed in this group of patients, a baseline examination and a follow-up one obtained 6.30 ± 0.23 years (range, 5.92–7.17 years) after the baseline study.

All MR imaging studies were performed on a 1.5T magnet (Magnetom Vision Plus; Siemens, Erlangen, Germany) using a quadrature transmit/receive head coil for the brain studies and a quadrature receive-only neck phased array coil for the cervical studies. In each brain examination, we obtained the following sequences: a transverse, T2-weighted, dual-echo turbo spin-echo sequence (TR, 3000 ms; TE, 14–85 ms; echo-train length, 5; acquisitions, 1); and a transverse T1-weighted, spin-echo sequence (TR, 667 ms; TE, 12 ms; acquisitions, 2). For both sequences, 46 interleaved contiguous axial sections with 3-mm thickness were acquired covering the whole brain, with a 192×256 matrix and 250-mm FOV, yielding an in-plane spatial resolution of approximately $1 \times 1 \text{ mm}^2$. Following the brain study, a 3D volume image centered on the cervical spine was obtained using a magnetization-prepared rapid acquisition of gradient echo sequence with 128 partitions in the sagittal plane of 1.25-mm thickness and the following parameters: TR/TE/TI, 9.7/450/4.2 ms; flip angle, 15°; 256 phase-encodings in the z-direction; 1 average; 250-mm FOV; 256×256 matrix.

MR Imaging Analysis

Cross-sectional area measurements were assessed using a semiautomatic segmentation method based on an active surface model of the cord surface with intrinsic smoothness constraints,¹⁸ provided in the Jim 6.0 software package (<http://www.xinapse.com/home.php>). Briefly, the sagittal 3D T1-weighted scans of the cervical cord from each patient were first reformatted in the axial plane and resampled to 1-mm section thickness. Then, the active surface method was applied to each scan to estimate the cord surface and cord centerline (Fig 1). An initial estimate of the cord centerline was manually provided by placing landmarks at the extremes of the cord region to be studied and at approximately each 10 mm between these landmarks. Thus, the region studied comprised the segment from the most cranial section in which the odontoid process was visible down to the C5 superior margin. A single operator placed all landmarks. The cord centerline and cord outlines at each section were calculated using a segmentation algorithm, with steadily increasing refinement of the active surface model describing the cord outline. The total cord length was calculated in each region as the distance along the centerline between the upper and lower landmarks. In each region, the mean cervical cord CSA was calculated as the total cord volume divided by the cord length, and CSA was also measured at the C2–C3 (CSA23), C3–C4 (CSA34), and C4–C5 (CSA45) discs. CSA measurements were then normalized (NMCSA, NCSA23, NCSA34, NCSA45)—in a manner similar to the proposal of Lin et al²¹—to the intracranial cross-sectional area measured at the inferior margins of the corpus callosum in an axial slice of the proton density-weighted image of each patient, as previously suggested.¹⁸ This adjustment was performed because cranial size was found to significantly correlate with the cord area in healthy controls.²² In addition to the normalized CSA measurements, the annualized (normalized) CSA loss rates between the baseline and follow-up

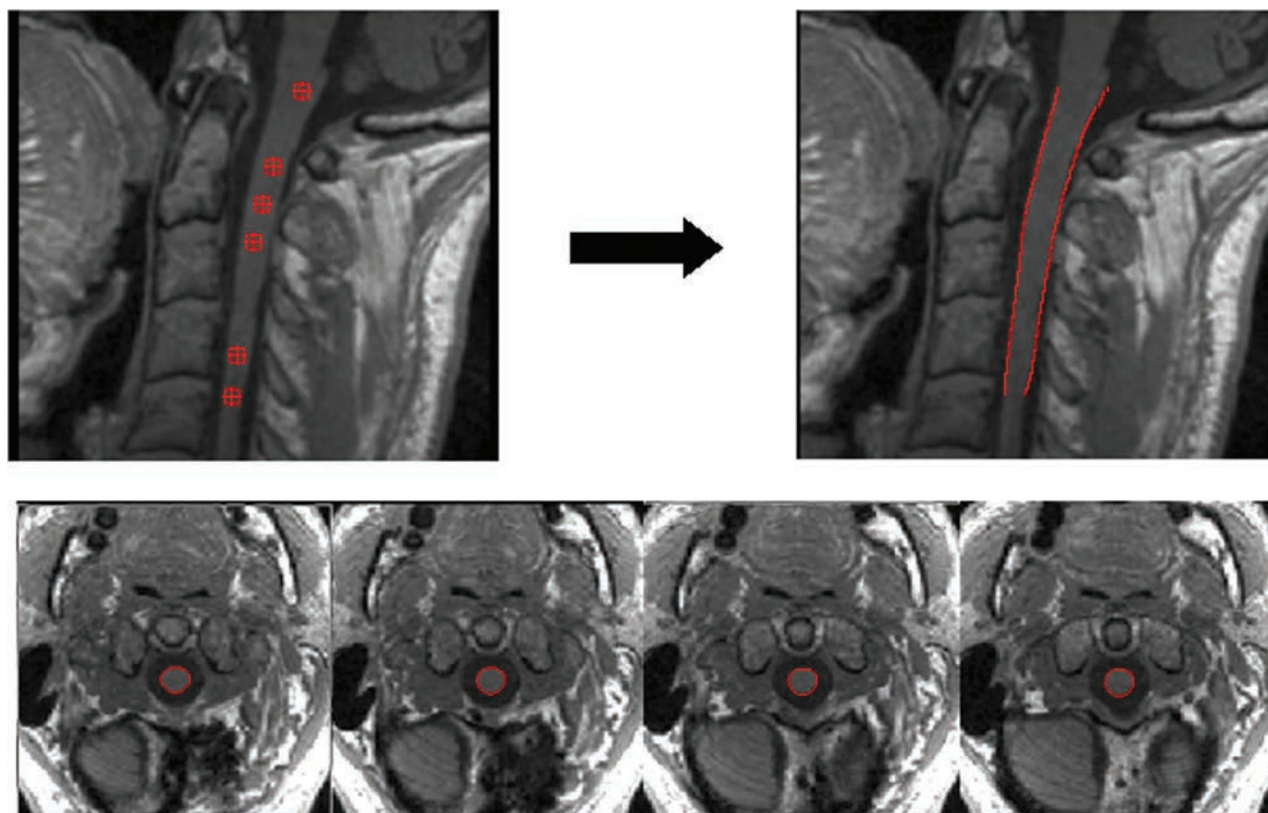


FIG 1. An example of the cord surface estimation obtained using the active surface method. The *upper left* image shows the location of the landmarks (*red markers*) that can be visualized in this sagittal slice. These landmarks were manually placed in the axial slices at the center area of the cord with a distance between them of approximately 10 mm. The *upper right* image shows the cord outline estimation (*red lines*). The lower axial slices show some examples of the spinal cord segmentation obtained (*region within red contour*).

examination (aNMCSA, aNCSA23, aNCSA34, aNCSA45) were also evaluated.

To calculate the brain T2 lesion volume (T2LV), the same neuroradiologist initially analyzed and marked lesions found on brain MR imaging on the proton density–weighted hard copies with cross-reference to the T2-weighted images. All lesions marked on the hard copies were outlined on the computer image using a semiautomatic local thresholding contour technique (D.L. Plummer; University College, London, England)²³; in cases in which the lesion could not be outlined satisfactorily with this approach, manual outlining was performed. A computer program then summed all the individual lesion volumes, and a final T2LV was generated and stored in a data base specifically designed for the study. To calculate the T1 lesion volume (T1LV), we used an automatic segmentation algorithm that measures T1LV from the initial T2 lesion segmentation that was used as a lesion mask.²⁴

Brain atrophy was evaluated by measuring the brain parenchymal fraction (BPF) according to a previously described algorithm.²⁵

Statistical Analysis

To evaluate the longitudinal cord CSA changes, differences between the baseline and follow-up CSA measurements were assessed using a *t* test for paired samples. Correlations of the cord CSA with the clinical and brain MR imaging measures were assessed using the Pearson correlation coefficient. To create a pre-

Table 1: Main baseline demographic, clinical, and conventional MRI characteristics

	Patients with MS
Median age (range) (yr)	51 (33–61)
Men/women	19:12
Mean disease duration at baseline (range) (yr)	11.74 (2–33)
Median EDSS score at baseline (range)	5.5 (3.0–6.5)
Mean brain T2LV at baseline (SD) (mL)	18.12 (20.63)
Mean brain T1LV at baseline (SD) (mL)	7.41 (8.47)
Mean BPF at baseline (SD)	73.13% (5.86%)

dictive model for the Δ EDSS, linear regression analysis was performed. A stepwise method was used to select the most relevant measures among the following: baseline CSA measures, annualized cord CSA loss rates, brain MR imaging measures, disease duration, and baseline EDSS scores. Age at baseline was also introduced in the model as a covariate. All statistical analyses were performed using SPSS (IBM, Armonk, New York). *P* values < .05 were considered statistically significant.

RESULTS

Clinical and Conventional MR Imaging Measures

The main baseline demographic, clinical, and conventional MR imaging characteristics of the patients are shown in Table 1. During clinical follow-up, the median EDSS score was 6.0 (range, 4.0–8.5) at 24 months and 7.5 (range, 4.0–9.5) at last measurement, approximately 14 years after baseline (14.12 ± 2.88 years) (Table 2). The mean T2 and T1 lesion volumes increased to

21.56 ± 20.65 mL and 9.53 ± 9.32 mL, respectively, whereas the mean BPF decreased by 3.83% at 6–7 years of radiologic follow-up (Table 3). The T2LV, T1LV, and BPF changes were statistically significant ($P < .001$).

Table 2: Evolution of the EDSS

	Baseline	2 Years	14 Years
Median EDSS score (range)	5.5 (3.0–6.5)	6.0 (4.0–8.5)	7.5 (4.0–9.5)

Table 3: MRI characteristics at follow-up

	Follow-Up
Mean brain T2LV (SD) (mL)	21.56 (20.65)
Mean brain T1LV (SD) (mL)	9.53 (9.32)
Mean BPF (SD)	70.33% (5.84%)

Table 4: Longitudinal cross-sectional area measurements

	NMCSA	NCSA23	NCSA34	NCSA45
Mean at baseline (SD) (mm ²)	71.49 (6.37)	67.76 (7.26)	68.21 (7.39)	71.51 (8.27)
Mean at follow-up (SD) (mm ²)	68.12 (8.91)	65.40 (10.27)	65.23 (10.61)	67.95 (9.97)
Cord area change averaged by year (SD) (%)	-0.77 (1.14)	-0.62 (1.20)	-0.74 (1.47)	-0.77 (1.61)
<i>P</i> value	.001	.006	.009	.006

Longitudinal Changes in Cervical Cord Cross-Sectional Area

Baseline CSA measurements, follow-up CSA measurements, and cord area changes averaged by year are shown in Table 4. The normalized CSA values decreased significantly in all the regions studied (Fig 2). The annualized CSA loss rates were similar for all the normalized CSA measurements.

Associations between Measurements

According to the Evans categorization system,²⁶ the normalized CSA measurements showed a weak-to-moderate negative association with the normalized area under the curve of the EDSS at baseline (NMCSA: $r = -0.357$, $P = .049$; NCSA23: $r = -0.418$, $P = .019$) and at follow-up (NMCSA: $r = -0.439$, $P = .013$; NCSA23: $r = -0.408$, $P = .023$; NCSA34: $r = -0.387$, $P = .032$).

No significant correlations were found between the annualized (normalized) cord CSA loss rates and the normalized area under the curve of the EDSS. Analysis of associations between the normalized CSA and brain MR imaging measurements showed no associations of the

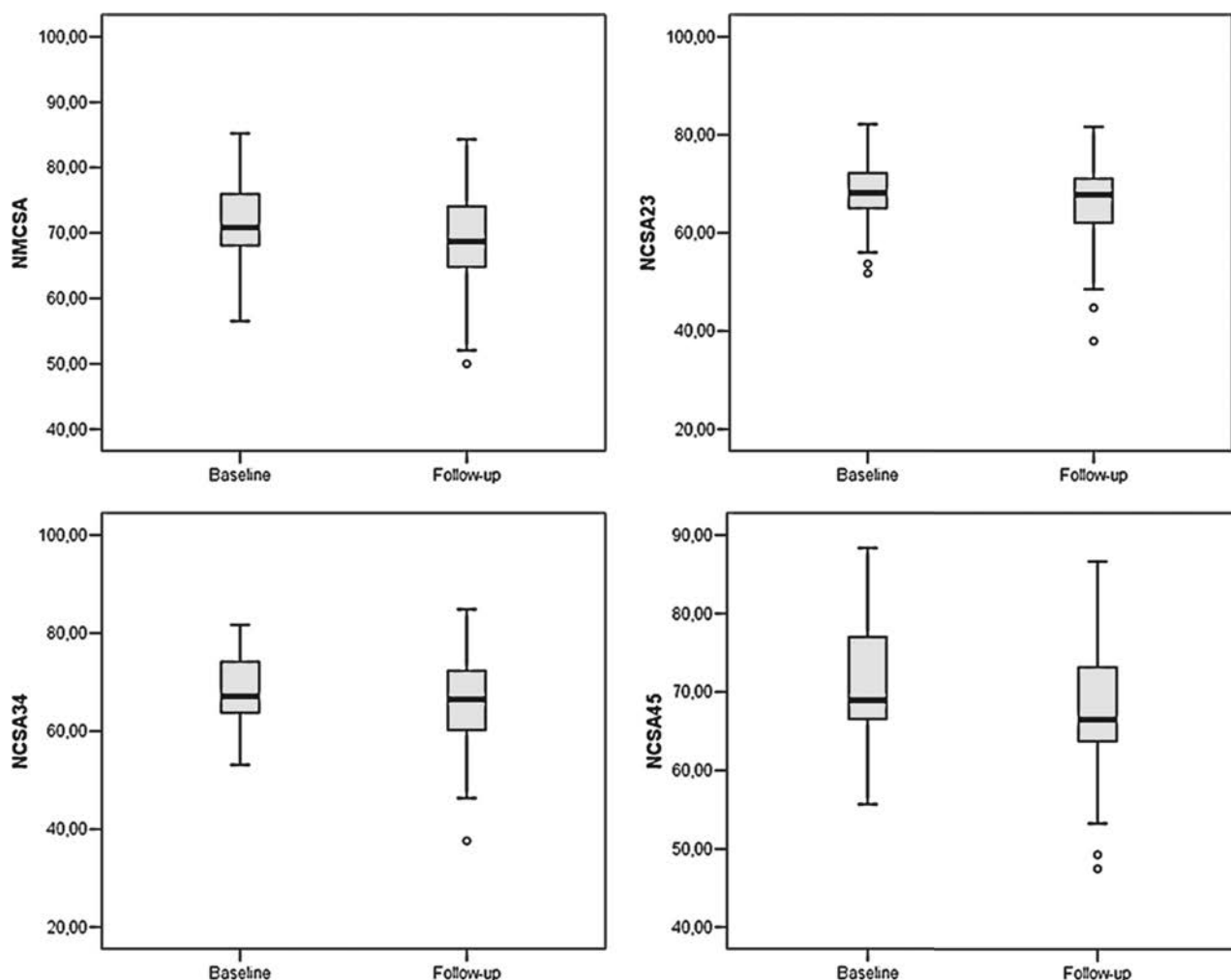


FIG 2. Box-and-whisker plots of normalized cross-sectional areas: NMCSA (upper left), NCSA23 (upper right), NCSA34 (lower left), and NCSA45 (lower right).

BPF, T2LV, or T1LV with the various CSA measurements. A moderate correlation was found between the baseline BPF and the annualized (normalized) CSA loss rates at C2–C3 ($r = -0.419$, $P = .019$) and C3–C4 ($r = -0.425$, $P = .017$), whereas a trend was observed between the baseline BPF and the aNMCSA ($r = -0.355$, $P = .05$).

Prediction of Long-Term EDSS Change

The long-term EDSS change was measured 14.12 ± 2.88 years after baseline to obtain an estimation on a time horizon of around 14 years. In the linear regression analysis to predict this change, the annualized mean cervical cord area loss rate (aNMCSA) and baseline EDSS ($EDSS_0$) were introduced in the model using the stepwise method, and age was introduced as a covariate. However, only aNMCSA and $EDSS_0$ with P values of .007 and .025, respectively, were statistically significant variables. The model obtained was then defined by the following expression:

$$\Delta EDSS = 4.0 - 0.628 \text{ aNMCSA} \\ - 0.476 \text{ EDSS}_0 + 0.006 \text{ Age.}$$

The F -test showed a significant P value (.004); thus, it was assumed that there was a linear relationship among the variables in our model. Finally, $R^2 = 0.390$, which indicated that the linear regression model explained 39.0% of the total variance in the data.

DISCUSSION

The present study investigated the role of cervical cord atrophy in a longitudinal study of a cohort of patients with PPMS to evaluate the association of this MR imaging finding with clinical progression of disability and with other MR imaging measures. We found a significant decrease in the normalized CSA values in all the regions studied. Moreover, some weak-to-moderate correlations were found between the weighted-average EDSS and normalized CSA values both at baseline and follow-up.

The annual loss of spinal cord tissue in our cohort was lower than that reported in previous studies.^{6,8,9,13,17,21,22} However, Lukas et al⁹ recently reported that spinal cord tissue loss may slow down with time, with already highly atrophied structures exhibiting slower atrophy rates. Our results support this notion: During the lengthy follow-up period, we found a smaller annualized CSA loss than other studies with a shorter follow-up.

To obtain the weighted-average EDSS, we used the area under the curve. The area under the curve becomes interesting when the longitudinal time intervals are unequally spaced, as was the case in the present study. Then the area under the curve reflects the weighted average of a certain outcome variable during the total follow-up period.²⁷ Area under the curve values were also normalized to facilitate their interpretation by an index in a range from 0 to 1, associated with patient disability.

Although the linear regression model predicting long-term EDSS change showed a strong correlation with the data according to the Evans categorization,²⁶ the only significant variables remaining in the model were the aNMCSA and baseline EDSS. None of the CSA measures or conventional MR imaging measures showed high enough significance to be included in the model. The model showed that the greater the progression of cervical cord atrophy, associated with a more negative aNMCSA, the greater

was the long-term EDSS change. Baseline EDSS acted as a limiting factor in the model, because the margin to a long-term EDSS increase was lower when baseline EDSS values were higher.

The lack of association between the BPF and cross-sectional area values is in agreement with a previous study in patients with PPMS.²⁸ At C2–C3 and C3–C4, a moderate negative correlation between the BPF and the annualized rate of spinal cord tissue loss was observed, whereas only a trend was seen between the baseline BPF and aNMCSA. These findings may be an indication that brain and cord pathology evolve differently and that measurement of brain and cord atrophy can provide complementary information about the severity of PPMS.²⁸

The data analysis did not include the effect of treatment. This factor was not considered essential because the study patients were part of a cohort participating in a clinical trial²⁰ in which one group was treated with interferon β 1-b, and the remainder, with placebo during the first 2 years; and there were no differences in EDSS progression or CSA measurements between the groups.

This study had limitations. First, the long follow-up made it difficult to enroll a larger sample that fulfilled the clinical and radiologic information required for the study. Second, images were acquired using a 1.5T MR imaging scanner. Most recent studies use 3T scanners to acquire cervical cord images because they provide a better signal-to-noise ratio in the same acquisition time. However, given the duration of our study, a 1.5T scanner was used at the first time point and we decided to maintain the same scanner throughout the study. Third, the sequence used to acquire cervical cord images was 3D T1-weighted MPRAGE. In a recent study, Kearney et al¹⁹ proposed the use of phase-sensitive inversion recovery sequences to take advantage of their better resolution and higher contrast. It is likely that reproducibility would improve if the active surface method were combined with a phase-sensitive inversion recovery rather than a 3D T1-weighted MPRAGE sequence. However, because of the retrospective nature of the study, it was not possible to introduce this sequence in the acquisition. Nonetheless, Kearney et al mentioned that when phase-sensitive inversion recovery cannot be used, combining active surface with 3D MPRAGE may be the most suitable approach. Fourth, EDSS values were not uniformly distributed across time. We tried to resolve this problem using a weighted-average measurement (normalized area under the curve), but a uniform distribution would have allowed further analysis. Finally, inclusion of a healthy control group would have helped to differentiate decreases in cervical cord values due to age and decreases due to MS-induced atrophy.

CONCLUSIONS

The results of this study suggest that cervical cord area measures are associated with disability in patients with PPMS. More interesting, this study supports MR imaging changes being taken into account when developing predictive studies. Specifically, we found that the rate of cervical cord area loss could play a relevant role in predicting clinical disability progression long term. Further longitudinal studies focused on the evaluation of cervical cord area changes in patients with PPMS, and their relation to disease progression for long periods would help to define the

value of cervical cord atrophy as a surrogate marker in MS clinical trials or for clinical management of these patients.

ACKNOWLEDGMENTS

The authors thank Celine Cavallo for English language support.

Disclosures: Cristina Auger—UNRELATED: Payment for Lectures Including Service on Speakers Bureaus: Novartis, Teva Pharmaceuticals, Biogen Idec, Stendhal. Jaume Sastre-Garriga—UNRELATED: Consultancy: Almirall; Grants/Grants Pending: Bayer AG, Sanofi Genzyme*; Payment for Lectures Including Service on Speakers Bureaus: Teva Pharmaceuticals, Biogen Idec, Novartis, Roche, Almirall, Merck Serono, Celgene, Sanofi Genzyme; Payment for Development of Educational Presentations: Merck Serono. Mar Tintoré—UNRELATED: Board Membership: Almirall, Bayer AG, Biogen Idec, Sanofi Genzyme, Merck Serono, Novartis, Sanofi-Aventis, Roche, Teva Pharmaceuticals; Grants/Grants Pending: Almirall, Bayer AG, Biogen Idec, Sanofi Genzyme, Merck Serono, Novartis, Sanofi Aventis, Roche, and Teva Pharmaceuticals*; Payment for Lectures Including Service on Speakers Bureaus: Almirall, Bayer AG, Biogen Idec, Sanofi Genzyme, Merck Serono, Novartis, Sanofi Aventis, Roche, and Teva Pharmaceuticals; Payment for Development of Educational Presentations: Almirall, Bayer AG, Biogen Idec, Sanofi Genzyme, Merck Serono, Novartis, Sanofi Aventis, Roche, and Teva Pharmaceuticals. Xavier Montalban—UNRELATED: Consultancy: Actelion, Almirall, Bayer AG, Biogen, Celgene, Hoffmann-La Roche, Merck Serono, Novartis, Orizon Genomics, Sanofi Genzyme, Teva Pharmaceuticals. Alex Rovira—UNRELATED: Board Membership: Novartis, Sanofi Genzyme; Payment for Lectures Including Service on Speakers Bureaus: Bayer AG, Stendhal Americas, Sanofi Genzyme, Bracco, Merck Serono, Teva Pharmaceuticals, Novartis, Roche, Biogen Idec; Payment for Development of Educational Presentations: Biogen Idec. *Money paid to the institution.

REFERENCES

1. Thompson AJ, Polman CH, Miller DH, et al. **Primary progressive multiple sclerosis.** *Brain* 1997;120:1085–96 CrossRef Medline
2. Thompson AJ, Montalban X, Barkhof F, et al. **Diagnostic criteria for primary progressive multiple sclerosis: a position paper.** *Ann Neurol* 2000;47:831–35 Medline
3. Bjartmar C, Kidd G, Mörk S, et al. **Neurological disability correlates with spinal cord axonal loss and reduced N-acetyl aspartate in chronic multiple sclerosis patients.** *Ann Neurol* 2000;48:893–901 Medline
4. Nijeholt GJ, van Walderveen MA, Castelijns JA, et al. **Brain and spinal cord abnormalities in multiple sclerosis: correlation between MRI parameters, clinical subtypes and symptoms.** *Brain* 1998;121:687–97 CrossRef Medline
5. Zivadinov R, Banas AC, Yella V, et al. **Comparison of three different methods for measurement of cervical cord atrophy in multiple sclerosis.** *AJNR Am J Neuroradiol* 2008;29:319–25 CrossRef Medline
6. Ingle GT, Stevenson VL, Miller DH, et al. **Primary progressive multiple sclerosis: a 5-year clinical and MR study.** *Brain* 2003;126:2528–36 CrossRef Medline
7. Stevenson VL, Ingle GT, Miller DH, et al. **Magnetic resonance imaging predictors of disability in primary progressive multiple sclerosis: a 5-year study.** *Mult Scler* 2004;10:398–401 CrossRef Medline
8. Agosta F, Absinta M, Sormani MP, et al. **In vivo assessment of cervical cord damage in MS patients: a longitudinal diffusion tensor MRI study.** *Brain* 2007;130:2211–19 CrossRef Medline
9. Lukas C, Knol DL, Sombekke MH, et al. **Cervical spinal cord volume loss is related to clinical disability progression in multiple sclerosis.** *J Neurol Neurosurg Psychiatry* 2015;86:410–18 CrossRef Medline
10. Losseff NA, Webb SL, O'Riordan JI, et al. **Spinal cord atrophy and disability in multiple sclerosis: a new reproducible and sensitive MRI method with potential to monitor disease progression.** *Brain* 1996;119:701–08 CrossRef Medline
11. Rocca MA, Horsfield MA, Sala S, et al. **A multicenter assessment of cervical cord atrophy among MS clinical phenotypes.** *Neurology* 2011;76:2096–102 CrossRef Medline
12. Lukas C, Sombekke MH, Bellenberg B, et al. **Relevance of spinal cord abnormalities to clinical disability in multiple sclerosis: MR imaging findings in a large cohort of patients.** *Radiology* 2013;269:542–52 CrossRef Medline
13. Furby J, Hayton T, Altmann D, et al. **A longitudinal study of MRI-detected atrophy in secondary progressive multiple sclerosis.** *J Neurol* 2010;257:1508–16 CrossRef Medline
14. Sastre-Garriga J, Ingle GT, Rovaris M, et al. **Long-term clinical outcome of primary progressive MS: predictive value of clinical and MRI data.** *Neurology* 2005;65:633–35 CrossRef Medline
15. Stevenson VL, Miller DH, Leary SM, et al. **One year follow up study of primary and transitional progressive multiple sclerosis.** *J Neurol Neurosurg Psychiatry* 2000;68:713–18 CrossRef Medline
16. Cawley N, Tur C, Prados F, et al. **Spinal cord atrophy as a primary outcome measure in Phase II trials of progressive multiple sclerosis.** *Mult Scler* 2017 May 1. [Epub ahead of print] CrossRef Medline
17. Valsasina P, Rocca MA, Horsfield MA, et al. **A longitudinal MRI study of cervical cord atrophy in multiple sclerosis.** *J Neurol* 2015;262:1622–28 CrossRef Medline
18. Horsfield MA, Sala S, Neema M, et al. **Rapid semi-automatic segmentation of the spinal cord from magnetic resonance images: application in multiple sclerosis.** *Neuroimage* 2010;50:446–55 CrossRef Medline
19. Kearney H, Yiannakas MC, Abdel-Aziz K, et al. **Improved MRI quantification of spinal cord atrophy in multiple sclerosis.** *J Magn Reson Imaging* 2014;39:617–23 CrossRef Medline
20. Montalban X, Sastre-Garriga J, Tintoré M, et al. **A single-center, randomized, double-blind, placebo-controlled study of interferon beta-1b on primary progressive and transitional multiple sclerosis.** *Mult Scler* 2009;15:1195–205 CrossRef Medline
21. Lin X, Tench CR, Turner B, et al. **Spinal cord atrophy and disability in multiple sclerosis over four years: application of a reproducible automated technique in monitoring disease progression in a cohort of the interferon beta-1a (Rebif) treatment trial.** *J Neurol Neurosurg Psychiatry* 2003;74:1090–94 CrossRef Medline
22. Rashid W, Davies GR, Chard DT, et al. **Increasing cord atrophy in early relapsing-remitting multiple sclerosis: a 3 year study.** *J Neurol Neurosurg Psychiatry* 2006;77:51–55 CrossRef Medline
23. Plummer DL. **Dispimage: a display and analysis tool for medical images.** *Riv Neuroradiol* 1992;19:1715–20
24. Aymerich FX, Sobrevilla P, Montseny E, et al. **Fuzzy approach to lesion load measurement in T1-weighted images.** *Mult Scler* 2001;7(suppl 1):87
25. Aymerich X, Sobrevilla P, Montseny E, et al. **Application of an automatic segmentation algorithm to brain atrophy assessment in multiple sclerosis.** *Rev Neurol (Paris)* 2000;156(suppl 3):103–04
26. Evans JD. *Straightforward Statistics for Behavioral Sciences.* Pacific Grove: Brooks/Cole Publishing; 1996
27. Twisk JW. *Applied Longitudinal Data Analysis for Epidemiology: A Practical Guide.* New York: Cambridge University Press; 2013
28. Rovaris M, Judica E, Sastre-Garriga J, et al. **Large-scale, multicentre, quantitative MRI study of brain and cord damage in primary progressive multiple sclerosis.** *Mult Scler* 2008;14:455–64 CrossRef Medline

Carotid Artery Wall Imaging: Perspective and Guidelines from the ASNR Vessel Wall Imaging Study Group and Expert Consensus Recommendations of the American Society of Neuroradiology

 L. Saba,  C. Yuan,  T.S. Hatsukami,  N. Balu,  Y. Qiao,  J.K. DeMarco,  T. Saam,  A.R. Moody,  D. Li,  C.C. Matouk,  M.H. Johnson,  H.R. Jäger,  M. Mossa-Basha,  M.E. Kooi, Z. Fan, D. Saloner, M. Wintermark, D.J. Mikulis, and B.A. Wasserman; on behalf of the Vessel Wall Imaging Study Group of the American Society of Neuroradiology

ABSTRACT

SUMMARY: Identification of carotid artery atherosclerosis is conventionally based on measurements of luminal stenosis and surface irregularities using in vivo imaging techniques including sonography, CT and MR angiography, and digital subtraction angiography. However, histopathologic studies demonstrate considerable differences between plaques with identical degrees of stenosis and indicate that certain plaque features are associated with increased risk for ischemic events. The ability to look beyond the lumen using highly developed vessel wall imaging methods to identify plaque vulnerable to disruption has prompted an active debate as to whether a paradigm shift is needed to move away from relying on measurements of luminal stenosis for gauging the risk of ischemic injury. Further evaluation in randomized clinical trials will help to better define the exact role of plaque imaging in clinical decision-making. However, current carotid vessel wall imaging techniques can be informative. The goal of this article is to present the perspective of the ASNR Vessel Wall Imaging Study Group as it relates to the current status of arterial wall imaging in carotid artery disease.

ABBREVIATIONS: CE = contrast-enhanced; DIR = double inversion recovery; FC = fibrous cap; IPH = intraplaque hemorrhage; IVUS = intravascular ultrasound; LRNC = lipid-rich necrotic core; MATCH = multicontrast atherosclerosis characterization; SNAP = simultaneous noncontrast angiography and intraplaque hemorrhage; SPACE = sampling perfection with application-optimized contrasts using different flip angle evolution; US = ultrasound

The word “atherosclerosis” is derived from the 2 Greek words “athera” (mush) and “sclerosis” (hardening), indicating hardening of the vascular wall. This disease is highly prevalent in

developed countries, with carotid artery narrowing reported in up to 75% of men and 62% of women 65 years of age and older.¹ Stroke is the second most common cause of death worldwide,² and approximately 18%–25% of all strokes are due to carotid atherosclerotic disease.³

Conventionally, identification of atherosclerosis affecting the carotid artery is based on measurements of the degree of luminal stenosis and surface irregularities^{4,5} by sonography, catheter-based angiography, and, nowadays, CTA or MRA.^{6,7} However, histopathologic studies initially performed on coronary arteries and subsequently on carotid arteries demonstrate considerable differences between plaques with identical degrees of stenosis. These observations led to research indicating that certain plaque features are associated with increased risk for ischemic events.^{8–10} The more recent introduction of fast multidetector row CT technology, high-field MR imaging, and advanced ultrasound (US) systems has enabled accurate characterization of plaque features that relate to risk of ischemic injury.^{11–14} The ability to look beyond the lumen using advanced wall imaging methods to identify “vulnerable plaque”^{15,16} is spurring a paradigm shift away from simple measurement of percent luminal stenosis for gauging the risk of ischemic injury. Currently, characterization of the vessel wall and atherosclerotic plaque is the focus of several ongoing research studies that are investigating the optimal approach to vulnerable plaque imaging.^{17–19}

From the Department of Medical Imaging (L.S.), University of Cagliari, Cagliari, Italy; Departments of Radiology (C.Y., N.B., M.M.-B.) and Surgery (T.S.H.), University of Washington, Seattle, Washington; The Russell H. Morgan Department of Radiology and Radiological Sciences (Y.Q., B.A.W.), Johns Hopkins Hospital, Baltimore, Maryland; Department of Radiology (J.K.D.), Walter Reed National Military Medical Center, Bethesda, Maryland; Department of Radiology (T.S.), Ludwig-Maximilian University Hospital, Munich, Germany; Division of Neuroradiology (D.J.M.), Department of Medical Imaging, University Health Network, and Department of Medical Imaging (A.R.M.), Sunnybrook Health Sciences Centre, University of Toronto, Toronto, Ontario, Canada; Biomedical Imaging Research Institute (D.L., Z.F.), Cedars-Sinai Medical Center, Los Angeles, California; Departments of Neurosurgery, Neurovascular and Stroke Programs (C.C.M., M.H.J.), Radiology and Biomedical Imaging (C.C.M., M.H.J.), and Surgery (M.H.J.), Yale University School of Medicine, New Haven, Connecticut; Neuroradiological Academic Unit (H.R.J.), Department of Brain Repair and Rehabilitation, University College London Institute of Neurology, London, UK; Department of Radiology (M.E.K.), CARIM School for Cardiovascular Diseases, Maastricht University Medical Center, Maastricht, the Netherlands; Department of Radiology and Biomedical Imaging (D.S.), University of California, San Francisco, California; and Department of Radiology (M.W.), Neuroradiology Division, Stanford University, Stanford, California.

The views expressed in this article are those of the authors and do not reflect the official policy of the Department of Army/Navy/Air Force, Department of Defense, or US Government. The identification of specific products or scientific instrumentation does not constitute endorsement or implied endorsement on the part of the authors, Department of Defense, or any component agency.

Please address correspondence to Luca Saba, MD, University of Cagliari, Azienda Ospedaliero Universitaria di Cagliari, Polo di Monserrato, Provincia di Cagliari, Italy; e-mail: lucasaba@tiscali.it

<http://dx.doi.org/10.3174/ajnr.A5488>

Further evaluation in randomized clinical trials is needed to establish the exact role of plaque imaging in clinical decision-making. However, carotid vessel wall imaging techniques may be beneficial at present. For example, improved visualization of the location and extent of atherosclerotic plaque would assist in surgical planning before endarterectomy or carotid artery stent placement. Vessel wall imaging may also be helpful in borderline clinical cases. Identification of carotid plaque harboring a large lipid-rich necrotic core (LRNC) with ulceration and intraplaque hemorrhage (IPH) despite guideline-based medical therapy in a patient with repeat strokes and 50% carotid stenosis may lead to consideration for carotid endarterectomy. In asymptomatic patients, vessel wall imaging with a large LRNC may represent the phenotype of atherosclerotic disease amenable to more intensive lipid-lowering therapy.²⁰ Similarly, progressive vulnerable plaque features with increasing IPH in asymptomatic carotid stenosis may benefit from more intensive lipid-lowering therapy.^{21,22}

The goal of this article is therefore to present the perspective of the ASNR Vessel Wall Imaging Study Group on the current status of arterial wall imaging in carotid artery disease.

CLINICAL BACKGROUND AND PHYSIOLOGY

For several years, digital subtraction angiography remained the primary imaging method for studying carotid arteries for detecting stenosis secondary to atherosclerotic plaque.^{23,24} The method provides optimal spatial resolution for defining the opacified lumen, the associated degree of luminal stenosis, and plaque-related luminal changes that include lumen irregularity and plaque ulcerations.^{25,26}

Carotid endarterectomy trials were undertaken during the 1980s to mid-1990s that quantified the benefit of carotid endarterectomy according to the degree of luminal stenosis.^{4,27-30} These studies became the basis for considering degree of stenosis as the primary metric for stratifying subsequent stroke risk and selecting the optimal therapeutic approach (surgery versus best medical management).²⁷ In particular, 3 multicenter randomized studies, the European Carotid Surgery Trial (ECST), NASCET, and Asymptomatic Carotid Atherosclerosis Study (ACAS) evaluated cutoffs for the degree of carotid stenosis as they relate to stroke risk reduction by carotid endarterectomy.²⁸⁻³⁰

NASCET, ECST, and ACAS used DSA to assess the percent reduction in the luminal diameter of the artery. The methodology for carotid stenosis quantification is debated because NASCET and ECST used indirect ratio-percent methods.³¹ Stenosis measurements with NASCET and ECST differ substantially: With the ECST method, twice as many stenoses were classified as severe, and less than one-third of the number of stenoses, as mild compared with the NASCET method.³² Techniques that enable identification of both outer and inner walls of the artery might lead to more accurate assessment of risk. Bartlett et al³³ suggested the use of this direct diameter-based measurement to overcome the limitations of the percent-based methods, and the results they found suggest that this technique could be efficient.

The degree of luminal stenosis as a marker of atherosclerotic disease severity has been criticized because of observations that plaques producing only mild-to-moderate stenosis may still lead to acute cerebral infarction.³⁴⁻⁴¹ Histopathologic evaluation of

these plaques showed that plaque erosion and disruption were common morphologic features found in symptomatic lesions, indicating that luminal narrowing was not the sole predictor of cerebrovascular events.³⁶⁻³⁸

These studies introduced the following new concepts: 1) The degree of carotid stenosis is a weak indicator of the volume and extension of carotid plaque⁴²⁻⁴⁴; 2) a set of plaque features identifiable by imaging are closely linked to the development of ischemic symptoms; and 3) these features can significantly increase the risk of stroke regardless of the degree of stenosis.⁴⁵⁻⁴⁸ Thanks to advancements in the imaging techniques to specifically target the vessel wall as opposed to the vessel lumen, considerable research effort is underway to identify those plaque-related parameters that, together with the degree of stenosis, can more accurately predict the presence of vulnerable plaque and the associated risk of ischemic events.

More than 30 years ago, Imparato et al⁸ found that there were certain plaque features, such as IPH, that were associated with an increased risk of plaque rupture and distal embolization. Since that time, roughly 1000 articles have been published on IPH as well as ones characterizing additional features associated with plaque vulnerability, including the thickness of the fibrous cap, rupture of the cap, the presence and size of the LRNC, and the presence of active plaque inflammation. Vulnerable plaques also tend to be characterized by an eccentric distribution, an irregular surface of the intimal layer, or superficial ulcerations with intimal exposure.

Imaging Features of Plaques at Risk for Stroke

US can assess plaque composition based on echogenicity with classification systems proposed by Geroulakos et al⁴⁹ and Bluth.⁵⁰ The presence of echogenic/hypoechoic elements is associated with the LRNC,^{51,52} whereas hyperechoic regions or the presence of acoustic shadowing is indicative of calcification. US is sensitive in identifying calcification, but when present, the ensuing acoustic shadowing limits visualization of tissues deep to the calcification.⁵³

CT has been used to type plaques based on Hounsfield attenuation. de Weert et al^{54,55} categorized plaques as fatty for attenuation values of <60 HU, mixed for attenuation values between 60 and 130 HU, and calcified for attenuation values of >130 HU. By applying these thresholds, it is possible to identify those plaques with an LRNC from others with a prevalent expression of myofibroblasts, hemorrhage, or calcification.⁵⁶ Based on this analysis, calcified plaques were found to be 21 times less likely to be symptomatic than noncalcified plaques,⁵⁷ whereas fatty plaques were clearly associated with an increased risk of rupture.^{48,58}

MR imaging has the ability to distinguish plaque components such as the LRNC, fibrous tissue, and IPH with high accuracy.⁵⁹⁻⁶⁴ The identification of calcified components can be more challenging than CT, but MR imaging typically offers good results.^{65,66}

Luminal Morphology and Ulcerations

The morphology of the luminal surface of carotid plaques can be classified as smooth, irregular, or ulcerated.⁶⁷ A smooth surface is identified as plain luminal morphology without any sign of ulceration or irregularity. An irregular surface indicates the presence of

small alterations of the luminal surface on the luminal profile of the plaque; this condition is considered a risk factor for embolism and is associated with an increased risk of TIA/stroke.⁶¹ The third type of morphology is ulceration. Plaque ulceration has been defined as “an intimal defect larger than 1 mm in width, exposing the necrotic core of the atheromatous plaque”⁶⁸; however, other authors suggested other (smaller) sizes.^{69–71} The NASCET study demonstrated a significantly increased risk of cerebrovascular events in plaques with ulcerations.⁴

Intraplaque Hemorrhage

IPH is a common feature of atherosclerotic plaques and is considered one of the identifying features of vulnerable plaque.⁴⁰ A number of studies have found a statistically significant association between the presence of IPH and cerebrovascular events,^{72,73} and IPH has been implicated in plaque progression.⁷⁴ It is thought that the rupture of neovessels or plaque rupture itself causes IPH; and some conditions such as inflammation, metabolic disease, or diabetes may precipitate this event.⁷⁵ Recent literature also indicates a potential role of blood pressure.^{76,77}

Fissured Fibrous Cap and Lipid Rich Necrotic Core

The fibrous cap (FC), which separates LRNC from the vessel lumen, is considered one of the most important features of the carotid artery vulnerable plaque model. The FC is a layer of fibrous connective tissue and contains macrophages and smooth-muscle cells within a collagen-proteoglycan matrix associated with T-lymphocytes.⁷⁸ Vulnerable plaques are characterized by the presence of a thin FC covering a large LRNC containing macrophages and inflammatory cells. In both cross-sectional and longitudinal studies,^{21,47} the LRNC size was found to be a strong predictor of fibrous cap disruption. The fissuring or rupture of the FC exposes the LRNC to luminal blood, activating the thromboembolic cascade. Therefore, LRNC and FC status are expected to be associated with a risk of cerebrovascular events, as shown in a single-center experience.^{73,79,80} The intact thick FC is associated with a low risk of plaque rupture, a thin FC is associated with a mild risk, while a fissured FC is associated with a high risk of plaque rupture.⁸¹ Additionally, percent LRNC area exceeding 40% of vessel wall area indicates a high risk for plaque rupture, while percent luminal stenosis did not correlate with plaque rupture.²¹

Neovascularization and Inflammation

Intraplaque neovascularization arises from newly formed microvessels that grow into the intima through breaks in the medial wall and are characterized by leaky capillaries with an endothelial lining that is immature and imperfect due to the harsh atherosclerotic environment. Histopathologic studies have demonstrated that neovessels can be found within carotid artery plaques, and the degree of neovascularity is associated with the “activity” of the plaque in terms of inflammation and increased risk of neovessel rupture and hemorrhage (IPH).^{82,83} Inflammation of unstable “vulnerable” atherosclerotic plaques was first identified in coronary artery lesions and subsequently demonstrated in carotid artery plaques.^{84,85}

The recruitment of inflammatory cells in atherosclerotic lesions is a constitutive phenomenon seen throughout the process of lesion initiation and plaque growth. In addition, inflammation

appears to play a role in the process of plaque disruption.⁸⁶ Inflammatory cells are typically found in the plaque shoulder, cap, or both.⁸⁵ In many instances and particularly in advanced plaques with a complex architecture, inflammatory cells tend to accumulate focally within plaques.^{85,86}

Several types of inflammatory cells are detected in the carotid artery vulnerable plaque, and some studies have found that the presence of macrophages is significantly associated with the risk of plaque rupture^{87–89}; therefore, the identification of macrophages has become the target of imaging studies devoted to the detection of plaque inflammation.^{90–94}

Plaque Remodeling (Positive versus Negative)

The concept of plaque remodeling was initially described for atherosclerotic lesions in coronary arteries but is largely accepted for other vascular beds, including the carotid arteries.^{95,96} Carotid plaques can show either positive or negative remodeling or both. Positive remodeling is dilation of the vessel wall in response to an increase in plaque volume with little or no compromise of the vessel lumen as the vessel initially attempts to maintain normal lumen diameter.⁹⁷ Negative remodeling is present when the vessel lumen diameter is decreased (stenosis).

Plaque Volume

Recent studies have demonstrated that the volume of the carotid artery plaque could play a role in determining plaque “vulnerability” and risk of cardiovascular events.^{98,99} Increasing plaque volume predicted cardiovascular events.^{43,100} Some authors have hypothesized that the plaque volume may be a better indicator of the severity of atherosclerotic disease than the degree of stenosis.²¹ Noninvasive in vivo assessment of atherosclerotic plaque volume and the relative contribution of different plaque components clearly have important clinical implications as they relate to risk assessment for ischemic events. In addition, it has been shown that higher LRNC volumes appear to be associated with the presence of plaque ulcerations, representing a significant risk factor for the development of cerebrovascular events.¹⁰¹ Furthermore, plaque composition is known to change with increasing plaque volume. More specifically, there is an increase in the proportion of lipid and calcification with increasing plaque volume.¹⁰¹ Plaque length, which relates more directly with plaque volume than the degree of stenosis, has been shown to be an independent risk factor for periprocedural complications and an excess restenosis rate in a secondary data analysis of the Carotid and Vertebral Artery Transluminal Angioplasty Study (CAVATAS).¹⁰²

Summary Concepts

It is clear that there are several plaque features of increased clinical risk supported by associations with endarterectomy specimen analyses. It is of utmost importance to test management strategies based on these MR imaging–defined features of risk before treatment guidelines can be established. Currently, there are several prospective trials intended to examine the value of prospective plaque imaging (Atherosclerosis Risk in Communities [ARIC], Plaque At RISK [PARISK], Carotid Plaque Imaging in Acute Stroke [CAPIAS], Chinese Atherosclerosis Risk Evaluation-Phase II [CARE-II], and Canadian Atherosclerosis Imaging Network

[CAIN]).¹⁰³⁻¹⁰⁸ In the meantime, it is possible that carotid plaque characterization may be of immediate clinical value today. Given that the presence of IPH, large LRNC, and/or a thin-ruptured FC is associated with a higher risk of future cardiovascular events, the presence of these plaque features may warrant closer clinical follow-up and consideration for more intensive medical therapy. Despite attempts to encourage all physicians to manage atherosclerosis medically with current evidence-based guidelines, many patients are not receiving high-intensity lipid-lowering therapy, even when indicated. Providing additional information based on carotid plaque MR imaging identification of IPH, large LRNC, and/or a thin-ruptured FC may improve patient/physician compliance with current therapeutic guidelines. If patients receiving standard-of-care medical therapy have repeat strokes ipsilateral to carotid plaque harboring “vulnerable” plaque features, they may warrant surgical intervention even if they do not meet the stenosis thresholds by the NASCET criteria.

CURRENT IMAGING STATE OF THE ART

In this section of the paper, we will summarize the imaging techniques that can be used in the imaging of the carotid artery wall.

US

US is generally accepted as the standard imaging technique for first-line diagnosis of atherosclerosis of the carotid artery.⁶⁷ US has shown very good results in the identification and characterization of high-risk plaques in patients with atherosclerosis.¹⁰⁹ In particular, the use of microbubble contrast material facilitates assessment of vulnerable plaque features such as the presence/absence of neovascularization.^{110,111} The recently introduced volumetric US technology seems to add further value to this technique by improving the interobserver concordance and increasing the spatial coverage.¹¹² Another US technique that could be used for carotid plaque characterization is intravascular US (IVUS). The advantage of IVUS is excellent spatial resolution, which is possible given the short distance between the probe and the carotid plaque, which permits the use of high-frequency (up to 50 MHz) insonation without excessive attenuation.

US, however, suffers from some key limitations. In patients with short muscular necks, it may be very difficult to identify the carotid bifurcation.¹¹³ In obese patients or in patients that have had radiation therapy, US assessment of the carotid arteries can be challenging. Another limitation of US is the evaluation of highly calcified plaques that create acoustic shadowing that can reduce visualization of the lesion.¹¹⁴ Furthermore, US is less capable of detecting additional, more distally located (“tandem”) stenoses than CTA or MRA. It is important to underline that IVUS is invasive and is only performed in selected cases that are largely treated with carotid artery stent placement; thus, no pathologic correlate is available. IVUS identification of the fibrous cap or visualization of friable plaque may correlate with increased risk of emboli. Moreover, the small cohorts of assessed IVUS patients as well as the potential risk related to the procedure need further analysis before IVUS can be included in the routine clinical work-up.¹¹⁵

Luminal Morphology and Ulcerations. It has recently been shown that 3D-US could be effective in the detection of ulceration in carotid artery plaques.^{116,117}

Intraplaque Hemorrhage. A few articles have assessed US performance in the detection of IPH, and the results demonstrated low sensitivity and specificity.^{118,119}

Fibrous Cap Status. Some authors have explored the potential of conventional US to characterize the FC, but the results obtained were suboptimal.¹²⁰⁻¹²² Recent articles^{123,124} have suggested that intravascular ultrasonography can assess in detail plaque structure and the FC but with associated procedural risk.

Neovascularization and Inflammation. Several recently published^{110,111,125,126} contrast-enhanced sonography studies found that sonographic enhancement correlates with intraplaque neovascularization in carotid endarterectomy specimens. However, the reproducibility and utility of this technique for clinical care are not well-established.¹²⁷

It is important to underline that US can also be used to assess those initial subtle wall alterations in the very early phases of atherosclerosis progression, for example, the intima-media thickness that is considered a significant predictor of coronary and cerebrovascular events.^{128,129}

Recent studies assessed the reliability of US for assessing certain plaque features. Bar et al¹³⁰ assessed plaques in 30 patients. Interrater agreement values for the following plaque features were as follows: homogeneity, 96% ($\kappa = 0.84$; $P < .001$); surface characteristics, 90% ($\kappa = 0.77$; $P < .001$); and echogenicity, 86% ($\kappa = 0.60$; $P < .001$). The correlation coefficient for plaque content and volume measurement agreement was 0.81, and measurements did not differ significantly ($P =$ not significant). In an article published in 1999 by Hartmann et al,¹³¹ the κ values and 95% confidence intervals for interrater reproducibility were 0.05 (−0.07 to 0.16) for plaque surface structure, 0.15 (0.02 to 0.28) for plaque heterogeneity, 0.18 (0.09 to 0.29) for plaque echogenicity, and 0.29 (0.19 to 0.39) for plaque calcification. The upper bounds of all the confidence intervals were below the 0.40 level, indicating very low reliability.

CT

Modern CT scanners can provide exquisite, rapid high-resolution imaging of the carotid artery lumen and the arterial wall. The introduction of multienergy technology provided a tremendous boost to the development of CT techniques; and constant advances in detector technology, in spatial and temporal resolution, and release of advanced software for image reconstruction have helped to consolidate this technique as a reliable tool for the evaluation of arterial pathology, with particular success in the detection and characterization of carotid atherosclerosis.

Because of its spatial resolution, CT imaging seems to be a promising tool for the quantification of the volume of the carotid plaque as well as for the volume quantification of plaque subcomponents (fatty, mixed, calcified) (Fig 1). Moreover, the introduction of multienergy technology is opening new options in tissue characterization because the different tissue components show different attenuation levels with varying kiloelectron volt values.^{132,133}

Luminal Morphology and Ulcerations. CT offers very good results in detecting ulcerations when compared with histopathology (Fig 2), with performance significantly better than US,¹³⁴⁻¹³⁶ but the presence of a halo or edge blur may hinder detection of smaller ulcerations.

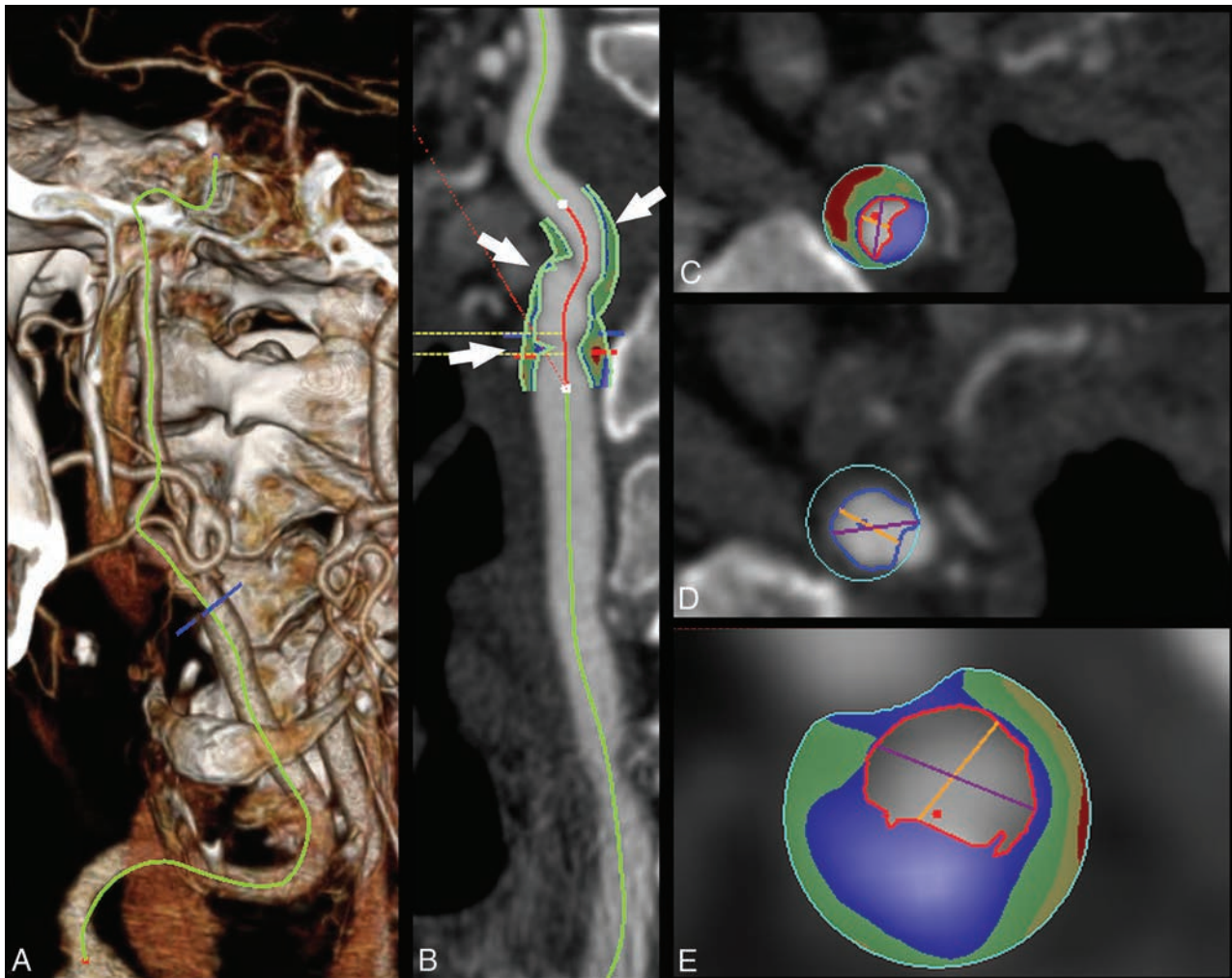


FIG 1. Plaque volume analysis in a 75-year-old man with a TIA. In the volume-rendered image, the carotid is traced (A), and in the curved-planar-reconstructed postprocessed image (CTA module, Aquarius iNtuition Edition, Version 44121382907; TeraRecon, San Mateo, California) (B), the plaque is identified based on the green contours (white arrows). The volume analysis with automated boundary detection and tissue segmentation is shown in panels C, D, and E (corresponding to the 3 arrows, proximal-to-distal) with contours delineating the lumen (red contour), outer wall (blue contour), and shading of calcium (blue), mixed tissue (green), and lipid component (red).

Intraplaque Hemorrhage. Detection of IPH using CT is challenging, and conflicting results have been reported. While some authors have found that CT density is slightly higher in fatty plaques with IPH identified by MR imaging compared with plaques without IPH,¹³⁷ others found no significant differences in Hounsfield units of fatty plaques with and without IPH identified by MR imaging.¹⁰⁴ Other authors found a correlation between the presence of IPH and low Hounsfield unit values (<30 HU),^{56,138,139} which might be explained by the associated presence of LRNC. Recently, some authors suggested that the rim sign on CTA (soft-tissue plaque with adventitial calcifications) as well as maximum soft-plaque thickness could be predictive of carotid IPH.¹⁴⁰

Fibrous Cap Status. The assessment of the status of the FC using CT is complex because of the artifacts related to the edge blur and halo effects, but authors suggest that CT can be used to assess the FC status, in particular to identify rupture.^{141,142} Notably, it seems that the rupture of the FC correlates with the presence of postcontrast plaque enhancement in CTA analysis.⁴⁵

Neovascularization and Inflammation. The degree of postcontrast plaque enhancement has been shown to be associated with the extent of neovascularization on CT.¹⁴³ The adventitial neovascularization has been assessed with both MR imaging¹⁴⁴ and CT.^{145,146} Romero et al¹⁴⁵ showed adventitial neovascularity on CTA to be significantly more common in symptomatic than in asymptomatic patients with $\geq 70\%$ stenosis and for stenosis between 50% and 70%,¹⁴⁶ and similar findings have been reported by MR imaging.¹⁴⁴

Plaque Remodeling. CT studies have found that positive carotid remodeling was significantly greater in patients with cerebral ischemic symptoms than in asymptomatic patients and that the extent of expansive remodeling may indicate underlying atherosclerotic plaque vulnerability.^{147,148}

Plaque Volume. CT can calculate the volume of the carotid artery plaque and determine the volume of the subcomponents, according to the Hounsfield unit threshold.¹⁴⁹ Further, it has been shown in a CT/MR imaging comparison study that the best discriminating factor for predicting a complicated American Heart Association type VI

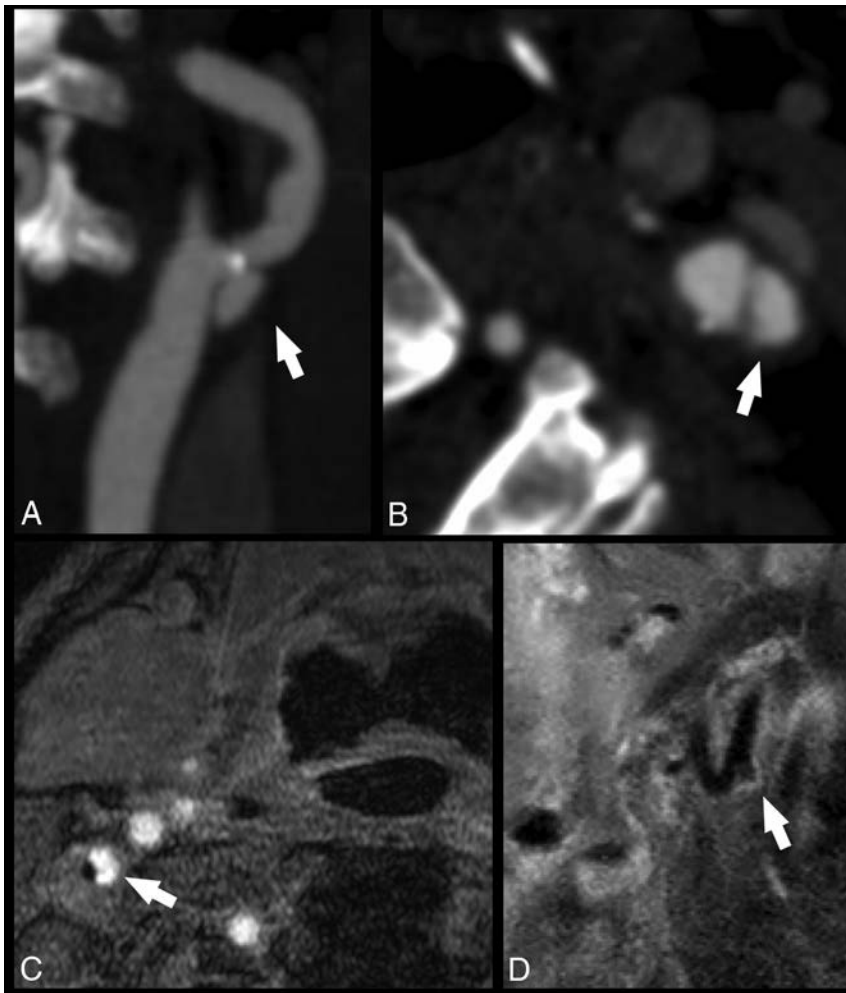


FIG 2. Ulcerated carotid artery plaques detected with CT and MR imaging. In the first case, the CTA of a 74-year-old man with a TIA demonstrates an ulcerated carotid artery plaque (white arrows) in the left internal carotid artery (white arrow) in the MIP (A) and axial source (B) images. In the second case, an MR imaging analysis of a 63-year-old man with a TIA shows a tiny ulceration (white arrows) in the right internal carotid artery visible in the axial (C) and paracoronar (D) planes.

plaque is the thickness of the fatty plaque component with a receiver operating characteristic area under the curve of 0.89.¹⁰⁴

CT Limitations. CT imaging has 3 main limitations: 1) the radiation dose delivered to patients, 2) the risk related to the administration of contrast material, and 3) the limited fatty tissue contrast. Diagnostic radiation exposure and the consequent potential radiation hazards represent a significant issue,^{150,151} particularly when longitudinal monitoring is required. The second limiting factor of CT is the potential anaphylactic reaction to contrast material^{152,153} and contrast-induced nephropathy, which is a common form of hospital-acquired acute renal failure.^{154,155} A further limitation of CT is the limited published information concerning the reliability of this technique and the prospective value of CT-based plaque features on stroke risk and/or stroke recurrence.

MR

The use of a high field strength (1.5T–3T) and dedicated surface radiofrequency coils improves the signal-to-noise ratio, which allows for the evaluation of plaque components and investigation beyond the simple assessment of stenosis measurements. Multi-

contrast carotid MR imaging (including T1WI, T2WI, and proton density and TOF) can characterize plaque components (eg, fibrous cap, LRNC, calcification, and intraplaque hemorrhage) without administration of contrast agents. Contrast-enhanced MR imaging improves tissue characterization^{60,61} and offers information on the presence of neovascularization (Figs 3 and 4).

Luminal Morphology and Ulcerations.

MR imaging detects plaque ulcerations with a sensitivity similar to CT (Fig 2).¹⁵⁶ Etesami et al¹⁵⁶ demonstrated that the use of contrast-enhanced MRA techniques improved the sensitivity for ulcerations by 37.5% compared with an unenhanced time-of-flight sequence.

Intraplaque Hemorrhage.

MR imaging is considered the best imaging technique for the detection of IPH (Figs 3 and 5). Several studies have shown that the appearance of IPH depends on the oxidative state of hemoglobin.^{157–159} Because of the sensitivity of MR imaging in detecting IPH and the risk attributed to this feature, some authors suggest that MR imaging is the best technique for imaging carotid artery vulnerable plaque.^{12,40,63,160,161} During the subacute and chronic phases, IPH appears bright on T1-weighted imaging due to the relatively short T1 of methemoglobin. This phenomenon has been exploited using widely available sequences such as MPRAGE, though other heavily

T1-weighted techniques have been developed to satisfy this purpose such as multicontrast atherosclerosis characterization (MATCH) and simultaneous noncontrast angiography and intraplaque hemorrhage (SNAP) (Figs 6 and 7). In MATCH, hyper-T1 contrast weighting is achieved using inversion preparation and data acquisition at the background nulling point, and thus IPH can be exclusively visualized with a near-dark background; on the other hand, background tissues can readily be visualized on other contrast weightings, thanks to the inherently coregistered multicontrast acquisition (Fig 7).^{162,163} IPH detection using 3D SNAP enables greater conspicuity of the lumen boundary compared with MPRAGE (Figs 5–7).¹⁶⁴ SNAP provides the advantage of 3D isotropic resolution as well as simultaneous bright-blood angiography to detect stenosis or ulceration that may be colocalized with IPH.¹⁶⁵ It is worth noting that it is not necessary to restrict carotid wall imaging to dedicated, small-FOV surface coils for IPH detection since this can be achieved at a lower spatial resolution using large-FOV neck coils (Fig 3).^{63,79,166} In fact, IPH detection can be achieved on the mask sequence acquired as part of a routine contrast-enhanced MRA (Fig 3).⁶³

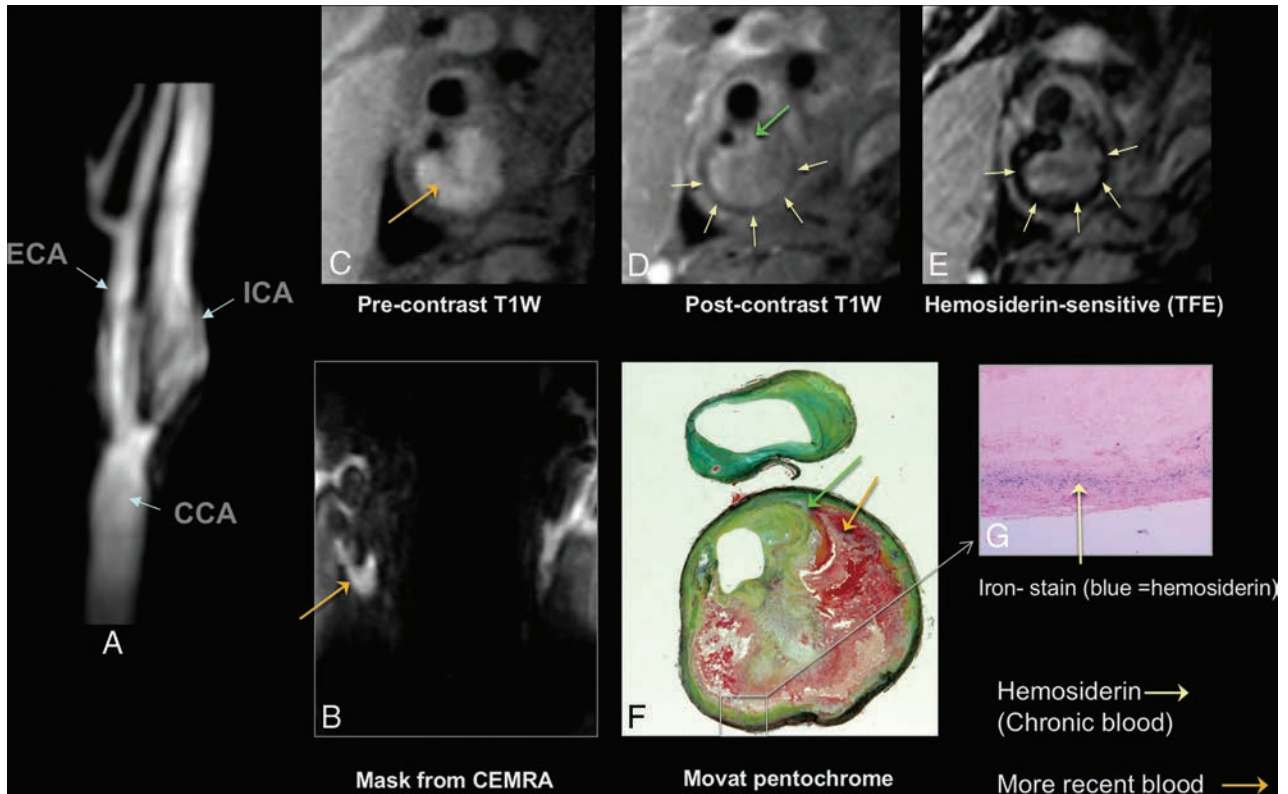


FIG 3. Carotid atherosclerotic plaque MR imaging and a specimen from a 73-year-old man with stenosis of the carotid bulb measuring 69% by the NASCET criteria demonstrated on a contrast-enhanced MRA (A). The precontrast (mask) image from the contrast-enhanced MRA demonstrates bright signal indicative of intraplaque hemorrhage, specifically subacute blood, or methemoglobin (B, arrow). Subacute blood is also identified as bright signal on the precontrast T1-weighted black-blood image (C, arrow). A rim of hemosiderin is identified as hypointense signal on the postcontrast black-blood image (D) and a hemosiderin-sensitive sequence (E) and is confirmed on the endarterectomy specimen (F and G). The fibrous cap is also delineated (green arrow, D and F). Black-blood imaging was achieved by using 2D cardiac-gated double inversion recovery turbo spin-echo. ECA indicates external carotid artery; CCA, common carotid artery; TFE, turbo field echo.

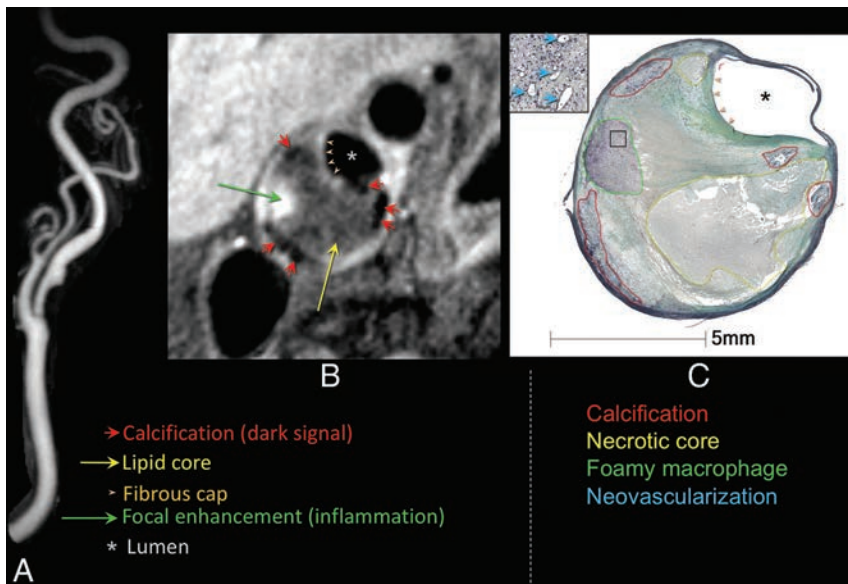


FIG 4. Carotid atherosclerotic plaque MR imaging and a specimen from a 76-year-old woman with transient ischemic attacks ipsilateral to carotid bulb stenosis, measuring 47% by the NASCET criteria demonstrated on a contrast-enhanced MRA. A, Narrowing is caused by the plaque characterized by 2D cardiac-gated double inversion recovery black-blood MR imaging (B). Regional enhancement (green arrow) within the lipid core (yellow arrow) suggests focal inflammation with neovascularity as confirmed on the endarterectomy specimen (C, green circle). Contrast enhancement is also useful for delineating the fibrous cap (B and C, orange arrowheads). Calcification is identified as areas of hypointensity (B, red arrows, and C, red circle).

Lipid-Rich Necrotic Core. Initial research demonstrated that LRNC could be detected as a focal hypointense region on T2WI (Fig 8).^{167,168} Multiple studies have confirmed the improved detection of LRNC seen as a focal nonenhancing region on contrast-enhanced T1WI within the carotid vessel wall.^{60,61} Larger LRNC size correlates with future ipsilateral carotid symptoms. All validation of LRNC detection/quantification and predictive features has been based on multicontrast carotid plaque MR imaging protocol using dedicated carotid coils. Recent work has suggested the ability to detect a large LRNC using commercially available 3D T1WI sequences and large-FOV neck coils. The Canadian Atherosclerosis Imaging Network has recently completed a prospective, multi-institution study using large-FOV neck coils and commercial sequences from a variety of MR imaging vendors to detect LRNC and IPH. When fully analyzed, CAIN may give us additional information about the ability of

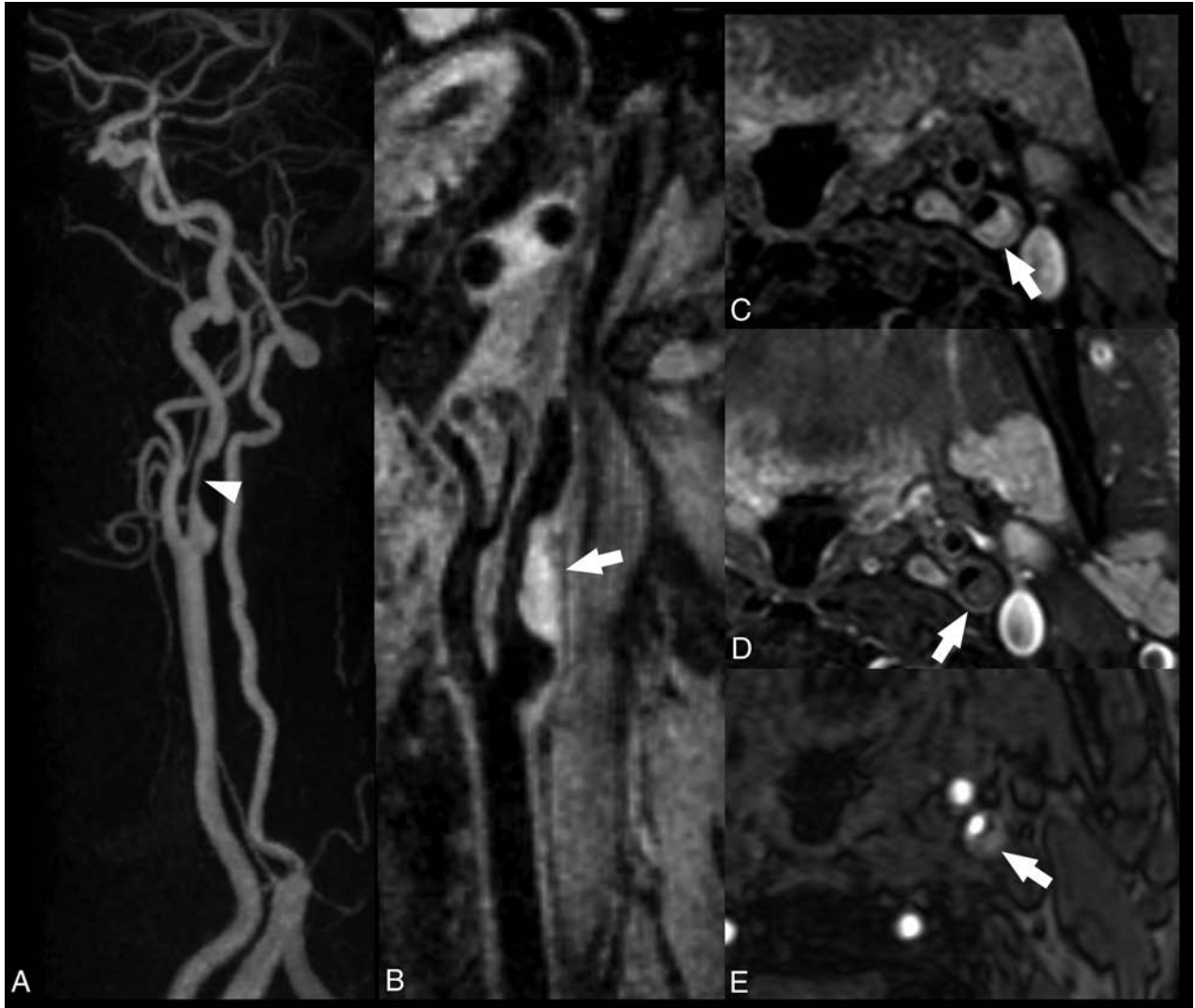


FIG 5. Smooth left internal carotid artery stenosis with intraplaque hemorrhage. All images were acquired with a 16-channel neurovascular coil at 3T. The CE-MRA demonstrates a smooth, nonulcerated stenosis in the bulbous and postbulbous parts of the left internal carotid artery (*white arrowhead, A*). Oblique reformat of a coronally acquired MPRAGE image shows extensive intraplaque hemorrhage, which appears hyperintense (*white arrow, B*). The IPH is hyperintense on the nonenhanced T1 fat-saturated spin-echo image (*C*) and isointense on the gadolinium-enhanced T1 fat-saturated spin-echo image (*D*). On the TOFMRA source data, the IPH also appears hyperintense but to a lesser degree than the intraluminal flow signal (*E*).

IPH and LRNC size detected with large-FOV neck coils and commercial sequences to predict future ipsilateral events.

Fibrous Cap Status. MR imaging can assess fibrous cap status,^{61,169} as opposed to the other noninvasive imaging modalities such as CT and US.¹⁴¹ A regular (thick) FC is characterized by the presence of a juxtaluminal band of low signal on time-of-flight MR images and/or a hyperintense juxtaluminal region on contrast-enhanced T1WI, whereas a thin FC is present when this band of low signal on TOF or the hyperintense region on contrast-enhanced (CE)-T1WI is not visible or when the juxtaluminal hyperintense region on CE-T1-weighted MR imaging is interrupted. The fissured fibrous cap is characterized by 2 distinct features: 1) the absence of the juxtaluminal band of low signal, and 2) the presence of a bright gray region adjacent to the lumen, corresponding to plaque hemorrhage and/or mural thrombus.^{60,170} As shown by Wasserman et al⁶¹ and Cai et al,⁶⁰ contrast-enhanced

imaging could be useful for improving delineation of the cap compared with noncontrast (T2), and CE-T1WI can be used to quantify the fibrous cap and the LRNC. Although resolving a thin fibrous cap defined by pathologic criteria would necessitate a higher field strength to overcome signal constraints, distinguishing thin/ruptured from thick fibrous cap thicknesses can be achieved at 1.5T (Fig 8).^{171,172}

Consistent visualization of the FC requires dedicated carotid surface coils. Yuan et al¹⁷⁰ and others have shown that the fissured FC has a statistically significant association with the presence of cerebrovascular symptoms⁸¹ and is associated with a higher risk of ischemic symptoms in prospective studies.^{79,80}

Neovascularization and Inflammation. There are new contrast agents using iron particles (ultrasmall superparamagnetic iron oxide or P947)^{173,174} that can evaluate plaque inflammation via uptake by phagocytic cells within the inflamed vessel wall. Small

particle-based MR imaging contrast agents (iron oxide) can be used to evaluate the presence of plaque inflammation. These iron oxide particles enter atherosclerotic plaques, with the agents accumulating in macrophages transformed from blood monocytes attracted by inflammatory mediators.⁹⁰ High-risk inflamed plaques contain a focal area of signal loss on MR images, due to iron oxide accumulation.⁹¹ Iron nanoparticles (10- to 300-nm-sized) are also bound to antibodies, drugs, peptides, and polysaccharides; and avidin-biotin cross-linked with polymers is used to assess endothelial function in animal models. Polymer hydroxyl acidic core (polylactic acid) and dendrimers (polyami-

doamine, diaminobutane) have been described as suitable to functionalize the surface of superparamagnetic iron oxide¹⁷⁵ (15- to 60-nm superparamagnetic iron oxide) particles, allowing for ligand binding. Ligand-bound superparamagnetic iron oxide (anti-VCAM-1 and anti-E-selectin antibody conjugated superparamagnetic iron oxide) can cause dephasing and loss of T2* signal intensity due to susceptibility effects and is suitable for passive targeted imaging of inflammation in cardiovascular tissue.¹⁷⁵ In addition to iron oxide nanoparticles, various other nanoparticles are being used for molecular imaging of atherosclerosis in animal models, eg, liposome vesicles (50–70 nm)

for US¹⁷⁶/MR imaging¹⁷⁷; perfluorocarbon core emulsions (200–300 nm) for MR imaging, US, fluorescence, and nuclear imaging; chemo-thermo-immuno¹⁷⁸; and high-density lipoprotein and low-density lipoprotein micelles for MR imaging.¹⁷⁹ Other types of particles such as gold, carbon nanotube fullerenes (4 nm), quantum dots cadmium selenide spheres (2–10 nm), and metal-based agents are in the process of standardization and may be useful in fluorescent imaging.¹⁸⁰ Moreover, other investigators have reported the possibility of viral capsid

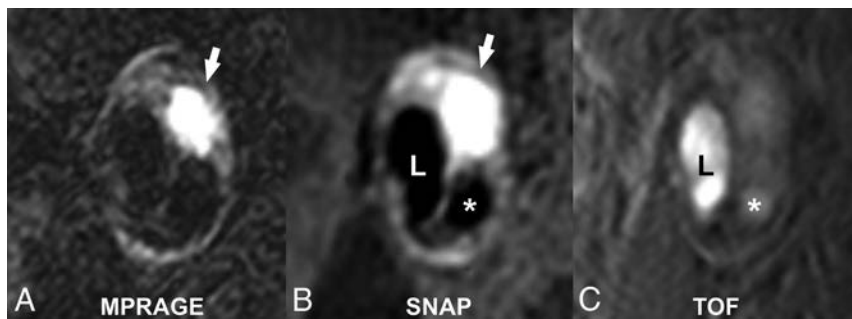


FIG 6. Matched cross-sectional images of a carotid plaque with high signal intensity (white arrows), consistent with the presence of intraplaque hemorrhage on MPRAGE (A) and SNAP MR imaging (B). Note the greater conspicuity of the carotid lumen (L) on SNAP compared with the MPRAGE image. There is a penetrating ulcer (asterisk) that is more easily detected on SNAP compared with the TOF MRA image (C).

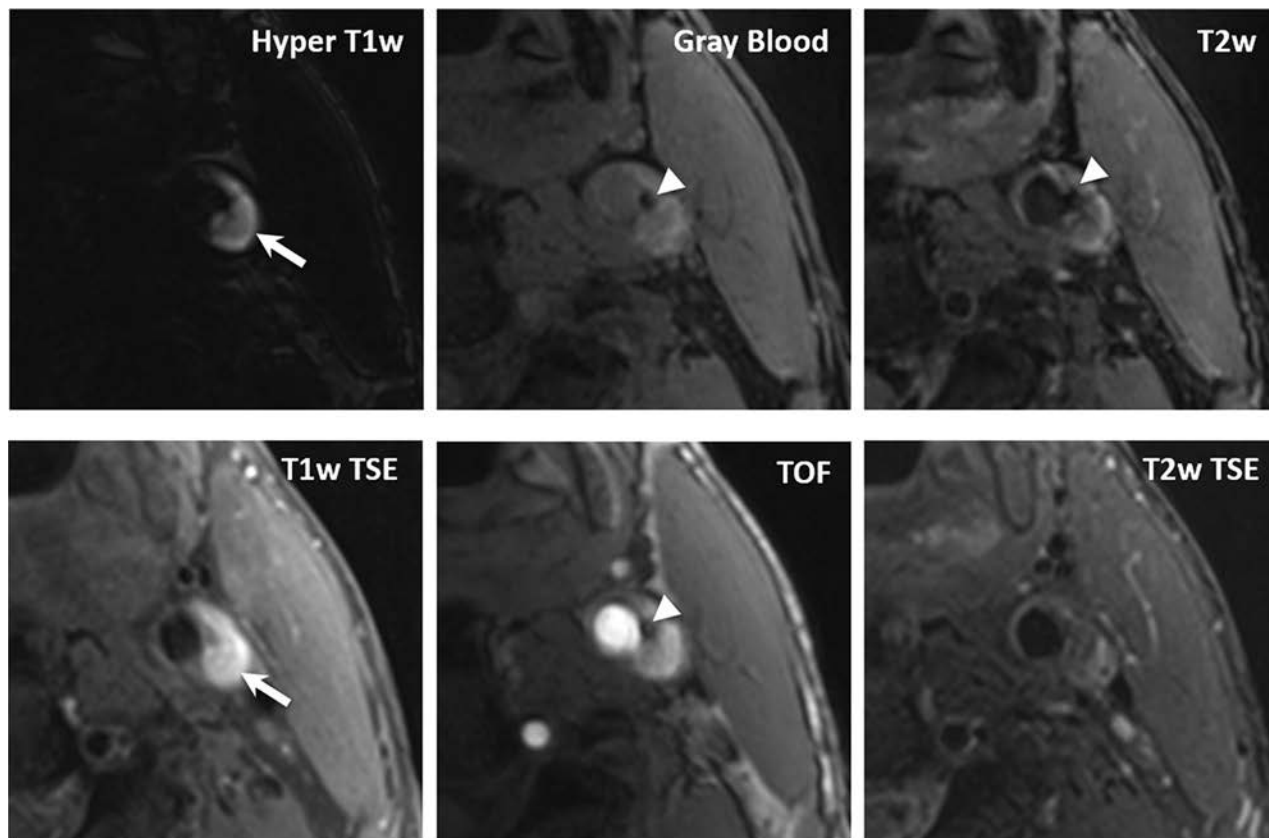


FIG 7. In a 68-year-old male patient, coexistent plaque components, fresh intraplaque hemorrhage (arrows), and superficial calcifications (arrowheads) are detected by MATCH (first row) and the conventional multicontrast protocol (second row). Compared with T1-weighted TSE and TOF, MATCH provides more conspicuous depiction of intraplaque hemorrhage on the hyper-T1-weighted image and calcification on the gray blood image. Notice that the calcification is also visible on the MATCH T2-weighted image but not on the T2-weighted TSE image.

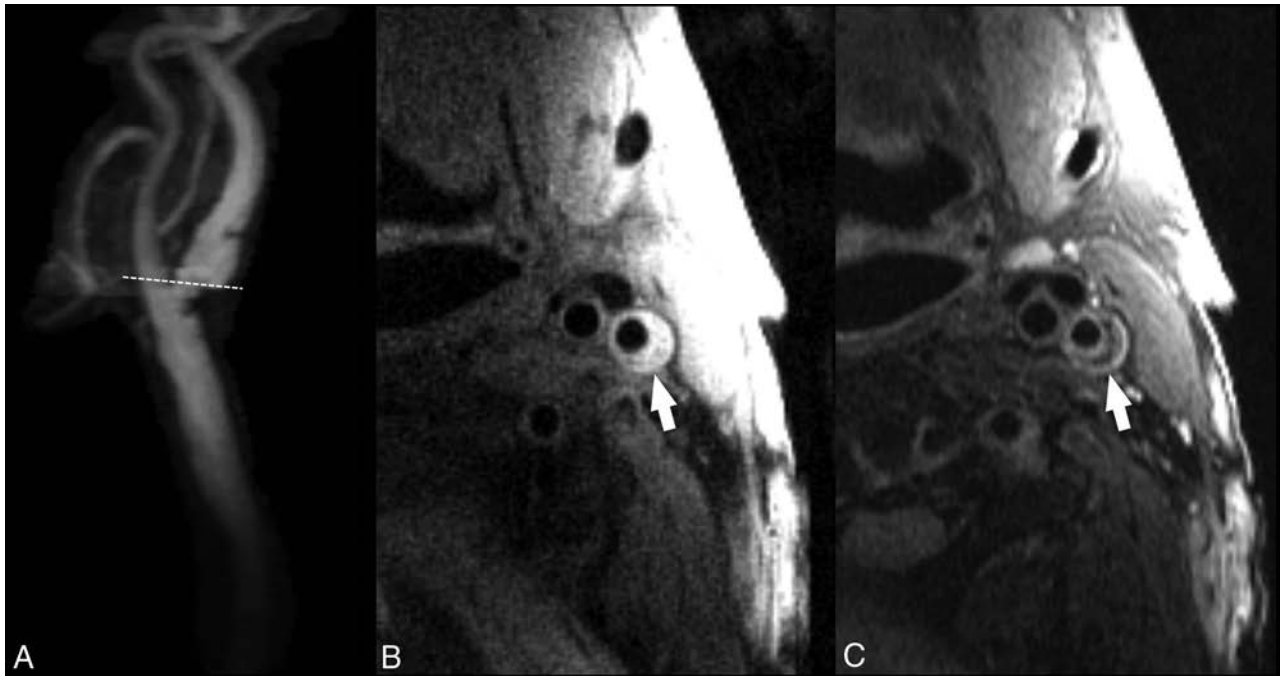


FIG 8. A, Contrast-enhanced MRA of the extracranial carotid bifurcation indicating the level of 2D-FSE images obtained with 1.5T. B, T1-weighted double inversion recovery black-blood FSE image shows an eccentric plaque (*arrow*) in the internal carotid artery. C, T2-weighted double inversion recovery black-blood FSE image at the same level shows a crescentic, hypointense signal from the necrotic core, which is separated by a higher intensity fibrous cap from the flow lumen.

protein cages with gadolinium as potential nanospheres for drug encapsulation and imaging.¹⁸¹

A recent MR imaging study¹⁸² showed that enhancement of carotid plaque after administration of gadolinium is associated with neovascularization ($P < .001$) (Fig 4). The correlation between the degree of plaque enhancement and the degree of neovascularization, which is itself linked to the degree of plaque inflammation, was also confirmed at histology in a recent study by Millon et al.¹⁸² Investigations have shown that inflammatory cells are also present at the interface with the underlying necrotic core and in the plaque shoulder region.^{183,184} From the imaging point of view, it is possible to distinguish 2 different types of neovascularization: 1) adventitial neovascularization, and 2) intraplaque neovascularization. The adventitial neovascularization has been assessed with MR imaging.¹⁴⁴ Ectopic neovascularization in the intima and media is a hallmark of advanced atherosclerotic lesions, but the adventitial layer is a fundamental target because it serves as the main source of in-growth of new vessels. The degree of neovascularity measured using gadolinium perfusion methods correlated with adventitial perfusion as measured by its transfer constant (Fig 9).¹⁸⁵ Wasserman¹⁷¹ categorized the circumferential enhancement (0, absent; 1, <50%; 2, $\geq 50\%$) on postcontrast MR imaging by finding an association between the grade of adventitial enhancement and cerebrovascular events. Plaque perfusion imaging using dynamic contrast-enhanced MR imaging has been shown to give reproducible physiologic measurements of the vasa vasorum.^{186,187} However, protocol compliance may be more important for functional imaging such as dynamic contrast-enhanced MR imaging as compared with anatomic imaging.

Plaque Volume. Recently published studies show the utility of MR imaging for this type of quantification.^{103,188} In general, the

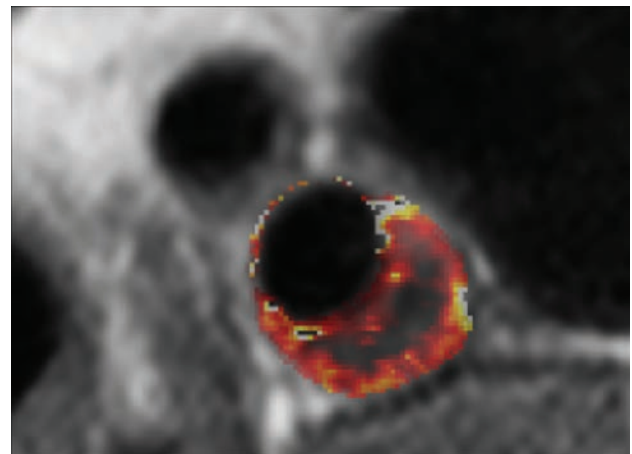


FIG 9. Volume transfer constant (K^{trans}) map of a patient with carotid plaque. Maps were generated using pharmacokinetic modeling of dynamic contrast-enhanced MR images. The parametric map is overlaid on the anatomic MR image, and voxel K^{trans} values (Patlak model) are color-coded. The necrotic core exhibits low K^{trans} values at the center of the plaque, while the highly vascularized adventitia at the outer rim exhibits high K^{trans} values. There is another region of higher K^{trans} values near the inner rim of the plaque.

reliability of MR imaging for plaque assessment has been very good. A study published by Wasserman in 2010¹⁰³ found that the scan reliability for common carotid artery lumen area was 0.94, whereas for the ICA lumen area, it was 0.89. In the assessment of the total wall volume, the value was 0.79, but in the assessment of LRNC volume, the value was very low (0.3). The authors found that overall reliability is primarily related to reader variability rather than scan acquisition. The coefficient of variation values for the plaque area or plaque volume are between 3% and 6%, as demonstrated by Saam et al.^{189,190}

Imaging studies have documented changes in atherosclerotic plaque volume and composition and progression of subclinical lesions into rupture-prone plaques.¹⁹¹⁻¹⁹⁶ The ability to monitor these changes might contribute to our ability to estimate risk and assess pharmaceutical treatment efficacy.¹⁹⁷ For example, changes in plaque structure that correspond with a clinical event help to identify that plaque as a culprit lesion, which puts it at a higher risk for future stroke.^{34,122,198} Several studies have reported using MR imaging for longitudinal analysis of carotid plaque variations,¹⁹¹⁻¹⁹³ with fewer reports using CTA.^{194,195}

MR Imaging Limitations. An important limitation to contrast-enhanced MR imaging evaluation of plaque that has recently emerged is the potential for gadolinium toxicity, particularly when longitudinal monitoring is required. Recent studies have reported the accumulation of gadolinium in various tissues of patients without renal impairment, including in bone, brain, and kidneys,¹⁹⁹⁻²⁰¹ and in July 2015, the US Food and Drug Administration published a safety announcement that it is investigating the risk of brain deposits associated with the repeat use of gadolinium contrast agents in MR imaging,²⁰² stating: “To reduce the potential for gadolinium accumulation, health care professionals should consider limiting GBCA [gadolinium-based contrast agents] use to clinical circumstances in which the additional information provided by the contrast is necessary. Health care professionals are also urged to reassess the necessity of repetitive GBCA MRIs in established treatment protocols.” This risk must now be weighed against the potential radiation hazard described earlier that limits longitudinal plaque monitoring by CT.

Advanced Algorithms to Carotid Artery Plaque Characterization

With the development of deep learning technology and plaque characterization algorithms applied to medical imaging, it is now possible to identify, classify, and quantify target features from imaging datasets such as total carotid artery plaque volume and plaque subcomponent detection (calcium, IPH, lipid core).^{203,204} Deep-learning technology has experienced rapid progress in health care over recent years, with early reports of implementation in carotid imaging²⁰⁴ raising the prospect of routine use in the clinical setting once validated.

Functional–Molecular Imaging

“Molecular” imaging techniques have been gaining popularity. The objective of molecular imaging is to provide biologic insight into the identification and classification of carotid artery plaques, especially those at high risk. In atherosclerotic plaques, multiple and complex reactions take place at the molecular and cellular level, with various atherosclerosis-related biomarkers present at different stages of disease progression.²⁰⁵ Conventional imaging with US, MR, or CT cannot identify these components because of limited imaging contrast; therefore, several methods have been proposed that use external contrast agents targeting these specific biomarkers.

A wide variety of studies has assessed the diagnostic potential of nuclear medicine techniques for imaging and quantifying plaque inflammation, such as by PET using the widely available [¹⁸F] FDG or newer radiotracers such as [¹⁸F] fluorocholine

(Fig 10).²⁰⁶⁻²⁰⁸ Nuclear medicine tracer techniques have also shown efficacy in the identification of neovascularization.^{209,210}

Because vulnerable plaques are infiltrated by lymphocytes and macrophages, with the latter cell population capable of taking up [¹⁸F] FDG from the interstitial spaces, [¹⁸F] FDG PET can be used to directly detect plaque inflammation in various anatomic locations.²¹¹ In recent years, a number of studies have assessed the diagnostic potential of [¹⁸F] FDG PET to image and quantify plaque inflammation^{206,207} as well as monitoring the reduction of plaque inflammation resulting from statin therapy.²⁰⁸

RECOMMENDATIONS

Carotid MRI

Background. Results from recently published meta-analyses support the hypothesis that MR imaging detection of carotid IPH is associated with increased risk for future primary and recurrent ischemic neurologic events.^{79,212,213} Furthermore, the absence of IPH portends a benign clinical course, even among patients with symptomatic 50%–99% carotid stenosis.²¹³ Other plaque features associated with increased risk include identification of a large LRNC and a thin or ruptured fibrous cap.⁷⁹

Goals. 1) To provide general guidelines for carotid MR vessel wall imaging with recommended imaging sequences, spatial resolution, and coverage. Guideline considerations are that the protocol can be applied broadly across a spectrum of clinical scanners and not require specialized software or research keys for implementation, and 2) to recommend future areas for technical development and clinical expansion needs.

Essential Features for Identification with Carotid Plaque Imaging. Any MR imaging protocol for plaque imaging should be able to identify the following atherosclerotic plaque characteristics:

- 1) Stenosis and luminal surface condition (fibrous cap and ulceration).
- 2) Presence of intraplaque hemorrhage.
- 3) Presence of lipid rich necrotic core.
- 4) Plaque burden and distribution.

Minimum MR Imaging Protocol Requirements for Identification of Essential Plaque Features (1.5T and 3T). Recommended minimum sequence requirements are the following:

- Resolution: In-plane 0.6 mm, through-plane 2 mm
- Longitudinal coverage: 3–4 cm centered on the carotid bifurcation
- Effective blood suppression for a plaque burden visualization sequence.

The protocol may include any combination of sequences that meets the minimum requirements set forth above. The sequences used can be either 2D or 3D or a combination, provided that they together meet the minimum sequence requirements above. Overall scan time can be adjusted based on field strength and the availability of specialized hardware such as carotid phased array coils. 3T scanners are recommended for improved SNR.

Example Protocols. Four protocols are presented based on considerations for 2D and 3D imaging and the use of gadolin-

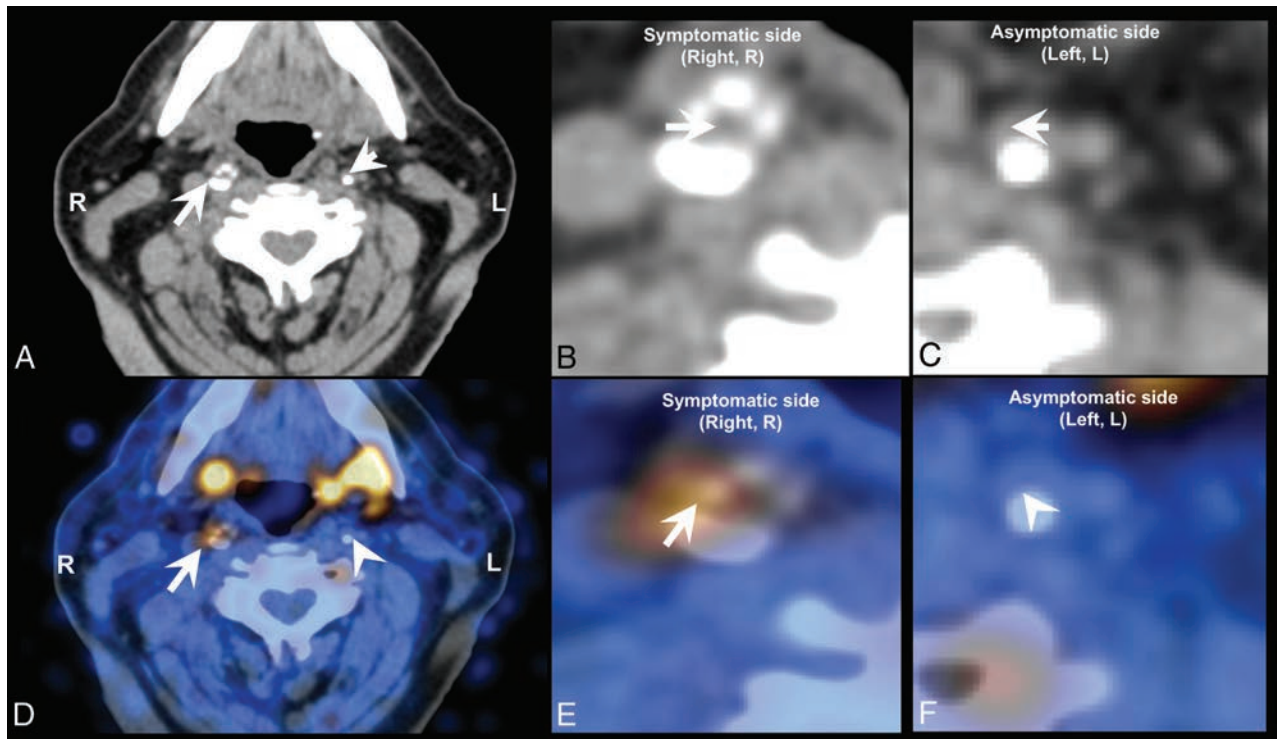


FIG 10. [¹⁸F] fluorocholine positron-emission tomography CT (¹⁸F-FCH PET CT) image of a symptomatic (arrow) and contralateral asymptomatic (arrowhead) carotid plaque of a patient who experienced right-sided stroke. A, Diagnostic contrast-enhanced CT shows a significant stenosis in the right internal carotid artery because of a calcified plaque, whereas a noncalcified atherosclerotic plaque can be seen on the contralateral internal carotid artery. B, CT, inset on the symptomatic plaque. C, CT, inset on the asymptomatic plaque. D, The fused PET CT image denotes a focal area of high [¹⁸F] FCH uptake in the right symptomatic carotid plaque, whereas there is no visible [¹⁸F] FCH uptake in the left asymptomatic carotid plaque. E, Fused PET CT, inset on the symptomatic plaque. F, Fused PET-CT, inset on the asymptomatic plaque.

Table 1: 3D Noncontrast protocol

Name	3D TOF	3D MPRAGE	3D TIWI SPACE/Cube/VISTA	3D T2WI SPACE/Cube/VISTA
Plaque feature	Stenosis, ulceration, calcification	Intraplaque hemorrhage	Plaque burden and distribution	LRNC
Sequence ^a	FFE/SPGR	IR-TFE/SPGR	TSE/FSE	TSE/FSE
Image mode	3D	3D	3D	3D
Scan plane	Axial	Coronal	Coronal	Coronal
TR (ms)	24	15	1000	2500
TE (ms)	4.6	Minimum	30	250
FOV (cm)	16 × 16	16 × 16	16 × 16	16 × 16
Resolution (mm ²)	0.6 × 0.6	0.6 × 0.6	0.6 × 0.6	0.6 × 0.6
Slice thickness (mm)	1 ^b	0.6	0.6	0.6
Blood suppression	Saturation—veins	None	MSDE/FSD ^c	MSDE/FSD
Special parameters	Flip angle = 20°	Flip angle = 15° TI = 500 ms Turbo factor = 30, IRTR = 800 ms	Echo-train: variable VFA T1	Echo-train: variable VFA T2
Fat suppression	No	Yes (water excitation)	Yes	Yes

Note:—SPGR indicates echo-spoiled gradient-echo; FFE, fast-field echo; IR-TFE, inversion recovery—turbo field echo; VFA, variable flip angle; IRTR, time interval between 2 consecutive IR pulses; MSDE, motion-sensitized driven equilibrium; FSD, flow-sensitized dephasing.

^a Siemens/Philips/GE acronyms.

^b Interpolated resolution.

^c Pulse gating not required for any sequence.

ium contrast agents (Tables 1–4). If patients are able to undergo gadolinium contrast injection, its use is recommended for the detection and quantification of LRNC and the delineation of the fibrous cap.^{60,214} Use of large-coverage 3D sequences can detect plaques extending beyond the 4-cm coverage centered on the bifurcation and is preferable. Carotid coils are recommended for use with all protocols, though large-FOV

neck coils can detect IPH. It is possible to add a 4-minute 3D MPRAGE sequence to routine clinical carotid MRA protocol. The protocol is similar to Table 1, but with 0.8-mm isotropic resolution using a large-FOV neck coil instead of 0.6 mm using dedicated carotid surface coils. Focal regions of T1 hyperintensity within the carotid plaque that are 15× greater than the adjacent sternocleidomastoid muscle can be used to identify IPH.

Table 2: 3D contrast protocol

Name	3D TOF	3D MPRAGE	Precontrast and Postcontrast ^a 3D TIWI SPACE/Cube/VISTA
Plaque feature	Stenosis, ulceration, calcification	Intraplaque hemorrhage	Plaque burden and distribution, LRNC
Sequence ^b	FFE/SPGR	IR-TFE/SPGR	TSE/FSE
Image mode	3D	3D	3D
Scan plane	Axial	Coronal	Coronal
TR (ms)	24	15	1000
TE (ms)	4.6	Minimum	30
FOV (cm)	16 × 16	16 × 16	16 × 16
Resolution (mm ²)	0.6 × 0.6	0.6 × 0.6	0.6 × 0.6
Slice thickness (mm)	1 ^c	0.6	0.6
Blood suppression	Saturation–veins	None	MSDE/FSD ^d
Special parameters	Flip angle = 20°	Flip angle = 15° TI = 500 ms Turbo factor = 30, IRTR = 800 ms	Echo-train: variable VFA TI
Fat suppression	No	Yes (water excitation)	Yes

^a Clinical CE-MRA per institutional protocol can be used before postcontrast sequence.

^b Siemens/Philips/GE acronyms.

^c Interpolated resolution.

^d Pulse gating not required for any sequence.

Table 3: 2D noncontrast protocol

Name	TOF MRA Localizer	Oblique TIWI Localizer	TIWI	T2WI	3D-TOF	MPRAGE
Plaque feature	Localize artery	Localize bifurcation	Plaque burden and distribution	LRNC	Stenosis, ulceration, calcification	Intraplaque hemorrhage
Sequence ^a	FFE/SPGR	TSE/FSE	TSE/FSE	TSE/FSE	FFE/SPGR	IR-TFE/IR-FSPGR
Image mode	2D	2D	2D	2D	3D	3D
Scan plane	Axial	Oblique	Axial	Axial	Axial	Axial
TR (ms)	25	2000	800	4800	24	13
TE (ms)	4	8	10	50	Minimum	Minimum
FOV (cm)	16 × 12	16 × 16	16 × 16	16 × 16	16 × 16	16 × 16
Resolution (mm ²)	0.63 × 0.83	0.63 × 0.63	0.63 × 0.63	0.63 × 0.63	0.63 × 0.63	0.63 × 0.63
Slice thickness (mm)	2	2	2	2	2/–1	2/–1
No. of slices	32	6	16	16	40	40
Blood suppression	None	DIR	DIR	DIR	None ^b	None
Special parameters	Flip angle = 40°	Echo-train = 14; 3 slices/TR	Echo-train = 10;	Echo-train = 12; 8 slices/TR	Flip angle = 20°	Flip angle = 15°, turbo factor = 30, TI = 500 ms, IRTR = 800 ms Water excitation
Fat suppression	No	Yes	Yes	Yes	No	Water excitation

Note:—DIR indicates double inversion recovery; FSPGR, fast-spoiled gradient recalled.

^a Siemens/Philips/GE acronyms.

^b Pulse gating not required for any sequence.

Motion-sensitized driven-equilibrium²¹⁵/flow-sensitive dephasing²¹⁶ flow suppression is required for 3D sampling perfection with application-optimized contrasts using different flip angle evolution (SPACE; Siemens, Erlangen, Germany)/Cube (GE Healthcare, Milwaukee, Wisconsin)/volume isotropic turbo spin-echo acquisition (VISTA; Philips Healthcare, Best, the Netherlands) to ensure effective blood suppression to accurately identify plaque lumen boundaries. Good blood suppression postcontrast requires the use of motion-sensitized driven-equilibrium or double inversion recovery (DIR)/quadruple inversion recovery²¹⁷ flow suppression. For DIR, the inversion time can be calculated based on estimated T1 values of blood at 5-minute intervals following contrast administration (0.1 mmol/kg) for 1.5T or 3T scanners.²¹⁸ We recommend a TI of 250 ms for 3T scanners for a TR triggered at a 1 RR interval, which generally produces adequate flow suppression beginning 5 minutes after injection despite variations in postinjection scan time and heart rate, which will affect the T1 blood values.

Discussion. Lumen. Quantifying luminal narrowing is a prerequisite, as stenosis severity is the cornerstone for treatment decisions in

current clinical guidelines. Furthermore, detection of ulceration provides prognostic value. Use of TOF MRA for lumen assessment avoids the need for IV contrast and may provide confirmatory evidence of intraplaque hemorrhage and sometimes calcification. Addition or substitution with CE-MRA should be considered for those without contraindication for contrast administration. This would also provide an opportunity to perform post-contrast-enhanced imaging of the vessel wall for direct identification of the LRNC and identification/confirmation of fibrous cap status and ulcerations.

IPH. MR imaging techniques are available for IPH detection across scanner platforms, and the predictive value of IPH for ischemic events has been extensively evaluated, both with and without custom carotid coils. In a review performed by Gupta et al,⁷⁹ studies were stratified by those utilizing multisequence, carotid coil–dependent protocols and those using a single sequence with standard large-FOV neck coils for IPH detection. Using either technique, IPH was associated with significantly increased risk for TIA or stroke (hazard ratio, 440; 95% CI, 210–923; and hazard ratio, 504; 95% CI, 215–1185, respectively). While IPH can be identified on TIWI sequences

Table 4: 2D contrast protocol

Name	TOF MRA Localizer	Oblique T1WI Localizer	Precontrast and Postcontrast ^a T1WI	3D-TOF	MPRAGE
Plaque feature	Localize artery	Localize bifurcation	Plaque burden and distribution, LRNC	Stenosis, ulceration, calcification	Intraplaque hemorrhage
Sequence ^b	FFE/SPGR	TSE/FSE	TSE/FSE	FFE/SPGR	IR-TFE/IR-FSPGR
Image mode	2D	2D	2D	3D	3D
Scan plane	Axial	Oblique	Axial	Axial	Axial
TR (ms)	25	2000	800	24	13
TE (ms)	4	8	10	Min	Min
FOV (cm)	16 × 12	16 × 16	16 × 16	16 × 16	16 × 16
Resolution (mm ²)	0.63 × 0.83	0.63 × 0.63	0.63 × 0.63	0.63 × 0.63	0.63 × 0.63
Slice thickness (mm)	2	2	2	2/-1	2/-1
No. of slices	32	6	16	40	40
Blood suppression	Saturation—veins	MSDE	QIR ^c	Saturation—veins	No ^d
Special parameters	Flip angle = 40°	Echo-train = 14; 3 slices/TR	Echo-train = 10	Flip angle = 20°	Flip angle = 15°, turbo factor = 30, TI = 500 ms, IRTR = 800 ms
Fat suppression	No	Yes	Yes	No	Water excitation

Note:—QIR indicates quadruple inversion recovery.

^a Clinical CE-MRA per institutional protocol can be used before postcontrast sequence.

^b Siemens/Philips/GE acronyms.

^c Double inversion recovery can be used, but blood suppression may be incomplete, and inversion time is a variable dependent on patient and contrast bolus.

^d Pulse gating not required for any sequence.

such as T1WI fast spin-echo, T1WI SPACE, TOF, and so forth, a highly T1-weighted sequence such as MPRAGE can provide higher sensitivity and specificity for IPH detection.²¹⁹

Lipid-Rich Necrotic Core. T2-weighted imaging can be used to detect the presence of LRNC.^{167,168} Direct assessment of the LRNC can also be done in patients undergoing contrast administration using a postcontrast T1WI scan. CE-MRA followed by post-CE vessel wall imaging in patients without contraindication will improve detection and quantification of the LRNC and delineation of the fibrous cap.²¹⁴

Plaque Burden and Distribution. Knowledge of the location and distribution of plaque assists in preprocedural planning. Time-efficient 3D large-coverage black-blood MR imaging may be better suited for this purpose.

Future Improvements and Needs for MR Imaging. Technical developments are urgently needed in the following areas:

- 1) Improved spatial resolution both in-plane and through-plane to better characterize finer structures such as fibrous caps.
- 2) More effective blood flow suppression for large-spatial-coverage imaging acquisition and pre- and postcontrast administration.
- 3) Dedicated carotid coils that are integrated with head and neck coils for extensive coverage.
- 4) Improved techniques for identifying the lipid rich necrotic core, especially without the need for contrast application.
- 5) More effective methods to deal with motion.
- 6) A streamlined imaging protocol that is able to identify multiple imaging targets in 1 or 2 imaging sequences.
- 7) Effective image-processing tools for efficient quantitative identification of imaging targets.
- 8) Development of training programs for MR imaging specialists on image acquisition and for radiologists on vessel wall image interpretation.
- 9) Ultimately, a guideline that clearly calls for the need for carotid plaque imaging and 1 simple protocol that can meet all the needs.

Currently, there are many new techniques being developed for carotid plaque imaging. 3D-SNAP provides non-contrast-enhanced MRA and simultaneous IPH detection.¹⁶⁴ 3D spoiled gradient-recalled echo pulse sequence for hemorrhage assessment using inversion recovery and multiple echoes (3D-SHINE) provides information about the state of IPH in addition to IPH detection.²²⁰ IPH can also be identified on a precontrast mask of CE-MRA if available.⁶³ MATCH provides comprehensive information regarding plaque composition in a single sequence.¹⁶³ 3D Multiple Echo Recombined Gradient Echo (3D-MERGE)²²¹ and 3D delay alternating with nutation for tailored excitation with fast low-angle shot (3D-DASH)²²² provide large-coverage blood suppression for plaque burden measurements. Diffusion-weighted imaging can detect LRNC without the use of contrast media.²²³ Self-gating has been used to reject data acquired during swallowing motion.²²⁴ T1-insensitive blood-suppression techniques such as quadruple inversion recovery²¹⁷ provide good blood suppression for post-contrast imaging. However, these supplementary techniques require specialized equipment (3T, custom carotid coils, custom sequences) and more intensive interpreter training.

Carotid CT

Background. Currently no meta-analyses or prospective trials have suggested that some specific CT features are associated with an increased risk for future primary and recurrent ischemic neurologic events, even if there are several prospective trials on their way or that have been published that examine the value of plaque imaging prospectively (PARISK, CAPIAS, CARE-II).¹⁰⁴⁻¹⁰⁶ However, cross-sectional studies have found that some CT characteristics (Hounsfield unit attenuation, the presence of neovascularization) are associated with increased risk of cerebrovascular events.^{48,225}

Goals. 1) To provide general guidelines for carotid CT vessel wall imaging with recommended desirable imaging techniques, tissue contrast, spatial resolution, and coverage. Guideline considerations are that the protocol can be applied

Table 5: Aquilion Vision^a

	Scanogram (AP–Lat)	Basal Scan (Optional)	Contrast Scan
Coverage	Sternum to midhead	Midneck to cover the bifurcation	From aortic arch to midhead
Scan mode	Scanogram	Helical	Helical
Start time	NA		Bolus tracking ^b
Range	500 mm	8 cm	Variable
Collimation	NA	0.5 × 80	0.5 × 80
Pitch	NA	1	1
kV	120	120	120
mA	50–200 ^c	350	350
Rotation time	NA	0.275 second	0.275 second
Direction	NA	Caudocranial ^d	Caudocranial ^d
Slice thickness	NA	1 mm	1 mm
Slice interval	NA	0.5 mm	0.5 mm
FOV	Wide	20 cm	20 cm
Filter	NA	Sharp (FL03)	Sharp (FL03)
CTDI (mGy)	–	15	15
DLP (mGy × cm)	–	0.6	0.6
Amount of CM	–	–	40–50 mL ^e
IDR	–	–	1.4–1.5 g I/s
Concentration ^f	–	–	370 mg I/mL
Flow rate ^f	–	–	4 mL/s

Note:—NA indicates not applicable; AP, anteroposterior; Lat, lateral; CTDI, CT dose index; DLP, dose-length product; IDR, iodine delivery rate; CM, contrast medium.

^a Toshiba Medical Systems, Tokyo, Japan.

^b Position of bolus tracking: aortic arch, threshold 100 HU.

^c 50 mA in AP and 200 in Lat.

^d Craniocaudal is also possible.

^e Variable according to the concentration.

^f Concentration × flow rate = IDR. The parameter to be considered is IDR.

Table 6: Somatom Sensation 64^a

	Scanogram (AP–Lat)	Basal Scan (Optional)	Contrast Scan
Coverage	Sternum to midhead	Midneck to cover the bifurcation	From aortic arch to midhead
Scan mode	Scanogram	Helical	Helical
Start time	NA		Bolus tracking ^b
Range	500 (mm)	8 cm	Variable
Collimation	NA	0.6 × 64	0.6 × 64
Pitch	NA	0.55	0.55
kV	120	120	120
mA	50–200 ^c	350	350
Rotation time	NA	0.28 second	0.28 second
Direction	NA	Craniocaudal ^d	Craniocaudal ^d
Slice thickness	NA	1 mm	1 mm
Slice interval	NA	0.5 mm	0.5 mm
FOV	Wide	20 cm	20 cm
Filter	NA	Sharp (B30f)	Sharp (B30f)
CTDI (mGy)	–	18	18
DLP (mGy × cm)	–	0.65	0.65
Amount of CM	–	–	40–50 mL ^e
IDR	–	–	1.4–1.5 g I/s
Concentration ^f	–	–	370 mg I/mL
Flow rate ^f	–	–	4 mL/s

^a Siemens, Malvern, Pennsylvania.

^b Position of bolus tracking: aortic arch, threshold 100 HU.

^c 50 mA in AP and 200 in Lat.

^d Caudocranial is also possible with optimal results.

^e Variable according to the concentration.

^f Concentration × flow rate = IDR. The parameter to be considered is IDR.

broadly across a spectrum of clinical CT scanners and not require specialized software or research keys for implementation. 2) To recommend future areas for technical development and clinical expansion needs.

Essential Features for Identification with Carotid Plaque Imaging. Any CT protocol for plaque imaging should be able to identify the following atherosclerotic plaque characteristics:

- 1) Stenosis and luminal surface condition (plaque morphology and ulceration).
- 2) Type of plaque (fatty versus mixed versus calcified).
- 3) Presence of plaque enhancement.
- 4) Plaque burden and distribution.

Minimum CT Protocol Requirements for Identification of Essential Plaque Features. Recommended minimum parameter requirements are the following:

- Resolution: isotropic voxel with 1-mm resolution
- Longitudinal coverage: from the aortic arch to intracranial vessels
- CT generation: third with at least 16-detector-row.

Example Protocols. Four protocols are presented (Tables 5–8). No CT study of carotid arteries must be performed without the administration of contrast material. The use of a biphasic approach (unenhanced scan followed by a contrast scan) allows the assessment of the carotid plaque neovascularization. This is becoming more important but is not considered currently necessary. To reduce the radiation dose delivered to the patients, the z-length of the basal scan should cover only the carotid artery plaque bifurcation (4-cm coverage centered on the bifurcation). The dual-energy CT technique¹⁴³ allows a virtual unenhanced image to assess plaque enhancement without the need for a biphasic approach.

Discussion. Lumen. Quantifying luminal narrowing is a prerequisite. To correctly assess the degree of stenosis, by avoiding the halo or edge blur, the correct window settings should be used.²²⁶ At the current level of technology, the status of the FC cannot be adequately explored by CT.

Type of Plaque. According to Hounsfield unit attenuation, the carotid plaque can be categorized as fatty (<60 HU), mixed (between 60 and 130 HU), and calcified (>130 HU). By applying these thresholds, it is possible to identify those plaques with a LRNC from others. Applying the Hounsfield unit classification, however, creates 2 problems

Table 7: ICT

	Scanogram (AP–Lat)	Basal Scan (Optional)	Contrast Scan
Coverage	Sternum to midhead	Midneck to cover the bifurcation	From aortic arch to midhead
Scan mode	Scanogram	Helical	Helical
Start time	NA		Bolus tracking ^b
Range	500 (mm)	8 cm	Variable
Collimation	NA	0.625 × 128	0.625 × 128
Pitch	NA	0.933	0.933
kV	120	120	120
mA	50–200 ^c	350	350
Rotation time	NA	0.5 second	0.5 second
Direction	NA	Craniocaudal ^d	Craniocaudal ^d
Slice thickness	NA	1 mm	1 mm
Slice interval	NA	0.5 mm	0.5 mm
FOV	Wide	20 cm	20 cm
Filter	NA	Sharp (B)	Sharp (B)
CTDI (mGy)	–	15	16
DLP (mGy × cm)	–	0.6	0.6
Amount of CM	–	–	40–50 mL ^e
IDR	–	–	1.4–1.5 g I/s
Concentration ^f	–	–	370 mg I/mL
Flow rate ^f	–	–	4 mL/s

^a Philips Healthcare.

^b Position of bolus tracking: aortic arch, threshold 100 HU.

^c 50 mA in AP and 200 in Lat.

^d Caudocranial is also possible with optimal results.

^e Variable according to the concentration.

^f Concentration × flow rate = IDR. The parameter to be considered is IDR.

Table 8: LightSpeed VCT^a

	Scanogram (AP–Lat)	Basal Scan (Optional)	Contrast Scan
Coverage	Sternum to midhead	Midneck to cover the bifurcation	From aortic arch to midhead
Scan mode	Scanogram	Helical	Helical
Start time	NA		Bolus tracking ^b
Range	500 (mm)	8 cm	Variable
Collimation	NA	0.625 × 64	0.625 × 64
Pitch	NA	0.984	0.984
kV	120	120	120
mA	50–200 ^c	350	350
Rotation time	NA	0.5 second	0.5 second
Direction	NA	Craniocaudal ^d	Craniocaudal ^d
Slice thickness	NA	1 mm	1 mm
Slice interval	NA	0.625 mm	0.625 mm
FOV	Wide	20 cm	20 cm
Filter	NA	Sharp (B)	Sharp (B)
CTDI (mGy)	–	15	16
DLP (mGy × cm)	–	0.6	0.6
Amount of CM	–	–	40–50 mL ^e
IDR	–	–	1.4–1.5 g I/s
Concentration ^f	–	–	370 mg I/mL
Flow rate ^f	–	–	4 mL/s

^a GE Healthcare.

^b Position of bolus tracking: aortic arch, threshold 100 HU.

^c 50 mA in AP and 200 in Lat.

^d Caudocranial is also possible with optimal results.

^e Variable according to the concentration.

^f Concentration × flow rate = IDR. The parameter to be considered is IDR.

that have recently come to light: 1) The Hounsfield unit value of the plaque is dependent on the level of energy applied, as demonstrated by Saba et al¹³² using multienergy systems, and 2) the carotid artery plaques may show contrast enhancement (by comparing the attenuation values of the basal and postcontrast scans), suggesting that the attenuation value of the plaque obtained after administration

of contrast material represents 2 different parameters: the type of the plaque and the degree of neovascularization of the tissue.^{143,227} This is not a problem if pre- and postcontrast scans or dual-energy is applied (capable of distinguishing plaque from contrast enhancement), but this is not usually done clinically secondary to an increase in x-ray dose.

Carotid Plaque Enhancement. Assessment of plaque enhancement is limited in the case of single-phase CTA, and multiphase CTA is rarely performed outside of research studies due to radiation concerns. An unenhanced axial CT scan obtained over 4 cm centered on the carotid bifurcation, followed by CTA, would theoretically be ideal in assessing plaque enhancement but carries a greater radiation penalty. Alternatively, some authors have employed dual-energy techniques with the use of the virtual nonenhanced image to assess plaque enhancement with less radiation dose.¹⁴³

Plaque Burden and Distribution.

Knowledge of the location and distribution of plaque assists in preprocedural planning. Moreover, CT can calculate the volume of the carotid artery plaque and determine the volume of the subcomponents, according to the Hounsfield unit threshold.¹⁴⁹

Future Improvements and Needs for CT. Technical developments are urgently needed in the following areas:

- 1) Improved contrast resolution for greater discrimination of tissue types in plaque.
- 2) Improved techniques such as multienergy applications for identifying the lipid-rich necrotic core, especially without the need for contrast application.
- 3) Evidence-based guidelines that invoke the need for carotid plaque imaging, preferably using 1 simple universal protocol that can meet all needs.

Currently, most of the research on carotid artery CT is focusing on methods that 1) reduce the radiation dose delivered to the patients, and 2) improve carotid artery

plaque characterization using multienergy tools that promise more accurate detection of plaque components.

CONCLUSIONS

In the last 20 years, there has been a paradigm shift in the imaging of the atherosclerotic carotid artery, from the assessment of the

degree of luminal stenosis to the characterization of plaque. Several features have been identified that are potentially associated with plaque rupture, and imaging has been used to identify these features in vivo.

Researchers and clinicians now have several imaging modalities that allow in-depth exploration of carotid artery plaque and its components. Sonography should be considered as a first-line examination, at least for screening, whereas CT and MR imaging improve identification of several plaque features associated with vulnerability.

Also promising are nuclear medicine and molecular imaging techniques that can further explore assessment of plaque vulnerability, especially inflammation, but these approaches are still investigational and not part of the main diagnostic algorithm of carotid atherosclerosis. In the future, larger prospective longitudinal studies investigating these technologic advances may fully exploit the clinical potential of vessel wall imaging.

ACKNOWLEDGMENTS

The authors would like to thank Drs Stefan Vöö and Wei Zu for their help in image selection for this article.

REFERENCES

1. Yanez ND, Burke GL, Manolio T, et al; CHS Collaborative Research Group. **Sibling history of myocardial infarction or stroke and risk of cardiovascular disease in the elderly: the Cardiovascular Health Study.** *Ann Epidemiol* 2009;19:858–66 CrossRef Medline
2. Truelsen T, Begg S, Mathers C. The global burden of cerebrovascular disease. Geneva: World Health Organization; 2000. http://www.who.int/healthinfo/statistics/bod_cerebrovasculardiseasestroke.pdf. Accessed December 6, 2017
3. Ooi YC, Gonzalez NR. **Management of extracranial carotid artery disease.** *Cardiol Clin* 2015;33:1–35 CrossRef Medline
4. Barnett HJ, Taylor DW, Eliasziw M, et al. **Benefit of carotid endarterectomy in patients with symptomatic moderate or severe stenosis: North American Symptomatic Carotid Endarterectomy Trial Collaborators.** *N Engl J Med* 1998;339:1415–25 CrossRef Medline
5. Howarth JC, Klotz JG. **The diagnostic value of carotid arteriography: a preliminary report.** *Cleve Clin Q* 1951;18:179–83 CrossRef Medline
6. von Arbin M, Britton M, de Faire U, et al. **Non invasive assessment of the internal carotid artery in stroke patients.** *Scand J Clin Lab Invest* 1983;43:275–83 CrossRef Medline
7. Weinberger J. **Clinical applications of noninvasive carotid artery testing.** *J Am Coll Cardiol* 1985;5:137–48 CrossRef Medline
8. Imparato AM, Riles TS, Gorstein F. **The carotid bifurcation plaque: pathologic findings associated with cerebral ischemia.** *Stroke* 1979;10:238–45 CrossRef Medline
9. Redgrave JN, Lovett JK, Gallagher PJ, et al. **Histological assessment of 526 symptomatic carotid plaques in relation to the nature and timing of ischemic symptoms: the Oxford plaque study.** *Circulation* 2006;113:2320–28 CrossRef Medline
10. Jeziorska M, Woolley DE. **Local neovascularization and cellular composition within vulnerable regions of atherosclerotic plaques of human carotid arteries.** *J Pathol* 1999;188:189–96 Medline
11. Choi CJ, Kramer CM. **MR imaging of atherosclerotic plaque.** *Radiol Clin North Am* 2002;40:887–98 CrossRef Medline
12. Moody AR. **Magnetic resonance direct thrombus imaging.** *J Thromb Haemost* 2003;1:1403–09 CrossRef Medline
13. Oliver TB, Lammie GA, Wright AR, et al. **Atherosclerotic plaque at the carotid bifurcation: CT angiographic appearance with histopathologic correlation.** *AJNR Am J Neuroradiol* 1999;20:897–901 Medline
14. Bluth EI. **Evaluation and characterization of carotid plaque.** *Semin Ultrasound CT MR* 1997;18:57–65 CrossRef Medline
15. Naghavi M, Libby P, Falk E, et al. **From vulnerable plaque to vulnerable patient: a call for new definitions and risk assessment strategies, part II.** *Circulation* 2003;108:1772–88 CrossRef Medline
16. Naghavi M, Libby P, Falk E, et al. **From vulnerable plaque to vulnerable patient: a call for new definitions and risk assessment strategies, part I.** *Circulation* 2003;108:1664–72 CrossRef Medline
17. Zavodni AE, Wasserman BA, McClelland RL, et al. **Carotid artery plaque morphology and composition in relation to incident cardiovascular events: the Multi-Ethnic Study of Atherosclerosis (MESA).** *Radiology* 2014;271:381–89 CrossRef Medline
18. van Dijk AC, Truijman MT, Hussain B, et al. **Intraplaque hemorrhage and the plaque surface in carotid atherosclerosis: the Plaque At RISK Study (PARISK).** *AJNR Am J Neuroradiol* 2015;36:2127–33 CrossRef Medline
19. Zhao XQ, Hatsukami TS, Hippe DS, et al; AIM-HIGH Carotid MRI Sub-study Investigators. **Clinical factors associated with high-risk carotid plaque features as assessed by magnetic resonance imaging in patients with established vascular disease (from the AIM-HIGH Study).** *Am J Cardiol* 2014;114:1412–19 CrossRef Medline
20. Underhill HR, Yuan C. **Carotid MRI: a tool for monitoring individual response to cardiovascular therapy?** *Expert Rev Cardiovasc Ther* 2011;9:63–80 CrossRef Medline
21. Xu D, Hippe DS, Underhill HR, et al. **Prediction of high-risk plaque development and plaque progression with the carotid atherosclerosis score.** *JACC Cardiovasc Imaging* 2014;7:366–73 CrossRef Medline
22. DeMarco JK, Spence JD. **Plaque assessment in the management of patients with asymptomatic carotid stenosis.** *Neuroimaging Clin N Am* 2016;26:111–27 CrossRef Medline
23. Croft RJ, Ellam LD, Harrison MJ. **Accuracy of carotid angiography in the assessment of atheroma of the internal carotid artery.** *Lancet* 1980;1:997–1000 Medline
24. Wardlaw JM, Chappell FM, Best JJ, et al; NHS Research and Development Health Technology Assessment Carotid Stenosis Imaging Group. **Non-invasive imaging compared with intra-arterial angiography in the diagnosis of symptomatic carotid stenosis: a meta-analysis.** *Lancet* 2006;367:1503–12 Medline
25. Liapis CD, Paraskevas KI. **Do carotid surface irregularities correlate with the development of cerebrovascular symptoms? An analysis of the supporting studies, the opposing studies, and the possible pathomechanism.** *Vascular* 2006;14:88–92 CrossRef Medline
26. Comerota AJ, Katz ML, White JV, et al. **The preoperative diagnosis of the ulcerated carotid atheroma.** *J Vasc Surg* 1990;11:505–10 Medline
27. Rothwell PM, Eliasziw M, Gutnikov SA, et al; Carotid Endarterectomy Trialists' Collaboration. **Analysis of pooled data from the randomised controlled trials of endarterectomy for symptomatic carotid stenosis.** *Lancet* 2003;361:107–16 CrossRef Medline
28. European Carotid Surgery Trialists' Collaborative Group. **Randomised trial of endarterectomy for recently symptomatic carotid stenosis: final results of the MRC European Carotid Surgery Trial (ECST).** *Lancet* 1998;351:1379–87 CrossRef Medline
29. Barnett HJ, Taylor DW, Haynes RB, et al; North American Symptomatic Carotid Endarterectomy Trial Collaborators. **Beneficial effect of carotid endarterectomy in symptomatic patients with high-grade carotid stenosis.** *N Engl J Med* 1991;325:445–53 Medline
30. Executive Committee for the Asymptomatic Carotid Atherosclerosis Study. **Endarterectomy for asymptomatic carotid artery stenosis.** *JAMA* 1995;273:1421–28 CrossRef Medline
31. Bladin CF, Alexandrov AV, Murphy J, et al. **Carotid Stenosis Index: a new method of measuring internal carotid artery stenosis.** *Stroke* 1995;26:230–34 CrossRef Medline
32. Rothwell PM, Gibson RJ, Slattery J, et al. **Equivalence of measurements of carotid stenosis: a comparison of three methods on 1001 angiograms—European Carotid Surgery Trialists' Collaborative Group.** *Stroke* 1994;5:2435–39 CrossRef Medline

33. Bartlett ES, Walters TD, Symons SP, et al. **Carotid stenosis index revisited with direct CT angiography measurement of carotid arteries to quantify carotid stenosis.** *Stroke* 2007;38:286–91 CrossRef Medline
34. Wasserman BA, Wityk RJ, Trout HH 3rd, et al. **Low-grade carotid stenosis: looking beyond the lumen with MRI.** *Stroke* 2005;36:2504–13 CrossRef Medline
35. Astor BC, Sharrett AR, Coresh J, et al. **Remodeling of carotid arteries detected with MR imaging: atherosclerosis risk in communities carotid MRI study.** *Radiology* 2010;256:879–86 CrossRef Medline
36. Lovett JK, Gallagher PJ, Hands LJ, et al. **Histological correlates of carotid plaque surface morphology on lumen contrast imaging.** *Circulation* 2004;110:2190–97 CrossRef Medline
37. Spagnoli LG, Mauriello A, Sangiorgi G, et al. **Extracranial thrombotically active carotid plaque as a risk factor for ischemic stroke.** *JAMA* 2004;292:1845–52 Medline
38. Lovett JK, Gallagher PJ, Rothwell PM. **Reproducibility of histological assessment of carotid plaque: implications for studies of carotid imaging.** *Cerebrovasc Dis* 2004;18:117–23 CrossRef Medline
39. Redgrave JN, Lovett JK, Rothwell PM. **Histological features of symptomatic carotid plaques in relation to age and smoking: the oxford plaque study.** *Stroke* 2010;41:2288–94 CrossRef Medline
40. Altaf N, Daniels L, Morgan PS, et al. **Detection of intraplaque hemorrhage by magnetic resonance imaging in symptomatic patients with mild to moderate carotid stenosis predicts recurrent neurological events.** *J Vasc Surg* 2008;47:337–42 CrossRef Medline
41. Freilinger TM, Schindler A, Schmidt C, et al. **Prevalence of nonstenosing, complicated atherosclerotic plaques in cryptogenic stroke.** *JACC Cardiovasc Imaging* 2012;5:397–405 CrossRef Medline
42. Mono ML, Karameshev A, Slotboom J, et al. **Plaque characteristics of asymptomatic carotid stenosis and risk of stroke.** *Cerebrovasc Dis* 2012;34:343–50 CrossRef Medline
43. Rozie S, de Weert TT, de Monyé C, et al. **Atherosclerotic plaque volume and composition in symptomatic carotid arteries assessed with multidetector CT angiography; relationship with severity of stenosis and cardiovascular risk factors.** *Eur Radiol* 2009;19:2294–301 CrossRef Medline
44. Saam T, Yuan C, Chu B, et al. **Predictors of carotid atherosclerotic plaque progression as measured by noninvasive magnetic resonance imaging.** *Atherosclerosis* 2007;194:e34–42 CrossRef Medline
45. Saba L, Tamponi E, Raz E, et al. **Correlation between fissured fibrous cap and contrast enhancement: preliminary results with the use of CTA and histologic validation.** *AJNR Am J Neuroradiol* 2014;35:754–59 CrossRef Medline
46. Albuquerque LC, Narvaes LB, Maciel AA, et al. **Intraplaque hemorrhage assessed by high-resolution magnetic resonance imaging and C-reactive protein in carotid atherosclerosis.** *J Vasc Surg* 2007;46:1130–37 CrossRef Medline
47. Ota H, Yu W, Underhill HR, et al. **Hemorrhage and large lipid-rich necrotic cores are independently associated with thin or ruptured fibrous caps: an in vivo 3T MRI study.** *Arterioscler Thromb Vasc Biol* 2009;29:1696–701 CrossRef Medline
48. Saba L, Montisci R, Sanfilippo R, et al. **Multidetector row CT of the brain and carotid artery: a correlative analysis.** *Clin Radiol* 2009;64:767–78 CrossRef Medline
49. Geroulakos G, Ramaswami G, Nicolaidis A, et al. **Characterization of symptomatic and asymptomatic carotid plaques using high-resolution real-time ultrasonography.** *Br J Surg* 1993;80:1274–77 CrossRef Medline
50. Bluth EI, Kay D, Merritt CR, et al. **Sonographic characterization of carotid plaque: detection of hemorrhage.** *AJR Am J Roentgenol* 1986;146:1061–65 CrossRef Medline
51. Grønholdt ML, Wiebe BM, Laursen H, et al. **Lipid-rich carotid artery plaques appear echolucent on ultrasound B-mode images and may be associated with intraplaque haemorrhage.** *Eur J Vasc Endovasc Surg* 1997;14:439–45 CrossRef Medline
52. Noritomi T, Sigel B, Swami V, et al. **Carotid plaque typing by multiple-parameter ultrasonic tissue characterization.** *Ultrasound Med Biol* 1997;23:643–50 CrossRef Medline
53. Schminke U, Motsch L, Hilker L, et al. **Three-dimensional ultrasound observation of carotid artery plaque ulceration.** *Stroke* 2000;31:1651–55 CrossRef Medline
54. de Weert TT, Ouhlous M, Zondervan PE, et al. **In vitro characterization of atherosclerotic carotid plaque with multidetector computed tomography and histopathological correlation.** *Eur Radiol* 2005;15:1906–14 CrossRef Medline
55. de Weert TT, Ouhlous M, Meijering E, et al. **In vivo characterization and quantification of atherosclerotic carotid plaque components with multidetector computed tomography and histopathological correlation.** *Arterioscler Thromb Vasc Biol* 2006;26:2366–72 CrossRef Medline
56. Ajduk M, Pavić L, Bulimbasić S, et al. **Multidetector-row computed tomography in evaluation of atherosclerotic carotid plaques complicated with intraplaque hemorrhage.** *Ann Vasc Surg* 2009;23:186–93 CrossRef Medline
57. Nandalur KR, Hardie AD, Raghavan P, et al. **Composition of the stable carotid plaque: insights from a multidetector computed tomography study of plaque volume.** *Stroke* 2007;38:935–40 Medline
58. Nandalur KR, Baskurt E, Hagspiel KD, et al. **Calcified carotid atherosclerotic plaque is associated less with ischemic symptoms than is noncalcified plaque on MDCT.** *AJR Am J Roentgenol* 2005;184:295–98 CrossRef Medline
59. Saam T, Ferguson MS, Yarnykh VL, et al. **Quantitative evaluation of carotid plaque composition by in vivo MRI.** *Arterioscler Thromb Vasc Biol* 2005;25:234–39 Medline
60. Cai J, Hatsukami TS, Ferguson MS, et al. **In vivo quantitative measurement of intact fibrous cap and lipid-rich necrotic core size in atherosclerotic carotid plaque: comparison of high-resolution, contrast-enhanced magnetic resonance imaging and histology.** *Circulation* 2005;112:3437–44 CrossRef Medline
61. Wasserman BA, Smith WI, Trout HH 3rd, et al. **Carotid artery atherosclerosis: in vivo morphologic characterization with gadolinium-enhanced double-oblique MR imaging initial results.** *Radiology* 2002;223:566–73 CrossRef Medline
62. Wasserman BA, Haacke EM, Li D. **Carotid plaque formation and its evaluation with angiography, ultrasound, and MR angiography.** *J Magn Reson Imaging* 1994;4:515–27 CrossRef Medline
63. Qiao Y, Etesami M, Malhotra S, et al. **Identification of intraplaque hemorrhage on MR angiography images: a comparison of contrast-enhanced mask and time-of-flight techniques.** *AJNR Am J Neuroradiol* 2011;32:454–59 CrossRef Medline
64. Moody AR, Murphy RE, Morgan PS, et al. **Characterization of complicated carotid plaque with magnetic resonance direct thrombus imaging in patients with cerebral ischemia.** *Circulation* 2003;107:3047–52 CrossRef Medline
65. Cai JM, Hatsukami TS, Ferguson MS, et al. **Classification of human carotid atherosclerotic lesions with in vivo multicontrast magnetic resonance imaging.** *Circulation* 2002;106:1368–73 CrossRef Medline
66. Hofman JM, Branderhorst WJ, ten Eikelder HM, et al. **Quantification of atherosclerotic plaque components using in vivo MRI and supervised classifiers.** *Magn Reson Med* 2006;55:790–99 Medline
67. Saba L, Anzidei M, Marincola BC, et al. **Imaging of the carotid artery vulnerable plaque.** *Cardiovasc Intervent Radiol* 2014;37:572–85 CrossRef Medline
68. Sitzer M, Müller W, Siebler M, et al. **Plaque ulceration and lumen thrombus are the main sources of cerebral microemboli in high-grade internal carotid artery stenosis.** *Stroke* 1995;26:1231–33 CrossRef Medline
69. Troyer A, Saloner D, Pan XM, et al; Assessment of Carotid Stenosis by Comparison with Endarterectomy Plaque Trial Investigators. **Major carotid plaque surface irregularities correlate with neurologic symptoms.** *J Vasc Surg* 2002;35:741–47 CrossRef Medline
70. Polak JF, O’Leary DH, Kronmal RA, et al. **Sonographic evaluation of carotid artery atherosclerosis in the elderly: relationship of dis-**

- ease severity to stroke and transient ischemic attack. *Radiology* 1993;188:363–70 CrossRef Medline
71. Anderson GB, Ashforth R, Steinke DE, et al. CT angiography for the detection and characterization of carotid artery bifurcation disease. *Stroke* 2000;31:2168–74 CrossRef Medline
 72. Altaf N, MacSweeney ST, Gladman J, et al. Carotid intraplaque hemorrhage predicts recurrent symptoms in patients with high-grade carotid stenosis. *Stroke* 2007;38:1633–35 CrossRef Medline
 73. Takaya N, Yuan C, Chu B, et al. Association between carotid plaque characteristics and subsequent ischemic cerebrovascular events: a prospective assessment with MRI—initial results. *Stroke* 2006;37:818–23 CrossRef Medline
 74. Takaya N, Yuan C, Chu B, et al. Presence of intraplaque hemorrhage stimulates progression of carotid atherosclerotic plaques: a high-resolution magnetic resonance imaging study. *Circulation* 2005;111:2768–75 CrossRef Medline
 75. Pasterkamp G, van der Steen AF. Intraplaque hemorrhage: an imaging marker for atherosclerotic plaque destabilization? *Arterioscler Thromb Vasc Biol* 2012;32:167–68 CrossRef Medline
 76. Selwaness M, van den Bouwhuisen QJ, Verwoert GC, et al. Blood pressure parameters and carotid intraplaque hemorrhage as measured by magnetic resonance imaging: the Rotterdam Study. *Hypertension* 2013;61:76–81 CrossRef Medline
 77. Sun J, Canton G, Balu N, et al. Blood pressure is a major modifiable risk factor implicated in pathogenesis of intraplaque hemorrhage: an in vivo magnetic resonance imaging study. *Arterioscler Thromb Vasc Biol* 2016;36:743–49 CrossRef Medline
 78. Cury RC, Houser SL, Furie KL, et al. Vulnerable plaque detection by 3.0 Tesla magnetic resonance imaging. *Invest Radiol* 2006;41:112–15 CrossRef Medline
 79. Gupta A, Baradaran H, Schweitzer AD, et al. Carotid plaque MRI and stroke risk: a systematic review and meta-analysis. *Stroke* 2013;44:3071–77 CrossRef Medline
 80. Kwee RM, van Oostenbrugge RJ, Mess WH, et al. MRI of carotid atherosclerosis to identify TIA and stroke patients who are at risk of a recurrence. *J Magn Reson Imaging* 2013;37:1189–94 CrossRef Medline
 81. Demarco JK, Ota H, Underhill HR, et al. MR carotid plaque imaging and contrast-enhanced MR angiography identifies lesions associated with recent ipsilateral thromboembolic symptoms: an in vivo study at 3T. *AJNR Am J Neuroradiol* 2010;31:1395–402 CrossRef Medline
 82. Virmani R, Kolodgie FD, Burke AP, et al. Atherosclerotic plaque progression and vulnerability to rupture: angiogenesis as a source of intraplaque hemorrhage. *Arterioscler Thromb Vasc Biol* 2005;25:2054–61 CrossRef Medline
 83. McCarthy MJ, Loftus IM, Thompson MM, et al. Angiogenesis and the atherosclerotic carotid plaque: an association between symptomatology and plaque morphology. *J Vasc Surg* 1999;30:261–68 CrossRef Medline
 84. Schroeder AP, Falk E. Vulnerable and dangerous coronary plaques. *Atherosclerosis* 1995;118(suppl):S141–49 CrossRef Medline
 85. de Boer OJ, van der Wal AC, Teeling P, et al. Leucocyte recruitment in rupture prone regions of lipid-rich plaques: a prominent role for neovascularization? *Cardiovasc Res* 1999;41:443–49 CrossRef Medline
 86. van der Wal AC, Becker AE, van der Loos CM, et al. Site of intimal rupture or erosion of thrombosed coronary atherosclerotic plaques is characterized by an inflammatory process irrespective of the dominant plaque morphology. *Circulation* 1994;89:36–44 CrossRef Medline
 87. Fleiner M, Kummer M, Mirlacher M, et al. Arterial neovascularization and inflammation in vulnerable patients: early and late signs of symptomatic atherosclerosis. *Circulation* 2004;110:2843–50 CrossRef Medline
 88. Moulton KS, Vakili K, Zurakowski D, et al. Inhibition of plaque neovascularization reduces macrophage accumulation and progression of advanced atherosclerosis. *Proc Natl Acad Sci U S A* 2003;100:4736–41 CrossRef Medline
 89. Lennartz MR, Aggarwal A, Michaud TM, et al. Ligation of macrophage Fcγ receptors recapitulates the gene expression pattern of vulnerable human carotid plaques. *PLoS One* 2011;6:e21803 CrossRef Medline
 90. Ruehm SG, Corot C, Vogt P, et al. Ultrasmall superparamagnetic iron oxide-enhanced MR imaging of atherosclerotic plaque in hyperlipidemic rabbits. *Acad Radiol* 2002;9(suppl 1):S143–44 CrossRef Medline
 91. Trivedi RA, Mallawarachi C, U-King-Im JM, et al. Identifying inflamed carotid plaques using in vivo USPIO-enhanced MR imaging to label plaque macrophages. *Arterioscler Thromb Vasc Biol* 2006;26:1601–06 CrossRef Medline
 92. Annovazzi A, Bonanno E, Arca M, et al. ^{99m}Tc-interleukin-2 scintigraphy for the in vivo imaging of vulnerable atherosclerotic plaques. *Eur J Nucl Med Mol Imaging* 2006;33:117–26 CrossRef Medline
 93. Tang TY, Howarth SP, Miller SR, et al. Correlation of carotid atheromatous plaque inflammation using USPIO-enhanced MR imaging with degree of luminal stenosis. *Stroke* 2008;39:2144–47 CrossRef Medline
 94. Howarth SP, Tang TY, Trivedi R, et al. Utility of USPIO-enhanced MR imaging to identify inflammation and the fibrous cap: a comparison of symptomatic and asymptomatic individuals. *Eur J Radiol* 2009;70:555–60 CrossRef Medline
 95. Fukuda K, Iihara K, Maruyama D, et al. Relationship between carotid artery remodeling and plaque vulnerability with T1-weighted magnetic resonance imaging. *J Stroke Cerebrovasc Dis* 2014;23:1462–70 CrossRef Medline
 96. Achenbach S, Ropers D, Hoffmann U, et al. Assessment of coronary remodeling in stenotic and nonstenotic coronary atherosclerotic lesions by multidetector spiral computed tomography. *J Am Coll Cardiol* 2004;43:842–47 CrossRef Medline
 97. Virmani R, Burke AP, Kolodgie FD, et al. Pathology of the thin-cap fibroatheroma: a type of vulnerable plaque. *J Interv Cardiol* 2003;16:267–72 CrossRef Medline
 98. Miura T, Matsukawa N, Sakurai K, et al. Plaque vulnerability in internal carotid arteries with positive remodeling. *Cerebrovasc Dis Extra* 2011;1:54–65 CrossRef Medline
 99. Vukadinovic D, Rozie S, van Gils M, et al. Automated versus manual segmentation of atherosclerotic carotid plaque volume and components in CTA: associations with cardiovascular risk factors. *Int J Cardiovasc Imaging* 2012;28:877–87 CrossRef Medline
 100. Wannarong T, Parraga G, Buchanan D, et al. Progression of carotid plaque volume predicts cardiovascular events. *Stroke* 2013;44:1859–65 CrossRef Medline
 101. Saba L, Sanfilippo R, Sannia S, et al. Association between carotid artery plaque volume, composition, and ulceration: a retrospective assessment with MDCT. *AJR Am J Roentgenol* 2012;199:151–56 CrossRef Medline
 102. Bonati LH, Ederle J, Dobson J, et al; CAVATAS Investigators. Length of carotid stenosis predicts peri-procedural stroke or death and restenosis in patients randomized to endovascular treatment or endarterectomy. *Int J Stroke* 2014;9:297–305 CrossRef Medline
 103. Wasserman BA, Astor BC, Sharrett AR, et al. MRI measurements of carotid plaque in the atherosclerosis risk in communities (ARIC) study: methods, reliability and descriptive statistics. *J Magn Reson Imaging* 2010;31:406–15 CrossRef Medline
 104. Trelles M, Eberhardt KM, Buchholz M, et al. CTA for screening of complicated atherosclerotic carotid plaque—American Heart Association type VI lesions as defined by MRI. *AJNR Am J Neuroradiol* 2013;34:2331–37 CrossRef Medline
 105. Bayer-Karpinska A, Schwarz F, Wollenweber FA, et al. The carotid plaque imaging in acute stroke (CAPIAS) study: protocol and initial baseline data. *BMC Neurol* 2013;13:201 CrossRef Medline
 106. Truijman MT, Kooi ME, van Dijk AC, et al. Plaque At RISK

- (PARISK): prospective multicenter study to improve diagnosis of high-risk carotid plaques. *Int J Stroke* 2014;9:747–54 CrossRef Medline
107. Chinese Atherosclerosis Risk Evaluation-Phase II (CARE-II). <https://clinicaltrials.gov/ct2/show/NCT02017756>. Accessed December 6, 2017
 108. Tardif JC, Spence JD, Heinonen TM, et al. **Atherosclerosis imaging and the Canadian Atherosclerosis Imaging Network.** *Can J Cardiol* 2013;29:297–303 CrossRef Medline
 109. Bluth EI. **Value of US in selecting patients for carotid angioplasty and stent placement.** *Radiology* 2005;237:374–75; author reply 375 CrossRef Medline
 110. Akkus Z, Hoogi A, Renaud G, et al. **New quantification methods for carotid intra-plaque neovascularization using contrast-enhanced ultrasound.** *Ultrasound Med Biol* 2014;40:25–36 CrossRef Medline
 111. van den Oord SC, van der Burg J, Akkus Z, et al. **Impact of gender on the density of intraplaque neovascularization: a quantitative contrast-enhanced ultrasound study.** *Atherosclerosis* 2014;233:461–66 CrossRef Medline
 112. Chiu B, Shamdasani V, Entrekin R, et al. **Characterization of carotid plaques on 3-dimensional ultrasound imaging by registration with multicontrast magnetic resonance imaging.** *J Ultrasound Med* 2012;31:1567–80 CrossRef Medline
 113. Gaitini D, Soudack M. **Diagnosing carotid stenosis by Doppler sonography: state of the art.** *J Ultrasound Med* 2005;24:1127–36 CrossRef Medline
 114. Grant EG, Benson CB, Moneta GL, et al; Society of Radiologists in Ultrasound. **Carotid artery stenosis: grayscale and Doppler ultrasound diagnosis—Society of Radiologists in Ultrasound consensus conference.** *Ultrasound Q* 2003;19:190–98 CrossRef Medline
 115. Dembo T, Tanahashi N. **Recurring extracranial internal carotid artery vasospasm detected by intravascular ultrasound.** *Intern Med* 2012;51:1249–53 CrossRef Medline
 116. Heliopoulos J, Vadikolias K, Piperidou C, et al. **Detection of carotid artery plaque ulceration using 3-dimensional ultrasound.** *J Neuroimaging* 2011;21:126–31 CrossRef Medline
 117. Madani A, Beletsky V, Tamayo A, et al. **High-risk asymptomatic carotid stenosis: ulceration on 3D ultrasound vs TCD microemboli.** *Neurology* 2011;77:744–50 CrossRef Medline
 118. Ajduk M, Bulimbasić S, Pavić L, et al. **Comparison of multidetector-row computed tomography and duplex Doppler ultrasonography in detecting atherosclerotic carotid plaques complicated with intraplaque hemorrhage.** *Coll Antropol* 2013;37:213–19 Medline
 119. Kume S, Hama S, Yamane K, et al. **Vulnerable carotid arterial plaque causing repeated ischemic stroke can be detected with B-mode ultrasonography as a mobile component: jellyfish sign.** *Neurosurg Rev* 2010;33:419–30 CrossRef Medline
 120. Huijbers A, de Borst GJ, Wan S, et al. **Non-invasive carotid artery imaging to identify the vulnerable plaque: current status and future goals.** *Eur J Vasc Endovasc Surg* 2015;50:563–72 CrossRef Medline
 121. Varetto G, Gibello L, Castagno C, et al. **Use of contrast-enhanced ultrasound in carotid atherosclerotic disease: limits and perspectives.** *Biomed Res Int* 2015;2015:293163 CrossRef Medline
 122. Funaki T, Iihara K, Miyamoto S, et al. **Histologic characterization of mobile and nonmobile carotid plaques detected with ultrasound imaging.** *J Vasc Surg* 2011;53:977–83 CrossRef Medline
 123. Sangiorgi G, Bedogni F, Sganzerla P, et al. **The Virtual histology In Carotids Observational Registry (VICTORY) study: a European prospective registry to assess the feasibility and safety of intravascular ultrasound and virtual histology during carotid interventions.** *Int J Cardiol* 2013;168:2089–93 CrossRef Medline
 124. Hitchner E, Zayed MA, Lee G, et al. **Intravascular ultrasound as a clinical adjunct for carotid plaque characterization.** *J Vasc Surg* 2014;59:774–80 CrossRef Medline
 125. Hoogi A, Zurakhov G, Adam D. **Evaluation of a 3D technique for quantifying neovascularization within plaques imaged by contrast enhanced ultrasound.** *Conf Proc IEEE Eng Med Biol Soc* 2013; 2013:1124–27 CrossRef Medline
 126. van den Oord SC, Akkus Z, Roeters van Lennep JE, et al. **Assessment of subclinical atherosclerosis and intraplaque neovascularization using quantitative contrast-enhanced ultrasound in patients with familial hypercholesterolemia.** *Atherosclerosis* 2013;231:107–13 CrossRef Medline
 127. Jaipersad AS, Shantsila A, Silverman S, et al. **Evaluation of carotid plaque neovascularization using contrast ultrasound.** *Angiology* 2013;64:447–50 CrossRef Medline
 128. O’Leary DH, Polak JF, Kronmal RA, et al; Cardiovascular Health Study Collaborative Research Group. **Carotid-artery intima and media thickness as a risk factor for myocardial infarction and stroke in older adults.** *N Engl J Med* 1999;340:14–22 CrossRef Medline
 129. Polak JF, Pencina MJ, Pencina KM, et al. **Carotid-wall intima-media thickness and cardiovascular events.** *N Engl J Med* 2011;365: 213–21 CrossRef Medline
 130. Bar M, Roubec M, Farana R, et al. **Inter-rater reliability of carotid atherosclerotic plaque quantification by 3-dimensional sonography.** *J Ultrasound Med* 2014;33:1273–78 CrossRef Medline
 131. Hartmann A, Mohr JP, Thompson JL, et al. **Interrater reliability of plaque morphology classification in patients with severe carotid artery stenosis.** *Acta Neurol Scand* 1999;99:61–64 Medline
 132. Saba L, Argiolas GM, Siotto P, et al. **Carotid artery plaque characterization using CT multienergy imaging.** *AJNR Am J Neuroradiol* 2013;34:855–59 CrossRef Medline
 133. Ertl-Wagner BB, Hoffmann RT, Bruning R, et al. **Multi-detector row CT angiography of the brain at various kilovoltage settings.** *Radiology* 2004;231:528–35 CrossRef Medline
 134. Saba L, Caddeo G, Sanfilippo R, et al. **CT and ultrasound in the study of ulcerated carotid plaque compared with surgical results: potentialities and advantages of multidetector row CT angiography.** *AJNR Am J Neuroradiol* 2007;28:1061–66 CrossRef Medline
 135. Saba L, Caddeo G, Sanfilippo R, et al. **Efficacy and sensitivity of axial scans and different reconstruction methods in the study of the ulcerated carotid plaque using multidetector-row CT angiography: comparison with surgical results.** *AJNR Am J Neuroradiol* 2007;28:716–23 Medline
 136. Kuk M, Wannarong T, Beletsky V, et al. **Volume of carotid artery ulceration as a predictor of cardiovascular events.** *Stroke* 2014;45: 1437–41 CrossRef Medline
 137. U-King-Im JM, Fox AJ, Aviv RI, et al. **Characterization of carotid plaque hemorrhage: a CT angiography and MR intraplaque hemorrhage study.** *Stroke* 2010;41:1623–29 CrossRef Medline
 138. Wintermark M, Jawadi SS, Rapp JH, et al. **High-resolution CT imaging of carotid artery atherosclerotic plaques.** *AJNR Am J Neuroradiol* 2008;29:875–82 CrossRef Medline
 139. Saba L, Francone M, Bassareo PP, et al. **CT attenuation analysis of carotid intraplaque hemorrhage.** *AJNR Am J Neuroradiol* 2017 Nov 30. [Epub ahead of print] CrossRef Medline
 140. Eisenmenger LB, Aldred BW, Kim SE, et al. **Prediction of carotid intraplaque hemorrhage using adventitial calcification and plaque thickness on CTA.** *AJNR Am J Neuroradiol* 2016;37:1496–503 CrossRef Medline
 141. Saba L, Potters F, van der Lugt A, et al. **Imaging of the fibrous cap in atherosclerotic carotid plaque.** *Cardiovasc Intervent Radiol* 2010;33: 681–89 CrossRef Medline
 142. Saba L, Mallarini G. **Fissured fibrous cap of vulnerable carotid plaques and symptomatology: are they correlated? Preliminary results by using multi-detector-row CT angiography.** *Cerebrovasc Dis* 2009;27:322–27 CrossRef Medline
 143. Saba L, Lai ML, Montisci R, et al. **Association between carotid plaque enhancement shown by multidetector CT angiography and histologically validated microvessel density.** *Eur Radiol* 2012; 22:2237–45 CrossRef Medline
 144. Qiao Y, Etesami M, Astor BC, et al. **Carotid plaque neovascularization and hemorrhage detected by MR imaging are associated with**

- recent cerebrovascular ischemic events. *AJNR Am J Neuroradiol* 2012;33:755–60 CrossRef Medline
145. Romero JM, Babiarz LS, Forero NP, et al. **Arterial wall enhancement overlying carotid plaque on CT angiography correlates with symptoms in patients with high grade stenosis.** *Stroke* 2009;40:1894–96 CrossRef Medline
 146. Romero JM, Pizzolato R, Atkinson W, et al. **Vasa vasorum enhancement on computerized tomographic angiography correlates with symptomatic patients with 50% to 70% carotid artery stenosis.** *Stroke* 2013;44:3344–49 CrossRef Medline
 147. Hardie AD, Kramer CM, Raghavan P, et al. **The impact of expansive arterial remodeling on clinical presentation in carotid artery disease: a multidetector CT angiography study.** *AJNR Am J Neuroradiol* 2007;28:1067–70 CrossRef Medline
 148. Ohara T, Toyoda K, Otsubo R, et al. **Eccentric stenosis of the carotid artery associated with ipsilateral cerebrovascular events.** *AJNR Am J Neuroradiol* 2008;29:1200–03 CrossRef Medline
 149. Adraktas DD, Tong E, Furtado AD, et al. **Evolution of CT imaging features of carotid atherosclerotic plaques in a 1-year prospective cohort study.** *J Neuroimaging* 2014;24:1–6 CrossRef Medline
 150. Brenner DJ, Hall EJ. **Computed tomography—an increasing source of radiation exposure.** *N Engl J Med* 2007;357:2277–84 CrossRef Medline
 151. Nickoloff EL, Alderson PO. **Radiation exposures to patients from CT: reality, public perception, and policy.** *AJR Am J Roentgenol* 2001;177:285–87 CrossRef Medline
 152. Cashman JD, McCredie J, Henry DA. **Intravenous contrast media: use and associated mortality.** *Med J Aust* 1991;155:618–23 Medline
 153. Morcos SK. **Acute serious and fatal reactions to contrast media: our current understanding.** *Br J Radiol* 2005;78:686–93 CrossRef Medline
 154. Rudnick MR, Kesselheim A, Goldfarb S. **Contrast-induced nephropathy: how it develops, how to prevent it.** *Cleve Clin J Med* 2006;73:75–80, 83–87 Medline
 155. Chappell FM, Wardlaw JM, Young GR, et al. **Carotid artery stenosis: accuracy of noninvasive tests—individual patient data meta-analysis.** *Radiology* 2009;251:493–502 CrossRef Medline
 156. Etesami M, Hoi Y, Steinman DA, et al. **Comparison of carotid plaque ulcer detection using contrast-enhanced and time-of-flight MRA techniques.** *AJNR Am J Neuroradiol* 2013;34:177–84 CrossRef Medline
 157. Moreno PR, Purushothaman KR, Sirol M, et al. **Neovascularization in human atherosclerosis.** *Circulation* 2006;113:2245–52 CrossRef Medline
 158. Cappendijk VC, Cleutjens KB, Kessels AG, et al. **Assessment of human atherosclerotic carotid plaque components with multi-sequence MR imaging: initial experience.** *Radiology* 2005;234:487–92 CrossRef Medline
 159. Chu B, Kampschulte A, Ferguson MS, et al. **Hemorrhage in the atherosclerotic carotid plaque: a high-resolution MRI study.** *Stroke* 2004;35:1079–84 CrossRef Medline
 160. Bitar R, Moody AR, Leung G, et al. **In vivo 3D high-spatial-resolution MR imaging of intraplaque hemorrhage.** *Radiology* 2008;249:259–67 CrossRef Medline
 161. Moody AR, Allder S, Lennox G, et al. **Direct magnetic resonance imaging of carotid artery thrombus in acute stroke.** *Lancet* 1999;353:122–23 Medline
 162. Dai Y, Lv P, Lin J, et al. **Comparison study between multicontrast atherosclerosis characterization (MATCH) and conventional multicontrast MRI of carotid plaque with histology validation.** *J Magn Reson Imaging* 2017;45:764–70 CrossRef Medline
 163. Fan Z, Yu W, Xie Y, et al. **Multi-contrast atherosclerosis characterization (MATCH) of carotid plaque with a single 5-min scan: technical development and clinical feasibility.** *J Cardiovasc Magn Reson* 2014;16:53 CrossRef Medline
 164. Wang J, Börner P, Zhao H, et al. **Simultaneous noncontrast angiography and intraplaque hemorrhage (SNAP) imaging for carotid atherosclerotic disease evaluation.** *Magn Reson Med* 2013;69:337–45 CrossRef Medline
 165. Chen S, Zhao H, Li J, et al. **Evaluation of carotid atherosclerotic plaque surface characteristics utilizing simultaneous noncontrast angiography and intraplaque hemorrhage (SNAP) technique.** *J Magn Reson Imaging* 2017 Aug 2. [Epub ahead of print] CrossRef Medline
 166. Wintermark M, Rapp JH, Tan J, et al. **Unmasking complicated atherosclerotic plaques on carotid magnetic resonance angiography: a report of three cases.** *J Vasc Surg* 2006;44:884–87 CrossRef Medline
 167. Trivedi RA, U-King-Im JM, Graves MJ, et al. **MRI-derived measurements of fibrous-cap and lipid-core thickness: the potential for identifying vulnerable carotid plaques in vivo.** *Neuroradiology* 2004;46:738–43 CrossRef Medline
 168. Toussaint JF, LaMuraglia GM, Southern JF, et al. **Magnetic resonance images lipid, fibrous, calcified, hemorrhagic, and thrombotic components of human atherosclerosis in vivo.** *Circulation* 1996;94:932–38 CrossRef Medline
 169. Hatsukami TS, Ross R, Polissar NL, et al. **Visualization of fibrous cap thickness and rupture in human atherosclerotic carotid plaque in vivo with high-resolution magnetic resonance imaging.** *Circulation* 2000;102:959–64 CrossRef Medline
 170. Yuan C, Zhang SX, Polissar NL, et al. **Identification of fibrous cap rupture with magnetic resonance imaging is highly associated with recent transient ischemic attack or stroke.** *Circulation* 2002;105:181–85 CrossRef Medline
 171. Wasserman BA. **Advanced contrast-enhanced MRI for looking beyond the lumen to predict stroke: building a risk profile for carotid plaque.** *Stroke* 2010;41(10 suppl):S12–16 CrossRef Medline
 172. Kwee RM, van Engelsehoven JM, Mess WH, et al. **Reproducibility of fibrous cap status assessment of carotid artery plaques by contrast-enhanced MRI.** *Stroke* 2009;40:3017–21 CrossRef Medline
 173. Ouimet T, Lancelot E, Hyafil F, et al. **Molecular and cellular targets of the MRI contrast agent P947 for atherosclerosis imaging.** *Mol Pharm* 2012;9:850–61 CrossRef Medline
 174. Chan JM, Monaco C, Wylezinska-Arridge M, et al. **Imaging of the vulnerable carotid plaque: biological targeting of inflammation in atherosclerosis using iron oxide particles and MRI.** *Eur J Vasc Endovasc Surg* 2014;47:462–69 CrossRef Medline
 175. Hayek SS, Sharma R, Kwon S, et al. **Temperature and magnetic resonance characteristics of zinc, manganese, gadolinium, gold, iron magnetic nanoparticles and cytokine synergy in hyperthermia.** *J Biomed Sci Eng* 2008;1:182–89 CrossRef
 176. Demos SM, Alkan-Onyuskel H, Kane BJ, et al. **In vivo targeting of acoustically reflective liposomes for intravascular and transvascular ultrasonic enhancement.** *J Am Coll Cardiol* 1999;33:867–75 CrossRef Medline
 177. Flacke S, Fischer S, Scott MJ, et al. **Novel MRI contrast agent for molecular imaging of fibrin: implications for detecting vulnerable plaques.** *Circulation* 2001;104:1280–85 CrossRef Medline
 178. Neubauer AM, Sim H, Winter PM, et al. **Nanoparticle pharmacokinetic profiling in vivo using magnetic resonance imaging.** *Magn Reson Med* 2008;60:1353–61 Medline
 179. Li H, Gray BD, Corbin I, et al. **MR and fluorescent imaging of low-density lipoprotein receptors.** *Acad Radiol* 2004;11:1251–59 CrossRef Medline
 180. Michalet X, Pinaud FF, Bentolila LA, et al. **Quantum dots for live cells, in vivo imaging, and diagnostics.** *Science* 2005;307:538–44 CrossRef Medline
 181. Winter PM, Cai K, Chen J, et al. **Targeted PARACEST nanoparticle contrast agent for the detection of fibrin.** *Magn Reson Med* 2006;56:1384–88 CrossRef Medline
 182. Millon A, Boussel L, Brevet M, et al. **Clinical and histological significance of gadolinium enhancement in carotid atherosclerotic plaque.** *Stroke* 2012;43:3023–28 CrossRef Medline
 183. Wahlgren CM, Zheng W, Shaalan W, et al. **Human carotid plaque calcification and vulnerability: relationship between degree of plaque calcification, fibrous cap inflammatory gene expression**

- and symptomatology.** *Cerebrovasc Dis* 2009;27:193–200 CrossRef Medline
184. Underhill HR, Yuan C, Yarnykh VL, et al. **Arterial remodeling in [corrected] subclinical carotid artery disease.** *JACC Cardiovasc Imaging* 2009;2:1381–89 CrossRef Medline
 185. Kerwin WS, Oikawa M, Yuan C, et al. **MR imaging of adventitial vasa vasorum in carotid atherosclerosis.** *Magn Reson Med* 2008;59:507–14 CrossRef Medline
 186. Gaens ME, Backes WH, Rozel S, et al. **Dynamic contrast-enhanced MR imaging of carotid atherosclerotic plaque: model selection, reproducibility, and validation.** *Radiology* 2013;326:271–79 CrossRef Medline
 187. Chen H, Sun J, Kerwin WS, et al. **Scan-rescan reproducibility of quantitative assessment of inflammatory carotid atherosclerotic plaque using dynamic contrast-enhanced 3T CMR in a multi-center study.** *J Cardiovasc Magn Reson* 2014;16:51 CrossRef Medline
 188. Ukwatta E, Yuan J, Rajchl M, et al. **3-D carotid multi-region MRI segmentation by globally optimal evolution of coupled surfaces.** *IEEE Trans Med Imaging* 2013;32:770–85 CrossRef Medline
 189. Saam T, Kerwin WS, Chu B, et al. **Sample size calculation for clinical trials using magnetic resonance imaging for the quantitative assessment of carotid atherosclerosis.** *J Cardiovasc Magn Reson* 2005;7:799–808 CrossRef Medline
 190. Saam T, Raya JG, Cyran CC, et al. **High resolution carotid black-blood 3T MR with parallel imaging and dedicated 4-channel surface coils.** *J Cardiovasc Magn Reson* 2009;11:41 CrossRef Medline
 191. Corti R, Fayad ZA, Fuster V, et al. **Effects of lipid-lowering by simvastatin on human atherosclerotic lesions: a longitudinal study by high-resolution, noninvasive magnetic resonance imaging.** *Circulation* 2001;104:249–52 CrossRef Medline
 192. Bousset L, Arora S, Rapp J, et al; MAPP Investigators. **Atherosclerotic plaque progression in carotid arteries: monitoring with high-spatial-resolution MR imaging—multicenter trial.** *Radiology* 2009;252:789–96 CrossRef Medline
 193. Saam T, Yuan C, Chu B, et al. **Predictors of carotid atherosclerotic plaque progression as measured by noninvasive magnetic resonance imaging.** *Atherosclerosis* 2007;194:e34–42 CrossRef Medline
 194. Anzidei M, Suri JS, Saba L, et al. **Longitudinal assessment of carotid atherosclerosis after radiation therapy using computed tomography: a case control study.** *Eur Radiol* 2016;26:72–78 CrossRef Medline
 195. van Gils MJ, Vukadinovic D, van Dijk AC, et al. **Carotid atherosclerotic plaque progression and change in plaque composition over time: a 5-year follow-up study using serial CT angiography.** *AJNR Am J Neuroradiol* 2012;33:1267–73 CrossRef Medline
 196. Fleg JL, Stone GW, Fayad ZA, et al. **Detection of high-risk atherosclerotic plaque: report of the NHLBI Working Group on current status and future directions.** *JACC Cardiovasc Imaging* 2012;5:941–55 CrossRef Medline
 197. Zhao XQ, Dong L, Hatsukami T, et al. **MR imaging of carotid plaque composition during lipid-lowering therapy a prospective assessment of effect and time course.** *JACC Cardiovasc Imaging* 2011;4:977–86 CrossRef Medline
 198. Inzitari D, Eliasziw M, Gates P, et al; North American Symptomatic Carotid Endarterectomy Trial Collaborators. **The causes and risk of stroke in patients with asymptomatic internal-carotid-artery stenosis.** *N Engl J Med* 2000;342:1693–700 CrossRef Medline
 199. Murata N, Gonzalez-Cuyar LF, Murata K, et al. **Macrocyclic and other non-group 1 gadolinium contrast agents deposit low levels of gadolinium in brain and bone tissue: preliminary results from 9 patients with normal renal function.** *Invest Radiol* 2016;51:447–53 CrossRef Medline
 200. Stojanov D, Aracki-Trenkic A, Benedeto-Stojanov D. **Gadolinium deposition within the dentate nucleus and globus pallidus after repeated administrations of gadolinium-based contrast agents-current status.** *Neuroradiology* 2016;58:433–41 CrossRef Medline
 201. Rogosnitzky M, Branch S. **Gadolinium-based contrast agent toxicity: a review of known and proposed mechanisms.** *Biometals* 2016; 29:365–76 CrossRef Medline
 202. FDA Drug Safety Communication: FDA evaluating the risk of brain deposits with repeated use of gadolinium-based contrast agents for magnetic resonance imaging (MRI). Safety Announcement 7-27-2015. <http://www.fda.gov/Drugs/DrugSafety/ucm455386.htm>. Accessed December 6, 2017
 203. Araki T, Ikeda N, Shukla D, et al. **A new method for IVUS-based coronary artery disease risk stratification: a link between coronary and carotid ultrasound plaque burdens.** *Comput Methods Programs Biomed* 2016;124:161–79 CrossRef Medline
 204. Lekadir K, Galimzianova A, Betriu A, et al. **A convolutional neural network for automatic characterization of plaque composition in carotid ultrasound.** *IEEE J Biomed Health Inform* 2017;21:48–55 CrossRef Medline
 205. Sanz J, Fayad ZA. **Imaging of atherosclerotic cardiovascular disease.** *Nature* 2008;451:953–57 CrossRef Medline
 206. Graebe M, Pedersen SF, Borgwardt L, et al. **Molecular pathology in vulnerable carotid plaques: correlation with [18]-fluorodeoxyglucose positron emission tomography (FDG-PET).** *Eur J Vasc Endovasc Surg* 2009;37:714–21 CrossRef Medline
 207. Graebe M, Pedersen SF, Højgaard L, et al. **18FDG PET and ultrasound echolucency in carotid artery plaques.** *JACC Cardiovasc Imaging* 2010;3:289–95 CrossRef Medline
 208. Ishii H, Nishio M, Takahashi H, et al. **Comparison of atorvastatin 5 and 20 mg/d for reducing F-18 fluorodeoxyglucose uptake in atherosclerotic plaques on positron emission tomography/computed tomography: a randomized, investigator-blinded, open-label, 6-month study in Japanese adults scheduled for percutaneous coronary intervention.** *Clin Ther* 2010;32:2337–47 CrossRef Medline
 209. Truijman MT, Kwee RM, van Hoof RH, et al. **Combined 18F-FDG PET-CT and DCE-MRI to assess inflammation and microvascularization in atherosclerotic plaques.** *Stroke* 2013;44:3568–70 CrossRef Medline
 210. Calcagno C, Ramachandran S, Izquierdo-Garcia D, et al. **The complementary roles of dynamic contrast-enhanced MRI and 18F-fluorodeoxyglucose PET/CT for imaging of carotid atherosclerosis.** *Eur J Nucl Med Mol Imaging* 2013;40:1884–93 CrossRef Medline
 211. Tawakol A, Migrino RQ, Bashian GG, et al. **In vivo 18F-fluorodeoxyglucose positron emission tomography imaging provides a noninvasive measure of carotid plaque inflammation in patients.** *J Am Coll Cardiol* 2006;48:1818–24 CrossRef Medline
 212. Saam T, Hetterich H, Hoffmann V, et al. **Meta-analysis and systematic review of the predictive value of carotid plaque hemorrhage on cerebrovascular events by magnetic resonance imaging.** *J Am Coll Cardiol* 2013;62:1081–91 CrossRef Medline
 213. Hosseini AA, Kandiyil N, Macsweeney ST, et al. **Carotid plaque hemorrhage on magnetic resonance imaging strongly predicts recurrent ischemia and stroke.** *Ann Neurol* 2013;73:774–84 CrossRef Medline
 214. Takaya N, Cai J, Ferguson MS, et al. **Intra- and interreader reproducibility of magnetic resonance imaging for quantifying the lipid-rich necrotic core is improved with gadolinium contrast enhancement.** *J Magn Reson Imaging* 2006;24:203–10 CrossRef Medline
 215. Wang J, Yarnykh VL, Hatsukami T, et al. **Improved suppression of plaque-mimicking artifacts in black-blood carotid atherosclerosis imaging using a multislice motion-sensitized driven-equilibrium (MSDE) turbo spin-echo (TSE) sequence.** *Magn Reson Med* 2007; 58:973–81 CrossRef Medline
 216. Fan Z, Zhang Z, Chung YC, et al. **Carotid arterial wall MRI at 3T using 3D variable-flip-angle turbo spin-echo (TSE) with flow-sensitive dephasing (FSD).** *J Magn Reson Imaging* 2010;31:645–54 CrossRef Medline
 217. Yarnykh VL, Yuan C. **T1-insensitive flow suppression using quadruple inversion-recovery.** *Magn Reson Med* 2002;48:899–905 CrossRef Medline
 218. Sharma P, Socolow J, Patel S, et al. **Effect of Gd-DTPA-BMA on blood and myocardial T1 at 1.5T and 3T in humans.** *J Magn Reson Imaging* 2006;23:323–30 CrossRef Medline
 219. Ota H, Yarnykh VL, Ferguson MS, et al. **Carotid intraplaque hemorrhage imaging at 3.0-T MR imaging: comparison of the diagnos-**

- tic performance of three T1-weighted sequences. *Radiology* 2010; 254:551–63 CrossRef Medline
220. Zhu DC, Vu AT, Ota H, et al. **An optimized 3D spoiled gradient recalled echo pulse sequence for hemorrhage assessment using inversion recovery and multiple echoes (3D SHINE) for carotid plaque imaging.** *Magn Reson Med* 2010;64:1341–51 CrossRef Medline
221. Balu N, Yarnykh VL, Chu B, et al. **Carotid plaque assessment using fast 3D isotropic resolution black-blood MRI.** *Magn Reson Med* 2011;65:627–37 CrossRef Medline
222. Li L, Chai JT, Biasiolli L, et al. **Black-blood multicontrast imaging of carotid arteries with DANTE-prepared 2D and 3D MR imaging.** *Radiology* 2014;273:560–69 CrossRef Medline
223. Xie Y, Yu W, Fan Z, et al. **High resolution 3D diffusion cardiovascular magnetic resonance of carotid vessel wall to detect lipid core without contrast media.** *J Cardiovasc Magn Reson* 2014;16:67 CrossRef Medline
224. Fan Z, Zuehlsdorff S, Liu X, et al. **Prospective self-gating for swallowing motion: a feasibility study in carotid artery wall MRI using three-dimensional variable-flip-angle turbo spin-echo.** *Magn Reson Med* 2012;67:490–98 CrossRef Medline
225. Saba L, Mallarini G. **Carotid plaque enhancement and symptom correlations: an evaluation by using multidetector row CT angiography.** *AJNR Am J Neuroradiol* 2011;32:1919–25 CrossRef Medline
226. Saba L, Mallarin G. **Window settings for the study of calcified carotid plaques with multidetector CT angiography.** *AJNR Am J Neuroradiol* 2009;30:1445–50 CrossRef Medline
227. Saba L, Piga M, Raz E, et al. **Carotid artery plaque classification: does contrast enhancement play a significant role?** *AJNR Am J Neuroradiol* 2012;33:1814–17 CrossRef Medline

Multiparametric Imaging Improves Confidence in the Diagnosis of Multinodular and Vacuolating Neuronal Tumor of the Cerebrum

We read with much interest the article by Nunes et al¹ in the July 2017 issue of the *American Journal of Neuro-radiology*, in which they presented an impressive series of 33 confirmed or presumed multinodular and vacuolating neuronal tumors (MVNT) of the cerebrum, an entity that has only recently been categorized in the 2016 revision of the *World Health Organization Classification of Tumors of the Central Nervous System*.²⁻⁴ Only a few cases of MVNT have been reported in the literature in the past 4 years with confirmed pathologic correlations.¹⁻³

The authors presented a detailed description of the entity, which involves the deep cortical ribbon and the adjacent subcortical white matter and is distributed into small coalescent nodules, hyperintense on FLAIR and T2-weighted imaging and hypointense on T1WI. On our 3T MR imaging, we noticed that these lesions were not homogeneous but had a central FLAIR hypointense signal as well as central punctiform T1 hyperintensities (white arrows, Fig 1), probably related to a high protein or solid component within the vacuolated areas. This specific feature was present in all our patients but requires reasonably high resolution to be seen. This simple sign can improve diagnostic confidence.

We believe that radiologists should always perform multiparametric imaging to characterize brain abnormalities consistent with an MVNT with a high-field MR imaging whenever possible. In our experience, diffusion-weighted imaging shows no restricted diffusion inside the lesion, and susceptibility-weighted imaging does not show an intratumoral susceptibility signal or intralesional hemorrhaging. Perfusion sequences such as dynamic-susceptibility contrast or arterial spin-labeling show no hyperperfusion, increasing neither cerebral blood volume nor cerebral blood flow. MR spectroscopy may show a mild decrease of NAA but no choline peak or lipid or lactate peaks, which might suggest malignancy (Fig 2). Multivoxel MR spectroscopy shows no abnormality in the surrounding brain parenchyma. All these features improve diagnostic confidence and support strong arguments in favor of this presumptive diagnosis, thus avoiding a potentially risky surgical biopsy.

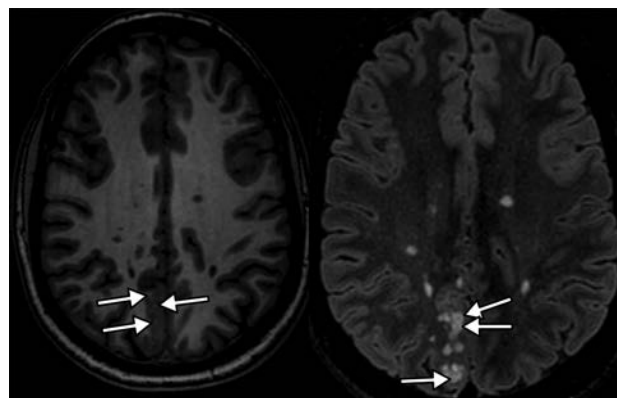


FIG 1. Axial T1 (*left*) and FLAIR (*right*) weighted imaging showing a right parietal lesion involving the deep cortical ribbon and the adjacent subcortical white matter distributed into small coalescent nodules, hyperintense on FLAIR, hypointense with punctiform hyperintensities on T1WI, and central hypointensities on FLAIR (*arrow*), characteristics of MVNT.

We think that this systematic approach best serves patients because this entity is provisionally considered a brain tumor by the World Health Organization and should be best understood using state-of-the-art MR imaging characterization. This management allows clinicians to reassure their patients who are often frightened by the term “tumor” and sometimes request surgical removal. In our experience, which is further echoed in the article, long-term follow-up MR imaging performed >10 years after the first discovery of a presumed MVNT shows perfect stability of brain abnormalities with rare or absent clinical symptoms.

We entirely agree with the authors’ conclusion suggesting that MVNT is more likely a malformative lesion as opposed to a neoplasm. Clinical and histologic analysis have not yet provided clear evidence for a neoplastic process. Molecular investigations in few cases have so far failed to reveal *IDH1/2*, *BRAF* V600E, *EGFR*, *ERBB2*, *KRAS*, *BRAF*, *NRAS*, *PIK3CA*, and *AKT1* mutations or obvious DNA copy number abnormalities. A point mutation involving *MEK1* (*MAP2K1*) p. Q56P (c.167A>C) in non-small-cell lung cancers has been found in 1 case.

Thus, we believe that the name of this entity should be changed to remove the term “tumor” and replaced by the term “hamar-

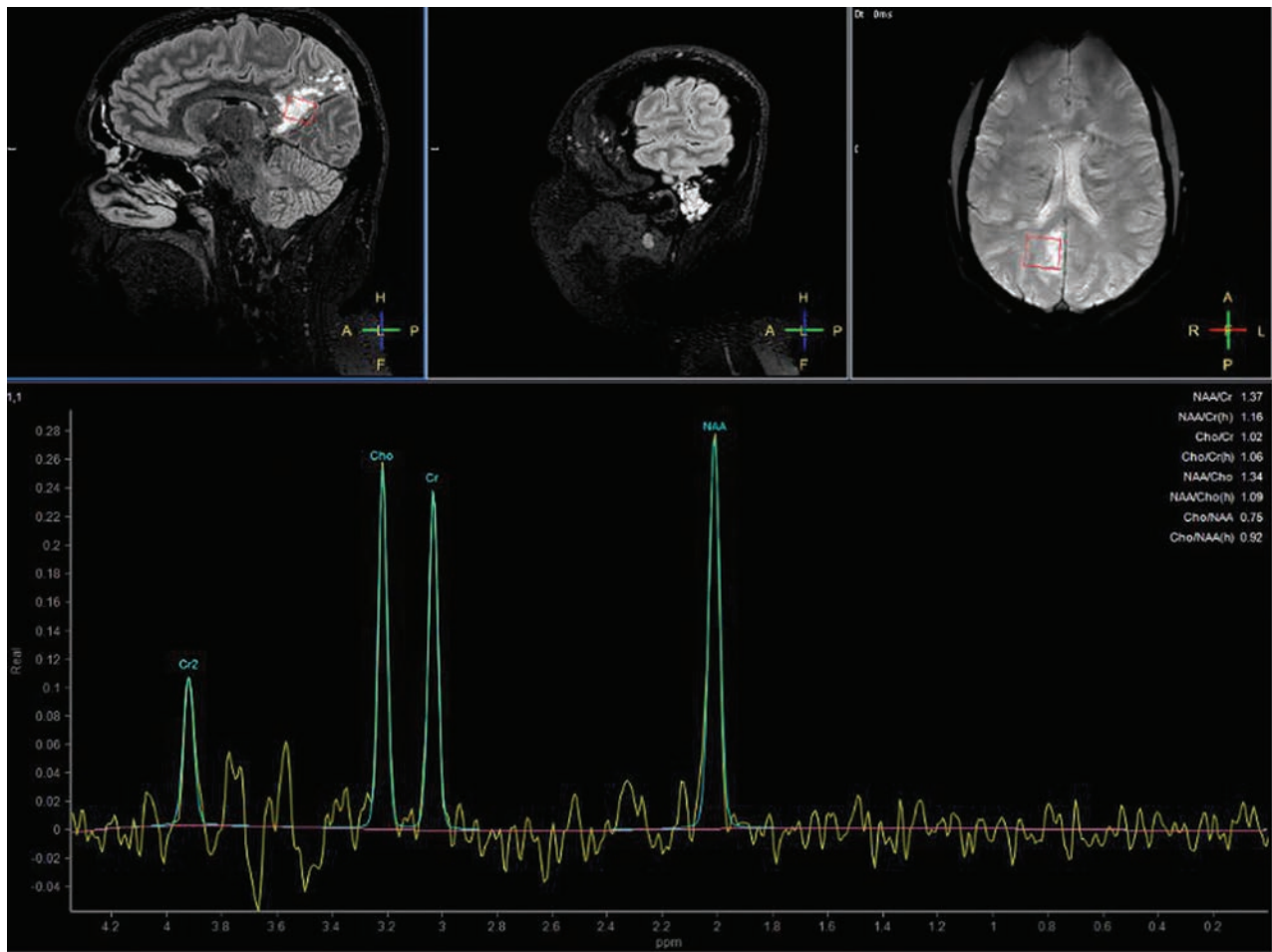


FIG 2. MR spectroscopy shows a mild decrease of *N*-acetylaspartate but no choline or lipids peaks.

toma,” “dysplasia,” or “malformation.” We also believe that larger series are needed to determine at what point the entity will be considered malignant.

Disclosures: Homa A. Biassette—UNRELATED: Grants/Grants Pending: DEVELAGE FP7 grant.* Comments: 2012–2015 “DEVELAGE: Pathways Common to Brain Development and Ageing: Defining Strategies for Preventive Therapy and Diagnostics.” Julien Savatovsky—UNRELATED: Grant: Association de la Recherche Sur le Syndrome Immuno-Deficitaire Acquis; Consulting Fee or Honorarium: Association de la Recherche Sur le Syndrome Immuno-Deficitaire Acquis, Madday Pharmaceutical, Bristol-Myers Squibb, GlaxoSmithKline; Support for Travel to Meetings for the Study or Other Purposes: GE Healthcare, Philips Healthcare, Bayer HealthCare; Expert Testimony: Philips Healthcare, Bayer HealthCare*; Payment for Lectures Including Service on Speakers Bureaus: Philips Healthcare, Association de la Recherche Sur le Syndrome Immuno-Deficitaire Acquis, Biogen.* *Money paid to the institution.

REFERENCES

1. Nunes RH, Hsu CC, da Rocha AJ, et al. **Multinodular and vacuolating neuronal tumor of the cerebrum: a new “leave me alone” lesion with a characteristic imaging pattern.** *AJNR Am J Neuroradiol* 2017;38:1899–904 CrossRef Medline
2. Fukushima S, Yoshida A, Narita Y, et al. **Multinodular and vacuolat-**

ing neuronal tumor of the cerebrum. *Brain Tumor Pathol* 2015;32:131–36 CrossRef Medline

3. Huse JT, Edgar M, Halliday J, et al. **Multinodular and vacuolating neuronal tumors of the cerebrum: 10 cases of a distinctive seizure-associated lesion.** *Brain Pathol* 2013;23:515–24 CrossRef Medline
4. Louis DN, Perry A, Reifenberger G, et al. **The 2016 World Health Organization Classification of Tumors of the Central Nervous System: a summary.** *Acta Neuropathol* 2016;131:803–20 CrossRef Medline

● **A. Lecler**

Department of Radiology

● **D. Chauvet**

Department of Neurosurgery

Fondation Ophtalmologique Adolphe de Rothschild
Paris, France

● **H.A. Biassette**

Department of Pathology

Lariboisière Hospital, Paris-Diderot, Paris-Cité-Sorbonne University
Paris, France

● **J. Savatovsky**

Department of Radiology

Fondation Ophtalmologique Adolphe de Rothschild
Paris, France

REPLY:

We appreciate the comments from Lecler et al regarding our publication “Multinodular and Vacuolating Neuronal Tumor of the Cerebrum: A New ‘Leave Me Alone’ Lesion with a Characteristic Imaging Pattern.”¹ Several valid points have been raised about improving the confidence of making the presumptive diagnosis of multinodular and vacuolating neuronal tumor (MVNT) using advanced MR imaging techniques. Most of the MVNTs in our series showed virtually a pathognomonic imaging appearance, and presumptive diagnoses were made solely on the basis of conventional MR imaging sequences acquired on either a 1.5T or 3T scanner. From our study, we had established several key neuroimaging features to assist in the presumptive diagnosis of MVNT, which include the following: 1) clusters of discrete or coalescent nodular lesions located within the deep cortical ribbon and superficial subcortical white matter with an otherwise normal-appearing cortex, 2) absent or minimal contrast enhancement, and 3) stability on imaging follow-up.^{1,2}

We do agree with Lecler et al that higher field strength and spatial resolution increase the conspicuity of the MVNT nodules, which range from 1 to 5 mm in diameter.¹ From our experience with the higher resolution 3D MR imaging sequences, either the FLAIR or steady-state sequences (CISS and FIESTA) offer the best contrast resolution to show the MVNT nodules, which appear hyperintense on both T2-weighted and FLAIR sequences.¹ In our experience, MVNT nodules can coalesce to form a larger dominant lesion. The largest MVNT encountered in our case series measured 57 mm in maximum diameter.¹ Although larger size MVNTs have the potential to mimic diffuse gliomas, there are usually imaging clues, such as the presence of satellite nodules and the absent or minimal mass effect.^{1,2}

Perhaps, in this rare category of MVNT, advanced neuroimaging techniques such as MR spectroscopy, MR perfusion, or

[¹⁸F]FDG PET/MR imaging may have a role in excluding worrisome parameters such as hypervascularity, increased Cho/NAA and Cho/Cr ratios, and FDG hypermetabolism. It is also logical that the smaller-sized MVNT with discrete nodules may not have sufficient imaging resolution for accurate assessment with advanced neuroimaging techniques.

In summary, we agree that the presumptive diagnosis of classic MVNT would benefit from improved spatial resolution.^{1,2} Advanced neuroimaging techniques may have a role for lesions not fulfilling our proposed criteria for MVNT or for the evaluation of symptomatic MVNTs for the consideration of surgical options. Ultimately, the neuroimaging appearance of MVNT is sufficiently pathognomonic, and recognition of these features is the key to clinching the diagnosis.

REFERENCES

1. Nunes RH, Hsu CC, da Rocha AJ, et al. **Multinodular and vacuolating neuronal tumor of the cerebrum: a new “leave me alone” lesion with a characteristic imaging pattern.** *AJNR Am J Neuroradiol* 2017;38: 1899–904 CrossRef Medline
2. Nunes RH, Hsu CC, Osborn AG. **Presumptive diagnosis of multinodular vacuolating tumor: “more than meets the eye!”** *Neuroradiology* 2017 Sep 8. [Epub ahead of print] CrossRef Medline

 **R.H. Nunes**

Division of Neuroradiology
Santa Casa de Sao Paulo School of Medical Sciences
Sao Paulo, Brazil
Division of Neuroradiology
Diagnosticos da America SA
Sao Paulo, Brazil

 **C.C.-T. Hsu**

Department of Medical Imaging
Princess Alexandra Hospital
Brisbane, Queensland, Australia

 **A.G. Osborn**

Department of Radiology
University of Utah
Salt Lake City, Utah

<http://dx.doi.org/10.3174/ajnr.A5447>

The Anesthesiologist, Rather Than the Anesthesia, May Influence the Outcomes following Stroke Thrombectomy

It is more than likely that systemic hypotension resulting from anesthesia, regardless of the technique used, can have deleterious effects in patients with ongoing acute ischemic stroke. Cerebral autoregulation is often impaired in these neurocritical patients, rendering cerebral blood flow entirely dependent on cerebral perfusion pressure. Hence, maintaining an optimal mean arterial blood pressure may be vital to improving survival outcomes. On the other hand, cerebral vasoreactivity to CO₂ is one of the most effective mechanisms to regulate the diameter of the cerebral arterioles. According to the Hagen-Poiseuille equation, the laminar flow rate is directly related to the differential pressure of the cerebral arterioles and the fourth power of the radius of these vessels. Consequently, optimizing arterial blood pressure while maintaining normocarbia should be one of the main goals when anesthetizing patients undergoing stroke thrombectomy to improve collateral circulation.

Not unexpectedly, Schönberger et al¹ have recently reported that in the Sedation versus Intubation for Endovascular Stroke Treatment (SIESTA) trial, which involved a cohort of 104 patients with acute ischemic stroke in the anterior circulation randomized to undergo either conscious sedation or general anesthesia, there was no significant difference in the neurologic improvement at 24 hours after the admission, measured by the National Institutes of Health Stroke Scale score. Furthermore, the same research group conducted a post hoc analysis of the data and reported in a recent issue of *AJNR* that the collateral status, which was strongly related to the thrombectomy success in the SIESTA trial, was not significantly influenced by the anesthetic technique used.²

There is ongoing debate as to whether patients undergoing stroke thrombectomy would benefit from conscious sedation or general anesthesia. In the SIESTA trial, the systolic blood pressure and end-tidal carbon dioxide were closely monitored and maintained in the range of 120–180 and 35–45 mm Hg, respectively. A

tight control of these variables, however, decreases the external validity of the results, as maintaining blood pressure and arterial partial pressure of carbon (PaCO₂) within physiologic ranges largely depends on the anesthesiologist's skills. Consequently, the potential advantages of general anesthesia may also be obscured by poor control of these crucial variables. Further clinical trials evaluating the variation of mean arterial blood pressure and CO₂ between anesthetic techniques, are needed to elucidate the role of these critical aspects in the neurological and functional outcomes of patients undergoing stroke thrombectomy.

While general anesthesia can be associated with cardiovascular instability in neurocritical patients, anesthesiologists play a very important role in preventing a substantial drop in blood pressure following the induction in most cases, while maintaining normocarbia. Induction techniques have also evolved to provide high-quality anesthesia in a quick and safe manner in the emergency environment, thus saving precious time for the neuroradiologist to perform a successful thrombectomy. On the other hand, patients undergoing thrombectomy under conscious sedation should be carefully selected because those with poor neurologic status are unlikely to cooperate and those having potentially difficult airways cannot always be safely sedated, especially considering that in this scenario, the airway access may be challenging.

REFERENCES

- Schönberger S, Uhlmann L, Hacke W, et al. **Effect of conscious sedation vs general anesthesia on early neurological improvement among patients with ischemic stroke undergoing endovascular thrombectomy: a randomized clinical trial.** *JAMA* 2016;316:1986–96 CrossRef Medline
- Schönberger S, Pfaff J, Uhlmann L, et al. **The impact of conscious sedation vs general anesthesia for stroke thrombectomy on the predictive value of collateral status: a post hoc analysis of the SIESTA trial.** *AJNR Am J Neuroradiol* 2017;38:1580–85 CrossRef Medline

W. Fandino

The Walton Centre National Health Service Foundation Trust
Liverpool, United Kingdom

<http://dx.doi.org/10.3174/ajnr.A5430>

Economic Considerations in MR Imaging of Patients with Cardiac Devices

Several recent high-profile publications have generated interest in MR imaging in patients with implantable cardiac devices, some of which were traditionally considered an absolute contraindication. In particular, an analysis published in the *New England Journal of Medicine* documented an overall safe experience performing 1500 nonthoracic, 1.5T MRIs in patients with nonconditional devices (1000 pacemakers and 500 implantable cardioverter-defibrillator studies) as part of a prospective registry (The MagnaSafe Registry; <http://magnasafe.org/>).¹ Given the wide dissemination of this article, coupled with the estimated 1.8 million patients with similar devices in the United States alone,² practical guidance for radiologists, who are on the front line of this decision-making process, is desperately needed.

In this setting, we wish to express our gratitude to Korutz et al³ for their recent article, “Pacemakers in MRI for the Neuroradiologist.” Their article includes a thorough assessment of safety considerations in performing MR imaging in patients with implantable cardiac devices. In addition to a detailed review of the recent literature, the authors provide their own multidisciplinary protocol as a helpful reference for radiologists who have instituted (or are considering implementing) MR imaging in this patient population. Furthermore, their own experience imaging 121 patients with nonconditional implants adds to the growing evidence that MR imaging can be performed in appropriately screened and carefully monitored patients.

One additional consideration, separate from any safety issue, must be noted. At present, the Centers for Medicare and Medicaid does not permit coverage for routine clinical MR imaging in patients with cardiac devices that are classified by the FDA as nonconditional. In fact, reimbursement is only permitted when imaging is performed within the narrow scope of a prospective registry assessing safety.⁴ Thus, for most of these patients, the cost of clinically indicated MRIs will not be covered. In our experience, many providers are unaware of this crucial issue. When informed, they appreciate the opportunity to discuss the implications with their patients and, when appropriate, may reconsider using a cov-

ered alternate technique. For radiologists, accurate reporting of the specific device and FDA category is essential to ensure remuneration for covered MRI-conditional devices and to avoid fraudulent billing for noncovered services.

Some institutions have elected to perform these studies regardless of the patient's ability to pay an out-of-pocket expense. However, this may not be feasible or desirable for other facilities, given the time-intensive and resource-consuming processes needed to screen these patients and coordinate their imaging. If a self-payment is expected, this should be clearly communicated and prospectively discussed with the patient, who may need to complete an Advance Beneficiary Notice. In certain situations, meeting with a hospital financial representative might help to minimize the impact of a large and unexpected bill following the patient's study.

While the financial considerations entail additional logistic considerations in an already complex process, a proactive approach can ensure financial informed consent and may refine decisions regarding clinical work-up.

REFERENCES

1. Russo RJ, Costa HS, Silva PD, et al. **Assessing the risks associated with MRI in patients with a pacemaker or defibrillator.** *N Engl J Med* 2017; 376:755–64 CrossRef Medline
2. Nazarian S, Hansford R, Roguin A, et al. **A prospective evaluation of a protocol for magnetic resonance imaging of patients with implanted cardiac devices.** *Ann Intern Med* 2011;155:415–24 CrossRef Medline
3. Korutz AW, Obajuluwa A, Lester MS, et al. **Pacemakers in MRI for the neuroradiologist.** *AJNR Am J Neuroradiol* 2017 Jul 13. [Epub ahead of print] CrossRef Medline
4. Centers for Medicare & Medicaid Services. Decision Memo for Magnetic Resonance Imaging (MRI) (CAG-00399R2). February 24, 2011. <https://www.cms.gov/medicare-coverage-database/details/nca-decision-memo.aspx?NCAId=246&bc=ACAAAAAAAgAAAA%3d%3d& Accessed August 30, 2017>

● M.U. Antonucci
● M.V. Spampinato
● E.R. Ritenour

Department of Radiology and Radiological Science
Medical University of South Carolina
Charleston, South Carolina

<http://dx.doi.org/10.3174/ajnr.A5450>

REPLY:

We would like to thank Dr Antonucci and his colleagues for their recent letter regarding our publication, “Pacemakers in MRI for the Neuroradiologist.” We agree with their assessment that there are factors beyond safety that must be considered before implementing a program for imaging patients with non-MR imaging–conditional cardiac implantable electronic devices. Specifically, the Centers for Medicare and Medicaid Services (CMS) currently does not cover MR imaging in patients with these devices. However, we hope that the recent data published through The MagnaSafe Registry (<http://magnasafe.org/>), a framework that has been recently proposed for securing coverage for these studies by CMS and private insurers, and studies such as ours demonstrating that these imaging studies can be performed safely will provide the necessary momentum to get these much-needed services covered in the near future.^{1,2}

Nevertheless, we wish to point out that ultimately, the number of patients with implantable devices who are imaged after going through the comprehensive screening protocol that we use is very low. Currently, we perform approximately 100 pacemaker studies per year of the nearly 50,000 MR neuroimaging examinations that are performed yearly at our hospital. As part of our screening protocol, a radiologist reviews the details of the case and discusses the need for the examination with the ordering physician, including whether an alternative imaging technique could provide a satisfactory answer to the clinical question. This step helps to filter out examinations that may be unnecessary.

Furthermore, while the reimbursement considerations regarding imaging patients with non-MR imaging–conditional devices are important and problematic, it is our belief that there are other factors, including certain intangible benefits, that ought to be considered when deciding whether to develop a protocol to image these patients. We have found that providing this service results in frequent positive feedback from our ordering clinicians

(emergency medicine, neurology, neurosurgery, and primary care) because it aids their clinical decision-making by giving them access to information often not available using other imaging strategies. Offering access to these studies has increased referrals to our institution, which may compensate, to some degree, for the lack of reimbursement for the MR imaging examination itself. For instance, the physicians in our Brain Tumor Institute are now receiving referrals of patients with pacemakers from surrounding areas who require MR imaging and who often also go on to use a wide array of other medical services that our institution can provide as well.

Finally, it is best practice, regardless of cost issues, to provide our patients with the most effective diagnostic examinations needed for their care. It is our hope that our article, “Pacemakers in MRI for the Neuroradiologist” and ensuing discussions on this topic will help provide radiology departments with a framework for developing their own pacemaker imaging programs. The momentum that is building on this topic in the medical community will hopefully lead to reimbursement for these valuable studies in the near future.

REFERENCES

1. Russo RJ, Costa HS, Silva PD, et al. **Assessing the risks associated with MRI in patients with a pacemaker or defibrillator.** *N Engl J Med* 2017; 376:755–64 [CrossRef Medline](#)
2. Kramer DB, Kesselheim AS. **Coverage of magnetic resonance imaging for patients with cardiac devices: improving the coverage with evidence development program.** *JAMA Cardiol* 2017;2:711–12 [CrossRef Medline](#)

● **A.W. Korutz**

● **E.J. Russell**

● **T.A. Hijaz**

● **J.D. Collins**

Department of Radiology

● **B.P. Knight**

Department of Medicine, Division of Cardiology

● **A.J. Nemeth**

Departments of Radiology and Neurology
Northwestern University Feinberg School of Medicine
Chicago, Illinois

<http://dx.doi.org/10.3174/ajnr.A5467>